STUDIA UNIVERSITATIS
BABEŞ-BOLYAI

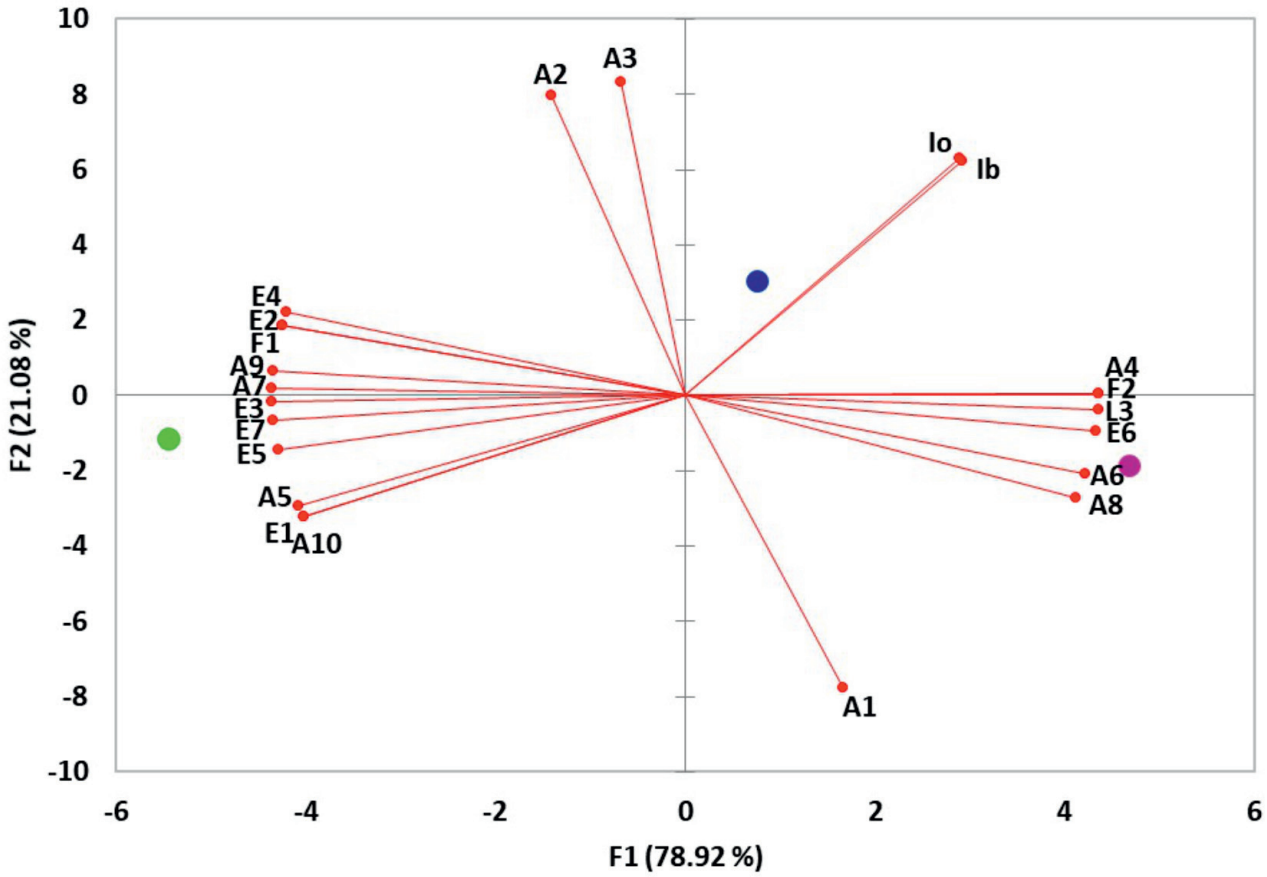

CHEMIA

4/2021

STUDIA UNIVERSITATIS BABEȘ-BOLYAI CHEMIA

4/2021

http://chem.ubbcluj.ro/~studiachemia/;
studiachemia@chem.ubbcluj.ro
http://www.studia.ubbcluj.ro/serii/chemia/index_en.html

YEAR **Volume 66 (LXVI) 2021**
MONTH **DECEMBER**
ISSUE **4**

S T U D I A
UNIVERSITATIS BABEŞ–BOLYAI
CHEMIA

4

ISSUE DOI:10.24193/subbchem.2021.4

STUDIA UBB EDITORIAL OFFICE: B.P. Hasdeu no. 51, 400371 Cluj-Napoca, Romania, Phone + 40 264 405300 * 6452

CUPRINS – CONTENT – SOMMAIRE – INHALT

Studia Universitatis Babes-Bolyai Chemia has been selected for coverage in Thomson Reuters products and custom information services. Beginning with V. 53 (1) 2008, this publication is indexed and abstracted in the following:

- Science Citation Index Expanded (also known as SciSearch®)
- Chemistry Citation Index®
- Journal Citation Reports/Science Edition

STUDIA UBB CHEMIA, LXVI, 4, 2021 (p. 7-22)
(RECOMMENDED CITATION)
DOI:10.24193/subbchem.2021.4.01

INFLUENCE OF THE CAFFEINE ON THE INTERACTION BETWEEN HALOPERIDOL AND HUMAN SERUM ALBUMIN: SPECTROSCOPIC AND MOLECULAR DOCKING APPROACH

MIROSLAV SOVRLIĆ[a], RATOMIR JELIĆ[a], MARKO ANTONIJEVIĆ[b], ZORAN MARKOVIĆ[b], JOVICA TOMOVIĆ[a*], EMINA MRKALIĆ[b]

ABSTRACT. The interactions between human serum albumin (HSA) and haloperidol (HPD) in the presence or absence of caffeine (CAF) with HSA were studied by fluorescence-absorption spectroscopy and molecular modeling. The results showed that the presence of CAF decreased binding constants of HPD-HSA with increasing temperature from 1.07×10^4 mol/dm^3 to 3.13×10^2 mol/dm^3. The results indicate that the HSA-HPD and HSA-CAF-HPD system is very thermally sensitive. The number of binding sites obtained at three different temperatures were close to 1 indicating the presence of one binding site of HPD, CAF on HSA. Fluorescence quenching was initiated by dynamic quenching procedure irrespective of the absence or presence of CAF. The negative value of the free energy change (ΔG) indicates a spontaneous binding process of both, HPD to HSA protein and HPD to the HSA-CAF protein complex. The values of $\Delta H^0<0$ and $\Delta S^0<0$ for binding interaction HSA-HPD and HSA-CAF-HPD, indicate that interaction is enthalpy driven. Docking simulation results are confirmed that the most preferable place for binding HPD and CAF is the active site I, in domain II subdomain IIA. The present study suggested that the combined actions of HPD and CAF, may lead to further changes in HSA conformation.

Keywords: *Caffeine; Interaction; Human serum albumin; Haloperidol; Fluorescence;*

INTRODUCTION

Within plasma proteins, human serum albumin (HSA) is undoubtedly the most important transporter of drugs and other small molecules. HSA accounts for about 60% of the proteins present in the plasma of healthy

[a] *University of Kragujevac, Faculty of Medical Sciences, Department of Pharmacy, Svetozara Markovića 69, Kragujevac 34000, Serbia*
[b] *University of Kragujevac, Institute for Information Technologies, Department of Science, Jovana Cvijića bb, Kragujevac 34000, Serbia*
[*] *Corresponding author: jovicatomovic2011@gmail.com*

individuals. It is smaller in mass (66,500 Da) than other plasma proteins [1]. Binding to HSA is often very specific, at least for low or therapeutic drug concentrations. Two binding sites in HSA, sites I and II, by Gail Sudlow classification and co-workers, are involved in tying up a large number class of compounds. Analysis of the crystal structure of albumin revealed that the two major binding sites of the hydrophobic cavity in subdomains IIA and IIIA [2].

Caffeine (CAF) is the most widely consumed psychoactive substance in the world and can be found in coffee seeds (2%), cola cotyledons (up to 3%), and in tea leaves (up to 4%) [3]. It is purine alkaloid that posses many different pharmacological effects such as: stimulation of the central nervous system, diuretic effect, a stimulating effect on the heart, muscle relaxation, stimulation of gastric secretion, etc. [3,4]. CAF binds to plasma proteins in a certain percentage (10-30%). Caffeine could bind to HSA via the hydrophobic interaction between the pyrimidine ring and aromatic stacking. The binding is carried out via 3 methyl groups by Van der Waals forces and hydrogen bonding [5]. The primary binding site was considered to be a hydrophobic cavity formed by Leu198, Lys199, Ser202, Phe211, Trp214, Val344, Ser454 and Leu481 in domain IIa, Sudlow's site I [6].

Haloperidol (HPD) is an antipsychotic drug from the group of butyrophenones which competitively blocks postsynaptic dopamine (D2) receptors in the mesolimbic system of the brain, thereby eliminating dopamine neurotransmission which is beneficial in patients with psychoses and delusions [7]. It is highly bound to plasma proteins (90%). Haloperidol is used extensively for the treatment of psychotic disorders, therefore monitoring of plasma haloperidol concentrations is clinically significant. The potential severity of the side effects is one of the reasons for monitoring the concentration of haloperidol in the blood [8]. Earlier binding experiments with HPD and HSA indicated that the binding site was located in a hydrophobic cavity near Sudlow's site I (subdomain IIA) [9,10].

Given that the actual volume of distribution and drug concentration at the receptor-binding site are associated with the amount of unbound fraction of the drug, the complete characterization of the mechanism of drug binding to plasma proteins became a necessary step for understanding the pharmacokinetic, pharmacodynamic and the toxicological profile of each drug [11]. Simultaneous administration of the two drugs may lead to competition at the level of binding to HSA, which may significantly affect the disposition of both drugs, with possible serious physiological consequences. Due to its characteristics, HSA is a unique protein model for the quantitative and qualitative study of protein-drug interactions [12]. Previous studies showed that CAF as well as other natural products present in food and beverages could have an effect on binding parameters of different drugs to HSA [13-15].

The aim of this study is to systematically characterize the interactions of HPD and CAF with HSA using spectroscopic and molecular modeling methods. The thermodynamic parameters, nature of forces responsible for drug binding and location of the probe in macromolecular architecture were discussed based on the results of temperature variation experiments as well as molecular docking results.

RESULTS AND DISCUSSION

Interaction mechanism of HSA-HPD and HSA-CAF-HPD

In order to demonstrate the binding of HPD and CAF to HSA, the fluorescence emission spectra of HSA were recorded. Fluorescence spectroscopy methodology is used to test small molecule binding for proteins. This test method can provide information on the binding mechanism, binding mode, binding constant, and number of binding sites [16]. The interaction of several antipsychotic drugs with serum albumin has been studied in the past [17,18]. Also, in previous studies has been shown that natural compounds from food and beverages can modulate interaction between HSA and antipsychotics [19]. However, a detailed analysis of interactions between HSA and HPD in the presence or absence of CAF is not available in the literature. The fluorescence spectra of HSA with different concentrations of HPD and same concentration CAF were recorded at temperatures 293, 303 and 310 K. Based on numerous papers, we can conclude that Trp213 residues are major drug targets in HSA [20]. The tryptophan (Trp) fluorescence intensity of HSA decreases continuously with the regular addition of raising concentration of HPD, indicating that HPD is interacting with HSA (Figure 1.-left). The interaction of HPD with HSA in the presence of a competitive compound was investigated (Figure 1.-right). It is clear that fluorescence intensity is significantly reduced in the presence of different HPD concentrations and fixed CAF concentrations at all recorded temperatures compared to the emission spectra recorded without CAF. The binding of HPD-induced a redshift in the fluorescence emission spectrum of HSA indicating that the polarity around the Trp213 was increased in the presence of HPD. In the presence of CAF, the binding of HPD also induced a redshift in fluorescence emission spectrum of the HSA-HPD complex, indicating that binding of CAF further increased the polarity around HPD bound to HSA. This was probably due to the loss of the compact structure of the hydrophobic subdomain IIA where Trp is located [21]. The presence of a red or blue shift λ_{max} indicates that there was a decrease or increase in the hydrophobicity of the microenvironment of the binding region of the drug.

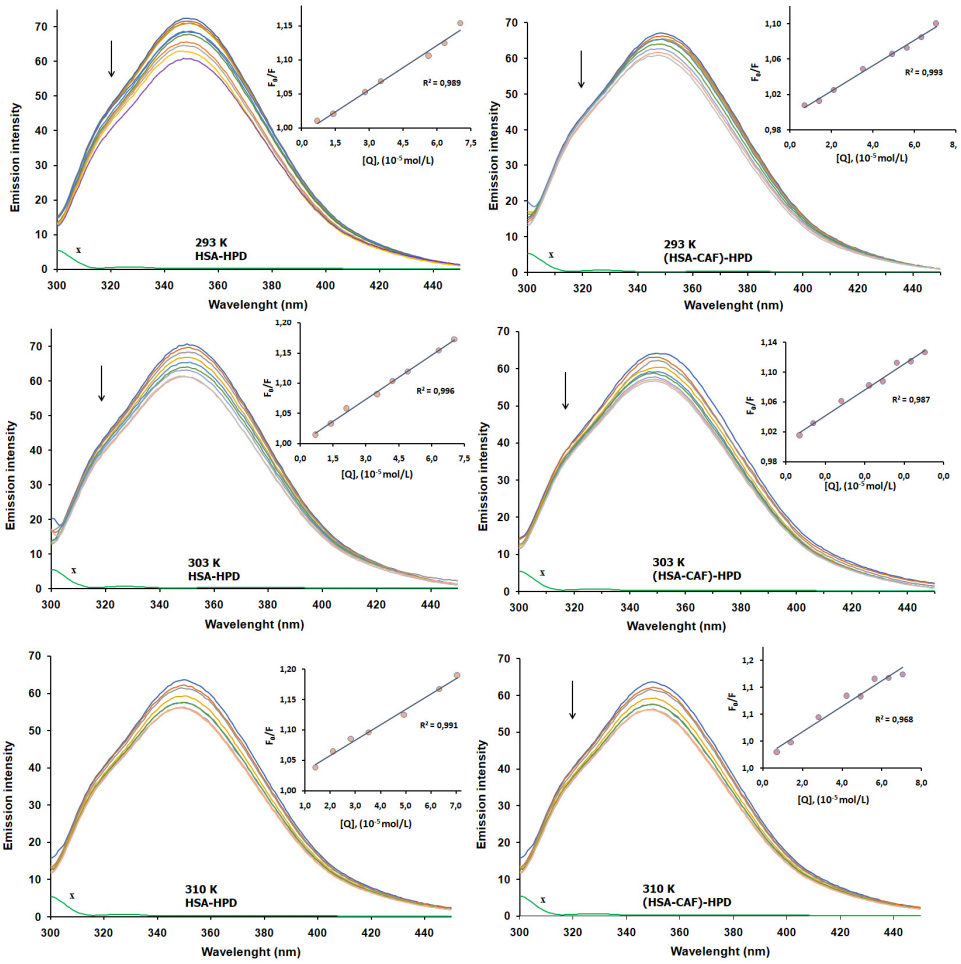

Figure 1. Fluorescence emission spectra and Stern–Volmer plots of the fluorescence quenching of HSA fluorescence with HPD (**left**) and HSA-CAF-HPD complex (**right**) (increasing concentration HPD along the arrow direction) at different temperatures. Curve *x* shows the emission spectrum of HPD only.

Fluorescence quenching data obtained at different temperatures is usually described by Stern–Volmer (SV) equation (1) [22]:

$$(1)\quad F_0/F = 1 + k_q \times \tau_0[Q] = 1 + K_D\,[Q] = 1 + K_{SV}$$

where F_0 and F are the fluorescence intensities of HSA in the absence and presence of the quencher, respectively, [Q] is the concentration of the quencher, K_D is the quenching constant, k_q is the quenching rate constant of biological macromolecule, τ_0 is the average lifetime of the molecule without any quencher and the fluorescence lifetime of the biopolymer is 10^{-8} s. K_{SV} and k_q values are given in Table 1. Given that in our experiments, te concentration of free HPD was not known, we took approximately corresponds to the total concentration of HPD.

Quenching can be defined as a decrease of fluorescence and under the conditions of fixed pH, temperature, and ionic strength. Fluorescence quenching can occur by a variety of mechanisms, most commonly classified as static and dynamic quenching. These mechanisms can be distinguished by their differing dependence on temperature and viscosity. This also means that only one type, either dynamic (interaction of the excited fluorophore with the quencher) or static (fluorophore and quencher interact in the ground state), mechanism of quenching occurs [23]. Basically, albumin-drug interaction is a dynamic and reversible process, and dissociation of bound drug molecules from the albumin-drug complex occurs very quickly, probably within a few milliseconds or in a shorter period of time [20].

Fluorescence data can also be used to calculate a constant of binding (K_a) and number of binding sites (n). When small molecules bind independently to a set of equivalent sites on a macromolecule, a balance between free and bound the molecule can be represented by modified Stern–Volmer equation (2) to confirm the mechanism [24].

$$(2)\quad log\frac{F_0-F}{F} = logK_a + nlog[Q]$$

where K_a is the binding constant and n is the number of binding sites. There are many binding sites per HSA molecule and [K] is the concentration of quenchers. Values K_a and n are obtained from the intersection and slope of the graph of the dependence of log (F_0 - F) / F on log [K] (Figure 2). The values of K_a and n are given in Table 1. From Figure 2, it was known that under certain HPD concentrations, the curves of $F_0/(F_0–F)$ versus 1/[Q] were linear.

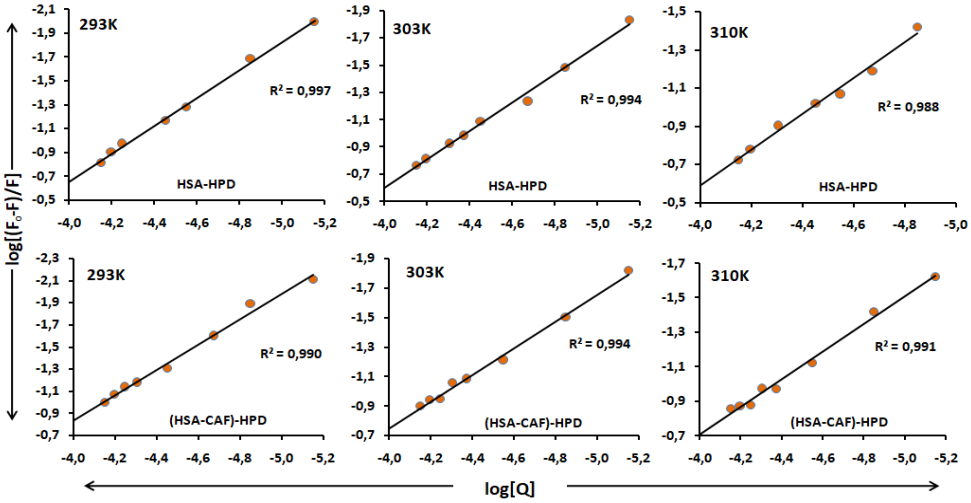

Figure 2. Modified Stern–Volmer Plots of log $(F_0 - F)/F$ versus log [Q] at different temperatures using equation 2.

The binding constants (K_a) and the number of binding sites (n)

The values of n obtained at three different temperatures were close to 1 indicating the presence of one binding site of HPD on HSA and HSA-CAF. In addition, an increase in temperature leads to an decrease in the (n) binding capacity of HSA for HPD and 1.17 values were obtained; 1.04 and 0.93 at 293, 303 and 310 K. Also, the values of n were decreased in the presence of CAF at all temperatures. Our report is an excellent agreement with the previous reports where antipsychotic drugs have shown to bind with HSA at one binding site [9]. Results from our study indicate that the binding of HPD at sites to HSA and HSA-CAF was a concentration-dependent saturable process.

Correlation coefficients above 0.9 indicate a good linear relationship. It is clear from Figure 1. and Table 1 that the values of K_a were decreased significantly upon an increase in the temperature indicating that the complex between HSA and HPD gets disrupted on increasing the temperature. Binding constant decreases with increasing temperature, both in the absence and in the presence of CAF. The value of quenching constant obtained for HSA-HPD interaction was in the range from 1.07×10^4 to 1.48×10^3 mol/dm^3, while the value of quenching for HSA-CAF-HPD was in the range 5.47×10^3 to 3.13×10^2 mol/dm^3, at three different temperatures. These results indicate that the HSA-HPD and HSA-CAF-HPD system is very thermally sensitive. In other words, even a small temperature change can lead to significant changes in the K_a value. The unstable compound would be partly decomposed with the rising temperature, therefore, the values of K_a decreased. As a rule, the

K_{SV} values increase with an increase in temperature for dynamic quenching, and the Kq values were on the order of 10^{11} L/mol·s. These results can be explained by more collisions between drug and fluorophores and faster diffusion at higher temperatures [25-26].

Based on the conventional concept, the cellular uptake is proportional to the unbound fraction of the drug. If a drug is weaker bound to serum albumins, the fraction of free drug available to act on target tissues may be significantly increased and the effect of the drug may consequently be higher [27]. The data indicate that the binding of HPD to HSA was largely inhibited in the presence of CAF. This may be explained by the competitive interference of HPD and CAF in the vicinity of the binding site of HSA which leads to increasing concentrations of free HPD in the plasma and its maximum effect [28]. Further, te mechanism by which CAF decreased the binding affinity and led to a decrease in the binding constant is not sufficiently elucidated, but indicates that probably there is a competition between CAF and HPD for binding to HSA.

The results presented in Table 1 indicate that the stability of the HSA-HPD complex decreases with increasing temperature and that HPD is better bound and transported by HSA at lower temperatures as well as due to the absence of CAF. All these results showed that there were obviously characters of dynamic quenching.

Table 1. The interaction parameters of the HSA–HPD and HSA-CAF-HPD systems at different temperatures

Systems	T/K	K_{SV}/dm^{3}mol^{-1}	Kq/dm^{3}mol^{-1}s	K/dm^{3}mol^{-1}	n	R
HSA-HPD	293	2.17×10^3	2.17×10^{11}	1.07×10^4	1.171	0.997
	303	2.43×10^3	2.43×10^{11}	3.72×10^3	1.042	0.994
	310	2.54×10^3	2.54×10^{11}	1.48×10^3	0.939	0.988
HSA-CAF-HPD	293	1.44×10^3	1.44×10^{11}	5.47×10^3	1.143	0.990
	303	1.74×10^3	1.74×10^{11}	7.48×10^2	0.905	0.994
	310	1.90×10^3	1.90×10^{11}	3.13×10^2	0.800	0.991

The decreasing trend of K_a with increasing temperature indicates that the HPD binding reaction for HSA was exothermic, both in the presence and in the absence of CAF [29].

UV–Vis measurements

In this part of the study, we examined changes in the UV absorption spectra of the HPD, HSA-CAF, and HSA-CAF-HPD systems, with varying concentrations of haloperidol. The contribution of HPD and competing for CAF was subtracted from the results in complexes. HSA has a weak absorption

maximum at about 278 nm due to the cumulative absorption of three aromatic amino acid residues (Trp, Tyr and Phe). The absorption spectra of HPD are characterized by an absorption peak at 247 nm. The absorption maximum at 278 nm slightly increased (Figure 3), which was largely caused by π – π * transitions of aromatic amino acid residues to HSA [30], indicating that a complex has formed between HSA and CAF and HSA-CAF and HPD. At the characteristic peak for haloperidol (247 nm) we notice that with increasing concentration of HPD, the absorption intensity of HSA-CAF increasing (Figure 3; inset), while the concentration of CAF remained the same, suggesting that we can exclude static quenching mechanism interactions between HSA-CAF and HPD. The dynamic quenching only affects the excited states of the fluorophores and, thus, no changes in the absorption spectra are expected. However, the ground state complex formation will result in perturbation of the absorption spectrum of the fluorophore [23]. We also found a similar phenomenon observed with the fluorescence method. It is evident from UV–Vis spectral results that the progressive increase of absorbance with the increase in drug concentration confirms the formation of new protein–drug–drug complexes (HSA-CAF-HPD).

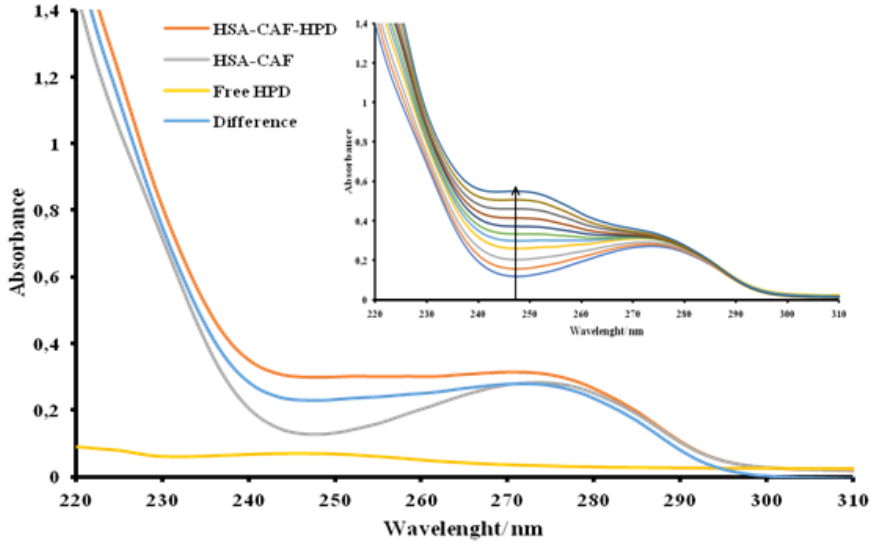

Figure 3. UV–Vis absorption spectra of HSA-CAF; absorption spectrum of HPD only; absorption spectrum of HSA-CAF-HPD complex; difference between absorption spectrum of HSA-CAF-HPD complex and free HPD. Inset: UV–Vis absorption spectra of HSA-CAF (1:1) in the presence of increasing amounts of HPD from 0.0 to 7.0 × 10^{-5} mol dm^{-3} (T = 298 K, pH = 7.4).

Thermodynamics of HSA-HPD and HSA-CAF-HPD interaction

There are essentially four types of non-covalent interactions that could play a role in ligand binding to proteins. These are electrostatic interaction, hydrogen bond formation, van der Waals interaction, hydrophobic and steric contacts [31]. To identify the binding force between HPD and HSA, and HPD to HSA-CAF complex, an examination of the binding was carried out at three different temperatures 293, 303 and 310 K. To find out the nature of the interaction of HPD with HSA and HPD with HSA-CAF complex, thermodynamic parameters (enthalpy change (ΔH_0) entropy change (ΔS_0) and Gibbs free energy change ($\Delta G0$)), were calculated using Van't Hoff and Gibbs–Helmholtz relations [32] using equation (3) and equation (4):

(3) $lnK_a = -\Delta H^0/RT + S^0/R$
(4) $\Delta G^0 = \Delta H^0 - T\Delta S^0$

where K_a is the binding constant at the appropriate temperature, R is the gas constant and T is absolute temperature (Figure 4). The values of ΔH^0, ΔS^0 and ΔG^0 at different temperatures are shown in Table 2. The negative value of the free energy change (ΔG) indicates a spontaneous (*exergonic*) binding process of both, HPD to HSA protein and HPD to HSA-CAF protein complex [33]. The values of $\Delta H^0 < 0$ and $\Delta S^0 < 0$ for binding interaction HSA-HPD and HSA-CAF-HPD, means that interaction is enthalpy driven. It can be seen that the binding reactions of these components are exothermic and are characterized by relatively large negative ΔH values. In this case, a spontaneous reaction is dependent upon the $T\Delta S$ term being small relative to the ΔH term, so that ΔG is negative [34,35]. The latter is consistent with dispersive van der Waals interactions of aromatic chromophores being the main contributors to bind formation. Dispersive van der Waals interactions are characterized both by negative enthalpy and negative entropy indicating an enthalpic origin for the binding process of these drugs to HSA protein [36].

Table 2. Thermodynamic parameters of the HSA–HPD and HSA-CAF-HPD systems at different temperatures

System	T/K	ΔH^0/kJ mol^{-1}	ΔS^0/J mol^{-1} K^{-1}	ΔG^0/kJ mol^{-1}
HSA-HPD	293			-22.70
	303	-87.15	-219.88	-20.50
	310			-18.96
(HSA-CAF)-HPD	293			-20.81
	303	-128.86	-368.56	-17.13
	310			-14.55

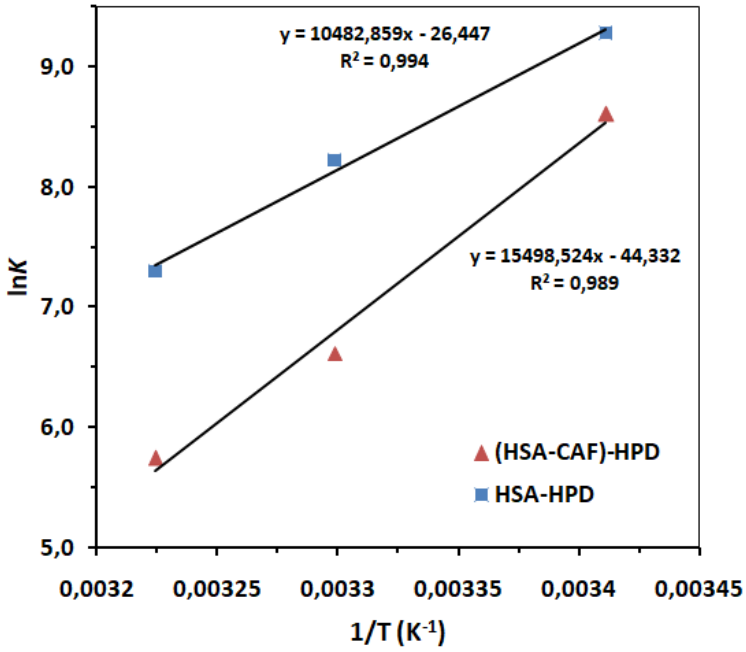

Figure 4. Van't Hoff plot of the interaction between HSA and HPD, and HSA-CAF complex and HPD, T = 293, 303, and 310 K.

Docking studies

The HSA protein is able to bind multiple molecules in six active binding sites [37-38]. In most cases, drugs are binding to sites I and II, because these sites have the highest binding affinities [37]. The reason for this is a high amount of different amino acid residues that are forming hydrophobic cavities inside subdomain IIA and IIIA where those active sites are found. The experimental work in this paper has shown that active site, which has the highest affinity for binding the HPD, is the same active site where CAF molecules are banded, alongside with other drugs like warfarin [9]. The AGFR software was employed for finding the active site by configuring and computing affinity maps for a receptor molecule (Figure 5). Obtained maps are further used in AutoDock4 for docking simulation. Docking simulation results are confirmed that the most preferable place for binding HPD and CAF is the active site I (Sudlow I) in domain II subdomain IIA (Figure 5).

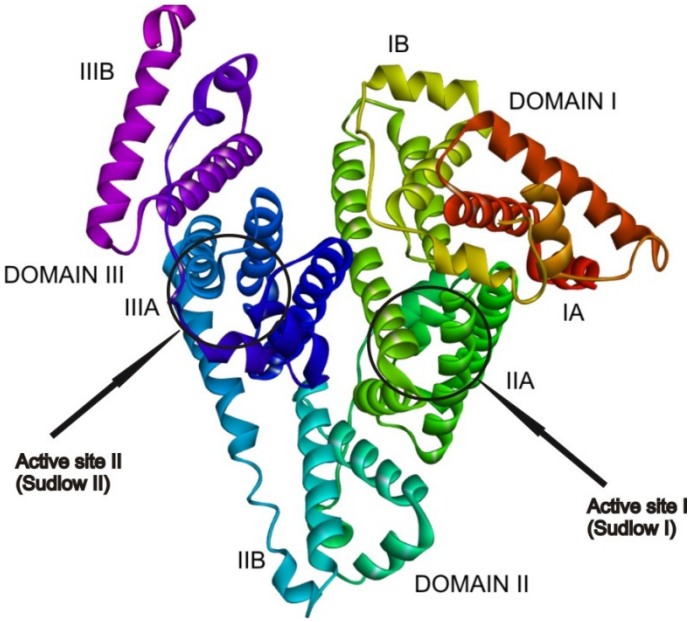

Figure 5. Active sites, domains and subdomains of HSA.

The presented results in Table 3 contain values of Gibbs energies, inhibition constants, and other thermodynamic parameters that describe the binding of HPD and CAF molecules to HSA, as well as binding of these molecules to HSA-HPD and HSA-CAF complexes.

Table 3. Estimated values of binding energies for HSA with HPD and CAF

Conformations	ΔG_{bind} (kJ mol^{-1})	K_i (μM)	ΔG_{inter} (kJ mol^{-1})	$\Delta G_{vdw+hbond+desol}$ (kJ mol^{-1})	ΔG_{ele} (kJ mol^{-1})	ΔG_{total} (kJ mol^{-1})	ΔG_{tor} (kJ mol^{-1})
HSA-HPD	-40.7	0.08	-43.2	-42.8	-0.38	-6.19	8.74
HSA-CAF-HPD	-39.8	0.11	-44.6	-43.9	-0.71	-3.93	8.74
HSA-CAF	-20.8	231.7	-20.8	-20.7	-0.04	0.00	0.00
HSA-HPD-CAF	-20.6	243.2	-20.6	-19.0	-1.59	0.00	0.00

As can be seen from Table 3, the obtained thermodynamic parameters from docking simulations are following the same trend that is established by the experiment (Table 2). The values of Gibbs energy from the docking calculation are equally lower in relation to the experimental values from Table 2. That partially can be explained by higher entropy values

in the experiment, solvent presence, and the usage of approximations in the equations for theoretical calculations, for example, the usage of the compact unbounded model.

It should be noted that the presence of CAF in the blood inhibits the binding of HPD. The reason for this lies in the fact that both molecules are binding in the same active place. It was found that there is a small difference in binding energy, which cannot be ignored if HPD binds only to HSA and / or to HSA-CAF complex (see values of binding constants Table 3).

CONCLUSIONS

In this paper, fluorescence-absorption spectroscopy and molecular modeling were used to investigate the interaction between HSA and HPD under simulative physiological conditions (*in vitro*) in the presence of CAF. CAF is an important phytonutrient, which if used with other drugs may cause interference. The presence of CAF, caused a decrease in the binding constants of the HPD with HSA (competitive interference), because CAF and HPD have almost the same binding site in HSA. This fact indicates that in the presence of caffeine there may be an increase in the free fraction of haloperidol in plasma, which may lead to the manifestation serious side effects or changes in effectiveness. In order to reduce side effects, the patience under HPD treatment should reduce their intake of beverages rich in CAF. This research illustrates that the simultaneous uptake of coffe, tea, …etc and drugs may cause interaction.

EXPERIMENTAL SECTION

Reagents and chemicals

CAF (Ph.Eur.-USP-FU, catalog No. 326356) was obtained commercially from the Carlo Erba reagents. HPD with purity over 95 % (Product No. H1512), HSA (Lyophilized powder ≥96 % by agarose gel, essentially fatty acid free, product No. A1887) and phosphate-buffered saline (PBS, Product No. P4417) were purchased from Sigma-Aldrich Chemical Company (St. Louis, MO, USA). All chemicals are used without further purification. Double-distilled water was used throughout the experiment.

Preparation of solutions

Solution of PBS (0.01 M) contains 0.0027 M KCl and 0.137 M NaCl, pH=7.4 at 298,15 K, was prepared by dissolving one tablet in 200 ml of distilled water. HSA stock solution ($2 \cdot 10^{-5}$ M) was prepared by dissolving

them in PBS. The stock solution of HPD ($3.2 \cdot 10^{-3}$ M) was prepared by dissolving them in 5% methanol and then diluted to $2.82 \cdot 10^{-4}$ M with solution of PBS. The CAF ($2 \cdot 10^{-4}$ M) stock solutions were dissolved in 5% ethanol and diluted with solution of PBS. All solutions were made fresh and stored in the refrigerator at 4 ˚C prior to use.

Fluorescence spectra measurements

All fluorescence spectra were measured on an RF-1501 PC spectrofluorometer (Shimadzu, Japan) with excitation at 295 nm, using a 150 W Xenon lamp source, 1.0 cm quartz cells and a thermostatic bath. Fluorescence spectra were recorded at 293, 303, 310 K in the range of 310—460 nm. The widths of the excitation and emission slit widths were both fixed at 5 nm. The specified temperatures were controlled by Julabo ED (v.2) open circulating bath (Julabo Labortechnik GmbH, Germany).

The fluorescence spectra were obtained with constant HSA concentration (2.0×10^{-6} M) and by varying the HPD concentrations from 0 to 7.0×10^{-5} M for HSA-HPD binary system. For the research on the effects of the CAF on the HSA-HPD system fluorescence spectra were also recorded at different temperatures (293, 303 and 310 K). In all series of solutions, the molar ratio of HSA to CAF is maintained at 1:1 ($2 \cdot 10^{-6}$ M). The solutions of HSA-CAF were left to stand for an hour, and then in the all of the solutions concentration of HPD varied from 0 to $5 \cdot 10^{-5}$ M. Resultant mixtures were incubated at different temperatures for half an hour, respectively.

Ultra-violet spectroscopy

All absorption maxima of the spectra were recorded in the range of 200 to 400 nm at a temperature of 298 K on a spectrophotometer (Agilent Cary 300 spectrophotometer equipped with 1.0 cm quartz cells). On the ordinate, the detection of absorbance values in the range from 0 to 3 was set. The scanning speed was set to 480 nm per minute, and the device entered values of absorbance at 1 nm. Before each new batch, a pure solution corresponding to the buffer was recorded, and the obtained absorption spectrum formed the baseline. Enabling the baseline correction option, the program corrected all recorded spectra by subtracting the values corresponding to the baseline. The absorption spectra were obtained with constant HSA and CAF concentrations (2.0×10^{-6} mol dm^{-3}) and by varying the HPD concentrations from 0.0 to 7.0×10^{-5} mol dm^{-3}.

Molecular docking

The molecular docking simulations were employed in order to better understand the inhibitor efficiency of the investigated compounds. Before molecular docking simulations, the pockets and binding sites of HSA protein were determined. AutoGridFR (AGFR) program [39] was used for this purpose. Ligands were prepared for docking by optimizing their geometries using the density functional theory (DFT) and employing B3LYP functional [40,41] that is implemented in the Gaussian 09W software package [42]. The crystal structure of HSA was obtained from the Brookhaven Protein Data bank (PDB ID:1HK1, [43]). Protein was prepared for docking in Discovery Studio 4.0 [44]. Polar hydrogen atoms, Kollman charges, and other parameters were added using the graphical interface from AutoDockTools (ADT) [45]. The AutoDock 4.2 software was used for molecular docking simulations. In the docking procedure, ligands are presented as flexible molecules and the docking software was free to rotate all single bonds to catch the best position inside the active site of HSA. The Lamarckian Genetic Algorithm (LGA) was used for protein-ligand and complex-ligand flexible docking. The conformer with the lowest binding energy was used for further analyses. Parameters for the LGA method were determined as follows: a maximum number of energy evaluations was 250.000, a maximum number of generations was 27,000, and mutation and crossover rates were 0.02 and 0.8, respectively. Algorithms, that AutoDock 4.2 software is based on, can predict positions within the protein target, for the ligand, and to assess them by scoring functions defined by setting the grid box. Grid box with dimensions 56×50×58 $Å^3$ in -x, -y, and -z directions of HSA was used to cover the protein binding site and accommodate ligand to move freely. A gridpoint spacing of 0.375 Å was used for auto grid runs. Results of the interactions between the target protein and investigated compounds were analyzed and illustrated in Discovery Studio 4.0 and AutoDockTools.

ACKNOWLEDGMENTS

This work was supported by the Ministry of Education, Science and Techological Development of the Republic of Serbia (Agreement No. 451-03-68/2020-14/200122)

REFERENCES

1. T. Peters Jr.; *All about albumin: biochemistry, genetics, and medical applications,* 1st ed; San Diego: Academic press, **1995;** pp. 382
2. F. Yang; Y. Zhang; H. Liang; *Int. J. Mol. Sci*., **2014**, *15*, 3580-3595.
3. I. Jerković; C.I. Tuberoso; P.M. Kuś; Z. Marijanović; M. Kranjac; *RSC Adv*., **2014**, *4*, 60557-60562.
4. A. Adan; J.M. Serra-Grabulosa; *Hum. Psychopharm*. Clin., **2010**, *25*, 310-317.
5. Q. Wu; C. Li; Y. Hu; Y. Liu; *Sci. China. Ser. B Chem*., **2009**, *52*, 2205-2212.
6. W. Wang; W. Zhang; Y. Duan; Y. Jiang; L. Zhang; B. Zhao; P. Tu; *Spectrochim. Acta. A Mol. Biomol. Spectrosc*., **2013**, *115*, 57-63.
7. S. Miyamoto; G.E. Duncan; C.E. Marx; J.A. Lieberman; *Mol. Psychiatry*., **2005**, *10*, 79-104.
8. S. Kudo; T. Ishizaki; *Clin. Pharmacokinet*., **1999**, *37*, 435-456.
9. J.D. Berić; S.D. Stojanović; E.M. Mrkalić; Z.D. Matović; D.R. Milovanović; M.M. Sovrlić; R.M. Jelić; *Monatsh. Chem*., **2018**, *149*, 2359-2368.
10. C.P. de Morais e Coura; E.T. Paulino; C.M. Cortez; V.M. da Silva Fragoso; *Serum albumin and the haloperidol pharmacokinectics. A study using a computational model.* AIP Publishing LLC, **2016**, p. 100009.
11. S. Schmidt; D. Gonzalez; H. Derendorf; *J. Pharm. Sci*., **2010**, *99*, 1107-1122.
12. O. Dömötör; C.G. Hartinger; A.K. Bytzek; T. Kiss; B.K. Keppler; E.A. Enyedy; *J. Biol. Inorg. Chem*., **2013,** *18*, 9-17.
13. Y.Q. Wang; H.M.Zhang; Q.H. Zhou; *Eur. J. Med. Chem*., **2009**, *44*, 2100-2105.
14. D. Raghav; S. Mahanty; K. Rathinasamy; *Spectrochim. Acta. A Mol. Biomol. Spectrosc*., **2020,** *226*, 117584.
15. M.M. Islam; V.K. Sonu; P.M. Gashnga; N.S. Moyon; S. Mitra; *Spectrochim. Acta. A. Mol. Biomol. Spectrosc*., **2016,** *152*, 23-33.
16. Z. Limpouchová; K. Procházka; *Theoretical principles of fluorescence spectroscopy*. *In Fluorescence Studies of Polymer Containing Systems*; Springer, Cham., **2016**; pp. 91-149.
17. K. Kitamura; A.A. Omran; C. Nagata; Y. Kamijima; R. Tanaka; S. Takegami; T. Kitade; *Chem. Pharm. Bull*., **2006**, *54*, 972-976.
18. N. Seedher; *Indian. J. Pharm. Sci*., **2000**, *62*, 16-20.
19. J.J. Jing; B. Liu; X. Wang; X. Wang; L.L. He; X.Y. Guo; M.L. Xu; Q.Y. Li; B. Gao; B.Y. Dong; *Lumin*., **2017**, *32*, 1056-1065.
20. A.B. Khan; J.M. Khan; M.S. Ali; R.H. Khan; *Spectrochim. Acta. A Mol. Biomol. Spectrosc*., **2012**, *97*, 119-124.
21. X. An; J. Zhao; F. Cui; G. Qu; *Arab. J. Chem*., **2017**, *10*, 1781-1787.
22. J.R. Lakowicz; *Principles of Fluorescence Spectroscopy*; Plenum Press, New York, **1999**; pp. 237-265.
23. J.R. Lakowicz; *Quenching of Fluorescence. In: (eds) Principles of Fluorescence Spectroscopy*; Springer, Boston, MA, **2006**; pp. 277-330.
24. S.K. Dutta; S.K. Basu; K.K. Sen; *Indian. J. Exp. Biol*., **2006**, *44*, 123–127.
25. Z.J. Cheng; Y.T. Zhang; *J. Mol. Struct*., **2008**, *889*, 20-27.

26. M. Shahlaei; B. Rahimi; M.R. Ashrafi-Kooshk; K. Sadrjavadi; R. Khodarahmi; *J. of Luminiscence*, **2015,** *158*, 91-98.
27. L. Brunton; J. Lazo; K. Parker; *Goodman & Gilman's The Pharmacological Basis of Therapeutics, 11th edn.*; McGraw-Hill, New York, **2005**.
28. N. Seedher; P. Agarwal; *Drug. Metab. Pers. Ther.*, **2010**, *25*, 17-24.
29. Y.Q. Wang; H.M. Zhang; G.C. Zhang; W.H. Tao; S.H. Tang; *J. Lumin.*, **2007**, *126*, 211-218.
30. M.G. Wen; X.B. Zhang; J.N. Tian; S.H. Ni; H.D. Bian; Y.L. Huang; H. Liang; *J. Solute. Chem.*, **2009**, *38*, 391-401.
31. D. Leckband; *Annu. Rev. Chem. Biomol. Eng*., **2010**, *1*, 365-389.
32. R.A. Alberty; *J. Phys. Chem. B*., **2010**, *114*, 17003-17012.
33. J.Q. Lu; F. Jin; T.Q. Sun; X.W. Zhou; *Int. J. Biol. Macromol*., **2007,** *40*, 299-304.
34. D.B. Davies; L.N. Djimant; A.N. Veselkov; *J. Chem. Soc. Faraday. Trans*., **1996**, *92*, 383-390.
35. D.B. Davies; D.A. Veselkov; L.N. Djimant; A.N. Veselkov; *Eur. Biophys. J*., **2001**, *30*, 354-366.
36. P.D. Ross; S. Subramanian; *Biochemistry*., **1981**, *20*, 3096-3102.
37. J. Ghuman; P.A. Zunszain; I. Petitpas; A.A. Bhattacharya; M. Otagiri; S. Curry; *J. Mol. Biol*., **2005**, *353*, 38-52.
38. L. Trynda-Lemiesz; *Bioorg. Med. Chem*., **2004**, *12*, 3269-3275.
39. P.A. Ravindranath; S. Forli; D.S. Goodsell; A.J. Olson; M.F. Sanner; *PLoS. Comput. Biol*. **2015**, *11*, e1004586.
40. A.D. Becke; *Phys. Rev. A*.,**1988,** *38*, 3098-3100.
41. A.D., Becke; *J. Chem. Phys*., **1993**, *98*, 5648.
42. [dataset] M.J. Frisch; G.W. Trucks; H.B. Schlegel; G.E. Scuseria; M.A. Robb; J.R. Cheeseman; G. Scalmani; V. Barone; B. Mennucci; G.A. Petersson; H. Nakatsuji; M. Caricato; X. Li; H.P. Hratchian; A.F. Izmaylov; J. Bloino; G. Zheng; J.L. Sonnenberg; M. Hada; M. Ehara; K. Toyota; R. Fukuda; J. Hasegawa; M. Ishida; T. Nakajima; Y. Honda; O. Kitao; H. Nakai; T. Vreven; J. Montgomery; J. A. Peralta; F. Ogliaro; M. Bearpark; J.J. Heyd; E. Brothers; K.N. Kudin; V.N. Staroverov; R. Kobayashi; J. Normand; K. Raghavachari; A. Rendell; J.C. Burant; S.S. Iyengar; J. Tomasi; M. Cossi; N. Rega; J.M. Millam; M. Klene; J.E. Knox; J.B. Cross; V. Bakken; C. Adamo; J. Jaramillo; R. Gomperts; R.E. Stratmann; O. Yazyev; A.J. Austin; R. Cammi; C. Pomelli; J.W. Ochterski; R.L. Martin; K. Morokuma; V.G. Zakrzewski; G.A. Voth; P. Salvador; J.J. Dannenberg; S. Dapprich; A.D. Daniels; Ö. Farkas; J.B. Foresman; J. V. Ortiz; J. Cioslowski; D.J. Fox; *Gaussian 09. Revision D*. Gaussian Inc, Wallingford, **2009**.
43. I. Petitpas; C.E. Petersen; C.E. Ha; A.A. Bhattacharya; P.A. Zunszain; J. Ghuman; N.V. Bhagavan; S. Curry; *Proc. Natl. Acad. Sci*., **2005**, *100*, 6440-6445.
44. D.S. BIOVIA; Discovery studio visualizer, Release. San Diego: Dassault Systèmes, **2017**.
45. G.M. Morris; R. Huey; W. Lindstrom; M.F. Sanner; R.K. Belew; D.S. Goodsell; A.J. Olson; *J. Comput. Chem*., **2009**, *30*, 2785-2791.

STUDIA UBB CHEMIA, LXVI, 4, 2021 (p. 23-31)
(RECOMMENDED CITATION)
DOI:10.24193/subbchem.2021.4.02

LEAD ISOTOPIC RATIO DETERMINATION IN CAVE SEDIMENTS USING TRIPLE-QUADRUPOLE INDUCTIVELY COUPLED PLASMA MASS SPECTROMETRY

ANAMARIA IULIA TÖRÖK[a], CLAUDIU TĂNĂSELIA[a,*], ANA MOLDOVAN[a,b], BOGDAN ANGYUS[a,c], ERIKA ANDREA LEVEI[a], CECILIA ROMAN[a]

ABSTRACT. Lead isotopic ratio determination is significantly affected by the isobaric interference of mercury (^{204}Hg), thus many studies lack ^{204}Pb/^{206}Pb values. Removal of ^{204}Hg from sample is resource consuming, while mathematical correction can be employed if the Hg isotope ratio in the sample is known. Triple quadrupole inductively coupled plasma mass spectrometry (TQ-ICP-MS) offers a mechanism for removing the ^{204}Hg, by pressurizing the reaction cell with ammonia, that reacts with ^{204}Hg positively charged ions rendering them neutral, thus filtering them out and removing them from the ion beam. The Pb isotope ratio determination can be used as "fingerprint" to identify the sources of contamination and environmental pollution. The method developed based on this mechanism was used for Pb isotopic ratio determination in cave sediment samples. Relative standard deviation of this method was between 0.36% - 0.59%.

Keywords: *ICP-MS, Pb isotopic ratio, lead, cave sediments, triple-quadrupole*

INTRODUCTION

Lead (Pb) is the 36th most abundant element in the Earth's crust (16 ppm crustal abundance), occurring with four naturally occurring stable isotopes: ^{204}Pb (1.4% abundance), ^{206}Pb (24.1% abundance) ^{207}Pb (22.1 % abundance)

[a] *INCDO-INOE2000, Research Institute for Analytical Instrumentation, 67 Donath, RO-400293, Cluj-Napoca, Romania*
[b] *Technical University, Faculty of Materials and Environmental Engineering, 103-105 Muncii Boulevard, 400641 Cluj-Napoca, Romania*
[c] *Babes-Bolyai University, Faculty of Chemistry and Chemical Engineering, 11 Arany Janos, 400028 Cluj-Napoca, Romania*
[*] *Corresponding author: claudiu.tanaselia@icia.ro*

and ^{208}Pb (52.4% abundance), with ^{204}Pb being the only isotope that is not radiogenic. The other three isotopes are the products of the radioactive decay of uranium (^{235}U, ^{238}U) or thorium (^{232}Th) [1]. Hence the geographically Pb abundance is correlated with former U and Th ore deposits, thus making Pb isotopic ratio determination an excellent geological tracer and an important geochronometer [2-4].

Pb isotopic measurements are used to determine the age of meteorites, Earth and other planetary bodies (Mars and Moon) [2]. Also, it can offer information on geochemical origins by "fingerprinting" minerals, lavas and pollutants as potential Pb sources and on the pathways by which Pb enters into the environment [5, 6]. Moreover, Pb isotopic studies can offer valuable information on the geogenic or anthropogenic sources of Pb in various environmental matrices (water, soil, sediments, rocks, plants etc.). Pb is considered one of the most toxic heavy elements that occurs naturally in the environment, with no known function in the human body [7]. Pb occurs in the atmosphere as fine particulate (<1 μm) from anthropogenic sources, and it can also be found in ore deposits such as galena (PbS), anglesite ($PbSO_4$), cerussite ($PbCO_3$), or minimum (Pb_3O_4) [3]. Distribution in the environment takes places through a series of complete well-balanced chemical and physical processes such as weathering, runoff, precipitation, stream/river flow, erosion, though which Pb is transferred to atmosphere (air, dust), hydrosphere (water), lithosphere (soil and sediments) and biosphere (biota) [3, 8].

Thermal ionization mass spectrometry (TIMS) or multi-collector inductively coupled plasma mass spectrometry (MC-ICP-MS) are the most used techniques to measure Pb isotopic ratios from various matrices. One of the biggest disadvantages of these techniques are the high cost and the labor-intensive sample preparation in ultraclean laboratories [9]. However, the precision of single detector ICP-MS instruments is at least one order of magnitude poorer when compared to MC-ICP-MS methods, due to inherent sequential reading that is affected by plasma variations between readings. Single detector ICP-MS offers a higher versatility and lower initial and maintenance costs, and its precision can be considered satisfactory for some applications.

If not chemically separated, the ^{204}Hg isotope (mass 203.973476 amu), will overlap ^{204}Pb isotope (mass 203.973029 amu) and separating them in a mass spectrometer requires a resolution of over 400000. That is well beyond the limits of current instruments as the ICP-MS resolution varies from 400 for a single detector, quadrupole instrument, to around 10000 for a sector field instrument, which is 40 times lower than the required value to separate ^{204}Hg from ^{204}Pb isotopes [10-12]. Thus, lead isotopic ratio studies are published incompletely, without specifying the ^{204}Pb isotope, since ^{204}Pb

analysis is often unreliable. As chemical separation is a resource consuming step in sample preparation, recent advances in ICP-MS design makes it possible to have an online chemical sample alteration that removes the ^{204}Hg, making ^{204}Pb determination possible to an acceptable precision level.

In the case of ^{204}Pb determination, a triple-quadrupole ICP-MS will filter out all the isotopes with masses different than 204 amu using the first quadrupole (Q1), leaving a mix of Pb and Hg passing through the rest of the mass spectrometer. The ion beam will enter the second quadrupole (Q2), that doesn't have a filtering role, but it guides the beam trough the collision/ reaction cell. The cell has the possibility to be pressurized with a collision and/or a reaction gas in case of the most ICP-MS instruments on the market. In this case, if the cell is pressurized with ammonia, it will react with $^{204}Hg^-$ ions much more often than with $^{204}Pb^-$ ions, transferring an electron to the Hg ions, rendering them neutral (due to instrument design, the ion beam in ICP-MS is usually made exclusively from negative ions). Thus, the third quadruple (Q3) will guide only the ^{204}Pb ions to the detector, filtering out the remaining $^{204}Hg^0$ atoms [13], a process depicted in Figure 4.

The main objective of this study was to optimize the determination of Pb isotopic ratio from cave sediment samples, using triple-quadrupole ICP-MS instrument with reaction cell by pressuring with ammonia, in order create a neutral ^{204}Hg species that is filtered out from the ion beam. Cave sediment samples are considered to be significant part of caves science, offering valuable information about the caves hydrogeological and palaeoclimatological records. Take into consideration further application possibilities, cave samples were used as test samples for Pb isotopic ratio method optimization. Five different caves from Romania were selected in order to study the scattered distribution of Pb isotopic ratio from the sediment samples.

RESULTS AND DISCUSSION

The Pb concentration is displayed in Figure 1. The highest Pb content was measured in case of the sampling sites from Ferice cave (19.4 mg/kg ± 4.53). High Pb values were found also in case of the sites from Lesu cave (12.3 mg/kg ± 0.84). The lowest Pb values were registered in case of Tausoare cave (3.9 mg/kg ± 1.28).

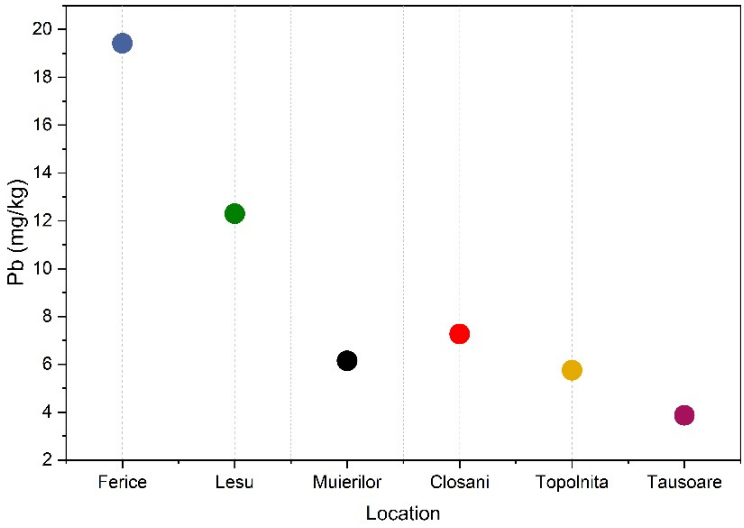

Figure 1. Pb concentration (mg/kg) in the cave sediment samples.

Table 1. Results of NIST 981 SRM reading for the Pb isotopes (n=10)

	204/206	**207/206**	**208/206**
Certified values (NIST 981 SRM)	0.059042 ±0.000037	0.91464 ±0.00033	2.1681 ±0.0008
Average measured values (this study)	0.059558 ±0.000865	0.91817 ±0.00842	2.1555 ±0.0062

A batch of 10 measurements of NIST 981 standard reference material (SRM) was performed and the results are listed in Table 1. Uncertainty was calculated as three times the standard deviation. The uncertainty for $^{204}Pb/^{206}Pb$ is not significantly different from than $^{207}Pb/^{206}Pb$, but it's higher (at least one order of magnitude) than the one reported for NIST 981 SRM, due to differences in employed techniques (Figure 2). Relative standard deviation of measurements was between 0.36% - 0.59%.

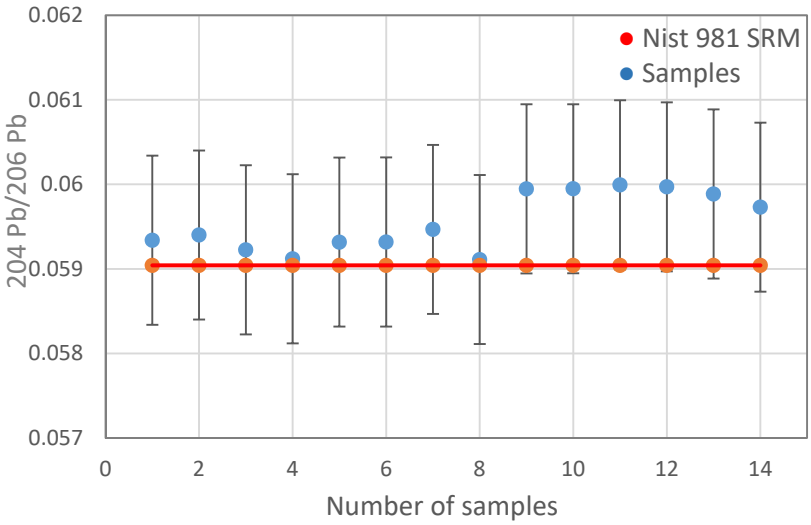

Figure 2. $^{204}Pb/^{206}Pb$ measured values (blue dots) and the NIST 981 SRM certified value (line).

The results for NIST981 measurements are displayed on Table 2 and graphically plotted on Figure 3. Pb isotope ratio data shows a clear distinction between NIST 981 SRM and the rest of the sample, as expected, due to different analytical techniques used in this study (triple-quadrupole, single-collector inductively coupled plasma mass spectrometry) and NIST laboratory (triple filament solid-sample mass spectrometry).

Table 2. Pb isotopic ratio in studied samples, including NIST 981 standard reference material for reference (5 readings/sample)

Sampling sites	204Pb/206Pb	207Pb/206Pb	208Pb/206Pb
Ferice	0.053859 ±0.0004	0.846714 ±0.0051	2.044527 ±0.0099
Lesu	0.05361 ±0.0001	0.845489 ±0.020	2.047661 ±0.048
Muierilor	0.052027 ±0.0017	0.816579 ±0.0187	1.992496 ±0.0353
Closani	0.052456 ± 0.0001	0.807570 ±0.020	1.971243 ±0.035
Topolnita	0.054545 ± 0.0001	0.832732 ±0.0008	2.006947 ±0.0017
Tausoara	0.05491 ±0.0002	0.83748 ±0.0024	2.013048 ±0.0010
NIST 981 SRM	0.059555 ±0.001019	0.918095 ±0.009818	2.145219 ±0.037757

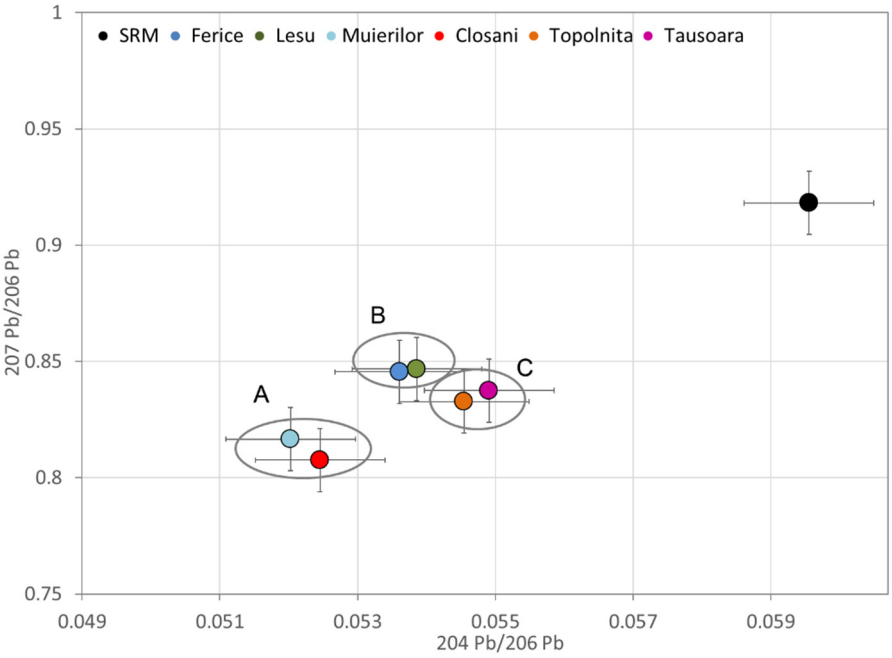

Figure 3. Sample results including NIST 981 SRM (top right): $^{207}Pb/^{206}Pb$ vs $^{204}Pb/^{206}Pb$ values. The error bars are calculated as three times standard deviations for each sample.

The samples from Muierilor and Cloșani (group A) are clearly separated from the other samples (Figure 3). Despite being sampled from different geographical locations, samples from Ferice and Lești (group B) seems grouped together, as well Topolnița and Tausoare (group C) (Figure 3). A low separation between groups B and C is observed, but the isotopic ratio data doesn't show a clear distinction for samples within groups B and C. This can be explained by insufficient precision, due to inherent plasma variation, associated with other geological factors that may be similar between the mentioned locations.

CONCLUSIONS

A triple-quadrupole ICP-MS was successfully used to determine Pb isotopic ratio from cave sediment samples, including data on ^{204}Pb, usually left out due to ^{204}Hg interference. The ^{204}Hg was removed in the reaction cell by pressuring the cell with ammonia, a reactive gas that would initiate a

charge transfer to ^{204}Hg, creating a neutral ^{204}Hg species that is filtered out from the ion beam. While further optimizations could improve the precision, this will remain an order of magnitude lower than multi-collector ICP-MS instruments, due to design limits. However, the achieved precision using this approach is satisfactory in some cases, especially if we consider the advantages of single collector ICP-MS (versatility, low initial and tunning costs) over more expensive and less flexible multi-collector ICP-MS instruments.

EXPERIMENTAL SECTION

Instrumentation

The Pb concentration and isotopic ratio measurements were performed using a Thermo Scientific iCAP TQ ICP-MS instrument. In order to minimize the effect of plasma variations, the dwell time was set to 0.02 seconds for ^{208}Pb, 0.04 seconds for ^{206}Pb and ^{207}Pb and respectively 0.2 seconds for ^{204}Pb, to increase the number of counts for the least abundant isotope, while keeping the counts low enough for the most abundant isotope so that the detector would stay in ion counting mode and won't switch to analog (Faraday) mode. For each isotope, one channel was used for reading its counts ("peak-hopping"). The number of sweeps was set to 250. Both Q1 and Q3 quadrupoles were used in "high resolution" mode, while the collision cell gas flow was set to 0.6 ml/min. Nickel cones were used for all the measurements in this study and the instrument was configured in "High-Matrix" mode. Data acquisition and ICP-MS operation were performed using Qtegra software (v. 2.10.3324.131), provided by the manufacturer. ICP-MS operating parameters are listed in Table 3.

Table 3. Thermo Scientific iCAP TQ ICP-MS parameters

ICP-MS parameter	Value
Nebulizer gas flow (Ar)	0.90 l/min
Ammonia reaction gas for the remove of ^{204}Hg	0.6 l/min
Extraction Lens	-132.1 V
Spray chamber temperature	2.7 °C
Q1 Focus Lens	-1 V
Q1 Bias	-0.9602 V
QCell Bias	-2.01 V
Q3 Bias	-1.0002
Focus Lens	19.20 V
RAPID Lens	-377 V
Plasma power	1550 W
Cool Flow	14 l/min
Auxiliary Flow	0.8 l/min

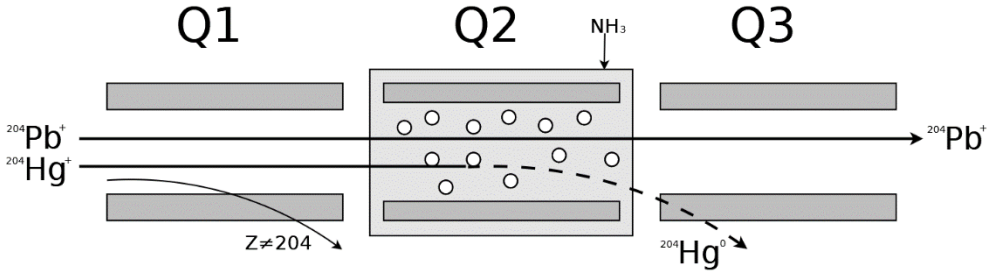

Figure 4. Removal of ^{204}Hg interference using a triple-quadrupole ICP-MS. Q1- first quadrupole, Q2- second quadrupole (inside the reaction cell pressurized with ammonia) and Q3- third quadrupole.

Description of SRM and cave sediment samples

For measuring the total Pb concentration, a calibration curve was used in the 1-100 µg/L range and ^{208}Pb was chosen, due to is highest abundance. The standard solutions for the calibration curve were prepared by successive dilutions from Perkin-Elmer Multi-Element Calibration Standard 3. For isotopic ratio calibration and to calculate the method uncertainty for each isotopic ratio, a NIST 981 standard reference material (SRM) was used. Blank values were subtracted from each measurement. The SRM was used in a bracketing technique: the reference material was measured before and after each sample, to avoid any signal shift in isotopic determination. Ultrapure deionized water from a water purification system (Elga Veolia, UK) with HNO_3 (5%) was used for the blank samples and the Pb counts were measured and subtracted from the subsequent sample values. The deionized water was also used to prepare the calibration standard solutions and for all dilutions. The sediment samples were dried at 60-65 °C for 12h. The dried samples were ground and sieved in order to obtain a fine powder. Three grams of the ground samples were dissolved in a 3:1 (v/v) mixture of HCl (30%) and HNO_3 (65%) on sand bath, then transferred and diluted with ultrapure water to a final volume of 100 mL in volumetric flask. NIST 981 SRM was acquired as a solid sample (wire) and it was purchased directly from NIST. For analysis, 1 g of the solid sample was digested in HNO_3 (65%) and 1 L stock solution was prepared, the diluted for daily use (down to 50 µg/L).

The sediment samples were collected in February 2020, from five Romanian caves: Ferice, Lesu, Muierilor, Tausoare, and Topolnita sampling sites.

ACKNOWLEDGMENTS

This work was supported by the Romanian Ministry of Research and Innovation, CCCDI-UEFISCDI, through projects 352PED/2020 (GLAZEX) and PN-III-P4-ID-PCCF-2016-0016 (DARKFOOD) within PNCDI III. The authors would like to thank Dr. Oana Teodora Moldovan for providing the samples collection.

REFERENCES

1. F. Vanhaecke K. Kyser, The Isotopic Composition of the Elements, in *Isotopic Analysis*. **2012**. p. 1-29.
2. D. Weis, Lead Isotopes, in *Encyclopedia of Geochemistry: A Comprehensive Reference Source on the Chemistry of the Earth*, W.M. White, Editor. **2017**, Springer International Publishing: Cham. p. 1-5.
3. A.M. Ghazi J.R. Millette, 4 - Lead, in *Environmental Forensics*, R.D. Morrison and B.L. Murphy, Editors. **1964**, Academic Press: Burlington. p. 55-79.
4. R.D. Vocke; *Pure Appl Chem*, **1999**, 71, 1593-1607.
5. L. Gao, L. Han, W. Peng, B. Gao, D. Xu; X. Wan; *Ecotoxicol Environ Safety*, **2018**, 164, 226-233.
6. H. Cheng Y. Hu; *Environmental pollution (Barking, Essex : 1987)*, **2010**, 158, 1134-46.
7. A.L. Wani, A. Ara; J.A. Usmani; *Interdisciplinary toxicology*, **2015**, 8, 55-64.
8. J. Zhou, B. Du, Z. Wang, W. Zhang, L. Xu, X. Fan, X. Liu; J. Zhou; *Sci Total Environ*, **2019**, 647, 932-941.
9. B. Gulson, G.D. Kamenov, W. Manton; M. Rabinowitz; *Int J Environ Res Public Health*, **2018**, 15, 723.
10. I. Gelaude, R. Dams, M. Resano, F. Vanhaecke; L. Moens; *Anal. Chem.*, **2002**, 74, 3833-3842.
11. G. Audi A.H. Wapstra; *Nuclear Physics A*, **1995**, 595, 409-480.
12. I. Gelaude, R. Dams, M. Resano, F. Vanhaecke; L. Moens; *Anal Chem*, **2002**, 74, 3833-42.
13. D. Asogan. *Using triple quadrupole interference removal to improve data quality in laser ablation ICP-MS for geochemical applications*. Application note 44387 2018; Available from: https://assets.thermofisher.com/TFS-Assets/CMD/Application-Notes/an-44387-icp-ms-interference-removal-geochemical-an44387-en.pdf.

STUDIA UBB CHEMIA, LXVI, 4, 2021 (p. 33-50)
(RECOMMENDED CITATION)
DOI:10.24193/subbchem.2021.4.03

ATTENUATED TOTAL REFLECTANCE – FOURIER TRANSFORM INFRARED SPECTROSCOPY APPLIED FOR THE EVALUATION OF ESSENTIAL OILS' PATTERN RECOGNITION AND THERMO-OXIDATIVE STABILITY: A COMPARATIVE STUDY

RAMONA MARIA POPA[a], FLORINELA FETEA[a], CARMEN SOCACIU[a,b,*]

ABSTRACT. The Attenuated Total Reflectance-Fourier Transform Infrared Spectroscopy was applied for the evaluation of specific patterns for six different essential oils obtained from aromatic plants (thyme, oregano, tea tree) or common spices (clove, cinnamon, juniper). The spectral fingerprints were recorded using a Shimadzu IR Prestige-21 spectrometer in the middle infrared region (3500-650 cm^{-1}) before and after thermal oxidation in hot air. In parallel, the peroxide index, *cis-trans* isomerization and lipoperoxidation were evaluated to determine their oxidative stability. Each oil showed specific FTIR spectra, especially in the fingerprint region (1650-650 cm^{-1}), in good agreement with our previous GC-MS analysis of the same samples. The spectral patterns in this region were also correlated with their oxidative stability, chemically determined. The spectral data were processed by multivariate analysis (Metaboanalyst 5.0 software) and the discriminatory analysis helped to identify each oil pattern.
This study combined the capability of ATR-FTIR-MIR spectroscopy to realize a pattern recognition of essential oils as a rapid and non-destructive method, as well the oxidative modifications, easier than chemical routine tests. This study contributes to the control of quality, authenticity, and safety of essential oils and can be extended to other extracts, used as additives or ingredients in food or cosmetic products.

Keywords: *essential oils fingerprinting, Attenuated Total Reflectance Mid Infrared Spectroscopy, thermal oxidation*

[a] *Department of Food Science, Faculty of Food Science and Technology, University of Agricultural Sciences and Veterinary Medicine Cluj-Napoca, Cluj-Napoca RO-400372, Romania*
[b] *Research Center for Applied Biotechnology, Proplanta, Cluj-Napoca, RO-400478 Romania*
[*] *Corresponding author: carmen.socaciu@usamvcluj.ro*

INTRODUCTION

The Fourier Transform Infrared Spectroscopy (FTIR) is a non-destructive, fast, reproducible analytical method useful to fingerprint different food products. It can identify specific vibration bands, characteristic to functional groups of different molecules [1-3]. The Attenuated Total Reflectance-Fourier Transform Spectroscopy (ATR-FTIR) is the most suitable technique to highlight the specific imprint of liquid samples, including plant oils and volatile essential oils (EOs), to check their authenticity, traceability and adulteration [2, 4-6]. Moreover, it is useful to identify oxidative processes that modify the functional groups (alcohols, aldehydes, ketones, epoxides, peroxides, acids). The ATR-FTIR spectral data are usually collected in the whole middle Infrared region (MIR), from 4000 to 400 cm^{-1} including the fingerprint region 1800-650 cm^{-1}.

It is also an excellent tool for quantitative analysis, because the intensities of the spectral bands are proportional to concentration. It helps to distinguish oils from different botanical origins using specific wavenumber domains coupled with non-supervised classification techniques [7-9].

Different reviews and experimental data have been published, about the FTIR spectroscopy applied for the characterization of edible oils, and to compare it with other physical and chemical properties, e.g. Iodine value peroxide and saponification index [6, 10-12], as well as for the freshness evaluation and detection of adulteration [13]. A large majority of data refer to olive oil adulteration with low-cost edible oils [12, 14] or to assess oil oxidation [15-17]. Moreover, the determination of edible oil authenticity, compared with the more accurate but time-consuming, laborious, and expensive chromatography-based methods (GC-MS) is advantageous being a more rapid and cheaper solution. Considering the advantages of being non-destructive, cost effective and environmentally friendly, using small amounts of liquid samples and simple preparation procedures [5,18]. Meanwhile FTIR spectroscopy was found to be superior for the discrimination and classification of edible oil comparing to FT-Raman and FT-NIR [19, 20].

The applicability of FTIR-MIR spectroscopy in assessing oils fingerprinting quality & safety parameters is crucially dependent on the chemometric methods, including calibrations with large and representative samples [13,21]. The common chemometric classification includes non-supervised approaches e.g. principal component analysis (PCA), cluster analysis (CA), while the supervised methods include partial least squares with discriminant Analysis (PLSDA), linear discriminating analysis (LDA) and principal component regression (PCR) [22]. The Random Forest (RF) algorithm is applied as a superior classifier useful for food adulteration, for

classification and authentication in chemometrics [23]. The web-based software MetaboAnalyst 5.0 (www.metaboanalyst.ca/) is a new integrated tool which accepts a variety of input data (from NMR and MS to FTIR peak lists) and offers several chemometric options for data processing, from univariate (ANOVA t-test) to multivariate statistical analysis, PCA, PLS-DA, CA, heatmaps, RF and more sophisticated statistical or machine learning methods [11].

EOs include a variety of volatile molecules such as terpenes and terpenoids (esters, aldehydes, acids, alcohols, ketones, and ethers derived from terpenes), phenol-derived aromatic and aliphatic components [24-27]. EOs proved to have multiple biological actions, such as antioxidant, bactericidal, virucidal, fungicidal, antiparasitic, insecticidal effects [28-30] being used in food industries, as natural flavors or in different pharmaceutical and cosmetic formulations. Therefore, the quality, authenticity and safety of EOs is of high scientific interest and involves high resolution analytical procedures, e.g. gas-chromatography coupled with mass spectrometry, infrared spectroscopy, magnetic resonance [4, 31, 32].

EOs are extracted from aromatic herbs and spices, vegetables and fruits, many of them being described in EMA monographies (https://www.ema.europa.eu/en/medicines/herbal) and in European pharmacopeia [33]. The ATR-FTIR-MIR method can be adapted for a global quantification of EOs free or dissolved in edible oils or encapsulated in hydrocolloids or powders and can be used also to compare their chemical profile during storage, as recently reported [34, 35]. This technique allows a short analysis time, minimum sample preparation [36, 37].

Recently, the characterization of the volatile fractions of EOs of some *Lamiaceae* spices in relation to their activities was reported [38, 39]. Thyme (*Thymus vulgaris L.)* includes different subspecies and varieties and is used frequently as a spice or medicinal remedy with anti-inflammatory and antibacterial effects, its oily extracts being rich in thymol and terpinene-4-ol [26,40,41] beside flavonoids and triterpenoids. Oregano (*Origanum vulgare L*.) is rich in monoterpenoids (thymol and carvacrol) and sesquiterpenoids with antiinflamatory, antispasmodic, antioxidant, antifungal and antibacterial activity [42, 43]. Juniperus (*Juniperus communis L.*) is a coniferous tree, its oil contains monoterpenes (approx. 58%), mainly α-pinene, β-myrcene and sabinene [44]. The industrial applications in relation to the chemical composition and antimicrobial activity obtained from its berries was recently confirmed [45]. Tea tree (*Melaleuca sp*.) is used for its essential oil, the main oil components are monoterpenes and sesquiterpenes, and their oxygenated analogues [46, 47] with antiseptic, cytotoxic, antibiotic, anti-inflammatory and antioxidant activity. Clove (*Syzygium aromaticum L*.) is a rich source of eugenol,

eugenol acetate, gallic acid, having a high potential for pharmaceutical, cosmetic and food applications due to its antioxidant and antimicrobial effect [48, 49]. Cinnamon (*Cinnamomi Cortex*) oil is extracted from its bark and contains mainly cinnamaldehyde (up to 87,23%) coumarin, cinnamic alcohol and acid, its biological activity (antioxidant, antidiabetic, thrombocyte anti-aggregation, antifungal and antibacterial) as recently described [50-53]. We applied previously the GC-MS analysis for a comparative identification of similar six EOs as well the behavior of EOs in different formulations [54, 55].

This study aims to apply the ATR-FTIR-MIR spectroscopy for the evaluation of the specific pattern of six types of essential oils obtained from aromatic plants (thyme, oregano, tea tree) or common spices (clove, cinnamon, juniper). The specific spectral fingerprints were recorded and the oxidative stability after an induced thermal oxidation in hot air was investigated. All data were processed by statistical multivariate analysis using the online Metaboanalyst 5.0 software and the specific patterns of their recognition, authenticity, and stability were established.

RESULTS AND DISCUSSION

Physical characteristics

Some physical characteristics of the studied EOs are presented in Table 1.

Table 1. Comparative physical characteristics of the 6 essential oils: density, refractive index, rotational power.

Essential oil	Relative Density	Refractive index	Rotational power
Thyme	0.9220	1.4980	-2.7
Oregano	0.9500	1.5120	+1.1
Juniper	0.8610	1.4770	-6.2
Cloves	1.0580	1.5320	-1.6
Cinnamon	1.0200	1.5860	-1.1
Tea tree	0.9020	1.4770	+10.2

The highest refractive index was seen for Cinnamon, Clove and Oregano oils, in parallel with highest density for these oils. The rotational power was very different, from +10.2 to -6.2 and was dependent on the sums of the different optical active terpenoids found in these essential oils. Tea tree had a high dextrogir rotational power which may be explained by its rich composition in (+)terpiene-4-ol, while Juniper the highset levogir power due to (-) alpha pinene.

ATR-FTIR-MIR spectra

The Infrared absorption bands observed before and after the induced thermal oxidation are characteristic to different types of bonds and functional groups found in EOs, considering two MIR domains, 1800-650cm^{-1}, 3600-2500 cm^{-1}), as presented in Figure 1 A-G.

For comparison, the same spectra were recorded, as a control, for Sunflower oil, before and after the induced thermal oxidation.

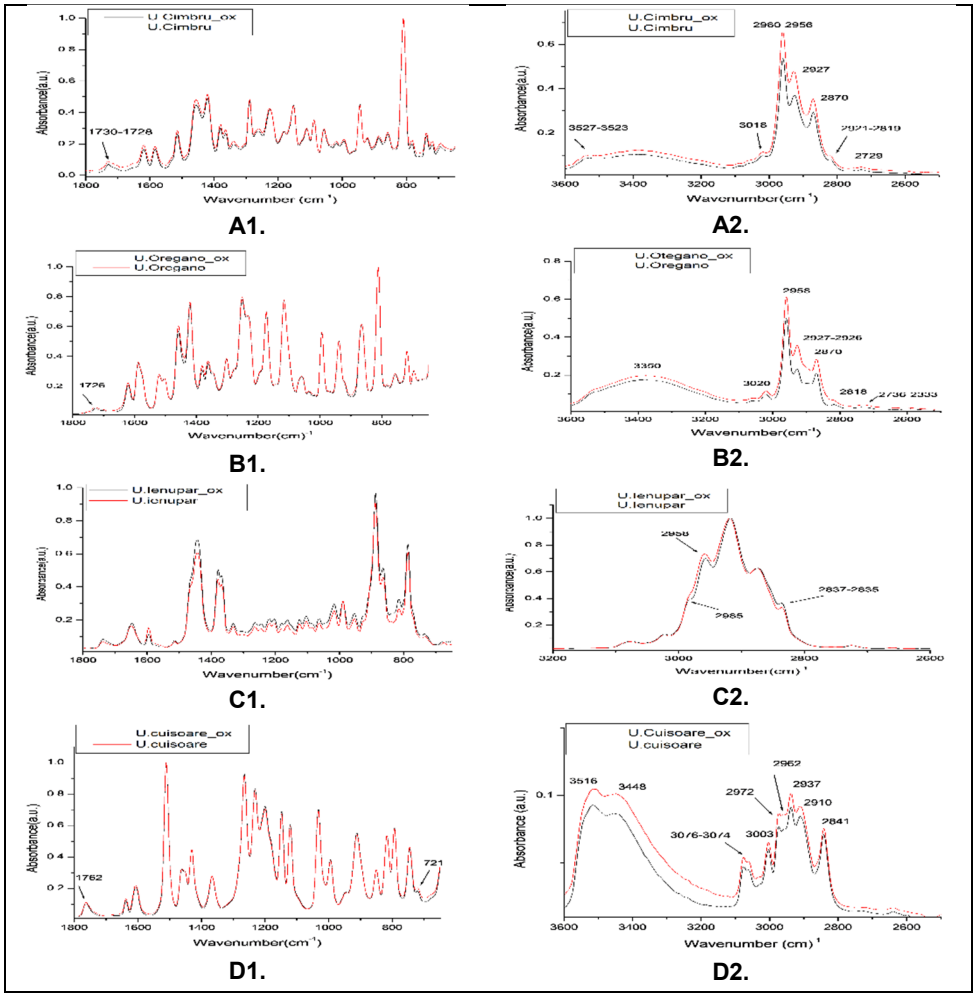

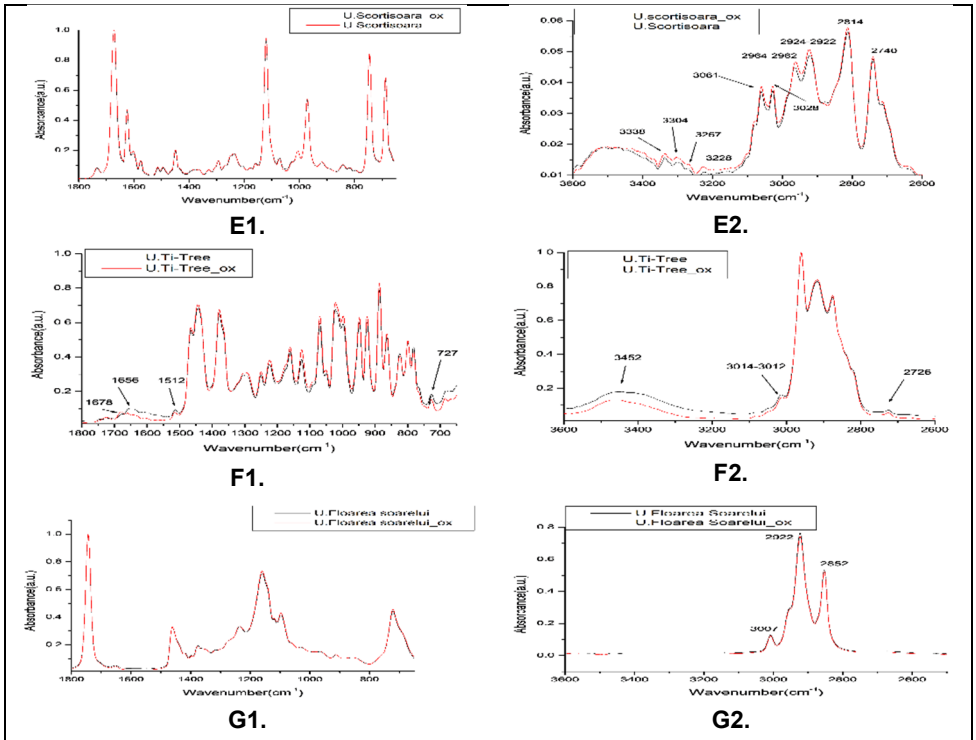

Figure 1. FTIR spectra in the region 1800-650 cm^{-1} and 3600-2500 cm^{-1} of six essential oils, before (black) and after induced thermal oxidation (red). A1-A2. Thyme (Cimbru). B1-B2. Oregano. C1-C2. Juniperus (Ienupăr). D1-D2. Clove (Cuişoare). E1-E2. Cinnamon (Scorţişoară). F1-F2. Tee tree (Ti-Tree). G1-G2. Sunflower oil (Floarea Soarelui) as control.

All spectra included peaks in four zones, disregarding the zones specific to nitrogen compounds: 1 (1000-650 cm^{-1}), 2 (1470-1000 cm^{-1}), 3 (1750-1500 cm^{-1}) and 4 (3600-2700 cm^{-1}), attributed to different stretching or deformation vibrations known to characterize oils (Table 4).

The spectral fingerprints for thyme oil (Figure 1A1-A2) show dominant signals with characteristic frequencies in zones 1-2 and 4, where the signal intensities were higher than 0.38. Such signals are good markers to fingerprint thyme: 810vs, 945m, 1551m, 1226m, 1419m, 1456m, 2927m, 2960s, 3527m (Table 2). No specific signals (fi, i, m) were identified in zone 3. Oxidation reduced some intensities only in zone 4, indicating small changes in aliphatic chain vibrations CH_2 and CH_3.

For oregano (Figure 1B1-B2), the fingerprints include specific wavenumbers and intensities at 717m, 866s, 939m, 993m, 1116s, 1172s, 1232s,

1251s, 1419s, 1458s, 2958s, 3350m. Oxidation reduced some intensities, but not significantly, indicating similar changes in vibrations in aliphatic chains.

For juniper (Figure 1C1-C2), the specific frequencies in zones 1-2 and 4, with signal intensities higher than 0.38 were identified. The specific pattern is different, include peaks at 786s, 864m, 889vs, 1367m, 1379m, 1442s, 2875s, 2918vs, 2985s. To notice in this case no peaks were visible at wavenumbers higher than 2985 cm^{-1}.

The spectral fingerprints of clove oil (Figure 1D1-D2) look different from thyme, oregano or juniper, some signals are dominant in both samples (clove oil and oxidized clove oil). These signals represent specific imprints of clove: 744m, 792m, 817m, 912m, 1120m, 1147s, 1232s, 1265vs, 1431m, 1510vs, 3448s and 3515s. Oxidation reduced some intensities, but only in zone 4 (2700-3600 cm^{-1}).

Cinnamon pattern (Figure 1E1-E2) is highly specific and different, with peaks at 686s, 746s, 972m, 1120vs, 1624m, 1672vs, 3338 and 3304m. Oxidation did not reduce intensities, insignificantly even in zone 4.The peak at 686 cm^{-1} corresponds to the vibration specific to alkenes, while peaks at 1672, 1624 cm^{-1} and 1734 cm^{-1} correspond to the C-O carbonyl bond from aldehydes vibration, indicators of cinnamic aldehyde, a marker of cinnamon.

Tea tree (Figure 1F1-F2) had also specific fingerprint, with multiple peaks, at 781m, 798m, 823m, 864m, 887s, 923s, 948s, 997m, 1022s, 1068m, 1126m, 1161m, 1379s, 1442s, 1465m, 2875s, 2916s, 3452m different from the other oils. Oxidation does not affect the pattern, only slight increases of the signals above 3014 cm^{-1}.

The sunflower oil imprint (Figure 1G1-G2) is the poorest in signals, some dominant signals can be seen at 721m, 1097m, 1120m, 1159s, 1743vs, 2852m, 2922s, 3007m and no signals at higher wavenumbers. No changes after induced oxidation are noted, since sunflower oil contains lipophilic antioxidants, mainly tocopherols and carotenoids which act as antioxidants.

To conclude, the absorption frequencies in the ATR-FTIR-MIR spectra in the fingerprint region (1800-650 cm^{-1}) were assigned to be specific to the different EOs: absorptions characteristic to the aromatic ring between 890-730 cm^{-1}(1), attributed to aliphatic long chain hydrocarbons at aprox. 720 cm^{-1} (2) and absorptions in the region 1750-1500 cm^{-1} attributed to carbonyl compounds at approx. 1750 cm^{-1} and to C = C absorption at 1600 cm^{-1}(3). In the region 3600-2700 cm^{-1} three spectral areas showed visible changes for all EOs: absorptions in the zone 2920-2850 cm^{-1} corresponding to stretching vibration in the CH_2 aliphatic chain (1), in the range 3003-3007 cm^{-1} corresponding to stretching vibration of the double bond *cis* specific to unsaturated fatty acids, the decreased intensity being a marker of *cis-trans* isomerization (2) and the band at 3473 cm^{-1} attributed to the O-H stretching vibration of hydroperoxides (3).

The comparative image of the patterns of different EOs and their specific FTIR markers are summarized in Table 2.

Table 2. Wavenumbers considered as markers for EOs pattern recognition*.

Nr.	EO	Very strong signals (vs)	Strong signals (s)	Medium signals (m)
1.	Thyme	810	2960	945, 1551, 1226, 1419, 1456, 2927, 3018
2.	Juniperus	889, 2918	786, 1442, 2875, 2958, 3022	864, 1367, 1379
3.	Oregano	-	866, 1116, 1172, 1232, 1251,1419, 1458, 2958, 3020	717, 939, 993
4.	Cloves	1265, 1510	1147, 1232	744, 792, 817, 912, 1120, 1431
5.	Cinnamon	1120,1672	686, 746	972, 162, 3061, 3308
6.	Tea tree	-	887, 923, 948, 1022, 1379, 1442, 2875, 2916	781, 798, 823, 864, 997, 1068, 1126, 1161, 1465
7.	Sunflower	1743	1159, 2922, 3007	721, 1097, 1120, 2852

*The abbreviations for intensities are marked in parentheses (vs =>0.9; s =>0.6; m => 0.38).

Chemometrics: Multivariate analysis for EOs pattern recognition

The PLSDA Analysis was first applied to identify the discrimination between samples from the two groups of EOs, a first one considered to belong to aromatic or medicinal plants MP (Thyme, Oregano and Tea tree) and the second one, the spice-group S (Juniperus, Clove and Cinnamon). Figure 2 A and B represents the score plot of PLSDA and the VIP scores derived from loadings, which identify the relevant features (IR ranges) that may explain the discrimination between groups MP and S.

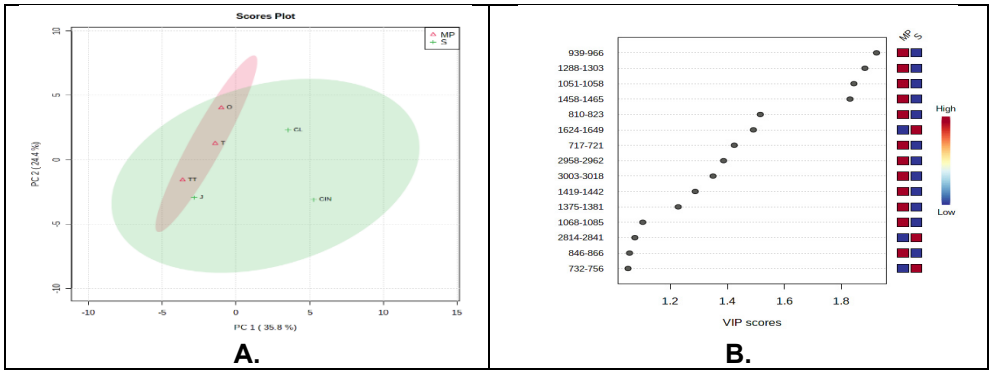

Figure 2. A. The PLSDA Score plot for samples' discrimination. **B.** VIP scores corresponding to wavenumbers (WN) which discriminate between groups MP and S. T-thymus; O-oregano; TT-Tea tree; J-Jenuper; CIN-Cinnamon; CL-clove.

As can be seen in Figure 1A, the co-variance of components PC1-PC2 was 60%, indicating an acceptable significance of discrimination. There are observed high similarities between T, O and TT, close to J. CL and CIN show distinct patterns. The WN ranges which may be considered most relevant for this discrimination are 939-966, 1288-1303, 1051-1058, 1458-1465 cm^{-1}. Applying the RF analysis (Mean Decrease Accuracy), the first 15 wavenumbers to be considered potential biomarkers for the discrimination of MP *vs* S groups are shown in Figure 3A.

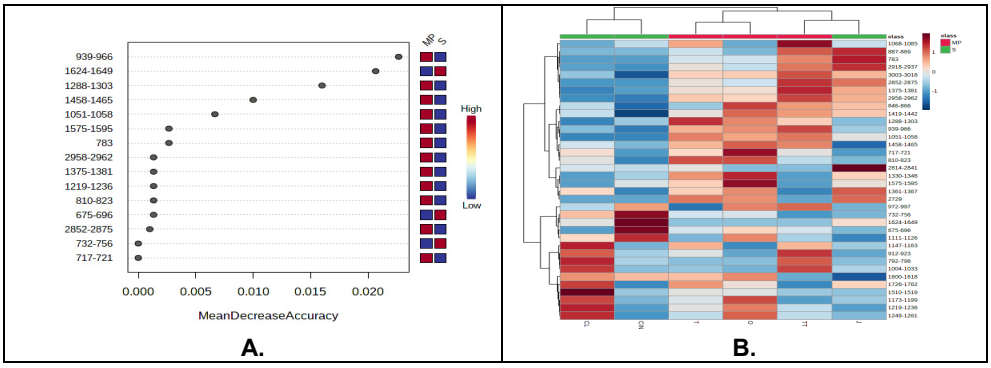

Figure 3. A. The MDA plot showing the wavenumbers to be considered biomarkers of discrimination between groups MP and S. **B.** The Heatmap showing above the sample clusters MP and S (red *vs* green) and the correlations between individual samples and FTIR intensities at different wavenumbers. T-thymus; O-oregano; TT-Tea tree; J-Jenuper; CIN-Cinnamon; CL-clove.

These are 939-966, 1624-1649, 1288-1303, 1458-1465 cm^{-1}, very similar to the previous analysis (Figure 2B.). The intuitive image of correlations between EOs samples and the WN ranges are presented in heatmap (Figure 3B). One can see distinct patterns of each EO and the ranges which can be considered as authenticity fingerprint, as well the sample clusters MP and S (red *vs* green).

Multivariate analysis to identify EOs stability against oxidation

Based on the spectral fingerprints and the matrices representing the peak wavenumbers *vs* intensity, for each EOs sample, before and after induced thermal oxidation, the PLSDA and RF analysis showed the differences between the initial (G) and final stage (Ox). Figure 4 A and B represents the score plot of PLSDA and the VIP scores which identified the features (wavenumbers) that may explain the discrimination between sample groups G and Ox.

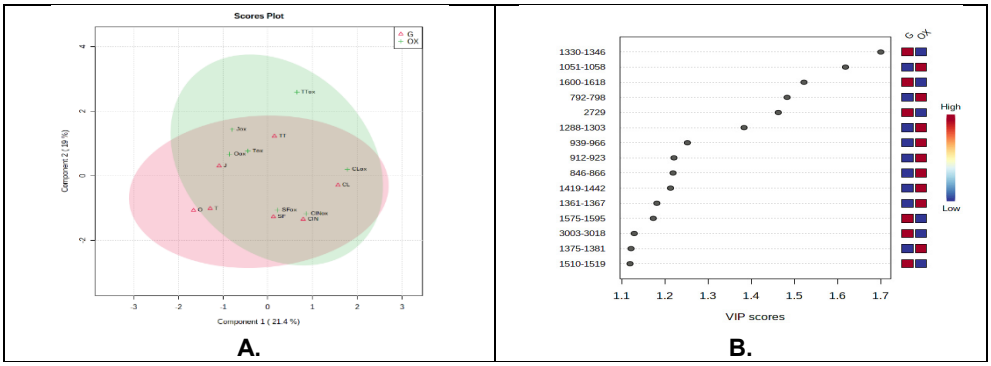

Figure 4.A. The PLSDA Score plot for the discrimination between EOs, at initial (G) and final stage (Ox). **B.** VIP scores corresponding to wavenumbers which discriminate between groups G and Ox. T-thymus; O-oregano; TT-Tea tree; J-juniper; CIN-Cinnamon; CL-clove.

As can be seen in Figure 4 A, the co-variance of components PC1-PC2 was 40.4%, indicating weak discriminations between samples in initial and oxidized form. This indicates a good stability of samples against induced thermal oxidation, especially visible for SF, CIN and CL. The most labile seems to be T and O as indicated by the distance between the two stages in the plot. The WN ranges which may be considered most relevant for this discrimination are 1330-1346, 1051-1058, 1600-1618, 792-798, 1288-1303 cm^{-1} with higher VIP scores (Figure 4B). Applying the RF analysis and considering Mean Decrease Accuracy (MDA), the first 15 wavenumbers to be considered potential biomarkers for the discrimination of G *vs* ox groups are shown in Figure 5A.

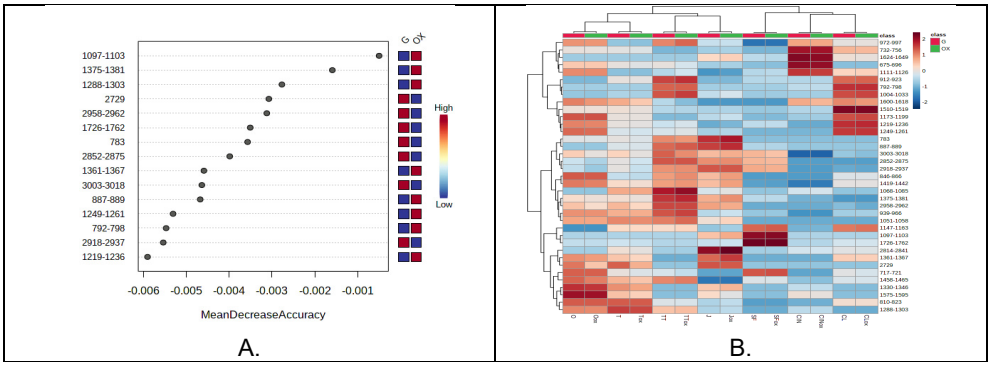

Figure 5.A. The MDA plot showing the wavenumbers to be considered biomarkers of discrimination between groups G and Ox. **B.** The Heatmap showing the sample clusters and their correlations with the FTIR intensities at different wavenumbers, before (G) and after thermal oxidation (Ox).

These are 1097-1103, 1375-1381, 1288-1303, 2729, 2958-2962, 1726-1762, 1458-1465 cm^{-1}, many being similar to the VIP score ranking (Figure 4B.). Here also, an intuitive image of correlations between EOs samples (at initial stage comparative to the final stage after induced oxidation) and the WN ranges are presented in heatmap (Figure 5B). One can see also the patterns of each EO and as well the similarities between the initial and oxidized forms (red *vs* green).

Oxidative stability and cis-trans *isomerization by induced thermal oxidation*

In parallel to FTIR spectroscopy, the usual parameters used for the identification of oxidation were determined, *e.g.,* Peroxide Index (IP) and Lipid peroxidation by MDA test. Figure 6 shows the correlation plot between these parameters and the wavenumbers which were identified above, as relevant for the ATR-FTIR-MID spectral modifications. For these correlations there were considered the ratios between the oxidized/initial stage (OX/I), for each of the six EOs.

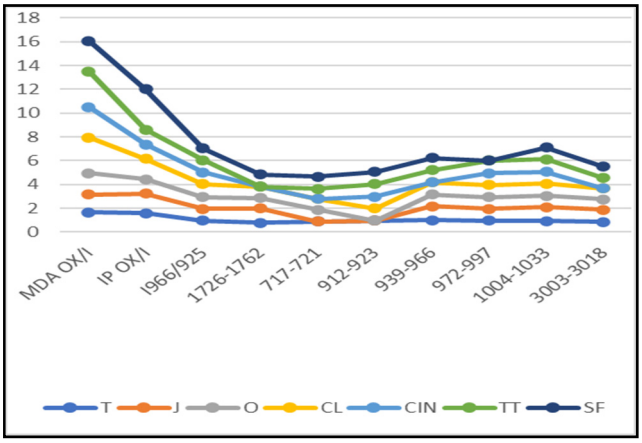

Figure 6. Correlations (expressed as ratios between the oxidized/initial stage) between the different parameters to characterize oxidation, from MDA-lipid peroxidation, to peroxide index (IP) and peak intensities of different FTIR ranges for the six EOs: Thyme(T), Juniper(J), Oregano(O), Clove (C), Cinnamon (CIN), Tea tree (TT), Sunflower (SF).

Also, considering that genuine plant-derived oils contain *cis* isomers of different unsaturated molecules, in agreement with FTIR application notes [56], the increase of the peak intensity at 966 cm^{-1} and of the intensity ratios

966 / 925 cm^{-1} can indicate the isomerization of *cis trans* isomers. It is known that *trans* fats are considered by-products of the thermal processing. Therefore, we considered these ratios to compare the behaviors of different EOs after induced thermal oxidation, as shown in table 3.

Table 3. Signal intensity ratios 966/925 cm^{-1}, as indicators of *cis-trans* isomerizations, before (I) and after induced thermal oxidation.

Essential oils	$I_{966/925}$ Ox/I
Thyme	0.985
Juniperus	0.988
Oregano	0.970
Cloves	1.088
Cinnamon	0.988
Tea tree	1.026
Sunflower	1.007

No significant changes were observed between these intensity ratios, therefore we consider that all essential oils, including sunflower oil did not undergo *cis-trans* isomerization during the induced thermal oxidation.

CONCLUSIONS

The data obtained reflected the potential of ATR-FTIR-MIR method to obtain detailed information and specific patterns of different essential oils (thyme, oregano, juniper, clove, cinnamon, and tea tree). The different plant-derived essential oils (from aromatic/medicinal and spices) showed specific FTIR spectra, and the qualitative features were identified in different zones, specific to molecular vibrations and related to their molecular composition. These data were in good agreement with our previous GC-MS analysis of the same samples [54].

Beside the qualitative patterns, semi-quantitative analysis was done, recording the peak intensities related to specific wavenumbers. Therefore, it was possible to realize specific “identity cards” of each oil, based on specific absorption wavenumbers and intensity range, to be markers of authenticity.

As a second goal, by an induced thermal oxidation it was demonstrated that almost all tested essential oils showed good oxidative stability. By routine chemical methods (peroxide index and malondialdehyde test) and evaluation of FTIR intensities at specific wavenumbers, there were find good, significant positive correlations. Therefore, specific FTIR wavenumbers from the fingerprint region can be considered as markers of oxidative stability of essential oils.

All data obtained by ATR-FTIR-MIR spectroscopy were further processed by chemometrics, via multivariate analysis bringing added-value information and biological significance. By PLSDA-and Random Forest analysis significant correlations and sample discrimination were identified and finally reflected by intuitive heatmaps.

This study combined the capability of ATR-FTIR-MIR spectroscopy to realize a pattern recognition of essential oils as a rapid and non-destructive method, as well the oxidative modifications, easier than chemical routine tests. This study contributes to the control of quality, authenticity, and safety of essential oils and can be extended to other extracts, used as additives or ingredients in food or cosmetic products.

EXPERIMENTAL SECTION

Materials

A few types of essential oils (Thyme, Juniperus, Oregano, Clove, Cinnamon, Tee Tree) and one sunflower oil were subjected to FTIR analysis. These were provided by the Fares Company Orăştie and were previously characterized by various physical and chemical parameters mentioned in their Technical Specifications. The controlled thermo-oxidation was performed in a hot air oven at 180ºC for 14 hours. The FTIR analysis was applied before and after oxidation to determine their specific pattern and to highlight the spectral changes induced by thermal oxidation.

ATR-FTIR-MIR Spectroscopy

The ATR-FTIR-MIR absorption spectra were recorded using the Shimadzu IR Prestige -21 spectrophotometer with horizontal ATR diamond accessory and a single PIKE reflection to hexane as background (control). The spectra were recorded on the wavelength range 3600-650 cm^{-1} at a resolution of 4 cm^{-1}, and 64 scans for one spectrum. The raw data obtained were processed using IR Solution Software (Shimadzu) and OriginR 7SR1 Software (OriginLab Corporation, Northampton, USA).

According to literature data, the different absorptions were especially followed [37]. Table 4 include the most significant bands which correspond to specific vibrations of the molecules found in different EOs.

From each FTIR spectrum a matrix representing the peak intensities as a function of wavenumber (WN) was built and used for statistical analysis and data interpretation.

Relative density

A pycnometer, before and after being filled with water at 20 ° C was weighed. The empty, dried pycnometer is filled with each sample (EO) brought to a temperature of 20°C and weighed. The difference represents the parameter (m). The relative density of the sample is calculated according to the formula: $D = m/m_1$ where D = relative density. Parameters m and m_1 represent EOs and water weight, respectively expressed in g.

Refractive index

A few drops from each EO were placed between the prisms of the refractometer. The boundary between the light and the dark area was brought to the intersection of the reticular wires. The value of the refractive index was read directly on the scale.

Table 4. Typical FTIR regions of volatile oils, correlated with the mode of vibration for specific functional groups, considered as predictor variables for statistical data processing.

Range (cm^{-1})	Functional Group	Mode of Vibration
3471	-C=O	Symmetric Stretching in esters
3006	-HC=CH- (*cis*)	Symmetric Stretching in *cis* olefins
2872, 2962	=C–H (*trans* and *cis*)	Symmetric Stretching C-H (CH_3)
2854, 2926	=C–H (*trans* and *cis*)	Symmetric Stretching C-H (CH_2)
1745	-C=O	Stretching
1635-1655	RHC=CH2	Stretching in cis olefins
1418,1458, 1463	$=CH_2$	Deformation in plane
1376, 1380, 1396	$-CH_2-$, dimethyl	Plane & out-of-plane deformations in *cis* olefins
1147–1159	-C–O, C-OH	Stretching, bending
1096, 1237	-C=O	Stretching of ester groups
967	-HC=CH- (*trans*)	Out of plane deformation for disubstituted olefins
850–920	$=CH_2$	Out of plane deformation
842-862	Isopropyl group	Out of plane deformation
723, 810	-C–H; -HC=CH- (*cis*)	Bending (out of plane) specific to olefins

Rotational power

The rotational power was determined by a polarimeter, as follows: the tube with the polarimeter was filled with the sample, avoiding the formation of air bubbles. The angle of rotation alpha (±) was read on the scale of the analyzer.

Peroxide Index

Reagents: Chloroform: Acetic acid, 2:1, saturated potassium iodide solution, Natrium thiosulphate 0.01 N, starch solution 1%. To 15 ml solvents mix there were added 2,5 g from each EO oil and fresh potassium iodide solution. After mixing 1 min, 30 ml water was added and titrated with thiosulfate, using starch as color indicator. In parallel, a blank (distilled water) was titrated. The value of peroxide index (IP) was calculated according to the formula: IP= 10x (V2 – V1)/m, where m= 2.5 g, V2 – thiosulfate volume used for samples titration; V1- thiosulfate volume used for blank.

Lipoperoxidation

Reactive oxygen species degrade polyunsaturated lipids to form malondialdehyde (MDA), which measure the degree of lipid peroxidation [57]. The spectrophotometric determination of MDA is done after its condensation with thiobarbituric acid (TBA) to give a fluorescent pink-red derivative (MDA-TBA complex) that can be measured by absorption at 535nm [58]. A temperature of 100ºC and a low pH (max. 3) are required to release MDA from oxidized lipids. To build the calibration curve for MDA, a solution 100μM 1,1,3,3 tetramethoxypropane was used. Shortly, in a centrifuge tube, to 100 μl oil there were added 0.9 ml Tris solution and 2ml of TBA reagent. After mixing 1 min and 15 min kept in a boiling water bath, the solution was centrifuged 10 min at 1000 rpm and the pink MDA-TBA complex, was measured at 535 nm against a blank containing 1ml Tris and 2ml TBA reagent. The results (Eq MDA) were calculated by multiplying the Absorbance (A535) with the value of its absorption molar coefficient (163.8).

Chemometrics

The raw FTIR data representing the absorption intensities at each wavenumber from the middle infrared region (3600-650 cm^{-1}) were statistically processed using the online software Metaboanalyst 5.0 (www.metaboanalyst.ca) and included the multivariate analysis by PLSDA (score plots and VIP value ranking), heatmaps, Random forest (RF) analysis.

ACKNOWLEDGMENTS

The technical support of the Spectroscopy laboratory - Institute of Life Sciences at University of Agricultural Sciences and Veterinary Medicine Cluj-Napoca is acknowledged.

REFERENCES

1. M.D. Guillén; N. Cobo; *J. Sci. Food Agric.,* **1997**, *75*, 1–11.
2. A.S. Franca; L.M.L. Nollet; *Spectroscopic Methods in Food Analysis*, CRC Press, NY, **2017**, 664 pg.
3. D.-W. Sun; *Infrared Spectroscopy for Food Quality Analysis and Control*; Academic Press: Cambridge, MA, USA, **2009**.
4. C. Socaciu; F. Ranga; F. Fetea; D. Leopold; F. Dulf; R. Parlog; *Czech J. Food Sci.,* **2009**, *27*, S70–S75.
5. W.-H. Su; D.-W. Sun; *Food Eng. Rev.,* **2019**, *11*, 142–158.
6. Q. Li; J. Chen; Z. Huyan; Y. Kou; L. Xu; X. Yu; J.-M. Gao; *Crit. Rev. Food Sci. Nutr.,* **2019**, *59*, 3597–3611.
7. G. Gurdeniz; F. Tokatli; B. Ozen; *Eur. J. Lipid Sci. Technol.,* **2007**, *109*, 1194–1202.
8. Y.W. Lai; E.K. Kemsley; R.H. Wilson; *J. Agric. Food Chem.,* **1994**, *42*, 1154–1159.
9. D.A. Rusak; L.M. Brown; S.D. Martin; *J. Chem. Educ.,* **2003**, *80*, 541–543.
10. L. Xu; X. Zhu; X. Yu; Z. Huyan; X. Wang; *Eur. J. Lipid Sci. Technol.,* **2018**, *120*, 1700396.
11. J. Xia; N. Psychogios; N. Young; D.S. Wishart; *Nucleic Acids Res.,* **2009**, *37*, W652–W660.
12. Y. Le Dreau; N. Dupuy; J. Artaud; D. Ollivier; J. Kister; *Talanta,* **2009**, *77*, 1748–1756.
13. L. Cerretani; A. Giuliani; R.M. Maggio; A. Bendini; T.G. Toschi; A. Cichell; *Eur. J. Lipid Sci. Technol.,* **2010**, *112*, 1150–1157.
14. N.Vlachos; Y. Skopelitis; M. Psaroudaki; V. Konstantinidou; A. Chatzilazarou; E. Tegou; *Anal. Chim. Acta*, **2006**, 459–465.
15. M.D. Guillen; N. Cabo; *J. Sci. Food and Agr.,* **2000***, 80,* 2028-2036.
16. B. Muik; B. Lendl; A. Molina-Diaz; M. Valcarcel; M.J. Ayora-Canada; *Anal. Chim. Acta,* **2007**, *593*, 54–67.
17. M.A. Poiana; E. Alexa; M.F. Munteanu; C. Mateescu; *Open Chemistry,* **2015**, *13*, 689–698.
18. C. Socaciu; F. Fetea; F. Ranga; A. Bunea; F. Dulf; S. Socaci; A. Pintea; *Appl. Sci.* **2020**, *10*, 8695.
19. H. Yang; J. Irudayaraj; M.M. Paradkar; *Food Chem.,* **2005**, *93*, 25–32.
20. L.E. Rodriguez-Saona; M.E. Allen Dorf; *Ann. Rev. Food Sci. Technol.,* **2011**, 2, 467–483.
21. A. Biancolillo; F. Marini; C. Ruckebusch; R. Vitale; *Appl. Sci.,* **2020**, *10*, 6544.
22. A.C. Godoy; P.D.S. dos Santos; A.Y. Nakano; R.A. Bini; D.A.B. Siepmann; R. Schneider; P.A. Gaspar; P.W.D. Pfrimer; R.F. da Paz; O.O. Santos; *Food Anal. Meth.,* **2020**, *13*, 1138–1147.
23. F. Bachion de Santana; W. Borges Neto; R.J. Poppi; *Food Chem.,* **2019**, *293*, 323–332.
24. C. Fisher; T.R. Scott; *Food Flavours: Biology and Chemistry, Royal Society of Chemistry*, **2007**, 176 pg, ISBN 9781847550866

25. J. Rivera Calo; P.G. Crandall, C.A. O'Bryan; S.C. Ricke; *Food Control*, **2015**, *54*, 111-119.
26. A. Wesołowska; D. Jadczak; Not. Bot. Horti. Agrobo., **2019**, *47*, 829-835.
27. V. Istudor; *Farmacognozie, Fitochimie, Fitoterapie,* vol. II, Ed. Medicală, Bucureşti, **2001**
28. S.A. Johnson; *Medicinal Essential Oils: The Science and Practice of Evidence-Based Essential Oil Therapy*, Lightning Source Inc. Publ, **2017**.
29. F. Bakkali; S. Averbeck; D. Averbeck; M. Idaomar; *Food and Chem Toxicol.,* **2008**, *46*, 446–475.
30. S. Baptista-Silva; S. Borges; O.L. Ramos; M. Pintado; B. Sarmento; *J. of Essential Oil Res.,* **2020**, *32*, 279-295.
31. T.K.T. Do; F. Hadji-Minaglou; S. Antoniotti; X. Fernandez; *Trends Anal Chem.,* **2015**, *66*, 146-157.
32. I.L. Milovanović; A.C. Mišan; M.B. Sakač; I.S. Čabarkapa; B.M. Šarić; J.J. Matić; P.T. Jovanov; *Food Process Quality Safety*, **2009**, *3-4*, 75-79.
33. *European Pharmacopoeia* (Ph. Eur.) 10th Edition, **2020**
34. O.Taylan; N. Cebi; O. Sagdic; *Foods,* **2021**, *10*, 202-212.
35. N. Cebi; O. Taylan; M. Abusurrah; O. Sagdic; *Foods,* **2021**,*10*, 27-32.
36. J.D. Wicochea Rodriguez; S. Peyron; P.Rigou; P.Chalier; *PLoS ONE,* **2018,***13,* e0207401.
37. S. Agatonovic-Kustrin; P. Ristivojevic; V. Gegechkori; T.M. Litvinova; D.W. Morton; *Appl. Sci.,* **2020**, *10*, 7294.
38. B. Bozin; N. Mimica-Dukic; N. Simin; G. Anackov; *J Agric Food Chem.,* **2006**, *54*,1822–1828.
39. C. Turek; F.C. Stintzing; *Compr. Rev. Food Sci. Food Safety*, **2013**, *12*, 40-53.
40. P. Satyal; B.L. Murray; R.L. Mcfeeters; W.N. Setzer; *Foods*, **2016**, *5*, 70-75.
41. A.K. Al-Asmari; T. Athar; A.A. Al-Faraidy; M.S. Almuhaiza; *Asian Pac. J. Trop. Biomed.,* **2017**, *7*, 147–150.
42. J. Kula; T. Majda; A. Stoyanova; E. Georgiev; *J. Essent. Oil Bear Plant.,* **2007**, *10*, 215-220.
43. X. Stoilova; S. Bail; G. Buchbauer; A. Krastanov; A. Stoyanova; E. Schmidt; et al ; Bosnia *Nat. Prod. Commun.*, **2008**, *3*, 1043-1046.
44. Salamon; P. Petruska; *Indian J.Pharmaceut.Educ. Res.,***2017**, *51*, S479-S482.
45. S. Falcãoa; I. Bacémb; G. Igrejasb; P.J. Rodriguesc; M. Vilas-Boasa; J.S. Amarala; *Ind Crops & Prod.,* **2018**,*124*, 878–884.
46. I. Amri; E. Mancini; L. De Martino; A. Marandino; H.Lamia; H. Mohsen; J. Bassem; M. Scognamiglio; E. Reverchon; V. De Feo; *Int.J.Mol.Sci,* **2012**, *13,* 16580-16591.
47. D. Gallart-Mateua; C.D. Largo-Arangoa; T. Larkmanb; S. Garriguesa; M. De La Guardia; *Talanta*, **2018**, 189, 404-410.
48. K. Chaieb; H. Hajlaoui; T. Zmantar; A. Ben Kahla-Nakbi ; M, Rouabhia; K. Mahdouani; *Phytotherapy Res.* **2007**, *21*, 501–506.
49. H. Boughendjioua; *IRJPMS*, **2018**, *11*, 26-28.
50. G. Jayaprakasha; L. Rao; *Crit Rev Food Sci Nutr.* **2011**, *51*, 547-562.

51. K.M. Brodowska; A.J. Brodowska; K. Śmigielski; E. Łodyga-Chruścińska; *Eur J Biol Res.,* **2016**, *6*, 310-316.
52. J. Shao; Y. Zhang; Z. Zhu; *Tropical J. Pharm. Res.,* **2018**, *17*, 1839-1845.
53. W. Zhou; Z. Liang; P. Li; Z. Zhao; J.Chen-Zhou; *Chem. Central J.,* **2018**, *12*, 71-78.
54. R.M. Popa; S. Socaci; A. Farcas; C. Socaciu; *Bull USAMV Food Sci Technol*, **2021**, *78*, 88-100.
55. R.M. Popa; F. Fetea; C. Socaciu; *Molecules*, **2021**, *in press.*
56. AOCS Official Method 14D-99, Rapid Determination of Isolated geometric trans Isomers in fats and oils by Attenuated Total Reflectance Infrared Spectrometry, 7th edition, revised **2020**.
57. M.W. Davey; E. Stals; B. Panis; J. Keulemans; R.L. Swennen; *Anal. Biochem.,* **2005**, *347,* 201–207.
58. V. Nair; C.L. O'Neil; P.G. Wang; *Malondialdehyde, Encyclopedia of Reagents for Organic Synthesis,* John Wiley & Sons, New York, **2008**.

STUDIA UBB CHEMIA, LXVI, 4, 2021 (p. 51-60)
(RECOMMENDED CITATION)
DOI:10.24193/subbchem.2021.4.04

THE INFLUENCE OF SOME TECHNOLOGICAL FACTORS ON THE FUNCTIONAL FOOD CHARACTERISTICS OF CARROTS IN THE HILLY AREA OF TRANSYLVANIA

LUCIAN DORDAI[a,*], CECILIA ROMAN[a], MARIUS ROMAN[a], ANCA NAGHIU[a]

ABSTRACT. The global warming and aridization process in Romania presents zonal risk situations that can strongly affect the production potential and quality of carrot crops. An experiment was designed which follows the effect of technological factors on the quantity and quality of production for three varieties of carrots *(Royal Chantenay, Atomic Red* and *Purple Haze* F_1), under organic cultivation conditions. 18 carrot samples were analyzed to evaluate the antioxidant capacity and total of mineral elements. For the antioxidant capacity a photochemiluminescence methods was used and the Photochem instrument from AnalytikJena togheter the ACL kit and for the total content of mineral elements was used the ICP-MS Elan Drc II Perkin-Elmer. By irrigating the carrot culture, the antioxidant capacity increases by 17.6% compared to the control sample (non-irrigated). Through chemical fertilization and zeolite fertilization of carrot culture, the antioxidant capacity increases by 3.2% and 18.8%, respectively, compared to the control sample (basic fertilization). By irrigating the carrot culture, the total content of mineral elements increases by 14.1% compared to the control sample (non-irrigated). Through chemical fertilization and fertilization with zeolite of carrot culture, the total content of minerals elements increases by 5.5% and 18.9% respectively with the control sample (basic fertilization).

Keywords: *carrots, zeolites, functional foods, fertilization, irrigation, organic farming*

INTRODUCTION

Carrot (*Daucus Carota L.*) is a vegetable and medicinal plant, the most important crop in the Apiaceae family [1]. Carrot root is widely used due to its richness in carotenoids, anthocyanins, dietary fiber, vitamins and other

[a] *INCDO-INOE 2000, Research Institute for Analytical Instrumentation, 67 Donath str., RO-400293, Cluj-Napoca, Romania*
[*] *Corresponding author: lucian.dordai@icia.ro*

nutrients. Carrot extracts, which serve as sources of antioxidants, have important functions in preventing many diseases [4].

Obtaining superior quantitative and qualitative carrot harvests involves using water and fertilizers rationally if it exploits irrigated land as correctly as possible [2].

Natural zeolites are part of a family of natural minerals, of volcanic origin, with three main properties that are of great interest for agricultural purposes: high cation exchange capacity; high water retention capacity in free channels; high adsorption capacity, which make them particularly attractive for use as fertilizers [3,5]. The exploitation and use of zeolites abroad is constantly growing. In the United States, Japan, South Korea, and Western European countries, 300,000 tons of zeolites were used in 1995 [6]. Great successes in the use of natural zeolites in various fields are obtained in Japan, Hungary, Bulgaria. There are more than 60 zeolite deposits in Russia with total projected reserves of clinoptilolite, mordenite and phillipsite of 3.5 billion tons. The trend is for zeolitic volcanic tuffs to become export materials for producing countries. Out of 45 countries that possess deposits of natural zeolites, only in 16 of them have they been exploited, respectively: USA (20 mining operations), Japan (10 mining operations), Russia (4 mining operations), South Korea, China and Yugoslavia, 2 mining operations [7]. In Romania, important deposits of clinoptilolytic tuffs are located in the Transylvanian Depression and in the adjacent basins such as Silvania and Maramureş. Taking into account the extension, thickness and content in zeolites, the most important volcanic tuff deposits in Romania are described as "Tuf de Dej" in the Transylvanian Depression, "Tuf de Slănic" in the Tarcău Unit and the Subcarpathian Depression, "Tuf de Perşani" in the Transylvanian Depression. The volcanic tuff deposits in our country are easily accessible, with possibilities of quarry exploitation. Of the 40 known zeolitic minerals, only six have large reserves and properties needed for practical use [8,14].

The promotion and sustainable use of natural resources is an opportunity to address issues related to food security, quality of life and the environment [9].

To successfully promote this type of agriculture, agricultural producers should meet several requirements and conditions, the most important of which are crop rotation, fertilization, weed and pest control as well as reducing energy consumption [10,13].

The transition of agricultural producers to sustainable agriculture has become a topic of great interest in most countries of the world. In Romania, in order to apply sustainable agriculture, it is necessary to establish certain goals and respect some principles and methods, such as increasing the quality of life in rural areas by increasing incomes from agricultural activities,

expanding more public services and utilities, diversifying certain non-agricultural activities. For now, Romania's agriculture is in a difficult situation, due to poor equipment and machinery, the unstable situation in rural infrastructure, low application of natural fertilizers, but also due to small irrigated areas and soil degradation. In this way, the major problem of agriculture in the future is not to produce more, but to produce sustainably [11,12].

The aim of this study was to identify ecological technological solutions to improve the functional food characteristics of three varieties of carrots: *Royal Chantenay, Atomic Red* and *Purple Haze* F_1 by synergistic use of irrigation and fertilization with natural zeolites. By protecting the environment and within the limits of economic efficiency, the aim was to identify methods to increase the production and quality of carrot cultivation.

RESULTS AND DISCUSSION

The influence of irrigation, fertilization and carrot variety on the antioxidants capacity of carrots

The quality of production of carrots was analyzed in terms of the content of antioxidants - molecules that protect the body from the effects of free radicals. The samples were taken from all experimental variants, on all 3 repetitions, choosing plants from the center and extremities of the experimental plots, diagonally, for each of the three years of experience. The antioxidants content was calculated as the average of the three years of experimentation (2016-2018) and is expressed in ascorbic acid equivalent.

As can be seen in Tables 1, irrigation, chemical fertilization as well as zeolite fertilization had a very significant effect on the antioxidants content of plants.

Table 1. The influence of irrigation, fertilization and carrot variety on the antioxidants capacity of carrots, 2016- 2018

Experimental condition	Antioxidant capacity (µg/mgTrolox)	Relative production (%)	Difference (µg/mg Trolox)	Significance
Not irrigated	235.26	100.0	0.00	Control sample
Irrigated	276.75	117.6	41.50	[a] ***
Basic Fertilization	238.53	100.0	0.00	Control sample
Chemical fertilization	246.07	103.2	7.54	***
Fertilization with zeolite	283.41	118.8	44.88	***
Royal Chantenay	24.22	100.0	0.00	Control sample
Atomic Red	25.19	104.0	0.98	[b] *
Purple Haze F_1	718.60	2967.4	694.38	***

[a] *** - very significant effect; [b] * - significant positive effect

The analysis of the results in Table 1 shows that for the carrot culture carried out under irrigation conditions, the antioxidant content increases by 17.6% compared to the control sample (non-irrigated). Through chemical fertilization and zeolite fertilization of carrot culture, the antioxidant capacity increases by 3.2% and 18.8%, respectively, compared to the control sample (basic fertilization). *Purple Haze F_1* show a very significant effect in antioxidant capacity compared with *Royal Chantenay* and *Atomic Red.*

The analysis of the results from Table 2 on the influence of the interactions between factors A x B x C, irrigation regime x fertilization x carrot variety at the carrot harvest, in the environmental conditions from Aiton - Cluj, between 2016 and 2018, indicated that the irrigation regime and fertilizers applied during the period of plant growth had a significant

Table 2. The effect of the interaction of the three technological factors on the carrot antioxidant content, 2016-2018

Experimental condition	Antioxidant capacity (µg/mgTrolox)	Relative production (%)	Difference (µg/mg Trolox)	Significance
[a]a_1 x [b]b_1 x [c]c_1	19.37	100.0	0.00	Control sample
[d]a_2 x b_1 x c_1	21.60	111.5	2.23	[i] -
a_1 x b_1 x [e]c_2	19.80	100.0	0.00	Control sample
a_2 x b_1 x c_2	22.40	113.1	2.60	-
a_1 x b_1 x [f]c_3	622.10	100.0	0.00	Control sample
a_2 x b_1 x c_3	725.90	116.7	103	[j] ***
a_1 x [g]b_2 x c_1	22.43	100.0	0.00	Control sample
a_2 x b_2 x c_1	25.50	113.7	3.07	[k] *
a_1 x b_2 x c_2	24.30	100.0	0.00	Control sample
a_2 x b_2 x c_2	26,60	109.5	2.30	-
a_1 x b_2 x c_3	632.60	100.0	0.00	Control sample
a_2 x b_2 x c_3	745.00	117.8	112.0	***
a_1 x [h]b_3 x c_1	27.23	100.0	0.00	Control sample
a_2 x b_3 x c_1	29.17	107.1	1.93	-
a_1 x b_3 x c_2	26.83	100.0	0.00	Control sample
a_2 x b_3 x c_2	31.23	116.4	4.40	**
a_1 x b_3 x c_3	722.63	100.0	0.00	Control sample
a_2 x b_3 x c_3	863.37	119.5	140.3	***

[a]a_1- not irrigated; [b]b_1-basic fertilization; [c]c_1- *Royal Chantenay*; [d]a_2-irrigated; [e]c_2-*Atomic Red*; [f]c_3-*Purple Haze F_1*; [g]b_2-chemical fertilization; [h]b_3-fertilization with zeolite; [i] - statistically positive; [j] ***-very significant effect; k*- significant positive effect.

influence on the content of antioxidants recorded in the experimental fields of the crop, which involves the recommendation for the application of irrigation and fertilization to obtain a quality production.

The influence of irrigation, fertilization and carrot variety on the total content of minerals element

The quality of production was analyzed in terms of the total content of minerals element of carrots which are biologically active substances, non-caloric, but which ensure the normal function of all cells and tissues of the body.

As can be seen in the Table 3, irrigation as well as all fertilization options had a very significant effect on the mineral content of plants. Through chemical fertilization and fertilization with zeolite of carrot culture, the total content of minerals elements increases by 5.5% and 18.9% respectively with the control sample (basic fertilization). *Atomic Red* and *Purple Haze F_1* had a very significant negative effect in total content of minerals element compared with *Royal Chantenay.*

Table 3. The influence of irrigation, fertilization and carrot variety on the total content of minerals element, 2016- 2018

Experimental condition	Total content of minerals element (mg/kg)	Relative production (%)	Difference (mg/kg)	Significance
Not irrigated	8711.55	100.0	0.00	Control sample
Irrigated	9937.04	114.1	1225.49	[a]***
Basic fertilization	8623.63	100.0	0.00	Control sample
Chemical fertilization	9069.54	105.5	472.91	***
Fertilization with zeolite	10252.71	118.9	1629.07	***
Royal Chantenay	10377.57	100.0	0.00	Control sample
Atomic Red	9321.27	8.,8	-1056.30	[b]000
Purple Haze F_1	8274.05	79.7	-2103.52	000

[a] ***- very significant effect; [b]000- very significant negative effect

The analysis of the results in Table 4 indicates that the irrigation regime and fertilizers applied during the plant growth period had a very significant influence on the total mineral content recorded in the experimental fields of the crop.

Table 4. The effect of the interaction of the three technological factors on the total content of minerals element, 2016-2018

Experimental condition	Total content of minerals element (mg/kg)	Relative production (%)	Difference (mg/kg)	Significance
[a]a_1 x [b]b_1 x [c]c_1	8878.23	100.0	0.00	Control sample
[d]a_2 x b_1 x c_1	10058.77	113.3	1180.53	[i]***
a_1 x b_1 x [e]c_2	8103.03	100.0	0.00	Control sample
a_2 x b_1 x c_2	9181.97	113.3	1078.93	***

Experimental condition	Total content of minerals element (mg/kg)	Relative production (%)	Difference (mg/kg)	Significance
$a_1 \times b_1 \times {}^{f}c_3$	7245.10	100.0	0.00	Control sample
$a_2 \times b_1 \times c_3$	8274.70	114.2	1029.60	***
$a_1 \times {}^{g}b_2 \times c_1$	9516.90	100.0	0.00	Control sample
$a_2 \times b_2 \times c_1$	10847.40	114.0	1330.50	***
$a_1 \times b_2 \times c_2$	8512.30	100.0	0.00	Control sample
$a_2 \times b_2 \times c_2$	9541.97	112.1	1029.67	***
$a_1 \times b_2 \times c_3$	7578.67	100.0	0.00	Control sample
$a_2 \times b_2 \times c_3$	8582.03	113.2	1003.37	***
$a_1 \times {}^{h}b_3 \times c_1$	10673.70	100.0	0.00	Control sample
$a_2 \times b_3 \times c_1$	12290.40	115.1	1616.70	***
$a_1 \times b_3 \times c_2$	9587.03	100.0	0.00	Control sample
$a_2 \times b_3 \times c_2$	11001.430	114.8	1414.27	***
$a_1 \times b_3 \times c_3$	8308.97	100.0	0.00	Control sample
$a_2 \times b_3 \times c_3$	9654.83	116.2	1345.87	***

[a]a_1- not irrigated; [b]b_1-basic fertilization; [c]c_1- Royal Chantenay; [d]a_2-irrigated; [e]c_2-Atomic Red; [f]c_3-Purple Haze F1; [g]b_2-chemical fertilization; [h]b_3-fertilization with zeolite; i - very significant effect.

Determination of heavy metal content in carrot samples

The effect of the interaction of the three technological factors on the content of heavy metals (mg / kg) in carrots (Table 5) is different.

The content of heavy metals: Pb, Cd, Cu, Zn, As, Hg was studied in the carrot samples from the experimental field Aiton, Cluj County, specifying the level of dangerous concentration in relation to the maximum allowed concentrations of heavy metals in food products, according to Order no. 640 of September 19, 2001 published in the OFFICIAL MONITOR no. 173 of March 13, 2002, on the safety and quality conditions for fresh vegetables and fruits intended for human consumption [15].

With, Cd, Zn are more concentrated in plants of the *Royal Chantenay* variety, the irrigated-chemically fertilized system.

Pb, As are more concentrated in plants of the *Purple Haze F_1* variety, the irrigated-basic fertilization system.

Table 5. Heavy metal content of carrot samples

Experimental condition	Pb	Cd	Cu	Zn	As	Hg
$a_1 \times b_1 \times c_1$	0.08	0.22	10.10	34.50	0.05	<0.05
$a_2 \times b_1 \times c_1$	0.1	0.21	9.80	32.7	0.05	<0.05
$a_1 \times b_1 \times c_2$	<0.05	<0.05	5.72	11.44	0.07	<0.05
$a_2 \times b_1 \times c_2$	<0.05	<0.05	5.43	12.11	0.06	<0.05
$a_1 \times b_1 \times c_3$	0.26	<0.05	9.29	22.13	0.12	<0.05
$a_2 \times b_1 \times c_3$	0.45	0.11	7.80	23.21	0.26	<0.05

Experimental condition	Pb	Cd	Cu	Zn	As	Hg
$a_1 x b_2 x c_1$	0.12	0.29	11.20	48.1	0.06	<0.05
$a_2 x b_2 x c_1$	0.12	0.31	10.27	47.30	0.05	<0.05
$a_1 x b_2 x c_2$	<0.05	<0.05	4.85	10.10	0.06	<0.05
$a_2 x b_2 x c_2$	0.21	0.21	6.23	33.20	0.05	<0.05
$a_1 x b_2 x c_3$	0.24	0.12	8.10	21.45	0.04	<0.05
$a_2 x b_2 x c_3$	0.32	<0.05	4.50	19.83	0.10	<0.05
$a_1 x b_3 x c_1$	0.09	0.11	6.78	35.76	0.06	<0.05
$a_2 x b_3 x c_1$	0.10	0.09	5.44	32.19	0.07	<0.05
$a_1 x b_3 x c_2$	0.19	0.16	5.80	28.45	0.05	<0.05
$a_2 x b_3 x c_2$	0.20	0.17	6.05	27.54	0.04	<0.05
$a_1 x b_3 x c_3$	0.28	0.07	4.32	22.34	0.06	<0.05
$a_2 x b_3 x c_3$	0.10	0.04	3.21	15.33	0.03	<0.05
CMA	0.5	0.2	-	-	-	0.03

CONCLUSIONS

The analysis of the results for the period 2016-2018 shows that for the carrot culture carried out under irrigation conditions, the antioxidant capacity increases by 17.6% compared to the control sample (non-irrigated).

Through chemical fertilization and zeolite fertilization of carrot culture, the antioxidant capacity increases by 3.2% and 18.8%, respectively, compared to the control sample (basic fertilization).

Purple Haze F_1 show a very significant effect in antioxidant capacity compared with *Royal Chantenay* and *Atomic Red.*

Throughout the research period, irrigation as well as all fertilization options had a very significant effect on total content of minerals elements of the plants.

Through chemical fertilization and fertilization with zeolite of carrot culture, the total content of minerals elements increases by 5.5% and 18.9% respectively with the control sample (basic fertilization).

Atomic Red and *Purple Haze* F_1 show a very significant negative effect in minerals element compared with *Royal Chantenay*.

EXPERIMENTAL SECTION

The experiments were performed in the hilly area of Transylvania, Aiton locality (46 ° 31 'and 46 ° 31' northern latitude; 23 ° 40 'and 23 ° 48' east longitude) containing 3 repetitions, 18 variants, 54 experimental plots. The comparative cultures were ordered in a multifactorial system, completely randomized, with subdivided plots.

The experimental factors studied were: irrigation regime - with two experimental variants (non-irrigated / irrigated), fertilization, with three experimental

variants (basic fertilization / chemical fertilization / zeolite fertilization) and carrot variety, with three experimental variants (*Royal Chantenay, Atomic Red and Purple Haze F_1*) (table 6).

The experiments contained a number of 3 repetitions (n = 3), the number of variants analyzed in the experiment was 18 (v = 2 x 3 x 3), the total number of experimental plots was 54 (18 x 3). We opted for a rectangular shape of the test plots (90x60 cm). The comparative cultures were ordered in a multifactorial system, completely randomized, with subdivided plots.

For the statistical analysis of the results, the POLIFACT statistical program was used - analysis of variance for completely randomized multifactorial experiments. As witnesses in the statistical analysis, a_1 (non-irrigated) was used for irrigation, b_1 (basic fertilization) for fertilization, c_1 (*Royal Chantenay*) for the carrot variety.

Table 6. Experimental factors and experimental variants

The factors studied	Experimental variants
Factor A Irrigation regime	a_1 – not irrigated
	a_2 – irrigated
Factor B Fertilization	b_1 – basic fertilization
	b_2 – chemical fertilization
	b_3 – fertilization with zeolite
Factor C Carrot variety	c_1 – *Royal Chantenay*
	c_2 – *Atomic Red*
	c_3– *Purple Haze F_1*

Methods and equipment used to determine the content of heavy metals and minerals

Instrumentation used: • Microwave digester Berghoff MWS-3+ (Eningen, Germania) • ICP-MS ELAN DRC II Perkin-Elmer

Reagents and materials used: • 65% HNO_3 (Merck, Germany); • H_2O_2 30% analytical purity (Merck, Germany); Multi-element stock solution 1000 mg / l (Merck, Darmstadt, Germany); • Ultrapure water, Milli-Q (Millipore, Bedford, MA, USA).

Procedure: Three replicates of 0.5 g of sample (dried at 40 ° C, ground and homogenized) were subjected to microwave digestion with 8 ml of 65% HNO_3 and 3 ml of 30% H_2O_2. After cooling to ambient temperature, the sample was diluted to 25 ml with ultrapure water, then filtered through a 0.45 µm cellulose membrane filter. The control samples were prepared analogously. Concentrations of total content of minerals in mineralized solutions were determined using ICP-MS. To verify the performance of the proposed method,

the sensitivity of the method was studied by determining and calculating the detection and quantification limits.

Methods and equipment used to determine total antioxidant capacity.

Instrumentation used • Plastic tubes; • Test tubes with 50 ml for centrifuge; • Photochem Analytics Jena; • Single-channel automatic pipettes (500-5000 µl, 100-1000 µl, 10-100 µl); • Centrifuge D-78532 HETTICH - Germany.

Reagents and materials used: • ACW kit consisting of: dilution solution for water-soluble samples, buffer solution, photosensitizer solution, standard antioxidant solution; • ACL kit consisting of: buffer solution, photosensitizer solution, standard antioxidant solution; • Methanol; • Ultrapure water

Procedure: Carrot samples for *Atomic Red, Purp Haze* F_1 and *Royal Chantenay* were analyzed. After homogenization and crushing, the carrot samples were extracted using methanol. The mixture was centrifuged at 3500 RPM for 8 minutes and analyzed using the Photochem instrument from Analytik Jena together with the ACL (Antioxidative Capacity of the Lipid Soluble Compounds) kit. Antioxidant capacity was expressed as Trolox equivalent. The determinations were performed according to the ACL kit.

For the statistical analysis of the results, the POLIFACT statistical program was used - analysis of variance for completely randomized multifactorial experiments.

ACKNOWLEDGMENTS

This research was funded by the Romanian Ministry of Research and Innovation, CCCDI-UEFISCDI, project number-18N/08.02.2019/PNCDI III.

REFERENCES

1. N.Y. Paniagua, Z. Rainer, C. Romero, *Ethnobotany of the Andes*, **2020**,1-8.
2. D.D. Carvalho, D.D.O. Neto, J.G.M. Guerra, J.R.C. Rouws, F.D.L Oliveira, *Revista Brasileira de Engenharia Agrícola e Ambiental*, **2018**, *22(7),* 445-450.
3. T. Melkon, M. Gunther, K.H. Stefan, *Micropor. Mesopor. Mat.,* **2018**, *264*, 70-75.
4. N.J. Hendrik, T. Wherle, C.C. Claus, *Food Qual. Prefer.,* **2019**, *72*, 98-108.
5. S. Wang, Y. Peng, *Chem. Eng. J.*, **2010**, *156*, 11-24.
6. C.J. Rhodes*, Sci. Prog.*, **2010**, *93(3)*, 223-284.
7. C.S. Colin, A.C. Paul, *Chem. Rev.*, **2003**, *103(3)*, 663–702.
8. J.J. Cochemé, P.J. Leggo, G. Damian, A. Fulop, B. Ledesert, O. Grauby, *Clays Clay Miner.*, **2003**, *51(6)*, 599–608.

9. M.I. Ardeleanu, *Sustainability,* **2016**, *8(3)*, 245.
10. R.V. Ionescu, M.L Zlati, V. M. Antohi, S. Stanciu, Florina O. Virlanuta, C. Serban, *Sustainability,* **2020**, *12(10)*, 4182.
11. C.V. Radulescu, I. Ioan, *The USV Annals of Economics and Public Administration,* **2015**, *15*, 1(21).
12. L.Scutaru, *Quality – Access to Success*, **2013**, *15 (10)*, 25-31
13. F.Bran, *Ecoforum,* **2014,** *2(1)*, 35-40.
14. I.Seghedi, A. Szakács, I. Vanghelie, C. Costea, *Romanian J. Mineral Deposits*, **2000**, *80*, 11-20.
15. ****Ordinul nr. 640 din 19 septembrie 2001 Publicat în MONITORUL OFICIAL nr. 173 din 13 martie 2002, privind condiţiile de securitate şi calitate pentru legume şi fructe proaspete destinate consumului uman*.

STUDIA UBB CHEMIA, LXVI, 4, 2021 (p. 61-76)
(RECOMMENDED CITATION)
DOI:10.24193/subbchem.2021.4.05

EVALUATION OF THE LEVEL OF CONTAMINATION WITH PHTHALATES IN DAIRY PRODUCTS FOUND ON THE ROMANIAN MARKET

ALINA IOANA FĂT[a,*], SORIN DANIEL DAN[a,*], ALEXANDRA TĂBĂRAN[a], GABRIELA VALENTINA VESA[a], FILIPPOS GEORGIOS NIKOLAOU[a], EMŐKE DALMA KOVÁCS[b], CECILIA ROMAN[b], MELINDA HAYDEE KOVÁCS[b], ROMOLICA MIHAIU[c], MARIAN MIHAIU[a]

ABSTRACT. Human exposure to phthalates (artificial phthalic acid esters) is ubiquitous because of the widespread use of these chemicals in consumer and industrial products. The aim of this study was to determine the presence and amount of the phthalates in milk and dairy products collected in Romania. Samples were gathered at several stages during the production, primary production (farm), milk collection center and retail level. Six types of phthalates were assessed by gas chromatography with mass spectrum detection (GC-MS, of which only 4 were detected in the samples - di-n-butyl phthalate (DBP), di-2-ethylhexyl phthalate (DEHP), di-n-octyl phthalate (DOP) and dibutylbenzyl phthalate (BBP). The obtained concentrations ranged between 0.060 – 0.298 mg/kg for DEHP, in raw milk samples and 0.038 - 0.173 mg/kg respectively, in commercial milk. DMP and DEP were not detected in any sample. The lowest quantity of phthalates was detected in yogurt with 0.1% fat – 0.042 mg/kg, and the largest amount was recorded in butter with 75% fat – 0.683 mg/kg. The level of total phthalates in all samples analysed did not exceed the maximum permitted limit of 60 mg/kg.

Keywords: *phthalates, milk, dairy products, GC-MS*

INTRODUCTION

Phthalates (PAEs) are esters of phthalic acid which are a class of chemicals with a wide use, since 1930. These substances are commonly used as plasticizers - additions to polymers (plastics, rubber, paints) designed to

[a] *Department of Animal Production and Food Safety, University of Agricultural Sciences and Veterinary Medicine, Faculty of Veterinary Medicine, 3-5 Mănăştur Street, 400372, Cluj-Napoca, Romania*
[b] *INCDO-INOE 2000, Research Institute for Analytical Instrumentation, Cluj-Napoca, Romania*
[c] *Babes-Bolyai University Faculty of Economics and Business, Teodor Mihali nr. 58-60, 400591 Cluj Napoca, Romania*
[*] *Corresponding authors e-mail: fat.alinaioana@yahoo.com, sorindan@usamvcluj.ro*

impart polymers (PVC) plasticity, extensibility and tear resistance. They are also used as solvents, lacquers, resins, or surfactants, alcohol denaturants in cosmetics, perfumes, pesticides, etc. [4, 8, 35].

Phthalates are compounds synthesized by double esterification of 1.2-benzenedicarboxylic acid (phthalic acid) with linear or branched alcohols [40].

These substances are classified into two groups: low-molecular-weight phthalates such as di-n-butyl phthalate (DBP) or benzyl butyl phthalate (BBP), and high-molecular-weight phthalates such as diisodecyl phthalate (DIDP) or diisononyl phthalate (DINP) [37].

Depending on the molecular weight, they can be used in various industrial applications. Low molecular weight phthalates, such as diethyl phthalate (DEP) and dibutyl phthalate (DBP), benzyl butyl phthalate (BBP) are used in personal care and hygiene products (as solvents and fixation agents in perfumes, in the preparation of shampoos, soaps, lotions, cosmetics, and softeners, or added as plasticizers of cellulose acetate), in the process industry (e.g., production of lacquers, paints, lubricating oils, adhesives, inks, waxes, insecticides) and also in the pharmaceutical industry (in some drugs, it is used to regulate the release speed) [38, 40].

On the other hand, high molecular weight phthalates, such as bis(2-ethylhexyl) phthalate (DEHP), diisononyl phthalate (DINP), and di-n-octyl phthalate (DnOP) are mainly used as plasticizers in the production of vinyl, which is often used in products such as flooring and wall covering or another construction materials, clothing and furnishings, toys, food packing, and medical devices [39, 40]. The plasticizing phthalates, which also include diisodecyl phthalate (DIDP), dimethyl phthalate (DMP), diethyl phthalate (DEP), dibutyl phthalate (DBP), and benzyl-butyl phthalate (BBP), are used as intermolecular lubricants conferring hardness, flexibility, malleability, and elasticity [3, 25, 31, 35, 40].

At room temperature, phthalates are oily liquids with low volatility and varying miscibility with polymers. Their addition reduces intermolecular interactions and increases the mobility of polymer chains [37, 40, 42]. Their solubility in water decreases with an increase in the length of the carbon chain or molecular weight [37].

The chemical and physical properties vary with the structure, with the length of the chain and the branches. They are generally colorless, odorless and lipophilic, they have a weak solubility in water and a satisfactory solubility in most organic solvents. Also, these substances show a high boiling point and a low vapor pressure, both parameters influencing their high stability and presence in the environment [37, 40, 42].

Humans can be exposed to phthalates after ingestion of food or water (orally), from the air (inhalation - indoor/outdoor air, hair/paint sprays), through

dermal contact (personal care products, toys, textiles, gloves, paints/adhesives, and dust particles) or parenteral application [7, 43]. Phthalates have been detected in environmental samples like rainwater, water, soil and sediments, indoor air or dust and aquatic systems, being considered ubiquitous substances in the environment [2, 3, 51].

The highest human exposure to phthalates comes from food, especially by those with high fat content which accumulates phthalates [18, 21, 30]. Due to their lipophilic nature, phthalates may also lead to accumulation from the feed and the environment in animal tissues, muscle, fat, and also the phthalates may pass through the digestive tract in the milk, which leads to another potential threat chain of the consumer [18, 23].

From the environmental point of view, phthalates have a duration of several hours in the atmosphere and of months in the soil, whereas they can persist for years in sediments [46]. They can bioaccumulate in invertebrates, fish, and plants, whereas in complex animals they are efficiently metabolized and excreted. This last consideration is very important because the possible presence of phthalates in tissues [47] indicates a very recent exposure/ contamination [23, 41, 47].

Once they enter the body, phthalates undergo a series of phase I hydrolysis and phase II conjugation reactions and are subsequently excreted in feces and urine [44, 48, 49]. In the first step, diester phthalate are hydrolysed to monoester in a process catalysed by lipases and esterases in the intestines or other tissues. While this step for xenobiotic in most of the cases bring to a detoxification, in such a case leads phthalates to become more bioactive as monoester. The second phase of metabolism, conjugation, is often catalysed by enzyme UDP-glucuronosyl-transferase to form the hydrophilic glucuronide conjugate, and the conjugates are easily excreted into urine [45].

Because phthalates have a short half-life in human bodies and are excreted quickly in urine as monoester metabolites, the metabolites are suitable biomarkers for human exposure to parent compounds. The half-life of phthalates in human bodies (in plasma and urine) is less than 24 h, and following metabolism, monoesters of phthalates are conjugated with glucuronide or sulfate and excreted in urine [50].

Phthalates do not form covalent bonds with the polymers they are mixed with. Therefore, they can freely migrate to the surface of products and further into food and beverages in contact with these surfaces. As a result, they can easily escape and spread to the environment during the production and the utilization of products that contain them [42].

Also, phthalate esters may migrate into foods during food processing and storage in plastic packing materials [11, 20, 35]. For instance, bottled milk, as well as milk products, can be contaminated with phthalates in several

ways: through water, air or soil, also during the bottling process or migration from packing material to milk or milk products, absorption from PVC tubing to raw milk during milking on dairy farms, etc. [1, 12, 21].

Moreover, due to their low vapor tension, phthalates are easily evaporated and diffuse into the atmosphere; they are trapped in aerosols and, through rainfall, end up in receiving water bodies and soil. As a result, the phthalates have been detected in samples taken from sewage, air, surface water, soil, and aquatic organisms [2, 3, 51].

Consequently, this has led to their widespread dispersion into the environment, providing an easy source of human exposure by inhalation, ingestion, dermal absorption, or even intravenous route [42].

In a literature review, Cao Xu-Liang [3], identified various sources of phthalate food contamination, including PVC tubing used in food production, food packaging films (also known as wrapping or cling films), PVC gaskets in jars, printer ink on labels, and other sources.

Many plasticizers and additives are listed as suspected endocrine disrupters or mutagens, which can have adverse effects on human health even at low levels. Several phthalates are able to act as anti-androgens, estrogens, anti-estrogens or inhibitors of steroidogenic enzymes and are able to act with thyroid hormones and their receptors through interaction, as well as within the brain and the immune system [20,15].

Due to the chemical composition (vitamins, minerals, carbohydrates, lipids, and proteins) milk is considered one of the most nutritionally complete natural foods [17, 28]. Also, many specialized milk products such as cheese, yogurt, butter, cream or ice cream are popular in diets worldwide. However, most commercial milk and milk products are packaged in plastic or other polymer materials. Therefore, it is extremely important for human health protection to evaluate and monitor phthalates in this type of products [20].

To guarantee human health, the European Union established limits for many compounds used in packaging and established regulations, specifying migration tests using food simulants to determine their probable migration into food. The EU fixed Specific Migration Limits (SMLs) for single contaminants or group of contaminants in Regulation 10/2011. These values are in particular 0.3 mg/kg food simulant (fs) for DBP, 30 mg/kg fs for BBP, 1.5 mg/kg fs for DEHP. For compounds for which there are not SML, a restriction value of 60 mg/kg of food product is applied. For containers and other articles, for sheets and films in contact with less than 500 mL or g or more than 10 L and for materials and articles for which it is not possible to estimate the relationship between the surface area of such materials and the quantity of food in contact, the SML are expressed in mg/kg applying a surface to volume ratio of 6 dm^2 per kg of food. Overall, the plastic packaging

must not be released to food simulants more than 10 mg of all compounds in one dm^2 of contact surface between food and packaging (Overall Migration Limit or OML) [6].

For infants and small children which have a higher consumption of food per kilogram bodyweight than adults and do not yet have a diversified nutrition, special provisions should be set in order to limit the intake of substances migrating from food contact materials.

Based on these findings, a careful analysis of these endocrine disrupters is mandatory, in order to respect the food safety legislation [34].

There are two main reasons to study the contamination of milk with phthalates. Firstly, especially for children, milk is a significant consumer product. In order to quantify the phthalate amount that humans are exposed to by means of their dietary, it is important to know the phthalate content of such food products.

Secondly, phthalates are likely to be concentrated in the lipid phase of the foods due to their lipophilic characters. Since dairy products like milk and other products can be classified as high-fat foods, they have higher tendency to be contaminated by phthalates than low-fat content foods.

In Romania, phthalate esters assessment was performed mainly on bottled water [9, 26, 29]. Regarding our knowledge, no literature is available dealing with the contamination levels of dairy products packaged in plastic containers. There is only a single study performed on milk by Miclean *et al.* (2012), where determined phthalates esters were DBP and DEHP.

Given the lack of knowledge regarding the level of phtalates in dairy products produced in Romania and the importance of this subject, our aim was to investigate a particular milk production chain and to evaluate the extent of this chemical hazard.

RESULTS AND DISCUSSION

The levels of phthalates detected in milk samples are shown in Table 1. These were calculated as the average means of concentrations obtained for the same analyzed milk samples. Only 4 out of the six phthalates taken into study were present in the samples.

In the case of commercial milk, the highest concentration of phthalates (DOP), respectively 0.3152±0.2441 mg/kg, was found in a milk sample with 3.5% fat content and the lowest, of 0.0201±0.0349 mg/kg (DBP) was determined in the case of milk samples with 1.5% fat content (Table 1).

Based on statistical analyses, significant differences regarding the level of phthalates were calculated only in the case of raw milk 4% fat content, when compared BBP and DEHP ($p=0.008$) (Table 1). Higher total

phthalates levels were observed in the case of raw milk with 4%, followed by pasteurized milk with 3.5%, raw milk with 3.5%, and pasteurized milk with 1.5% fat content. Significant differences were noticed only when compared raw milk with 4% versus pasteurized milk with 1.5% (p=0.01). Thus, between the level of total phthalates and fat content there is direct correlation (Table 1).

Table 1. Phthalate esters level (mean ±SD, mg/kg) in raw and pasteurized milk samples (n=5)

Milk samples	BBP	DEHP	DOP	DBP	DMP	DEP	Total phthalates
Control sample	<LOD	<LOD	<LOD	<LOD	<LOD	<LOD	<LOD
Raw milk 3.5%	0.104± 0.018	0.1454±0 1057	0.1005± 0.0222	0.497± 0.06	<LOD	<LOD	0.3996± 0.085
Raw milk 4%	0.1115± 0.0155	0.1685±0 0773*	0.2172± 0.2284	0.0573± 0.0632	<LOD	<LOD	0.5678± 0.2687
Pasteurized milk 1.5%	0.0352± 0.0601	0.1277±0 0485	0.099± 0.0992	0.0201± 0.0349	<LOD	<LOD	0.2818± 0.1756
Pasteurized milk 3.5%	0.0794± 0.0701	0.1075±0 0605	0.3152± 0.2441	0.0224± 0.0388	<LOD	<LOD	0.5245± 0.3301

* Significant differences between BBP, DEHP, DOP and DBP ($p<0.05$)

For milk products, analyses were made from the following ingredients: sour cream, yogurt, different types of cheese (fresh, salted, ripened, cream), cream, ice cream and butter. The results of phthalates from the investigated milk products are presented in Table 2.

In the case of sour cream, the highest concentration of phthalates (DMP) respectively 0.0831±0.0214 mg/kg, was found in a sample with 20% fat. By comparison of the values obtained for sour cream samples, significant differences were observed for BBP (p=0.035) and DOP (p=0.0089). In the yogurt samples, the only significant difference was observed by comparing the total amount of phthalates (p=0.001) (Table 2).

For fresh fat cheese, based on statistical analyses, significant differences regarding the level of phthalates were calculated when compared BBP and DEHP (p=0.002), BBP and DOP (p=0.00074), respectively BBP and DBP (p=0.006). Higher total phthalates levels were observed in the case of maturated cheese (0.5905±0.0175 mg/kg), followed by burduf cheese (kneaded cheese), cream cheese, fresh fat cheese and telemea cheese. When comparing telemea cheese with cream cheese and burduf cheese, significant differences were noticed only for total phthalates (p=0.00001) (Table 2).

Following analyses, the lowest quantity of total phthalates was detected in yogurt with 0.1% fat - 0.042±0.0052 mg/kg, and the highest concentration was recorded in butter with 85% fat - 0.683±0.0072 mg/kg (Table 2).

Table 2. Phthalate esters level (mean ±SD, mg/kg) in different dairy products (n=5)

Dairy product	BBP	DEHP	DOP	DBP	DMP	DEP	Total phthalates
Sour cream 20%	0.0315±0.0027	0.0672±.0007*	0.062±0.0031*	0.0831±0.0214*	<LOD	<LOD	0.244±0.0225
Sour cream 33%	0.0541±0.0122	0.0729±.0058	0.0224±.0139*	0.0819±0.0177	<LOD	<LOD	0.231±0.0251
Yogurt 0.1%	<LOD	0.0185±.0038	<LOD	0.0237±0.0015	<LOD	<LOD	0.042±0.0052
Yogurt 2%	0.0135±0.0042	0.0180±.0062	0.0279±.0137	0.0431±0.0154*	<LOD	<LOD	0.102±0.012
“Telemea” cheese	0.0224±0.0048	0.0052±.0001*	0.034±0.0062	0.0568±0.0044*	<LOD	<LOD	0.118±0.0031
Cream cheese	0.0873±0.0147	0.1106±.0123	0.1620±.0147*	0.1164±0.0105*	<LOD	<LOD	0.4764±0.0228
Maturated cheese	0.1301±0.0122	0.1324±.0043	0.1707±.0215*	0.1573±0.0225	<LOD	<LOD	0.5905±0.0175
Fresh fat cheese	0.0642±0.0068	0.1079±.0088*	0.1322±.0101*	0.1407±0.024*	<LOD	<LOD	0.4451±0.029
Burduf cheese	0.0887±0.0225	0.1562±.0179*	0.1446±.0106*	0.1216±0.0049	<LOD	<LOD	0.5112±0.0216
Raw cream	0.1399±0.0127	0.2321±.0278*	0.1796±.023	0.1173±0.021	<LOD	<LOD	0.669±0.0426
Ice cream	<LOD	0.0431±.0096	0.0713±.0065*	0.0611±0.013	<LOD	<LOD	0.1755±0.0099
Butter	0.1455±0.0174	0.1854±.0182	0.2122±.0147*	0.139±0.023	<LOD	<LOD	0.683±0.0072

* Significant differences between BBP, DEHP, DOP and DBP ($p<0.05$) for each dairy product analysed. Among the six phthalates examined, DEHP was the most commonly detected phthalate compound, followed by DOP, BBP and DBP. Two phthalates, DMP and DEP, were not detected in any sample.

For the last three decades, various researchers have reported phthalate levels in milk and dairy products. Fierens *et al.* (2013), for example, mentioned in their review more studies conducted between 1985 and 2012, to investigate the presence of phthalates in milk and dairy products. Other researchers also continued analyzing phthalates in these types of food [2, 3, 10, 16, 19, 33].

In most of the studies, phthalate levels were determined in retail milk and dairy products while only a few surveys reported phthalate concentrations in raw milk and/or in samples collected from dairy factories. However, in

order to reduce the risk of phthalate contamination of milk or dairy products, it is important to know how these compounds can enter into milk during the technological stages of milk processing. Therefore, phthalates should not only be investigated at the retail level, but also at other stages of milk processing. [13].

Studies also demonstrated that milk and dairy products are contaminated with phthalates (especially DEHP) during collection due to the use of flexible milking tubes [5, 12, 27].

In a subsequent study, Fierens *et al.* (2013), evaluated how the quantity of phthalates increases with the milk processing and packaging. The authors revealed that during pasteurization, the DEHP content in milk increased from 364 μg/kg^{-1} fat (mean level) in raw milk to 426 μg/kg^{-1} fat and the reason of this increase was most likely due to DEHP containing food contact materials (tubings and sealants). The DEHP migration might have been facilitated by increasing temperature during pasteurization. After packaging, the level further increased to 630 μg/kg^{-1} fat in cans and to 523 μg/kg^{-1} fat in plastic pouches. DBP was detected only at the point just before packaging (32 μg/kg^{-1} fat) and after packaging the concentrations increased to 52 and 60 μg/kg^{-1} fat, respectively, when packaged in cans and in pouches. BBP was detected only in milk after packaging at 12 μg/kg^{-1} fat in cans and 53 μg/kg^{-1} fat in pouches. The possible sources of the contamination were labelled as mechanical milking process and intake of the feed by the cattle [14].

In a comprehensive study conducted by Wendi *et al.* (2009) in 3 European countries (UK, Norway and Spain), DEHP and total phthalate esters were determined in milk obtained during different stages of collection, transportation and packaging and also cream, butter and cheese samples. The author reported that after processing the milk contaminated with DEHP, the dairy products obtained lead to high concentrations of DEHP, while low-fat milk while maintaining lower concentrations of phthalates. The same authors added that the total levels of contamination in the raw milk were between 0.12 – 0.28 mg/kg. They suggested that on processing the DEHP phthalate is concentrated in the cream at levels up to 1.93 mg/ kg, whereas low fat milk contained from 0.01 to 0.07 mg/kg. In the cheese samples collected from the UK, the maximum allowed limit for DEHP was exceeded, obtaining 17 mg/kg, respectively for total phthalates - 114 mg/kg [24, 32].

Also, our results are in accordance with those published by Miclean *et al.* (2012), with the concentrations of DBP and DEHP in the range of 2.85-6.28 ng/g and 36.84-112.3 ng/g.

According to the study conducted by MeeKyung *et al*., 15 out of 30 raw bovine milk samples monitored in their study contained DEHP, the concentrations in raw milk ranging from non-detectable under the LOD level

to 154 μg/kg^{-1}, and the mean concentration was 57 μg/kg^{-1}. DBP was observed at concentration from non-detectable to 99 μg/kg^{-1} in twenty samples and the mean concentration was 30 μg/kg^{-1} [36].

J. Lin *et al.* (2015), conducted a study to determinate the concentrations of phthalates from commercial whole milk products packaged in plastic materials, metal or glass containers. The concentrations of phthalates (DEHP) in milk samples packaged in plastic materials (79.3±2.6 ng/g) were much higher than those in metal (8.8±0.7 ng/g) or glass containers (6.6±0.5ng/g). The amounts of phthalates were much higher in milk samples packaged in plastic containers compared with glass or metal containers, indicating that plastic packaging materials are the likeliest source of phthalate contamination in commercial whole milk products. These findings are in accordance with our results, because in the case of samples collected directly from the cattle, in glass bottles, the phthalates were not detected. In contrast, all milk and dairy product samples that came into contact with plastic packaging recorded different levels of phthalates. The phthalates are more soluble in fat, higher level of these residues is usually recorded in the case of products rich in fat, like ripened cheeses and butter [18, 21, 30].

The differences between phthalates levels in dairy products, could be represented by different types of packaging materials, with different levels of PAEs in the plastic material. Even if the Commission Regulation No. 10/2011, the maximum accepted concentration (MAC) of phthalates were established, ranged from 0.3 mg/kg in the case of DBP to 30 mg/kg for BBP, the manufactures of packaging materials must follow those rules. Also, the following phthalates, DEHP, DBP and BBP are not allowed to be used in the manufacture of packaging materials for food products containing fats [6,34].

Recent studies observed that phthalates were found in all environmental (air, water, soil and sediment) at different concentrations in many countries which reflect the widespread usage of plastic products [24].

CONCLUSIONS

Even the total phthalates levels in all the samples analyzed do not exceed the maximum limit (60 mg/kg), rich fat milk and dairy products could be considered as a high-risk food category, being a potential source of human exposure to phthalates. Analyses should be performed at a more extent level to accurately evaluate the extent of this risk for human health.

The protocol used in this research for the detection of the phthalates can be applied for further implementation in food agencies laboratories for a more thorough investigation. Promoting the substitution of phthalates with other non-toxic substances could be a way to reduce the risk of food contamination with these types of compounds that are dangerous to human health.

EXPERIMENTAL SECTION

Sample collection

For this study, samples of milk and dairy products were collected randomly, at several stages in the milk chain, from farm, milk collection center and retail level. From each dairy product, seven samples were collected.

Milk samples were collected from several specific sources: milk obtained by manual milking, milk obtained by mechanically milking - collected from the bulk tank and commercial milk.

The control milk sample was collected from a dairy farm in Maramures County, by manual milking into a glass container, avoiding any contact with plastic materials. This milk was not pasteurized before analysis.

The milk samples collected from farm and milk collection center were packed in plastic (polyethylene terephthalate, PET) bottles. For each milk sample, the fat content was also determined, using standard Gerber method. The samples collected represent raw milk with 3.5% fat and 4% fat, respectively. The shelf life of milk is 10 days after packaging and the milk was used within this period.

To investigate phthalate contamination at retail level, samples of milk with different quantity of fat were purchased from supermarket, with 1.5% fat and 3.5% fat. All milk samples (1.5% fat and 3.5% fat), were packed in plastic cans and were from the same brand.

The dairy products were bought from supermarket and were represented by sour cream with 20% fat and 33% fat, yoghurt with 0.1% and 2% fat content, butter with 75% fat, raw cream and ice cream, all with varied validity period. All samples were packed in various plastic containers.

In order to investigate phthalates in cheese samples, 5 different variety were collected, depending on the amount of fat contained, the shelf life and the production method. The types of cheese collected were fresh cheese with 25% fat, telemea cheese (fresh salted cheese maturated in brine) with 50% fat content, maturated cheese with 45% fat, cream cheese with 60% fat in dry matter and burduf cheese. Burduf cheese is a traditional Romanian cheese made from sheep's milk. The name burduf cheese means kneaded cheese, referring to the method of production in which a traditional sweet cheese called *caș* is cut, salted, and then kneaded in a large wooden bowl. The mixture is then placed in a sheep's stomach or skin that has been cleaned and sawed on the edges. Alternatively, it can be stored in a tube made of pine bark. Burduf cheese is a salty and fermented cheese, quite compact but pasty, with 45% FDM (fat in dry matter).

All samples were transported to the laboratory in a cool box and were stored at −18 °C prior to analysis.

Reagents and standards

The standard solutions of individual phthalates consisted of di-n-butyl phthalate (DBP), di-2-ethylhexyl phthalate (DEHP), di-n-octyl phthalate (DOP), benzyl butyl phthalate (BBP), dimethyl-phthalate (DMP) and diethyl-phthalate (DEP), all dissolved in methanol, each at a concentration of 1 $mg \cdot L^{-1}$ were purchased as Pestanal®, analytical standards from Merk (Darmstadt, Germany).

All reagents and water used for the analyses were checked for contamination with phthalates. The solvents used had an analytical purity (suitable for GC) > 99 %.

To avoid phthalate contamination, all the employed laboratory dishes were made of glass, previously washed with water, rinsing with hexane and dried at 60 °C for 2 hours.

Milk samples liquid-liquid extraction

For phthalates analysis from milk samples, 50 mL of sample was placed in separatory funnel with 15 mL methanol – n-hexane solvent (1:2 v/v) and subjected for shake (LaboShake, Gerhardt Analytical System, Germany) for 30 min at 130 rpm. Phase equilibration was allowed for 10 min. Emulsion was removed with 2.5 mL salt solution (15 % NaCl). The extraction was repeated once again in the same manner and the obtained supernatant was combined with the previously obtained. Na_2SO_4 was added at this extract to remove potential remained water. In finally, the extract was transferred at an Erlenmeyer flask and subjected for fully evaporation at 40°C with a rotary evaporator (Laborota 4010, Heidolph Instruments, Germany). Finally, samples were redissolved in 1 mL n-hexane and analyzed by GC-MS.

Dairy products ultrasound assisted extraction

In case of each studied dairy products 15 g of samples was weight in a 150 mL volume Erlenmeyer flask. Extraction solvent was a mixture of 30 mL methanol – n-hexane (1:2 v/v). In the following ultrasound assisted extraction was performed using a Sonorex ultrasound bath (Bandelin, Germany). The extraction was allowed for 1 h at 35 kHz ultrasonic frequency. Resulted extract was filtered on Whatman filter paper and cleaned on a high purity grade silica column with average pore size 60 A (52-73A) and 70-230

mesh. Resulted extract was fully evaporated with a rotary evaporator. After this procedure, the samples were redissolved in 1 mL n-hexane and analyzed by GC-MS.

GC-MS analysis of phthalates

Phthalate analysis was performed on gas chromatograph with mass spectrometer system (6890 series Agilent GC system, 5975 series Agilent MS detector). From each extract 1 µL was injected in SSL injector used in splitless mode. The mass spectrometer was operated at the electron impact mode with 70 eV. Phthalates were separated on a HP-5MS, 5 % diphenyl 95 % dimethyl polysiloxane capillary column (Agilent Technologies) with the following characteristics: 30 m x 0.25 mm i.d. x 0.25 µm film thickness. The compounds were separated using the following oven program: 100ºC, increased at 8ºC/min up to 260ºC, increased at 35ºC/min up to 310ºC and held for 10 min and the running time being 31.43 min. The MSD transfer line heater, ion source and quadrupole analyzer temperatures were set at 320, 230 and 150 ºC, respectively.

The qualitative and quantitative analyses were performed by comparison with the external standards. Full scan mode with the mass/charge ratio ranging from 100 to 550 m/z was applied. In Figure 1 is presented a TIC (Total Ion Chromatogram) of a blank sample and a cheese sample.

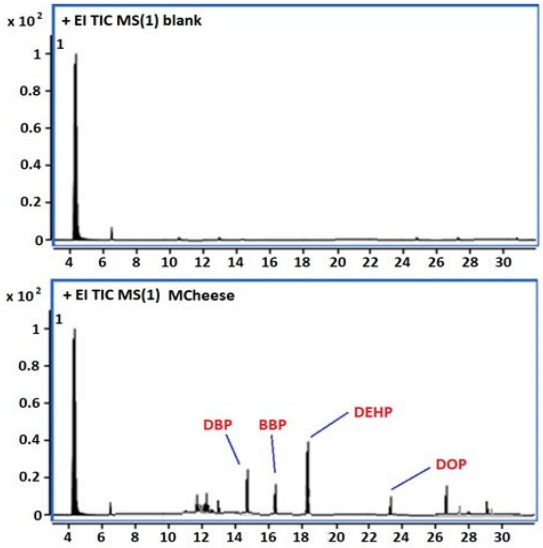

Figure 1. GC-MS analysis of phthalates from a blank and a cheese sample

Methods performance

Efficiency of applied analytical method was evaluated considering parameters as linearity, limit of detection (LOD), limit of quantitation (LOQ), and recovery. Stock solutions of individual phthalate standards (10 mg of each phthalate in part as BBP, DEHP, DOP, DBP, DMP and DEP) were weighted and dissolved in 10 mL of methanol. Working standard mixture was obtained after combining the six stock solutions and dilution until to reach 1 $mg \cdot L^{-1}$. Series of five calibration standards within range of 0.01 – 500 $\mu g \cdot g^{-1}$ were obtained after serial dilution of working standard solution. Obtained linear regression curves were used for quantification of phthalates. LOD and LOQ were determined based on standard error of the calibration curve at y-intercept multiplied three and ten times, respectively (see Table 3).

Table 3. Calibration curve correlation coefficient, LOD and LOQ of applied analytical method

Parameter	BBP	DEHP	DOP	DBP	DMP	DEP
R^2	0.9925	0.9954	0.9961	0.9938	0.9971	0.9962
LOD ($\mu g \cdot g^{-1}$)	0.0052	0.0034	0.0061	0.0042	0.0035	0.0029
LOQ ($\mu g \cdot g^{-1}$)	0.0173	0.0113	0.0203	0.014	0.0117	0.0097

Method recovery was established by spiking each sample matrix with 100 $\mu g \cdot g^{-1}$, respectively. Obtained values for each phthalate are presented in Table 4.

Table 4. Method recovery (%) for milk and dairy products matrices

Sample matrix	BBP	DEHP	DOP	DBP	DMP	DEP
Milk	75.9	85.5	74.8	105.5	88.6	84.5
Sour cream	88.2	95.6	86.9	115.3	76.9	90.5
Yogurt	87.2	75.9	84.6	91.2	77.7	103.5
Cheese	91.8	95.6	102.5	93.5	84.4	95.6
Butter	77.6	84.2	68.9	105.2	102.3	84.6

Statistics

The statistical analyses were realized with Origin 8.5 software (OriginLab Corporation, Northampton, MA 01060, USA). Mean differences between dairy products were analyzed using analysis of variance ANOVA.

The results were expressed according to the standard deviation (SD), with significance level established at $P < 0.05$. Post-hoc test comparation using Bonferoni, Tukey's and Scheffe's was performed.

REFERENCES

1. D. Amiridou, D. Voutsa, *J. Hazard. Mater.*, **2011**, *185*, 281
2. E. L. Bradley, Determination of phthalates in foods and establishing methodology to distinguish their source, **2012**, FSA PROJECT C01048, Report FD 10/05
3. Xu-L. Cao, *Compr. Rev. Food Sci. Food Saf.*, **2010**, *9*, 21-43
4. N. Casajuana, S. Lacorte, *J. Agric. Food Chem.*, **2004**, *52 (12)*, 3702-3707
5. L. Castle, J. Gilbert and T. Eklund., *Food Addit. Contam*., **1990***, 7*, 591-596
6. COMMISSION REGULATION (EU) No 10/2011 of 14 January 2011 on plastic materials and articles intended to come into contact with food, https://eur-lex.europa.eu/legal-content/EN/TXT/PDF/?uri=CELEX:32011R0010&from=EN
7. National Research Council (US) Committee on the Health Risks of Phthalates. *Phthalates and Cumulative Risk Assessment: The Tasks Ahead*. Washington (DC): National Academies Press (US); **2008**
8. Gh. Duca, B. Gaina, R. Sturza, *Akademos*, **2010**, *3(18)*, 96-100
9. I. Dumitraşcu. *Aerul şi Apa: Componente ale Mediului*, **2012**, p.337
10. M.A. Farajzadeh, D. Djozan, M.R. Afshar and M.J. Norouzi, *J. Sep. Sci*., **2012**, *35*, 742-749
11. E. Fasano, F. Bono-Blay, T. Cirillo, P. Montuori, S. Lacorte, *Food Control*, **2012**, *27*, 132–138
12. Y.-L. Feng, J. Zhu, R. Sensenstein, *Anal. Chim. Acta*, **2005**, *538*, 41-48
13. T. Fierens, M. Van Holderbeke, H. Willems, S. De Henauw, I. Sioen. *Food Chem. Toxicol.*, **2012**, *50*, 2945-2953
14. T. Fierens, M. Van Holderbeke, H. Willems, S. De Henauw, I. Sioen. *Environ. Int.*, **2013**, *51*, 1-7
15. J.S. Fisher, *Reproduction*, **2004**, *127*, 305-315
16. H. Fromme, L. Gruber, E. Seckin, U. Raab, S. Zimmermann, M. Kiranoglu. *Environ Int*, **2011**, *37*, 715–22
17. T. C. Jenkins, M. A. McGuire, *J. Dairy Sci.*, **2006**, *89*, 1302–1310
18. M. Krejčíková, A. Jarošová. *MENDELNET*, **2013**, 593-596
19. Z. Li, F. Xue, L. Xu, C. Peng, H. Kuang, T. Ding. *J Chromatogr Sci*, **2011**, *49*, 338–43
20. J. Lin, W. Chen, H. Zhu, C. Wang, *J. Dairy Sci*., **2015**, *98 (12)*, 8278–8284
21. M. Miclean, O. Cadar, C. Roman. *Studia UBB Chemia*, *LVII*, *1*, **2012**, pp. 127 – 133
22. M. A. Mohamed, A. S. Ammar. *Am. J. Food Technol.*, **2008**, *3*, 341-346
23. S. M. Rhind, C. E. Kyle, C. Mackie, G. Telfer, *Sci. Total Environ.*, **2005**, *383*, 70-80
24. M. Saad, M. Ahmed, Y. Sultan. *World J. Pharm. Res*. **2015**, *4990*, 1799-1807

25. T. Schettler, *Int. J. Androl.*, **2006**, *29*, 134–139
26. I. Schiopu, A. Gurzau, E. Gurzau*. Wulfenia*, **2015**, *22*, 345-358
27. M. Sharman, W.A. Read, L. Castle, J. Gilbert. *Food Addit. Contam.*, **1994**, *11*, 375-385
28. H. Soyeurt, I. Misztal, N. Gengler*, J. Dairy Sci*., **2010**, *93*, 1722–1728
29. R.O. Sulentic, I. Dumitrascu, N.C. Deziel, A.E. Gurzau. *Int. J. Environ. Res. Public Health*, **2018**, *15*, 2109
30. J. VELÍŠEK, *Chemie potravin 3. Tábor: OSSIS*, **2002**, 343
31. C.K. Wei, L.C. Fung, M. Pang, *MJAS*, **2011**, *15 (2)*, 167 – 174
32. A. Wendi, L. Reed and G. John. *Food Addit Contam.*, **2009**, *111(3)*, 375-385
33. H. Yan, X. Cheng, B. Liu*. J Chromatogr*, **2011**, 879:2507–12
34. EFSA Scientific Committee, J.M.B. Baviera, C. Bolognesi, A. Chesson, P.S. Cocconcelli, R. Crebelli, D.M. Gott, K. Grob, E. Lampi, A. Mortensen, G. Rivière, V. Silano, I.-L. Steffensen, C. Tlustos, H. Van Loveren, L. Vernis and H. Zorn. *EFSA Journal*, **2019**, *17(12)*, 5838
35. A. Giuliani, M. Zuccarini, A. Cichelli, H. Khan and M. Reale*. Int. J. Environ.Res. Public Health,* **2020**, *17*, 5655
36. K. MeeKyung, J.Y. Seon, C. Gab-Soo*. Food Addit. Contam. Part A Chem. Anal. Control. Expo. Risk Assess*. **2009**, *26*, 134–138
37. P. A. Przybylińska, M. Wyszowski. *Ecol Chem Eng S*., **2016,** *23(2)*, 347-356
38. P.M. Lorz, F.K. Towae, W. Enke, R. Jäckh, N. Bhargava, W. Hillesheim. Phthalic acid and derivatives. In *Ullmann's Encyclopedia of Industrial Chemistry*, 7th ed., B. Elvers Eds., Wiley-VCH, Weinheim, Germany, **2007,** Volume 27, pp. 132-180
39. S.E. Root, S. Savagatrup, A.D. Printz, D. Rodriquez, D.J. Lipomi. *Chem. Rev.* **2017**, *117*, 6467–6499
40. E.N. Peters. Plastics: Information and Properties of Polymeric Materials. In *Mechanical Engineers' Handbook: Materials and Mechanical Design,* 3rd ed.; M. Kutz Eds., **2005**, Volume 1, pp. 335-379
41. I. Notardonato, C. Protano, M. Vitali, B. Bhattacharya and P. Avino. *Appl. Sci*. **2019**, *9*, 2945
42. M. Tankiewicz, E. Olkowska, A. Berg and L. Wolska. *Front. Chem.*, **2020,** *7*, 928
43. M.A. Kamrin. *J. Toxicol. Environ. Health B: Crit. Rev.*, **2009**, *12*, 157–174
44. A.M. Calafat, X. Ye, M.J. Silva, Z. Kuklenyik, L.L. Needham, *Int. J. Androl.,* **2006**, *29*, 166–171
45. P. Ventrice, D. Ventrice, E. Russoa, G. De Sarroa. *Environ. Toxicol. Pharmacol.,* **2013**, *36*, 88-96
46. N. Sopheak, R. Sempere, A. Delmont, A. Paluselli, B. Ouddane. *Environ. Sci. Technol.,* **2015**, *49*, 4019–4035
47. D. Savoca, M. Arculeo, S. Barreca, S. Buscemi, S. Caracappa, A. Gentile, M.F. Persichetti, A. Pace. *Mar. Pollut. Bull.,* **2018**, *127*, 165–169
48. H. Frederiksen, N. E. Skakkebæk, and A. M. Andersson. *Mol. Nutr. Food Res.*, **2007**, *51(7)*, 899–911
49. S. J. Genuis, S. Beesoon, R. A. Lobo and D. Birkholz. *Sci. World J.,* **2012,** *2012*, 615068
50. Y. Wang, H. Zhu, K. Kannan. *Toxics*. **2019**, *7(2)*, 21

51. K. Stamatelatou, C. Pakou, G. Lyberatos; Occurrence, Toxicity and Biodegradation of Selected Emerging Priority Pollutants in Municipal Sewage Sludge. In *Comprehensive Biotechnology,* 3rd ed.; Murray Moo-Young Eds.; Pergamon, **2011**, Volume 6, pp. 421-432

STUDIA UBB CHEMIA, LXVI, 4, 2021 (p. 77-95)
(RECOMMENDED CITATION)
DOI:10.24193/subbchem.2021.4.06

THE INFLUENCE OF CLIMATIC FACTORS ON THE AROMA COMPOUNDS OF FETEASCA REGALA WINE FROM THREE SOUTHERN REGIONS OF ROMANIA

DIANA IONELA STEGARUS[a,*], DANIELA SANDRU[b], PETRU ALEXE[c], ADINA FRUM[d], OANA BOTORAN[a], ECATERINA LENGYEL[b]

ABSTRACT. Climatic factors have a great influence on the quality of grapes and wines, thus the identification and quantification of aroma compounds from Feteasca regala wine manufactured in 2019 in three established winemaking centers from Romania (Samburesti, Corcova and Dragasani) was performed. After liquid/liquid extraction, the aromatic composition was identified and quantified by gas chromatography coupled with mass spectrometry (GC-MS). 42 aroma compounds were analyzed depending on the region of origin of the vineyards and climatic factors. Results showed significant differences between the wines regions of origin. The quantities of long-chain alcohols varied between 28644.54 µg/L and 33969.27 µg/L and esters between 4221.10 µg/L and 7901.25 µg/L. Significant quantities were determined for fatty acids and ranged between 5310.99 µg/L and 6045.15 µg/L and lactones between 727.39 µg/L and 988.01 µg/L. The most significant results regarding the aroma profile were determined for the wine from Avincis Dragasani vinery, where the climatic indicators ratio was optimum, thus conferring specific and quantifiable elements to the wine.

Keywords: *GC-MS, oenological climate index, wine aroma compounds*

INTRODUCTION

Natural factors have a great influence on the quality of grapes and wines, because the harvest of the same variety of grapes, transformed by the same winemaking technology provides wines of different quality if the

[a] *National Research and Development Institute for Cryogenics and Isotopic Technologies – ICSI Ramnicu Valcea, Romania; diana.stegarus@icsi.ro; oana.dinca@icsi.ro*
[b] *Lucian Blaga University of Sibiu, Faculty of Agricultural Sciences, Food Industry and Environmental Protection, Sibiu, Romania; ecaterina.lengyel@ulbsibiu.ro; daniela.sandru@ulbsibiu.ro*
[c] *Dunărea de Jos University of Galati, Faculty of Food Science and Engineering, Galati, Romania; petru.alexe@ugal.ro*
[d] *Lucian Blaga University of Sibiu, Faculty of Medicine, Sibiu, Romania; adina.frum@ulbsibiu.ro*
[*] *Corresponding author: diana.stegarus@icsi.ro*

regions of the grapes' cultivation is different. These influences are currently being studied intensively, especially since there is a change in climate and, implicitly, the effects are major. Technological factors lead to obtaining quality, harmonious or specific wines. All the elements below are significant in the appreciation and cataloging of wines [1].

Climate is the main factor that conditions and determines the global spread of vines, being, through its elements, the most important natural factor. Through temperature, light, humidity, air movement, climate decisively influences the growth and fruiting of the vine, in fact it directly influences the physiological and biochemical processes [2]. The process of photosynthesis is influenced by temperature and light, and the rate of accumulation of sugars depends on the difference between the amount produced by photosynthesis and that consumed by respiration.

The vine is a light-loving plant, hence its classification among heliophilous plants. Within one hemisphere, both light and temperature decrease from the equator to the poles, but at the same time the aroma and sugars content of the grapes decrease, and the acidity registers an intense evolution. Too strong shade lowers the sugar content of grapes and promotes increased malic acid production and, climate change influences the growth and quality of vines [3].

In relation to its physical, chemical, and biological properties, the soil strongly influences the viticultural production and the quality of the grapes. It could be appreciated that the vine grows properly on forest soils, rendzinas, brown soils, alluvial soils and degraded chernozems. To the qualitative differences of the wines determined by the type of soil and the presence of limestone are added those determined by the texture of the soil. The most favorable texture of soil for growing vines is the clay – sandy one and the most favorable is clay [4].

In terms of altitude, famous vinicultural regions of the world are located between 80 and 150 m above sea level. However, there are vineyards that are located in mountainous areas at 1500 m altitude. In Romania, many vine plantations are located between 100 and 300 m altitude. If the plantations are at altitudes of approximately 167 m, with an ideal exposure to the sun, slopes in a southerly and westerly direction, and a wide variety of soil types, from forest reddish brown to soils high in iron oxides or calcareous, they are appropriate for vine cultivation. Sun exposure is an important factor for sloping vineyards. Wines obtained from vine plantations that are organized in slopes are superior to those organized in plateaus [5,6].

The mechanical composition of grapes is the gravimetric ratio between the constituent uvological units, clusters, skins, seeds, and pulp. The change in the chemical composition shows the influences on the technological

process, especially on the chemical and organoleptic characteristics of the wine. Both mechanical and chemical composition are influenced by the nature of the soil, the degree of ripeness of the grapes, phytosanitary status, pedoclimatic conditions and agrotechnical processes applied [7,8]. Most of the grape flavors are transmitted to the wine, but because of the processes that take place through alcoholic fermentation, other new components appear, components that can lead to the wine's specific characteristics. Many flavors are found in small amounts in wines, but they confer the specificity of it. They accumulate under the beneficial action of the sun and proper soil or climatic factors, especially in young wines [9].

The aromatic differentiation of a wine obtained from the same grape variety can be achieved by sensorial methods, but more precisely by gas-chromatographic methods, which have the possibility to highlight elements more precisely. The aroma of a wine is complex and depends on the concentrations of various compounds such as long-chain alcohols, esters, volatile fatty acids, lactones, phenolic compounds, and other essential compounds [10-13]. Studies show that one of the most cultivated grape varieties in Romania is Feteasca regala, the wines obtained from this cultivar present floral, citrus, or apricot notes. To potentiate some flavors, a series of pre-fermentative treatments can be used. Their role is to obtain finer, less acidic, or tastier wines [12,14-17].

Climate changes can lead to the differentiated accumulation of flavor compounds, and can influence the production of grapes, regardless of variety [18,19].

The aim of this study is to identify and quantify the aroma compounds that are formed in Feteasca regala wine, under the influence of specific climatic factors. The wine samples were obtained in 2019 by using the same technological conditions and they came from three established wine centers in Romania.

RESULTS AND DISCUSSION

To provide a proper correlation between the aromatic profile of the analyzed wines and the geographic region from which they come from; a pedo-climatic characterization of those regions is mandatory. Thus, in the Samburesti region, the soils are mostly loamy, loamy-clayey, and clayey-loamy, a structure that influences the vine culture. These soils are characterized by a medium to weak supply of organic and mineral substances with a variable texture from loamy-sandy to clayey, with an important content of iron in the form of colloidal hydroxyl. The vine plantations are located on smooth slopes and plateaus with southern, south-eastern, and south-western exposure.

The oenoclimatic aptitude index from 2019 was calculated at a value of 4568, and the viticultural bioclimatic index reached 7.42.

The values for the climatic indexes were calculated by using the readings from the meteorological stations near to the viticultural centers. The analyzed parameters were temperature, solar radiation, and precipitations.

Irimia et al. (2014) established a series of suitability intervals for bioclimatic indexes and ecological factors for the temperate continental climatic conditions of Romania. The quantification was performed by using classes and points [20].

The bioclimatic index is representative for the winegrowing regions from the temperate continental climate areas. This index was calculated for the growing season (from April 1st to September 30th). In order to obtain a high-quality white wine, the Ibcv has to be between 5.1 and 13. The formula used for the calculus was:

$$Ibcv = (ASD \cdot \Sigma t_a / PP \cdot N_d) / 10$$

where: Ibcv = bioclimatic index; ASD = actual sunshine duration, expressed as hours; Σt_a = the sum of daily average temperatures (greater than 10°C); PP = precipitations, expressed as mm and N_d = the number of days in the growing season [20].

The oenoclimate aptitude index (IAOe) shows the winemaking suitability, thus the optimum index is situated between 3790 and 4600. The values that are greater than 4301 show the obtaining of high-quality white wines. This index was calculated for the growing season as well (from April 1st to September 30th) by using the following formula:

$$IAOe = ASD + \Sigma t_a – (PP – 250)$$

where: IAOe = oenoclimate aptitude index; ASD = actual sunshine duration, expressed as hours; Σt_a = the sum of daily average temperatures (greater than 10°C); PP = precipitations, expressed as mm and 250 = the minimum precipitations required for vines that are not irrigated, expressed as mm [20].

In the Corcova region, the soils are reddish-brown with leached chernozems, medium texture, locally coarse or clayey-loamy. These types of soils have several advantageous physical and chemical characteristics for the cultivation of vines. The bottom soils are normal or slightly-moderately eroded on the slopes, followed by brown soils or weakly podzolite soils, moderately to strongly eroded on slopes and alluvial soils on the meadow terraces of Topolnita. The characteristic wines of this region are alcoholic wines, full-bodied, rich in extract and with a high content of mineral

substances, these features being due to the existing soil types. The oenoclimatic aptitude index from 2019 was calculated at the value of 4532, and the viticultural bioclimatic index reached 7.34.

In the Dragasani region, the vine plantations are located at altitudes exceeding 400 m, with brown, forest reddish-brown soils, some of them are podzolites and rich in limestone and located on alluvial gravels. The dominant soils are luviosols and luvic brown soils which, together with the thermohydric conditions allow and recommend the cultivation of white grape varieties. The oenoclimatic aptitude index from 2019 was calculated at the value of 4596, and the viticultural bioclimatic index at 7.48, which induces favorable climatic conditions for the vine culture.

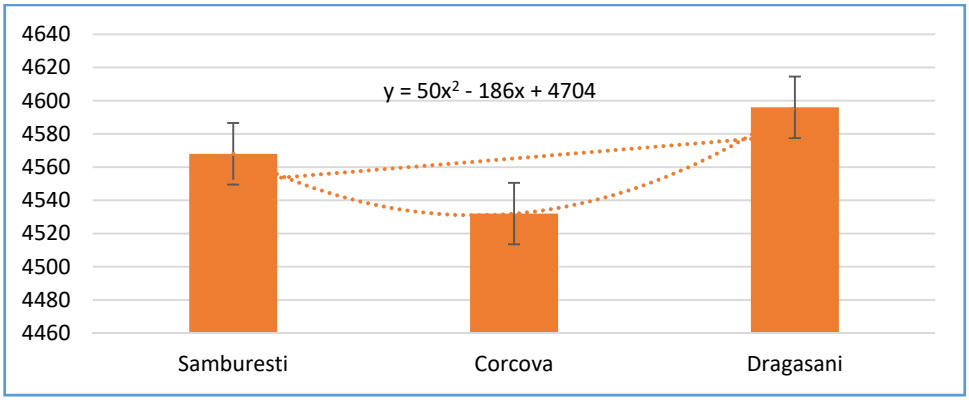

Figure 1. The oenoclimatic aptitude index calculated for the year 2019 for the investigated regions of origin of the Feteasca regala wine samples

Figures 1 and 2 show the differences between the three studied regions regarding the oenoclimatic aptitude index and the viticultural bioclimatic index. The highest values were registered in the Dragasani region and the lowest in the Corcova one, thus the flavors of the wines were influenced.

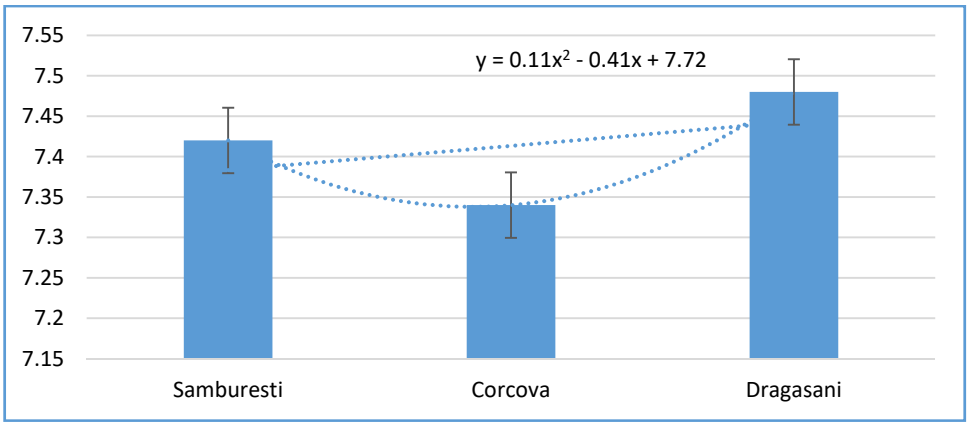

Figure 2. The viticultural bioclimatic index calculated for the year 2019 for the investigated regions of origin of the Feteasca regala wine samples

Table 1 shows the results obtained for the GC-MS analysis of the volatile aroma compounds of the wine samples in order to be able to correlate these results to the pedo-climatic indexes calculated.

Table 1. GC-MS analysis of volatile aroma compounds from the Feteasca regala wine samples

Compounds	Feteasca regala wine samples (µg/L)		
	Samburesti	Corcova	Avincis Dragasani
Alcohols			
Iso butanol	139.45	126.24	113.03
Butanol	4.97	5.98	3.08
Isopentyl alcohol	13214.01	12036.71	14001.15
1-hexanol	716.25	588.06	667.25
4-methyl-1-pentanol	0.00	1.02	0.62
E-3-hexenol	14.36	10.66	12.12
Z-3-hexenol	19.25	14.55	21.02
2-nonanol	9.05	12.18	16.07
1-heptanol	412.15	315.74	512.36
2,3-butandiol	1296.54	1406.36	874.24
3-(methylthio)-1-propanol	447.11	612.05	228.69
Linalool	229.51	425.11	309.25
Terpineol	99.36	129.27	202.14
2-phenyl ethanol	14355.20	12221.10	16214.50

Compounds	Feteasca regala wine samples (µg/L)		
	Samburesti	Corcova	Avincis Dragasani
Trans-geraniol	90.36	62.33	41.08
Glycerin	836.06	508.51	615.47
Benzyl alcohol	111.05	168.54	137.20
3-hydroxy-butanone	0.00	0.12	0.00
Total alcohols (µg/L)	*31994.68*	*28644.54*	*33969.27*
Esters			
N-amyl acetate	10.25	6.25	14.36
Hexyl-acetate	0.00	1.25	0.00
Ethyl caproate	31.25	58.36	51.21
Ethyl lactate	415.25	303.54	501.08
Ethyl octanoate	98.56	215.71	166.52
Ethyl-3-hydroxy butyrate	81.06	136.08	101.42
Ethyl decanoate	88.21	102.37	96.95
Ethyl hydrogen succinate	2355.19	5236.64	3021.14
Phenethyl acetate	101.30	60.37	81.47
Diethyl malate	114.67	155.54	184.20
Methyl-4-hydroxy-butanoate	925.36	1625.14	1147.14
Total esters (µg/L)	*4221.10*	*7901.254*	*5365.49*
Fatty acids			
Isobutyric acid	92.25	74.14	51.69
Hexanoic acid	847.54	1205.11	741.40
Fatty acids (continued)			
Isovaleric acid	100.28	141.79	168.73
Lactic acid	315.41	197.57	229.54
Octanoic acid	3215.41	1998.10	2318.19
Decanoic acid	1005.51	1354.09	1208.11
Hexadecanoic acid	91.25	101.47	74.54
Malic acid	354.25	471.67	499.25
2-oxoadipic acid	23.25	13.47	19.54
Total fatty acids (µg/L)	*6045.15*	*5557.41*	*5310.99*
Lactones			
Pantolactone	51.23	29.15	34.66
Isovaniline	22.15	11.09	14.14
Butyrolactone	914.63	687.15	817.66
Total lactones (µg/L)	*988.01*	*727.39*	*866.46*
Total volatiles (µg/L)	***43248.94***	***42830.59***	***45512.21***

Table 1 shows aroma compounds found in the analyzed samples. Long-chain alcohols, like isopentyl had concentrations between 12036.71 µg/L for Feteasca regala wine from Corcova and 14001.15 µg/L for Avincis Dragasani. Isopentyl confers banana aromas to wines, caranda being a

volatile cyanobacterial organic compound, and combined with other aroma compounds it contributes to the aroma palette of the wine. Terpenic alcohols (which give wines floral, fresh, and invigorating aromas) are present in the wine samples, like linalool with concentration between 229.51 μg/L for Samburesti region and 425.11 μg/L for Corcova region, terpineol with concentrations between 99.36 μg/L for Samburesti region and 202.14 μg/L for Dragasani region and trans-geraniol with concentrations between 41.08 μg/L for Dragasani region and 90.36 μg/L for Samburesti region. 4-methyl-1-pentanol (which gives wines a walnut aroma) was not detected in the Samburesti region wine sample, instead 1.02 μg/L was quantified in the one from the Corcova region and 0.62 μg/L in the one from the Dragasani region. Glycerin gives the wines sweetness and velvety properties, being found in the analyzed samples in amounts of 836.06 μg/L for the Samburesti region sample, 508.50 μg/L for the Corcova region sample and 615.47 μg/L for the Dragasani region sample. The results obtained are consistent to the values provided by specialists in the field for the wines to be balanced and harmonious [6]. Significant amounts of 2-phenyl-ethanol were identified in the wine samples, the results were between 12221.10 μg/L for the Corcova region sample and 16214.50 μg/L for the Dragasani region sample. This compound participates in the aromatic palette of the wine through the floral notes conferred, being present in all the assortments of wines in significant quantities. 3-hydroxy-butanone is a compound that results from the alcoholic fermentation of must under the influence of *Saccharomyces* wine yeasts and gives butter aroma to wines. In the wine samples, this compound was present only in the one from Corcova region with an amount of 0.12 μg/L. This amount does not lead to imbalances in the wine's aromatic palette.

Figure 3 shows the evolution of the total long-chain alcohols in the wine samples analyzed. The highest values were recorded for the wine sample from the Dragasani region (33969.27 μg/L), followed by the one from the Samburesti region (31994.68 μg/L) and the lowest value was recorded for the sample from the Corcova region (28644.54 μg/L).

Esters are valuable compounds for wines, as they play an important role in their aromatic palette. Thus, fruit aromas as banana are conferred by the presence of the N-amyl acetate, which was quantified in the samples analyzed at 10.25 μg/L in the wine from the Samburesti region, 6.25 μg/L for the one from the Corcova region and 14.36 μg/L for the one from the Dragasani region. Hexyl acetate was not detected in the samples from the Samburesti and Dragasani regions and a low quantity was determined for the sample from the Corcova region (1.25 μg/L). This compound leads to aromas of green apple and sweet cherries. These aromas were not found in

the wine samples analyzed. Ethyl caproate constitutes a valuable compound if found in wines because of the fruity aroma of pineapple that it confers to wines and combined with other esters they provide a harmonious and pleasant aroma to wines. This compound was quantified for the wine samples analyzed at 31.25 µg/L for the wine from the Samburesti region, 58.36 µg/L for the one from the Corcova region and 51.21 µg/L for the one from the Dragasani region.

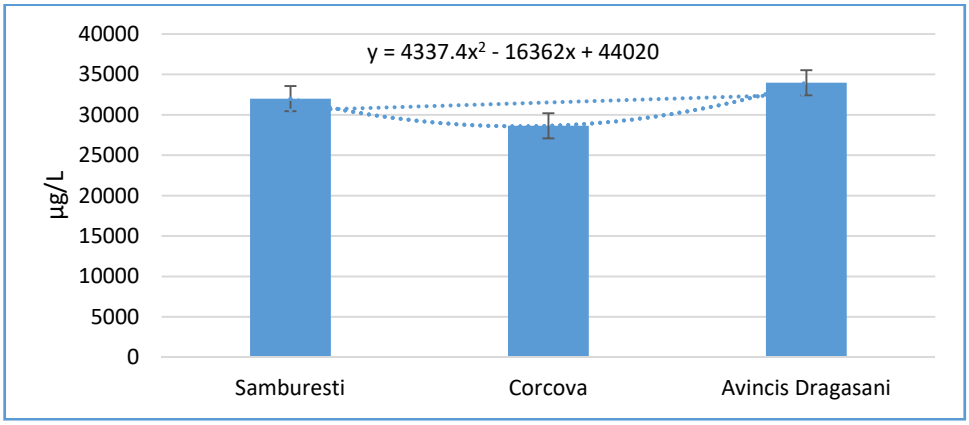

Figure 3. The variation of the total long-chain alcohols from the wine samples analyzed

Ethyl lactate is an ester that exists in every wine. It confers sweet or buttery, fruity, creamy, or rum aromas to wines. The analyzed wine samples had 303.54 µg/L for the wine from the Corcova region, 501.08 µg/L from the one from the Dragasani region and 415.25 µg/L for the one from the Samburesti region. Ethyl hydrogen succinate is an ester that confers fruity melon aromas. It was quantified at 2355.19 µg/L for the wine from the Samburesti region, 5236.64 µg/L for the one from the Corcova region and 3021.14 µg/L for the one from the Dragasani region. Significant differences were observed between the analyzed wine samples from the three regions, regarding this compound.

Other esters such as ethyl octanoate or ethyl decanoate contribute to the aromatic palette of the wine giving it fruity or sweet notes, in even larger amounts of soap. The amounts determined for these compounds are similar to the ones listed in literature [9]. Figure 4 shows the amounts of total esters determined for the wine samples analyzed. 4221.10 µg/L were determined for the wine sample from the Samburesti region, 7901.25 µg/L for the one from the Corcova region and 5365.49 µg/L for the one from the Dragasani region.

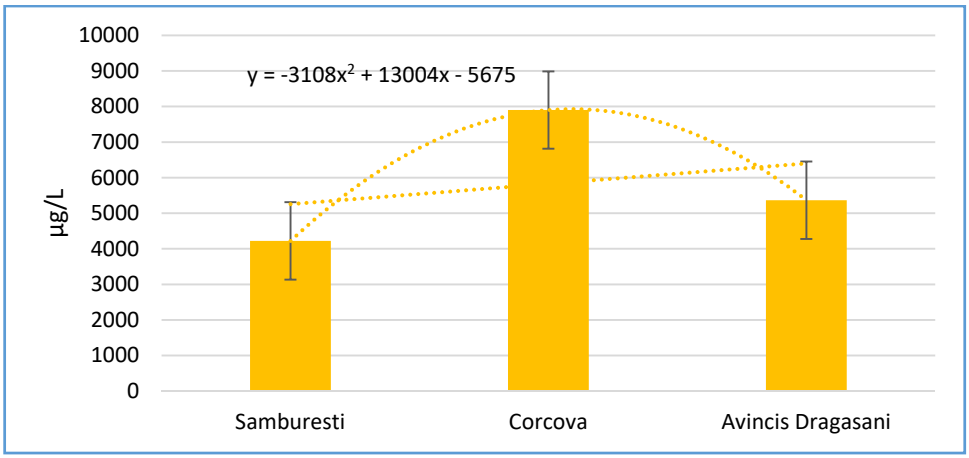

Figure 4. The variation of the total esters from the wine samples analyzed

Fatty acids participate along with the other volatile compounds in completing the aromatic palette of wines. Although the aromas conferred by volatile fatty acids tend to be in less pleasant areas (rancid, sour, cheesy, greasy, even mold), in small amounts they have a decisive role in the formation of the sensory properties of wines. Certain compounds confer hints of sweat, hot, sour, or harsh which led to a complex aromatic profile. In the Feteasca regala wine samples, a series of volatile fatty acids were quantified, such as isobutyric acid with values of 92.85 µg/L for the Samburesti area, 74.14 µg/L for the Corcova area and 51.69 µg/L for the Dragasani area. These compounds give the acidic aroma of the wines. The isovaleric acid (3-methylbutanoic acid) gives a sweat and cheese odor was identified in the analyzed samples in amounts starting from 100.28 µg/L for the Samburesti region and reaches 168.73 µg/L for the Dragasani region. The octanoic and decanoic acids that give an odor of sweat or harsh showed significantly higher amounts reaching maximum values of 3215.41 µg/L in the wine from the Samburesti region and 1354.09 µg/L in the wine from the Corcova region. Lactic and malic acids lead to the adjustment of the unpleasant aromas given by volatile fatty acids so that their presence is considered beneficial to the aromatic palette of wines. The values obtained were at a maximum amount of 315.41 µg/L in the wine from the Samburesti region and respectively 499.25 µg/L in the one from the Dragasani region.

Figure 5 shows the total of the fatty acids identified and quantified in the Feteasca regala wine samples. 6045.15 µg/L were determined for the wine from the Samburesti area, 5557.41 µg/L for the one from the Corcova region and 5310.99 µg/L for the one from the Dragasani region.

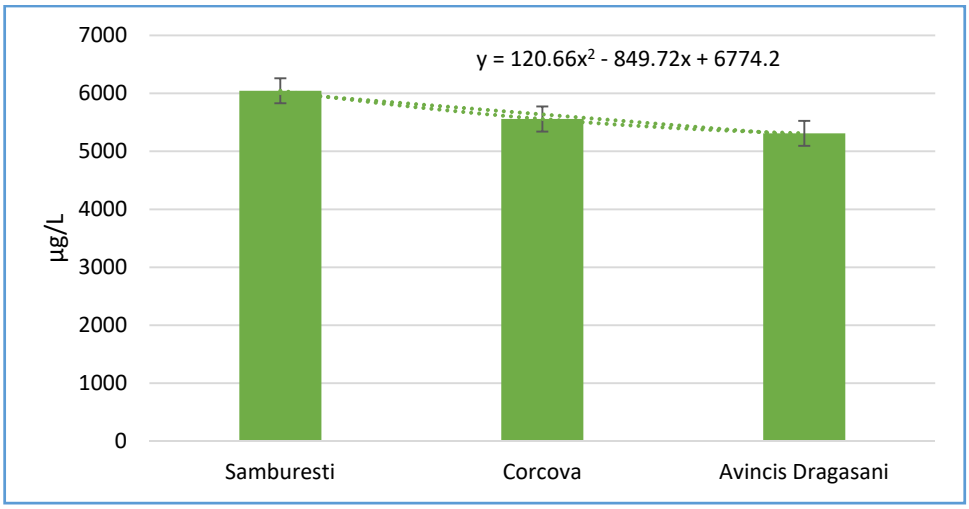

Figure 5. The variation of the total fatty acids from the wine samples analyzed

Lactones have an important role in completing the odorizing palette of wines. The aromas are sugar cotton wool (pantolactone) and caramel (butyrolactone). The amounts identified were 988.01 µg/L for the Samburesti region, 727.39 µg/L for the Corcova region and 866.46 µg/L for the Dragasani as can be observed in figure 6.

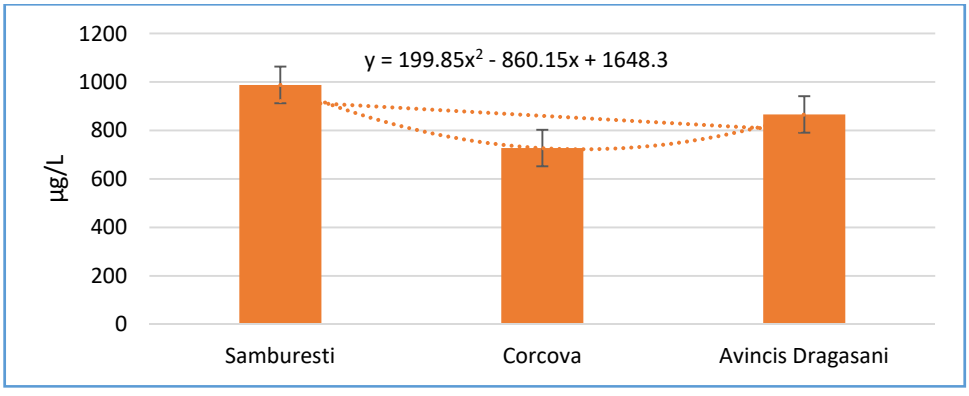

Figure 6. The variation of the total lactones from the wine samples analyzed

The total volatile compounds determined from the Feteasca regala wines analyzed led to the differentiation of the wines even though the parameters and technological processes used for their manufacturing were similar. Figure 7 shows that the highest quantity of total volatile compounds was registered for the Dragasani region wine with 45512.21 µg/L, followed by the Samburesti region with 43248.94 µg/L and then Corcova region with 42830.59 µg/L.

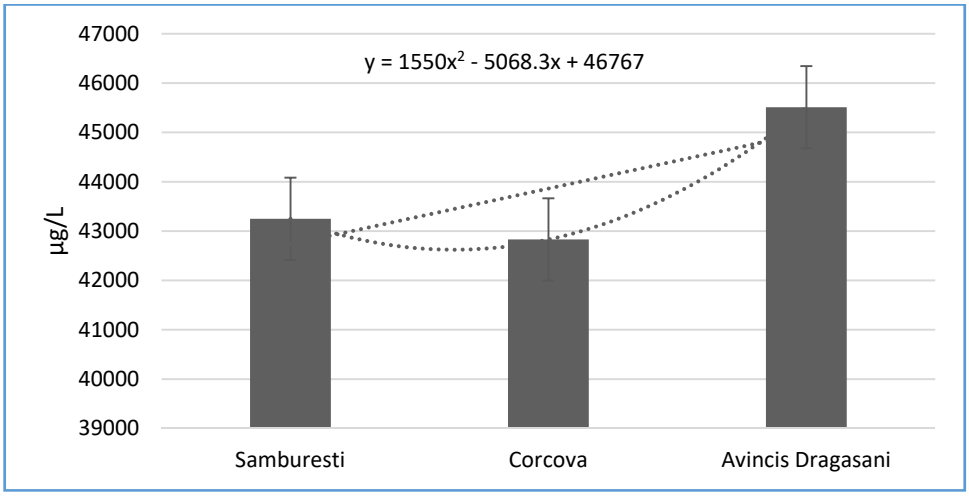

Figure 7. The variation of the total volatile compounds from the wine samples analyzed

PCA was applied to the matrix formed by the total minor volatile compounds corresponding to all of the different wine samples. The maximum number of PCs was set at three; however, the first two components explained the data variance (63.2% and 36.8%), as shown in the score plot in figure 8. The PCA score plots of evaluated volatile compounds showed the best separation of points for Feteasca Regala wine originating from three different vineyards located in the same area.

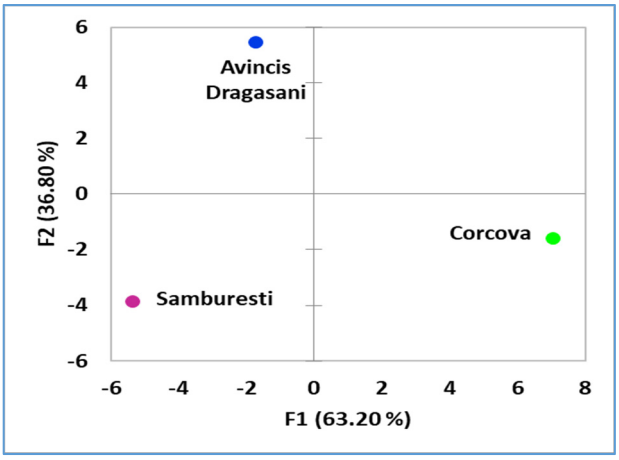

Figure 8. PCA score plot of the total minor compounds by geographical origin of Feteasca Regala wine

The separation between Samburesti and Avincis Dragasani can be seen through the second principal component (PC2), which describes 36.8 % of the total variance. The PCA loadings showed that iso butanol, 2-nonanol, terpineol, trans-geraniol, 2,3-butandiol, isobutyric acid and isovaleric acid had the highest role in the formation of PC2. The majority of these volatile compound belong to the alcohols group. Corcova region was separated from the other two through the first principal component (PC1), consisting of esters and fatty acids. PCA represents one of the most versatile of all chemometric techniques that involves data dimensionality reduction by mathematical modelling using a covariance analysis between factors and exploring the hidden trends in a data matrix without much loss of information [21]. Even though the results obtained from the PCA revealed obvious clustering of the samples according to their provenance, which indicated differences in Feteasca Regala wine samples composition, and was in fact mostly coherent with the previously explained results. For a more precise determination regarding variables contribution, in the next part, we reduced the measurement to most relevant factors by applying Kaiser-Meyer-Olkin measure of sampling adequacy to assess which of the data were the most suitable for PCA at an accepted level of significance of $\alpha = 0.60$. The goal was to reduce the number of items by finding correlations between them and abstracting a smaller number of factors (figure 9).

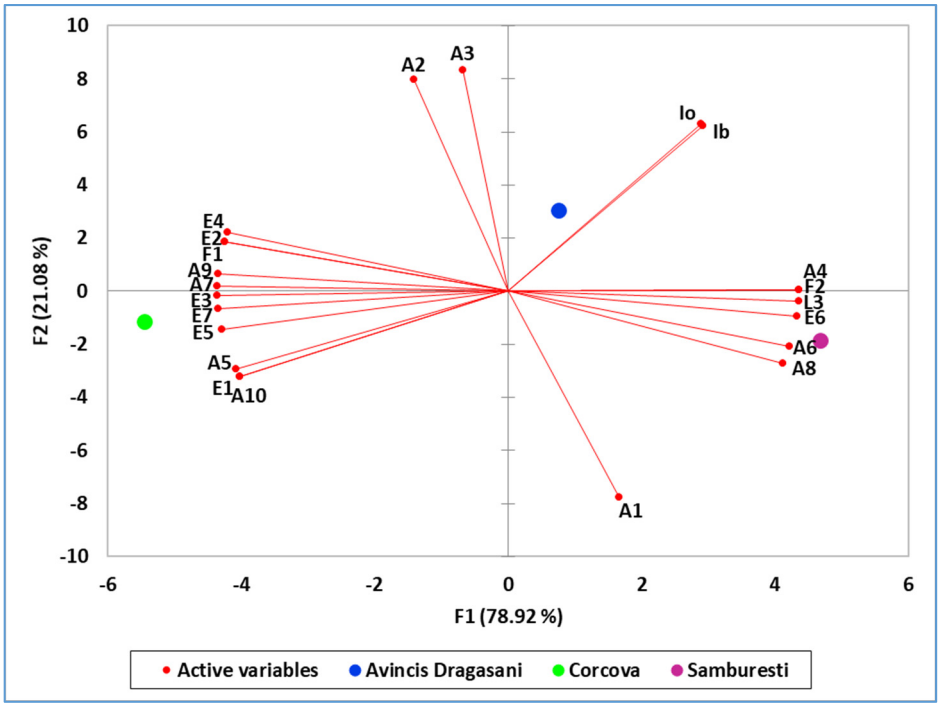

Figure 9. PCA score plot using Kaiser-Meyer-Olkin determined variables at an accepted level of significance of α = 0.60 (Io - oenoclimatic aptitude index; Ib - viticultural bioclimatic index; A1 – iso butanol; A2 – 2-nonanol; A3 – Terpineol; A4 – 1-Hexanol; A5 – 4-methyl-1-pentanol; A6 – E-3-hexenol; A7 – Linalool; A8 – Glycerin; A9 – Benzyl alcohol; A10 – 3-hydroxy-butanone; E1 – Hexyl-acetate; E2 – Ethyl octanoate; E3 – Ethyl-3-hydroxy butyrate; E4 – Ethyl decanoate; E5 – Ethyl hydrogen succinate; E6 – Phenethyl acetate; E7 – Methyl-4-hydroxy-butanoate; F1 – Decanoic acid; F2 – 2-Oxoadipic acid and L3 – Butyrolactone)

After considering the Kaiser-Meyer-Olkin selected components, the performed PCA analysis revealed that the first two components explained 100% of the total variation. The first principal component (PC1) explained 78.9% of the total variance and presented a high negative correlation with most of the ester group, separating Samburesti region from Corcova. PC2 explained 21.1% of the total variance and separated Avincis Dragasani area from the other and mostly corresponded to the oenoclimatic aptitude index and viticultural bioclimatic index. Multivariate statistical methods were essentially useful to reduce a large number of correlated variables into a small

number of uncorrelated vectors, allowing a clearer graphical representation. Therefore, the attempt to eliminate the elements to define better the variables responsible for origin separation was made, but the percentage of explained variance remained the same. The wine volatile profile and climatic factors along with chemometric analysis methods successfully differentiate the geographical locations. Even if the provenance regions were close in distance, each of them has their own particularities in terms on pedoclimate offering to the same variety unique features.

CONCLUSIONS

Following the evaluation of aroma compounds in the wine samples analyzed, the highest amounts were determined for wines obtained from grapes harvested from vineyards that were situated on brown or brown-reddish soils, rich in limestone and located on alluvial gravels, where the oenoclimatic aptitude index and the viticultural bioclimatic index were high. This was possible in the Dragasani region, the results obtained being superior to those in Samburesti and Corcova regions. These indicators have led to a more significant accumulation of long-chain alcohols. A slightly lower pedoclimatic index was reported in the Samburesti region where aroma compounds such as long-chain alcohols and esters showed amounts below those of Dragasani region. These values can also be influenced by soils that have a different configuration: clayey, loamy-clayey. Instead, crops that are oriented on the southern, south-eastern, and south-western slopes lead to the accumulation of volatile compounds such as fatty acids and lactones at significantly higher values than Dragasani and Corcova regions. The lowest values of the calculated climatic indexes were in the Corcova region (about 10-12%), although the soil has favorable properties for growing vines (reddish-brown with leached chernozems, medium texture, locally coarse or clay-loam). These qualities have led to wines with a rich ester content which gives them specific aromas and bouquet.

In perspective of the outcomes achieved inside this preliminary investigation, it can be concluded that a classification approach based on the combination of volatile compounds and climatic factors, together with appropriate chemometric techniques is a promising and effective way for differentiating Feteasca regala wine variety conforming to their geographical origin. The analyzed wines surprised only a segment of the multitude of factors that lead to the formation of the aromatic palette of a wine, but as it is observed for the same variety volatile compounds can accumulate in variable amounts contributing to the formation of their sensory properties.

EXPERIMENTAL SECTION

The samples analyzed were 2019 production Feteasca regala wines from three wine centers from Romania, Valcea county, namely: Samburesti (44° 48' N 24°23' E), Corcova (44°41′ N 23° E) and Avincis Dragasani (44°39′ N 24°15′ E) as illustrated in figure 10.

Figure 10. The representation of the studied wine centers from Romania

Reagents

All the reagents used were analytical grade. Isobutanol 95%, butanol 98%, isopentyl alcohol 98%, 1-hexanol, 4-methyl-1-pentanol 99%, E-3-hexenol, Z-3-hexenol 98%, 2-nonanol, 1-heptanol, 2,3-butanediol 99%, 3-(methylthio)-1-propanol 97%, linalool, terpineol 98%, 2-phenyl ethanol, trans-geraniol, glycerin, benzyl alcohol, 3-hydroxy-butanone 98%, N-amyl acetate, hexyl-acetate 97%, ethyl caproate, ethyl lactate, ethyl octanoate 98%, ethyl-3-hydroxy butyrate, ethyl decanoate 99%, ethyl hydrogen succinate, phenethyl acetate, diethyl malate, methyl-4-hydroxy-butanoate 97%, isobutyric acid, hexanoic acid 99%, isovaleric acid 98%, lactic acid 99%, octanoic acid, decanoic acid 99%, hexadecanoic acid 97%, malic acid 95%, 2-oxoadipic acid 97%, pantolactone 98%, isovaniline 95%, butyrolactone 97%, methylene chloride and sodium sulfate were purchased from Sigma-Aldrich, (Milwaukee, WI, SUA) and Fluka (Buchs, Switzerland).

Sample preparation

100 mL of wine sample were extracted 3 times with dichloromethane (10 mL, 10 mL, and 5 mL) for 15 minutes at 700 rpm. The organic extract was dried on anhydrous sodium sulfate, concentrated up to 1.0 mL and analyzed.

The samples were collected from three different bottles for each wine and the analysis was performed in triplicate for each sample collected. The results were expressed as the average of all determinations performed for the same type of sample.

GC-MS analysis

The analysis of the minor volatile compounds from the wine samples was performed by using a gas chromatograph (GC) coupled with a mass spectrometer (MS) Varian 450-GC with Varian 240-MS equipment. The GC was equipped with a Thermo Scientific TG-WAXMS (60 m x 0,32 mm, 0,25μm film thickness) capillary column. The carrier gas was helium at a flow of 1.2 mL/min and a splitting injection system was used. The injection volume was 1μL. The column temperature was programed as follows: 35℃ for 2.8 min., then it increases up to 120℃ with 4℃/min. for 4 min., ramped up to 190℃ with 10℃/min. maintained for 7 min. The mass detector was used at 70 eV in the scan mode, and the mass range for ion scan was between 40 and 300 m/z (mass to charge ratio).

The analysis of the volatile compounds was done by comparing the relative retention times and mass fragmentation of each compound from the sample chromatogram to the chromatograms that show compounds analyzed by using standard solutions and by comparison to the spectral library (NIST Mass Spectral Library 08) as well.

Statistical analysis

The primary aim of the chemometric evaluation was to show the relationship between the wine samples and the minor volatile compounds in order to generate a visual plot of the samples and their distribution on a score plot and interpret their trends. To process the minor volatile compounds from the wine samples, PCA (principal component analysis) was applied [22]. Principal component analysis was selected because of its capability to explore and model experimental data, assess variable significance and correlations, and create simple bidimensional plots in which the wine samples (also known as objects) and the minor volatile compounds are visualized (scores plot and loadings plot, respectively). In order to use the appropriate statistical

tests for PCA, it was first necessary to reduce the measurement to most relevant factors. For this purpose, Kaiser-Meyer-Olkin measure of sampling adequacy was used to assess which data are suitable for PCA s for the accepted level of significance α = 0.60. The goal was to reduce the number of items by finding correlations between them and abstracting a smaller number of factors. During statistical evaluation of the data, Microsoft Excel 2016 was used for the descriptive statistics, while XLSTAT Addinsoft 2014.5.03 version (Addinsoft Inc., USA) software was used for the chemometrical evaluation of the results.

ACKNOWLEDGMENTS

This work is supported by the project ANTREPRENORDOC, in the framework of Human Resources Development Operational Programme 2014- 2020, financed from the European Social Fund under the contract number 36355/23.05.2019 HRD OP /380/6/13 – SMIS Code: 123847.

REFERENCES

1. R. Baumes R.; Wine Aroma Precursors, Wine Chemistry and Biochemistry, Springer, New York, **2009**, pp. 251-265
2. I. Rebenciuc; O. Tița; *Management of Sustainable Development*, **2019**, *11 (2)*, 59-64
3. L.M. Irimia; C.V. Patriche; B. Roșca; *Theor. Appl. Climatol.*, **2018**, *133*, 1–14
4. R.R. Walker; D.H. Blackmore; P.R. Clingeleffer; Aust. J. Grape Wine R., **2010**, *16(1)*, 243–257
5. A. Dobrei; M. Mălăescu; A. Ghiță; T. Cristea; A. Drăgunescu; *J Hortic, Forestry and Biotechnology,* **2010**, *14(1)*, 298-301
6. I. Rebenciuc; Vinurile moldovenești – aromă și savoare, *Editura Universitatii Lucian Blaga din Sibiu*, **2020**
7. N. Pomohaci; V.V. Cotea; V. Stoian; I. Năməloşanu; Oenology, *Ceres*, Bucharest, **2001**
8. H.A. Gomez-Gomez; I.O. Minatel; C.V. Borges; M. Ortiz Mayo Marques; E. Tadeu da Silva; G.C. Monteiro; M.J.R. da Silva; M.A. Tecchio; G.P. Pereira Lima; *J. Agr. Sci.*, **2018**, *10(12)*, 65-77
9. L. Louw; A. Tredoux; P. Van Rensburg; M. Kidd; T. Naes; H. Nieuwoudt; *S. Afr. J. Enol. Vitic.*, ***2016****, 31*(2), 213-225
10. C. González-Barreiro; R. Rial-Otero; B. Cancho-Grande; J. Simal-Gándara; 2013, *Crit. Rev. Food Sci.*, **2013**, *55(2)*, 202-218
11. D.I. Popescu; Repere analitice in autentificarea vinurilor românești, Editura Universitatii Lucian Blaga din Sibiu, **2019**

12. I.S. Pretorius; P.B. HØj; *Aust. J. Grape Wine R.*, **2005**, 11(12), 83-108
13. I. Rebenciuc; O. Tița; D.I. Popescu; *Manag Sustain Dev*, **2019**, *11(2)*, 55-58
14. A.M. Moroșanu; C.E. Luchian; M. Niculaua; C.L. Colibaba; A.C. Tarțian; V.V. Cotea; *Not. Bot. Horti. Agrobo.*, **2018**, *46(1)*, 247-259
15. J.H. Swiegers; R. Willmott; A. Hill-Ling; D.L. Capone; K.H. Pardon; G.M. Elsey; K.S. Howell; M.A. de Barros Lopes; M.A. Sefton; M. Lilly; I.S. Pretorius; *Dev. Food Sci.*, **2006**, *43*, 113-116
16. A.G. Reynolds; J. Schlosser; D. Sorokowsky; R. Roberts; J. Willwerth; C. de Savigny; *Am. J. Enol. Vitic.*, **2007**, *58*, 25-41
17. I. Rebenciuc; O. Tița; *Bulletin UASVM Animal Science and Biotechnologies*, **2018**, *75(1)*
18. A. Popa; G. Condei; D. Popa; F. Dragomir; M. Seiculescu; M. Nica; C. Genoiu; A. Dunoiu; *Buletin USAMV-CN*, **2006**, *63*
19. A. Popescu; V. Enache; C. Simion; A. Donici; G. Tabaranu; 2009, *Bulletin UASVM*, **2009**, *66(1)*
20. L.M. Irimia; C.V. Patriche; H. Quenol; *J Int Sci Vigne Vin*, **2014** *48(3)*,145-167
21. H. Kaygusuz; F. Tezcan; F.B. Erim; O. Yildiz; H. Sahin; Z. Can; S. Kolayli; *LWT -Food Sci. Tech.,* **2016**, *68*, 273–279
22. M. Gajek; A. Pawlaczyk; M.I. Szynkowska-Jozwik; *Molecules*, **2021**, *26*, 214

STUDIA UBB CHEMIA, LXVI, 4, 2021 (p. 97-106)
(RECOMMENDED CITATION)
DOI:10.24193/subbchem.2021.4.07

EFFECTS OF SWEETENERS AND STORAGE ON THE ACIDITY, SOLUBLE SOLIDS AND SENSORIAL PROFILE OF LINGONBERRY JAMS

TEODORA SCROB[a,*], SÂNZIANA MARIA VARODI[a], GEORGIANA ALEXANDRA VINTILĂ[a]

ABSTRACT. In this study, seven jam formulations were prepared, starting with the basic formulation, containing sucrose. This sweetener was replaced by fructose, erythritol, brown sugar, coconut sugar, stevia and saccharine, making these formulations a good alternative, some of them being also suitable for diabetic patients. Titratable acidity (TA) and total soluble solids (TSS) of lingonberry jams were evaluated for changes in jam quality during storage at 4°C, 25°C (under light conditions) and 25°C (under dark conditions) for 60 days. Moreover, a sensory evaluation was performed after 180 days of storage at 4°C to assess its consumer acceptance as compared to jam made with sucrose. During storage, TA and TSS increased in the case of all samples regardless of temperature conditions. ANOVA analysis of results revealed that the changes in TA and TSS were significantly affected by the type of sweetener used in jam formulation ($p<0.05$). Jams formulated with coconut sugar and stevia were assessed by the sensory panel as the most acceptable.

Keywords: *titratable acidity, total soluble solids, sucrose, sweeteners, sensory properties*

INTRODUCTION

Due to the growing health concerns and higher incidence of obesity, metabolic syndrome and diabetes, during the recent decades there has been an increase in interest for low calorie food consumption [1,2]. These days' consumers are looking for high quality foods and there is considerable demand for fresh fruits and their products. Lingonberry fruit (*Vaccinium vitis-*

[a] *Babeş-Bolyai University, Faculty of Chemistry and Chemical Engineering, 11 Arany Janos str., RO-400028, Cluj-Napoca, Romania,*
[*] *Corresponding author: teodora.scrob@ubbcluj.ro; teodora_scrob@yahoo.com*

idaea) is attaining popularity, as it is rich in bioactive compounds including anthocyanins, proanthocyanidins, flavonols or hydroxycinnamic acids [3] and also possesses various biochemical activities such as antioxidant and antibacterial effects [4]. However, these fruits are perishable and the lack of appropriate techniques for postharvest, transport and storage results in great losses. Fruit preservation techniques like candying, production of jams and fruit preserves extend significantly their shelf-life allowing their consumption all year [5]. In this way, jams are most preferred by consumers mainly due to their availability, sensory quality and low cost.

Sugar has a key technological role in the traditional jam's confection, as it influences the soluble solids content. Therefore, sugar plays an important role in physical, chemical, and sensorial properties of jams, also increasing its microbiological stability and hence safety [6]. However, large sugar consumption has been correlated with adverse effects on health, such as cardiovascular diseases, obesity and diabetes [7]. During the recent decades there has been an increase in interest for replacing sugar with other constituents. Fructose is the most commonly used sugar in jam formulations for people with diagnosed diabetes mellitus type 2 [8]. Sugar alcohols (erythritol, isomalt, lactitol, maltitol, mannitol, sorbitol), are attractive alternatives to sucrose as they are minimally metabolized (and thus we draw fewer calories from them), taste relatively similar to sucrose, and are naturally occurring [9]. Coconut sugar has become a popular alternative to white sugar due to its distinctive aroma, slightly acidic and smelling caramel, with a lower glycemic index than white sugar. Stevia is another natural sweetener, which is increasingly popular in the last years. It represents extract from the leaves of the plant *Stevia rebaudiana (Bert.)* which contains a high level of low-calorie sweetening compounds, known as steviol glycosides. Besides sweetening properties, Stevia rebaudiana extracts possess antioxidant, antimicrobial and antifungal activity [10,11]. Among synthetic sweeteners, saccharin is the oldest of this sweeteners category, with sweetness from 200 to 700 times more potent than sucrose. Synthetic sweeteners are in principle designed to mimic the sensory properties of sucrose, but in actuality usually exhibit additional taste notes other than sweetness, most frequently bitterness, or temporal characteristics that do not match that of sucrose [12]. This can lead to a lingering sweetness that consumers find off-putting [11].

Fruit jam incorporating alternative sweetener should have similar textural and rheological characteristics, as well as sensory properties to that of the traditional product [13]. Sugar-free jams are possible using alternative sweeteners also called low-calorie sweeteners, such as sorbitol, maltitol, and/or sweeteners like saccharin and cyclamate, responsible to cause

weight gain [14]. However, the attainment of a suitable texture may be more difficult in sugar-free jams than in jams with other sweeteners. So the new product formulation has to result in similar texture, flavor, and other characteristics of the traditional product. Therefore, understanding of the factors that may influence the texture of processed foods is essential for the development of new products [5].

To our knowledge, the literature available at present is deficient in references about effects of different sweeteners on lingonberry jams properties during storage. Thus, the aim of this work was the development of lingonberry jam's formulations with different nutritional properties. For this purpose, the sucrose used in traditional jams was replaced by fructose, erythritol, brown sugar, coconut sugar, stevia and saccharine. The sensory properties of the products were evaluated in order to ascertain their acceptability. In addition, the changes in total soluble solids (TSS) and titratable acidity (TA) of lingonberry jams during storage at 4°C, 25°C (under light conditions) and 25°C (under dark conditions) for 60 days were monitored.

RESULTS AND DISCUSSION

Effects of storage time and temperature on titratable acidity (TA) of jams samples

Because acidity protects against the development of microorganisms, measuring TA is an important step in evaluating the quality of a jam. The TA values of jams samples obtained during 60 days of storage are presented in Table 1. TA increased during storage in the case of all samples regardless of temperature conditions. After 15 days of storage, maximum increase was observed in Jam 6 stored under light conditions (63.3%), while the lowest increase was observed in Jam 3 stored at 4°C (4.16%). Storage at 4°C after 30 days determined an evident increase of TA in the case of Jam 2, from 7.69% to 34.5%, respectively. After 60 days of storage, at 25 °C (under light), in Jams 5 and 6 total acids increased to highest values of 0.364% and 0.385 %, respectively. Storage at 4°C after 60 days determined an acidity level between 0.192 (Jam 1) and 0.301 (Jam 6). Maximum increase was observed in Jam 7 (43.3%) followed by Jam 6 (36.6%), while minimum increase was observed in Jam 1 (19.5%) followed by Jam 3 (20.8%). The results are in agreement with Muhammad et al. [15], which observed increased in % acidity from 42.22% to 71.88 % in apple diet jams. Formation of organic acids due to degradation of polysaccharides and breaking of chemical bonds might be the reason for this increase in acidity [16]. Under light conditions, the

increasing of TA was more pronounced than under dark conditions, due to a higher degradation of jam components. Also, there was a higher increase of TA at 25°C than at 4°C, suggesting that temperature of storage affects this parameter. This is also confirmed by one-way ANOVA test. Thus, it was observed that the differences on TA were not significant ($p>0.05$) after 15 days of storage at 4°C, but after 30 and 60 days of storage, respectively, the changes became significant for all jams samples ($p<0.05$). Storage at 25°C both under dark and light conditions induced significant differences reported to the control values ($p<0.05$). It was noticed that the changes in TA were significantly affected by the type of sweetener used in jam formulation ($p<0.05$). In addition, two-way ANOVA shows that between storage conditions and jams formulations no significant interaction effect exists ($p>0.05$).

Effects of storage time and temperature on total soluble solids (TSS) of jams samples

In this study, TSS of the products served as control parameter. When TSS reached 56.0-57.0 °Brix, jams heating was stopped, excepting Jam 6 and Jam 7, formulated with stevia and saccharine, respectively. In the case of these jams, heating was stopped when TSS reached about 22.0 °Brix, as previously reported by [16]. The TSS is primarily represented by sugars, with acids and minerals contributing, being an important parameter for evaluating jams quality [17]. Prior storage, TSS values of lingonberry jams were: 56.2 °Brix (Jam 1), 56.7 °Brix (Jam 5), 56.8 °Brix (Jam 2 and 3), 57.0 °Brix (Jam 4), while in the case of Jams 6 and 7, Brix values were much lower (22.0 and 21.7 °Brix, respectively). °Brix values of the jams samples analyzed during 60 days are presented in Table 1.

The data obtained for TSS revealed that there was a very slight change occurred during 60 days of storage at 4°C. Generally, all samples show an increasing in TSS during storage. Maximum increase was observed in Jam 6 (3.63%), while minimum increase was observed in Jam 2 (0.176%). These results are in agreement with the results of Muhammad et al. [15] who observed an increase in TSS of apple jams during storage. In another study Ehsan et al. [18] reported a slight increase in TSS of watermelon lemon jam from 68.6 to 68.9 during 60 days of storage. The increase in TSS contents may be explained by the solubilization of jam constituents during storage [15].

The high content of TSS might also be due to hydrolysis of polysaccharide especially pectin into simple sugar in the presence of acid during storage [16]. Moreover, increasing of TSS content was more visible in the case of samples stored at 25°C, exposed to light conditions, than those

stored under refrigeration. The highest mean value was recorded for Jam 6 (23.0 ºBrix) and Jam 4 (57.7 ºBrix) after 60 days of storage, both under light conditions, indicating that light and temperature influence the TSS.

Table 1. The TA and TSS values of jams samples obtained during storage.

Time (days)	Titratable acidity (%)			Total soluble solids (°Bx)		
	4 °C	25°C (dark)	25°C (light)	4 °C	25°C (dark)	25°C (light)
Jam 1						
0	0.161	0.161	0.161	56.2	56.2	56.2
15	0.168	0.168	0.175	56.3	56.4	56.6
30	0.189	0.189	0.192	56.4	56.8	56.8
60	0.192	0.195	0.203	56.5	56.9	56.9
Jam 2						
0	0.182	0.182	0.182	56.8	56.8	56.8
15	0.196	0.210	0.224	56.8	56.8	56.9
30	0.245	0.248	0.315	56.8	56.8	57.0
60	0.273	0.280	0.315	56.9	56.9	57.4
Jam 3						
0	0.168	0.168	0.168	56.9	56.9	56.9
15	0.175	0.175	0.182	43.4	44.3	45.2
30	0.182	0.182	0.196	43.7	44.6	44.8
60	0.203	0.189	0.217	44.0	44.1	44.2
Jam 4						
0	0.161	0.161	0.161	57.0	57.0	57.0
15	0.175	0.182	0.280	57.1	57.1	57.3
30	0.189	0.199	0.343	57.2	57.2	57.6
60	0.196	0.210	0.343	57.3	57.3	57.7
Jam 5						
0	0.175	0.175	0.175	56.7	56.7	56.7
15	0.210	0.217	0.315	56.8	56.8	56.8
30	0.224	0.238	0.332	56.9	56.9	56.9
60	0.252	0.273	0.364	56.9	57.0	57.2
Jam 6						
0	0.210	0.210	0.210	22.0	22.0	22.0
15	0.280	0.311	0.343	23.2	23.4	23.4
30	0.287	0.318	0.350	22.8	23.0	22.9
60	0.301	0.343	0.385	22.9	22.9	23.0
Jam 7						
0	0.210	0.210	0.210	21.7	21.7	21.7
15	0.273	0.273	0.315	21.7	21.7	22.0
30	0.294	0.308	0.322	21.9	21.9	22.0
60	0.301	0.308	0.336	22.1	22.0	22.0

The samples stored at 25°C at the dark followed a similar trend as samples stored under refrigeration. The results of statistical processing by one-way ANOVA test revealed that during jam storage, the differences reported to the control were quantified as non-significant ($p>0.05$), regardless of temperature storage. However, it could be noticed that the changes in TSS content was affected by jam's formulation ($p<0.05$). Also, two-way ANOVA show that no significant interaction effect between storage conditions and formulation is observed ($p>0.05$).

Sensory evaluation of jams samples

The sensory profile of the lingonberry jams was evaluated in terms of color, taste, texture, spreadability and overall acceptability. The sensory evaluation indicated that the majority of jams were acceptable to the consumers after 180 days of storage at 4 °C (Table 2). Result showed that Jam 5 recorded the best sensory evaluations, except for the color. Color is an important sensory attribute on which the consumer preference depends. Color acceptability was highest for Jam 6 and Jam 7 (8.80) while Jam 3 gave lowest (5) means value color acceptability.

Table 2. Sensory parameters of the jams samples.

Jam / **Parameter**	1	2	3	4	5	6	7
Color	8.60	8.00	5.00	8.60	6.20	8.80	8.80
Taste	7.80	7.00	4.20	7.20	8.80	8.00	6.80
Texture	8.80	7.40	4.20	8.40	8.80	8.00	8.00
Spreadability	8.80	6.40	4.00	8.60	8.80	8.40	8.20
Overall Acceptability	8.20	7.60	3.80	8.20	8.80	8.40	8.00

For taste, the maximum mean value was obtained in the case of Jam 5 (8.80), followed by Jam 6 (8) and Jam 1 (7.80). The high value of Jam 5 could be as a result of the presence of coconut sugar, that has a distinctive aroma, slightly acidic and smelling caramel. Texture ranged from 4.20 to 8.80 with Jam 3 having the lowest value while Jam 1 and Jam 5 had the highest. The low texture of Jam 3 could be attributed to the sweetener agent that crystallized during storage. Decrease in texture quality might be also due to hydrolysis of pectin contained in fruits and sweeteners during storage. These results are in agreement with Abolila et al. [1] who observed decreasing trend in texture of low calorie orange jam during storage. Concerning spreadability, Jam 3 and Jam 2 obtained the lowest scores (4 and 6.40, respectively).

Overall acceptability of the jam samples ranged from 3.80-8.80 and Jam 5 and 6 were rated most preferred while Jam 3 was least preferred. The sensory scores indicate that lingonberry jam samples were highly acceptable by the consumers except for the jam containing erythritol (Jam 3), which had the least preference scores compare to other jams. Overall acceptability is beyond 7.60 on a 9-point hedonic scales in the case of all jams, excepting Jam 3, revealing that they were equally acceptable by the panelists. The high sensory values of these jams could be due to the color and flavor of lingonberry fruits that are transferred to the final products on processing. Additionally, jam prepared with stevia (Jam 6) was evaluated as being better than jam prepared with sucrose. Since stevia extracts possess antioxidant, antimicrobial and antifungal activity [10,11], jams formulated with stevia could be commercialized as functional products. Moreover, although the bitterness level for the Jam 7 was expected to be very high, due to the saccharine content, it seems that the combination of this sweetener with lingonberry fruits reduced bitterness of jam, being preferred by the panelists, especially for its color and spreadability.

CONCLUSIONS

The results of our study supplies information regarding the replacement of sucrose from lingonberry jams with other sweeteners (natural and synthetic) and describes the sensorial stability of these jams during storage. The use of several sweeteners in the manufacture of lingonberry jam was shown to be satisfactory, resulting in a product with jam characteristics, taste and texture similar to conventional jam with sucrose, excepting jam prepared with erythritol. Storage at 4°C induced changes on TA and TSS parameters of lingonberry jams, but not as important as a storage at 25°C, indicating a better preservation of jams under refrigeration, regardless sweetener agent. Sugar formulation affected sensorial parameters of jams. Jams formulated with stevia and saccharine maintained the best color during storage, while jam formulated with coconut sugar obtained the lowest scores regarding color. The formulations containing sucrose or coconut sugar were the easiest to spread and resulted in the highest maintenance of texture. Coconut sugar led to the best scores for taste, mainly due to its distinctive flavor. Although jams prepared with stevia and saccharine did not reach the same concentration of soluble solids as jams made with sucrose, they were stable over the storage period considered. Moreover, the use of natural sweetener stevia in the manufacture of lingonberry jam resulted in a product with a higher overall acceptability than jam prepared with sucrose, this study being useful for diabetics or even for weight maintaining persons.

EXPERIMENTAL SECTION

Chemicals and reagents

All chemicals and reagents used in this study were of analytical grade and were purchased from Merck, Germany. Distilled water was used for solutions preparation.

Fruit material and jams preparation

Fresh lingonberries (*Vaccinium vitis-idaea L.*) were harvested from Apuseni Mountains, Romania, in August, 2019. Lingonberry jams were prepared in the laboratory, according to a traditional procedure. Basic formulation used for of each type of jam is presented in Table 3. White sugar was purchased from a local market in Cluj-Napoca, while all the other sweeteners used in this study were purchased from a health food store. The ingredients were heated at low temperature (50 °C), which was monitored during the entire process. Boiling process was stopped when TSS (total soluble solids) reached 56-57 °Brix, excepting Jam 6 and Jam 7, formulated with stevia and saccharine, respectively. In the case of these jams, heating was stopped when TSS reached about 22 °Brix, as previously reported by [16]. Each jam was packed into glass jars with screw caps, without being pasteurized. The jams were stored at 5°C, at 25°C (under light conditions) and at 25°C (under darkness conditions). Samples were analyzed immediately and after 15, 30 and 60 of storage.

Table 3. Jams formulation

	Lingonberry fruits (g)	**Sweetener (g)**
Jam 1 (with white sugar)	100	50.0
Jam 2 (with fructose)	100	29.4
Jam 3 (with erythritol)	100	77.0
Jam 4 (with brown sugar)	100	50.0
Jam 5 (with coconut sugar)	100	50.0
Jam 6 (with stevia)	100	0.180
Jam 7 (with saccharine)	100	0.180

Titratable Acidity (TA) determination

Titratable acidity (TA) was determined as previously described by Awolu et al. [19]. About 1 g of each sample was weighed and put into 50 ml centrifuge tube. Distilled water was added the centrifuge tube, mixed with the sample and filtered. About 1 ml aliquot of the filtered solution was taken and diluted with 10 ml of distilled water. Aliquotes of diluted samples (10 ml) were titrated with volumetric solution of 0.1N NaOH and the volume of NaOH was converted to percentages of citric acid, using equation (1):

$$\% \text{ citric acid} = V_{NaOH}/V_{sample} \times 0.007 \times 100 \quad (1),$$

where V_{NaOH} –volume of alkali used in titration and V_{sample}-volume of the sample titrated (10 ml).

Total Soluble Solids (TSS) determination

Total concentrations of soluble solids were determined using a Bellingham + Stanley refractometer (Bellingham + Stanley Ltd., Kent, UK) and expressed as degrees Brix (°Brix). The instrument prism was covered with about 1–2 drops of cooled lingonberry jam and soluble solids value was directly recorded from the digital reading display at ambient temperature.

Sensory analysis

All evaluation sessions were held in an analytical laboratory from our university and were conducted by an untrained panel consisting of 5 students with 24 years mean age. Color, taste, texture, spreadability and overall acceptability were evaluated according to the hedonic scale of nine points (9 = like extremely to 1 = dislike extremely) as reported by [17]. Jam samples were tempered for 30 min at room temperature (22 ± 2 °C) and drinking water was provided after each sample testing.

Statistical analysis

The experimental results were subjected to statistical analysis using Microsoft Excel. One-way analysis of variance (ANOVA) was used to determine significant differences between values. The significance level was defined as $p<0.05$ for 95% probability. Two-way ANOVA was used to identify the interdependence between factors.

ACKNOWLEDGMENTS

The authors would like to thank the project POCU/380/6/13/123886- "Entrepreneurship for innovation through doctoral and postdoctoral research" for the financial support given to this investigation.

REFERENCES

1. R. M. Abolila; H. Barakat; H. A. El-Tanahy; H. A. El-Mansy; *Food Sci. Nutr.*, **2015,** *6*, 1229–1244.
2. V. R. Souza; P.A. Pereira; A. C. M. Pinheiro; H. Bolini; S.V. Borges; F. Queiroz; *Int. J. Food Sci. Technol*., **2013**, *48*, 1541–1548.
3. C. Mane; M. Loonis; C. Juhel; C. Dufour; C. Malien-Aubert; *J. Agric. Food Chem,* **2011**, *59,* 3330-3339.
4. M. Toivanen; S. Huttunen; S. Lapinjoki; C. Tikkanen-Kaukanen; *Phytother Res.*, **2011**, *25,* 828-832.
5. A. Vilela; S. Matos; A. S. Abraão; A. M. Lemos; F. M. Nunes; *J. Food Process,* **2015***, 2015,* 1-14.
6. S. Basu; U. S. Shivhare; *J. Food Eng*., **2010**, *100 (2),* 357–365.
7. Y. Akanksha; G. Gulia; Y. Bhuvnesh; *Int. J. Sci. Eng.,* **2020**, *9(1),* 4079-4083.
8. M. Belovik; A. Torbika; I. P. Lijakovic; J. Mastilovik; *Food Chem*., **2017,** *237*, 1226-1233.
9. M. Grembecka*; Eur Food Res Technol*., **2015**, *241*, 1–14.
10. R. Lemus-Mondaca; A. Vega-Gálvez; L. Zura-Bravo; K. Ah-Hen; *Food Chem*., **2012**, *132*, 1121–1132.
11. M. R. Mora; R. Dando; *Compr Rev Food Sci Food Saf.,* **2021**, 1–30.
12. G. E. DuBois; I. Prakash; *Annu Rev Food Sci Technol.*, **2012**, *3*, 353–380.
13. S. Basu; U. S. Shivhare; T. V. Singh; *J. Food Eng*, **2013**, *114*, 465–476.
14. K. C. Foletto; B. A. Melo Batista; A. M. Neves; F. deMatos Feijó; C.R. Ballard; M. F. Marques Ribeiro; M. C. Bertoluci; *Appetite*, **2016**, *96*, 604–610.
15. A. Muhammad; Y. Durrani; A. Zeb; M. Ayub; J. Ullah; *Sarhad J. Agric.,***2008**, *24 (3)*, 461-467.
16. R. Sutwal; J. Dhankhar; P. Kind; R. Mehla; *Int. J. Curr. Res.*, **2019**, *11(4)*, 9-16.
17. N. Touati; M. P. Tarazona-Díaz; E. Aguayo; H. Louaileche; *Food Chem*., **2014**, *145*, 23–27.
18. E.B. Ehsan; Z.P. Naeem; A. Ghafoor; M.S. Bahtti; *Pak. J. Food Sci*., **2002**, *12 (3-4)*, 21-24.
19. O. O. Awolu; G. O. Okedele; M. E. Ojewumi; G. F. Oseyemi; *J. Int. J. Biotechnol. Food Sci.*, **2018**, *3(1)*, 7-14.

STUDIA UBB CHEMIA, LXVI, 4, 2021 (p. 107-122)
(RECOMMENDED CITATION)
DOI:10.24193/subbchem.2021.4.08

TRYPTOPHAN DERIVATIVES, PHENOLIC COMPOUNDS AND ANTIOXIDANT POTENTIAL OF SOME WILD *TANACETUM* TAXA FROM TURKEY

EMEL DIRAZ-YILDIRIM[a,*], SENGUL KARAMAN[a], MUHITTIN KULAK[b], AHMET ILCIM[c]

ABSTRACT. The important molecule tryptophan and its derivatives serotonin and melatonin have vital functions in human and plant biosystem. Recent reports claimed these molecules and parthenolide may also have a role in COVID-19 treatments. Herewith the study, contents of chlorogenic acid, cynarin, quinic acid, parthenolide, and tryptophan derivatives in leaf and flowers of seven species of *Tanacetum* from Turkey were examined using HPLC. The methanolic extracts of the species were also screened for their total phenolic content and DPPH scavenging activity. Regarding to HPLC data, the highest amount of chlorogenic acid and cynarin were detected in *T. cilicicum*, quinic acid in *T. densum* subsp. *amani* and parthenolide in *T. argenteum* subsp. *argenteum* leaves. Also, the highest amount of tryptophan and serotonin were estimated in *T. argenteum* subsp. *argenteum*. Melatonin content was highest in *T. densum* subsp. *amani*. All *Tanacetum* species exhibited potent antioxidant activities. *T. densum* subsp. *amani* (Afşin) flowers had higher DPPH activity than control group BHT and *T. cilicicum* leaves and flowers had the highest total phenolic content. Herewith, phenolic profiles of *T. argenteum* subsp. *argenteum, T. armenum* and *T. densum* subsp. *amani* and tryptophan derivates of the species were reported for the first time.

Keywords: *Tanacetum, parthenolide, antioxidant activity, tryptophan, serotonin, melatonin*

INTRODUCTION

The genus *Tanacetum* L. belonging to Asteraceae (Compositae) family includes over 200 species and is widespread in many countries of North America, Asia and Europe [1]. In Turkey, 61 taxa of *Tanacetum* exhibit

[a] *Kahramanmaras Sutcu Imam University, Science and Letter Faculty, Biology Department, 46100, Kahramanmaraş,Turkey*
[b] *Department of Herbal and Animal Production, Vocational School of Technical Sciences, Igdir University, 76000, Igdir, Turkey*
[c] *Mustafa Kemal University, Science and Letter Faculty, Biology Department, 31060, Hatay, Turkey*
[*] *Corresponding author: emeldiraz@hotmail.com*

distribution and 24 of them are endemic [2]. *Tanacetum* taxa has been widely used as medicinal plants over 2000 years due to their bitter substances, sesquiterpene lactones, resins, flavonoids, coumarins, tannic acid, essential oils. The plants have been well-documented to exhibit antimicrobial, antibacterial, antioxidant, expectorants, antiseptic vermifuges, insect-repelling and spasmolytic effects [1,3,4]. Of the species among *Tanacetum*, *T. parthenium* (feverfew) and *T. vulgare* (tansy) are the common species.

T. parthenium was used in treatment for ailments of the nervous system based on anecdotal and historical evidence. In 1978, British health magazine reported that feverfew leaves had chronic relieving effects and the plant gained popularity as a phytomedicine. The main molecule parthenolide was isolated from *T. parthenium* shoots and amount of the molecule was changed among 0.1-0.2% as approved pharmacologically active. Also, anticancer and anti-inflammatory activities of parthenolide have been shown [5,6]. Recent studies regarding chemical probe development from parthenolide showed that parthenolide-induced microtubule modulation and the currently characterized tubulin carboxypeptidase enzymes involved in nerve (re)growth, cardiac muscle cell function, and metastasis development [7]. Bahrami et al. claimed that parthenolide may be one of the herbal candidates for clinical evaluation of COVID-19 with a support of reduced mortality. Parthenolide reduced L-1, IL-2, IL-6, IL-8, and TNF-α production pathways which IL-6 in cytokine storm has significant role diabetes mellitus, and cardiovascular diseases as principal comorbidities [8].

The other active compound melatonin (N-acetyl-5-methoxytryptamine) is synthesized from the amino acid L-tryptophan via serotonin (5-Hydroxytryptamine). Therefore, L-tryptophan is the precursor for melatonin and serotonin [9]. Murch et al. highlighted that chronic migraine headaches are associated with lower circulation levels of melatonin [3]. Furthermore, melatonin was proved to be associated with a number of nervous diseases such as epilepsy, insomnia, depression, Alzheimer, Parkinson's illness and regulating circadian rhythm, improving immunity and anti-aging [10,11]. In a recent study, in COVID-19 patients, the expression of genes part of tryptophan metabolism was increased, so that tryptophan-rich sources could be beneficial for COVID-19 [12]. Reasearches about melatonin, serotonin and tryptophan content of foods, drinks and medicinal plants is fast increasing because requirement to synthetic melatonin is rising. According to a report published by Transparency Market Research entitled "Melatonin Market for Food & Beverages, Dietary Supplements, Medicine and Other Applications", the global demand of synthetic melatonin was valued at USD 504 million in 2012 and was expected to reach USD 1300 million in 2019, the latter involves about 4000 tons of synthetic melatonin [13]. Considering that the consumption of rich phytomelatonin

foods increases the level of melatonin in humans, it is inevitable that the need for phytomelatonin supplements will increase. Phytomelatonin is a potential option to substitute synthetic melatonin.

Of the studies, Murch et al. [3] investigated the melatonin level of some medicinal plants and detected rich melatonin content in feverfew. Feverfew is recommended as a migraine prophylactic since clinical researches have approved its potent effect against headaches and migraine [14]. Also, serotonin agonists were used in migraine treatments [15]. Hitherto, no documents regarding serotonin and tryptophan content of *Tanacetum* taxa have been reported. The present study was designed to investigate phenolics profile, antioxidant activity, parthenolide, tryptophan, serotonin and melatonin content of seven wild *Tanacetum* taxa (*T. argenteum* subsp. *argenteum*, *T. armenum, T. cadmeum* subsp. *orientale*, *T. cilicicum*, *T. densum* subsp. *amani*, *T. kotschyi, T. nitens*) for first time.

RESULTS AND DISCUSSION

HPLC–UV analyses of some secondary metabolites in Tanacetum taxa

The distribution of chlorogenic acid, cynarin, quinic acid and parthenolide in leaf and flowers of some *Tanacetum* species has been reported herein. The quantitative analysis of the individual compounds in the polar extracts was performed using HPLC–UV and the results were represented in Table 1 and representative HPLC-UV chromatograms were given in Figure 1.

The compounds were confirmed by comparing the retention times with the standards. Herewith the results, the contents of the compounds exhibited significant differences according to the species and organs (p<0.01). For the present study, *T. argenteum* subsp. *argenteum* was collected lately of flowering period and the plant material of *T. cadmeum* subsp. *orientale* and *T. nitens* were not enough for all biochemical analyses. Therefore, flowers of *T. argenteum* subsp. *argenteum* and other two taxa were not screened for their chlorogenic acid, cynarin, quinic acid and parthenolide contents. Of the species, chlorogenic acid and cynarin were detected highest in *T. cilicicum* (15.61±0.03 and 19.68±0.14 mg/g DW, respectively) leaves and quinic acid in *T. densum* subsp. *amani* (Afşin) (84.82±0.45 mg/g DW) leaves. Quinic acid was the most abundant secondary metabolite identified herein (19.27±2.30 to 84.82±0.45 mg/g DW in leaves and 12.36±0.30 to 31.73±0.20 mg/g DW in flowers). Regarding parthenolide content, the contents were higher in leaves than those in flowers. The highest parthenolide content was determined in *T. argenteum* subsp. *argenteum* leaves (1.48%). In addition, *T. densum* subsp. *amani* collected from two different locations (Afşin and Ahırdağı) exhibited significant differences concerned with metabolites reported herein. In the

previous studies, chlorogenic acid content in *T. parthenium* were reported to be 2.13-7.62 ppm [16], 80-100 mg/g [17], 0.286-2.976 mg/g [18], 6.45 g/kg [19], and 0.784% [20]. In *T. cilicicum*, chlorogenic acid content was found as 2.30 µg/mg [21]. Also, cynarin (1.48-7.49 ppm) and quinic acid (4-5.5 ppm) in *T. parthenium* were reported by Wu et al. [16]. The present results are similar to those values of previous studies.

Table 1. Phenolic compounds and parthenolide amount of *Tanacetum* taxa

	Chlorogenic acid (mg/g)		**Cynarin (mg/g)**		**Quinic acid (mg/g)**		**Parthenolide (mg/100g)**	
Taxa	**Leaf	**Flower	**Leaf	**Flower	**Leaf	**Flower	**Leaf	**Flower
T. argenteum subsp. *argenteum*	4.31± 0.02^{c}	ns	4.89± 0.02^{b}	ns	42.51± 1.37^{b}	ns	1.480± 0.050^{a}	ns
T. armenum	3.22± 0.01^{d}	2.65± 0.09^{b}	0.22± 0.01^{f}	0.60± 0.03^{d}	29.47± 1.24^{d}	31.73± 0.20^{a}	0.036± 0.001^{d}	0.010± 0.005^{c}
T. cilicicum	15.61± 0.03^{a}	2.38± 0.05^{c}	19.68± 0.14^{a}	7.96± 0.04^{b}	19.27± 2.30^{e}	23.78± 2.30^{c}	0.117± 0.009^{c}	0.020± 0.002^{b}
T. densum subsp. *amani* (Afşin)	13.91± 0.18^{b}	0.32± 0.04^{d}	3.69± 0.01^{c}	0.69± 0.02^{d}	84.82± 0.45^{a}	27.55± 0.24^{b}	0.120± 0.000^{c}	0.010± 0.005^{c}
T. densum subsp. *amani* (Ahır Mount)	2.86± 0.02^{e}	0.81± 0.02^{e}	1.73± 0.08^{e}	1.57± 0.05^{c}	38.32± 0.50^{c}	29.34± 0.04^{ab}	0.035± 0.002^{d}	0.018± 0.001^{b}
T. kotschyi	1.75± 0.02^{f}	7.06± 0.07^{a}	2.12± 0.08^{d}	11.14± 0.07^{a}	27.80± 1.30^{d}	12.36± 0.30^{d}	0.200± 0.050^{b}	0.080± 0.000^{a}

The data were statistically significant as compared with the control (**p < 0.01); letters indicate the significantly differing content of metabolites one from other taxa according Duncan test, ns: not studied

For parthenolide content of *Tanacetum* species, Orhan Erdoğan et al. [22], determined the parthenolide content of *T. argenteum* subsp. *argenteum* (2.261-1.585%), *T. parthenium* (0.186-0.279%, 0.231-0.505%) and *T. densum* subsp. *laxum* (0.832-0.090%) in leaves and flowers, respectively but parthenolide was not quantified in *T. cilicicum*. Furthermore, Özbilgin et al. [23], reported the parthenolide content in *T. argenteum* subsp. *argenteum* as 242.66 µg/100 mg but parthenolide was not detected in *T. densum* subsp. *sivasicum*. As seen in previous studies, *T. argenteum* subsp. *argenteum* showed highest parthenolide content. These results support our findings. Along with the study, parthenolide in *T. cilicicum* and *T. densum* subsp. *amani* were reported. The availability or detection of the compounds might be attributed to the extraction methods, solvents, sampling periods or time of the plant vegetation.

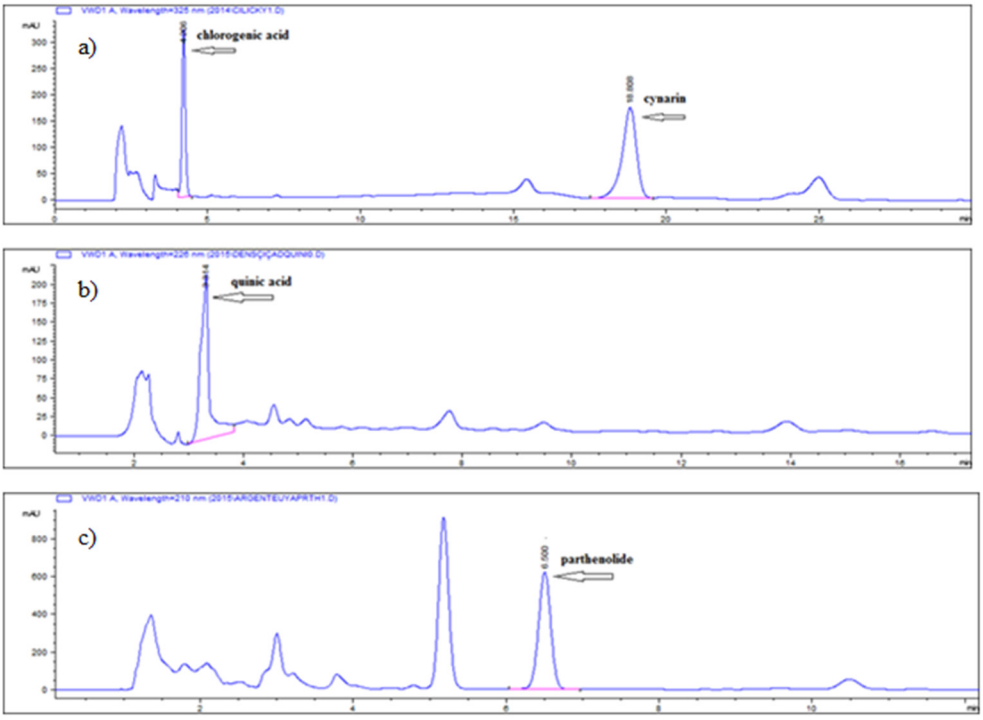

Figure 1. HPLC. **a)** Chromatograms of chlorogenic acid, cynarin; **b)** Chromatograms of quinic acid; **c)** Chromatograms of parthenolide.

HPLC analyses of tryptophan derivates in Tanacetum taxa

The concentrations of tryptophan, serotonin and melatonin in leaf and flowers of seven *Tanacetum* taxa were reported herein. The quantitative analysis of the individual compounds in the polar extracts was performed using HPLC–UV and the results were represented in Table 2 and representative HPLC-UV chromatograms were given in Figure 2.

Peak identifications were accomplished by comparing retention time of tryptophan, serotonin and melatonin in a standard solution with the chromatograms obtained from plant extract. HPLC chromatographic peaks for standard solutions and *T. argenteum* subsp. *argenteum* leaf extract peaks were overlapped and given in Figure 2a. These metabolites amount differed not only inter-specific but also among plant tissue of the same species (p<0.01). Content of tryptophan varied from 13.480-169.57 ppm in leaves and 11.56-63.02 ppm in flowers. Of the species, *T. argenteum* subsp. *argenteum* had

Table 2. Tryptophan, serotonin and melatonin content of *Tanacetum* taxa

	Tryptophan (ppm)		Serotonin (ppm)		Melatonin (ppm)	
Taxa	**Leaf****	**Flower****	**Leaf****	**Flower****	**Leaf****	**Flower****
T. argenteum subsp. *argenteum*	169.57± 1.40^{a}	40.66± 0.80^{c}	78.20± 0.79^{a}	79.78± 0.69^{a}	5.48± 0.50^{c}	2.57± 0.13^{d}
T. armenum	13.480± 1.30^{f}	63.02± 1.78^{a}	17.88± 1.90^{f}	43.88± 2.87^{d}	5.33± 0.20^{c}	4.42± 0.30^{c}
T. cadmeum subsp. *orientale*	20.050± 2.70^{e}	40.63± 0.26^{c}	31.04± 0.98^{e}	17.10± 0.05^{f}	8.12± 0.20^{a}	7.02± 0.50^{a}
T. cilicicum	22.360± 0.30^{e}	11.56± 1.10^{f}	64.22± 0.30^{b}	14.34± 0.60^{g}	4.94± 0.20^{c}	1.05± 0.20^{f}
T. densum subsp. *amani* (Afşin)	157.94± 1.21^{b}	37.46± 0.69^{d}	77.81± 1.05^{a}	71.61± 1.17^{b}	3.03± 0.19^{d}	2.39± 0.26^{d}
T. densum subsp. *amani* (Ahır M.)	20.200± 0.59^{e}	36.42± 0.30^{d}	19.23± 0.13^{f}	33.21± 0.70^{e}	8.46± 0.50^{a}	6.33± 0.40^{b}
T. kotschyi	31.830± 0.40^{d}	33.02± 1.20^{e}	38.18± 0.40^{d}	42.34± 0.80^{d}	1.99± 0.10^{e}	1.45± 0.10^{e}
T. nitens	64.470± 0.80^{c}	58.60± 0.70^{b}	47.46± 1.20^{c}	59.50± 1.20^{c}	6.52± 0.22^{b}	6.27± 0.30^{b}

The data were statistically significant as compared with the control (**p < 0.01); letters indicate the significantly differing content of metabolites one from other taxa according Duncan test

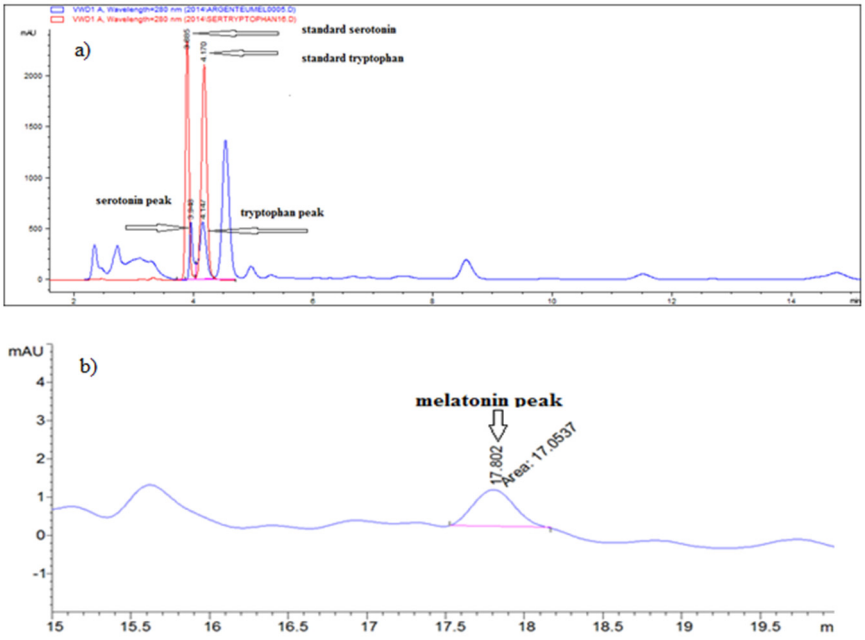

Figure 2. a) Chromatograms of tryptophan and serotonin standard solution and plant extract in HPLC chromatogram, b) Melatonin peak of the *T. cilicium* leaves extract in HPLC chromatogram

the highest content of tryptophan in their leaves (169.57±1.40 ppm DW) whereas the lowest content was determined in *T. armenum* (13.480±1.30 ppm DW). However, the highest content of tryptophan in flower was found in *T. armenum* (63.02±1.78 ppm DW). Furthermore, *T. argenteum* subsp. *argenteum* had the highest content of serotonin in both leaves (78.20±0.79 ppm DW) and flowers (79.78±0.69 ppm DW). Melatonin content was found at low levels using HPLC-UV. In order to confirm the reliability of the results, further LC-MS/MS analyses were performed. In the previous studies, Liquid chromatography–Mass Spectrometry (LC-MS/MS) is considered to be the effective method of detecting melatonin in plant material/food [24, 25]. On the basis of the mass fragmentation interpretation, standard melatonin (m/z 233) was identified by LC/MS-MS (Figure 3a).

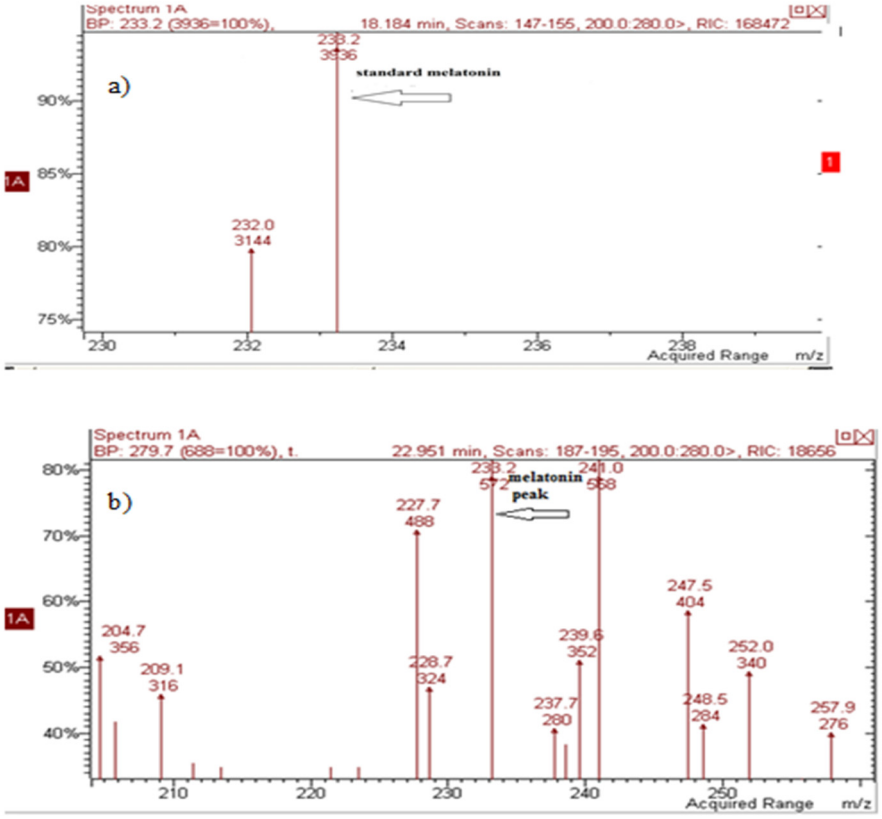

Figure 3. Mass spectra of a) melatonin peak in standard solution, b) of melatonin peak in plant extract

The LC/MS-MS spectra of *T. armenum* extracts were given in Figure 3b and melatonin peak in HPLC chromatogram of the *T. cilicicum* leaves was given in Figure 2b. Melatonin level was detected higher in leaves than in flowers in all taxa but serotonin and tryptophan levels exhibited differences. Melatonin content was found higher in *T. densum* subsp. *amani* (Ahır Mount location) leaves (8.46 ppm) and flowers (6.33 ppm) than other taxa. *T. densum* subsp. *amani* collected from Afşin (3.03 ppm in leaves, 2.39 ppm in flowers). Although Ahır Mount and Afşin had similar altitudes, ecological characteristics of the locations exhibited differences. While Ahır Mountain belongs to Mediterranean floristic region, Afşin location belongs to İran-Turan floristic region. Differences in time of harvest and environmental impact during plant growth and development cause variations in melatonin and serotonin levels [26,27].

The amounts of serotonin, tryptamine, and tyramine were reported in several commonly consumed fruits and vegetables [28]. In the study by Huang and Mazza [26], serotonin content was ranged from 1.800 to 221.900 ng/g and melatonin levels varied between 0.006 and 34.500 ng/g in some edible plants. Chen et al. [29], determined that the melatonin levels ranged from 10 ng-3.771 µg/g among 108 chinese medicinal plant. Murch et al. [3], used different dried techniques for *T. parthenium* and detected melatonin level among 1.37-2.45 µg/g. Ansari et al. [30], used different analytical and extraction methods for *T. parthenium* leaves and determined the melatonin level as 1010.6-2086.9 ng/g. Pérez-Llamas et al. [13], detected melatonin content of a herbal mix and improving a final product from mix as 5.5 µg/g, 7.2 mg/g respectively. Of the examined studies, the quantification methods were different and therefore the documented results regarding the content of the metabolites might be not consistent [26]. Herewith, in addition to the analytical techniques, the differences might be attributed to the ecological conditions, stress factors, genetic factors and harvesting time.

Antioxidant activity and phenolics content of Tanacetum taxa

The percentage of DPPH scavenging activity and total phenolics content of *Tanacetum* taxa were given in Table 3. The species showed significant differences with respect to antioxidant potential of leaves and flowers (p<0.01). As seen in Table 3, *Tanacetum* taxa had potent antioxidant activity. *T. densum* subsp. *amani* (Afşin) (96.20%) flowers were more effective than those in control group BHT. DPPH activities of flowers were higher than leaves. *T. cilicicum* had the highest total phenolic compounds in their leaves (84.01 mg GAE/g). Leaves of the taxa contained more total phenolics content than those of flowers except *T. kotschy*.

Table 3. Antioxidant activity and total phenolic contents of *Tanacetum* species

	DPPH Activity (%)		Total Phenolics (mg/g GAE)	
Taxa	**Leaf	**Flower	**Leaf	**Flower
T. argenteum subsp. *argenteum*	95.60±0.05^{a}	ns	51.79±0.11^{c}	ns
T. armenum	93.50±0.50^{bc}	95.66±1.50^{ab}	36.79±3.70^{d}	28.58±1.2^{c}
T. cilicicum	95.00±0.00^{ab}	96.00±0.01^{a}	84.01±3.50^{a}	46.63±1.9^{b}
T. densum subsp. *amani* (Afşin)	95.80±0.08^{a}	96.20±0.58^{a}	65.52±2.26^{b}	16.58±1.5^{d}
T. densum subsp. *amani* (Ahır Mount)	92.33±1.52^{c}	95.16±0.20^{b}	25.39±2.48^{e}	17.88±2.8^{d}
T. kotschyi	92.30±0.50^{c}	95.00±0.01^{b}	33.50±1.30^{f}	53.36±2.9^{a}
BHT (control)	96.00±0.00^{a}	96.00±0.00^{a}		

The data were statistically significant as compared with the control (**$p < 0.01$); letters indicate the significantly differing content of metabolites one from other taxa according Duncan test, ns: not studied

As in previous studies, Savcı et al. [31], reported some *Tanacetum* species showed similar DPPH activity with BHT. Arıtuluk et al. [4], determined that percentage of DPPH scavenging activity of aerial parts of *T. armenum* and *T. cilicicum* were 81.67% and 77.61%, respectively, whereas total phenolic contents of aerial parts of *T. armenum* and *T. cilicicum* were 58.86 mg GAE/g and 33.14 mg GAE/g, respectively. Esmaeili et al. [32], reported that *T. kotschyi* showed high antioxidant activity and included total phenolic compounds as 44.40 mg GAE/g while 90% DPPH scavenging activities of *T. kotschyi* were reported [33].

Gecibesler et al. [21], determined the total phenolic content of *T. cilicicum* among 99.53-268.02 mg GAE/g. Tepe and Sökmen [34], Emre [35], investigated the amount of total phenolics and antioxidant activity of *T. densum* subsp. *amani* (77.42%, 158.44 µg/ GAE mg- 94.9 %, 137.01 µg/ GAE mg). Köse et al. [36], reported total phenolic amount as 63 mg/GAE g in *Tanacetum argenteum* (Lam.) willd. subsp. *flabellifolium*. As it can be seen from the previous studies revealing the antioxidant potential of *Tanacetum* species showed similarity with our results and these wild species showed remarkable antioxidant activity. Higher activities might be attributed to low-temperature at higher altitude and subsequently increased rate of biosynthesis of antioxidant molecules [37]. As well as, Zengin et al. [38], declared that extraction techniques significantly effected phenol and flavonoid content of *Tanacetum parthenium*.

Principal component analysis

The discrimination can be evaluated from the principal component analysis scores plot between different *Tanacetum* taxa using identified metabolites identified herein as shown in Figure 4. With this visualization, the more expressed metabolites in plant species are located in the same area of the graph coupled with similar metabolite contents. Discrimination was shown on the plotted scores, where two principal components accounted for 76.59% of total variance. The first axis and second axis explained 39.26% and 37.33% of total variance. According to the results, *T. armenum* and *T. densum* (Ahır Mount), *T. densum* (Afşin) and *T. cilicicum* as well as *T. kotschyi* corresponded to three groups.

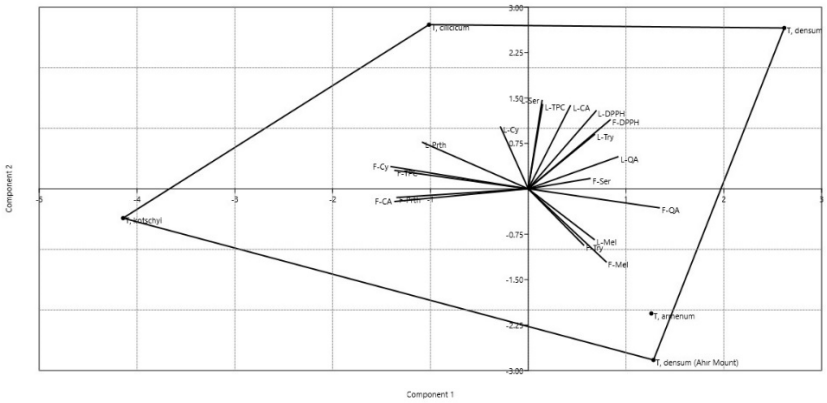

Figure 4. Principal component analysis of *Tanacetum* taxa

CONCLUSIONS

Along with the present study, the contents of chlorogenic acid, cynarin, quinic acid and parthenolide were for the first time reported for some *Tanacetum* species. Cynarin is of the biologically active chemical constituent of artichoke (*Cynara scolymus* L.), exhibit in potent choleretic, antimicrobial, antioxidant, antiradical, anticholinergic activities [39]. The content of cynarin were reported as 95-529.5 mg/kg [40], 10.15-0.67 mg/g [41] in artichoke. As our results, especially *T. cilicicum* can be shown as alternative source for cynarin. Of the significant compounds, parthenolide was found in large amounts. In European Pharmacopeia, required percentage of parthenolide was 0.2%. Herein, most of the *Tanacetum* species included higher amount than required, especially endemic species *T. argenteum* subsp. *argenteum* and *T. densum* subsp. *amani* (Afşin). Besides, *T. argenteum* subsp. *argenteum* had a large amount of tryptophan and serotonin. Furthermore, melatonin level of many taxa was

higher than those levels in common taxon *T. parthenium*. For the first time, no studies regarding the levels tryptophan, serotonin and melatonin have been performed in those *Tanacetum* species in present research hitherto. These components were found at important concentrations. The results obtained from this study demonstrate that these species might be evaluated commercially for their rich amount of biological active components in medicinal, pharmaceuticals and food industry.

EXPERIMENTAL SECTION

Plant material

Tanacetum species were collected from Kahramanmaraş city between 2012 and 2013. The plant species were identified by Dr. Ahmet Ilcim using Flora of Turkey and East Aegean Islands [42]. Plant materials, their origins and collection areas were listed in Table 4. The plants were collected at flowering period and then dried at room conditions. *T. densum* subsp. *amani* was collected from two different locations, namely Afşin and Ahır Mountain.

Table 4. Wild *Tanacetum* species along with site of collections and distribution range

Taxa	Diversity	Locality/Habitat	Collection date	Altitude	Collection No
T. argenteum (Lam.) Willd subsp. *argenteum* (L.) All.	Endemic	Afşin, Güvek Plateau calcareous rocks	26.08.2013	1800 m	KSUH 1001
T. armenum (DC.) Schultz Bip	İran-Turan	Işık Mountain calcareous, limy rocks	11.07.2012	2800 m	KSUH 1002
T. cilicicum (Boiss.) Grierson	E.Mediterra-nean element	Başkonuş Roadside	19.07.2012	1800 m	KSUH 1003
T. cadmeum (Boiss.) Heywood subsp. *orientale* Grierson	Endemic	Işık Mountain calcareous, limy rocks	09.07.2012	2600 m	KSUH 1004
T. densum (Lab.) Schultz Bip. subsp. *amani* Heywood	Endemic	Ahır Mountain Yedikuyular calcareous rocks	28.06.2012	1800 m	KSUH 1005
T. densum (Lab.) Schultz Bip. subsp. *amani* Heywood	Endemic	Afşin, Güvek Plateau calcareous rocks	26.08.2013	1800 m	KSUH 1006
T. kotschyi (Boiss.) Grierson	İran-Turan	Berit Mountain, Karagöl Site calcareous, limy rocks	11.07.2012	3100 m	KSUH 1007
T. nitens (Boiss. &Noë) Grierson	Endemic	Işık Mountain calcareous, limy rocks	09.07.2012	2650 m	KSUH 1008

Chemicals

All of the analytical grade solvents were purchased from Merck. 2,2-Diphenyl-1-picrylhydrazyl (DPPH) was provided from Aldrich, chlorogenic acid (dissolved in ethanol), cynarin (dissolved in methanol), quinic acid (dissolved in dd-H_2O), tryptophan (dissolved in warm dd-H_2O), serotonin (dissolved in dd-H_2O with 0.1 M HCl) melatonin (dissolved in 80% methanol), Folin-Ciocalteu reagent (2N), gallic acid and quercetine were obtained from Sigma. Parthenolide was purchased from Cayman (dissolved with dimethyl sulfoxide), BHT (Butylated Hydroxy Toluene) and aluminium chloride were procured from Fluka.

Sample extractions

Extraction for phenolics, antioxidant activity and parthenolide analyses: 1 g leaf or flower samples were initially crushed in porcelain mortar and then transferred to durham bottle. 50 ml methanol was added and mixed on magnetic stirrer for homogenization along 15 mins. Following homogenization, the samples were placed into ultrasonic-bath for 1 h. Finally, the samples were centrifuged at 5000 rpm for 15 minutes [19].

Extraction for tryptophan, serotonin and melatonin analyses: 2 g dried plant material was crushed in porcelain mortar and homogenized on magnetic stirrer with 60 ml solvent (2 methanol: 1 dd-H_2O) for 20 mins. Then, the samples were placed into ultrasonic bath for 1 h and incubated at -20 ºC for two weeks. After this period, samples were sonicated for 30 mins. in sonic bath and then centrifuged for 10 mins. in 6000 rpm at 4 °C. Finally, supernatants of the extracts were used for HPLC analyses. Extractions were kept at -80 ºC until used [30]. The study was carried out in dim light.

HPLC analyses

Separation of the compounds in the extracts was performed by a liquid chromatography system (HPLC) Agilent 1100 series(Agilent Technologies, Santa Clara, CA, USA) equipped with four Ecom pumps (Prague, Czech Republic), and a ACE C-18 column (5 µM, 4.6 mm × 150 mm) coupled with a UV detector (Hewlett-Packard 1100 model). For phenolics and parthenolide analyses: Standards were prepared at 1.95-3.9-7.8-15.6-31.2-62.5-125-250-500 ppm concentrations. Chlorogenic acid and cynarin were detected at 325 nm; quinic acid was detected at 226 nm. Mobile phase: Acetonitrile 20%, dd-H_2O 80% with 0.05% trifluoroacetic acid and flow rate was 1.2 mL/min. Total analyses time was 35 minutes. Column heat was adjusted to 30 ºC. The

peaks corresponding to chlorogenic acid, cynarin and quinic acids were seen at 4.29 min, 19.06 min, 3.3 min, respectively [16].

For parthenolide analyses: Mobile phase was isocratic including 55% acetonitrile (A), 45% water (B) per 22 min at 1.5 mL/min flow rate. The peaks were analyzed at 210 nm with UV detector. The parthenolide peak was seen at 6.5. min [22].

For tryptophan, serotonin and melatonin analyses: Standards were prepared with 1.95-3.9-7.8-15.6-31.2-62.5-125-250 ppm concentrations. Mobile phase was 0.1% formic acid + 0.1 M KH_2PO_4 with dd-H_2O (20%) and acetonitrile (80%) per 35 min at 1mL/min flow rate. The peaks were analyzed at 280 nm with UV detector and column heat was adjusted to 28 ºC. Tryptophan, serotonin and melatonin peaks were seen at 4.1 min, 3.9 min and 17.6 mins. respectively. 20 µl samples were injected to HPLC system. Before HPLC analyses, extracts were filtered with HPLC filter (0.2-25 mm millipore). All injections were performed in triplicate.

LC/MS-MS analyses

Since melatonin peak was visualized at a very small rate, standard melatonin and two samples were run in LC-MS/MS (Zivak Tandem Gold) according to the method proposed by [26]. These assays were performed in order to support and verify HPLC analysis. The ionization techniques included electrospray ionization (ESI) and the optimized voltage was applied to monitor the precursor ions, mass fragments occur as molecular ions (m/z) are either (M - H) + or (M + H)+ so, m/z 232.28 for melatonin,+1 and -1 ion charged form were determined in the chromatogram as 231.28 and 233.28. According to this method, mobile phase involved A- 0.1% (V / V) formic acid-acetonitrile, B-0.1% formic acid / dd-H_2O, flow rate was adjusted 0.2 ml / min, 5% A- 95% B for the first 5 min, 35% A- 65% B for 30 min, it was held for 5 min, 100% A-5 min, it was held for 5 min, 5% A- 95% B-5 min, it was held for 5 min. Total analysis time was set to 60 min.

Total phenolic compounds

Total phenolic content was determined using Folin Ciocalteu reagent. 2 mL of Folin Ciocalteu reagent was added to the 400 µL extract. After 3 mins, 1.6 mL of sodium carbonate (7.5%) was added and the mixture was allowed to stand for 30 min. Absorption was measured at 765 nm using a spectrophotometer (Agilent Rochester, NY, USA). A multipoint linear curve was obtained with gallic acid standard (Sigma) ranging from 20 to 400 ppm ($y=0.0078x + 0.0763$). The results were expressed as mg/g GA [43].

Antioxidant activity

The antioxidant activity of extracts were determined using 2,2-diphenyl-1-picrylhydrazyl (DPPH) radical scavenging activity. 1 mM DPPH and the positive control BHT (1 mM) was dissolved in methanol. 100 µl extract was poured into spectrophotometer baths and 3 ml DPPH added to extracts and incubated at dark for 30 min. Baths were read at 517 nm in spectrophotometer and calculated with the following formula; Radical scavenging activity: $\{(A_0-A_1/A_0) \times 100\}$. A_0: DPPH solution, A_1: extract with DPPH [43].

Statistical analysis

Three replications were used for each treatment. Data were expressed as mean and standard deviations. The means were compared using the one-way ANOVA followed by Duncan's multiple range tests. The differences between individual means were considered to be significant at $p<0.05$. Moreover, a principal component analysis (PCA) was performed in order to discriminate *Tanacetum* species on the basis of the components identified along with the study.

ACKNOWLEDGMENTS

This study was supported by grants from Kahramanmaraş Sütçü Imam University Scientific Research Projects Unit with 2013/4-20D project number. We would also like to thank Dr. Cihangir Uygun and Dr. İsa Başköse for their helps during collecting the plant material.

REFERENCES

[1] V. Kumar; D. Tyagi; *J Pharmacogn. Phytochem*., **2013,** *2*,159-63.
[2] M. Korkmaz; A. Kandemir; V. Ilhan; N. Yildirim Doğan; *Turk. J. Bot.,* **2015**, *39*, 96-104.
[3] S.J. Murch; B.S. Colleen; K.S. Praveen; *The Lancet*., **1997**, *350*,1598-1599.
[4] Z. C. Arituluk; I. I. T. Çankaya; A. M. G. Özkan; *FABAD J. Pharm. Sci*., **2016**, *41*, 17-25.
[5] B. H. Kwok; B. Koh; M. I. Ndubuisi; M. Elofsson; C. M. Crews; *Chem. & biol*., **2001**, *8*, 759-766.
[6] A. Ghantous; A. Sinjab; Z. Herceg; N. Darwiche; **2013**, *Drug Discov*., *18*, 894–905.
[7] R.R. Freund; P. Gobrecht; D. Fischer; H. D. Arndt; *Nat. Prod. Rep*., **2020**, *37,* 541-565.

[8] M. Bahrami; M. Kamalinejad; S. A. Latifi; F. Seif; M. Dadmehr; *Phytother Res*., **2020**, *34*, 2429–2430.
[9] S.J. Murch; R.S. Krishna; PK Saxena; *Plant Cell Rep*., **2000**, *19*, 698–704
[10] R. Long; Y. Zhu; S. Zhou; *Medicine*., **2019**, *98*, e14099.
[11] Y. Yan; Q. Shi; B. Gong; Review of melatonin in horticultural crops, IntechOpen Book Series, London UK, **2020**, *9,* pp. 107-115.
[12] M. M. Essa; H. Hamdan; S. B. Chidambaram; B. Al-Balushi; G. J. Guillemin; D. M. Ojcius; M. W. Qoronfleh; *Int J Tryptophan Res.,* **2020**,*13*, 1-2.
[13] F. Pérez-Llamas; J. Hernández-Ruiz; A. Cuesta; S. Zamora; M. B. Arnao; *Antioxidants*., **2020**, *9*, 158-176.
[14] S. Agatonovic-Kustrin; D. W. Morton; *Stud. Nat. Prod. Chem*., **2018**, *58*, 61-91.
[15] M. D. Ferrari; K. I. Roon; R. B. Lipton; P. J. Goadsby; *The Lancet*., **2001**, *358,* 1668-1675.
[16] C. Wu; F. Chen; X. Wang; Y. Wu; M. Dong; G. He; R.D. Galyean; L. He; G. Huang; *Phytochem Anal.,* **2007**, *18,* 401-410.
[17] S. Farzadfar; F. Zarinkamar; M. Hojati; *Plant Physiol Biochem*. **2017**, *112*, 207-217.
[18] A. Nieto-Trujillo; L. Buendía-González; C. García-Morales; A. Román-Guerrero; F. Cruz- Sosa; M.E. Estrada-Zúñigin; *Rev Mex **Ing** Quim.*, **2017**, *16*, 371-383.
[19] D. Fraisse; C. Felgines; O. Texier; J.L. Lamaison; *Food Nutr Sci.*, **2011**, *2,* 181-192.
[20] K. R. Hordiei, T. M. Gontova, A. G. Serbin, A. G. Kotov, E. E. Kotova; *Ukr. biopharm. j.*, **2019**, *3*, 64-70.
[21] I. H. Gecibesler; A. Kocak; I. Demirtas; *Nat. Prod. Res*., **2016**, *30*, 2850-2855.
[22] İ. Orhan Erdoğan; F. Tosun; A.R. Gülpınar; M. Kartal; A. Duran; F. Mihoğlugil; D. Akalgan; *Phytochem. Lett.*, **2015**,*11*, 347-352.
[23] S. Ozbilgin; E.K. Akkol; B. Ergene Oz; M. Ilhan; G. Saltan; O.B. Acikara; İ. Suntar; *Iran J Basic Med Sci*., **2018**, *2*,145-152.
[24] M. B. Arnao, J. Hernández-Ruiz; *Stud. Nat. Prod. Chem.*, **2015**, *46*, 519-545
[25] D. J. Kennaway; *Food Funct*., **2020**, *11*, 9359-9369.
[26] X. Huang, G. Mazza; *Crit Rev Food Sci Nutr*., **2011***, 51*, 269-284.
[27] M. H. Chung, T.S. Deng; *Bot Stud*., **2020**, *61*, 1-9.
[28] D. Ly; K. Kang; J. Choi; A. Ishihara; K. Back; S. Lee; *J Med Food.,* **2008***, 11*, 385-389
[29] G. Chen; Y. Huo; D.X. Tan; Z. Liang; W. Zhang; Y. Zhang; *Life Sci*., **2003**, *73*, 19–26.
[30] M. Ansari; K.H. Rafiee; N. Yasa; S. Vardasbi; S.M. Naimi; A. Nowrouzi; *Daru*. **2010***, 18*, 173–178.
[31] A. Savcı; E. F. Koçpınar; Y. Alan; M. Kurşat; *Int. Food Res. J.* **2020**, *27*, 160-170.
[32] M. A. Esmaeili; A. Sonboli; M. A. Noushabadi; *Food chem*., **2010**, *121*,148-155.
[33] A. Savcı; A. Yusuf; E. F. Koçpinar; M. Kurşat; S. Topdemir; M., Karataş; B. Çakmak; *SDÜFEFFD*, **2019**, *14*, 112-126.
[34] B. Tepe; A. Sokmen; *Bioresour. Technol.*, **2007**, *98*, 3076-3079.
[35] İ. Emre; *Braz. J. Biol.,* **2021**, *81* -1114
[36] B. Kose; Y. Iscan; G. Goger; F. B. Demirci; C. Elmacı; *Pak. J. Pharm. Sci.*, **2017**, *30*, 2047-2052.

[37] S. Gharibi; B. E. S. Tabatabaei; G. Saeidi; S. A. H. Goli; M. Talebi; *Ind Crops Prod*., **2013**, *50*, 154-158.
[38] G. Zengin; A. Cvetanović; U. Gašić; A. Stupar; G. Bulut; I. Şenkardes; *Ind Crops Prod*., **2020**, *146*, 112-202.
[39] M. Topal; H. Gocer; F. Topal; P. Kalin; L. P. Köse; İ. Gülçin; S. H. Alwasel; *J Enzym Inhib Med Ch*., **2016**, *31*, 266-275.
[40] K. Schütz; D. Kammerer; R. Carle; A. Schieber; *J. Agric. Food Chem*., **2004**, *52*, 4090−4096
[41] N. J. Jun; K. C. Jang; S. C Kim; D. Y. Moon; K. C. Seong; K. H. Kang; K. H. Park; *J. Appl. Biol. Chem.*, **2007**, *50*, 244-248.
[42] A.J.C. Grierson; Tanacetum L. In: Davis PH, editor. Flora of Turkey and the East Aegean Islands, Vol. 5. Edinburgh, UK: Edinburgh University Press, **1975**, pp. 256–292.
[43] P.H. Davis; Flora of Turkey and The East Aegean Island Vol. 5, Edinburgh Univ. Press., Edinburgh, 1965-1985.
[44] J. M. Fonseca; J.W. Rushing; N.C. Rajapakse; *J. Appl. Hortic.*, **2008**, *10*, 36-39.

STUDIA UBB CHEMIA, LXVI, 4, 2021 (p. 123-132)
(RECOMMENDED CITATION)
DOI:10.24193/subbchem.2021.4.09

BIOACTIVE POLYPHENOLIC COMPOUNDS FROM MOTHERWORT AND HAWTHORN HYDROETHANOLIC EXTRACTS

ANDREEA-MIRUNA NEAGU[a], CORNELIU-MIRCEA CODREANU[b], VASILE STAICU[a,c], RALUCA STAN[a,*]

ABSTRACT. Motherwort (*Leonurus cardiaca*) and Hawthorn (*Crataegus monogyna*) are known from traditional phytotherapy as being effective in alleviating many cardiovascular system disorders. This paper presents the studies made to assess the phytochemical compozition of the herbal extracts prepared from Motherwort (aerial parts), Hawthorn (fruits) and Hawthorn (flowers and leaves) by maceration, percolation and reflux using a mixture of ethanol and water as solvent. Optimum extraction conditions were evaluated for enhancing the content of the active substances (certain flavones and polyphenols: anthocyanins, etc.) present in the two studied plants, that are useful in the prevention of many cardiovascular disorders. Their chemical composition was investigated using UV-VIS spectroscopy methods: total polyphenolic content, total flavones content and the antioxidant activity were determined. The study showed that reflux extraction technique is more effective for extracting polyphenolic compounds from the two studied medicinal plants. Varying the extraction parameters led to the attainment of new phytotherapeutic extracts that are optimally beneficial in the phytotherapy of cardiovascular diseases.

Keywords: *Hawthorn, Motherwort, reflux, percolation, maceration, polyphenols*

INTRODUCTION

Hawthorn (*Crataegus monogyna*) belongs to the Rosaceae family and it is found in Europe, East Asia and eastern North America. Hawthorn fruits, leaves and flowers have been used as food and medicine around the world for centuries, being the most potent parts of the plant. Their chemical

[a] *University Politehnica of Bucharest, Faculty of Applied Chemistry and Materials Science, 1-7 Gheorghe Polizu Street, district 1, RO-011061, Bucharest, Romania*
[b] *"Dunarea de Jos" University of Galati, Faculty of Physical Education and Sport, 63-65 Garii Street, RO-800003, Galati, Romania*
[c] *Research and Development Department, S.C. Hofigal Export-Import S.A., 2 Intrarea Serelor Street, district 4, RO-042124, Bucharest, Romania*
[*] *Corresponding author: rl_stan2000@yahoo.com*

composition includes flavonoids, triterpene saponins and amines which confer cardiotonic, diuretic and antiatherosclerotic properties. Past and ongoing studies also suggest that flavonoids, particularly oligomeric proanthocyanidins present in the hawthorn extract, are the major bioactive constituents that possess potent antioxidant activity. Hawthorn extract has the potential to be a viable, natural alternative treatment for heart disease, as well as a promoter of general cardiovascular health [1,2].

Motherwort (*Leonurus cardiaca*) is a representative of the Lamiaceae family and it is native to Asia and southeastern Europe. It has been proven to be very effective in treating several cardiovascular disorders and some female-specific diseases due to its composition (sterols, alkaloids, furanic diterpenes and iridoids) that provides a complex biological activity (antimicrobial, analgesic, antioxidant, cardioprotective) [3,4].

Cardiovascular diseases are a group of disorders of the heart and blood vessels that, according to the World Health Organization, are the main source of death around the world. In 2016, around 17.9 million people died from cardiovascular diseases. Albeit these conditions stay pervasive in worldwide death rates, people can begin finding a way to forestall them [5]. The potential application in alleviating several cardiac disorders, as well as female-specific afflictions, made Motherwort and Hawthorn very good candidates for the development of alternative treatments.

The bioactive potential of Motherwort and Hawthorn are for the most part related to their phenolic constituents, which are usually the main components in the polar extracts. The antioxidant capacity of extracts acquired with polar solvents from these two plants has been recently evaluated through chemical antiradical assays [6].

The present paper aims to investigate the relationship between the antioxidant properties and the specific phenolic composition of some natural extracts from Hawthorn (fruits), Hawthorn (flowers and leaves) and Motherwort (aerial parts). Hawthorn flowers were extracted together with the leaves. That is due to the fact that Hawthorn leaf and flower have been subject to numerous clinical trials demonstrating the usefulness of Hawthorn leaf and flower extract in the management of cardiovascular diseases [7].The individual herbal extracts are known from traditional phytotherapy as being effective in alleviating many cardiovascular system disorders.

RESULTS AND DISCUSSION

Polyphenolic phytochemicals are of great interest due to the recognition of their antioxidant capacities and their great abundance in our diet and in medicinal plants. Polyphenols include flavonoids, phenolic acids, stilbenes and lignans.

Flavonoids are naturally occurring antioxidants widely present in fruits, vegetables and beverages (tea, wine, juice, etc.). They may be divided into several subclasses such as flavanols (catechin and proanthocyanidin), flavanones (naringin and hesperidin), isoflavanones, flavonols (quercetin and myricetin), flavones (luteolin and apigenin) and anthocyanidins. Epidemiologic studies have shown an association between the intake of flavonoids and reduced risks of cardiovascular diseases, such as myocardial infarction and stroke. It appears to be attributed to their antioxidant properties [8].

Anthocyanins are water-soluble secondary plant metabolites that are responsible for making bright-colored flowers and fruits attractive to pollinators or animals. Anthocyanins also protect cells from damage due to exposure to UV-light. They may also act as antioxidants in the cell vacuoles. Plants rich in anthocyanins include blueberries, cranberries, raspberries, blackberries, strawberries, cherries and grapes, among many other species.

The correlation between the total polyphenolic constituents of Motherwort and Hawthorn and the bioactive properties of their hydroethanolic extracts was herein evaluated.

In the present study, the phytochemical profile of hydroethanolic extracts of Motherwort (aerial parts), Hawthorn (fruits) and Hawthorn (flowers and leaves) was analyzed using UV-Vis Spectrophotometry. The results of the qualitative and quantitative analyses are summarized in **Figures 1–10**. Data are reported as the average of three analyses.

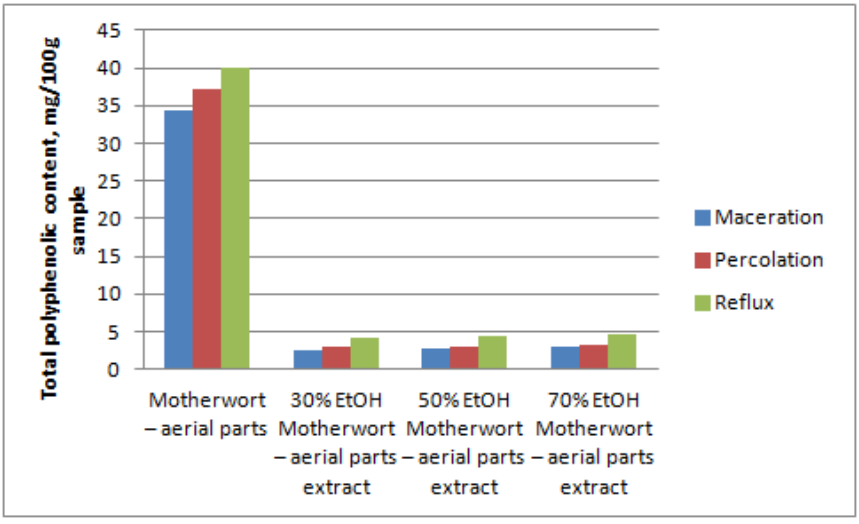

Figure 1. Total polyphenolic content from Motherwort – aerial parts and Motherwort – aerial parts extracts, expressed as gallic acid

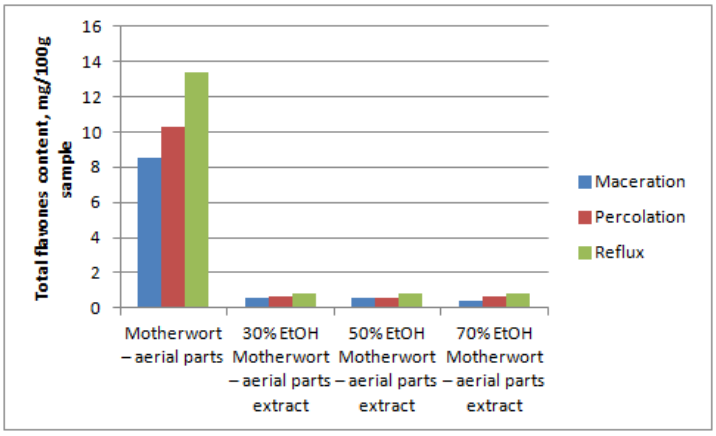

Figure 2. Total flavones content from Motherwort – aerial parts and Motherwort – aerial parts extracts, expressed as rutin

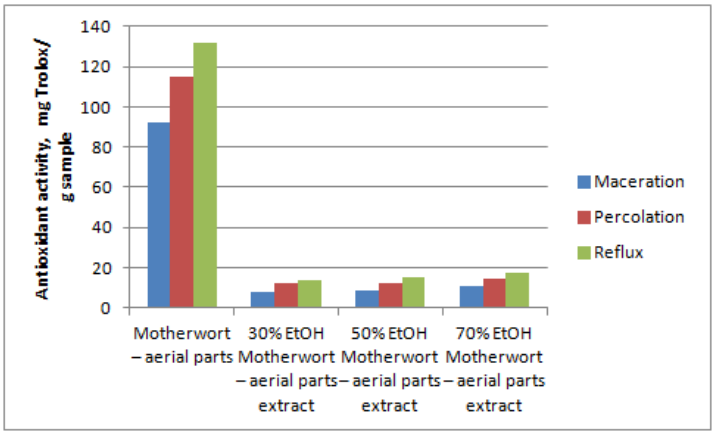

Figure 3. Antioxidant activity of Motherwort – aerial parts and Motherwort – aerial parts extracts, expressed as Trolox equiv.

Figures 1-3 depict the results for the Motherwort – aerial parts and Motherwort – aerial parts extracts for polyphenols, flavones and the antioxidant activity. According to reported studies, the total polyphenolic content in Motherwort – aerial parts extracts is between 0.4 and 7.3 mg/100g sample, so the values obtained in our study are above this range [3]. The best results were obtained for the 70% ethanol extracts (total polyphenolic content – approx. 5 mg/100g sample, total flavonoid content – approx. 1 mg/100 g sample). Reflux with 70% ethanol is the most suitable extraction method of the Motherwort - aerial parts. It promoted the highest contents of total phenolics, total flavonoids, major active compounds, and the most potent antioxidant activity.

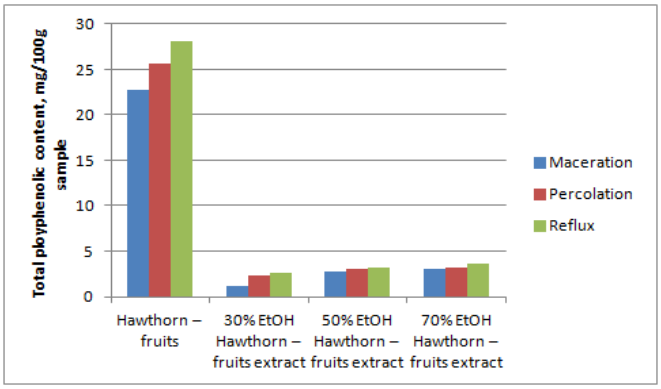

Figure 4. Total polyphenolic content from Hawthorn – fruits and Hawthorn – fruits extracts, expressed as gallic acid

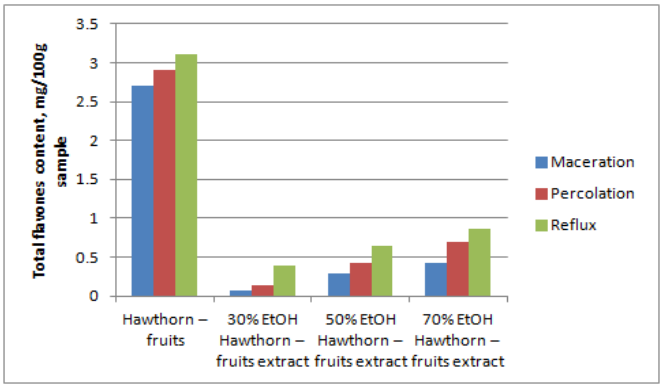

Figure 5. Total flavones content from Hawthorn – fruits and Hawthorn – fruits extracts, expressed as rutin

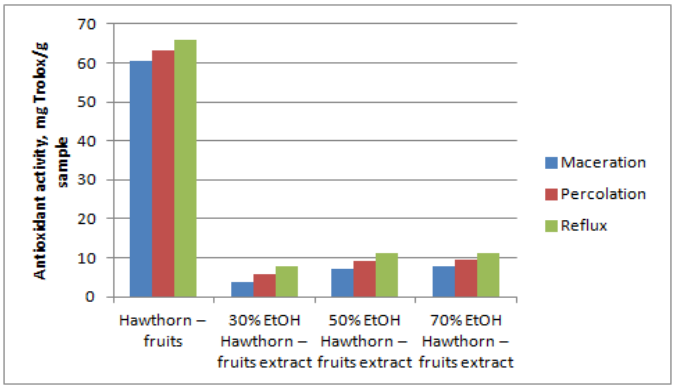

Figure 6. Antioxidant activity of Hawthorn – fruits and Hawthorn – fruits extracts, expressed as Trolox equiv.

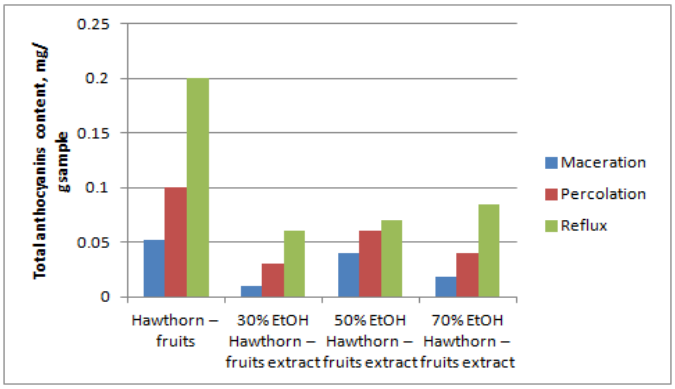

Figure 7. Total anthocyanins content from Hawthorn – fruits and Hawthorn – fruits extracts, expressed as cyanidin 3-*O*-glucoside chloride

Figures 4-7 depict the results for the Hawthorn – fruits and Hawthorn – fruits extracts for polyphenols, flavones, anthocyanins and the antioxidant activity. Polyphenols have similar values in the 50% and 70% ethanol extracts, but much lower values in the 30% ethanol extracts, also the results are higher for the reflux extracts. In addition to total polyphenolic content, spectrophotometric methods are also used in the determination of total contents of individual groups of phenolic compounds, such as total flavones and total content of anthocyanins as cyanidin 3-glucoside. Flavones determination show better results for the reflux-obtained extracts, ranging from 0.4 to 0.8 mg/100 g sample. As for the total content of anthocyanins in the Hawthorn – fruits extracts, we can note better extraction by percolation in 50% ethanol solution (0.06 mg/g sample) and by reflux in 70% ethanol solution (0.09 mg/g sample).

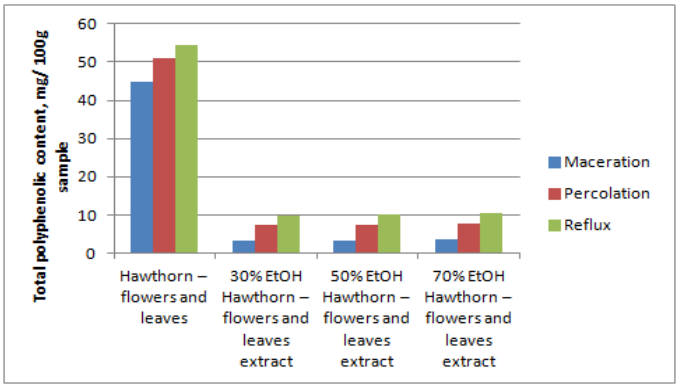

Figure 8. Total polyphenolic content from Hawthorn – flowers and leaves and Hawthorn – flowers and leaves extracts, expressed as gallic acid

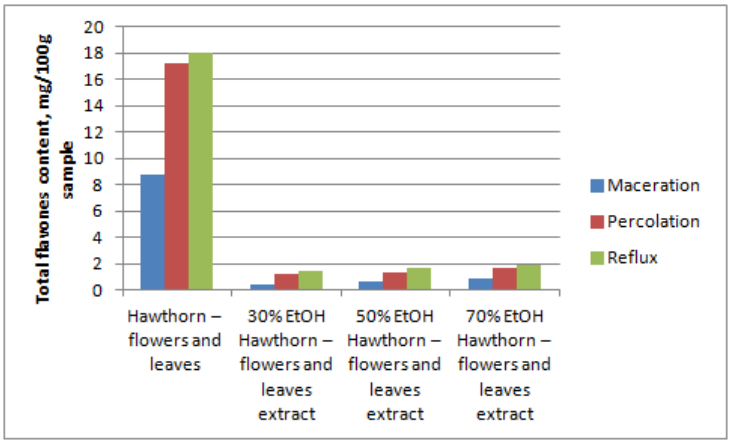

Figure 9. Total flavones content from Hawthorn – flowers and leaves and Hawthorn – flowers and leaves extracts, expressed as rutin

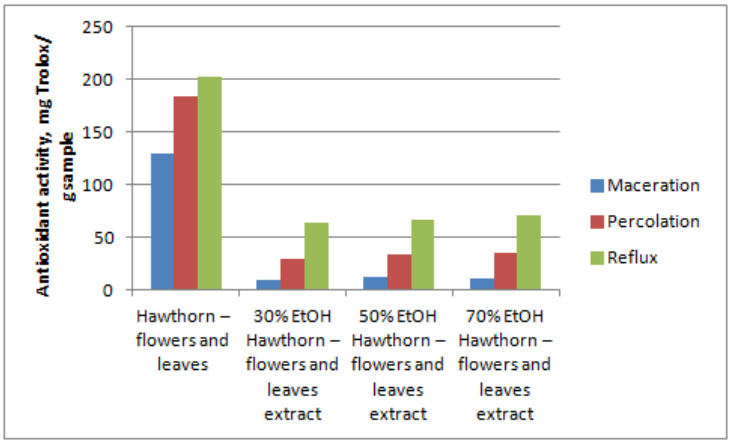

Figure 10. Antioxidant activity of Hawthorn – flowers and leaves and Hawthorn – flowers and leaves extracts, expressed as Trolox equiv.

Figures 8-10 depict the results for the Hawthorn – flowers and leaves and Hawthorn – flowers and leaves extracts for polyphenols, flavones and the antioxidant activity. They have similar values regardless the extraction method applyed, with higher values for the total polyphenolic content of about 10 mg/100g sample.

The hydroethanolic extracts of Hawthorn (fruits), Hawthorn (flowers and leaves) and Motherwort (aerial parts) exhibited promising antioxidant potential, as evaluated by the CUPRAC assay, with potencies order of Hawthorn (flowers and leaves) > Motherwort (aerial parts) > Hawthorn

(fruits) and values ranging from 3.6 to 70.5 mg Trolox/g sample. The results for the antioxidant activity of the studied extracts indicate the influence of the polyphenols and flavones present in each extract.

All in all, it can clearly be stated that the pharmacological activities of the examined traditionally used medicinal plants cannot be traced to one active compound but have to be regarded as the orchestrated effect of the entire spectrum of their phenolic constituents.

CONCLUSIONS

A detailed quantitative analysis of the phenolic compound spectrum of both Motherwort (*Leonurus cardiaca)* and Hawthorn (*Crataegus monogyna)* was conducted in order to understand their pharmacological activity.

The results show an increased content of anthocyanins in ethyl alcohol:water solution 50:50 *V/V* Hawthorn – fructus extract. Also, we can observe that reflux extraction technique is more effective for extracting polyphenols and flavones from the two studied medicinal plants. Focusing on the phenolic characteristics of the most-active extracts, their content in flavones and in anthocyanins is possibly connected with the antioxidant capacity of Motherwort and Hawthorn, respectively. Therefore, the extracts are considered as helpful sources of natural metabolites with possible health-benefit properties.

Varying the extraction parameters led to the attainment of new phytotherapeutic extracts that are optimally beneficial in the phytotherapy of cardiovascular diseases.

EXPERIMENTAL SECTION

UV-VIS Spectrophotometry was performed on a Jasco V-530 UV-Visible Spectrophotometer, with 2.0 nm Resolution and Double-beam Configuration.

Extraction of phenolic compounds:

The extracts were prepared from Motherwort (aerial parts), Hawthorn (fruits) and Hawthorn (flowers and leaves). The Hawthorn flowers and leaves were used as a mixture for the extraction in a 1:1.5 flowers:leaves ratio.

The plant samples of Motherwort (aerial parts), Hawthorn (fruits) and Hawthorn (flowers and leaves) were extracted in order to determine the total flavones content, total polyphenolic content and the antioxidant activity using the following method: an extract was prepared in a 1:10 of plant:solvent ratio in 50% ethanol by refluxing for 30 minutes. The obtained extract was filtered hot.

In order to determine total anthocyanins content from Hawthorn (fruits), the sample was previously submitted to extraction with methanol solvent as it follows: an extract was prepared in a 0.5:9.5 of plant:solvent ratio in methanol by mechanically stirring for 30 minutes. The obtained extract was filtered and diluted to 100 mL with methanol in volumetric flask. After that, a 50-fold dilution of this solution was prepared in a 0.1% V/V solution of hydrochloric acid in methanol.

The herbal extracts from Motherwort (aerial parts), Hawthorn (fruits) and Hawthorn (flowers and leaves) were obtained by conventional extraction methods as shown in **Table 1.** The plant:solvent ratio used depends on the actual volume of the dried, powdered plant material. Therefore, based on our previous experiments, we used the volume of solvent that completely soaked the powdered plant material and added excess to completely immerse.

Table 1. Experimental conditions for the three conventional methods used

	Extraction technique		
	Maceration	**Percolation**	**Reflux**
Solvent used	30%/50%/70% ethanol solution	30%/50%/70% ethanol solution	30%/50%/70% ethanol solution
Plant:solvent ratio	1:7	1:15	1:10
Temperature	Room temperature	Room temperature	82-86°C
Pressure applied	Not applicable	Not applicable	Not applicable
Time required	6 days	6 days	30 minutes
Volume of solvent required	500 mL	500 mL	50 mL

Determination of total polyphenolic content expressed as gallic acid equivalents: the polyphenols in the extracts are determined colorimetrically using Folin-Ciocalteu phenol reagent [9].

Determination of total flavones content expressed as rutin equivalents: the flavone derivatives content was determined by the reaction with aluminum chloride and total content was expressed in rutin [10].

Determination of total content of anthocyanins as cyanidin 3-glucoside: in the European Pharmacopoeia, a specification for total content of anthocyanins, calculated as cyanidin 3-glucoside, is given in the monographs for fresh bilberry fruit and fresh bilberry fruit dry extract, refined and standardized. The latter monograph also specifies a maximum limit for anthocyanidins, calculated as cyanidin, describes a certain chromatographic profile of 15 anthocyanins and 5 anthocyanidins to confirm identity [11].

Determination of antioxidant activity: the CUPRAC - cupric ion reducing antioxidant capacity - method is a simple and versatile antioxidant capacity assay useful for a wide variety of polyphenols, including phenolic acids, hydroxycinnamic acids, flavonoids, carotenoids, anthocyanins, as well as for thiols, synthetic antioxidants, and vitamins C and E. This method is based on electron transfer – it detects the ability of a potential antioxidant substance to transfer an electron to reduce any compound (**Figure 11**). The calibration curve was performed with a Trolox solution of known concentrations, 10-60 μg/mL [12].

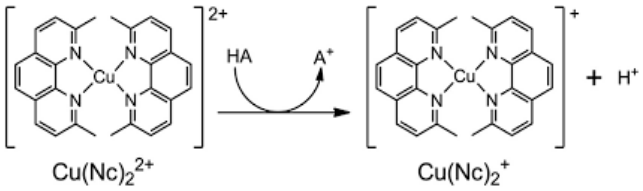

Figure 11. Reaction mechanism of copper reducing antioxidant capacity assay (CUPRAC)

REFERENCES

1. W-T. Chang; J. Dao; Z-H. Shao; *Am. J, Chin. Med.*, **2005**, *33*, 1–10.
2. L. Barros; A. M. Carvalho; I. C. F. R. Ferreira; *Phytochem. Anal.*, **2011**, *22*, 181-188.
3. R. C. Fierascu; I. Fierascu; A. Ortan; I. C. Fierascu; V. Anuta; B. S. Velescu; S. M. Pituru; C. E. Dinu-Pirvu; *BioMed Res. Int.*, **2019,** *2*, 1-13**.**
4. B. Sadowska; B. Micota; M. Rozalski; M. Redzynia; M. Rozalski; *Innate Immun.*, **2017**, *0*, 1-10.
5. J. Stewart; G. Manmathan; P. Wilkinson; *JR. Soc. Med. Cardiovasc. Dis.*, **2017**, *0*, 1-9.
6. A. Altemimi; N. Lakhssassi; A. Baharlouei; D. G. Watson; D. A. Lightfoot; *Plants*, **2017**, *42*, 1-23.
7. Hawthorn leaf and flower, Crataegus spp., folium cum flore; *European Medicines Agency*, **2016**, 268358.
8. M. L. McCullough; J. J. Peterson; R. Patel; P. F. Jacques; R. Shah; J. T. Dwyer; *Am. J. Clin. Nutr.*, **2012**, *95*, 454-464.
9. ISO 14502-1:2005(E), Determination of substances characteristic of green and black tea – Part 1: Content of total polyphenols in tea – Colorimetric method using Folin-Ciocalteu reagent.
10. L. Silva; B. Pezzini; L. Soares; *Pharmacogn. Mag.*, **2015**, *11*, 96-101.
11. Bilberry Fruit, fresh, Monograph, in *European Pharmacopoeia*, **2017**, *I*, 1173.
12. R. Apak; K. Güçlü; M. Özyürek; S. Esi̇n Karademi̇r; M. Altun; *Free Radic. Res.*, **2005**, *39*, 949-961.

STUDIA UBB CHEMIA, LXVI, 4, 2021 (p. 133-148)
(RECOMMENDED CITATION)
DOI:10.24193/subbchem.2021.4.10

BIOANALYSIS OF TOTAL PHENOLIC CONTENTS, VOLATILE COMPOUNDS, AND RADICAL SCAVENGING ACTIVITIES OF THREE WILD EDIBLE MUSHROOMS

AHMET METİN KUMLAY[a], MEHMET ZEKİ KOÇAK[b], MUBİN KOYUNCU[c], UĞUR GÜLLER[c,*]

ABSTRACT. Mushrooms are popular food for a long time because of their high nutritional value and many pharmaceutical properties. In that context, analyzing the contents and some antioxidant properties of three wild edible mushrooms, *Paxina queletii, Chlorophyllum agaricoides*, and *Mycenastrum corium*, is important in terms of emphasizing the values of these species in nutrition. For this propose, firstly total phenolic and flavonoid contents and radical scavenging activities were assayed. Then, quantitative analysis of phenolic and volatile compounds was performed by HPLC and GC-MS. The findings of the study revealed that *Mycenastrum corium* has the highest total phenolic and flavonoid content with the amount of 4.17 mg GAE/g and 1.58 mg QE/g respectively. However, $DPPH^{\cdot}$ and $ABTS^{\cdot+}$ radical scavenging activities of *C. agaricoides* were found higher with the IC_{50} values of 20.0 µg/mL and 6.4 µg/mL. Chromatographic analysis revealed that 5 alcohols, 14 aldehydes and ketones, 2 esters, 17 alkanes-heterocyclic compounds, and 4 acids were the major contributors of the antioxidant activities of the extracts. Regarding HPLC analysis, gallic acid, naringin and trans-cinnamic were found to be major phenolic compounds available for three species.

Keywords: *Chlorophyllum agaricoides, volatile compounds, Mycenastrum corium, Paxina queletii, phenolic content, radical scavenging*

INTRODUCTION

Mushrooms are functional foods that can provide additional benefits to human physiology and metabolic functions beyond meeting the essential nutrients. So, they can show effectiveness in preventing diseases [1]. Fungi

[a] *Iğdır University, Faculty of Agriculture, Department of Field Crops, Iğdır, Turkey*
[b] *Iğdır University, College of Applied Science, Department of Organic Farming, Iğdır, Turkey*
[c] *Iğdır University, Faculty of Engineering, Department of Food Engineering, Iğdır, Turkey*
[*] *Corresponding author: ugur.guller@igdir.edu.tr*

are a large family of eukaryotic organisms. Mushrooms are generally accepted as macrofungi with distinctive fruit parts that can be seen with the naked eye and can be collected by hand [2]. It has been estimated that more than 5.1 million different types of mushrooms are available [3]. Mushrooms are generally divided into two groups as medicinal and edible and have become more remarkable due to their nutritious, medicinal and economic potential [4].

In addition to their high-protein (200-250 g/kg dry matter), low-fat (20-30 g/kg dry matter) and low energy (240-310 kcal/kg) content they are good source of dietary fiber (220-300 g/kg dry matter) and sources of vitamins and minerals [5, 6]. 70% of the protein in mushrooms can be easily digested by the body [7]. Mushrooms are an important protein source for vegetarians because the proteins of some species are nutritionally equivalent to muscle proteins and they contain some essential amino acids found in animal proteins [8, 9]. Many mushroom species have been reported to contain L-ergothioneine, an important antioxidant, 12 times more than wheat germ and 4 times more than chicken liver [10-15]. The antioxidant potential of mushrooms is due to the rich phenolic compound contents [16-18]. Mushrooms are rich in B-group vitamins (folic acid, cobalamin, niacin, pantothenic acid, pyridoxine, thiamine, and riboflavin), ergosterol, phytoquinone, and tocopherols. Moreover, they are the only non-animal source of vitamin D in edible form [19-21]. It has also been reported that mushrooms are the source of beta-glucan, a polysaccharide preferred in cancer and HIV treatments because of its antitumor effects [22, 23]. Besides they are rich in mineral composition. Basic minerals known in their composition are calcium, potassium, iron, copper, and zinc. Potassium and phosphorus concentrations are higher than most vegetables, and most importantly are selenium contents not found in many fruits or vegetables [24].

When evaluated from a medical point of view, many types of fungi have been reported to contain substances that can prevent or alleviate cancer, heart disease, diabetes, viral infections, hypertension and hypercholesterolemia [25-27]. Besides, many medical benefits have been attributed to mushroom consumption, including the treatment of chronic and degenerative diseases, obesity, and cardiovascular disease [28, 29]. Due to the importance of mushrooms' nutritional content, in this study, the research team aimed to reveal the chemical composition and radical scavenging activities of three wild edible mushrooms, namely *Paxina queletii, Chlorophyllum agaricoides, Mycenastrum corium*.

RESULTS AND DISCUSSION

As a result of *in vivo* and *in vitro* experiments, it has been reported that mushrooms have bioactive substances (phenolics, antioxidants, anti-inflammatory, and antitumor agents) that are beneficial for health. Due to

their bioactive content, fungi show antibacterial, antifungal, antioxidant, antiviral, antitumor, cytostatic, immunosuppressive, antiallergic, antiatherogenic, hypoglycemic, anti-inflammatory and hepatoprotective activity [37]. Therefore, it is possible to be protected from diseases with a well-balanced diet associated with mushroom consumption due to the beneficial nutritional content of them [24, 38-40]. So in this study, total phenolic contents (TPC), total flavonoid contents (TFC), radical scavenging ability, volatile compounds and phenolic acid compositions of *Paxina queletii, Chlorophyllum agaricoides*, *Mycenastrum corium* were analyzed by using spectrophotometric and chromatographic methods to clarify their nutritional value.

TPC in ethanolic extracts of mushrooms (*Paxina queletii, Chlorophyllum agaricoides, Mycenastrum corium*) were found as 2.94±0.58, 1.36±0.35, and 4.17±0.67 mg GAE/g respectively (Table 1).

Table 1. $DPPH^{\bullet}$ and $ABTS^{\bullet+}$ radical scavenging activity, total phenolic and total flavonoid contents of mushroom extracts.

Mushroom Species	Total Phenolic Content (mg GAE/g)	Total Flavonoid Content (mg QE/g)	IC_{50} for DPPH Radical Scavenging (µg/mL)	IC_{50} for ABTS Radical Scavenging (µg/mL)
P. queletii	2.94±0.58	1.0±0.15	27.5	7.2
C. agaricoides	1.36±0.35	0.49±0.06	20.0	6.4
M. corium	4.17±0.67	1.58±0.62	25.9	7.5
Ascorbic acid	-	-	1.4	1.59
Trolox	-	-	-	2.15

The results of the current study were found lower than formerly reported studies. Liu et al. (2017) reported that TPC in different solvent fractions of *Inonotus sanghuang* ranged from 0.79 to 43.60 mg GAE/g [41]. Smolskaitė et al. (2015) determined that TPC in various organic solvent extracts of eight mushroom species ranged from 4.21 to 31.88 mg GAE/g [42]. Besides, our results appeared similar with the ethanolic extract of *A. bisporus* (6.18 mg GAE/g) and methanolic extract of *A. bisporus* (3.4 mg GAE/g dw) [43]. Specifically, Sezgin et al. (2020) reported that TPC value for *Chlorophyllum agaricoides* was reported as 46.5±1.4 mg equivalent (eq.) GA /g DW [44]. Those values were relatively much higher than those of values in the present study but higher than the report of Azieana et al. (2017) and our findings were similar to the report of López-Vázquez et al. (2017) [45, 46]. Different from the

study conducted by Sezgin et al. (2020) [44], we also carried out DPPH$^{\cdot}$ and ABTS$^{\cdot+}$ radical scavenging activities and characterized total flavonoid content with respect to quercetin equivalent of *Chlorophyllum agaricoides*.

Furthermore, TFC contents were 1.0±0.15, 0.49±0.06, and 1.58±0.62 mg equivalent QE /g DW for *P. queletii, C. agaricoides* and *M. corium,* respectively. As the case of total phenolic reports, TFC values of the current study was lower in comparison with the previous reports in different mushroom species analyzed by Abugri and Mc Elhenney (2013) but higher than the report by Azieana et al. (2017) and the current values were relatively close to the former reports [45, 47-49].

We performed DPPH$^{\cdot}$ and ABTS$^{\cdot+}$ assays to determine the radical scavenging activities of the relevant mushroom species. Through the ability to donate hydrogen, antioxidants can reduce the DPPH$^{\cdot}$ radical (purple) to the non-radical form DPPH-H (yellow) [43]. In order to compare the percentage of radical scavenging potencies with standards, radical scavenging % were calculated at a constant concentration (3 µg/ml). At 3 µg/ml concentration, DPPH$^{\cdot}$ radical scavenging activity% of the ethanolic extract of *Paxina queletii, Chlorophyllum agaricoides, Mycenastrum corium*, and standard ascorbic acid were found 13.19%, 14.32%, 9.2%, and 95.44% respectively. These results indicated that DPPH$^{\cdot}$ scavenging abilities of mushroom samples are lower than standard chemicals (Figure 1).

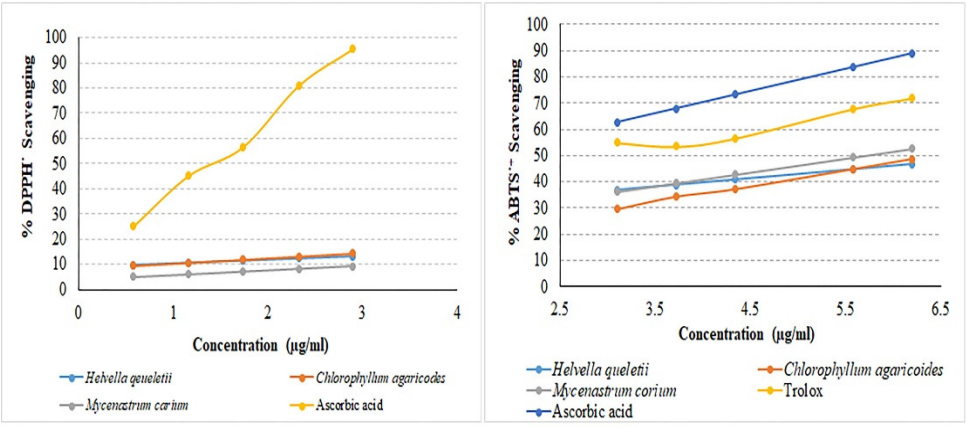

Figure 1. DPPH$^{\cdot}$ and ABTS$^{\cdot+}$ radical scavenging activities of the relevant mushroom species and standards

The IC_{50} values of mushroom extracts and standard were 27.5, 20.0, 25.9, and 1.4 µg/ml respectively (Table 1). $DPPH^{\cdot}$ scavenging abilities of mushroom samples are higher than extracts of *A. bisporus* [50-53] and lower than the ethanolic extract of *I. Sanghuang* [41]. $DPPH^{\cdot}$ radical scavenging activity of ethanolic extract of *P. queletii* were found considerably higher than methanolic extract of it (87.65% of 20 mg/ml extract) [54].

At 3 µg/ml concentration of samples and standards, $ABTS^{\cdot+}$ radical scavenging activity% of the ethanolic extract of *Paxina queletii, Chlorophyllum agaricoides, Mycenastrum corium*, trolox and ascorbic acid were determined as 36.84, 29.67, 36.31, 54.954, and 62.76% respectively. $ABTS^{\cdot+}$ scavenging activity of all mushroom extract were lower than that of both standards (Figure 1). The IC_{50} values of ethanolic extracts of mushroom samples and standards were 7.2, 6.4, 7.5, 1.59, and 2.15 µg/ml respectively (Table 1). The results of this study are close to those of *G. lucidum, G. esculenta, L. decastes, P. ostreotus*, and *F. trogii*, collected from Uşak, western Turkey, that reporting IC_{50} values was found in the range of 1.27 - 192.1 µg/ml [55]. Besides, $ABTS^{\cdot+}$ scavenging activities of *Paxina queletii, Chlorophyllum agaricoides*, and *Mycenastrum corium* determined higher than those of *I. Sanghuang* [55] and *Armillaria tabescens, Leucopaxillus gentianeus* and *Suillus granulates* methanolic extracts. Tel et al. (2014) reported the $ABTS^{\cdot+}$ radical scavenging activity % of mushroom species at issue, in the range between 12.73%-79.86% for 50 µg extracts [56].

A total of 42 compounds were detected by SPME/GC-MS, including 5 alcohols, 14 aldehydes and ketones, 2 esters, 17 alkanes-heterocyclic compounds, and 4 acids (Table 2). Similar volatile compound groups have been identified in many studies on mushrooms [35, 57-59]. Of those relevant components, volatile compounds common to mushroom samples are hexanal, nonanal, and dodecane. The main volatiles in *Mycenastrum corium* was nonanoic acid (22.40%) and 2-pentylfuran (15.71%). 2-pentylfuran (16.30%) and hexanal (16.21%) in *Paxina queletii*, and benzaldehyde (26.50%) in *Chlorophyllum agaricoide* were the main volatile compounds.

Paxina queletii has the highest content of alcohols and aldehydes-ketones compared to the other mushrooms. The highest content of alkanes-heterocyclic compounds is in *Chlorophyllum agaricoides*, and the highest acid content is in *Mycenastrum corium*. This content difference of volatile components in mushrooms reveals the unique character of each one. *Mycenastrum corium* and *Paxina queletii* have almost the same amount of 2-pentylfuran.

Table 2. Volatile compounds of Mycenastrum corium, Paxina queletii, and Chlorophyllum agaricoides

				Mycenastrum corium	***Paxina queletii***	***Chlorophyllum agaricoides***
No	RT[a]	Compound Name	Cas Number	Area %[b] (SD)[c]		
Alcohols						
1	4.16	1-Butanol, 3-methyl-	123-51-3	0.91± 0.05	-	-
2	6.45	1-Hexanol	111-27-3	0.63± 0.02	-	-
3	9.58	1-Octen-3-ol	3391-86-4	-	9.21± 1.12	-
4	11.02	1-Hexanol, 2-ethyl-	104-76-7	6.43± 0.11	-	-
5	12.29	1-Octanol	111-87-5	1.18± 0.08	3.09± 0.66	-
Total alcohols				9.15	12.30	-
Aldehydes-ketones						
6	4.81	Hexanal	66-25-1	5.76± 0.90	16.21± 0.05	2.94± 0.05
7	6.98	2-Heptanone	110-43-0	2.29± 0.60	9.04± 0.98	-
8	7.33	Heptanal	111-71-7	0.81± 0.05	-	-
9	9.03	Benzaldehyde	100-52-7	-	3.47± 0.22	26.50± 1.60
10	11.29	3-octen-2-one	18402-82-9	-	1.07± 0.09	-
11	12.89	2-Nonanone	821-55-6	-	2.81± 0.21	-
12	13.32	Nonanal	124-19-6	7.96± 1.01	3.29± 0.42	9.53± 1.05
13	15.58	2-Heptenal, 2-propyl-	34880-43-8	-	1.17± 0.06	-
14	15.85	2-Decanone	693-54-9	-	0.91± 0.12	-
15	16.28	Decanal	112-31-2	2.79± 0.05	1.36± 0.26	-
16	19.00	2-Undecanone	112-12-9	1.06± 0.18	-	-
17	19.51	Undecanal	11-44-7	-	-	1.97± 0.06
18	21.23	2-Octenal, 2-butyl-	13019-16-4	-	7.58± 0.88	-
19	22.11	Dodecanal	112-54-9	-	-	1.21± 0.05
Total aldehydes-ketones				20.67	45.91	42.15
Esters						
20	7.66	Aceticacid, pentyl ester	628-63-7	-	0.36± 0.02	-
21	32.85	9,12,15-Octadeca-trienoic acid 2-trime-thylsilyloxy-1-[(trimethylsilyloxy) methyl]ethyl ester	55521-23-8	-	1.39± 0.00	-
Total esters				-	1.75	-
Alkanes-heterocycliccompounds						
22	5.15	Hexamethylcyclo-trisiloxane	541-05-9	-	-	2.26± 0.16
23	6.51	p-Xylene	106-42-3	-	-	1.36± 0.30
24	7.13	Guanosine, 2'-deoxy-	961-07-9	-	-	1.15± 0.09
25	9.89	2-pentylfuran	3777-69-3	15.71± 2.24	16.30± 1.22	-

				Mycenastrum corium	***Paxina queletii***	***Chlorophyllum agaricoides***
26	10.60	Serotonin	50-67-9	-	-	0.50± 0.00
27	10.93	o-Cymene	527-84-4	-	0.80± 0.15	-
28	11.08	2-Carene	554-61-0	-	6.10± 0.74	7.47± 2.00
29	11.85	Undecane	1120-21-4	2.49± 0.35	-	2.67± 0.09
30	11.94	γ-terpinene	99-85-4	-	1.35± 0.22	-
31	15.09	Trehalose	99-20-7	1.02± 0.42	-	-
32	15.66	Azulene	275-51-4	1.00± 0.09	-	2.19± 0.44
33	16.15	Dodecane	112-40-3	4.10± 0.24	1.09± 0.00	8.29± 0.98
34	18.29	Eucalyptol	470-82-6	-	7.92± 2.08	-
35	19.95	Pentadecane	629-62-9	1.55± 0.12	-	-
36	21.94	Tetradecane	629-59-4	2.17± 0.60	1.36± 0.30	8.01± 0.29
37	24.36	Eicosane	112-95-8	0.89± 0.07	-	-
38	25.36	Hexadecane	544-76-3	-		1.70± 0.09
Total alkanes-heterocycliccompounds				28.93	34.92	35.77
Acids						
39	17.96	Nonanoic acid	112-05-0	22.40± 3.10	-	6.44± 0.86
40	20.99	Decanoic acid	334-48-5	5.39± 0.63	-	2.25± 0.16
41	27.33	Tetradecanoic acid	544-63-8	0.47± 0.00	-	0.47± 0.06
42	29.53	Hexadecanoic acid	57-10-3	0.35± 0.09	-	0.67± 0.03
Total acids				28.61	-	9.83

- : Not detected.
[a] RT: Retention time.
[b] Area %: The ratio between the peak area of a particular component in the sample and all the sample components' total peak area.
[c]SD: Standard deviation.

This volatile compound was reported in Nordic wild edible mushrooms, nearly the same amount in *Chanterelus cibarius* and close to twice in *Boletus edulis* [57]. In the same study, in *Chanterelus cibarius, Craterellus tubaeformis,* and *Lactarius camphoratus*, the hexanal content was detected twice the value we found in *Paxina queletii*. Hexanal and nonanal are two of the volatile compounds common to mushrooms studied in Aisala et al. (2019), just as in our study [57]. Hexanal and nonanal are also known as oxidation indicators in oils and butter. Some volatile compounds have functional properties. 1-Octen-3-ol produced by *Paxina queletii* was used successfully to control dry bubble disease in *Agaricus bisporus* [60].

Volatile compounds in dried mushrooms were content 1-octen-3-ol, 3-octen-2-one, 1-octanol, 2-octenal, 2-butyl-, 3-octanone, etc. the consequence was on aroma and sweetness in edible mushrooms. However, in another studies, main volatile compounds in fresh mushrooms were C8 compounds, content 1-octen-3-ol, 3-octanol, 2-octen-1-ol, 1-octanol, 2-octenal, 3-octanone, etc. the result was in conformity with other reports focusing on aroma in edible fungus [59, 61-63].

Nonanoic acid, the main volatile of *Mycenastrum corium*, is used for biocontrol of plants' fungal diseases [64]. New herbicides and blossom thinners based on nonanoic acid started to be used as an alternative to synthetic chemical herbicides [65]. *Mycenastrum corium* has the acidest content compared to *Chlorophyllum agaricoides*. Benzaldehyde is the main volatile in *Chlorophyllum agaricoides* and reported that benzaldehyde could be degraded from benzoic acid during the samples' drying process [59].

Generally, mushrooms are widely grown and consumed as an important food source due to their taste, low calorie and high sodium content, and vitamin, mineral, phenolic antioxidative compound content. Therefore, it is important to know edible mushrooms and to explain their disease-healing properties and physiological and biological active ingredients [42, 66]. HPLC analysis revealed that gallic acid, naringin and trans-cinnamic were predominant major compounds identified in three mushroom species and the individual profile of the relevant compounds are presented in Figure 2.

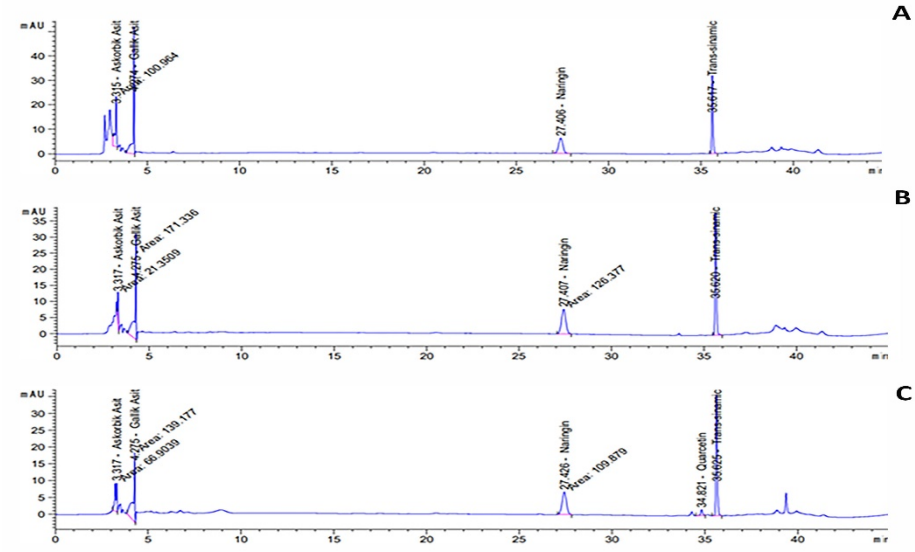

Figure 2. HPLC chromatogram of A) *P. queletii,* B) *C.agaricoides* and C) *M. corium*

Of the revealed compounds, gallic acid is a naturally occurring low molecular weight triphenolic compound [67], being versatile for its biological functions, *viz.* radical quenching as well as interfering acts with cell-signaling pathways and in apoptosis of cancer cells [67]. Herewith the current findings, the highest content of gallic acid was observed in *P. queletii* (12.4 µg/ml) and followed by *C.agaricoides* (10.32 µg/ml) and *M. corium* (8.22 µg/ml). In relative to other mushroom species, gallic acid ranged between 5.4 and 38.9 mg/g extract in sequential extracts of *Lycoperdon utriforme*, suggesting that the content was solvent dependent [44]. Regarding naringin as a natural flavanone glycoside, multiple therapeutic effects, such as effect on genetic damage, central nervous system diseases, oxidative stress, and metabolic syndrome have been well-reviewed by Chen et al. (2016) [67]. Indeed, no big differences were observed in naringin content of the mushroom species herein (Table 3). Trans-cinnamic has been reported to possess antioxidant [68], antimicrobial [69, 70] and α-glucosidase inhibition [71]. As the case of naringin, the values of trans-cinnamic were close to each other.

Table 3. Phenolic acid profile of wild mushrooms extracts

Compounds	***P. queletii***	***C.agaricoides***	***M. corium***
Gallic acid (µg/ml)	12.4	10.32	8.22
Naringin (µg/ml)	5.23	6.58	5.72
Trans-cinnamic (µg/ml)	6.59	8.08	7.4
Quercetin (µg/ml)	ND	ND	2.83

ND: Not detected

CONCLUSIONS

The present study is the first report on chemical compositions and radical scavenging activities of three wild-edible mushroom samples including *Paxina queletii, Chlorophyllum agaricoides* and *Mycenastrum corium* from Turkey. Regarding antioxidant activities, in general, scavenging activities of mushrooms were lower in comparison to the former reports. 42 volatile compounds of *Mycenastrum corium, Paxina queletii*, and *Chlorophyllum agaricoides* were detected. The extracts were found as rich sources of alkanes-heterocyclic compounds (2-pentylfuran, 2-carene, γ-terpinene, azulene, dodecane, eucalyptol, pentadecane, tetradecane, eicosane, hexadecane), acids (nonanoic, decanoic, tetradecanoic, hexadecanoic acids), esters and aldehydes and ketones. Considering the phenolic acid composition, the extracts were found to be rich in gallic acid, naringin and trans-cinnamic.

EXPERIMENTAL SECTION

Materials

Mushroom samples (*Paxina queletii (Bres.) Stangl, Chlorophyllum agaricoides (Czern.) Vellinga and Mycenastrum corium (Guers.) Des.* were collected from Zilan Valley (Erciş-Van, Turkey) (Table 4).

Table 4. The relevant information regarding species and their collection

Mushroom species	Altitude (m)	Coordinates	Location	Collection date
***Paxina queletii* (Bres.) Stangl**	1860	39°13'780"N, 43°23'560"E	Zilan Valley (Erciş-Van, Turkey)	2013-2014
***Chlorophyllum agaricoides* (Czern.) Vellinga**	1805	39°09'991"N, 43°19'614"E	Zilan Valley (Erciş-Van, Turkey)	2013-2014
***Mycenastrum corium* (Guers.) Desv.**	1835	39°13'793"N, 43° 23'575"E	Zilan Valley (Erciş-Van, Turkey)	2013-2014

After transferring to the laboratory and drying mushrooms at room temperature, the relevant mushroom samples were preserved in polyethylene bags at -20^{o}C until further analysis. The species (Figure 3) were defined by Mehmet Zeki Koçak and Deceased Prof. Dr. Kenan Demirel. A specimen was deposited in Mycology Research Fungarium, Faculty of Science, Van Yüzüncü Yıl University, Turkey (Fungarium codes: KOCAK 120, 155 and 106, respectively). All relevant chemicals used for analysis were purchased from Merck, unless otherwise stated. All chemicals were of HPLC grade.

Figure 3. Edible mushroom materials of A) *P. queletii*, B) *C. agaricoides* and C) *M. Corium*

Determination of total phenolic (TPC) and total flavonoid contents (TFC)

The TPC of ethanol extracts of mushrooms was determined based on Slinkard and Singleton (1977)'s method (FCR assay) [30]. Gallic acid (GA) (1 mg/ml) was used as the standard phenolic compound. TPC of extracts were calculated as milligrams of gallic acid equivalent (mg GAE/ g dried extract).

The TFC of extracts was determined according to the method described by Park et al. (1997) [31]. Quercetin (0.1 mg/ml) was used as the standard flavonoid compound. TFC of the extracts was calculated as milligrams of quercetin equivalent (mg QE/g dried extract).

Radical scavenging activities

The 1,1-diphenyl-2-picryl hydrazyl ($DPPH^{\cdot}$) radical scavenging activities were assayed according to method put by Brand-Williams et al. (1995) [32] with some modifications [33]. Alcohol solution of $DPPH^{\cdot}$ was added to various concentrations of mushrooms extracts ranging from 5 µg/ml to 14.5 µg/ml. The sample tubes were kept at room temperature in the dark and after 30 min the absorbance were measured at 517 nm. Both IC_{50} values and scavenging percentages of the extracts and standard chemicals regarding $DPPH^{\cdot}$ scavenging were calculated in order to compare with the literature.

The 2,2'-azino-bis [3-ethylbenzothiazoline-6-sulphonic acid] ($ABTS^{\cdot+}$) scavenging activities of the mushroom extracts were determined according to the method described by Cemeroğlu (2010) [34]. After $ABTS^{\cdot+}$ solution was prepared absorbance of blank sample was adjusted to 0.700±0.025 at 734 nm in the spectrophotometer by diluting with 20 mM acetate buffer (including 2.45 mM potassium persulfate). The concentrations ranging from 30 µg/ml to 55 µg/ml of mushroom extracts were assayed. The IC_{50} values for each mushroom was quantified and also, scavenging percentages of the extracts and standard chemicals were calculated.

Analysis of volatile compounds

A 2 cm (50/30 µm divinylbenzene/carboxen/polydimethylsiloxane) SPME fiber (Supelco Co., Bellefonte, PA, USA) was used for the extraction of volatile compounds from samples. 5 ml of the ultra-pure water was added to 0.5 g of the sample in the glass vials (Supelco, USA) and allowed to equilibrate at 40°C for 30 min [35]. Identification of volatile compounds was performed with Thermo Fisher Trace ISQ GC-MS (USA) gas chromatography-mass spectrometry system and run in split (ratio was 1:10) mode. The volatile compounds were separated on a DB-5MS column (30 m × 0.25 mm × 0.25 µm;

Agilent, USA). The oven was held at 40°C for 1 min, then increased at 5°C per min to 120°C, it was held for 2 min, then rose again at 10°C per min to 240°C and caught 3 min. The mass spectrometer was set to scan from 45 to 450 amu (threshold 1000) at a sampling rate of 1.11 scans/s [36]. Compounds were identified by comparison to the Wiley9 and Mainlib mass spectral libraries. The quantitative analysis was based on the ratios between the terminal area of a given component in the sample and the total terminal area of all components in the sample [35].

Extraction and quantification of phenolic compounds using HPLC

The relevant mushroom samples were firstly dried and then powdered. A shaker-assisted sequential extraction was performed with 5 mg of fungus samples in 10 ml methanol at 120 rpm for 24 hours at room temperature. The extraction was repeated three times with the same materials to collect all residues after extraction. The filtrates of three extractions were evaporated using a rotary evaporator (Heidolph 94200, Bioblock Scientific). The vacuo-dried samples were preserved at +4°C until chromatographic analysis.

The methanol extracts of the relevant mushrooms were filtered through a 0.45 µm disk prior to HPLC analysis. For analysis, Agilent 1260 CA, USA series liquid chromatograph equipped with a diode array detector was used. The separation was performed using 10 µL of extract on a ACE Generix 5C18 (GEN-7444) Scotland, column (4.6 x 250 mm, 5 µm) thermos stated at 30°C. The mobile phase was (A) 0.1% phosphoric acid in water and (B) HPLC-grade 100% acetonitrile. The gradient was performed as specified in Table 5. The relevant phenolics were quantified with the comparing of the peak recorded at 300 nm with the standard curves of each acid. The calibration curves were obtained from a concentration range between 20-1000 µg/ml and 0.5-50 µg/ml for Gallic acid, naringin and trans-cinnamic. The results are expressed in µg per ml of dry mushroom.

Table 5. HPLC conditions

Time (min.)	Solvent %		Flow Rate (mL/min)
	A	B	
0	83	17	0.8
7	85	15	0.8
20	85	15	0.8
24	70	30	0.8
30	65	35	0.8
40	83	17	0.8

A: 0.1% phosphoric acid in water
B: HPLC-grade 100% acetonitrile

ACKNOWLEDGMENTS

The taxonomic definition of wild mushroom species used in this study has been enlightened in M. Z. K.'s master's thesis. The analyses performed in the article were later designed and carried out. The authors thank to Dr. Muhittin Kulak for language editing of manuscript.

Author Contribution

MZK: Field survey, collection and identification of the species, elemental and phenolic analysis, co-writing of the draft; AMK: Co-writing of the draft, formal analysis; MK: GC-MS analysis, co-writing of the draft; UG: Antioxidant analysis, co-writing of the draft. All co-authors read and approved the last draft for submission.

Conflicts of interest

There are no conflicts to declare.

REFERENCES

1. M. Dimitrijević; V. Stankov Jovanović; J. Cvetković; M. Mitić; G. Petrović; A. Đorđević, and V. Mitić; *Anal. Lett.*, **2017**, 50(10), 1691-1709.
2. M. Zhang; S. Cui; P. Cheung, and Q. Wang; *Trends Food Sci. Technol.*, **2007**, 18(1), 4-19.
3. J. Falandysz and J. Borovička; *Appl. Microbiol. Biotechnol.*, **2013**, 97(2), 477-501.
4. A.S. Bengu; *Prog. Nutr.*, **2019**, 21(1), 189-193.
5. M.J. Feeney; A.M. Miller, and P. Roupas; *Nutr. today*, **2014**, 49(6), 301.
6. P. Kalač; *J. Sci. Food Agric.*, **2013**, 93(2), 209-218.
7. W.M. Breene; *J. Food Protect.*, **1990**, 53(10), 883-894.
8. E.E. Ak; Y. Tüzel; E. Eren, and F. Atilla; *Türk Tarım-Gıda Bilim ve Teknoloji dergisi*, **2016**, 4(3), 239-243.
9. S.N. Lotfy; H.H. Fadel; A.H. El-Ghorab, and M.S. Shaheen; *Food Chem.*, **2015**, 187, 7-13.
10. H.N. Bao; H. Ushio, and T. Ohshima; *J. Agric. Food Chem.*, **2008**, 56(21), 10032-10040.
11. C.L. Dikeman; L.L. Bauer; E.A. Flickinger, and G.C. Fahey; *J. Agric. Food Chem.*, **2005**, 53(4), 1130-1138.
12. P. Kalač and L.r. Svoboda; *Food chemistry*, **2000**, 69(3), 273-281.
13. W.Y. Lee; E.-J. Park; J.K. Ahn, and K.-H. Ka; *Mycobiology*, **2009**, 37(1), 43-47.
14. A.S. Logan; U. Nienaber, and X.S. Pan; Lipid oxidation: Challenges in food systems. **2015,** Elsevier.
15. A.J. Weigand-Heller; P.M. Kris-Etherton, and R.B. Beelman; *Prev. Med.*, **2012**, 54, S75-S78.
16. L. Barros; M.-J. Ferreira; B. Queiros; I.C. Ferreira, and P. Baptista; *Food Chem.*, **2007**, 103(2), 413-419.

17. S. Khatun; A. Islam; U. Cakilcioglu; P. Guler, and N.C. Chatterjee; *NJAS-Wageningen J. Life Sci.*, **2015**, 72, 1-5.
18. C. Rice-Evans; N. Miller, and G. Paganga; *Trends Plant Sci.*, **1997**, 2(4), 152-159.
19. E. Bernaś; G. Jaworska, and Z. Lisiewska; *Acta Scientiarum Polonorum Technologia Alimentaria*, **2006**, 5(1), 5-20.
20. I. Fasidi and M. Kadiri; *Food/Nahrung*, **1990**, 34(5), 415-420.
21. H. Sivrikaya; L. Bacak; A. Saraçbaşı; I. Toroğlu, and H. Eroğlu; *Food Chem.*, **2002**, 79(2), 173-176.
22. S. Hazama; S. Watanabe; M. Ohashi; M. Yagi; M. Suzuki; K. Matsuda; T. Yamamoto; Y. Suga; T. Suga, and S. Nakazawa; *Anticancer Res.*, **2009**, 29(7), 2611-2617.
23. P. Yang; M. Liang; Y. Zhang, and B. Shen; *Adv. Ther.*, **2008**, 25(8), 787-794.
24. P. Kalač; *Food Chem.*, **2009**, 113(1), 9-16.
25. R. Genders; Mushroom growing for everyone. **1982,** Faber and Faber.
26. P. Oei; Manual on mushroom cultivation: techniques, species and opportunities for commercial application in developing countries. **1991,** Tool.
27. A. Turkoglu; M.E. Duru; N. Mercan; I. Kivrak, and K. Gezer; *Food Chem.*, **2007**, 101(1), 267-273.
28. S. Kavishree; J. Hemavathy; B. Lokesh; M. Shashirekha, and S. Rajarathnam; *Food Chem.*, **2008**, 106(2), 597-602.
29. B. Ribeiro; R. Lopes; P.B. Andrade; R.M. Seabra; R.F. Gonçalves; P. Baptista, and I. Quelhas; *Food Chem.*, **2008**, 110(1), 47-56.
30. K. Slinkard and V.L. Singleton; *Am. J. Enol. Vitic.*, **1977**, 28(1), 49-55.
31. Y.K. Park; M.H. Koo; M. Ikegaki, and J. Contado; *Arq. Biol. Tecnol*, **1997**, 97-106.
32. W. Brand-Williams; M.-E. Cuvelier, and C. Berset; *LWT-Food Sci Technol.*, **1995**, 28(1), 25-30.
33. U. Güller; P. Güller, and M. Çiftci; Alternative Therapies in Health and Medicine, **2020**.
34. B. Cemeroğlu; *Gıda Analizleri (Editör: B. Cemeroğlu). Ankara, Türkiye: Gıda Teknolojisi Derneği Yayınları*, **2010**, (34), 87-93.
35. Y. Tian; Y. Zhao; J. Huang; H. Zeng, and B. Zheng; *Food Chem.*, **2016**, 197, 714-722.
36. M. Koyuncu and Y. Tuncturk; *Oxidation Commun.*, **2017**, 40(2), 785-798.
37. S.P. Wasser and A.L. Weis; *Critical Reviews™ in Immunology*, **1999**, 19(1).
38. N.G. Puttaraju; S.U. Venkateshaiah; S.M. Dharmesh; S.M.N. Urs, and R. Somasundaram; *J. Agric. Food Chem.*, **2006**, 54(26), 9764-9772.
39. P. Roupas; J. Keogh; M. Noakes; C. Margetts, and P. Taylor; *J. Funct. Foods*, **2012**, 4(4), 687-709.
40. D. Stojković; F.S. Reis; L. Barros; J. Glamočlija; A. Ćirić; L.J. van Griensven; M. Soković, and I.C. Ferreira; *Food Chem.Toxicol.*, **2013**, 59, 289-296.
41. K. Liu; X. Xiao; J. Wang; C.-Y.O. Chen, and H. Hu; *LWT-Food Sci. Technol.*, **2017**, 82, 154-161.
42. L. Smolskaitė; P.R. Venskutonis, and T. Talou; *LWT-Food Sci. Technol.*, **2015**, 60(1), 462-471.
43. J. Liu; L. Jia; J. Kan, and C.-h. Jin; *Food Chem. Toxicol.*, **2013**, 51, 310-316.

44. S. Sezgin; A. Dalar, and Y. Uzun; *J. Food Sci. Technol.*, **2020**, 57(5):1866–1876.
45. J. Azieana; M. Universiti Teknologi; S. Alam; M. Universiti Teknologi; S. Alam; M. Universiti Teknologi; S. Alam; M. Universiti Teknologi, and S. Alam; *Open Access Library Journal*, **2017**, 4(11), 1.
46. E. López-Vázquez; F. Prieto-García; M. Gayosso-Canales; E.O. Sánchez, and J.V. Ibarra; *Italian J. Food Sci.*, **2017**, 29(4).
47. D.A. Abugri and W.H. McElhenney; *J Nat Prod Plant Resour*, **2013**, 3(3), 37-42.
48. C. Gan; N.B. Amira, and R. Asmah; *Int. Food Res. J.*, **2013**, 20(3), 1095.
49. F.C. Wong; T.-T. Chai; S.-L. Tan, and A.-L. Yong; *Tropical J. Pharm. Res.*, **2013**, 12(6), 1011-1016.
50. L. Barros; S. Falcão; P. Baptista; C. Freire; M. Vilas-Boas, and I.C. Ferreira; *Food Chem.*, **2008**, 111(1), 61-66.
51. A.C. Ramírez-Anguiano; S. Santoyo; G. Reglero, and C. Soler-Rivas; *J. Sci.Food Agric.*, **2007**, 87(12), 2272-2278.
52. F.S. Reis; A. Martins; L. Barros, and I.C. Ferreira; *Food Chem. Toxicol.*, **2012**, 50(5), 1201-1207.
53. J.M. Savoie; N. Minvielle, and M.L. Largeteau; *J. Sci. Food Agric.*, **2008**, 88(6), 970-975.
54. A. Dundar; V. Okumus; S. Ozdemir; K.S. Celik; M. Boga; E. Ozcagli; G. Ozhan, and A. Yildiz; *J. Horticulture*, **2015**, 1-6.
55. G. Tel; M. Ozturk; M.E. Duru, and A. Turkoglu; *Pharm. Biol.*, **2015**, 53(6), 824-830.
56. G. Tel; E. Deveci; S. Küçükaydın; M.A. Özler; M.E. Duru, and M. Harmandar; *Eurasian J. Anal. Chem.*, **2014**, 8(3), 136-147.
57. H. Aisala; J. Sola; A. Hopia; K.M. Linderborg, and M. Sandell; *Food Chem.*, **2019**, 283, 566-578.
58. R.L. Berendsen; S.I. Kalkhove; L.G. Lugones; J.J. Baars; H.A. Wösten, and P.A. Bakker; *Appl. Microbiol. Biotechnol.*, **2013**, 97(12), 5535-5543.
59. F. Pei; W. Yang; N. Ma; Y. Fang; L. Zhao; X. An; Z. Xin, and Q. Hu; *LWT-Food Sci. Technol.*, **2016**, 72, 343-350.
60. J.L. Mau; R.B. Beelman, and G.R. Zigler; *J. Food Sci.*, **1992**, 57(3), 704-706.
61. M. Aneja; T.J. Gianfagna, and P.K. Hebbar; *Physiol. Mol. Plant Pathol.*, **2005**, 67(6), 304-307.
62. J. Bennett; R. Hung; S. Lee, and S. Padhi; *Fungal associations*, **2012**, 373-393.
63. S. Grosshauser and P. Schieberle; *J. Agric. Food Chem.*, **2013**, 61(16), 3804-3813.
64. R. Ciriminna; A. Fidalgo; L.M. Ilharco, and M. Pagliaro; *Biofuel Bioprod Biorefin*, **2019**, 13(6), 1476-1482.
65. S. Sezgin; A. Dalar, and U. Yusuf; *Int. J. Second. Metab.*, **2018**, 5(2), 163-170.
66. B. Badhani; N. Sharma, and R. Kakkar; *Rsc Advances*, **2015**, 5(35), 27540-27557.
67. R. Chen; Q.-L. Qi; M.-T. Wang, and Q.-Y. Li; *Pharm. Biol.*, **2016**, 54(12), 3203-3210.
68. M. Sova; *Mini Rev. Med. Chem.*, **2012**, 12(8), 749-767.
69. K.S. Letsididi; Z. Lou; R. Letsididi; K. Mohammed, and B.L. Maguy; *Lwt*, **2018**, 94, 25-32.

70. S. Yilmaz; M. Sova, and S. Ergün; *J. Appl. Microbiol.*, **2018**, 125(6), 1714-1727.
71. S. Adisakwattana; K. Sookkongwaree; S. Roengsumran; A. Petsom; N. Ngamrojnavanich; W. Chavasiri; S. Deesamer, and S. Yibchok-anun; *Bioorg. Med. Chem. Lett.*, **2004**, 14(11), 2893-2896.

STUDIA UBB CHEMIA, LXVI, 4, 2021 (p. 149-158)
(RECOMMENDED CITATION)
DOI:10.24193/subbchem.2021.4.11

ASSESSMENT OF NON-AQUEOUS SOLVENTS IN THE ELECTROOXIDATION OF RESORCINOL, PHLOROGLUCINOL, PYROGALLOL, AND ROLE OF CO-SOLVENT IN DETERMINATION OF PYROGALLOL WITH MICROELECTRODE VOLTAMMETRY

LÁSZLÓ KISS[a,b,*], SÁNDOR KUNSÁGI-MÁTÉ[b,c]

ABSTRACT. This study reveals the behavior of resorcinol, phloroglucinol and pyrogallol in several non-aqueous solvents (acetonitrile, acetone, dimethyl sulphoxide, dimethyl formamide, nitrobenzene, nitromethane, dichloromethane, methanol). The voltammetric curves showed that the results obtained with the outlined compounds depend strongly on the solvent used. Resorcinol and phloroglucinol undergo some fouling during their electrooxidation while pyrogallol gave reproducible voltammograms in many solvents. The optimal solvent was chosen then for the determination of pyrogallol in cooking oil taking into consideration the antifouling, miscibility, permittivity and viscosity effects with steady-state voltammetry by using microelectrode.

Keywords: *Resorcinol; Phloroglucinol; Pyrogallol; Co-solvent; Microelectrode*

INTRODUCTION

Polyhydroxy phenols are investigated due to several applications mainly in aqueous solvents considerably due to their antioxidant properties. Hydroquinone, resorcinol and catechol can be determined simultaneously so numerous works are based on their quantification in lower concentrations [1-5]. The low oxidation potential is utilized by using pyrogallol as antioxidant also in apolar environments such as biodiesel and cooking oil so some works aimed at measuring it by using special electrochemical detection techniques [6-8].

[a] *University of Pécs, Department of General and Physical Chemistry, Faculty of Sciences, Ifjúság street 6, H-7624 Pécs, Hungary*
[b] *János Szentágothai Research Center, Ifjúság útja 20, Pécs H-7624, Hungary*
[c] *University of Pécs, Institute of Organic and Medicinal Chemistry, Faculty of Pharmacy, Honvéd street 1, Pécs H-7624, Hungary*
[*] *Corresponding author: kissl@gamma.ttk.pte.hu*

In several electroanalytical procedures a co-solvent is used due to different reasons, for example improving the transport properties, solution permittivity and altering favourably the molecular environment. The higher diffusion coefficient enhances the sensitivity towards the analytes and the higher permittivity contributes to the reduction of the ohmic distortion. In the viewpoint of reproducibility of current signals the solvent has essential role as deactivation processes can take place and moreover, the rapid fouling already diminishes remarkably the magnitude of the peak currents of the subsequent scans after the first one. This process is difficult to describe quantitatively as porosity of film and the nature of solvent highly affects electrode deactivation as it was shown in earlier works [9-11]. Therefore, these requirements should be taken into consideration when choosing the appropriate co-solvent for analysis of compounds prone to fouling and on the other hand the solvent is miscible with the sample. So, the electrochemical behavior of widely used polihidroxi benzenes was the aim of this work in different non-aqueous solvents and the introduction of an analytical procedure.

RESULTS AND DISCUSSION

In the first part of studies the examination of electrochemistry of the three polyhydroxy phenols was carried out in different non-aqueous solvents dissolved in 50 mM concentration scanning in the potential range between 0 and 2 V with 0.1 V/s scan rate. It is clearly seen from Fig. 1 that resorcinol and phloroglucinol deactivates the working electrode (1 mm in diameter platinum) in all solvents. The low values of the first current peaks in nitrobenzene, nitromethane and dichloromethane are due to the limited solubility of solutes well below 50 mM. The curves obtained in methanol displayed in Fig. 2 show the usual fouling behavior for resorcinol and phloroglucinol but after the second scan a slight increase of peak currents appears indicating that there is only a weak adherence of formed deposit on the electrode surface. It also suggests that porosity of film varies during the experiment.

Dimethyl sulphoxide highlights the importance of solvent in the behavior of a compound namely resorcinol and phloroglucinol (Fig. 3a and b) as the peak currents of curves show that no tendency can be observed in the subsequent scans which is a sign of formation of weakly bound organic layer. Its thickness was high enough to see with naked eye as a brownish deposit and it was easy to remove mechanically.

The position of hydroxyl groups determines significantly the ability to fouling as resorcinol and phloroglucinol showed previously as these groups are in 1,3 position relative to each other. On the other hand, this is also indicated by pyrogallol (Fig. 1c). The magnitude and reproducibility of peak currents in majority of solvents suggest that pyrogallol undergoes also non-fouling processes reinforced also by the curves in Fig. 3c. The part of molecule

where neighbouring hydroxyl groups can be found oxidizes similarly to catechol (1,2-position). In parallel to this process polymerization reaction can take place but the removal of the products depend significantly on the solvent. Nitrobenzene has an identical effect on its electrochemistry. However, the solute dissolved completely in 50 mM concentration the peak height of the first voltammogram is unprecedently low compared with the other solvents. The reason is the very low polymer solubility and on the other hand it deposits as a compact layer.

The only solvent where pyrogallol could not be dissolved in 50 mM concentration was dichloromethane but reproducibility of currents show the lack of deactivation and therefore appropriateness for analytical purposes.

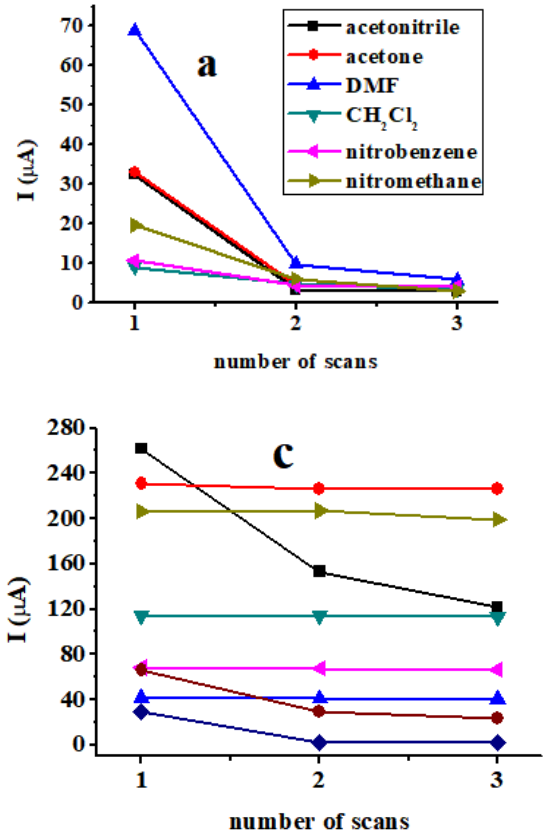

Figure 1. Voltammetric peak currents of 50 mM resorcinol (a), phloroglucinol (b) and pyrogallol (c) in the different non-aqueous solvents (scan rate 0.1 V/s, supporting electrolyte 70 mM TBAP). In part c: ■: acetonitrile, ●: acetone, ▲: CH_2Cl_2 (saturated solution), ▼: dimethyl formamide, ►: methanol, ◄: dimethyl sulphoxide, ●: nitromethane, ♦: nitrobenzene.

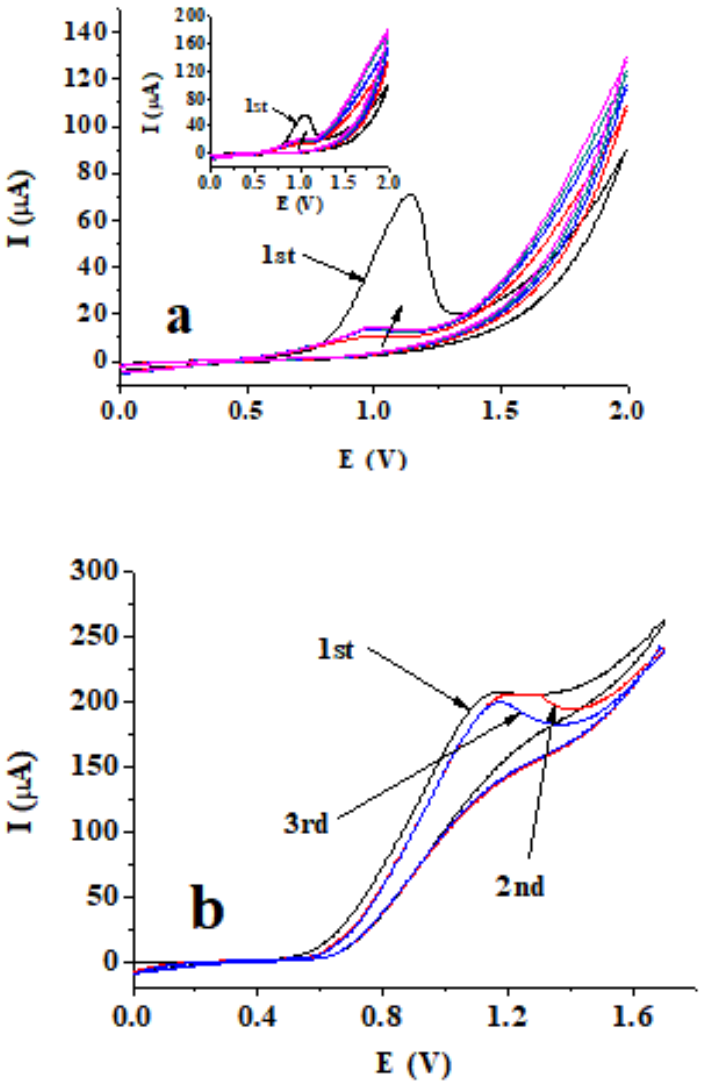

Figure 2. Subsequent cyclic voltammetric curves of 50 mM resorcinol (a), phloroglucinol (inset graph in part a) and pyrogallol (b) in methanol (scan rate 0.1 V/s, supporting electrolyte 70 mM TBAP)

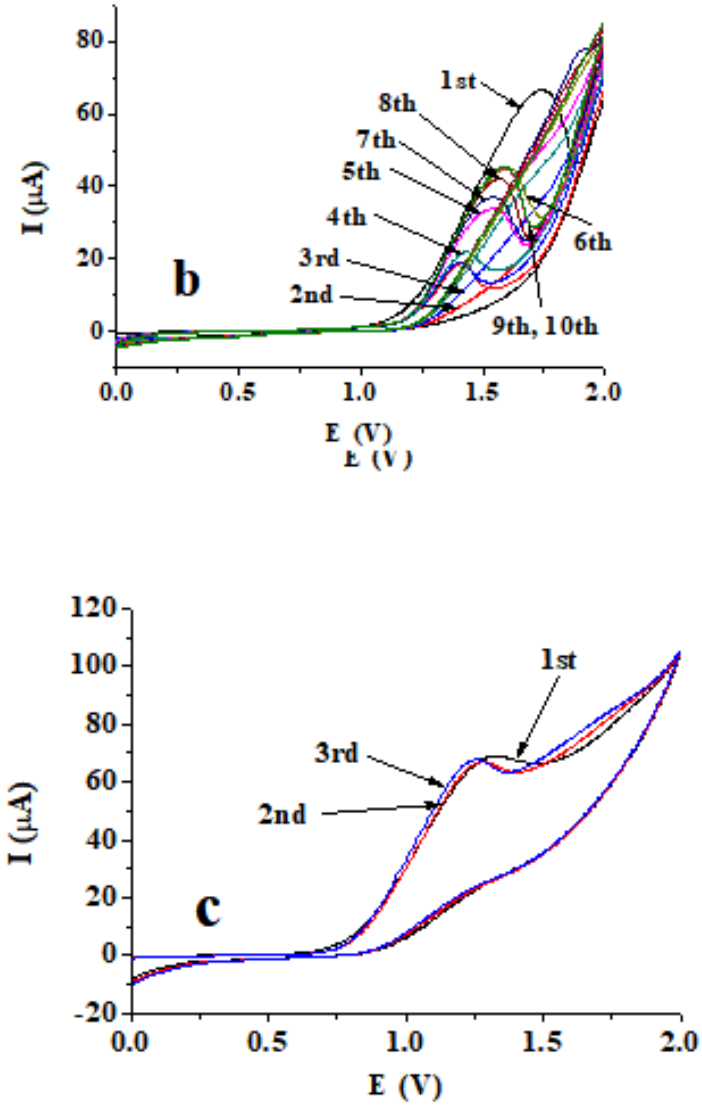

Figure 3. Subsequent cyclic voltammetric curves of 50 mM resorcinol (a), phloroglucinol (b) and pyrogallol (c) in dimethyl sulphoxide (scan rate 0.1 V/s, supporting electrolyte 70 mM TBAP)

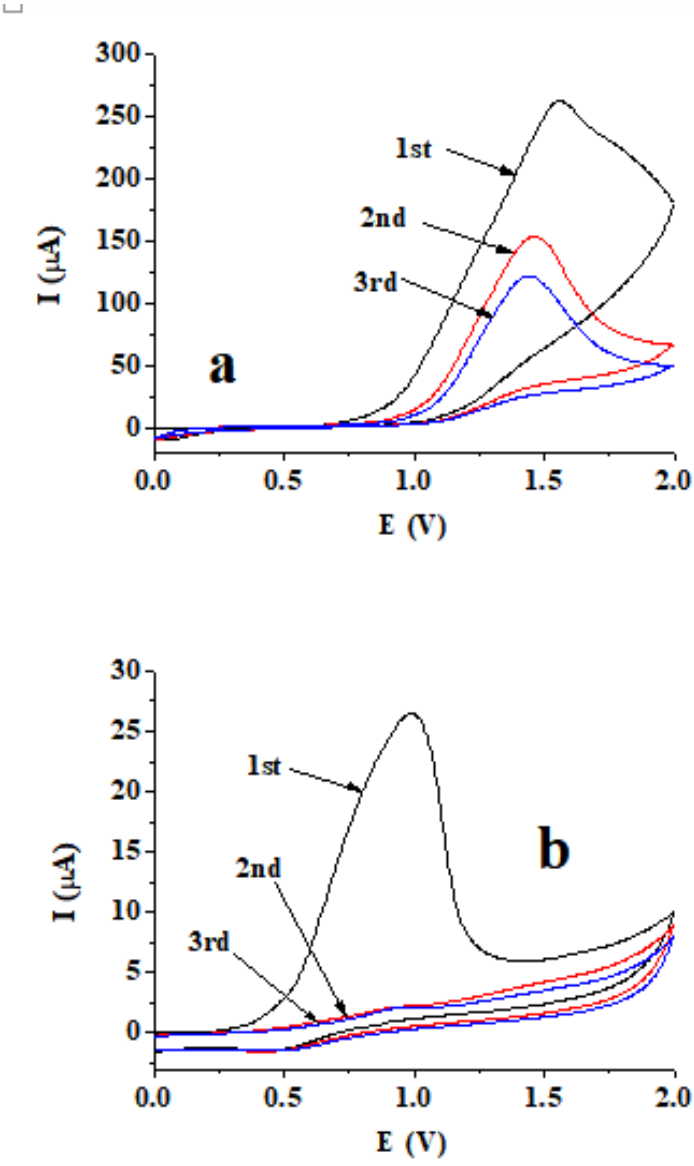

Figure 4. Cyclic voltammetric curves of 50 mM pyrogallol in acetonitrile (a) and in nitrobenzene (b) (scan rate 0.1 V/s, supporting electrolyte 70 mM TBAP)

The results of the above experiments showed that pyrogallol differs significantly from the other polyhydroxy compounds especially in signal reproducibility which is essential in analytical purposes. On the other hand, pyrogallol has an outstanding role as antioxidant in many applications so its quantification has gained high importance. The real sample used here was a cooking oil purchased from a supermarket. Taking into consideration the anti-fouling properties and sensitivity (magnitude of current signal) acetone seemed to be the most appropriate co-solvent for further analytical purposes. Moreover acetone has high miscibility with the majority of apolar samples. During the procedure a 25 μm in diameter platinum microelectrode was used which is suitable in highly resistive environments. The permittivity of acetone will be drastically diminished by mixing with oily samples but being enough for electroanalysis in this way. On the other hand the mixing with oil the addition of acetone increases significantly viscosity highly affecting the current signals of electroactive materials. The real sample may contain additives being electrochemically active in the potential range where pyrogallol oxidation occurs. Therefore for taking these facts into account the standard addition method was applied in the analytical procedure.

The cooking oil and acetone were mixed in 50-50 v/v% and concentration of added pyrogallol was varied for carrying out the calibration experiments so the viscosities of all solution were uniform. All solutions contained 10 mM TBAP supporting electrolyte. The steady-state voltammograms were measured with the platinum microelectrode between 0 and 2 V with 0.1 V/s scan rate and the current values read at the beginning of the current plateaus were utilized for calibration. The electrodes were thoroughly washed with acetone after each measurement to avoid the contamination of calibration solutions with each other, and working electrode was polished.

By examining the microelectrode voltammograms of added pyrogallol (Fig. 5), some deviations can be observed from the regular steady-state voltammograms. The current plateaus are not parallel at all to the x-axis. This is attributable to pyrogallol not to the other components which was verified by studies of pyrogallol alone in acetone as the shapes of its voltammograms were very similar to that obtained in the mixture prepared with the chosen cooking oil sample. These results suggest a complicated process described in a previous paragraph but the voltammetric curves were reproducible after renewing the electrode surface.

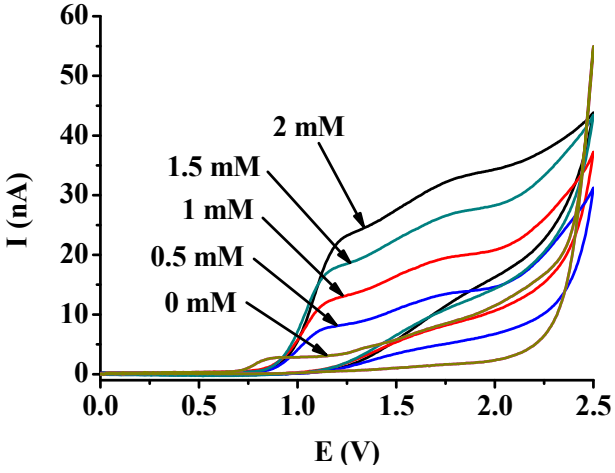

Figure 5 Steady-state voltammograms for the determination of pyrogallol in cooking oil

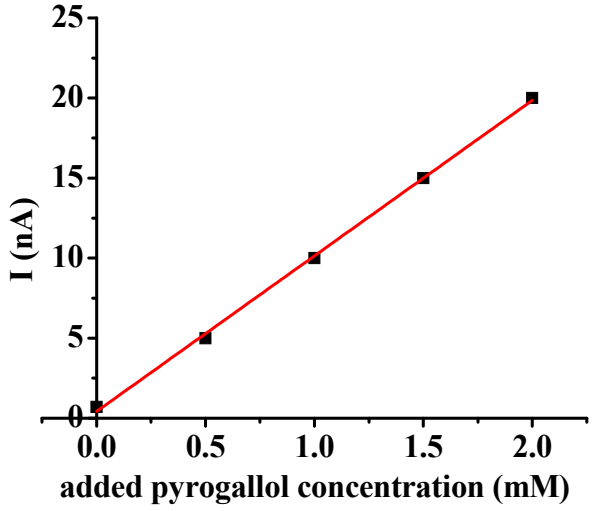

Figure 6. The calibration curve of the standard addition procedure for pyrogallol in 50-50 v/v% mixture of cooking oil and acetone (supporting electrolyte 10 mM TBAP, v=0.1 V/s, working electrode 25 μm platinum microdisc)

The calibration curve of standard addition method can be seen in Fig. 6 for added pyrogallol. It was linear and it enabled the determination of pyrogallol. Without added pyrogallol a current plateau appeared at a lower anodic potential than that characteristic of pyrogallol. It suggests that an other additive more suscepticle to oxidation is present in the cooking oil. Its plateau current was therefore subtracted from the other ones measured in presence of added pyrogallol and these corrected values served for making the calibration plot. By using the intercept at the x-axis 43.2 μM pyrogallol could be determined, but this measured concentration value is only the half of the true value due to addition of acetone so it should be taken into consideration. Finally, the concentration of pyrogallol in cooking oil was 86.4 μM.

The determined pyrogallol concentration is in the range of that usually found in non-aqueous real samples by using indirect electrochemical methods [12-14]. The method introduced in this work seems to be appropriate for the assessment of antioxidant content.

CONCLUSION

The obtained results showed that in non-aqueous solvents resorcinol and phloroglucinol has high susceptibility to electrode fouling while pyrogallol showed obviously larger and more reproducible current signals. Thanks to these facts determination of the latter compound is possible in apolar liquids with microelectrode voltammetry.

EXPERIMENTAL SECTION

High purity solvents and solid materials were used for the investigation of polyhydroxy phenols throughout the entire work which were products of Sigma Aldrich and Acros Organics. The solutions used for the studies were always freshly prepared particularly in case of pyrogallol which is very susceptible to the oxidation. The working electrode was a 1 mm in diameter platinum disc and a 25 μm in diameter platinum microdisc, a platinum wire served as counter and silver wire as quasi reference electrode. A potentiostat (Dropsens, Spain) was used for carrying out the measurements. Before all studies the surfaces of working electrodes were thoroughly polished on a polishing cloth with aqueous suspension of 1 μm average particle size alumina powder. The subsequent ultrasonication in deionized water and thorough washing with deionized water ensured the removal of physically adsorbed particles from the electrode surfaces. In all solutions tetrabutylammonium perchlorate (TBAP) was dissolved as supporting electrolyte.

ACKNOWLEDGEMENT

Project no. TKP2020-IKA-08 has been implemented with the support provided from the National Research, Development and Innovation Fund of Hungary, financed under the 2020-4.1.1-TKP2020 funding scheme.

REFERENCES

1. M. Buleandra, A. A. Rabinca, I. A. Badea, A. Balan, I. Stamatin, C. Mihailciuc, A. A. Ciucu, *Microchim. Act.*, **2017**, *184*, 1481.
2. H. Ershadifar, M. Akhond, G. Absalan, *IEEE Sensor J.*, **2017**, *17*, 5030.
3. N. Sabbaghi, M. Noroozifar, M. Tohidinia, M. Farsadrooh, *Int J. Electrochem. Sci.*, **2017**, *12*, 8777.
4. P. Feng, S. Wang, W. Su, S. Cheng, *J. Chinese Chem. Soc.*, **2012**, *59*, 231.
5. O. V. Karunina, L. I. Skvortsova, V. N. Kiryushov, *J. Anal. Chem.*, **2009**, *64*, 48.
6. R. M. Cardoso, R. M. Dornellas, A. P. Lima, R. H. O. Montes, E. M. Richter, R. A. A. Munoz, *J. Brazilian Chem. Soc.*, **2017**, *28*, 1650.
7. J. Chylkova, M. Tomaskova, L. Janikova, R. Selesovska, T. Navratil, P. Chudobova, *Chem. Papers*, **2017**, *71*, 1047.
8. A. S. A. Araujo, R. P. Caramit, L. C. S. Oliveira, V. S. Ferreira, *Electroanal.*, **2015**, *27*, 1152.
9. L. Kiss, D. Bősz, F. Kovács, H. Li, S. Kunsági-Máté, *Polymer Bull.*, **2019**, *76*, 215.
10. L. Kiss, D. Bősz, F. Kovács, H. Li, G. Nagy, S. Kunsági-Máté, *Polymer Bull.*, **2019**, *76*, 5849.
11. L. Kiss, F. Kovács, S. Kunsági-Máté, *Periodica Polytechnica Chemical Engineering*, **2021**, *65*, 139.
12. C. Hung, W. Chang, W. Su, S. Cheng, *Electroanalysis*, **2014**, *26*, 2237.
13. J. Tashkhourian, S. M. Ghaderizadeh, *Russian J. Electrochem.*, **2014**, *50*, 959.
14. J. S. Bonini, F. Q. Mariani, E. G. de Castro, A. Galli, R. Marangoni, F. J. Anaissi, *Orbital: Electron. J. Chem.*, **2015**, *7*, 318.

STUDIA UBB CHEMIA, LXVI, 4, 2021 (p. 159-170)
(RECOMMENDED CITATION)
DOI:10.24193/subbchem.2021.4.12

EFFECTS OF HEATING TEMPERATURE AND *β*-CAROTENE ON QUALITY AND FATTY ACIDS COMPOSITION OF VEGETABLE OILS

FLAVIA POP[a,*], CRINA PAȘCU[a]

ABSTRACT. The purpose of the study was to investigate the effects of temperature and *β*-carotene addition on the quality parameters of corn and palm oils subjected to heating. Vegetable oils and 0.005% *β*-caroten additivated oils were heated at varying temperatures (100, 130, 160, 190 and 220°C for 30 minutes) to follow quality alterations. Peroxide value, total polar compounds, refractive index value, iodine value and fatty acids composition were determined to measure the degree of oxidative rancidity. Peroxide value was significantly ($p < 0.001$) influenced by the type of oil, additivation and heating temperature. Palm oil with added antioxidant showed the smallest increase in polar compounds during the heat treatment. Corn oil fatty acids profile was rich in oleic (C18:1), arachidonic (C20:4), eicosenoic (C20:1), and linoleic (C18:2) fatty acids, followed by alphalinolenic (C18:3) and palmitoleic (C16:1) acids. Polyunsaturated fatty acids and monounsaturated fatty acids content decreased during heat treatment. Statistical analysis of the data revealed that the development of rancidity in vegetable oils subjected to heating was significantly ($p < 0.01$) reduced by the addition of *β*-carotene in concentration of 0.005%.

Keywords: *corn oil, palm oil, heating, fatty acids profile, peroxide index, total polar compounds*

INTRODUCTION

Vegetable oils are essential ingredients in every single kitchen. Frying is delivering products with desirable sensory properties such as a crispy texture, golden crust, and unique fried food flavours in a short period of time [1].

[a] *Technical University of Cluj-Napoca, North University Center of Baia Mare, Chemistry and Biology Department, 76A Victoriei Str., 430122, Baia Mare, Romania*
[*] *Corresponding author: flavia_maries@yahoo.com*

Vegetable oils are an important source of liposoluble vitamins and essential fatty acids, which are necessary in the formation of cell membranes and in maintaining their operation. Fatty acids participate in the regulation of cholesterol metabolism and are the precursors of the hormones involved in wound healing, reducing of inflammation and blood clotting. Vegetable food oils are used for many purposes. In the countries with warm climate are used very much for cooking. In Western countries they are used in processed form, the most common product being margarine. Much of the vegetable oils are used to prepare meals, salads and ice cream [2].

Corn oil is extracted from the germ of corn, its main use is in cooking, where its high smoke point makes refined corn oil a valuable frying oil. It is also a key ingredient in some margarines and is generally less expensive than most other types of vegetable oils. It contains compounds that may promote heart health, such as phytosterols, vitamin E and linoleic acid [3].

The highly saturated nature of palm oil renders it solid at room temperature, making it a cheap substitute for butter or hydrogenated vegetable oils in uses where solid fat is desirable, such as the making of pastry dough and baked goods. The health concerns related to trans fats in hydrogenated vegetable oils may have contributed to the increasing use of palm oil in the food industry [4].

Thermal oxidation of oils occurs as a self-oxidation reaction, through the formation of free radicals. In the first stage, the reaction is initiated by the loss of a proton and the formation of an alkyl radical (R·). In the propagation step, the radical binds oxygen and form a peroxy radical (R-O-O·). Termination of the reaction involves the recombination of radicals with the formation of stable compounds such as: hydroperoxides, epoxies, epidioxides, hydroperoxy-epidioxides, etc. The autooxidation process of oils is accelerated by the following factors: temperature, heavy metals, the presence of oxygen, the fatty acids degree of unsaturation, the absence of self-oxidation inhibitors like natural or added antioxidants [5-7].

The presence of antioxidants in frying fats can extend both the fry-life of the fats and the shelf-life of the fried products. A number of studies focused on the positive effects of the addition of plant extracts to frying fats and oils: oregano, rosemary, sage, tea, lavender and thyme [8, 9, 10, 11, 12]. Also, it has been reported that tocopherols show a rapid loss at frying temperatures due to their degradation, but α-tocopherol is less stable at high temperature than δ-tocopherol, while β- and γ-tocopherols degrade at an intermediate rate [13]. Zeb and Murkovic have studied the thermal stability of corn oil fortified with β-carotene and reported the degradation of β-carotene during accelerated thermal oxidation [14, 15].

Several studies report quality degradation of vegetable oils during heating, fatty acids degradation, reduction in bioactive compounds and properties, pigments destruction, sensorial changes, and color modifications, as well as physical and rheological changes [16-20].

The purpose of this research was to investigate the effect of temperature (100, 130, 160, 190 and 220°C for 30 minutes) and β-carotene addition on corn and palm oils by analysing peroxide value, total polar compounds, refractive index value, iodine value and fatty acids content.

RESULTS AND DISCUSSION

Peroxide value, total polar compounds, refractive index value, iodine value and fatty acids profile were determined in order to asses the effect of heating temperature and β-carotene addition on corn and palm oils quality.

Peroxide value is a measure of primary lipid oxidation, indicating the amount of peroxides formed during oil oxidation. The products of lipid oxidation such as peroxides, free radicals, malonaldehyde and other cholesterol oxidation products are reported to promote coronary heart disease and atherosclerosis [5].

Unheated oils showed lower values of the peroxide index. Peroxide value was significantly ($p < 0.001$) influenced by treatments: additivation and heating temperature. In corn oil was found the highest level of peroxide value (Table 1) followed by the palm oil. Regardless of the heating temperature, the highest peroxide index level was found in non-additivated oil. In the case of corn oil, the most intensive peroxide formation was found at 190°C, while over this temperature the decomposition was dominant. The reason of this trend may be that peroxides are not heat-resistant, and high temperature lowers their concentration. Antioxidant application had a statistically significant ($p < 0.01$) effect on the peroxide index of corn and palm oil samples. The results showed that palm oil was more stable to heating, producing smaller amounts of peroxides (Table 2). The addition of β-carotene in a proportion of 0.005% significantly retarded the development of oxidation products, but antioxidant activity decreased with temperature due to an increased rate of initiation reactions.

Zeb and Murkovic, studied the thermal stability of corn oil fortified with 50-300 μg/g β-carotene using a Rancimat apparatus at 110 °C for 14 h. The research showed that most of the β-carotene was degraded during the first 5 h of the thermal oxidation and the addition of β-carotene produces significant effects ($p < 0.05$) on the peroxide index, free fatty acid values and radical scavenging activity of the corn oil [14].

Table 1. Changes in quality parameters of corn oil and *β*-carotene additivated oil during heating

Heating temperature	Corn oil				0.005% *β*-Carotene additivated oil			
	PV	TPC	RIV	IV	PV	TPC	RIV	IV
Unheated	2.07[a]	2.5[a]	1.4847[a]	99.5[a]	2.05[a]	2.5[a]	1.4848[a]	99.5[a]
100°C	2.93[b]	6.7[c]	1.4839[a]	98.4[a]	2.61[b]	6.0[c]	1.4841[a]	99.1[a]
130°C	4.74[c]	10.6[e]	1.4828[b]	97.1[b]	4.03[bc]	8.2[d]	1.4835[a]	98.4[ab]
160°C	6.82[d]	16.8[f]	1.4791[bc]	94.2[bc]	6.12[c]	14.5[e]	1.4806[b]	96.7[b]
190°C	9.14[e]	20.4[g]	1.4759[c]	91.3[c]	8.55[d]	18.7[f]	1.4784[bc]	93.8[bc]
220°C	8.45[de]	25.3[h]	1.4721[cd]	90.1[d]	9.36[e]	21.4[g]	1.4752[c]	92.1[c]
p	<0.001	<0.001	<0.05	<0.01	<0.01	<0.01	<0.05	<0.01

[a)] PV, peroxide value (meq O_2/kg); TPC, total polar compounds (%); RIV, refractive index value (refractometric degrees); IV, iodine value (g I_2/100 g).
[b)] Values are expressed as mean.
[c)] Different letters in the same column indicate statistically significant differences (Tukey's test $p < 0.05$).
[d)] Significant differences are denoted by asterisks: *$p < 0.05$; **$p < 0.01$; ***$p < 0.001$; $p \geq 0.05$, non-significant.

The degradation of *β*-carotene in corn oil during accelerated thermal oxidation was also observed [15]. The study showed that *β*-carotene promoted oxidation of triacylglycerols especially at longer exposure times and the researchers identified new classes of oxidized triacylglycerols in corn oil, which were epidioxy bis-hydroperoxides and hydroxy bis-hydroperoxides.

Several authors have reported an increase in peroxide index of oils during heating or frying [21, 22]. Filip et al., investigated the influence of two natural antioxidants on *trans* fatty acids formation during heat treatment of sunflower oil at 180°C for 120 hours.The study showed that the addition of rosemary extract and lutein significantly reduced the formation of *trans* fatty acids, with lutein suppressing the formation of *trans* fatty acids to a greater extent than the rosemary extract. The researchers also observed that the natural antioxidants tested proved to be useful additives to frying oils; they did not only prevent oxidation, but they also prevented *trans* isomerisation in the early stages of heat treatment, and reduced the formation of polar compounds [23].

Polar compounds include all oxidized triglycerides, dimerized triglycerides, free fatty acids, monoglycerides, diglycerides, sterols, antifoamers, hydrogenation catalyst residues and soaps formed during repeated heating of oils [24].

Total polar compounds indicate the state of oil deterioration and in all samples it was noticed that oils with added *β*-carotene were more stable.

According to some researchers the degradation of oils can be measured by polar compounds, which indicate the breakdown of triglycerides. During frying process the polar compounds accumulate on the surface of frying pan and foods. It can be imagined that the most poisonous components exist in the polar compounds of oil [25].

If the total polar compounds exceed more than 24%, the oil should be disposed according to Banu et al. [24]. It is observed from Table 1, that the total polar compound values exceeded 24% when corn oil was heated at 220°C. Polar compounds are found to be 21.4% for additivated corn oil and 19.6% for additivated palm oil subjected to heating at 220°C. The results indicate that β-carotene was an effective antioxidant in delaying oxidation for these edible oils.

The initial values of total polar compounds were not significantly different between the oil samples, indicating that the added antioxidant had no effects on the initial contents of polar compounds in the oil. With the heat treatment, there were noticed increases in the polar compounds in all of the samples, with and without β-carotene and the highest final content of polar compounds was noticed in the corn oil sample. β-Carotene had significant effects ($p < 0.01$) on the total polar compounds and palm oil with added antioxidant showed the smallest increase in polar compounds during the heat treatment (Table 2). In both oils, the polar compounds were significantly reduced ($p < 0.01$) by the addition of β-carotene. Significantly less polar compounds were formed in samples with added antioxidant at all stages of the heat treatment.

Table 2. Changes in quality parameters of palm oil and β-carotene additivated oil during heatin

Heating temperature	Palm oil				0.005% β-Carotene additivated oil			
	PV	TPC	RIV	IV	PV	TPC	RIV	IV
Unheated	1.56[a]	2.1[a]	1.4657[a]	79.1[a]	1.54[a]	2.0[a]	1.4658[a]	79.2[a]
100°C	2.28[b]	5.6[c]	1.4648[a]	78.5[a]	2.10[b]	4.7[c]	1.4653[a]	78.8[a]
130°C	3.93[c]	9.8[d]	1.4641[b]	77.7[b]	3.16[bc]	7.9[cd]	1.4644[a]	78.1[ab]
160°C	5.71[cd]	14.3[e]	1.4609[c]	75.1[c]	4.96[c]	12.8[d]	1.4619[b]	76.2[b]
190°C	7.69[d]	18.4[f]	1.4587[cd]	72.5[cd]	6.85[cd]	16.5[e]	1.4594[bc]	73.7[bc]
220°C	9.62[e]	22.7[g]	1.4569[d]	70.8[d]	8.97[d]	19.6[f]	1.4577[c]	71.9[c]
p	<0.001	<0.001	<0.05	<0.01	<0.01	<0.01	<0.05	<0.01

[a] PV, peroxide value (meq O_2/kg); TPC, total polar compounds (%); RIV, refractive index value (refractometric degrees); IV, iodine value (g I_2/100 g).

[b] Values are expressed as mean.

[c] Different letters in the same column indicate statistically significant differences (Tukey's test $p < 0.05$).

[d] Significant differences are denoted by asterisks: *$p < 0.05$; **$p < 0.01$; ***$p < 0.001$; $p \geq 0.05$, non-significant.

Refractive index value and iodine value are measures of the degree of unsaturation of fatty acids. Corn oil presented a higher value of refractive index compared to palm oil and the values decreased significant ($p < 0.05$) with the increase in heating temperature, in samples with and without β-carotene.

Iodine index values also decreased significant ($p < 0.01$) with the increase in heating temperature, as a result of the reduction in the degree of unsaturation, by the split of unsaturated fatty acids double bonds. Between the iodine index and the refractive index values, there was found a direct correlation (r = 0.97).

Fatty acids represent the main constitutes of the saponifiable fraction of vegetable oils, the fatty acids profile for unheated and oils subjected to heating at 220°C is presented.

Corn oil fatty acids profile was dominant in oleic acid (C18:1), with levels exceeding 29%, followed by arachidonic acid (C20:4) with near 17%, eicosenoic acid (C20:1) with 10%, palmitic acid (C16:0) with 9.1%, linoleic acid (C18:2) with 8.7% and alphalinolenic acid (C18:3) containing approximately 7.6% (Fig. 1). The palmitoleic (C16:1) and vaccenic acid ($C18:1_i$) amounts were also important (6.5 respectively 5.8%).

Palm oil fatty acids profile was rich in palmitic (C16:0), stearic (C18:0), oleic (C18:1), vaccenic ($C18:1_i$) and palmitoleic (C16:1) fatty acids, followed by myristic (C14:0) and linolenic (C18:2) acids (Fig. 3). Corn oil was predominantly polyunsaturated, while palm oil was mainly monounsaturated.

Heating at a temperature of 220°C, inflicted changes in fatty acids profile of both oils. Analyzing the fatty acids by their common nature, the most affected fraction was the polyunsaturated fatty acids (PUFA), directly related with their higher number of double bonds, with higher susceptibility to oxidation (Fig. 2, Fig. 4). With high heating temperature, PUFA content decreased with 14% in corn oil, and around 9% in palm oil. The heat treatment of oils induces modifications of unsaturated fatty acids, these may undergo isomerization from cis to trans form. The fatty acid profile of the heated fats changed as a result of cyclization, polymerization and hydrolytic, oxidative and other chemical reactions promoted by heat treatment.

Stojanovski et al. studied the influence of heat treatment on fatty acids composition in poultry meat after frying in different types and combinations of animal and vegetable fats. The researchers observed that during the thermal processing of the poultry in lard, the content of C18:1 increased from 45.84% to 49.05%, while C18:0 decreased from 10.18% to 7.45%, C16:0 also decreased from 29.55% to 27.45%. The changes that occur in fatty acid composition of fats after thermal processing of the meat were minimal and did not show statistical significance [26].

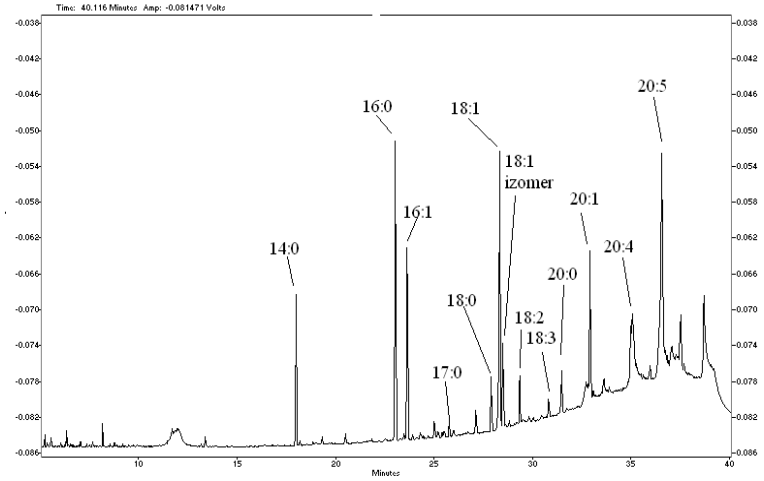

Figure 1. Gas chromatogram of unheated corn oil

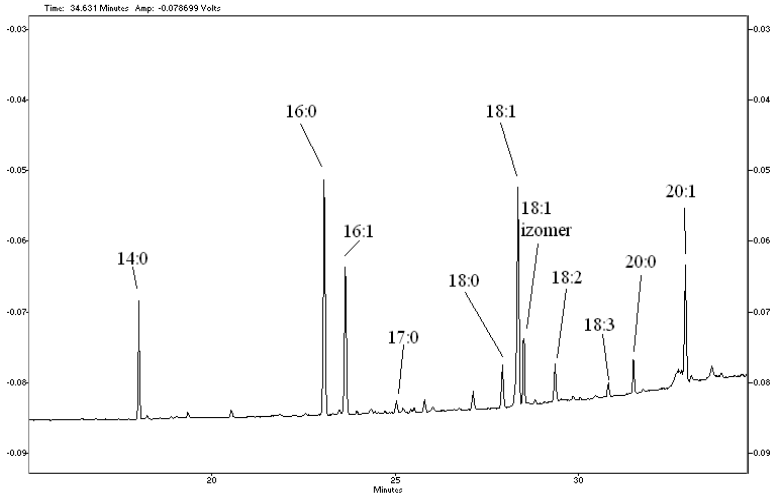

Figure 2. Gas chromatogram of corn oil subjected to heating at 220°C

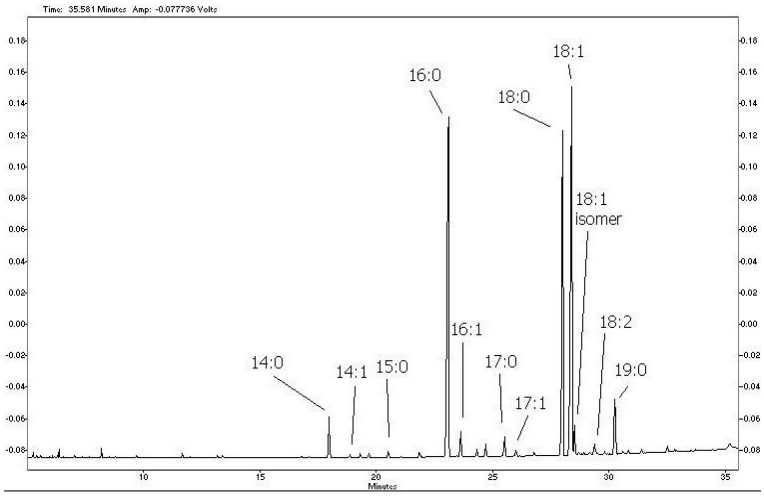

Figure 3. Gas chromatogram of unheated palm oil

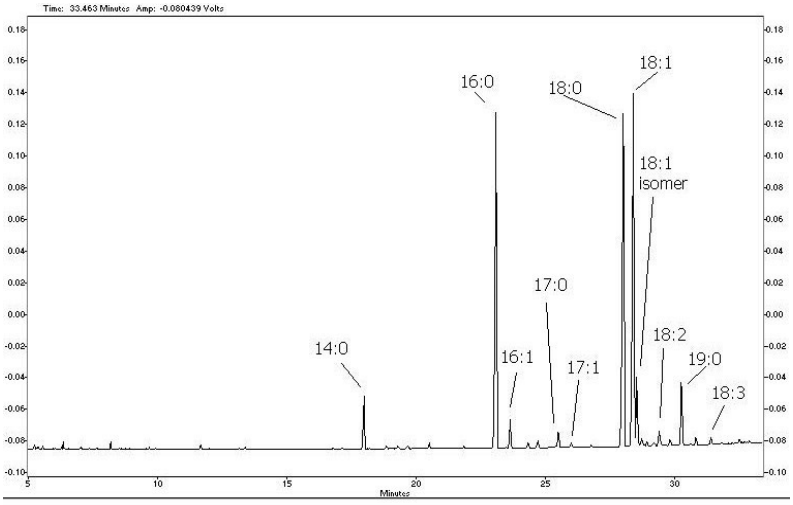

Figure 4. Gas chromatogram of palm oil subjected to heating at 220°C

CONCLUSIONS

Lipid oxidation in vegetable oils varied with the heating temperature and antioxidant addition. Unheated oils showed lower values of the peroxide index. In corn oil was found the highest level of peroxide value followed by the palm oil. Regardless of the heating temperature, the highest peroxide index level was found in non-additivated oil. Corn oil was more unstable at heat treatment, producing higher amounts of hydroperoxides.

β-Carotene had significant effects on the total polar compounds and palm oil with added antioxidant showed the smallest increase in polar compounds during the heat treatment. In both oils, the polar compounds were significantly reduced by the addition of β-carotene.

Heating inflicted changes in fatty acids profile of both oils, the most affected fraction was the polyunsaturated fatty acids, directly related with their higher number of double bonds, with higher susceptibility to oxidation.

Statistical analysis of the data revealed that the development of rancidity in vegetable oils subjected to heating at varying temperatures was significantly reduced by the addition of β-carotene in concentration of 0.005%.

EXPERIMENTAL SECTION

Samples

To assess the behavior of corn and palm oils under heating conditions, commercial samples were obtained from local markets. β-Carotene was dissolved in oils in the concentration of 0.005% (0.005 g/100 g of oil). Approximately 50 mL of oil were individually subjected to heating in an electric oven (FM11, Ariston, Fabriano, Italy) at 100, 130, 160, 190 and 220°C for 30 minutes. We used glass vessels with 80 cm^2 of exposure area with air. The cold samples were transferred to glass tubes and kept in refrigeration until analysis. For each studied oil, one sample was used as control sample (unheated). Three replications were carried out to examine each sample. All chemicals were of analytical grade and obtained from Merck (Germany); β-carotene was purchased from Sigma (Sigma Chemicals, Shanghai, China).

Physicochemical examination

Peroxide value was determined using UV-VIS spectrophotometer (Bibby Scientific, London, UK). A test portion was dissolved in a mixture of

chloroform/methanol (2:1, v/v), then iron(II) chloride and ammonium thiocyanate were added. This protocol was based on the spectrophotometer determination of ferric ions (Fe^{3+}) derived from the oxidation of ferrous ions (Fe^{2+}) by hydro peroxides, in the presence of ammonium thiocyanate (NH_4SCN). Thiocyanate ions (SCN^-) react with Fe^{3+} ions to give a red-violet homogeny that can be determined spectrophotometrically; the absorbance of each solution was read at 500 nm. To quantify PV, a calibration curve (absorbance at 500 nm vs. Fe^{3+} expressed in µg) was constructed. Peroxide value was expressed as meq O_2/kg sample [27].

The measurement of the polar compounds was carried out using a rapid method: Testo 265, based on dielectric constant measurements. This method shows high correlations between dielectric readings using the food oil sensor compared with the percent polar compounds obtained by liquid chromatography [28].

To determine the refractive index we used the PAL-RI (Tokyo, Japan) with the following technical characteristics: field: 1,3306-1,5284; resolution: 0.0001; accuracy: ± 0.0003; measuring temperature: 5-45^{o}C (resolution 1^{o}C); measuring time: 3s; in accordance with the requirements of EMC Directive 93/68/EEC.

Iodine value was determined using Hanus method. Approximately 0.5 g sample (dissolved in 15 mL CCl_4) was mixed with 25 mL Hanus solution (IBr) to halogenate the double bonds. After storing the mixture in the dark for 30 minutes, excess IBr was reduced to free I_2 in the presence of 20 mL of KI (100 g/L) and 100 mL distilled water. Free I_2 was measured by titration with 24.9 g/L $Na_2S_2O_3 \cdot 5H_2O$ using starch (1.0 g/100 mL) as an indicator. Iodine value was calculated as g I_2/100 g sample [27].

Fatty acids composition was determined using a Shimadzu GC-17 A gas chromatograph (Tokyo, Japan) coupled with a flame ionization detector.

To obtain methyl esters, 2 mL sample was introduced in a round-bottomed flask to which was added 20 mL of sulphuric acid methanol solution and 3 pieces of porous porcelain; a reflux cooler was fitted to the flask and it was boiled for about 60 minutes in a water bath. The content of the flask was cooled to room temperature and then was passed quantitatively in a separatory funnel using 20 mL of water, and the methyl esters were extracted in two stages with 20 mL of heptanes. The extracts were combined into another separatory funnel and washed with 20 mL of water until the sulphuric acid was completely removed, the removal being controlled with methyl orange. The extracts were then dehydrated by the addition of anhydrous sodium sulphate and filtered into a flask. Methyl esters were collected in 1 mL hexane, and 1µL sample was injected in the gas chromatograph.

The gas chromatography column is Alltech AT-Wax, (60 m x 0.32 mm x 0.5 μm), stationary phase (polyethylene); helium was used as a carrier gas at a pressure of 147 kPa, temperature of the injector and detector was set to 260°C, and the oven program was the following: 70°C for 2 minutes, then the temperature was raised to 150°C with a gradient of 10°C/minute, a level of 3 minutes, and the temperature was raised to 235°C with a gradient of 4°C/minute. Identification and quantification of FA were performed by comparison with standards. Results were expressed as % [28].

Statistical analysis

All analytical determinations were performed at least in triplicate. Values of different parameters were expressed as the mean ± standard deviation (X ± SD). Tukey's honest significance test was carried out at a 95% confidence level ($p < 0.05$). The Pearson's correlation (α=0.05) with two-tailed probability values was used to estimate the strength of association between chemical parameters.

ACKNOWLEDGMENTS

This work was financial supported by Technical University of Cluj-Napoca in the framework of the GNaCARUT competition, research Contract no. 3015/2019.

REFERENCES

1. V. K. Tyagi; A. K. Vasishtha; *J. Am. Oil Chem. Soc.*, **1996**, *73*, 499-507.
2. C. A. Costa; A. S. Carlos; G. P. Gonzalez; R. P. Reis; *Eur. J. Nutr.,* **2012**, *51*, 191-198.
3. S. Wang; K. A. Meckling; M. F. Marcone; Y. Kakuda; R. Tsao; *J. Agric. Food Chem.,* **2011**, *59*, 960-967.
4. E. Valantina; S. Sahayararaj; A. Prema; *Rasayan J. Chem.*, **2010**, *3*, 44-53.
5. Z. P. Pai; T. B. Khlebnikova; Y. V. Mattsat; V.N. Parmon; *React. Kinet. Catal. Lett.*, **2009**, *98*, 1-8.
6. O. Roman; B. Heyd; B. Broyart; R. Castillo; M. N. Maillard; *LWT - Food Sci. Technol.,* **2013**, *52*, 49-58.
7. A. H. Noor Armylisas; M. F. Siti Hazirah; S. K. Yeong; A. H. Hazimah; *Grasas Aceites*, **2017**, *68*, 130-136.
8. R. De Guzman; S. Haiying Tang; K. Y. S. Salley; *J. Am. Oil Chem. Soc.*, **2009**, *86*, 459-467.
9. M. Wroniak; K. Krygier; M. Kaczmarczyk; *Pol. J. Food Nutr. Sci.,* **2008**, *58*, 85-93.

10. A. Biswas; A. Adhvaryu; D. G. Stevenson; B. K. Sharma; *Ind. Crops Prod.,* **2007**, *25*, 1-9.
11. A. Bendini; E. Valli; L. Cerretani; E. Chiavaro; G. Lercker; *J. Agric. Food Chem.*, **2009**, *57*, 1055-1063.
12. A. M. El Anany; *Electron. J. Food Plants Chem.*, **2007**, *2*, 14-21.
13. S. Ernest; P. Kavitha; *Int. J. Chem. Environ. Pharm. Res.*, **2011**, *2*, 111-118.
14. A. Zeb; M. Murkovic; *J. Am. Oil Chem. Soc.*, **2013**, *90*, 881-889.
15. A. Zeb; M. Murkovic; *Food Res. Int.*, **2013**, *50*, 534-544.
16. N. Rodrigues; R. Malheiro; S. Casal; M. C. Manzanera; *Food Chem. Toxicol.,* **2012**, *50*, 2894-2902.
17. E. S. Shaker; *LWT - Food Sci. Technol.*, **2006**, *39*, 883-892.
18. K. Warner; *J. Agric. Food Chem.*, **2005**, *23*, 9906-9913.
19. H. Yoshida; S. Takagi; *J. Sci. Food Agric.,* **1999**, *62*, 41-50.
20. F. A. Aladedunye; *Eur J. Lipid Sci. Technol.,* **2014**, *116*, 688-695.
21. F. Caponio; A. Pasqualone; T. Gomes; *Int. J. Food Sci. Technol.,* **2003**, *38*, 481-488.
22. F. Kreps; L. Vrbiková; S. Schmidt; S. Sekretár; O. Híreš; *Eur. J. Lipid Sci. Technol.,* **2014**, *116*, 1685-1694.
23. S. Filip; J. Hribar; R. Vidrih; *Eur. J. Lipid Sci. Technol.,* **2011**, *113*, 224-233.
24. M. Banu; N. Prasad; N. Siddaramaiah; *Int. Food Res. J.*, **2016**, *23*, 528-537.
25. W. W. Nawar, *Lipids*. In: Fennema COR (ed.) Food chemistry, 3rd edn. Marcel Dekker, New York, **1996**, pp. 225-234.
26. M. Stojanovski; A. Čakarova; A. Kuzelov; E. Joshevska; G. Dimitrovska; D. Tomovska; K. Bojkovska; *J. Agric. Plant Sci.*, **2018**, *16*, 103-112.
27. F. Pop; *Studia UBB Chemia*, **2009**, *LIV(4),* 187-193.
28. F. Pop; *Studia UBB Chemia*, **2018**, *LXIII(2)*, 43-52.

STUDIA UBB CHEMIA, LXVI, 4, 2021 (p. 171-187)
(RECOMMENDED CITATION)
DOI:10.24193/subbchem.2021.4.13

UTILIZATION OF BANANA PEEL AS A BIOSORBENT FOR THE REMOVAL OF BASIC RED 29 FROM AQUEOUS SOLUTION

JEN-KAI CHONG[a], SIEW-TENG ONG[a,b,*]

ABSTRACT. The banana peel powder (BPP) was used as a low-cost adsorbent for the adsorption of Basic Red 29 (BR29) dye from aqueous solution. The FTIR, AFM and SEM analysis were conducted for the characterization of BPP. The effects of initial dye concentrations, contact time, pH, adsorbent dosage and agitation rate on the adsorption of BR29 were studied. The uptake was very rapid during the first 30 minutes and slowed down as the contact time increased. The adsorption decreased as the initial dye concentration increased while it increased as the adsorbent dosage increased. The uptake of BR29 was highest at pH 8 and the percentage uptake increased as the agitation rate increased. The adsorption kinetics of BR29 onto BPP fitted well to the pseudo-second order kinetic model. Three different isotherm models, which include Langmuir, Freundlich and Brunauer-Emmett-Teller (BET) were used to analyze the equilibrium adsorption data of BR29. The adsorption isotherm of BR29 onto BPP was better described by the Freundlich isotherm model with the coefficient of determination (R^2) of 0.9956.

Keywords: *Basic Red 29, Dye, Adsorption, Banana peel, Kinetic study*

INTRODUCTION

Dyes are colored substances that can be applied to impart color to other materials such as textiles, paper, plastics, foods and leather. Presently, there are more that hundred thousand varieties of dyes and these can be obtained commercially [1]. The textiles and textile products industries are consider as important and growing sectors in Malaysia. According to the

[a] *Department of Chemical Science, Faculty of Science, Universiti Tunku Abdul Rahman, Jalan Universiti, Bandar Barat, 31900 Kampar, Perak, Malaysia*
[b] *Centre for Agriculture and Food Research, Universiti Tunku Abdul Rahman, Jalan Universiti, Bandar Barat, 31900 Kampar, Perak, Malaysia*
[*] *Corresponding authors: ongst@utar.edu.my; ongst_utar@yahoo.com*

statistics, the industry was the eleventh largest export earner in 2017. The industry had export valued of approximately RM15.3 billion which comprised 1.6% of the total manufacturing exports of Malaysia [2]. However, the wet processing operation in textile industry which involves dyeing process produces a lot of dye wastewater. It has been estimated that about 280000 tons of textile dyes effluent is being generated annually around the world [3].

Apart from that, batik, which is the famous textile art in Malaysia has also continuously increased and there are more than a thousand batik factories located on the east coast of Malaysia. As most of the batik industries are comparatively small scale and family-based, they do not have proper wastewater treatment system and therefore, the discharge of the colorants used can cause a serious environmental issue. Moreover, the scattered location of the batik industries has increased the difficulties to create a centralized and comprehensive wastewater treatment system [4].

The release of dye wastewater to the surroundings without prior treatment will inflicts great damage to the ecosystem as dyes are potentially hazardous to aquatic animals and plants [5,6]. The bioaccumulation of the dyes in aquatic animal will be passed along the food chain and eventually affects all the organisms. Some of the dyes may cause allergic reaction and/or irritation when in contact with skin, inhaled and ingested. As cationic dyes such as Basic Red 29 (BR29), is much more toxic than all-purpose dyes or fiber reactive dyes, therefore this type of dye must be treated with correspondingly greater respect and caution.

A low-cost yet effective method for wastewater treatment is very crucial for both large scale and small scale textile industries. Adsorption approach is extensively applied for the colorant removal from wastewater. This is because the adsorbent can be prepared using low cost materials such as agricultural waste. Although the conventional adsorption method employed activated carbon (AC) as the adsorbent has exhibited a high efficiency performance, AC remains as a relatively expensive adsorbent. Therefore, nonconventional adsorbents have gained a lot of attention for the reduction of hazardous waste from wastewater.

Nonconventional adsorbents can be categorized into five separate groups including fruit waste, plant remains, living and nonliving biomass, agricultural and industrial waste materials, and natural inorganic materials. These items are used as economical bioadsorbent as they tend to be obtained easily and have good adsorption capacity [7].

Banana is considered as a main fruit crops in Malaysia. According to Department of Agriculture Malaysia (2017), the production of banana was around 350000 metric tons in 2017 which was accounted for 26.4% of the total major fruits production. The high production of banana will create a large amount of banana peel waste. Although banana peel is commonly used as

animal feed or fertilizer, efforts have been made to utilize banana peel in other applications, for instance, as an inexpensive bioadsorbent for the withdrawal of dyes and other contaminants [8]. Banana peel consists of large amount of cellulose, hemicelluloses, pectin and lignin that contain hydroxyl, carboxylic and various functional groups [9] that are essential important in the adsorption process The species of banana used in this study was Pisang Nangka or jackfruit banana with the scientific name *Musa x paradisiaca*. They are categorized as plantains which are members of the banana family with high starch content.

RESULTS AND DISCUSSION

Characterization of adsorbent

FTIR Analysis. FTIR spectroscopy was used to analyze the functional groups present on the surface of BPP. The FTIR spectra of BPP before and after the adsorption of BR29 were obtained in the range of 4000 to 400 cm^{-1} as depicted in Figure 1. There are various functional groups that can be found on the surface of BPP as multiple peaks were shown in the spectra. BPP with various functional groups shows that it has a complex nature and it can act as a good adsorbent [10].

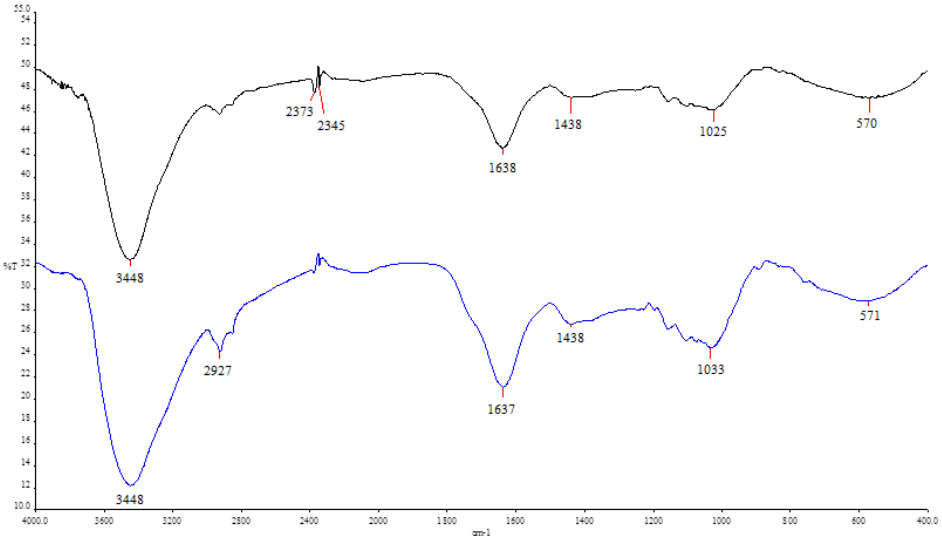

Figure 1. FTIR spectra of BPP before adsorption (black) and after adsorption (blue) of BR29

The broad and strong adsorption band at 3448 cm^{-1} was due to the vibration of O-H group. This indicates that the hydroxyl group was present on the surface of BPP as the banana peel consists of large amount of cellulose, hemicelluloses, pectin and lignin that contain hydroxyl and carboxylic groups [9]. The peak at 2927 cm^{-1} represents the stretching vibration of C-H group in alkanes. The strong adsorption at 1638 cm^{-1} represents the stretching of carbon-carbon double bond of aromatic ring that is present in lignin. The peak at 1025 cm^{-1} indicates the C-O stretching vibration and similar findings were reported by Mondal and Kar [11].

The spectrum of BPP after the adsorption of BR29 demonstrated a very close similarity with the one before the adsorption. The peak at 1638 cm^{-1} was changed to 1637 cm^{-1} whereas the peak at 1025 cm^{-1} was shifted to 1033 cm^{-1}. The slight changes observed are most probably because the adhesion of dye molecules onto the BPP is involving adsorption. As this kind of interaction is a surface chemistry process, therefore the spectrum before and after adsorption bear a lots of similarities [12].

Atomic Force Microscope (AFM) Analysis. AFM analysis was performed to inspect the surface topography of the BPP before and after adsorption of the dye. Figures 2(a) and 2(b) represent the AFM micrographs of BPP before and after adsorption, respectively. In Figure 2(a), the surface of BPP without addition of BR29 was observed to be rough and uneven. On the contrary, the micrograph in Figure 2(b) showed that the surface of BPP was relatively more even and smoother after adsorption of BR29. This suggests that the surface of BPP was covered by the dye molecules.

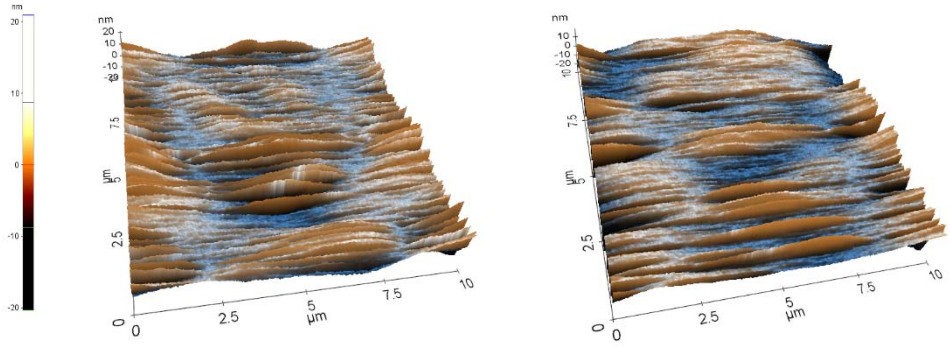

(a) (b)

Figure 2. AFM image of BPP (a) before adsorption (b) after adsorption

Scanning Electron Microscope (SEM) Analysis. The surface morphology of the BPP before and after adsorption was observed using SEM. This analysis can help to determine the size, the shape and the texture of the sample. The SEM micrographs of BPP before and after adsorption of BR29 with the magnification of 50000× were presented in Figures 3(a) and 3(b), respectively. By comparison, the micrograph of BPP before adsorption showed a porous, rough and uneven surface. Conversely, the surface of the BPP becomes smoother and relatively less porous after the adsorption process. This observation agrees well with the previous suggestion whereby after the dye adsorption, the surface will become more even due to the adhesion of dye molecules. Similar result was reported by Pishgar et al. [13] in which the surface morphology of banana peel became smoother after the adsorption of dye as compared to the one before adsorption.

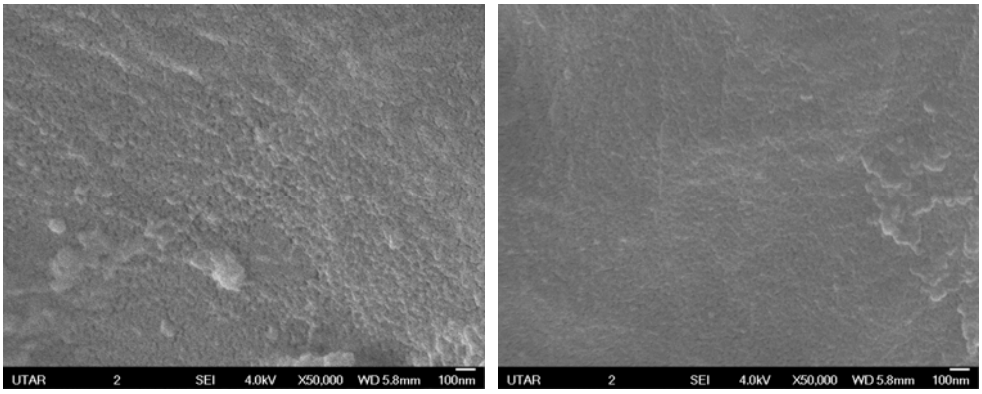

(a) (b)

Figure 3. SEM micrograph of BPP (a) before adsorption (b) after adsorption

Adsorption Studies

Effect of initial dye concentration and contact time. The trend of the dye uptake for the effect of initial dye concentrations and contact time was illustrated in Figure 4. Generally, the uptake trends of BR29 at different concentrations followed the same pattern in which the percentage uptake increased as the contact time lengthens. The percentage uptake of BR29 was rapid during the first 30 minutes and then followed by a more gradual process until 120 minutes. Thereafter, the rate of adsorption slowed down as it achieves equilibrium. Similar uptake profile was also reported in some of the previous works in the removal of dyes [14,15].

As large amount of surface sites were available for the adsorption of BR29 at the beginning, therefore, the uptake rate was very rapid. As the time progress, the number of remaining surface sites decreased and the adsorption

rate decreased [16]. The rapid initial rate of adsorption was related to the dye molecules produced a monolayer on the exterior of the BPP. Then, the leisurely internal mass transport stage caused the lower speed of adsorption [17].

When the BR29 concentration was increased from 100 to 500 mg/L, the maximum uptake decreased from 99.55% to 97.84%. The uptake decreased at higher concentration because the ratio of surface sites available to the amount of BR29 in the solution decreased. As a result, some of the dye molecules were not able to interact with the BPP and the uptake decreased. This also indicated that the dynamic equilibrium of the adsorption was affected by the initial concentration [18]. Similar observation was reported in the adsorption of Maxilon Blue GRL using white marble [19].

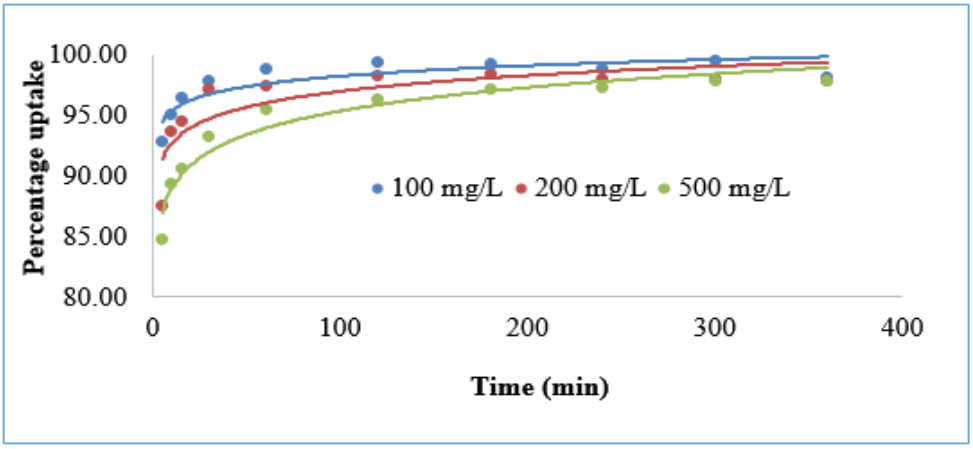

Figure 4. Effect of initial dye concentrations and contact time on percentage uptake of BR29

Effect of pH. The pH of the dye solution has a large impact on the adsorption process as the surface characteristic of the adsorbent will be changed according to the pH of the solution. The characteristic of dye molecules will also be altered by the solution's pH through ionization or dissociation process [10]. The influence of pH of solution was studied in the pH range from 2 to 10. The results showed that the uptake of BR29 increased with increasing pH until the maximum uptake was achieved at pH 8 and then decreased. The maximum uptake was 96.21% which occurred at pH 8 whereas the uptake was only 87.69% at pH 2 which was the lowest uptake compared to other pH values. In acidic condition, the surface active sites of BPP will be protonated as they accept H^+ ions from the aqueous dye solution. Thus, the surface will be positively charged. Conversely, the BPP will be negatively charged as the functional groups like hydroxyl and carboxylic groups are deprotonated under alkaline condition.

The pH_{pzc} of BPP was determined to be 5.45. Theoretically, the adsorption BR29 as a cationic species onto the BPP will be favored if the pH of the dye solution was higher than the pH_{pzc} of the BPP as the surface carried a net negative charge. Under the alkaline condition and at the pH greater than pH_{pzc} value, the negatively charged BPP will be having electrostatic attraction with the cationic dye molecules and this explained the favorable uptake. However, the uptake decreased from 96.21% at pH 8 to 95.31% at pH 10 and this can be related to the dissociation of the dye molecules. According to Washabaugh et. al. [20], the thiazolium ring that is present in the structure of BR29 molecule can undergoes ring opening under the alkaline condition via hydrolysis reaction.

Effect of adsorbent dosage. The results for the influence of adsorbent dosage ranging from 0.01 to 0.10 g were illustrated in Figure 5. Initially, the percentage uptake increased as the adsorbent dosage increased. The maximum uptake was achieved maximum when the adsorbent dosage was 0.06 g. The further increase in the adsorbent dosage caused a slight decrease in the uptake of the dye. When the mass of BPP used was greater, the number of surface area accessible for the BR29 increased. The highest uptake achieved was 96.94% with the adsorbent dosage of 0.06 g. The saturation occurred at 0.06 g at which further increase in adsorbent dosage had caused a slight decrease in the uptake. A lower percentage uptake when the dosage was probably caused by the aggregation of the BPP and thus reducing the sites available for the adsorption of the BR29 species when the adsorbent dosage increased [11].

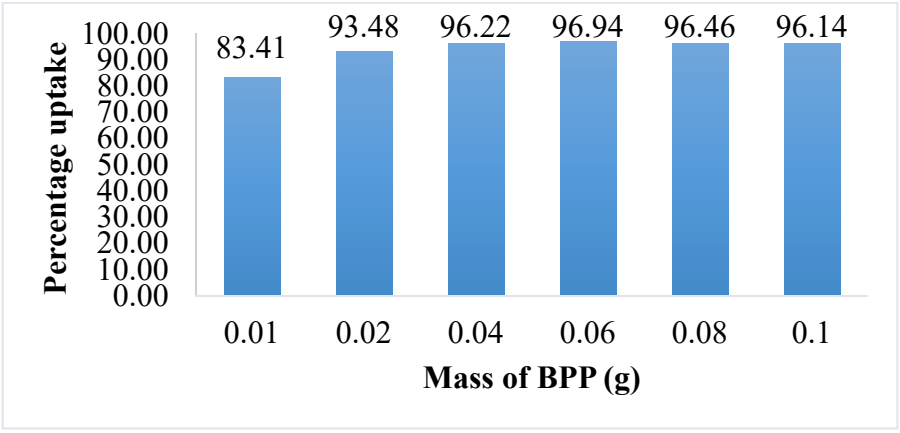

Figure 5. Effect of adsorbent dosage on percentage uptake of BR29

Effect of agitation rate. The influence of agitation rates was studied using 50 and 100 rpm agitation speed for a period of 240 minutes. The uptake of BR29 occurred very rapidly during the first 60 minutes and then slowed down in for both agitation rates. It was noted that a higher agitation rate resulted in higher percentage uptake of BR29. This is because an increase in the agitation rate will decrease the film resistance to mass transfer surrounding the adsorbent particles thus increase the adsorption of dye molecules. Similarly, Al-Tufaily and Al-Qadi [21] also reported that a higher uptake with increasing agitation speed is due to the increase in turbulence and caused the thickness of boundary layer around the BPP to decrease.

Adsorption kinetics. The kinetic studies can provide insight on the mechanism of the adsorption in a given systems. It also gives information about its possible rate determining stage like chemical interactions or mass transfer process [22]. The pseudo-first order and pseudo-second order kinetic models were applied in this analysis. For pseudo-first order kinetic model, it was developed by Lagergren [23] and thereafter, it has been commonly applied for the adsorption in liquid-solid systems. This linearized equation for this model can be expressed by the formula below:

$$\log (q_e - q_t) = \log q_e - \frac{k_1}{2.303} t \tag{1}$$

where:

q_e = amount of BR29 adsorbed at equilibrium (mg/g)
q_t = amount of BR29 adsorbed at time t (mg/g)
k_1 = rate constant of pseudo-first order kinetics (1/min)
t = time (min)

This model considers that the speed of adsorption is relative to the amount of vacant spots available [24]. The R^2 values for the initial BR29 concentrations of 100, 200 and 500 mg/L were 1.0000, 0.8683 and 0.9370, correspondingly while the k_1 values were 0.1175, 0.0569 and 0.0136 with unit of 1/min in that order. The value of k_1 represents the rate for the system to achieve equilibrium condition. It decreases when the initial concentration increases because the duration required to achieve equilibrium will increase at higher initial BR29 concentration [25].

On the other hand, the values of calculated q_e were 1.9297, 3.1747 and 8.4723 mg/g for 100, 200 and 500 mg/L of BR29 solution, respectively. The calculated q_e values were considerably different from the q_e obtained experimentally (Table 1). This proves that the adsorption of BR29 onto BPP

does not fit well to the pseudo-first order kinetic model. According to Ho and Mckay [26], the Lagergren model typically only relevant during first 20-30 min of the adsorption progression but it is generally not applicable for the whole adsorption process.

Therefore, the pseudo-second order kinetic model was also applied to study the adsorption kinetics of BR29 onto BPP. In this model, the rate determining stage of an adsorption activity was assumed to be the chemical adsorption process. The valence forces in chemisorptions process involves the electrons sharing or exchange between the BR29 and BPP [27]. The linear form equation based on this model is shown below:

$$\frac{t}{q_t} = \frac{1}{k_2 q_e^{\ 2}} + \frac{1}{q_e} t \tag{2}$$

In which

q_t = amount of BR29 adsorbed at time t (mg/g)
q_e = amount of BR29 adsorbed at equilibrium (mg/g)
k_2 = rate constant of pseudo-second order kinetics (g/mg·min)
t = time (min)

The initial adsorption rate, h can be determined using the formula:

$$h = k_2 q_e^2 \tag{3}$$

Table 1. Summary of values obtained for pseudo-first and pseudo-second order kinetics model

Initial BR29 concentration (mg/L)	Pseudo-first order				Pseudo-second order				
	$q_{e\,cal}$ (mg/g)	$q_{e\,exp}$ (mg/g)	k_1 (1/min)	R^2	$q_{e\,cal}$ (mg/g)	$q_{e\,exp}$ (mg/g)	k_2 (g/mg·min)	h (mg/g·min)	R^2
100	1.9297	19.6380	0.1175	1.0000	19.7628	19.6380	2.3276	909.0909	0.9999
200	3.1747	39.1380	0.0569	0.8683	39.2157	39.1380	0.0856	131.5789	1.0000
500	8.4723	97.8405	0.0136	0.9370	98.0392	97.8405	0.0074	70.9220	1.0000

The theoretical values of q_e calculated were 19.7628, 39.2157 and 98.0392 mg/g for 100, 200 and 500 mg/L of BR29, correspondingly. The values were comparable to the q_e values attained experimentally. The R^2 values for the three different initial dye concentrations achieved unity or approaching 1. These showed that the adsorption kinetics of BR29 onto BPP followed closely to the pseudo-second order kinetic model. The k_2 values were 2.3276, 0.0856 and 0.0074 g/mg·min for 100, 200 and 500 mg/L of

BR29 solution, respectively. The higher k_2 value means that the adsorption process will achieve equilibrium in shorter time. The parameters obtained for each of the kinetic model were summarized in Table 1.

In order to obtain the generalized predictive model for BR29 at any contact time and initial concentration, the corresponding linear plots of the pseudo-second order equation were regressed to obtain the constants related to the respective equations [28]. The theoretical model for the amount of BR29 adsorbed at any initial concentration, C_o and time was expressed by the formula:

$$q_t = \frac{C_o t}{0.0166C_o - 1.5918 + (0.000076C_o + 5.0863)t} \quad (4)$$

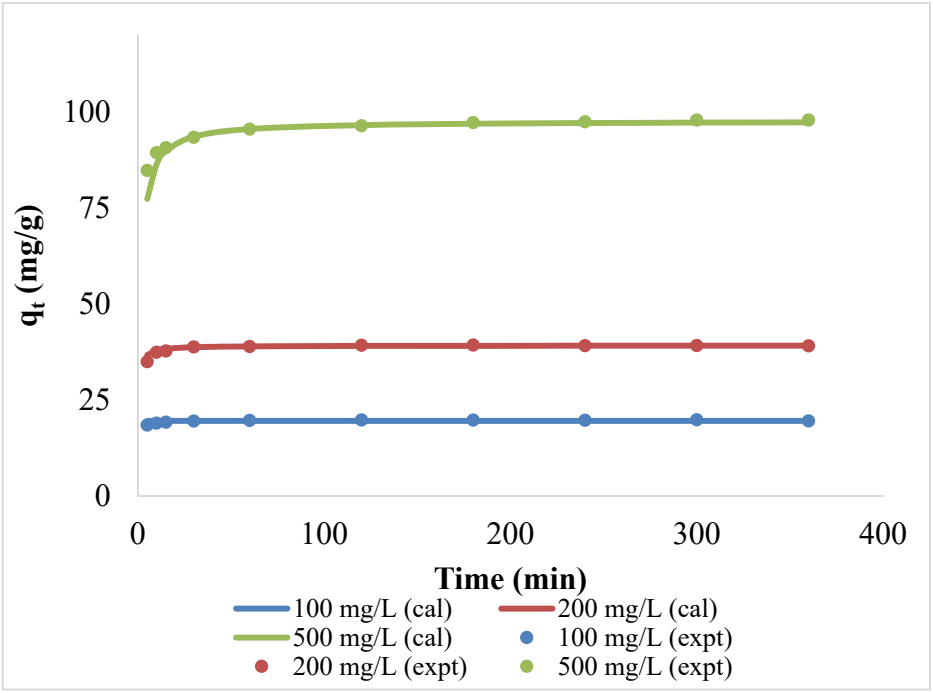

Figure 6. Comparison between the experimental values (expt) and theoretical values (cal) of q_t

Figure 6 showed the correlation between the data obtained during the analysis and theoretical data of q_t for the adsorption of BR29 by BPP. The experimental data showed an appreciable consistency with the graphs generated for the theoretical values. The graph also showed that the amount

of BR29 adsorbed was higher when the starting BR29 concentration was higher. The greater initial BR29 concentration offers a greater propulsive strength of concentration gradient to surpass the mass transfer resistances of the BR29 between the BPP and the solution [29].

Adsorption isotherm. The adsorption isotherm involves the equilibrium situation in which the speed of adsorption of BR29 onto the surface of BPP is equal to the speed of desorption of the BR29 from the BPP. Therefore, the concentration of BR29 solution will remain constant at equilibrium [30]. Three different isotherm models including Langmuir [31], Freundlich [32] and Brunauer-Emmet-Teller (BET) [33] models were applied in the study. The Langmuir model assumes monolayer adsorption over a homogenous adsorption sites with no association happens between the adsorbed species. The following linear form of the equation was proposed for this model:

$$\frac{C_e}{q_e} = \frac{C_e}{q_m} + \frac{1}{K_L q_m} \tag{5}$$

In which
C_e = concentration of BR29 at equilibrium (mg/L)
q_e = amount of BR29 adsorbed at equilibrium (mg/g)
q_m = maximum amount of BR29 adsorbed (mg/g)
K_L = Langmuir constant (L/mg)

From the graph of C_e/q_e against C_e, the values of q_m and K_L were 175.4386 mg/g and 0.1011 L/mg, respectively and these were obtained from the y-intercept and the slope of the graph. The R^2 for the linear plot was 0.9866.

The separation factor (R_L) is a dimensionless constant and act as an indispensable feature of Langmuir isotherm. R_L can be represented by the formula below:

$$R_L = \frac{1}{1 + K_L C_o} \tag{6}$$

In which
R_L = separation factor
K_L = Langmuir constant (L/mg)
C_o = initial dye concentration (mg/L)

The R_L values for all of the BR29 concentration fell in the category $0 < R_L < 1$, and therefore, the adsorption of BR29 onto BPP was favorable.

The Freundlich isotherm is an exponential equation and can be applied in the situation involving multilayer adsorption, adsorption on heterogeneous surfaces and possibility of reversible adsorption. The linear form of the equation is shown as below:

$$\log q_e = \frac{1}{n}\log C_e + \log K_F \quad (7)$$

In which
q_e = amount of BR29 adsorbed at equilibrium (mg/g)
n = Freundlich constant for adsorption intensity
C_e = concentration of BR29 at equilibrium (mg/L)
K_F = Freundlich constant for adsorption capacity (mg/g)(mg/L)^n

A high R^2 value of 0.9956 was obtained for the Freundlich model. The similar findings were reported in the uptake of Basic Blue 9 by using rise husk [34] and the uptake of Basic Violet 10 dye using outer skin of fruit [35] in which the adsorption processes were well described by this model. The number of 1/n and K_F obtained were 0.4962 and 26.0615, correspondingly. The figure of 1/n signifies the strength of the adsorption. If 1/n falls within the range of 0 to 1, it is related to the chemisorption process and the heterogeneity increases as the value approaches 0. If the value goes above 1, it shows that cooperative adsorption occurred [36].

The BET isotherm model is the extended theory for multilayer adsorption from Langmuir equation with the following assumption: (i) all surface adsorption sites are homogeneous; (ii) the heat of adsorption of second and following layers are equal to heat of liquefaction; (iii) no sideways association happens between the adsorbed species.
The formula below was proposed for this model:

$$q_e = \frac{q_m K_B C_e}{(C_s - C_e)[1 + (K_B - 1)(C_e / C_s)]} \quad (8)$$

Rearrangement of Equation (8) into linear form:

$$\frac{C_e}{(C_s - C_e)q_e} = \frac{(K_B - 1)}{K_B q_m}\left(\frac{C_e}{C_s}\right) + \frac{1}{K_B q_m} \quad (9)$$

In which
C_e = concentration of BR29 at equilibrium (mg/L)
C_s = monolayer saturation concentration of BR29 (mg/L)
q_e = amount of BR29 adsorbed at equilibrium (mg/g)

q_m = maximum amount of BR29 adsorbed (mg/g)
K_B = BET adsorption constant

The parameters and R^2 values obtained for all the isotherm models were summarized in Table 2. Based on the R^2 value, the adsorption of BR29 is better described by Freundlich model as compared to Langmuir and BET models.

Table 2. Values obtained from Langmuir, Freundlich, and BET isotherm model

Langmuir			Freundlich			BET		
q_{max} (mg/g)	K_L (L/mg)	R^2	K_f	n	R^2	K_B	q_{max} (mg/g)	R^2
175.439	0.101	0.987	26.062	0.496	0.996	175.052	28.563	0.987

CONCLUSIONS

Banana peel powder (BPP) was selected as an economical adsorbent for the adsorption of BR29 from aqueous solution. From the FTIR spectrum, a slight shifting of the peaks was observed. Both AFM and SEM micrographs showed that the surface of the BPP was relatively smoother and more even after the adsorption of BR29. Based on the results obtained from the initial dye concentrations and contact time, the percentage uptake increased significantly during the first 30 minutes and slowed down after that. The uptake improved at higher adsorbent quantity and it achieve maximum when the mass of adsorbent was 0.06 g. The adsorption of BR29 was favored under alkaline condition and the efficiency of uptake amplified as the agitation rate increased.

The adsorption kinetics of BR29 onto BPP was associated with the pseudo-second order kinetic model. The adsorption isotherm of BR29 onto BPP can be better described by the Freundlich isotherm model with a higher R^2 value. Based on Langmuir isotherm, the maximum amount of BR29 adsorbed onto BPP was 175.4386 mg/g.

EXPERIMENTAL SECTION

Preparation of adsorbent

Banana peels were obtained from a banana fritters stall in Kampar, Perak. The banana peels collected were cut into smaller sizes. Then, tap water was used to clean the banana peels followed by washing with distilled water to remove any dirt or impurities. The peels were dried using an oven at

60°C for period of one day. The dried banana peels were ground into powder form. The banana peel powder (BPP) was soaked in distilled water at 60°C with occasional stirring for decolorizing purpose. Furthermore, the BPP was filtered through filter bag and then rinsed with distilled water. The decolorizing process was repeated for another 5 times. After that, the powder was dried again for 24 hours. The BPP obtained was sieved through a sieve with the size of 1 mm. Finally, the dried BPP was stored in plastic bag with seal for further experiment.

Preparation of Basic Red 29 (BR29)

BR29 was selected as an adsorbate in the studies. BR29 or also known as Basacryl Red GL with the formula of $C_{19}H_{17}ClN_4S$ is having a molecular mass of 368.88 g/mol. The BR29 was acquired from Sigma-Aldrich Co. and employed directly without alteration. 1 gram of BR29 was weighed accurately and dissolved in 1 liter of distilled water to prepare a stock solution of 1000 mg/L. The stock solution was covered with aluminum foil and kept in the cabinet to prevent exposure to light. This is because the dye solution might degrade when exposed to light. The stock solution was diluted to different concentrations needed throughout the experiment.

Characterisation of adsorbent

Fourier Transform Infrared (FTIR) Spectroscopy

The BPP before adsorption and after adsorption were analyzed using Perkin Elmer FTIR Spectrum RX1 to identify the functional groups associated with the adsorbent. The spectra were obtained in the infrared region with the wavenumber range from 4000 to 400 cm^{-1}. The KBr pellet method was used in the analysis. The BPP was finely ground with KBr salt. The mixture was compacted under high pressure to form the KBr pellet. Finally, the pellet was analyzed using the FTIR spectrometer.

Atomic Force Microscope (AFM)

The surface topography of the BPP was examined using AFM with the model of Park Systems EX-7 with a scan area of 10 μm × 10 μm.

Scanning Electron Microscope (SEM)

Field emission scanning electron microscope was used to study the surface morphology of the BPP before and after adsorption. The model used was JEOL JSM 6701F FESEM with emission current of 4kV and working distance of 5.8 mm.

Point of zero charge (pH_{pzc}) of adsorbent

The pH at point of zero charge (pH_{pzc}) was analyzed for the BPP. The sodium chloride (NaCl) solutions with the pH of 2, 4, 6, 8, 10 and 12 were prepared. 0.01/0.1 M of HCl and 0.01/0.1 M NaOH were used to adjust the pH of the solution to the selected pH. Then, 0.10 g of BPP was added to 50 mL of 0.1 M sodium chloride solution at each pH. The mixture was shaken for 24 hours. The final pH of each solution was examined after 24 hours. The change in the pH (ΔpH) of each solution was calculated. A graph of ΔpH versus initial pH was plotted and the pH_{pzc} was obtained as the x-intercept of the plot.

Batch experiments

The batch study was performed in duplicates and the presented result was the average value obtained from the experiment. The concentration of BR29 solution was measured using Shimadzu UV-Vis Double Beam Spectrophotometer at the maximum wavelength of 510 nm. Dilution of sample was carried out if the absorbance value exceeds the highest point in the standard calibration graph. The percentage uptake of BR29 solution was evaluated using the equation:

$$\text{Percentage uptake} = \frac{C_o - C_t}{C_o} \times 100\ \% \qquad (10)$$

In which

C_o = Initial concentration of BR29 (mg/L)
C_t = Concentration of BR29 at time t (mg/L)

The BR29 solutions with the concentration of 100, 200 and 500 mg/L were used to analyze the effect of initial concentration on the uptake of the dye. A 20 mL of BR29 solution at the respective concentration was placed in centrifuge tubes. Then, 0.10 g of BPP was added to the BR29 solutions. The mixture was agitated at 150 rpm for 5, 10, 15, 30, 60, 90, 120, 180, 240, 300 and 360 minutes.

The pH of the BR29 solution was regulated with drop wise addition of 0.01/0.1 M hydrochloric acid (HCl) and 0.01/0.1 M sodium hydroxide (NaOH). A series of solutions with the pH 2, 4, 6, 8 and 10 were prepared. The parameter was conducted using 100 mg/L of BR29 at the corresponding pH.

Different adsorbent dosage of 0.01, 0.02, 0.04, 0.06, 0.08 and 0.10 g of BPP were used for this study. Each different mass of adsorbent was added to 100 mg/L of BR29 during the analysis.

A 100 mg/L of BR29 solution with BPP was agitated at 50 rpm at the time interval of 5, 10, 15, 30, 60, 90, 120, 180 and 240 minutes. This step was repeated by using 100 rpm agitation rate.

Different concentrations of BR29 solution were used in the isotherm study. The BR29 solutions with the concentration of 200, 300, 400, 500, 600 and 700 mg/L were prepared. A 0.10 g of BPP was added to 20 mL of BR29 solution at each concentration and shaken at 150 rpm for 240 minutes.

ACKNOWLEDGEMENTS

The financial support and research facilities by Universiti Tunku Abdul Rahman are acknowledged.

REFERENCES

1. S.L. Lee, S.W. Liew, S.T. Ong; *Acta Chim. Slov*., **2016**, *63*, 144-153.
2. Malaysian Investment Development Authority, *Textiles and Textile Products* [Online], **2019** Available at: http://www.mida.gov.my/home/textiles-and-textile-products/posts/
3. Y.L. Pang, A.Z. Abdullah; *CLEAN - Soil, Air, Water*, **2013**, *41*, 751-764.
4. P.M. Birgani, N. Ranjbar, R.C. Abdullah, K.T. Wong, G. Lee, S. Ibrahim, C. Park, Y. Yoon, M. Jang; *J. Environ. Manage.,* **2016**, *184*, 229-239.
5. D.A. Yaseen, M. Scholz; *Environ. Sci. Pollut. Res. Int.,* **2018**, *25*, 1980-1997.
6. S. Syafalni, I. Abustan, I. Dahlan, K.W. Chan, G. Umar; *Mod. Appl. Sci.,* **2012**, *6*, 37-51.
7. P.D. Pathak, S.A. Mandavgane, B.D. Kulkarni; *Rev. Chem. Eng.,* **2015**, *31*, 361-381.
8. G. Annadurai, R.S. Juang, D.J. Lee; *J. Hazard. Mater.*, **2002**, *92*, 263-274.
9. P.D. Pathak, S.A. Mandavgane, B.D. Kulkarni; *Curr. Sci.*, **2017**, *113*, 444-454.
10. M. Dahiru, Z.U. Zango, M.A. Haruna; *Am. J. Mater. Sci.*, **2018**, *8*, 32-38.
11. N.K. Mondal, S. Kar; *Appl. Water Sci.*, **2018**, *8*, 157-169.
12. H. Y. Gan, L. E. Leow, S. T. Ong; *Acta Chim. Slov*., **2017**, *64*, 144-158.
13. M. Pishgar, M.E. Yazdanshenas, M.H. Ghorbani, K. Farizadeh; *J. Appl. Chem. Res.*, **2013**, *7*, 51-62.
14. S.W. Liew, S.T. Ong; *Asian J. Chem.*, **2014**, *26*, 3808-3814.
15. H.J. Lee, S.T. Ong; *Environ. Prot. Eng. J.*, **2017**,*43*, 169-181.
16. M.N. Idris, Z.A. Ahmad, M.A. Ahmad; *Int. J. Basic Appl. Sci.*, **2011**, *11*, 38-43.
17. A. Salama, H.A. Aljohani, K.R. Shoueir; *Mater. Lett.*, **2018**, *230*, 293-296.
18. Ü. Geçgel, G. Özcan, G.Ç. Gürpınar; *J. Chem.*, **2013**, Article ID 614083,1.
19. A.M.K. Aljebori, A.N. Alshirifi; *Asian J. Chem.*, **2012**, *24*, 5813-5816.
20. M.W. Washabaugh, M.A. Gold, C.C. Yang; *J. Am. Chem. Soc.*, **1995**, *117*, 7657-7664.
21. M.A.M. Al-Tufaily, Z.S.R. Al-Qadi; *Int. J. Civ. Eng. Technol.*, **2016**, *7*, 1-14.

22. S.K. Kim, J. Venkatesan, Introduction to Marine Biotechnology, in *Handbook of Marine Biotechnology,* S.K. Kim Ed.; Springer-Verlag, Berlin Heidelberg, Swizerland, **2015**, Chapter 1, pp. 1-10.
23. S. Lagergren; *Handlingar*, **1898**, *24*, 1-39.
24. M. Ghasemi, N. Ghasemi, G. Zahedi, S.R.W. Alwi, M. Goodarzi, H. Javadian; *Int. J. Environ. Sci. Technol.*, **2014**, *11*, 1835-1844.
25. F.E. Soetaredjo, S. Ismadji, K. Foe, G. L. Woworuntu, Removal of Hazardous Contaminants from Water or Wastewater Using Polymer Nanocomposites Materials, in *Nanotechnology for sustainable water resources*, A.K. Mishra, C.M. Hussain Eds.; Scrivener Publishing, New Jersey, USA, **2018**, Chapter 4, pp. 103-139.
26. Ho, and McKay, G.; *Trans. Inst. Chem. Eng*., 1**998**, *76*, 332-340.
27. Y.S. Ho, G. McKay; *Pr. Biochem.*, **1999**, *34*, 451-465.
28. Y. S. Ho, G. McKay; *Water Res.*, **2000**, *34*, 735-742.
29. G.L. Dotto, S.K. Sharma, L.A.A. Pinto, Biosorption of Organic dyes: Research Opportunities and Challenges, in *Green chemistry for dyes removal from wastewater,* S.K. Sharma Ed.; Scrivener Publishing, New Jersey, USA, **2018**, Chapter 8, pp. 295-323.
30. Y.T. Huang, M.C. Shih, *Int. J. Sci. Res. Pub.*, **2016**, *6*, 548-554.
31. I. Langmuir; *J. Am. Chem. Soc.*, **1916**, *38*, 2221-2295.
32. H. M. F. Freundlich; *J. Phys. Chem.,* **1906**, *57*, 385-471.
33. S. Brunauer, P. H. Emmett, E. Teller; *J. Am. Chem. Soc.*, **1938**, *60*, 309-319.
34. A.N. Labaran, Z.U. Zango, U. Armaya'u, Z.N. Garba; *Sci. World J.*, **2019**, *14*, 66-70.
35. A.A. Inyinbor, F.A., Adekola, G.A. Olatunji; *Water Resour. Ind.*, **2016**,*15*, 14-27.
36. A. Sa, A.S. Abreu, I. Moura, A.V. Machado, Polymeric materials for metal sorption from hydric resources, in *Water Purification*, A. M. Grumezescu Ed., Academic Press, London, UK, **2017**, Chapter 8, pp. 289-322.

STUDIA UBB CHEMIA, LXVI, 4, 2021 (p. 189-204)
(RECOMMENDED CITATION)
DOI:10.24193/subbchem.2021.4.14

SYNTHESIS OF HYDROCARBON FUELS VIA SELECTIVE REFORMING OF KEROSENE OVER VARIOUS NI/ZEOLITE CATALYSTS

ELHAM SAIDI[a], MAHMOUD ZIARATI[a,*], NAHID KHANDAN[b], HOSSEIN DEHGHANI[a]

ABSTRACT. In this study, the reforming of kerosene was performed in a fixed-bed reactor in order to investigate the synthesis of hydrocarbon fuels. For this purpose, five Ni-based catalysts supported on Y, Mordenite, ZSM-5, Beta, and Ferririte zeolites were prepared by deposition-precipitation method. Four main composition groups of hydrocarbons including normal paraffins, isoparaffins, cycloparaffins, and aromatics were analyzed in feed and liquid products and the effects of key parameters of the catalysts namely acidity, diameter of pores in channels, and surface area on the progress of the reforming process were surveyed. According to the analysis results, Y zeolite with higher acidity, larger pore diameter, and more surface area led to produce the most aromatic contents (57.60%) in the products. Beta increased both cycloparaffins (34.91%) and isoparaffins (34.07%) in the product. Mordenite and Ferririte effectively increased the formation of isoparaffins by 38.22% and 38.85% respectively. Meanwhile, ZSM-5 with moderate acidity, surface area, and pore size increased the cycloparaffin contents of the product (46.28%). These results highlighted the potential of each zeolite to produce a valuable product via reforming process, which meets the requirement of standard hydrocarbon fuels. Ultimately, the pathway to reforming process over each prepared catalyst was proposed.

Keywords: *Reforming process, Bi-functional catalysts, Zeolite, Kerosene, Jet fuel, Reaction pathway*

INTRODUCTION

Fossil fuels including petroleum, natural gas, and coal produced 80% of the energy consumed worldwide in 2018. This share is estimated to decrease only slightly (70%) by 2050 [1]. The transportation as a fast growing

[a] *Malek- Ashtar University of Technology (MUT), Faculty of Chemistry and Chemical Engineering, Lavizan, P.O. BOX 158751774, Tehran, Iran*
[b] *Iranian Research Organization for Science & Technology (IROST), Department of Chemical Technologies, P.O. BOX 33535111, Tehran, Iran*
[*] *Corresponding author: maziarati@mut.ac.ir*

sector, particularly in developing countries, however is relied almost entirely (95%) on petroleum. Hence, it has lower probability to undergo these changes [2, 3]. By development of modernity in the world, the aviation as a transportation sector developed highly more than other sectors such that the need to jet fuels grew annually [4]. The petroleum-derived fuels utilized in these sections commonly contain four main compositions including line and branched paraffins, cycloparaffins, and aromatics [5]. There are several processes to produce or enhance the fuels by conversion of these components to each other through various reactions such as isomerization, hydrogenation and dehydrogenation, which are categorized as the reforming of hydrocarbons [6]. According to the previous literatures, many researchers have produced hydrocarbon fuels from several sources such as Fisher- Tropsch process [7], biomass and other wastes [8, 9], vegetable oils, etc. [10, 11]. However, the availability, easy access, and low price of oil-derived fuels makes them this chance to be applied as a feed for reforming process. Among them, kerosene is the third fraction of crude oil, which has the lowest H/C ratio and between 9 to 16 carbons. It was applied as a base for many jet fuels. Therefore, it was selected as a feed to reforming process in this research.

Several catalysts were employed for conversion of the hydrocarbons due to their undeniable advantages in comparison to traditional thermal reforming [12]. Catalytic reforming of hydrocarbon fractions is among the crucial processes in the oil refineries and petrochemical companies [13-15]. Among the various classifications of the homogeneous and heterogeneous catalysts namely acid, base, and zeolite catalysts, several valuable abilities of zeolites such as having acid-base character, low cost, environmentally friendly, uniform pore structure, high surface area and porosity, and reusability caused many researchers apply them widely to reforming of hydrocarbons [16]. In fact, their Lewis and Brønsted acid sites can efficiently go the reactions ahead the desirable route. This helps to form a final liquid product with high H/C ratios, which has the capability to utilize as a high energy fuel [17]. Zeolite catalysts have commonly employed as support of catalysts for major refining processes such as fluid catalytic cracking, distillate dewaxing by cracking, hydrocracking, lube dewaxing by cracking, gasoline desulfurization, distillate dewaxing by isomerization, light paraffin isomerization, lube dewaxing by isomerization, reformate upgrading and diesel aromatics saturation, and they have shown promising catalytic performance in the reforming process [18, 19]. As the individual advantage of zeolite in comparison to the conventional catalysts, they could provide the unique feature of shape selectivity due to their repeatable pore structure useful to the reaction under consideration. For example, zeolite with more dimensional pore channel structure can provide a higher cracking activity than 1D ones. It is because of longer contact time of molecules in the pore [20].

Introduction of metals to zeolites is favorable for catalytic reforming process, because of preserving acid sites and increasing the production of the lighter hydrocarbons by progress the reaction towards the desirable pathway. Nickel (Ni) with low cost, effective activity, and more availability is the most widely used with zeolites for the reforming of hydrocarbons [11, 21-27]. High metal loadings cause bulk Ni particles (> 10 nm) in the catalysts that harden access to internal zeolite pores [28]. Therefore, an ideal metal loading is necessary to influence the porosity and acidity of the zeolite in a positive way [29-31]. In this work, the 5% Ni loading for Ni/Y catalysts were employed to prepare the catalysts.

However, reports on the reforming of kerosene over zeolites are still rare and the vital role of various zeolites in the reforming of the hydrocarbon fuels has rarely studied in details. In light of this, five different zeolites (Ferririte, Mordenite, ZSM-5, β-zeolite, and Y-zeolite) were employed for catalytic reforming of kerosene in this research. Ultimately, the composition of products over each zeolite was discussed to determine the suitable zeolites to produce a standard fuel via reforming of kerosene.

RESULTS AND DISCUSSION

Structural properties

As indicated in Figure 1, XRD patterns reported for the calcined catalysts is clearly displayed the structures of catalysts without any contamination by impure phases. Therefore, the framework of zeolite seems to be maintained well after incorporation of nickel but its crystallinity slightly changed by synthesis. In this study, only some of the peaks of NiO were distinguished. One reason may be the size of the particles, which might be below the detection limit of XRD. As suggested in some literatures, the characteristic diffraction peaks of Ni crystallized from some prepared zeolite catalysts such as Ni/β are very weak (Figure 1) which means the poor crystallinity of Ni on these catalysts. It is in agreement with the highly dispersive of oxide on the support and smaller sizes than detected by XRD [32].

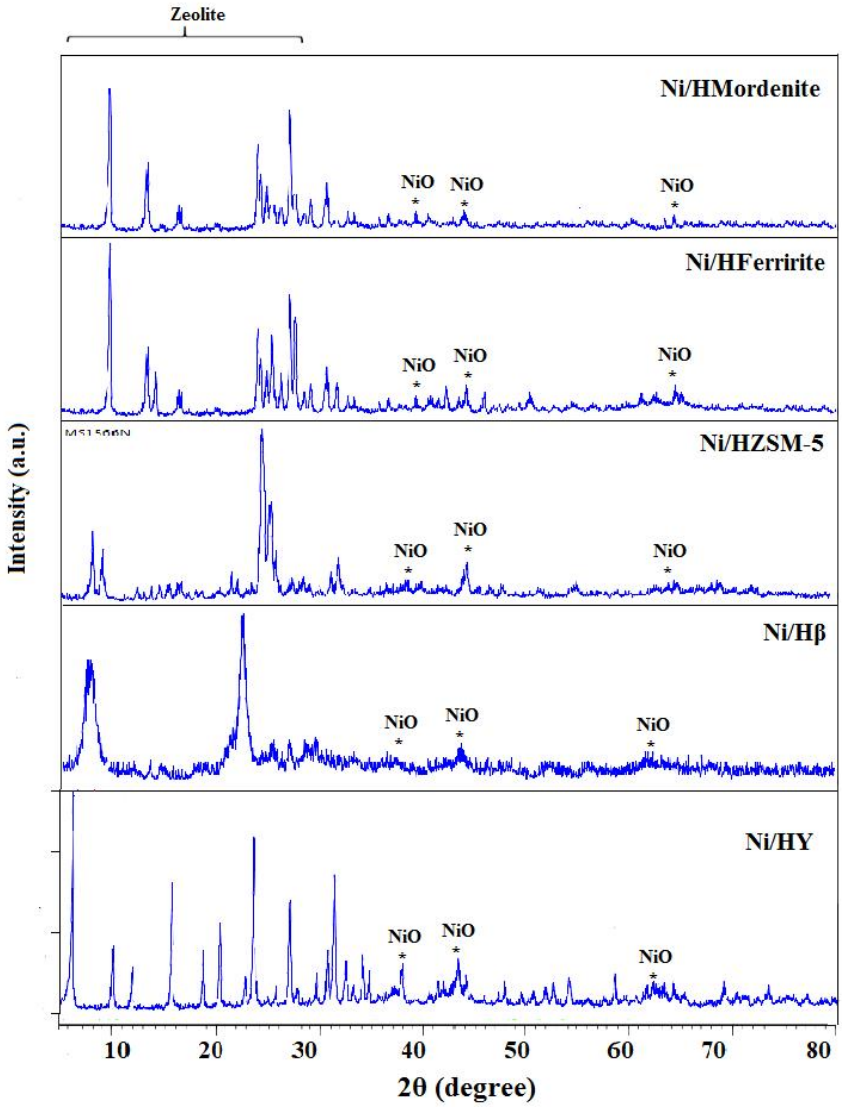

Figure 1. XRD patterns of the prepared catalysts

Textural properties and chemical composition

N_2 adsorption-desorption was applied to determine the textural properties of the prepared catalysts. The results of N_2 adsorption-desorption, surface areas, and other textural properties of the prepared catalysts were indicated in Table 1.

By comparison of the textural properties of the synthesized catalysts listed in Table 1 with the manufactured properties of net zeolites, it was found that the surface area of the catalysts decreased after the incorporation of Nickel species into the zeolites. This may be due to the higher dispersion of the nanosized crystallites [33].

Table 1. The textural properties of the prepared catalysts

Row	Catalyst	S_{BET} (m^2 g^{-1}) [(a)]	V_{total} (cm^3/g) [(b)]	Ni loading (wt. %) [(c)]
1	Ni/Y	540	0.35	5.20
2	Ni/β	370	0.66	4.97
3	Ni/ZSM-5	290	0.14	5.36
4	Ni/FER	260	0.11	5.08
5	Ni/MOR	310	0.16	5.29

(a) BET surface area obtained by analyzing nitrogen adsorption data at -196°C in a relative vapor pressure ranging from 0.05 to 0.30 (m^2/g); (b) Total pore volume estimated based on the volume adsorbed at P/P_o = 0.99 (cm^3/g); (c) The metal loading measured by EDX

The amount of Ni in the prepared catalysts was determined by the EDX analysis. As shown in the last column of Table 1, a proper approximation to the theoretical Ni loading was performed for Ni/β using this analysis, while the Ni-loading in the other catalysts is more than one expected during preparation. As mentioned in some literatures, this exceeding amount of metal may be due to the uneven embedded metal in the support on the area detected by the EDX instrument, which generated by the microwaves applied to separate particles with rapid heating. Another reason may be the probable fewer Ni particles in the area that is not analyzed using EDX [34].

TPR analysis

The H_2-TPR curves of the calcined Ni/zeolite catalysts were presented in Figure 2, which attributed to the reduction of the NiO. For all prepared Ni/zeolites, one obvious H_2 consumption peak was observed at approximately 350°C, which was ascribed to the peaks of NiO species reducing to Ni. In fact, the TPR curves had ascending route from 280°C to 350°C. Therefore, the optimum temperature for the reduction of the prepared samples was proposed to be in in this range.

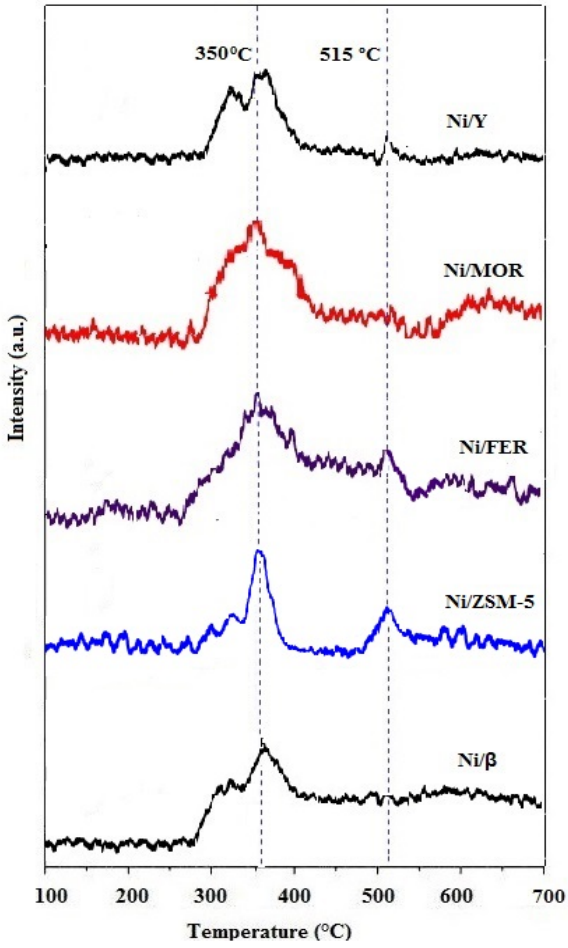

Figure 2. H_2-TPR curves of the calcined Ni/zeolite catalysts

Acidity analysis

The acidic properties of the zeolites determined from NH_3-TPD profiles with the corresponding strong and weak acid sites amounts were summarized in Figure 3. As observed, the acid strength of the various zeolites was different.

According to the previous studies, the reason of having a different acidity profile mainly is the difference in their intensity which refers to the amount of NH_3 desorbed from the samples pretreated with NH_3 chemical adsorption [35].

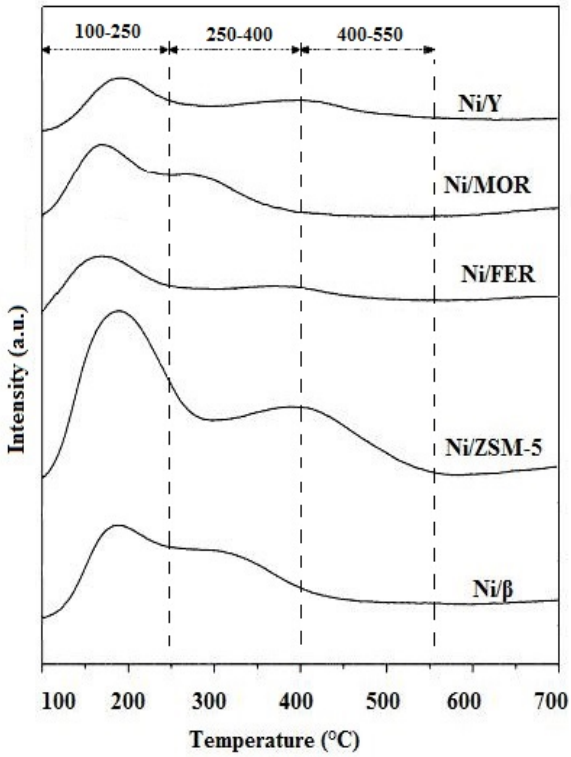

Figure 3. The profiles of NH_3-TPD for the prepared catalysts

As the profiles of NH_3-TPD revealed, the Ni/Y appeared to be the sample with more weak acid sites than strong acid sites. Ni/MOR showed to have relatively high weak and medium acidity. No obvious strong acid sites observed in the case of this sample. The TPD profile of the Ni/FER presented a little acidity for all weak, medium, and strong acid sites.

The highest weak acid site was remarkable in the case of Ni/ZSM-5 catalyst. In addition, it showed significantly the most amounts of medium and strong acid sites.

Ni/β sample had more weak acidity, which went towards medium acid sites. The amounts of its strong acid sites were not appeared to be remarkable. In comparison, both weak and strong acid sites was observed to be the most in the case of the Ni/ZSM-5 and the highest acidity in the range of the medium acid sites belonged to Ni/β among five prepared samples.

Performance test results

The collected produced liquids were subjected to physicochemical analytical tests using the methods specified by the American Standard for Testing and Materials (ASTM D1655). Among the analyzed properties, four significant properties namely density, final boiling point (FBP), flash point, and freezing point were selected to be discussed. The analysis results of these properties and their comparison to some standard fuels were given in Table 2.

Table 2. Physicochemical data of feed, produced liquids, and some standard fuels

products	Property	Density at 15.6 °C (kg/m^3)	FBP (°C)	Flash point (°C)	Freezing point (°C)
Standard method	**ASTM D**	4052	86	3828	2386
	IP	365	123	303	16
Products over Catalysts	**Feed**	797.4	280	50	-52
	No cat.	800.0	290	47	-53
	Ni/Y	799.8	295	46	-55
	Ni/Mordenite	800.1	289	49	-51
	Ni/β	797.4	294	51	-53
	Ni/ZSM5	799.6	282	46	-55
	Ni/Ferririte	799.2	297	48	-44
Standard fuels	**Gasoline**	Report	170	---	-60
	kerosene	799-815	275	43.3	-37.8
	Gasoil	820-860	385	51-54	---
	Jet fuel (ATK)	775-840	300	38	-47
	JP-4	751-802	270	---	-58
	JP-5	788-845	300	60	-46
	JP-7	779-806	288	60	-43.3
	JP-8	775-840	300	38	-47

Compositions of liquid products

All components of reformed kerosene in heterogeneous conditions by hydrocarbon groups and their carbon atom number Cn were identified or organized. The weight percentage of reformed produced liquids were identified and calculated with the same method as described for the kerosene fractions. The results were summarized in Table 3. In details, the identified peaks belonged to the carbon range of C8 to C24 in the presence of three prepared catalysts of Ni/Ferririte, Ni/Mordenite and Ni/Y, while the identified compounds of produced liquid in the presence of Ni/β catalyst were in the range of C8 to C17. On the other hand, feed and the produced liquid in the presence of Ni/ZSM-5 catalyst had the compounds ranged from C8 to C20.

Table 3. Summarization of compound analyses of produced liquids (wt. %)

Row	Catalyst type	N- paraffins	Isoparaffins	Cycloparaffins	Aromatics
1	Fresh feed	27.426	27.911	23.489	21.234
2	Ni/Y	24.6987	12.4439	5.2609	57.5965
3	Ni/Mordenite	24.1737	38.2285	7.8715	29.7263
4	Ni/β	22.7547	34.0740	34.9075	8.2639
5	Ni/ZSM-5	4.3875	30.3861	46.2826	18.9438
6	Ni/Ferririte	25.6899	38.8542	4.7488	30.7071

As the Figure 4 shows, the amounts of some compositions are more than other ones in produced fuels.

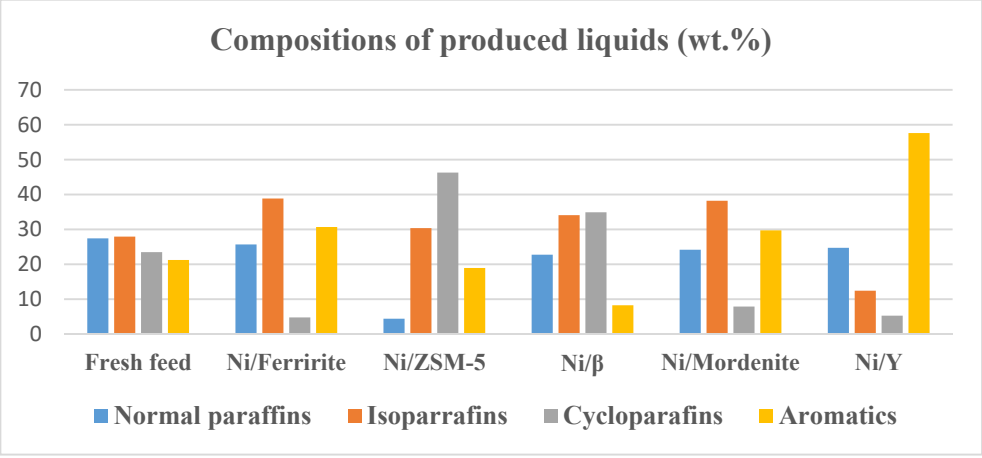

Figure 4. Distribution of the hydrocarbon groups contained in the produced liquids

The hydrocarbons are categorized by their carbon chain length into the gasoline (C5–C10), jet fuel (C9–C15), diesel (C14–C20), and lubricant (C19-C25) [34, 44]. As shown in the Table 4, the liquid products were classified according to these carbon chain ranges.

Table 4. The classification of liquid products according to the carbon chain range

Row	Catalyst	Gasoline (C5–C10)	Jet fuel (C9–C15)	Diesel (C14–C20)	Lubricant (C19-C25)
1	Ni/Y	18.65	64.72	16.52	0.11
2	Ni/ZSM-5	17.37	80.42	2.19	0.02
3	Ni/β	28.40	68.72	2.88	0
4	Ni/MOR	18.26	64.93	16.71	0.10
5	Ni/FER	18.96	64.49	16.42	0.13

According to these results, Ni/β produced the lowest fuels with no carbon numbers in the range of lubricants. As anticipated, the reforming of kerosene showed an enhanced capability of jet fuel products. This process led to at least 64% jet fuel over each catalyst. However, the Ni/ZSM-5 produced more cycloparaffins in comparison to other samples. Therefore, this catalyst produced highest jet fuel with the highest quality.

Effect of catalyst characters on the liquid products

The effect of some characters of the prepared catalysts on compositions of produced liquids is discussed in this section.

Pore sizes of the applied zeolite were in the order of Ni/Ferririte< Ni/ZSM-5< Ni/Mordenite< Ni/β< Ni/Y. Generally, micropore zeolites such as Ferririte have lower activity than those with mesopore (ZSM-5) and macropore (Y, Mordenite, and Beta). It is not in conflict with increasing the catalytic activity with decreasing the particle size. The kerosene- range molecules diffuse toward pores and react on the surface of catalyst. Since the Ferririte pore is smaller than some molecules such as cycloparaffins, a few amounts of these components were produced over this zeolite.

In the case of Y and Mordenite catalysts, however the few amounts of cycloparaffins may be due to the difference of acid sites strength and concentration. Instead, their polyaromatics were more, which may be due to macroporous structures of these catalysts. As already noted the acidity of the catalysts directly influences on some properties of the produced liquids. The acidity power (less Si/Al ratio) of applied catalysts was in the order of Ni/β< Ni/ZSM-5< Ni/Ferririte< Ni/Mordenite< Ni/Y. Note that acidity of Mordenite and Y has increased after ion exchange of Na-form zeolite samples to NH_4^+ form. Strong acid sites on catalysts would be the main reason for the catalyst deactivation (i.e. coke deposition and weak acid site may go forwards reforming process through multi-step pathway and therefore undesired side reactions. In other words, an optimum Si/Al ratio would be desirable [36]. As shown in Figure 5, zeolites have an important role to go selectively the dehydrocyclization reaction towards and supported metals can promote the formation of aromatics. The stronger- acidic catalysts have greater activity than that of the weaker-acidic catalyst. In this paper, Y zeolite with highest acidic power produced the most aromatic contents.

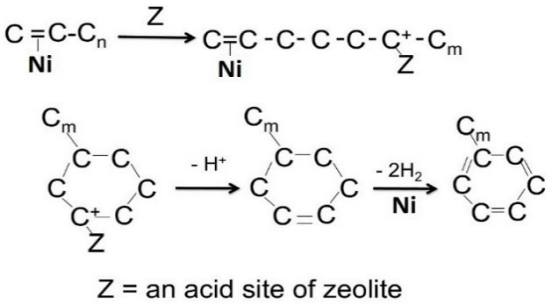

Figure 5. Formation routes of aromatic hydrocarbons from aliphatic ones on a Ni/ zeolite catalyst [37]

Reforming process in the presence of zeolites with 2 or 3D channel pore leads to produce a different fuel than 1D pore channel. As a result, a strong dependence of reforming process on the channel structures of catalysts was observed in order that some huge hydrocarbon components could not be formed or passed through 1D channel zeolites such as Mordenite. As well, 2D channel ZSM-5 zeolite made the limpidity of passing some components in comparison to 3D zeolites such as Y and β. In other words, shape selectivity of ZSM-5 is a key parameter in improving quality of products [38].

CONCLUSIONS

In this paper, reforming of kerosene was investigated over five 5%Ni/zeolite catalysts. Among the series studied, ZSM-5 and β catalysts direct the reaction forwards the dehydrocyclization by increasing the naphthenic compounds of fuel and hence it would be proposed to apply these catalysts to production of some type of jet fuels. These two catalysts had the weaker acidic power than other prepared catalysts. Therefore, they did not favor the formation of aromatics in comparison to Y, Mordenite and Ferririte catalysts, which would improve octane number of gasoline if they were applied to aromatization reactions. Y zeolite had the ability to produce more aromatics, which is suitable to produce high quality gasoline by increasing its octane number. Mordenite produced a product with high isoparaffin content. The high strong acid sites in the Y, Mordenite and Ferririte zeolites lead to side reactions such as cracking, and consequently more aromatic formation in the liquid products.

Its macroporous structure along with lowest Si/Al ratio and 3D channel structure would be the best reason to introduce Y zeolite as a suitable catalyst to further researches in the field of aromatization. The similarity of products to high-energy jet propellant fuels was maximized when Ni/ZSM-5 was used in this study.

EXPERIMENTAL SECTION

Materials

The properties of kerosene supplied by Tehran Oil Refinery Company (TORC) were reported in Table 5.

Table 5. Specifications of supplied kerosene by TORC

Property	Unit	Test method	Feed properties
Density at 15.6 ˚C	kg/m^3	D 1298	797.4
Distillation			
IBP	˚C	D 86	156
185 ˚C	% vol.		23.9
200 ˚C	% vol.		48.4
210 ˚C	% vol.		64.1
235 ˚C	% vol.		90.9
FBP	˚C		260
Sulfur	% wt.	D 1552	0.09
Flash point	˚C	D 3828	50
Freezing point	˚C	D 2386	-52
Acidity	% vol.	D 3242	0.5mL/0.5mL
Aromatic content	% vol.	D 6379	21.3%

Nickel nitrate hexahydrate ($Ni(NO_3)_2.6H_2O$), sodium carbonate (Na_2CO_3) applied to prepare the Ni/zeolite catalysts and ammonium nitrate (NH_4NO_3) used for zeolite ion exchange were purchased from Merck Company (Germany). Five applied zeolites to the reforming of kerosene were purchased from Zeolyst Company (USA) with the typical properties reported by manufacturer and more details of their properties were illustrated in Table 6.

Table 6. Physical characteristics of zeolite powders as reported by manufacturer

Row	Properties	Y	Mordenite	β	ZSM-5	Ferririte
1	Zeolyst product	CVB 100	CVB 10A	CP 814 E	CVB 2314	CP 914 C
2	IZA code	FAU	MOR	BEA	MFI	FER
3	Si/Al ratio	5.1	13	25	23	20
4	Channel system	12–12	12–12	12–12	10–10	8–8
5	Pore size (Å)	7.4 × 7.4	6.5 × 7.0	7× 6.5	5.6 × 5.3	3.5×4.8
6	Pore shape	Circular	Circular	Elliptical	Elliptical	Elliptical
7	Surface area	900	425	680	425	400
8	Average pore	55.95	42.73	39.89	41.85	37.32

Catalyst preparation and characterization

To prepare the catalysts, two Na-form zeolites i.e. Mordenite and Y zeolites were ion-exchanged to ammonium form using NH_4NO_3 solution (0.1mol/L). The deposition- precipitation method was applied to prepare the catalysts. In detail, the Na_2CO_3 (1M) solution was added into the aqueous solution of 1M metal nitrate ($Ni(NO_3)_2.6H_2O$) at 70ºC in a controlled rate. The solution was subject to continuous stirring by 700-1000rpm and the pH of the solution was kept up around 7±0.2. After that, the solution was aged at room temperature for 30min, followed by filtering three times, and rinsing to obtain precipitate. To deposit the support on the catalyst, zeolite was added to the deionized water and stirred in the room temperature to form a uniform mixture. Then, the precipitate was added to the performed solution. The obtained solution was aged 1h while stirred slowly in order to deposit the support on the catalyst suitably, followed by filtration. Subsequently, the obtained solid was dried at 110°C in air overnight and calcined at 550ºC in airflow for 5h in order to convert to the H form. Sieve analysis was performed using two US standard test sieves (ASTM E.11) with mesh numbers of 20 and 40 with the sieve opening of 0.850mm and 0.420mm, respectively.

X-ray powder diffraction (XRD) method was used to analyze the crystal structure of the catalysts. In fact, higher peaks confirm more crystallinity of the catalysts. XRD measurements of the samples were performed using a Philips PW-3710 diffractometer equipped with a nickel filtered Cu- Ka radiation (λ = 1.5418˚A) covert 2θ between 5º and 80º. The formation of cubic phase of NiO (JCPDS Card 47-1049) investigated to XRD patterns, in which the distinct peaks at 2θ of 37.26º, 43.29º, 62.88º, 75.42º, and 79.41º as peaks of cubic NiO crystals with various diffraction (111), (200), (220), (311), and (222) planes of the face-centered cubic NiO (JCPDS 47-1049), respectively [39].

The Ni content of the prepared catalysts was determined by an energy dispersive X-ray (EDX) spectrometer (Zeiss Gemini Leo 1530). The surface area and pore volume of the samples were measured at −196ºC (77K) using nitrogen adsorption according to the Brunauer–Emmett–Teller method (BET) method (by a CHEMBET-3000, Quantachrome Instruments, Germany). ICP (Inductively coupled plasma) emission spectrometer (Ultimo Expert, Horiba Scientific) was employed for measurement of the chemical composition of zeolites in this study. Temperature-programmed reduction (TPR) measurements of the catalysts were carried out at 550°C for 30min in air. The second stage ramped the temperature from 100°C to 700°C at 5°C/min in 3% H_2 diluted in argon. To investigate the consumption of H_2, a thermal conductivity detector (TCD) was applied.

Ammonia temperature programmed desorption (NH_3-TPD) with a BELCAT-M instrument (BEL Japan Inc.) with a TCD detector was employed to study the acid properties of the catalysts. A calibration curve was applied to calculate the ammonia amount by converting the peak area to concentration, and the number of weak, medium, and strong acidic sites was calculated by dividing the integrated peak area into ranges of 100–250, 250–450, and 450–600ºC, respectively [40].

Catalyst performance tests

Catalytic tests via reforming process were carried out in a stainless steel fixed-bed reactor with an internal diameter of 10mm and a length of 150mm. A schematic diagram of the experimental setup for the catalytic reforming of kerosene is shown in Scheme 1.

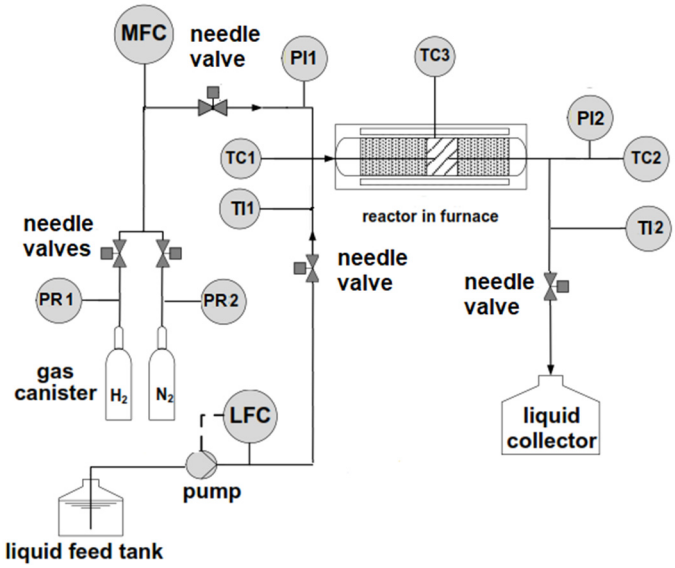

Scheme 1. Schematic diagram of the laboratory- scale experimental setup of reforming system. LFC- liquid flow controller; MFC- mass flow controller; pump–peristaltic pump; TC-thermocouple; TI– temperature indicator; PI – pressure indicator; PR – pressure regulator

Prior to the reforming of kerosene, reduction was performed at 300ºC for 1h in pure H_2 with a flowrate of 50mL/min. To activate the catalyst, N_2 was flowed in-situ for 10min with 70cc/min rate. A preheater was applied to heat kerosene initially with temperature of 300ºC. Kerosene with a flow rate of

5mL min^{-1} was introduced into the preheater by the peristaltic pump (TEC1, AQUA, Italy). Then, the heated feed was entered to the reactor at the temperature reaction (450ºC). A mass flow controller (Brooks, 5850) was employed for controlling of the feed flow rate. The liquid products were collected using two-step traps to be analysed. The products of reforming reaction were first collected in a hot trap followed by a cold trap with ice water to avoid produced liquid phase condensed and stranded in the system.

The collected liquid products were analysed by an Agilent 6890N gas chromatography (GC) equipped with a flame ionization detector (FID) and a DH capillary column (40m). Injection temperature was set to 300˚C. Column temperature was initially increased from 40 to 100˚C at a rate of 2˚C/min, and then increased to 300˚C at a rate of 10˚C/min for 8min.

ACKNOWLEDGMENTS

Financial support of this work by the faculty of chemistry and chemical engineering of Malek-Ashtar University of Technology (MUT) is gratefully acknowledged.

REFERENCES

1. Global Energy & CO_2 Status Report; International Energy Agency (IEA): Paris, France, **2018**.
2. J.C. Serrano-Ruiz; J.A. Dumesic; *Energy Env. Sci.*, **2011**, *4*, 83–99.
3. M. A. Díaz-Pérez; J. C. Serrano-Ruiz; *Molecules*, **2020**, *25*, 802-820.
4. S. Toamasek; Z. Varga; J. Hancsók; *Fuel Process. Technol.*, **2020**, *197*, 106197. https://doi.org/10.1016/j.fuproc.2019.106197
5. J.D. Woodroffe; B. G. Harvey; *energy fuels*, **2020**, https://dx.doi.org/10.1021/acs.energyfuels.0c00274
6. F. Zaera; *Appl. Catal. A.*, **2002**, *229*, 75–91.
7. A. Klerk; Molecules, **2018**, 23, 115-126.
8. M. Shahabuddin; M.T. Alam; B.B. Krishn; T. Bhaskar; G. Perkins; Bior Tech., **2020**, 312, 123596.
9. T.K. Habibie; B. H. Susanto; M. F. Carli; E3S Web of Conferences 67, **2018**.
10. S. Tomasek; Z. Varga; J. Hancsók; Fuel Process. Technol., **2020**, 197, 106197.
11. H. Wang; S. Yan; M. Kim; S.O. Salley; K.Y.S. Ng; Current Catalysis, **2012**, 1, 132-139.
12. X. Li; A.A. Alwakwak; F. Rezaei; A.A. Rownaghi; *ACS Appl. Energy Mater.*, **2018**, *1 (6)*, 2740–2748.
13. G.J. Antos; A.M. Aitani; *Catalytic Naphtha Reforming*, 2nd ed., Marcel Dekker, New York, **2004**, pp. 335–349.
14. C.E. Xu; *Catalytic Reforming Process and Engineering*, China Petrochemical Press, Beijing, **2006**, pp. 1–26.

15. P. Zhang; Y. Yang; Z. Li; B. Liu; C. Hu; *Catal. Today*, **2019**, https://doi.org/10.1016/j.cattod.2019.07.032.
16. M. Shahinuzzamana; Z. Yaakob; Y. Ahmed; *Renew. Sust. Energ. Rev.,* **2017**, http://dx.doi.org/10.1016/j.rser.2017.01.162.
17. J. Y. Kim; J. Moon; J.H. Lee; X. Jin; J.W. Choi; *Fuel*, **2020**, *279*, 118484.
18. F. Thomas; J. Degnan; *Top Catal.,* **2020**, *13*, 349–356.
19. A. Ishihara; *Fuel Process Technol*., **2019**, *194*, 106-116.
20. W. Namchota; S. Jitkarnka; *J Anal Appl Pyrolysis.*, **2016**, *118*, 86–97.
21. H. Kim; D. Kim; Y. K. Park; J. K. Jeon; *Res Chem Intermed*, **2018**, *44*, 3823–3833.
22. D. Yao; H. Yang; H. Chena; P.T. Williams, *Appl. Catal. B Environ.*, **2018**, *227*, 477- 487.
23. X. Yang; J. Da; H. Yu; H. Wang; *Fuel*, **2016**, *179*, 353–361.
24. L. Liu; L. Hong; *AIChE Journal*, **2011**, *57,* 3143-3152.
25. A.J. Maia; B. Louis; Y.L. Lam; M.M. Pereira; *J. Catal.*, **2010**, *269 (1)*, 103-109.
26. M. Lallemand; O.A. Rusu; E. Dumitriu; A. Finiels; F. Fajula; V. Hulea; *Appl. Catal. A.*, **2008**, *338*, 37-43.
27. L. Chen; X. Wang, H. Guo; X. Guo; Y. Wang; H. Liu; G. Li, *Catal. Commun.*, **2007**, *8*, 416–423.
28. P. Yan; J. Mensah; A. Adesina; E. Kennedy; M. Stockenhuber; *Appl. Catal. B Environ.,* **2020**, *267*, 118690.
29. A. Marcilla; A. Gómez-Siurana; F. Valdés; *J. Anal. Appl. Pyrolysis*, **2007**, *79*, 433-442.
30. A. Kant; Y. He; A. Jawad; X. Li; F. Rezaei; J.D. Smith; A. A. Rownaghi; *Chem. Eng. J.,* **2017**, *317*, 1-8.
31. M. A. Atanga, F. Rezaei, A. Jawad, M. Fitch, A. A. Rownaghi, *Appl. Catal. B Environ.*, **2018**, *220*, 429-445.
32. S. C. Qi; X. Y. Wei; Z. M. Zong; J. Hayashi; X. H. Yuan; L. B. Sun; *Chem Cat Chem.*, **2013**, *5*, 3543-3547.
33. K.B. Golubev; K. Zhang; X. Su; N.V. Kolesnichenko; W. Wu; *Catal Commun.*, **2021**, 149, 106176.
34. T. K. Habibie; B.H.Susanto; M. F. Carli; E3S Web of Conferences 67, 02024, **2018**, 3rd i-TREC 2018.
35. M.Y. Choo; L. E. Oi; T. J. Daou; T. C. Ling; Y.C. Lin; G. Centi; E. P. Ng; J. C. Juan; *Materials*, **2020**, *13*, 3104.
36. X. Zou; X. Wang; L. Li; K. Shen; X. Lu; W. Ding; *Int J Hydrog Energy*, **2010**, 35, 12191- 12200.
37. A. Ishihara; R. Ishida; T. Ogiyama; H. Nasu, T. Hashimoto, *Fuel Process. Technol.*, **2017**, 161,17–22.
38. R. Nishu; M. Liu; M. Rahman; M. Sarker, M. Chai; C. Li; J. Cai; *Fuel Process. Technol.,* **2020**, https://doi.org/10.1016/j.fuproc.2019.106301.
39. S. Zulkepli; J.C. Juan; H.V. Lee; N.S.A. Rahman; P.L. Show; E.P. Ng; *Energy Convers. Manag.*, **2018**, 165, 495–508.
40. C. Wang; Q. Liu; J. Song; W. Li; P. Li; R. Xu; H. Ma; Z. Tian, *Catal. Today*, **2014**, 234, 153-160.

STUDIA UBB CHEMIA, LXVI, 4, 2021 (p. 205-224)
(RECOMMENDED CITATION)
DOI:10.24193/subbchem.2021.4.15

DIASTEREOSELECTIVE SYNTHESIS OF (8*E*,10*Z*)-TETRADECA-8,10-DIENAL, THE SEXUAL PHEROMONE OF THE HORSE-CHESTNUT LEAF-MINER *Cameraria ohridella* (LEPIDOPTERA: GRACILLARIIDAE)

IULIANA VASIAN[a*], TEODORA FLORIAN[b], ALEXANDRINA NAN[c], EMESE GAL[d], MONICA GORGAN[a], ȘTEFANIA MARIA TÖTÖS[a], VASILE FLORIAN[b], ION OLTEAN[b]

ABSTRACT. Versatile classical and modern methods for a new synthesis of (8*E*,10*Z*)-tetradeca-8,10-dienal based on Sonogashira cross-coupling, Cahiez-Fürstner reaction as well as other reactions using palladium, iron or copper as catalysts were described. We designed two ways employing two different strategies one of that involves an *E*-reduction and the other a *Z*-reduction with crucial importance in terms of diastereoselective synthesis. From the variously formulated pheromone baits, the one containing only the active isomer showed superior activity compared to the mixture of all isomers of 8,10-tetradecandienal. The synthesis of the pure *E,Z* diastereoisomer allowed to clarify their structure-bioactivity relationships to reveal the diversity in the stereochemical aspects of pheromone communications.

Keywords: *Cameraria ohridella, (8E,10Z)-tetradeca-8,10-dienal, Pheromone, Lure, Field Tests*

INTRODUCTION

Cameraria ohridella (Lepidoptera: Gracillariidae), the horse-chestnut leaf miner is a micro moth whose larvae create mines in the leaves of horse chestnut trees *Aesculus hippocastanum* L., and it was discovered in Macedonia by Deschka and Dimic around the Ohrid Lake (Macedonia) as early as 1986 [1].

[a] *Babeș-Bolyai University, Raluca Ripan Institute for Research in Chemistry, Pheromones Production Centre, Fântânele 30, 400084, Cluj-Napoca, Romania.*
[b] *University of Agricultural Sciences and Veterinary Medicine Cluj-Napoca, Faculty of Agriculture, Department of Entomology, 3-5 Mănăştur Street, 400372, Cluj-Napoca, Romania.*
[c] *National Institute for Research and Development of Isotopic and Molecular Technologies, 67-103 Donat Str., 400293 Cluj-Napoca, Romania.*
[d] *Babeș-Bolyai University, Faculty of Chemistry and Chemical Engineering, 11 Arany Janos str., RO-400028, Cluj-Napoca, Romania.*
* *Corresponding author: iuliana.vasian@ubbcluj.ro, iulianavasian@yahoo.com.*

At that time, they considered this area being the place of origin of this species. Nevertheless, according to the later literature data, its authentic origin was Asian [2]. It was then spread throughout Europe after 1985 and was first reported in Romania in 1998 in Lovrin area [3].

(8*E*,10*Z*)-Tetradeca-8,10-dienal has been identified by Svatoš, 1999 [4] and Kalinova, 2003 [5] with EAD activity experiments as the female sex pheromone of the horse chestnut leaf miner *Cameraria ohridella* (Lepidoptera, Gracillariidae).

From synthetic point of view, some publications have reported the synthesis of (8*E*,10*Z*)-tetradeca-8,10-dienal such as Hoskovec [6], Francke [7], Marcia de Figueiredo [8], Gânscă [9]. Recently, a method of stereoselective synthesis of (8*E*,10*Z*)-tetradeca-8,10-dienal has been developed by Chourreu, 2020 [10] with good results based on an iron-catalyzed Kumada cross-coupling. The most important syntheses from the point of the strategy were reported by Svatoš [4] and Grodner [11]. The first synthesis of (8*E*,10*Z*)-tetradeca-8,10-dienal achieved by Svatoš employs a C7+C2+C5 carbon chain units strategy. (*E*)-14-(*tert*-butoxy)tetradec-6-en-4-yne, the key intermediate in this synthesis, was prepared using Sonogashira cross-coupling reaction [12]. The synthesis by Grodner [11] involves a C5+C5+C4 carbon chain units strategy, the stereospecific introduction of double bonds being achieved through the same methodology based on the Pd(0)-catalysed cross-coupling between suitable halo alkene and the known 1-pentynylmagnesium bromide.

Most of the syntheses described in the literature involve a reduction reaction with boranes or $LiAlH_4$ [13]. Any attempt to reproduce the described syntheses has conducted to low yields and low selectivity. When $LiAlH_4$ was used, a mixture of 4 isomers in different proportions was formed. In this paper we described a versatile method for the synthesis of (8*E*,10*Z*)-tetradeca-8,10-dienal which can be successfully apply at large scale for production purposes.

Herein, we report a practical method for the synthesis of (8*E*,10*Z*)-tetradeca-8,10-dienal (**1**) based on Sonogashira and Cahiez-Fürstner cross-coupling reaction using palladium, iron and copper catalysts, to obtain **1** as a single diastereoisomer in large quantities.

RESULTS AND DISCUSSION

1. Synthesis of 8,10-tetradecadienal (1') as a mixture of all its four diastereomeric forms

We first synthesized 8,10-tetradecadienal (**1**) as a mixture of four geometric diastereomers (*E*,*Z*), (*E*,*E*), (*Z*,*E*) and (*Z*,*Z*). This synthesis followed a C7+C2+C2+C3 carbon chain strategy. 1,7-Heptanediol was brominated in

the presence of 48% aq. HBr (yield 79%) followed by the protection of the hydroxyl group with DHP (3,4-dihydro-2*H*-pyran) to give 2-(9-bromoheptyloxy)-tetrahydro-2*H*-pyran (**3**) in 83 % yield (**Scheme 1**) [14].

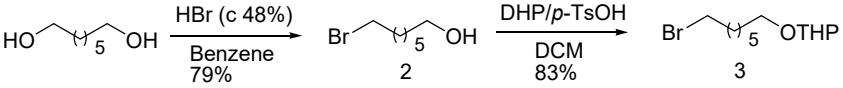

Scheme 1. Synthesis of 2-(9-bromoheptyloxy)-tetrahydro-2*H*-pyran (**3**)

2-(9-Bromoheptyloxy)-tetrahydro-2*H*-pyran (**3**) was coupled with commercial lithium acetylene ethylenediamine complex to give 2-(dec-9-ynyloxy)-tetrahydro-2*H*-pyran (**4**) in 90% yield [15]. The Sonogashira cross-coupling reaction of 2-(dec-9-ynyloxy)-tetrahydro-2*H*-pyran (**4**) with 5 equivalents of commercial (*Z*)-1,2-dichloroethene in the presence of a catalytic amount of Pd(PPh3)3Cl2, CuI and piperidine as base in THF afforded 2-[(*Z*)-11-chloroundec-10-en-8-ynyloxy]-tetrahydro-2*H*-pyran (**5**) in 67% yield and high isomeric purity (>95% by GC) (**Scheme 2**).

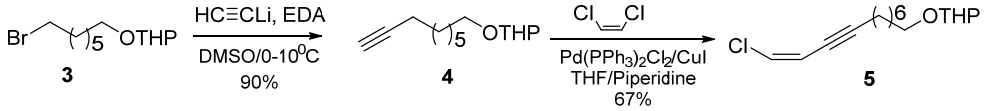

Scheme 2. Synthesis of 2-[(Z)-11-Chloroundec-10-en-8-ynyloxy]-tetrahydro-2*H*-pyran (**5**)

Next, the 2-[(*Z*)-11-chloroundec-10-en-8-ynyloxy]-tetrahydro-2*H*-pyran (**5**) was alkylated with propyl magnesiumbromide through a Cahiez-Fürstner cross-coupling reaction [16, 17] to provide 2-[(*Z*)-tetradec-10-en-8-ynyloxy]-tetrahydro-2*H*-pyran (**7**) in 75 % yield. Thus, the entire fourteen carbon skeleton of the pheromone (**1**) has been achieved (**Scheme 3**).

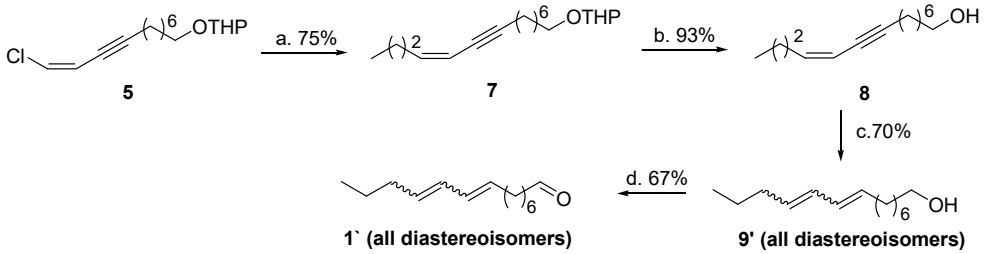

Scheme 3. Synthesis of 8,10-tetradecadienal (**1`**). *Reagents and catalysts:*
a) 1. *n*-Pr-Br (**6**), Mg (1.2 eq.), I_2, THF, reflux 2h; *n*-PrMgBr was added to a solution of $Fe(acac)_3$ (0.01 eq.), NMP, THF, **b)** *p*-TsOH (0.01 eq.), MeOH; c) $LiAlH_4$ (4 eq.), diglyme, 125-130^{0}C, 4 h; d) PCC (1.35 eq.), DCM, r.t., 4 h

Deprotection of (*Z*)-enynol **7** after Boom's procedure [18] (*p*-TsOH as catalyst) in methanol gave (*Z*)-tetradec-10-en-8-yn-1-ol (**8**) in 93 % yield.

The (*Z*)-enynol **8** was reduced to the corresponding diene **9'** according to the method of Rossi [13], with $LiAlH_4$ in diglyme at 125-130°C, to give a mixture of four isomers. Thus, it has been observed that the (*Z*)-double bond at position 10 of the enynol undergoes isomerization to the more stable *E*-diastereoisomer to give (8*E,*10*E*)-tetradeca-8,10-dien-1-ol. The identification of isomers was assumed based on the literature data [4] and GC-MS analysis. Thus the mixture of **9'** consisted of 43 % of (Z,E), 29% (E,Z), 9% (Z,Z) and 19% (E,E), RT (ZE,EZ,ZZ,EE)= 17.42,17.61,17.71,17.88. The isomeric compounds thus obtained were oxidized with PCC (pyridinium chlorochromate) [19] in CH_2Cl_2 to the corresponding aldehydes **1'** with a diastereomeric ratio, *ZE*:*EZ*:*ZZ*:*EE* = 49:27:7:17, identified by GC analysis with retention time, RT (*ZE*,*EZ*,*ZZ*,*EE*) = 16.51,16.72,16.82,16.99. (**Scheme 3**) [20].

The ratio of diastereoisomers was determined by GC-MS (**Figure 1)** and the presence of isomers mixture was confirmed by NMR analysis (**Figure 3**). The identification of the diastereoisomers was assumed based on the studies of Svatoš [4] and Kalinova [5].

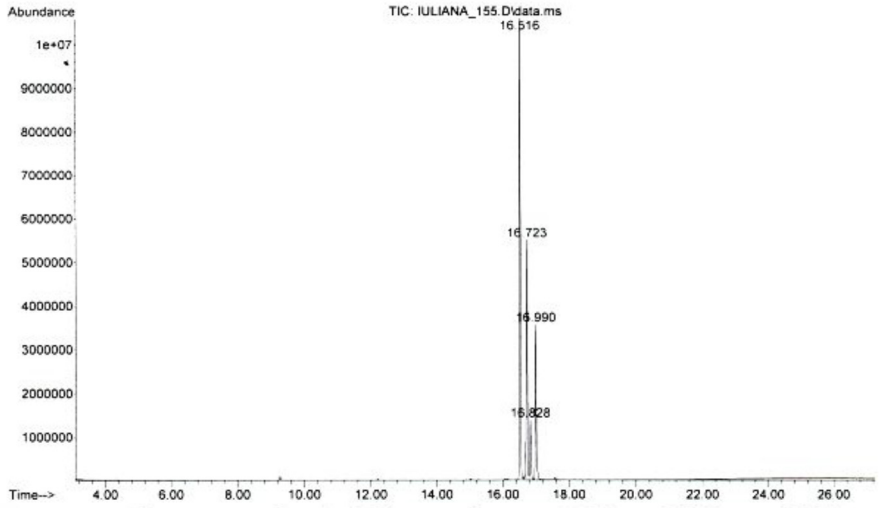

peak #	R.T. min	first scan	max scan	last scan	PK TY	peak height	corr. area	corr. % max.	% of total
1	16.516	3834	3857	3887	BV	10557251	222723127	100.00%	49.372%
2	16.723	3905	3916	3934	VV	5453140	119213475	53.53%	26.426%
3	16.828	3934	3946	3977	VV 2	1362504	31054191	13.94%	6.884%
4	16.990	3977	3993	4041	VB	3546226	78124090	35.08%	17.318%

Figure 1. GC chromatogram of synthesized 8,10-tetradecadienal (**1'**) as a mixture of all four diastereomeric forms

2. Synthesis of (8*E*,10*Z*)-tetradeca-8,10-dienal (1)

We have succeed to develop a very reliable method to synthesize the pure (8*E*,10*Z*)-Tetradeca-8,10-dienal (**1**) diastereoisomer, following a C5+C2+C7 carbon chain strategy. The key step was the stereoselective *cis*-reduction of the triple bond by H_2/P-1 Ni boride according to the Brown method [21]. Borane reduction [22] led to a degradation of the compound in the presence of acetic acid. In our case the reduction with borane of 400 mg of (*E*)-enynol **8** gave only 90 mg (22.5% yield) of the corresponding diene **9**.

The synthesis method of the pure (8*E*,10*Z*)-tetradeca-8,10-dienal (**1**) diastereoisomer also used protected bromide compound **3**. In order to avoid the *E*-reduction with lithium aluminium hydride, which gave an isomeric mixture, we have decided to employ (*E*)-cloroenyne **12** as coupling partner. This was obtained in good yield and high stereoisomeric purity by Sonogashira cross-coupling reaction of the 1-pentyne (**11**) with commercial *trans*-1,2-dichloroethylene in the presence of $Pd(PPh_3)_3Cl_2$ and CuI as catalysts in piperidine in THF (**Scheme 4**).

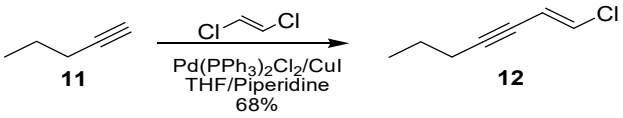

Scheme 4. Synthesis of (*E*)-1-chlorohept-1-en-3-yne (**12**)

Further, the alkylation of (*E*)-chloroenyne **12** with the corresponding Grignard reagent, obtained from 2-(9-bromoheptyloxy)-tetrahydro-2*H*-pyran (**3**) and Mg/I2/THF, in the presence of iron catalyst, after Cahiez cross-coupling reaction [16], afforded (*E*)-enyne **13** in moderate yield and high diastereoisomeric purity. Thus, the entire skeleton of fourteen carbon atoms has been reached after a C5+C2+C7 chain strategy (**Scheme 5**).

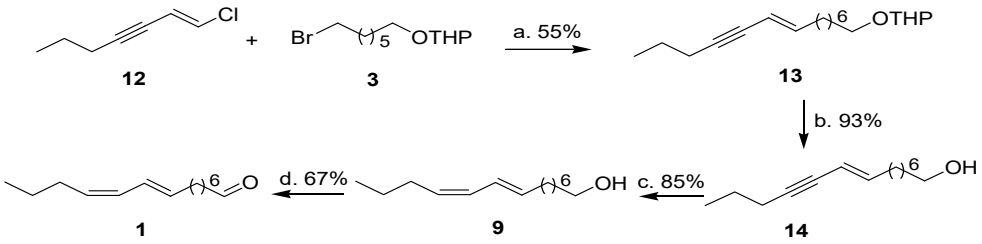

Scheme 5. Synthesis of (8*E*,10*Z*)-Tetradeca-8,10-dienal (**1**). *Reagents and conditions*: **a.** Mg (1.2 eq.), I_2, THF, reflux, 2h, Grignard formed was added to a solution of $Fe(acac)_3$ (0,01 eq.), NMP, THF, r.t.; **b.** *p*-TsOH, MeOH, r.t., over night; **c.** H_2/P-1 Ni boride, 1 atm., r.t., 4h; **d.** PCC (1.35 eq.), DCM, r.t., 4 h

After deprotection of 2-((*E*)-Tetradec-8-en-10-ynyloxy)-tetrahydro-2H-pyran (**13**), the prepared (*E*)-Tetradec-8-en-10-yn-1-ol (**14**) was hydrogenated in the presence of H_2/P-1 Ni boride [21] to the corresponding (8*E*,10*Z*)-tetradeca-8,10-dienol (**9**) in high yield (85%) and high stereoisomeric purity (> 95% from GC-MS analysis). Corey oxidation [19] of (8*E*,10*Z*)-tetradeca-8,10-dienol (**9**) with PCC (pyridinium chlorochromate) in CH_2Cl_2 gave the desired pheromone component (8*E*,10*Z*)-tetradeca-8,10-dienal (**1**) in good yield (67%) and high diastereoisomeric purity (> 99% from GC-MS analysis **Figure 2**).

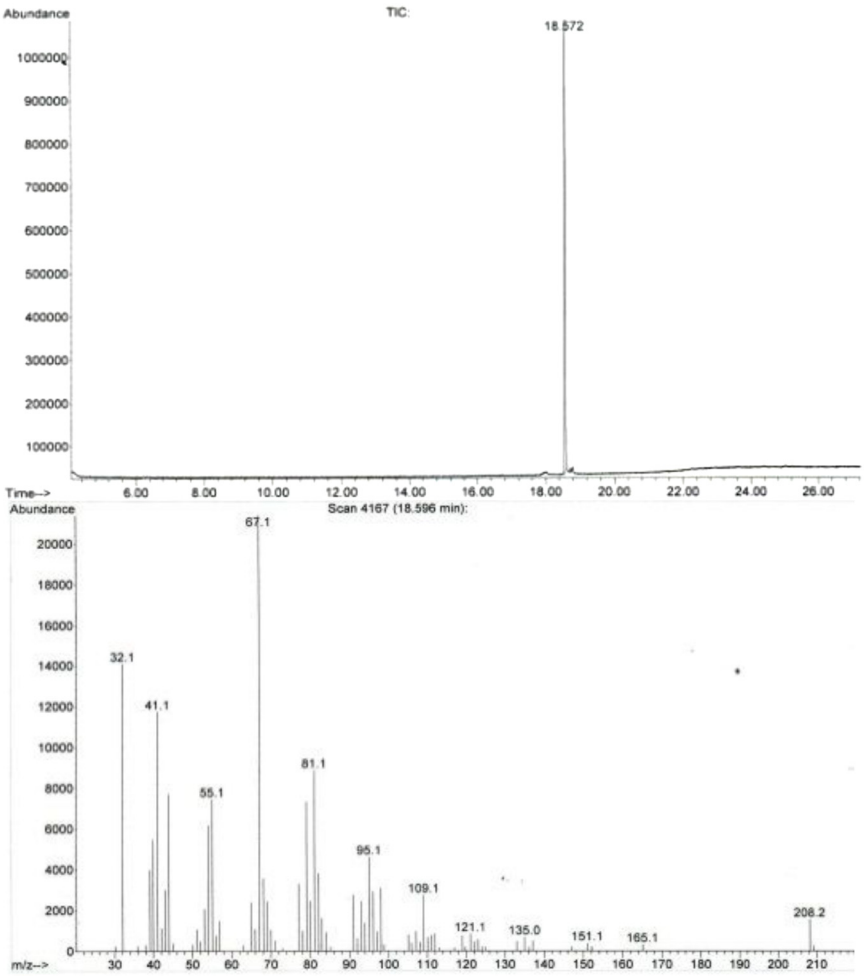

Figure 2. GC-MS analysis of (8*E*,10*Z*)-tetradeca-8,10-dienal (**1**)

The compounds **5**, **13** and **14** obtained by Sonogashira coupling reaction, respectively by Grignard reaction, were identified by GC-MS analysis, and the yield of the reaction was calculated from the obtained chromatograms.

Purification of 2-((*E*)-Tetradec-8-en-10-ynyloxy)-tetrahydro-2H-pyran (**13**) and (E)-Tetradec-8-en-10-yn-1-ol (**14**) is quite difficult due to the presence of by-products, for this reason these intermediates were used without any purification.

The ^{1}H-NMR spectrum of the pure isomer (**1**) has clear signals for the four dienic protons (b), while the signals in the mixture of isomers are overlapped (a) due to the presence of all four isomers with different intensity (**Figure 3**).

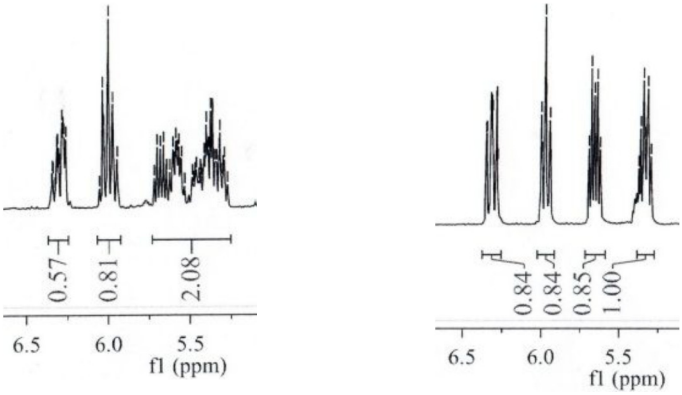

a) Mixture of diastereoisomer **1`** b) Pure (8*E*,10*Z*)-tetradeca-8,10-dienal (**1**)

Figure 3. Fragment of ^{1}H-NMR (400 MHz, $CDCl_3$) δ (ppm) 5.35-6.29 of 8,10-tetradecadienal (**1`**) and (8*E*,10*Z*)-tetradeca-8,10-dienal (**1**), 4 protons of the conjugated diene

Although the structure of the compounds *ZE*:*EZ*:*ZZ*:*EE* was elucidated by physico-chemical analysis [4], and the action of these was tested in the wind tunnel by Svatoš [4], the field trials (experiments) in nature may differ from those in the laboratory.

3. The efficiency of pheromone variants in field trials for capturing adults of *Cameraria ohridella*

In order to obtain a new formulation of the pheromone we have developed three pheromone variants, which have been tested in the field experiments. Variant F1 was loaded with 0.1 mg of isomers mixture, variant

F2 with 0.5 mg and variant F3 with 0.1 mg of pure active substance (F2 contains the same quantity of active as F3). The field experiments revealed that the variant F3 loaded with 0.1 mg of pure active pheromone has a net superior attractiveness to the other variants. The increase in the concentration of isomers has reduced the attractiveness of the *Cameraria* males. From the Svatoš analysis [4], it can be observed that the (*Z,Z*) isomer may have a negative effect on the pheromonal bait, thus assuming that the increase in the concentration of this in excess can have an antagonistic effect, as shown in Table 1, a decrease by half of F2 catches with 0.5 mg/lure compared to the variant F1 with the same compounds but with 0.1 mg isomers/lure (**Figure 4**).

Table 1. The captures of *Cameraria ohridella* males for blends F1, F2, F3

Repetition	Variant formulation*	Capture no. of *Cameraria ohridella* males					TOTAL No. of males
		4.07 2018	23.07 2018	31.07 2018	4.09 2018	24.09 2018	
R1	F1 - 0,1 mg isomeric mixture	1320	1628	2100	2000	227	**7275**
	F2 - 0,5 mg isomeric mixture	548	408	311	2849	11	**4127**
	F3 - 0,1 mg pure isomer	2600	3979	2700	6300	244	**15823**
R2	F1 - 0,1 mg isomeric mixture	2250	1790	1980	1260	57	**7337**
	F2 - 0,5 mg isomeric mixture	528	835	1420	2080	67	**4930**
	F3 - 0,1 mg pure isomer	2300	3778	2840	5160	92	**14170**

*The variant formulation of *Cameraria ohridella* blend: F1 = 0,1 mg/bait isomeric mixture, F2 = 0,5 mg/bait isomeric mixture, F3 = 0,1 mg/bait pure compound.

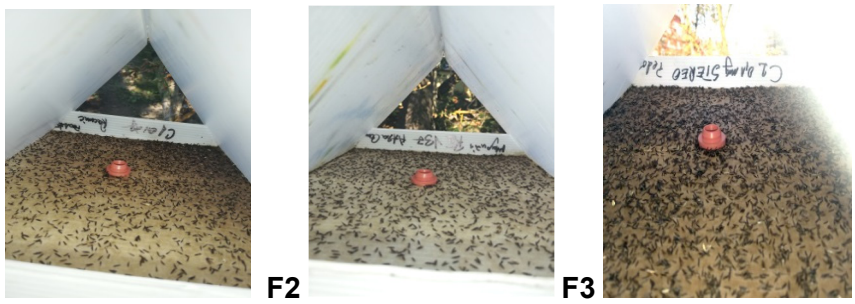

Figure 4. The catches of *Cameraria ohridella* in the traps of variants F1, F2, F3

The graph analysis presented in **Figure 5** shows that there are significant differences between the three pheromone variants (p = 0.0003). However, the Duncan analysis shows that there are no significant differences

between F1 and F2 assortment. Due to the fact that over 75% of the data recorded using pheromone variant F3 had higher values than the other two variants, this pheromone variant is significantly different from the other two variants.

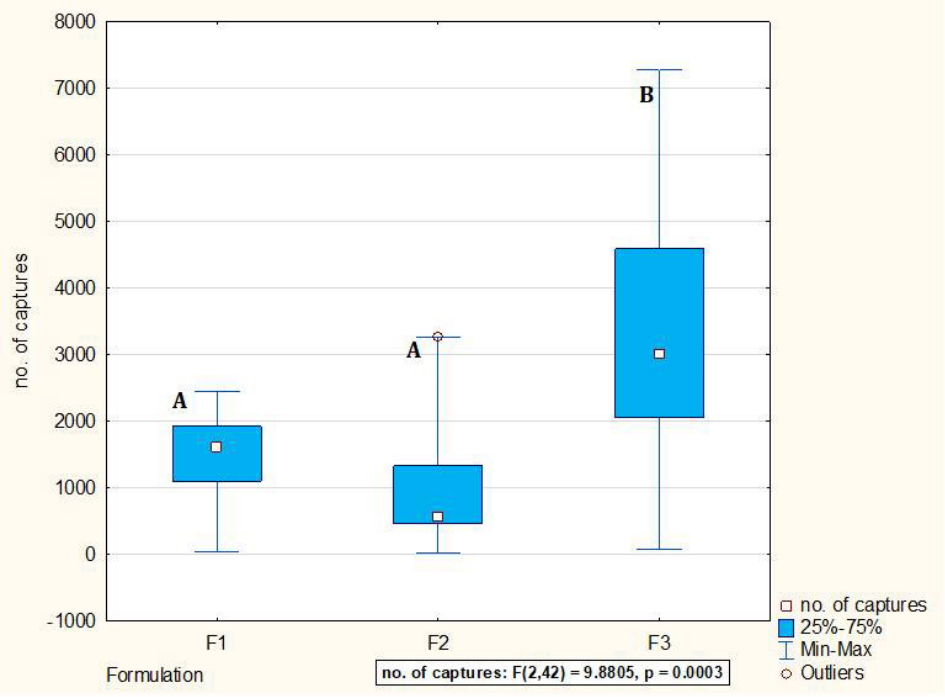

Figure 5. Pheromonal variants efficiency in capturing adult *Cameraria ohridella*

The records started on 04.07.2018 and were completed on 24.09.2018. There is a gradual increase in the average number of shots until the beginning of September and then in the third decade of captures it decreases greatly at just a few doses.

Compared to the average of the experiment, it can be seen that the number of catches in pheromone F3 exceeded this value at all observation data, except of course the last reading at which adult flight drops significantly (**Figure 6**).

There is a significant increase in catches, especially at the beginning of September. This is mainly due to the efficiency of pheromone variant F3 (**Table 1** and **Figure 7**).

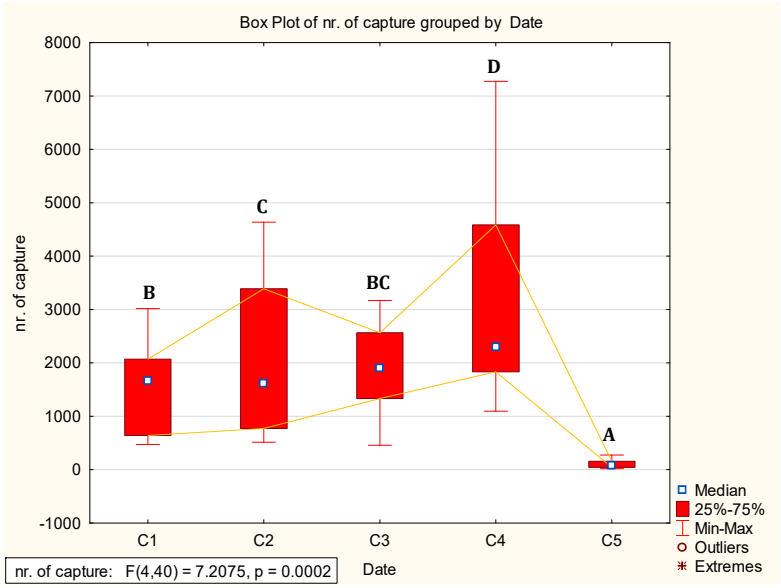

Figure 6. Evolution of catches depending on the date on which they were made

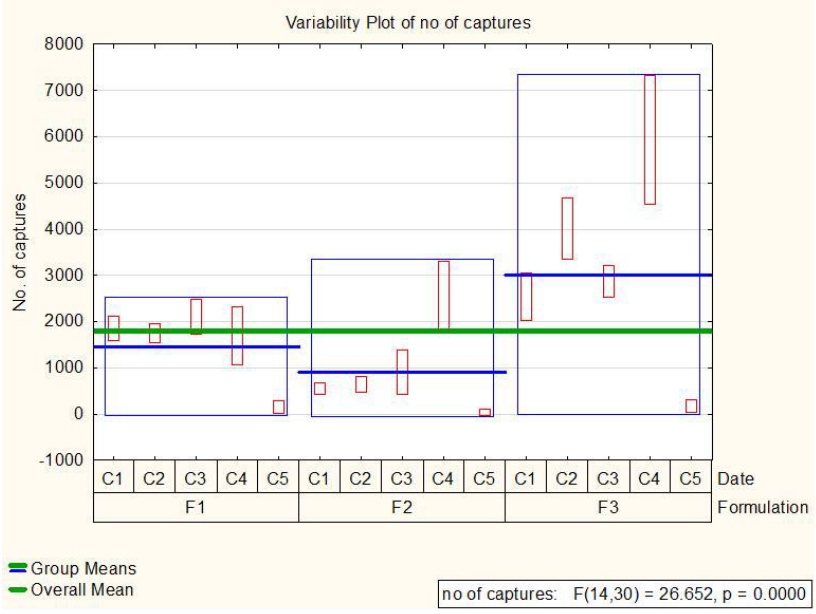

Figure 7. Number of pheromone-captured digits and reading data

The effectiveness of pheromone F2 is only demonstrated at the time of the maximum flight of these pests. On average, this pheromone has been shown to have lower efficiency than pheromone F1, with other readings being very small.

CONCLUSIONS

In conclusion, in this research work we describe a versatile stereoselective method for the synthesis of pure (8*E*,10*Z*)-tetradeca-8,10-dienal using cross-coupling reactions in the key steps after a C5+C2+C7 carbon chain strategy and a *Z*-reduction with crucial importance. The described methods were successfully applied on a large scale for production purposes in our production plant. Based on the field experiments, a new formulation of the pheromone lure was obtained for the product atraCAM, which employ a much smaller amount of the pheromone.

EXPERIMENTAL SECTION

Synthesis. All reaction products were analysed by GC-MS and NMR spectroscopy. Electron impact (70 eV) mass spectra were obtained on Hewlett-Packard MD 5972 GC-MS respectively on a GC-MS Shimadzu QP 2010 Plus instruments. GC analyses were performed on a Hewlett-Packard HP 5890 gas chromatograph. A HP-5MS capillary column (30 m x 0.25 mm x 0.33 μm) and helium gas were used for separations. ^{1}H-NMR (400 MHz or 600 MHz) and ^{13}C-NMR (101 MHz or 151 MHz) spectra were recorded at room temperature in $CDCl_3$ on a Bruker Advanced 400MHz/600MHz spectrometer, using the solvent line as reference. Thin layer chromatography (TLC) was performed on silica gel 60 F254 TLC plates purchased from Merck. Chemicals were purchased from Aldrich, Merck and Alfa Aesar and were used without further purification. All chemical reactions occurred in dry installations under argon stream.

Field tests. Different pheromone mixtures were tested for field activity. Delta traps, produced at the Pheromone Production Center of “Babes-Bolyai” University, “Raluca Ripan” Institute for Research in Chemistry, were used in the field trials. Red bromobutyl rubber septa 19 mm, loaded with the desired semiochemical mixture of lure in 50 μl *n*-hexane solution and 0,1% BHT (Butylated hydroxytoluene) were used for field trials. After loading, the solvent was allowed to evaporate in a hood at room

temperature for 30-45 min. Lures were wrapped in aluminium envelope and deposited in refrigerator until they were mounted in the field. The traps with pheromone were installed in different locations in the Cluj-Napoca area and in the experimental fields/park at University of Agricultural and Veterinary Medicine University. They were hung at crop canopy level ~ 150 cm above ground level, checked every 5-7 days. The pheromone bait capsule was changed every 6 weeks. Statistical analyses of trap catches from each test were compared with Duncan analysis.

***Preparation of compound* 2**

To a benzene (300 mL) solution containing 1,7-heptanediol (11.00 g, 83.33 mmol), HBr (1.2 eq., 48% aq., 8.09 g, 11.32 mL, 99.96 mmol) was added with vigorous stirring. The reaction mixture was azeotropically distilled using a Dean Stark trap to complete removal of water (about 10.55 ml). The reaction mixture was TLC checked and other 3.00 mL HBr (48% aq.) was then added and the resulted solution was allowed to stand for about 5 h. After cooling at rt, the reaction mixture was washed to neutrality with 7% aq. soln. $NaHCO_3$ 50 mL) then with water (75 mL) and, finally, with brine 75 mL). The organic layer was dried over anh. $MgSO_4$ and then evaporated to dryness under reduced pressure. Purification by flash column chromatography (silica gel, eluent *n*-hexane: Et_2O = 2:1 v/v, visualization with H_2SO_4 in ethanol, R_f = 0.68) gave the desired compound 7-bromoheptan-1-ol (**2**) (12.9 g, 79% yield with respect to 1,7-heptanediol) as pure (>98%) compound.

7-Bromoheptan-1-ol 2. Incolor liquid. 1H-NMR (400 MHz, CDCl3): δ (ppm) 3.60 (t, 3JH,H=6.0 Hz, 2H), 3.30 (t, 3JH,H=6.0 Hz, 2H), 3.10 (br s, 1H, -OH), 1.80-2.10 (overlapped signals, 4H), 1.20-1.70 (overlapped signals, 6H); 13C-NMR (100 MHz, CDCl3): δ (ppm) 61.7, 32.9, 32.5, 32.2, 29.3, 27.7, 26.6 [23].

***Preparation of compound* 3**

A mixture of 1-bromoheptan-7-ol (**2**), (7.70 g, 39 mmol), 3,4-dihydro-2*H*-pyran (1.5 eq., 5.00 g, 58.5 mmol) and *p*-toluenesulfonic acid (0.03 eq., 222 mg, 1.17 mmol) in dichloromethane (50 mL) was stirred at room temperature for 12 h. The mixture was diluted with diethyl ether (300 mL), the organic layer was washed with 2x75 ml water and 75 ml brine. The organic layer was dried over anh. $MgSO_4$ and then evaporated to dryness under reduced pressure. Purification by flash column chromatography (silica gel, eluent *n*-hexane: Et_2O = 10:1 v/v, visualization with H_2SO_4 in ethanol, R_f = 0.57) gave the desired compound 2-(7-Bromoheptyloxy)-tetrahydro-2H-

pyran **3** (9.00 g, 83% yield with respect to 7-Bromoheptan-1-ol (**3**) as pure (>95%) compound.

2-(7-Bromoheptyloxy)-tetrahydro-2H-pyran **3**. Incolor liquid. ^{1}H NMR (400 MHz, $CDCl_3$): δ (ppm) 4.56 (t, ^{3}J = 4.0 Hz, 1H), 3.89-3.83 (m, 1H), 3.75-3.69 (m, 1H), 3.52-3.46 (m, 1H), 3.41-3.34 (m, 3H), 1.88-1.78 (overlapped signals, 3H), 1.74-1.66 (m, 1H), 1.62-1.29 (overlapped signals, 12H); ^{13}C NMR (101 MHz, $CDCl_3$): δ (ppm) 99.0, 67.7, 62.5, 34.1, 32.9, 30.8, 29.7, 28.7, 28.2, 26.2, 25.6,19.8 [7]; MS (EI, 70 eV), m/z (I_{rel}, %): M^+, 279(1), 277(<1), 250, 252(<1), 223(<1), 207, 209(<1), 177, 179(<1), 135, 137(2), 121, 123(1), 97(7), 85(100), 55(40), 41(41), 29(18).

Preparation of compound 4

Lithium acetylide ethylenediamine complex (90% pure, 2 eq., 7.00 g, 0.076 mmol) was placed in 38 mL of dry dimethyl sulfoxide (DMSO). The suspension was cooled down to 5-10 °C and after few minutes 2-(7-bromoheptyloxy)-tetrahydro-2*H*-pyran (**3**) (10.60 g, 38 mmol) was added dropwise with stirring. The reaction mixture was allowed to warm up at room temperature and stirred for 6 h, after this time, *n*-hexane (100 mL) was added and the mixture was poured on 100 g ice. The organic layer was separated and the aqueous layer was extracted with *n*-hexane (3 x 100 mL). The combined organic layers were washed to neutrality successively with 100 mL water, 50 ml dil. aq. hydrochloric acid, 100 ml water and 100 ml brine. The organic layer was dried over anh. $MgSO_4$ and then evaporated to dryness under reduced pressure. Purification by flash column chromatography (silica gel, eluent *n*-hexane: Et_2O = 10:1 v/v, visualization with H_2SO_4 in ethanol, R_f = 0.50) gave the desired compound 2-(non-8-ynyloxy)-tetrahydro-2H-pyran (**4**) (7.6 g, 90% yield with respect to heptan-1,7-diol) as pure (>95%) compound.

2-(Non-8-ynyloxy)-tetrahydro-2H-pyran **4**. Incolor liquid. ^{1}H NMR (400 MHz, $CDCl_3$): δ (ppm) 4.57-4.55 (m, 1H), 3.89-3.83 (m, 1H), 3.73 (dt, *J* = 9.6 Hz, 6.8 Hz, 1H), 3.52-3.46 (m, 1H), 3.52-3.46 (m, 1H), 3.37 (dt, *J* = 9.6 Hz, 6.8 Hz, 1H), 2.19-2.15 (m, 2H), 1.93 (t, ^{3}J = 2.6 Hz, 1H), 1.88-1.66 (m, 2H), 1.62-1.23 (overlapped signals, 13H); ^{13}C NMR (101 MHz, $CDCl_3$): δ (ppm) 98.9, 84.9, 68.2, 67.7, 62.5, 30.9, 18.5, 29.8, 29.1, 28.8, 28.5, 26.2, 25.6, 19.8 [24]; MS (EI, 70 eV), m/z (I_{rel}, %): M^+-1, 223(<1); 169(<1); 151(<1); 128(<1); 115(<1); 101(27); 85(100); 67(27); 55(40); 41(78); 29(27).

Preparation of compound 5

A solution of $PdCl_2(PPh_3)_2$ (0.05 eq., 1.37 g, 1.7 mmol) in tetrahydrofuran (THF) (234 mL) was added to a solution of (*Z*)-1,2-dichloroethene (5 eq., 16.66 g, 171 mmol) and terminal alkyne **4** (7.7 g, 34.37 mmol) (under argon).

After 10 min., piperidine (3 eq., 8.76 g, 103 mmol) was added. The reaction mixture became clear yellow. After 15 min. CuI (0.1 eq., 0.656 g, 3.4 mmol) was added. The reaction mixture turned from blue to green, then to orange and finally a white precipitate was formed. The mixture was stirred at room temperature overnight. The solid was filtrated and the precipitate washed with diethyl ether (3X100 mL) and then poured into water (100 mL). The combined organic layers were washed with ammonia solution 50 mL and successively with 100 mL water, and 100 ml brine. The organic layer was dried over anh. $MgSO_4$ and then evaporated to dryness under reduced pressure. Purification by flash column chromatography (silica gel, eluent *n*-hexane: Et_2O = 10:1 v/v, visualization with UV lamp and H_2SO_4 in ethanol, R_f = 0.48) gave the desired compound *2-((Z)-11-chloroundec-10-en-8-ynyloxy)-tetrahydro-2H-pyran (**5**)* (6.4 g, 67% yield with respect to *2-(Hept-6-ynyloxy)-tetrahydro-2H-pyran* (**4**) as pure (>95%, isomeric purity) compound.

2-((Z)-11-chloroundec-10-en-8-ynyloxy)-tetrahydro-2H-pyran **5**. Brown liquid. MS (EI, 70 eV), m/z (Irel, %): 283(<1), 269(<1), 249(2), 231(<1), 211(<1), 191(<1), 177(<1), 164(2), 147(2), 131(1,5), 119(7), 105(16), 85(100), 67(20), 55(26), 41(29).

Preparation of compound 7

The synthesis of compound **7** took place in two steps, two installations were used concurrently. The first step was the formation of Grignard compound (5 eq.). The Grignard compound was prepared from Mg turnings (2.18 g, 90.48 mmol), in THF (20 mL) and I_2 crystal as an initiator. 1-Bromopropane (**6**) (10.74g, 87.35mmol) suspended in THF (50 mL) was added dropwise. The mixture was refluxed for 3h. Meanwhile, the other reaction flask was prepared by adding Z-chloroenyne **5** (5 g, 17.47 mmol), *N*-methyl-2-pyrrolidone (NMP) (17.5 mL), THF (22.3 mL) and $Fe(acac)_3$ (0.17 mmol, 0.01 eq.). The formed Grignard compound was poured under argon into a funnel and dropped over the mixture already prepared with protected Z-chloroenyne **5**. Heating and darkening of the reaction mixture were observed. The reaction mixture was stirred at room temperature overnight (TLC: eluent *n*-hexane: Et_2O = 10:1 v/v, visualization with UV lamp and H_2SO_4 in ethanol, R_f = 0.60). Water (100 mL) was added, and the organic layer was extracted with *n*-hexane (3x100 mL). The combined organic layers were washed successively with 100 mL water and 100 mL brine, until neutralization, dried over anhydrous $MgSO_4$ and evaporated under reduces pressure. The desired compound **7** (3.8 g) was obtained in 75% yield and >95% isomeric purity.

2-((Z)-Tetradec-10-en-8-ynyloxy)-tetrahydro-2H-pyran **7***.* Incolor liquid. ^{1}H NMR (400 MHz, $CDCl_3$): δ (ppm) 5.81 (dt, ^3J = 10.7, 7.4 Hz, 1H), 4.58-4.56 (m, 1H), 5.44 (dm, ^3J = 10.7 Hz, 1H), 3.89-3.84 (m, 1H), 3.73 (dt, ^3J =

9.6 Hz, 6.8 Hz, 1H), 3.52-3.47 (m, 1H), 3.38 (dt, ^3J = 9.6 Hz, 6.8 Hz, 1H), 2.33 (td, ^3J = 6.9 Hz, 2.0 Hz, 2H), 2.26 (qd, ^3J = 7.4 Hz, 1.1 Hz, 2H), 1.86-1.68 (m, 2H), 1.62-1.26 (overlapped signals, 16 H), 0.92 (t, ^3J = 7.4 Hz, 3H); ^{13}C NMR (101 MHz, $CDCl_3$): δ (ppm) 142.5, 109.5, 98.9, 94.4, 77.6, 67.7, 62.5, 32.2, 30.9, 29.8, 29.1, 28.9 (2C), 26.3, 25.6, 22.3, 19.8, 19.6, 13.9; MS (EI, 70 eV), m/z (I_{rel}, %): M^+ 292(<1), 277(<1), 263(<1), 249(<1), 233(<1), 221(<1), 208(<1), 191(1), 177(1), 161(1), 147(2), 133(3), 121(3), 108(14), 85(100), 79(34), 67(23), 55(26), 41(29).

***Preparation of compound* 8**

To a solution of the protected compound **7**, (7.19 mmol) in methanol (68 mL) *para*-toluenesulfonic acid (PTSA) (0.1 eq., 0.7 mmol) was added. After stirring for about 12 h the methanol was evaporated under reduce pressure. The residue was diluted with diethyl ether (300 mL), washed successively with 75 mL water, 75 mL $NaHCO_3$ solution and 75 mL brine, dried over anhydrous $MgSO_4$ and concentrated with a rotary evaporator. It was used in the next steps without purification or was purified on a chromatographic column with silica gel (eluent: *n*-Hex: EtOAc = 2: 1). The product **8** was obtained in 93% yield and > 95% isomeric purity.

(Z)-Tetradec-10-en-8-yn-1-ol **8***.* Incolor liquid. ^{1}H NMR (400 MHz, $CDCl_3$): δ (ppm) 5.81 (dt, ^3J = 10.7, 7.4 Hz, 1H), 5.43 (dm, ^3J = 10.7 Hz, 1H), 3.63 (t, ^3J = 6.6 Hz, 2H), 2.33 (td, ^3J = 6.9 Hz, 1.9 Hz, 2H), 2.25 (qd, ^3J = 7.4 Hz, 1.0 Hz, 2H), 2.17 (s, 1H, -OH overlapped), 1.60-1.33 (overlapped signals, 12H), 0.92 (t, ^3J = 7.4 Hz, 3H); ^{13}C NMR (101 MHz, $CDCl_3$): δ (ppm) 142.5, 109.5, 94.4, 77.6, 63.1, 32.8, 32.2, 29.0, 28.9, 25.8, 22.3, 19.6, 13.9; MS (EI, 70 eV), m/z (I_{rel}, %): M^+, 208(<1); 191(<1); 179(<1); 186(<1); 165(1); 147(1); 133(3); 121(4); 108(36); 91(48); 79(100); 67(36); 55(27); 41(34); 31(22).

***Preparation of compound* 9`. (Rossi R. method with $LiAlH_4$) [13]**

A solution of (*Z*)-enynol **8** (650 mg, 3.57 mmol) in diglyme (2 mL) under argon was added to a stirred suspension of $LiAlH_4$ (556 mg, 4 eq., 14.6 mmol) in diglyme (10 mL) at room temperature. The reaction mixture was warmed up to 125-130 ^{0}C for 15h. After cooling the suspension, cold aq. HCl (10%, 10 mL) was added to decompose the unreacted hydride. Diethyl ether (50 mL) was added and the mixture was extracted with diethyl ether (2 x 75 mL). The combined organic layers were successively washed with 50 mL water, 30 mL $NaHCO_3$ sat., and 50 mL brine. The organic layer was dried over anh. $MgSO_4$ and then evaporated to dryness under reduced pressure. Purification by flash column chromatography (silica gel, eluent *n*-hexane: EtOAc = 2:1 v/v,

visualization with UV lamp and H_2SO_4 in ethanol, R_f = 0.66) gave the desired compound 8,10-tetradecadien-1-ol (**9`**) (525 mg, 75% yield with respect to *(Z)-Tetradec-10-en-8-yn-1-ol (**8**)* (>90%, chemical purity) compound.

8,10-Tetradecadien-1-ol **9`**. Incolor liquid. MS (EI, 70 eV), m/z (I_{rel}, %): M^+, 210(<1); 192(<1); 181(<1); 167(<1); 150(1); 135(3); 121(9); 110(42); 95(31); 81(85); 67(100); 54(87); 41(64); 31(26).

Preparation of compound 12

(*Z*)-1,2-Dichloroethene (5 eq., 16.66 g, 171 mmol) and 1-pentyne (**11**) (3.34 g, 34.37 mmol) were added under stirring to a solution of catalyst $PdCl_2(PPh_3)_2$ (0.05 eq, 1.37 g, 1.7 mmol) in THF (234 mL). After 10 min. piperidine (3 eq., 8.76 g, 103 mmol) was added. The reaction mixture became clear yellow and was stirred for 15 min. CuI (0.1 eq, 0.656 g, 3.4 mmol) was then added. After the reaction mixture turns from blue to green then to orange, a white precipitate was formed and a yellow solution. The mixture was stirred at room temperature overnight and filtered. The precipitate was washed with diethyl ether (100 mL) and poured into water (100 mL), and then was extracted with diethyl ether (3 x 100 mL). The combined organic layers were successively washed with ammonia solution, water and brine until neutral pH. The combined organic layers were washed with ammonia solution 50 mL and successively with 100 mL water, and 100 ml brine. The organic layer was dried over anh. $MgSO_4$ and then evaporated to dryness under reduced pressure. Purification by flash column chromatography (silica gel, eluent *n*-hexane: Et_2O = 10:1 v/v, visualization with UV lamp and H_2SO_4 in ethanol, R_f = 0.92) gave the desired compound **12** (3 g, 68% yield with respect to 1-pentyne (**11**) as pure (>80%, chemical purity) compound.

(E)-1-Chlorohept-1-en-3-yne **12**. Brown liquid. ^{1}H NMR (400 MHz, $CDCl_3$) δ (ppm) 6.45 (d, ^3J = 13.6 Hz, 1H), 5.94 (dt, , ^3J = 13.6 Hz, 1H), 2.29 (dt, 2H), 1.57 (m, 2H), 1.0 (t, 3H); ^{13}C NMR (101 MHz, $CDCl_3$): δ (ppm) ^{13}C NMR (101 MHz, $CDCl_3$) δ (ppm) 128.7, 114.3, 92.67, 75.78, 21.9, 21.4, 13.5; MS (EI, 70 eV), m/z (I_{rel}, %): M^+, 128(35); 115(1); 133(7); 99(43); 91(100); 86(15); 77(89); 63(69); 61(15); 51(33); 39(33); 29(14).

Preparation of compound 13

The synthesis of the compound was performed in two steps and two installations were used concurrently. In the first stage, the Grignard -compound was prepared by dropwise addition of a solution of 2-(7-bromoheptyloxy)-tetrahydro-2*H*-pyran (**3**) in THF (20 mL) to a suspension of Mg turnings (0.860 g, 35.8 mmol) in THF (2 mL) and one crystal of I_2 for activation. The

suspension was refluxed for 3h. Meanwhile, the other reaction flask was prepared by adding anhydrous **12** (1.76 g, 13.7 mmol), NMP (13.7 mL), THF (17.5 mL) and $Fe(acac)_3$ (49 mg, 0.01 eq.). The formed Grignard compound was poured under argon into a funnel and dropped over the mixture already prepared with the protected (*E*)-chloroenyne **12**. Heating and darkening of the reaction mixture were observed. The reaction mixture was stirred at room temperature overnight (TLC: eluent *n*-hexane: Et_2O = 40:1 v/v, visualization with UV lamp and H_2SO_4 in ethanol, R_f = 0.54). Water (100 mL) was added, and the organic layer was extracted with *n*-hexane (3x100 mL). The combined organic layers were washed successively with 100 mL water and 100 mL brine, until neutralization, dried over anhydrous $MgSO_4$ and evaporated under reduces pressure. The desired compound **13** (2.2 g) was obtained in 55% yield and >90% isomeric purity.

2-((E)-Tetradec-8-en-10-ynyloxy)-tetrahydro-2H-pyran **13***.* Incolor liquid. MS (EI, 70 eV), m/z (I_{rel}, %): M^+, 292(1); 277(<1); 263(<1); 249(1); 235(<1); 219(1); 205(<1); 191(1); 177(1); 161(1); 147(2); 133(4); 121(5); 105(13); 85(100); 67(22); 55(39); 41(33).

Preparation of compound 14

To a solution of the protected compound **13** (2.2 g, 7.5 mmol) in methanol (70 mL) PTSA (0.1 eq., 140 mg, 0.7 mmol) was added. The mixture was stirred at rt overnight. The solvent was removed on a rotary evaporator. The residue was diluted with diethyl ether (200 mL), washed successively with 75 mL water, 50 mL $NaHCO_3$ solution and 75 mL brine, dried over anhydrous $MgSO_4$ and concentrated with a rotary evaporator. The compound can be used in the next steps without purification or can be purified on a silica gel column (Eluent: *n*-Hex: EtOAc = 2:1 v/v, visualization with UV lamp and H_2SO_4 in ethanol, R_f = 0.72). The deprotected compound **14** was obtained in 93% yield and 80% chemical purity.

(E)-Tetradec-8-en-10-yn-1-ol **14**. MS (EI, 70 eV), m/z (I_{rel}, %): M^+, 208(<1); 193(<1); 179(1.5); 165(1); 151(8); 133(3); 121(8); 105(23); 91(56); 79(100); 67(29); 55(34); 41(37); 31(23).

Preparation of compound 9 (Brown CA method, 1970) [21]

The hydrogenation reaction was performed with H_2 at rt and 1 atm. in a personalized installation. The installation is composed by a burette with a three-way valve filled with hydrogen, a water tank to maintain pressure in the burette, a hydrogen bottle, a flow regulator, a magnetic stirred, and a Schlenk flask. First $Ni(OAc)_2 \cdot 4H_2O$ (0.1556 g, 0.625 mmol) was dissolved in ethanol

95% (95 mL) under stirring (eventually by slight heating), then a solution of $NaBH_4$ (0.0238 g, 0.625 mmol) in ethanol 95%, 0.625 mL was added in hydrogen current and the catalyst NiP_2 was formed. The reaction mixture became darker and warm. Ethylenediamine (0.0835 mL, 1.39 mmol) was added dropwise, and the stirring was stopped. (*E*)-tetradec-8-en-10-yn-1-ol (**14**) (1.05 g, 5 mmol) was added in one portion and the hydrogen stream was closed. All the external valves were closed, the valve from the burette was opened and the stirring was started until no hydrogen consumption was observed (theoretical consumption 119 ml H_2, depending on the temperature and the atmospheric pressure). Then, the valve of the burette was closed and the flow regulating valve was opened. The reaction mixture was diluted with diethyl ether (50 mL) and filtered on a G4 filter funnel, the precipitate was washed with 200 mL diethyl ether. The filtrate was washed successively with 75 mL water, and 75 mL brine, to neutral pH. The organic layer was dried over anh. $MgSO_4$ and then evaporated to dryness under reduced pressure. Purification by flash column chromatography (silica gel, eluent *n*-hexane: Et_2O = 2:1 v/v, visualization with UV lamp and H_2SO_4 in ethanol, R_f = 0.4) gave the desired compound (8*E*,10*Z*)-tetradeca-8,10-dien-1-ol (**9**) (0.89 g, 85% yield with respect to compound **14** as pure (> 95% isomeric purity) compound.

(8E,10Z)-Tetradeca-8,10-dien-1-ol **9** [6]. ^{1}H NMR (400 MHz, $CDCl_3$) δ (ppm) 6.29 (ddd, $^3J_{trans}$ = 15.1 Hz, 11.0 Hz, 0.9 Hz, 1H), 5.94 (t, ^3J = 11.0 Hz, 1 H), 5.63 (dt, $^3J_{trans}$ = 15.1 Hz, 7.3 Hz, 1 H), 5.33-5.26 (m, 1 H), 3.62 (t, ^3J = 6.6 Hz, 2 H), 2.16-2.05 (overlapped signals, 4 H), 1.58-1.49 (overlapped signals, 4 H), 1.42-1.25 (overlapped signals, 8 H), 0.91 (t, ^3J = 7.3 Hz, 3 H); ^{13}C NMR (101 MHz, $CDCl_3$) δ (ppm) 134.6, 130.0, 128.8, 125.8, 63.1, 32.8, 29.9, 29.45, 29.4, 29.3, 25.8, 23.0, 13.9; MS (EI, 70 eV), m/z (I_{rel}, %): M^+, M^+, 210(6); 194(<1); 179(<1); 163(<1); 149(1); 135(3); 121(6); 109(10); 95(22); 81(51); 67(100); 55(43); 41(51); 31(22).

Preparation of compound **1**

PCC (1.35 eq., 2.49 g) was added to a solution of alcohol **9** or **9`** (8.57 mmol, 1.8 g) in CH_2Cl_2) (137 mL) at room temperature. The reaction mixture was stirred at room temperature for 3-5 h and the progress of the reaction was checked by thin-layer chromatography (TLC). CH_2Cl_2 was removed by a rotary evaporator and the residue was diluted with 300 mL diethyl ether, filtered on a G4 filter funnel, washed successively with 75 mL water and 75 mL brine until a neutral pH. The organic layer was dried over anh. $MgSO_4$ and then evaporated to dryness under reduced pressure. Purification by flash column chromatography (silica gel, eluent *n*-hexane: Et_2O = 10:1 v/v, visualization with UV lamp and H_2SO_4 in ethanol, R_f = 0.7) gave the desired

compound (8*E*,10*Z*)-Tetradeca-8,10-dienal (**1**) (1.2 g, 67% yield with respect to compound **9** or **9`** as pure (> 95% isomeric purity or isomers mixture) compounds.

(8E,10Z)-Tetradeca-8,10-dienal **1** [4, 6]. ^{1}H NMR (400 MHz, $CDCl_3$) δ (ppm) 9.76 (t, ^{3}J = 1.8 Hz, 1H), 6.29 (ddd, $^{3}J_{trans}$ = 16.0 Hz, 1 H), 5.95 (t, ^{3}J = 10,0 Hz, 1 H), 5.63 (dt, $^{3}J_{trans}$ = 16 Hz, 1 H), 5.35-5.27 (m, 1 H), 2.44-2.40 (m, 2 H), 2.17-2.04 (overlapped signals, 4 H), 1.66-1.59 (m, 2 H), 1.44-1.23 (overlapped signals, 8 H), 0.91 (t, ^{3}J = 8 Hz, 3 H); ^{13}C NMR (101 MHz, $CDCl_3$) δ (ppm) 203.04, 134.44, 130.15, 128.81, 125.94, 44.02, 32.89, 29.88, 29.28, 29.13, 29.03, 23.02, 22.14, 13.93; MS: (EI, 70 eV), m/z (I_{rel}, %): M^+, 208(3); 179(<1); 165(<1); 151(1); 135(1); 121(4); 109(9); 95(18); 81(41); 67(100); 55(31); 41(48).

ACKNOWLEDGMENTS

The authors thank Dr. Mircea Varga for his field test work. This work was supported by „Babes-Bolyai" University, „Raluca Ripan" Institute for Research in Chemistry, Pheromone Production Center.

REFERENCES

1. G. Deschk; N. Dimic; *Acta Entomol. Jugosl.,* **1986**, *22*, 11–23.
2. T. Perju; I. Oltean; I. Oprean; M. Ecobici; *J. Centr. Eur. Agric.,* **2004**, *4*, 331-336.
3. D. I. Șandru; *Sănătatea plantelor*, **1998**, *6*, 29-34.
4. a. A. Svatoš; B. Kalinová; H. Michal; J. Kindl; O. Hovorka; H. Ivan; *Tetrahedron Lett.*, **1999b**, *40*, 7011-7014. b. A. Svatoš; B. Kalinová; H. Michal; J. Kindl; O. Hovorka; H. Ivan; *IOBC wprs Bulletin*, **2001**, *24*, 5-12.
5. B. Kalinová; A. Svatoŝ; J. Kindl; O. Hovorka; I. Hrdý; J. Kuldová; M. Hoskovec; *J. Chem. Ecol.*, **2003**, *29*, 387-404.
6. M. Hoskovec; A. Šaman; A. Svatoš; *Collect. Czech. Chem. Commun.*, **2000**, *65*, 511-523.
7. W. Francke; S. Franke; J. Bergmann; T. Tolasch; M. Subchev; A. Mircheva; T. Toshova; A. Svatos; B. Kalinova; Z. Karpati; G. Szocs; M. Toth; *Naturforsch. C: Biosci.*, **2002***, 57*, 739-752.
8. R. Marcia de Figueiredo; R. Berner; J. Julis; T. Liu; D. Türp; M. Christmann; *J. Org. Chem.*, **2007**, *72*, 640-642.
9. L. Gânscă; S. Maxim; I. Ciotlăuș; A. Andreica; I. Oprean; *Rev. Roum. Chim.*, **2011**, *56*, 895-899.
10. P. Chourreu; O. Guerret; L. Guillonneau; E. Gayon; G. Lefèvre; *Org. Process Res. Dev.*, **2020**, *24*, 1335−1340.
11. J. Grodner; *Tetrahedron,* **2009**, *65*, 1648-1654.

12. K. Sonogashira; Y. Tohda; N. Hagihara; *Tetrahedron Lett.,* **1975**, *16*, 4467-4470.
13. a. R. Rossi; A. Carpita; *Synthesis*, **1977**, *8*, 561-562. b. A. Parenty; J. -M. Campagne; *Tetrahedron Lett.*, **2002**, *43,* 1231-1233.
14. T. Turki; S. Khamri; H. Amri; *J. Soc. Chim. Tunis*., **2007**, *9*, 17-22.
15. W. N. Smith; O. F. Beumel Jr.; *Synthesis*, **1974**, *1*, 441-442.
16. G. Cahiez; H. Avedissian*; Synthesis*, **1998**, *8*, 1199-1205.
17. A. Fürstner; A. Leitner; M. Méndez; H. Krause; *J. Am. Chem. Soc.*, **2002**, *124*, 13856-13863.
18. J. H. V. Boom; J. D. M Herschied; C.B. Reese; *Synthesis*, **1973**, 167-169.
19. E.J. Corey; J.W. Suggs; *Tetrahedron Lett.*, **1975**, *16*, 2647-2650.
20. I. Vasian; I. Oprean; T. Florian; I. Oltean; Ecomoni utilizati in protectia plantelor, Editura Bioflux, **2018**, ISBN 978-606-8887-28-9, chapter 1.
21. C. A. Brown; *J. Org. Chem.*, **1970**, *35*, 1900-1904.
22. H. C. Brown; Organic Syntheses via Boranes; Wiley-Interscience: New York, **1975**.
23. A. Singh; M. L. Sharma; J. Singh; *Indian Journal of Chemistry*, **2010**, *49B*, 1648-1652.
24. O. Loreau; A. Maret; J. M. Chardigny; J. L. Sébédio; J. P. Noël; Chemistry and Physics of Lipids, **2001**, *110*, 57-67.

STUDIA UBB CHEMIA, LXVI, 4, 2021 (p. 225-233)
(RECOMMENDED CITATION)
DOI:10.24193/subbchem.2021.4.16

INFLUENCE OF FILLER, MONOMER MATRIX AND SILANE COATING ON COMPOSITE RESIN ADHESION

MIHAELA PĂSTRAV[a], MARIOARA MOLDOVAN[b], ANDREA CHISNOIU[a,*], CODRUȚA SAROȘI[b], FILIP MIUȚA[b], OVIDIU PĂSTRAV[a], ADA DELEAN[a], RADU CHISNOIU[a]

ABSTRACT. This study compared marginal microleakage in case of two dental composite resins: a consecrated commercial Bis- GMA resin- IPS Empress Direct (Ivoclar Vivadent, Lichtenstein)- group A, and a recently introduced Bis- MEPP resin - Gaenial A'Chord (GC R&D Japan)- group B and to observe, by means of scanning electron microscopy (SEM), the differences between these two restorative materials when using the same adhesive system and restorative layering technique. Microleakage testing scores were higher in IPS Empress group, but the results were not statistically validated. SEM images on group A presented a highly developed hybrid layer, while for group B resin extension intersecting the hybrid layer were observed, having a similar electronic density with the adhesive layer, which demonstrates a continuity of the nanoparticles in depth. On dentin-composite interface increased number of gaps and fissures were observed, comparing to enamel-composite interface. The result from the research showed that the two compared composite resin present similar properties in terms of adhesion and microleakage.

Keywords: *composite resin, Bis-GMA, Bis-MEPP, silane coating.*

INTRODUCTION

For the past several decades, resin composites have been proposed as an alternative to amalgam, gold and ceramic restorations due to their unique optical, electrical, physical, chemical, and magnetic properties [1].

Fundamentally, the composition of dental composite is represented by an inorganic filler, organic matrix and coupling agent. The fillers represent

[a] *Iuliu Hatieganu University, Faculty of Dental Medicine, 8 Babes str., RO-400012, Cluj-Napoca, Romania.*
[b] *Babes-Bolyai University,Raluca Ripan Instutite for Research in Chemistry, 31 Fantanele str., RO-400294 , Cluj-Napoca, Romania.*
* *Corresponding author: maria.chisnoiu@umfcluj.ro.*

the main component which ameliorates the poor mechanical and physical properties of the unfilled resin [2]. Therefore, the ratio of resin/filler content directly affects the material's properties and increasing the filler content will increase wear resistance, strength and will reduce shrinkage properties. The components and ratio of the resin matrix, the shape, size and content of filler and the silane treatment will affect the viscosity improving the handling characteristics of the material, ensuring interlocking between filler particles and interfacial interaction between filler particles and the resin matrix [3].

The organic matrix consists of several monomers, such as BisGMA (2,2-bis[p-(2'-hidroxy-3'-methacryloxypropoxy)phenyl]- propane), UDMA (urethane dimethacrylate), TEGDMA (trietylenglycol dimethacrylate), DMAEMA (dimethylaminoethyl methacrylate- mostly used as an additive as light curing accelerator), BisMEPP (bisphenole A ethoxylate dimethacrylate) and various additives (photoinitiators-camphoroquinone, inhibitors, stabilizers). After the polymerization reaction of the monomer mixture of resin composites, an organic matrix as a three-dimensional cross-linked network is formed [4].

Physical and chemical properties of nanostructured composite materials can be adjusted by controlling the composition and the relative sizes of various components.

The composite nanostructures with High-performance Pulverized CERASMART (HPC) filler and Full- Coverage Silane Coating (FSC) technologies combine properties of the original components but also possess novel and collective performances which are not seen in the original constituents.

The silane coating of the FSC, creates a strong bond between particles in the resin matrix, resulting in a high wear resistance, color retention and excellent radiopacity for long-lasting and natural-looking restorations. HPC filler technology enables improved handling with minimal gaps, providing substantial marginal integrity for virtually eliminating the occurrence of secondary caries. In addition, its ceramic content contributes to the material's durability and ease of handling [5].

The present study was designed to compare marginal microleakage in case of two dental composite resins (a recently introduced Bis- MEPP resin - Gaenial A'Chord (GC R&D Japan) and a consecrated commercial Bis-GMA resin- Ips Empress Direct (Ivoclar Vivadent, Lichtenstein), and to observe, by means of scanning electron microscopy (SEM), the differences between these two restorative materials when using the same adhesive system and restorative layering technique.

RESULTS AND DISCUSSION

Microleakage testing showed higher number of samples with score 0 in group B, comparing to group A. Differences were also observed in case of samples with scores > 0, but the results were not statistically validated (Figure 1, Table 1).

Marginal microleakage

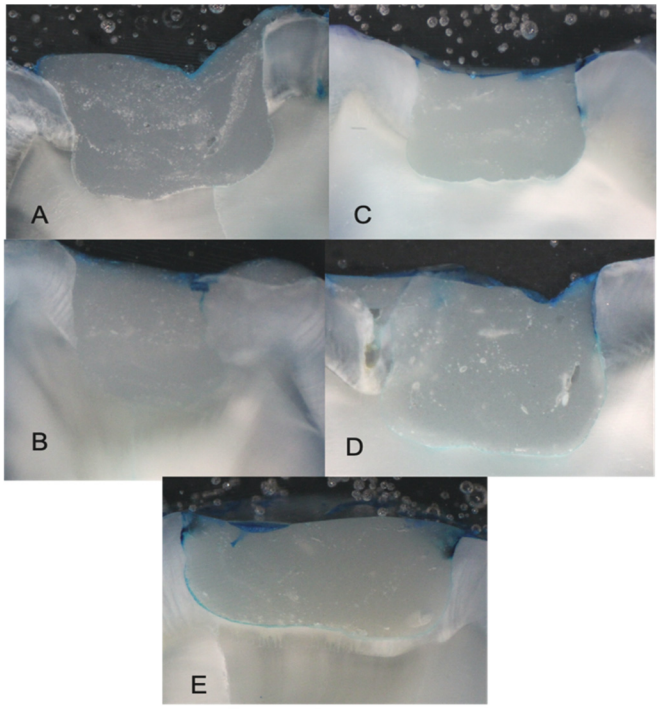

Figure 1. Representative images of degrees of microleakage for Gaenial A'Chord. (A-no evidence of dye penetration, B-1st degree, C-2nd degree, D-3rd degree, E-4th degree).

Table 1. Microleakage scores of the two composite groups

Group	score 0 N (%)	score 1 N (%)	score 2 N (%)	score 3 N (%)	score 4 N (%)	p
A (IPS Empress)	19 (63.4)	6 (20)	1 (3.33)	3 (10)	1 (3.33)	0.206
B (G-aenial A'Chord)	22 (73.34)	4 (13.34)	2 (6.67)	1 (3.33)	1 (3.33)	

SEM analysis

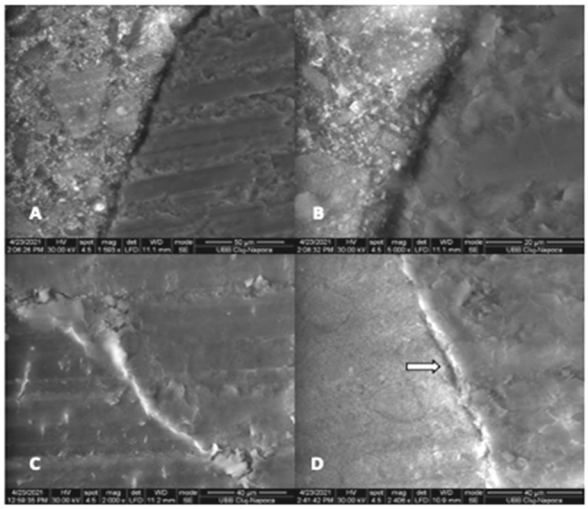

Figure 2. Representative images of the interface composite-dental tissues of the two composite groups. A- Enamel – IPS Empress direct interface; B- Dentin- IPS Empress direct interface; C- Enamel- Gaenial A'Chord interface; D- Dentin- Gaenial A'Chord interface. Arrow- cracks and gaps at material- dentin interface.

SEM analysis was performed to observe the adhesion between the coronary restorative materials and dental tissues for the situations when no microinfiltration was observed (score 0), as well as for the situations when the dye penetrated the composite/dental tissue interface (scores >0) (Figure 2).

In case of samples from group A with score 0 completely adapted adhesive interface was observed, indicating highly developed hybrid layers. SEM images show a uniform and efficient polymerization on the entire restored cavity. The hybrid layer presents a thin, homogenous and electron dense structure with relatively uniform width (~ 2 μm), closely following the dental surface and forming a hybrid layer (5-10 μm) which penetrates the dentin (Figure 2-B).

In case of samples from group B and score 0, resin extension intersecting the hybrid layer have a similar electronic density with the adhesive layer, which demonstrates a continuity of the nanoparticles in depth. The periphery of the dentinal canals was also hybridized and the hybrid layer was extended on the entire depth of the demineralized area (Figure 2-C).

In samples with score higher than 0, interfacial fissures between the dentin and the hybrid layer were observed on samples from group B. On dentin- composite interface increased number of gaps and fissures were observed, comparing to enamel-composite interface, indicating that dentin adhesion is probably influenced by higher number of factors comparing to enamel adhesion (Figure 2-D).

In case of Bis GMA resin a porous texture was observed on the SEM photographs, which led to the conclusion that the remaining monomer enabled water molecules to gain better access to the polymer matrix through this porous structure (Figure 2-B).

Characteristics of dental resin composites depend upon several factors including monomer composition, coating chemistry, filler content and irradiation protocol [6,7,8].

The resin matrix influences the properties of dental composites. In the current study the samples contained a Bis-GMA resin and a Bis MEPP resin. Bis-GMA resin in group A present two hydroxy groups which are capable of forming intermolecular bonding. These characteristics were observed on SEM images showing a deep penetration into the dentinal tubules. Previous studies present that the composites based on dimethacrylates with hydroxy groups (Bis-GMA) present improved mechanical properties under dry conditions, comparing to Bis-MEPP resin. Under wet conditions, these composites showed a relatively lower flexural strength than the composites based on dimethacrylates without hydroxy groups (Bis MEPP) [9]. However, Bis-MEPP-based resin presented a lower water sorption and high colour stability comparing with BisGMA resin in a study realized by Mizukami et al [10].

Resin-based dental composites contain filler materials such as barium glass, silica, apatite and a silane coupling agent. The latter enhances the bonding between the filler particles and the resin matrix. The filler particles added to the resin matrix also improve the physical and mechanical properties of the resin composite. Moreover, the addition of fillers reduces volume shrinkage after polymerization, and improves the aesthetic appearance and radiopacity [11].

Generally, surface of inorganic filler is hydrophilic, while resin monomer is hydrophobic. It is important for filler to be treated by silane coupling agent because the interface between filler and resin matrix impact on physical, chemical and mechanical properties of composite. Previous study by Higuchi et al, reported that FSC treated glass filler showed significantly less hydroxy-groups than glass filler of control resin and was uniformly covered with silane coupling agents. Results could be from higher chemical reaction rate between SiOH on the surface of filler and silane coupling agents. FSC has potential to produce higher physical, chemical and mechanical properties on composite product line [12].

From a clinical point of view, composite restoration requires good mechanical properties, such as a high viscosity of the composites and reduced polymerization shrinkage to avoid marginal micro infiltration, but also adequate aesthetics and wear resistance. Therefore, the ratio of resin/filler content directly affects the material's properties. Increasing the filler content results in enhanced wear resistance, strength and reduced shrinkage properties [2].

The fillers are the inorganic component of resin composites which are incorporated to enhance the mechanical properties and reduce polymerization shrinkage of resin composites. Pre-polymerized fillers were introduced to improve the filler volume fraction. They are processed using ground cured composite containing a variety of submicron particles [13].

In the present study, SEM images analysis showed that composite resin in group B (containing HPC fillers) which ensured the formation of the hybrid layer presented a deep penetration into the dentinal tubules. The addition of PPFs also aids in reducing the polymerization shrinkage and provides improved polishing when compared to conventionally filled resin composites [14-16].

CONCLUSIONS

Within the limitations of the current study, the material filler content as well as the resin matrix composition and silane coating influences microleakage of dental composites. Both investigated materials presented similar properties in terms of adhesion and microleakage.

EXPERIMENTAL SECTION

Preparation of the samples

Sixty maxillary and mandibular molars were included in the study. The teeth were extracted on orthodontic indication maximum 4 weeks prior to the study. All teeth were caries and filling free, without coronal destruction of other etiology and maintained in distilled water to ensure adequate hydration conditions.

Cavity preparation

On the occlusal surface of each tooth a Black class I cavity was realized with maximum depth of 3 mm. The preparation was made using 0,12 round turbine burs (MDT, Mc Drill Technology, Parma, Italy) on the enamel layer and 0,14 round tungsten carbide contra-angle burs (Dendia, Dendia GmbH, Austria). The bur was changed after every 5 cavity preparations.

The depth of the cavity was measured from the center of central fissure using UNC 15 probe (Hu-Freidy Mfg. Co. Inc., IL, USA). The width of the cavity was standardized using a divider and scale.

Sample distribution

The prepared 60 teeth were randomly divided into 2 groups of thirty teeth each based on the restorative material as Group A – Ips Empress Direct (n=30) and Group B –Gaenial A'Chord (n=30).

Table 2. Chemical composition of the two materials

Ips Empress Direct (Ivoclar Vivadent, Lichtenstein)	Nanohybrid	UDMA Bis-GMA TEGDMA Barium glass filler 0.4 μm Prepolymer 1-10 μm Ytterbium trifluoride 100 nm
GC Gaenial A'Chord (Dental Products, Alsip, IL, USA)	Microhybrid	UDMA, Bis-MEPP TEGDMA Silicon dioxide (16 nm), Strontium glass (200 nm), Pigment

Figure 3 shows the chemical structure of Bis-MEPP and Bis-GMA monomers.

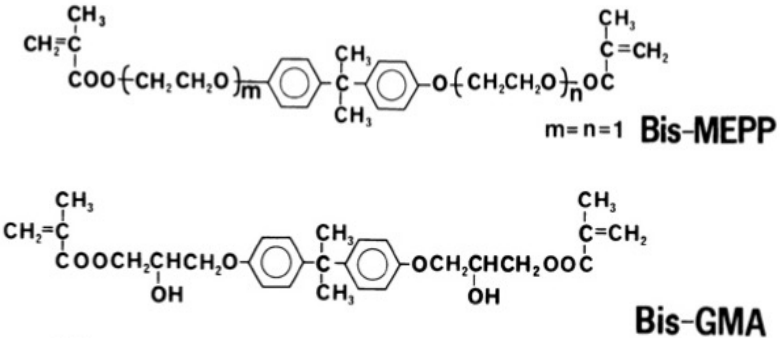

Figure 3. Chemical structure of Bis-MEPP and Bis-GMA monomers.

Restoration technique

As adhesive system, we used a 3 steps system, considering that this is the golden standard in dental adhesion. For both groups (A, B), the enamel was etched for 30 seconds and dentin for 15 seconds using 37% Meta Etchant Gel (Meta Biomed Co. Ltd), then washed and gently dried for approx.

5 sec. The new G2 - BOND Universal (GC Europe) was applied, according to the manufacturer instructions – first the Primer, for 10 sec., with a microbrush and dried for 5 sec., then the Bond, spread evenly using a gentle stream of air and light cured for 10 seconds, using a LED light-curing lamp (Translux-Wave, Kulzer). Teeth were then filled (using oblique layering technique and with 1 mm thick increments and light-curing for 20 seconds) with a nanohybrid composite IPS Empress Direct (Ivoclar, Vivadent, Lichtenstein G) - (group A) and G-aenial A'Chord (GC R&D, Japan)- (group B).

The shade of the composite was different from the tooth in order to facilitate the assessment. In the end, the restorations were finished and polished with red and yellow ring burs and rubber cups.

All specimens were thermocycled for 1000 cycles (5/55ºC, 30 seconds) in Eppendorf Master cycler gradient (Eppendorf AG, Hamburg, Germany). After thermocycling, apices of the teeth were sealed with a layer of sticky wax, and the roots surfaces were covered with two coats of nail polish. All samples were immersed in 2% methylene blue dye for 24 hours. Following immersion teeth were washed with distilled water then dried. Then they were embedded in acrylic resin (Duracryl Plus, SpofaDental) and, later, sectioned mesio-distally using the microtome (IsoMet TM1000, Buehler, IL, USA). There were selected those teeth slices that have not damages after cutting. Each tooth slice was 1.5 mm thick.

For marginal microleakage assessment, the cut sections were observed under 20X magnification and the area of maximum dye penetration was considered. For the magnification, a stereomicroscope was used (Zeiss CL 1500 ECO) and each sample was photographed using a digital photo camera (Canon EOS 1300D).

Two examiners scored extent of dye penetration using an ordinal scale (0-4) by consensus. Examiners were blind to material and/or technique used.

The scoring criteria:

0 – no evidence of dye penetration

1 – dye penetration along the axial cavity walls up to 1/3

2 – dye penetration along the axial cavity walls up to 2/3

3 – dye penetration along the whole axial cavity wall

4 – dye penetration on the pulpal wall

Samples for scanning electron microscopy (SEM) evaluation were prepared similar as for optical microscopy, in order to evaluate the enamel-composite and dentin-composite interface, as well as enamel and dentin structure. All measurements were performed using (SEM) QUANTA 133 microscope system (FEI Company USA). Several units of image magnification were used and all registrations were performed on enamel- composite interface and dentin-composite interface.

The statistical analysis was conducted using MedCalc Statistical Software version 18.11 (MedCalc Software bvba, Ostend, Belgium; http://www.medcalc.org; 2018). Qualitative data were analyzed with Chi-square and Fisher exact test and a 5% level of significance.

REFERENCES

1. C. P. Turssi; J. L. Ferracane; K. Vogel. *Biomat.,* **2005,** *26,* 4932-4937.
2. L. D. Randolph; W. M. Palin; G. Leloup; J. G. Leprince. *Dental Mat.*, **2016** *32*, 1586-1599.
3. J. H. Lee; C. M. Um; I. Lee. *Dental Materials*, **2006**, *22*, 515-526.
4. A. C. Obici; M. A. C. Sinhoreti; E. Frollini; L. C. Sobrinho; S. Consani. *Mat. Res.* **2004**, *7*, 605–610.
5. GC Group. *Br Dent J* **2020**, *229***,** 695.
6. L. Feng; B. I. Suh. *Macromol Chem and Phys,* **2007**, *208*, 295-306.
7. N. Emami; K. J. Söderholm. *J Mat Sci*, **2005,** *16,* 47-52.
8. A. Peutzfeldt; E. Asmussen. *J Dent Res.* **2005,** *84,* 659-62.
9. M. Kawaguchi; T. Fukushima; T. Horibe. *Dent Mat J*, **2009,** *8,* 40-45.
10. H. Mizukami; H. Kobayashi; M. Niizuma; Y. Sugai; R. Iketani; Y. Yamada; M. Manabe. *IADR/AADR/CADR*, **2019**, ID: 3652.
11. C.Y.K. Lung; J.P. Matinlinna. *Dent Mat,* **2012**, *28*, 467-477.
12. K. Higuchi; D. Usuki; T. Ueno; T. Kumagai. *IADR/AADR/CADR*, **2019**, 3678-3679.
13. J. L. Ferracane; W.V. Giannobile. *J Dent Res.* **2014**, *93,* 1185-1186.
14. P. Senawongse; P. Pongprueksa. *J Esthet Restor Dent.* **2007**, *19*, 265-273.
15. J. A. Arsecularatne; N. R. Chung; M. Hoffman. *Biosurf. Biotribol.* **2016,** *2*, 102-113.
16. M. Moldovan; R. Balazsi; A. Soanca; A. Roman; C. Sarosi; D. Prodan, M. Vlassa; I. Cojocaru; V. Saceleanu; I. Cristescu. *Materials,* **2019**, *12***,** 2109-2123**.**

STUDIA UBB CHEMIA, LXVI, 4, 2021 (p. 235-251)
(RECOMMENDED CITATION)
DOI:10.24193/subbchem.2021.4.17

IN VITRO STUDIES ON ENAMEL AND DENTIN ADHESION OF COMPOSITE RESINS IN PATIENTS WITH CHRONIC KIDNEY FAILURE AND HEALTHY PATIENTS

GEORGIANA FLORENTINA GHEORGHE[a], OANA ELENA AMZA[a], IOANA SUCIU[a], BOGDAN DIMITRIU[a], LILIANA GARNEATA[b], ANDREA MARIA CHISNOIU[c,*], DOINA PRODAN[d], MIHAELA PĂSTRAV[c,‡], SANDA ILEANA CIMPEAN[c,‡], RADU MARCEL CHISNOIU[c]

ABSTRACT. The objective of this study was to compare the structure, morphology and enamel-composite and dentin-composite interface in the teeth of patients with chronic renal failure, predialysis and healthy patients, using two methods: atomic force microscopy (AFM) and scanning electron microscopy (SEM). Most of the tested enamel specimens showed a mixed type of failure. The AFM examination indicated a deep engraving for enamel and dentin in sick people compared to healthy people. The average value of the roughness (Ra) in enamel and dentin from healthy patients were significantly different ($p < 0.001$) than from enamel and dentin in patients with renal failure. Regarding the SEM images, the dentin-composite material interface in teeth extracted from healthy patients, has uniformity, compared to the dentin-composite interface in teeth extracted from predialysis patients where a discontinuous hybrid layer with some gaps was identified.

Keywords: *atomic force microscopy, scanning electron microscopy, enamel-composite interface, dentin-composite interface, predialysis.*

[a] *Carol Davila University of Medicine and Pharmacy, Faculty of Dentistry, 17-23 Calea Plevnei, Bucharest, Romania.*
[b] *Carol Davila University of Medicine and Pharmacy, 8 B-dul Eroilor Sanitari, Bucharest, Romania.*
[c] *Iuliu Hatieganu University, Faculty of Dental Medicine, 8 Babes str., RO-400012, Cluj-Napoca, Romania.*
[d] *Babes-Bolyai University,Raluca Ripan Institute for Research in Chemistry, 31 Fantanele str., RO-400294 , Cluj-Napoca, Romania.*
* *Corresponding author: maria.chisnoiu@umfcluj.ro.*
‡ *Contributed equally to the study with the first author and can be considered main author.*

INTRODUCTION

The chronic renal failure is a condition whose incidence is constantly increasing, the consequence being the presentation of a large number of patients requesting dental treatments. Moreover, the orodental status considerably influences the evolution and prognosis of the underlying condition. For a correct dental treatment of this category of patients, the dentist must know and understand the systemic and oral manifestations that this condition has and implicitly its treatment.

The alterations in the hard tissue mineralisation of patients with chronic kidney disease are well known today. They are caused by disorders in the metabolism of calcium and phosphorus, increased parathyroid activity and abnormal metabolism of vitamin D [1]. The bone-like changes in dentin were not recognized until 1983, when a study showed the existence of a thinner layer of predentin in the teeth of patients with chronic kidney disease [2]. Moreover, dental changes such as hypoplasia of the enamel of temporary but also permanent teeth, narrowing or calcification of the pulp chamber have been reported [3, 4].

It is evident from the literature that the atomic force microscopy (AFM) and scanning microscopy (SEM) are commonly used methods for the analysis of dental structures [12, 16]. They are especially useful in the studies of the dentin collagen network and changes caused by different chemical agents on the dentin [17]. The changes in the intertubular and peritubular dentin caused by interaction with phosphoric acid, adhesion, structure and other changes in the restoration process can be investigated [13]. It can also be seen the interaction of dentinal adhesives with the hard tissues of the tooth. AFM has been applied in ultramorphological investigations of superficial and deep dentin and its mechanical properties or the identification of the functional width of the enamel-dentin junction [14, 15]. This method also provides information about the roughness of dentin, enamel and restorative materials, which we tried to highlight in this study [16, 17].

Taking into account the previous information but also the fact that modern aesthetic restorative dentistry is completely dependent on the quality and performance of adhesion of dental materials to the dental substrate, there is the possibility of changes in the teeth of patients with chronic renal failure.

The aim of the current study was to compare the structure, morphology and enamel-composite and dentin-composite interface in the teeth of patients with chronic renal failure, predialysis and healthy patients, using two methods: atomic force microscopy (AFM) and scanning electron microscopy (SEM).

RESULTS AND DISCUSSION

The observed morphological characteristics of the teeth are described qualitatively and quantitatively. For the quantitative assessment, imaging data and software package available for image analysis were used. In order to meet the statistical nature of the quantitative analysis, images were collected from a variety of different locations (enamel, dentin, composite, and the composite/dentin, enamel/composite interface) on the tooth specimens. Several samples of each type, collected from different patients, were also used. Below are the images obtained and the scanning parameters for each image and the roughness analysis (Figures 1-12).

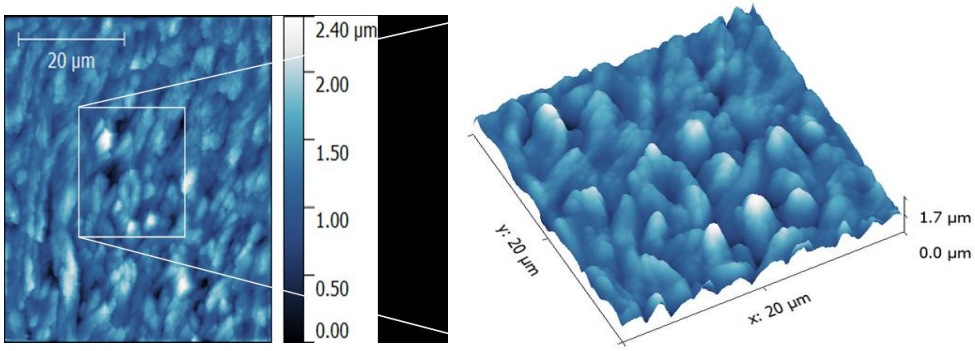

Figure 1. Bidimensional and tridimensional AFM image of the enamel on a healthy patient.

Table 1. Roughness parameters for scanned areas showed in Figure 2

Enamel	Av [µm]	Ra(Sa) [nm]	RMS (Sq) [nm]	Sk	Sku
20 × 20 µm^2	0.91	161 (±2.26)	210	0.00574	0.778
50 × 50 µm^2	1.202	241(±4.67)	307	0.0118	0.367

The analysis of the surfaces presented in **Figures 1-9** leads to the data presented in **Tables 1**, **2**, **3**, **4**, **5** and **6** where the parameters presented refer to:

- Av – mean of heights;
- Ra (Sa) arithmetic mean roughness;
- RMS (Sq) mean square deviation (standard deviation) calculated by the formula

$$S_q = \sqrt{\frac{1}{MN}\sum_{k=0}^{M-1}\sum_{l=0}^{N-1}[z(x_k, y_l)]^2}$$

A positive correlation was registered for the parameter Ra and RMS, for which higher values indicate a greater variation of the surface topography.

- S_{sk} asymmetry of the height distribution histogram (*skewness*) calculated by the formula

$$S_{sk} = \frac{1}{MN \cdot S_q^3}\sum_{k=0}^{M-1}\sum_{l=0}^{N-1}[z(x_k, y_l)]^3$$

For $S_{sk} = 0$, the height distribution is symmetric (Gaussian distribution, totally random variations). The positive asymmetry, Ssk > 0, indicates a smooth surface with peaks above average, while the negative values *Ssk* < 0 indicate the presence of many below average heights (pits or depressions in the surface).

- S_{ku} flattening the distribution curve of the height values (*kurtosis*) calculated by the formula

$$S_{ku} = \frac{1}{MN \cdot S_q^4}\sum_{k=0}^{M-1}\sum_{l=0}^{N-1}[z(x_k, y_l)]^4$$

reflects the number of extreme heights, '*peakedness'* of the surface topography and is a measure of the degree of flattening or vaulting of the distribution curve.

Value $S_{ku} = 0$ shows a normal Gaussian distribution, which is a Mesokurtic distribution. An area with a small number of extreme heights (several very high peaks or very deep valleys) will have a large S_{ku}, as opposed to an area with mostly moderate heights, which will generate small or negative S_{ku}.

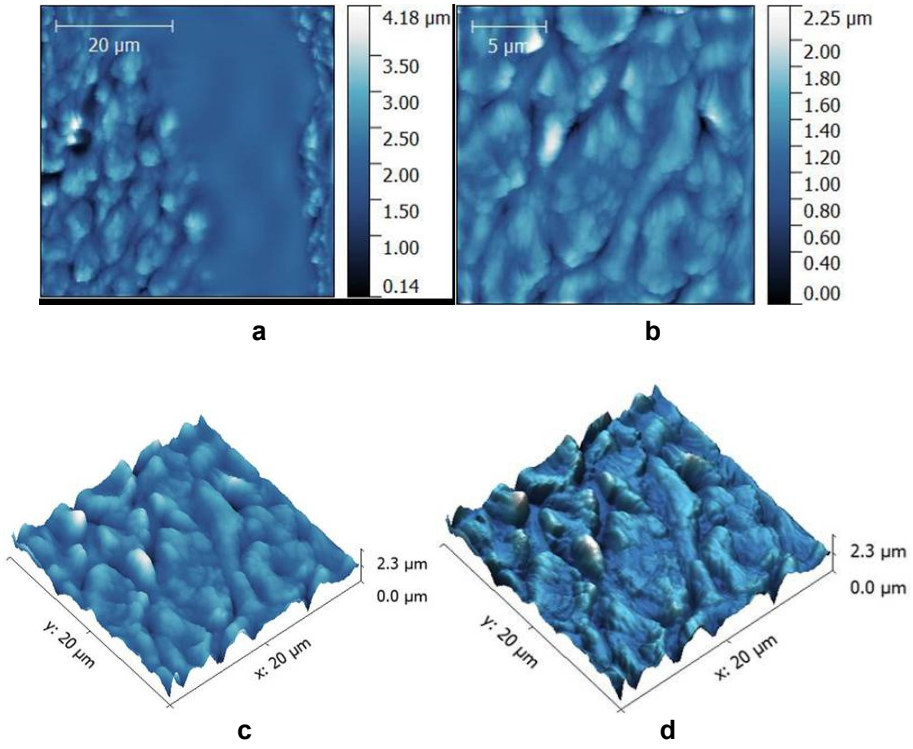

Figure 2. AFM images: a,b- bidimensional; c,d – tridimensional of the enamel from the enamel-composite area for extracted teeth in healthy patients.

Table 2. Roughness parameters for the scanned areas showed in Figure 3

	Av [µm]	**Ra(Sa) [nm]**	**RMS (Sq) [nm]**	**Sk**	**Sku**
Enamel					
20 × 20 µm^2	1.177	195 (± 3.56)	252	-0.197	0.824
50 × 50 µm^2	1.134	212 (±4.76)	269	-0.26	0.212
Composite					
50 × 50 µm^2	0.776	140 (±2.15)	180	-0.129	0.571
20 × 20 µm^2	1.295	112 (± 5,12)	147	-0.414	1.43

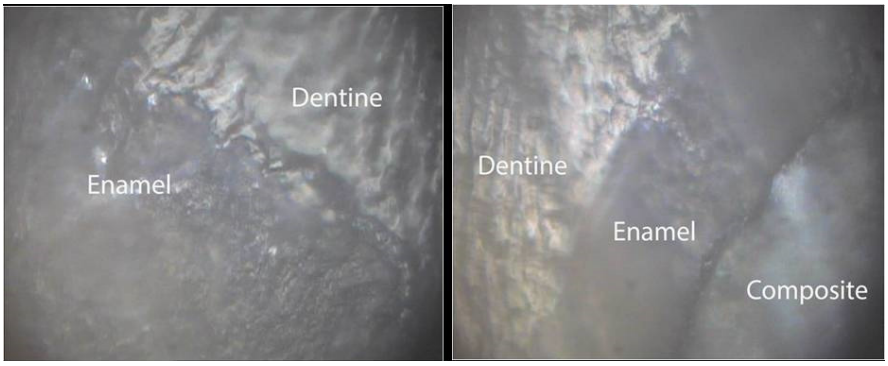

Figure 3. Images of the contact areas: a – enamel-dentin; b – enamel-dentin-composite for extracted teeth in healthy patients

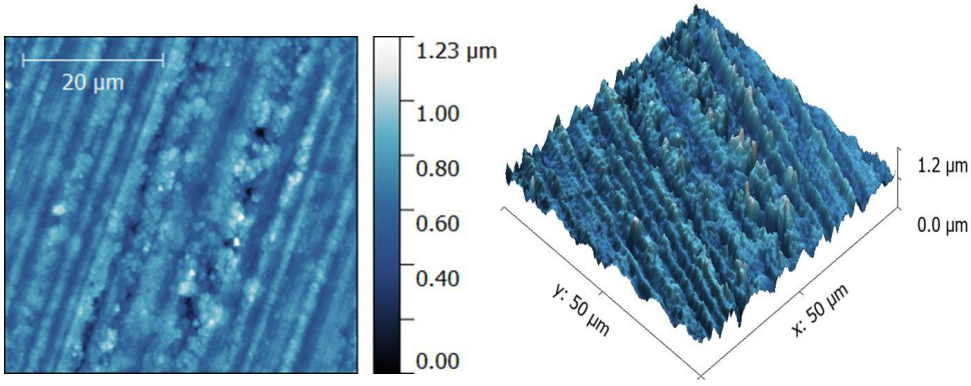

Figure 4. Bidimensional and tridimensional AFM images for *Tetric EvoCeram Bulk Fill* composite used in this study.

Table 3. Roughness parameters for the scanned areas showed in Figure 4

Composite	**Av** [µm]	**Ra(Sa)** [nm]	**RMS (Sq)** [nm]	**Sk**	**Sku**
50 × 50 µm^2	0.6733	95.5 (± 3,45)	122	-0.231	0.654
20 × 20 a µm^2	0.3269	68.2 (± 2,13)	88.2	0.081	0.284

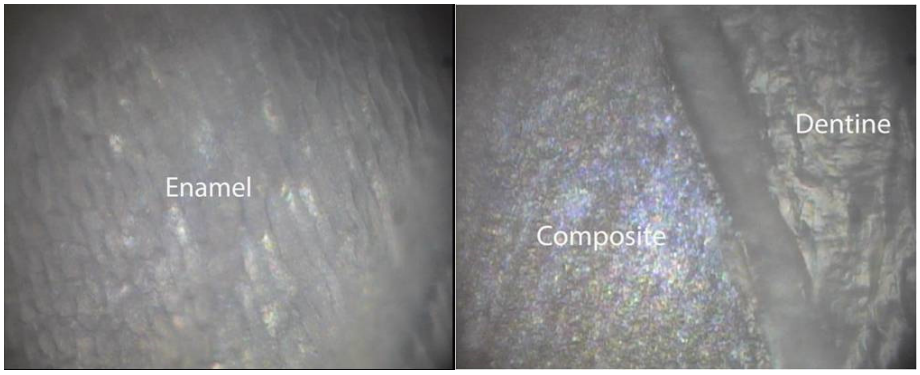

Figure 5. Enamel and composite-dentin interface images, registered on extracted teeth from predialysis patients

Comparing the images in **Figures 1** and **6** it is observed that the surface of the healthy tooth is much more uniform and significantly homogeneous. The AFM images show us similar morphological features, clearly emphasizing that the tooth enamel was not damaged during microscopy recordings.

Roughness is a very important surface property for technological applications, being used for quantitative analysis of changes that the surface may suffer; for example, surface erosion will naturally lead to an increase in its roughness.

Following the assessment of tooth enamel from healthy patients, we found that the surface is irregular, with an average height of 190 nm. The arithmetic roughness of 161 nm and the mean square deviation of 210 nm are large values indicating a rough surface. The value 0.00574 of the parameter Ssk indicates an almost symmetrical distribution (**Figure 1a**), a surface with generally random variations in height, and the value Sku 0.778 also indicates the presence on this surface of several lower heights (**Figure 1b**).

The images for tooth enamel from predialysis patients also show irregular surfaces. The Ra value of 178 nm and the average square roughness Sq 231 nm indicate a rougher surface than the enamel from healthy teeth. The negative value of -0.273 of the S_k parameter indicates a surface with recesses, and Sku 0.54 indicates a lower distribution of height values compared to the enamel from healthy teeth.

The assessment of the morphology and roughness at the enamel/ composite contact surface (**Figure 7**) for teeth extracted from predialysis patients indicates an irregular surface, and the negative value of the parameter S_k indicates a surface with recesses for both composite and enamel.

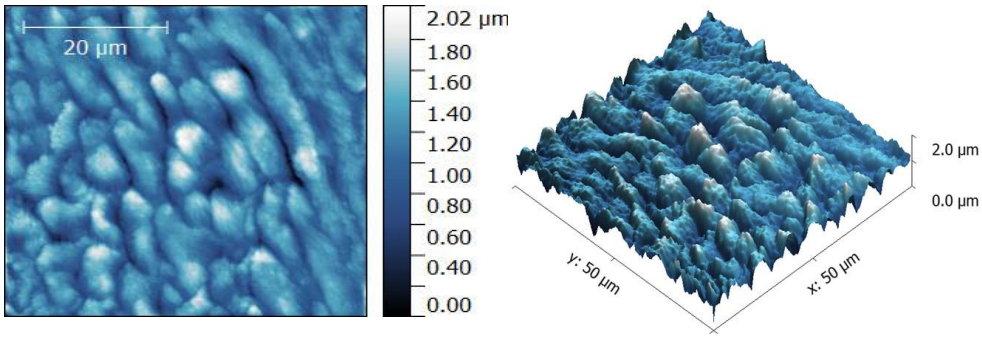

a **b**

Figure 6. AFM images: a- bidimensional; b – tridimensional of the enamel for extracted teeth in predialysis patients.

Tabel 4. Roughness parameters for the scanned areas showed in Figure 6

Enamel	**Av** [µm]	**Ra(Sa)** [nm]	**RMS (Sq)** [nm]	**Sk**	**Sku**
20 × 20 µm^2	1.181	178 (± 2.34)	231	-0.273	0.54
50 × 50 c µm^2	0.985	269 (±4.78)	327	-0.374	-0.446

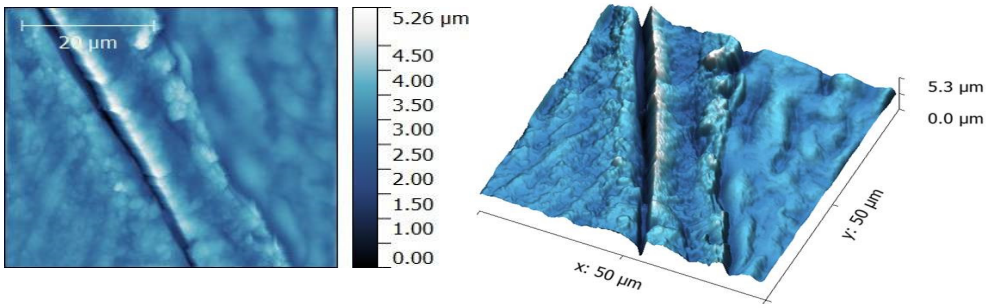

a **b**

Figure 7. AFM images: a- bidimensional; b – tridimensional at the composite –dentin interface for extracted teeth in predialysis patients.

Table 5. Roughness parameters for the scanned areas showed in Figure 7

	Av [µm]	**Ra(Sa)** [nm]	**RMS (Sq)** [nm]	**Sk**	**Sku**
Dentin					
20 × 20 µm2	0.6657	71.7 (± 4,56)	94.1	-0.318	1.61
Composite					
50 × 50 µm2	1.052	176 (± 3,24)	228	-0.583	1.01
20 × 20 µm2	0.3435	56.5 (± 4,12)	72.0	-0.39	0.466

The arithmetic roughness value of 51.3 nm at dentin (**Figure 8**) for teeth from predialysis patients indicates a less rough surface than the composite and enamel from the same samples taken. The high degree of porosity of the dental surfaces is also the most probable reason why the predialysis tooth seems to be fragile and weak; this was frequently noticed during the restoration and recording of both AFM and SEM images. According to these morphological findings, it can be deduced that the influence of treatments on predialysis patients on the teeth is real.

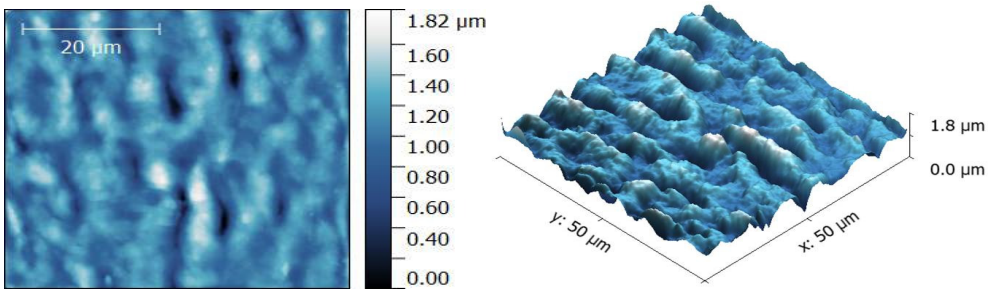

a **b**

Figure 8. AFM images: a- bidimensional; b – tridimensional of dentin from extracted teeth in predialysis patient.

Table 6. Roughness parameters for the scanned areas showed in Figure 9

Dentin	**Av** [µm]	**Ra(Sa)** [nm]	**RMS (Sq)** [nm]	**Sk**	**Sku**
50 × 50 µm^2	1.642	177 (± 2,57)	229	-0.605	1.63
20 × 20 µm^2	0.7229	51.3 (± 3,45)	67.9	-0.283	4.59

The kidneys play an important role in the endocrine control of calcium and phosphorus metabolism, largely through the formation of vitamin D_3. During the evolution of the chronic kidney disease, a secondary hyperparathyroidism appears, that is compensating due to the decrease of serum calcium levels in those patients. The main causes of progressive hypocalcemia are: phosphate retention due to decreased renal excretion capacity, decreased production of renal hormone 1,25-$(OH)_2D_3$ and a reduced skeletal response to the calcium action of parathyroid hormone [5].In the case of chronic renal failure, the decrease in the formation of 1,25-$(OH)_2D_3$ leads to a decrease in the production of calcium-binding protein in the intestinal mucosa, thus causing a decrease in calcium absorption and initiating the hypocalcemia with increasing serum parathyroid hormone levels [6] .

The mechanism of phosphate retention cannot be separated from alterations in vitamin D metabolism when considering the pathogenesis of secondary hyperparathyroidism [6].

Most of the enamel specimens tested showed a mixed type of failure, but the bond between the adhesive and the dentin was predominant in several samples. The AFM examination indicates a deep engraving for enamel and dentin in sick people compared to healthy people. The average value of the roughness (Ra) in enamel and dentin from healthy patients were significantly different ($p < 0.001$) than from enamel and dentin in patients with renal failure.

The statistical analysis showed a significant difference between the roughness values obtained for tooth enamel from patients with chronic renal failure and those for tooth enamel of healthy patients. These results could be determined by differences in the micromorphology of demineralised enamel surfaces. The patients with chronic renal failure may have elevated phosphate levels in saliva, as a result of alterations in calcium and phosphorus metabolism. As a result, we can speculate that a high level of phosphates in saliva can lead to the formation of a calcium-phosphate complex that forms a barrier on the tooth surface. Therefore, the diffusion of phosphate ions through the semipermeable enamel via the network of microchannel openings to the external surface can make the enamel more resistant to acid demineralisation, thus causing a low adhesion resistance.

A number of studies have investigated saliva composition and salivary flow in patients with chronic renal failure [7, 8, 9]. Thus, increased salivary concentrations of proteins and minerals were observed, as well as a decrease in salivary flow for both stimulated and unstimulated saliva in patients with chronic kidney disease. The buffer capacity and salivary pH have been shown to be increased in hemodialysis patients [9].It can be speculated that all these changes recorded at the salivary level may cause increased resistance to enamel demineralisation.

The results obtained in this study are similar to those presented in the study by Mahmoud et al. [10] on 44 molars collected from healthy patients and hemodialysis patients, to investigate the influence of uremia on the adhesion of composite resins to enamel and dentin, through AFM. Their conclusion was that uremia affects the adhesion of composite resins to enamel and dentin and provides an altered pattern of micromorphology of the demineralised tissues.

Also, in another study, Mahmoud et al. [11] investigated the effect of phosphoric acid concentration and duration of demineralisation on the enamel and dentin of the teeth of hemodialysis patients compared to healthy patients. The authors found that the enamel is much more resistant to acid attack, the higher concentration and longer duration of demineralisation being more effective in patients with chronic renal failure.

The results of the study on the assessment of the composite-enamel and dentin-composite interface by scanning electron microscopy after restoration are highlighted by the SEM images from **Figures 9, 11.**

The scanning electron microscopy images recorded the characteristics for the adhesive interface and structure in the case of the two lots of extracted teeth studied. Smaller magnifications (40-100x) were initially used for the overall assessment of the restorations and the adhesive interface, then magnifications of 200-1000x for the analysis of the structure of the composite material (C), respectively 1000-1500x for the study of the hybrid layer (SH).

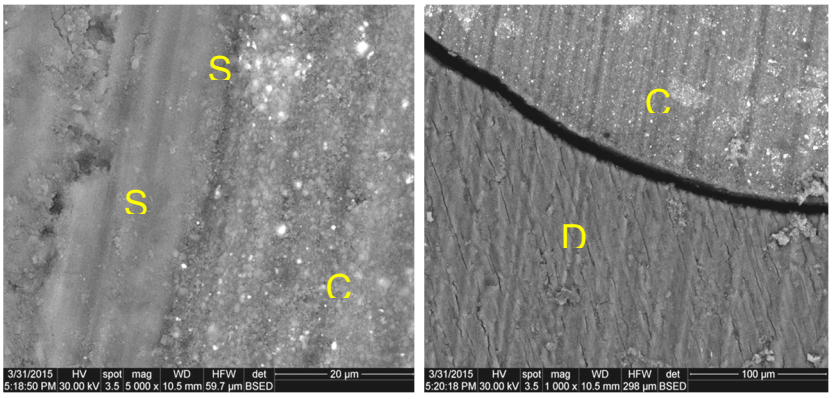

Figure 9. SEM image for extracted teeth from predialysis patients: a: – enamel-composite interface, magnification of x5000; b- dentin-composite interface, magnification of x1000;C- composite; D-dentin; SH- hybrid layer; S- enamel

In the case of samples from lot 1 of teeth extracted from predialysis patients, a continuous interface between composite-adhesive-dental hard tissues was observed, with a thin layer of adhesive, which infiltrated the smear layer (**Figure 9.a,b**). In several situations, fractures of the dentin were observed in the immediate proximity of the adhesive layer or partial detachment of the adhesive from the dentinal surface (**Figure 9**). **Figures 10 and 12** highlight the elements in the composition of the composite material, enamel and dentin.

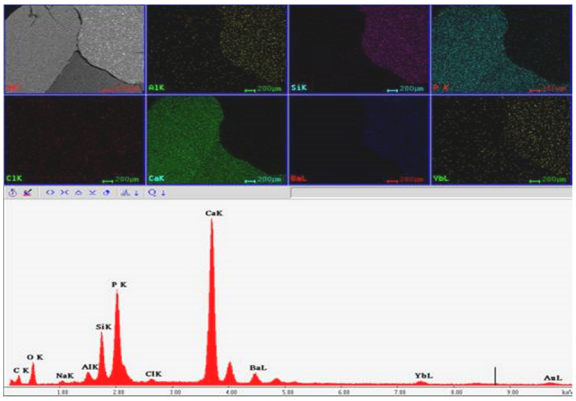

Figure 10. EDAX specters which highlight the elements from the composite-enamel-dentin interface from extracted teeth in predialysis patients. Coloured image according to the presented elements

The structure of the *Tetric EvoCeram Bulk Fill* composite material (**Figure 11b**) presented a hybrid, homogeneous appearance, highlighting 2 types of particles: light in colour, irregular in shape, with diameters varying between 1 and 10 μm, and dark in colour, with rounded or ovoid shape and diameter between 10-20 μm.

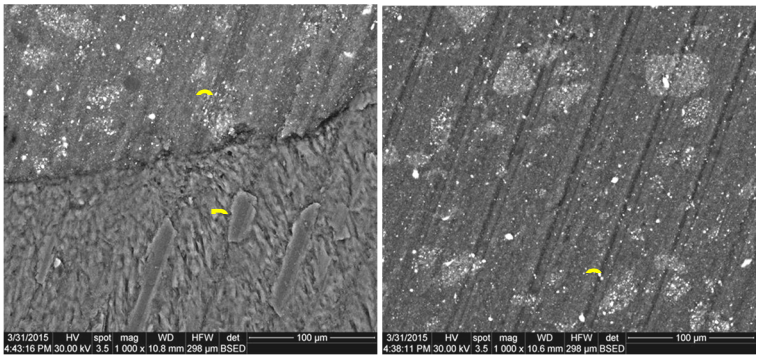

Figure 11. SEM image from extracted teeth in healthy patients: a – dentin-composite interface, magnification of x1000; b- composite material, magnification of x1000; C- composite; D-dentin; S- enamel

The dentin-composite material interface on teeth extracted from healthy patients, has a uniformity, compared to the dentin-composite interface in predialysis patients where the formation of a discontinuous hybrid layer was identified. The SEM assessment at the composite-enamel interface for the samples from lot 2 shows a hybrid, well-formed, uniform layer. The morphological changes observed at the enamel-composite interface in the samples from predialysis patients are probably due to the existence of a more porous and fragile dental structure.

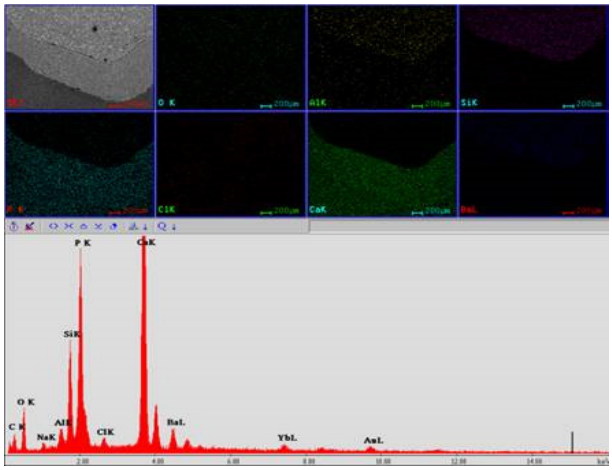

Figure 12. EDAX specters which highlight the elements from the composite-enamel-dentin interface from extracted teeth in healthy patients Coloured image according to the presented elements

The recent introduction of *Bulk Fill* restorative materials has rekindled the progressive volume ratio debate, with the introduced composites having a more pronounced polymerization shrinkage compared to the filling volume because the entire mass polymerizes at one time, faster than in small steps. Currently, the *Bulk Fill* restorative materials are available in different viscosities, low, variable or medium.

A number of studies have investigated the bonding capacity of adhesive systems to either enamel, dentin, or both [18- 24]. Most clinical points of view are for complex prepared cavities and include not only exposed enamel areas and superficial dentin, but also deep dentin areas. The hybrid layer is visualized in SEM images, and is possible only by sectioning the resin/dentin/enamel interfaces, being uniformly formed in the case of teeth from healthy patients.

Gaps and cracks have been observed in the areas of the composite/ dentin interface, indicating that adhesion to dentin is likely to be influenced by several factors than to enamel. The differences observed in these areas may be due to the air drying of the tooth slices and the dehydration of the specimens under vacuum during SEM recordings. However, because these

gaps or cracks were not only evident in the teeth of predialysis patients, since all samples were treated in the same way, they can be attributed to poorly polymerized hybrid adhesive layers.

The clinical relevance of porosities is unclear: their presence in large numbers at the composite-dental tissue interface can lead to microinfiltrations and failure of restoration by secondary caries or pulpal damage; however, clinical failures due to such porosities are rarely reported. The main purpose of dental adhesives is to ensure retention for composite restorations or cements. In addition to the resistance to mechanical stress, especially to those generated by the stress of the polymerization shrinkage of the composite, a good adhesive must also prevent microinfiltration along the edges of the restoration. Clinical failure of restorations occurs mainly through inadequate sealing rather than loss of retention, resulting in marginal dyschromia.

CONCLUSIONS

The structure, morphology and enamel-composite-dentin interface on teeth extracted from patients with chronic renal failure, predialysis patients and teeth from healthy patients were compared using two methods: atomic force microscopy (AFM) and scanning electron microscopy (SEM).

The AFM examination indicated a deep engraving for enamel and dentin in predialysis patients compared to healthy patients. The average value of the roughness (Ra) in enamel and dentin from healthy patients were significantly different ($p < 0.001$) than from enamel and dentin in patients with renal failure.

The hybrid layer is visualized in SEM images and is uniformly formed in the case of teeth from healthy patients, while in predialysis patients the formation of a continuous hybrid layer with some gaps was identified.

The morphological changes observed at the enamel-composite interface in the samples from predialysis patients are probably due to the more porous and fragile existing dental structure, probably with influences of alterations in the metabolism of calcium and phosphorus.

The clinical relevance of porosities is unclear: their presence in large numbers at the composite-dental tissue interface can lead to microinfiltrations and failure of restoration by secondary caries or pulpal damage; however, clinical failures due to such porosities are rarely reported.

EXPERIMENTAL SECTION

To perform this study, we used a total of 40 whole human teeth (molars), free of caries, extracted due to periodontal damage.

Lot 1 - 20 teeth were obtained from patients with chronic renal failure, predialysis patients, who came to the personal dental office for dental treatment. The patients were sent by the nephrologist from the Nephrology II department of the 'Dr. Carol Davila' Clinical Hospital of Nephrology, Bucharest, where they were monitored for their condition.

Lot 2 - 20 extracted teeth were collected from clinically healthy patients, free of chronic renal failure. All teeth were obtained after signing the patient's informed consent form.

Immediately after extraction, the teeth were washed and subjected to ultrasonic scaling (P5 Newtron, Satelec, Acteon, France) to remove deposits of calculus but also remaining soft tissue, being subsequently stored in physiological saline until use, in order to prevent dehydration.

Cavity preparation protocol

For the application of composite resin restorations, class I cavities were prepared at the level of all teeth with the help of a round bur (Komet, Germany) using light movements and water cooling. After preparation, the cavities were cleaned with physiological saline and the restorations were performed by applying the appropriate adhesive system and then the composite material. The technique used for demineralisation was total etch, with 37% phosphoric acid in gel form (Total Etch, Ivoclar Vivadent; Schaan, Liechtenstein) for 15 seconds, according to the manufacturer's instructions. The acid was then washed with water for 30 seconds.

The cavities were lightly air dried to avoid the desiccation phenomenon, then the adhesive was applied (*Adhese Universal*, Ivoclar Vivadent; Schaan, Liechtenstein) according to the manufacturer's recommendations. With the help of an LED photopolymerisation lamp (*Bluephase Style*, Ivoclar Vivadent; Schaan, Liechtenstein) we photopolymerised the adhesive for 10 seconds.

As a composite material we used a nano-hybrid composite resin (*Tetric EvoCeramBulk Fill*, Ivoclar Vivadent; Schaan, Liechtenstein; shade IVA) placed in a single layer, molded, photopolymerised for 10 seconds with the same LED lamp and then polished.

After filling all the cavities, the teeth were embedded in transparent self-polymerisable acrylic resin (Duracryl Plus, Spofa Dental, Cehia; shade 0) in order to be subjected to further tests.

After embedding the teeth in acrylic resin, all samples were sectioned longitudinally with a Microtom Buehler-IsoMet1000 sectioning machine at 1 mm intervals. The sectioned teeth were stored in physiological saline before and after the restorative treatment, in order to avoid their dehydration.

Study of the morphology and roughness of dental surfaces, by atomic force microscopy (AFM)

The atomic force microscopy (AFM) was used to investigate the morphology and roughness of dental surfaces before and after the restoration of cavities on teeth extracted from healthy patients compared to patients with chronic renal failure, predialysis patients. The surface morphology of the initial samples provides an important reference point for the correct and clear assessment of the effects induced by subsequent treatments.

The images were obtained with a commercial Ntegra Spectra microscope (NT-MDT, Russia), at room temperature, in air, in intermittent contact (semicontact), with rectangular silicon cantilever, with Au reflecting surface (NSG30-A, NT -MDT), nominal elasticity constant k = 40 N / m, resonance frequency 240-440 kHz, peak radius <10 nm.

After acquisition, the images were processed using Nova v1.1.0.1837 (NT-MDT).

For each sample, measurements were performed at three different surfaces for composite, enamel, enamel-composite, dentin-composite contact areas. For the roughness analysis, the statistical parameters calculated for the image on which the 'fit lines' correction was applied were used, through which a second-degree polynomial is found and extracted for each scan line. As the image processing history is important for the validity of the roughness comparison of two or more surfaces - the levelling procedure applied to each image directly affecting the roughness values, as well as the image size for which they are calculated - all AFM data were processed identically: for scan areas, 50 x 50 μm^2, 20 x 20 μm^2, recorded at a resolution of 256 x 256 scan points per image at the same correction (second degree polynomial 'fit lines') applied to each image.

Study of the interface by scanning electron microscopy

The electron microscopy determinations for tooth samples prepared as for the AFM study, in order to investigate the enamel/composite/dentin interfaces, and the structure of enamel and dentin in healthy patients compared to predialysis patients, were performed using the scanning electron microscope (SEM)QUANTA 133 (FEI Company USA). Several image magnification units were used and recordings were made at the enamel/composite/dentin interface. The tooth samples that were examined by SEM scanning electron microscopy were coated with a conductive layer consisting of gold. The analysis of the chemical composition of the tooth surface was performed using the EDAX method; this is a method of quantifying the elements in the composition of enamel, dentin and composite.

REFERENCES

1. G.P. Wysocki; T.D. Dalley; R.A. Ulan. *Oral Surg, Oral Med, Oral Pathol*, **1983**, *56*, 167-173.
2. F. Costantinides; G. Castronovo; E. Vettori; C. Frattini; M.L. Artero; L. Bevilacqua; F. Berton; F. Nicolin; R. Di Lenarda. *Int J Dent*, **2018**, *11,* 1-8.
3. S.M. Alamo; C.G. Esteve; G. Sarrion Perez. *J Clin Exp Dent,* **2011**, 3, e112-119.
4. C.Y. Yang; Z.F. Chang; Y.P. Chau. *Calcif Tissue Int,* **2015**, *97***,** 466–475.
5. D.B. Clark; G.P. Wysocki. *J Oral Pathol & Med*, **1988**, *17*, 60-69.
6. J. Bacchetta; J. Bernardor; C. Garnier. *Calcif Tissue Int* ,**2021**,*108***,** 116–127.
7. I. Tomás; J.S. Marinho; J. Limeres; M.J. Santos; L. Araújo; P. Diz. *Arch oral biol*, **2008**, *53*, 528-532.
8. A.M. Abdellatif; S.A. Hegazy, J.M. Youssef. *J Advanced Res,***2011**, *2,* 313–318.
9. C.P. Bots; H.S. Brand; J.H. Poorterman; B.M. Van Amerongen; M. Valentijn-Benz; E.C. Veerman. *Br Dent J* **2007***, 202,* E7-E7.
10. S.H. Mahmoud; M.A. Sobh; A.R. Zaher; M.H. Ghazy; K.M. Abdel Aziz. *J Adhes Dent*, **2008**, *10*, 335-338.
11. S.H. Mahmoud; M.E. Ahmed; K.M. Mahmoud; M.A. Grawish; A.R. Zaher. *The J Adhes Dent*, **2012**, *14,* 215-221.
12. F.H. Jones. *Surf Sci Rep*, **2001**, *42,* 75-205.
13. G.W. Marshall; M. Balooch; R.J. Tench; J.H. Kinney; S.J. Marshall. *Dent Mat*, **1993**, *9,* 265-268.
14. C. Cassinelli; M. Morra. *J Biomed Mat Res*, **1994**, *28*, 1427-1431.
15. L. Silaghi-Dumitrescu; A. Mihăilescu; A. Muntean; C. Sarosi; D. Prodan; M. R. Simu; M. Moldovan; A. Kui; M. Pastrav. *Studia UBB Chemia.* **2019**, *1,* 44.
16. O.H. Orasan; A.M. Chisnoiu; M.L. Dascălu; O. Păstrav; M. Păstrav; M. Moldovan; R. Chisnoiu. *Studia UBB Chemia.* **2017,** *1,* 62.
17. F. El Feninat; S. Elouatik; T.H. Ellis; E. Sacher; I. Stangel. *Appl Surf Sci*, **2001**, *183,* 205-215.
18. M. Ferrari; A. Vichi; S. Grandini. *Dent Mat*, **2001**, *17,* 422-429.
19. C. Poggio; M. Lombardini; P. Vigorelli; M. Ceci. *Scanning*, **2013**, *35,* 366-374.
20. B. Van Meerbeek; J. De Munck; Y. Yoshida; S. Inoue; M. Vargas; P. Vijay; G. Vanherle. *Oper Dent-Univ of Washington,* **2003**, *28,* 215-235.
21. M. Toledano; R. Osorio; G. De Leonardi; J.I. Rosales-Leal; L. Ceballos; M. Cabrerizo-Vilchez. *Am J of Dent*, **2001**, *14,* 205-210.
22. E.R. Hewlett. *J California Dent Assoc* **2003**, *31,* 469-476.
23. L. Brache; M. Özcan. *J Adhes Sci and Tech*, **2018**, *32,* 258-271.
24. D. Sucală; C. Sarosi; C. Popa; I. Cojocaru; M. Moldovan; A.G. Mohan. *Studia UBB Chemia.* **2018,** *1,* 2.

STUDIA UBB CHEMIA, LXVI, 4, 2021 (p. 253-265)
(RECOMMENDED CITATION)
DOI:10.24193/subbchem.2021.4.18

NEW MATERIAL USING CEMENT-BASED MATRIX WITH SELF-REPAIR PROPERTIES BASED ON REACTIVE GRAINS WITH PROTECTIVE COATING

MIRON ZAPCIU[a,*], CONSTANTIN VOINIȚCHI[b], NICOLETA IONESCU[c], MARIUS OLTEANU[d]

ABSTRACT. This research relates to cement-based matrix materials with self-repairing properties, based on reactive grains (Portland clinker) having the dimensions 90…160 μm and using a protective coating layer with a thickness of 4-7 μm. The material involves the use in mortars or concretes of a smart additive of a clinker reactive material covered with an impermeable polymeric coating that breaks when a crack appears in the material and allows the reaction between water and cement stone components and, consequently, the formation of a crack plugging product consisting in calcium silicate hydrates gels (CSH), superior to that of calcium carbonate precipitation. The intelligent addition is obtained by mixing the reactive material with the solution of a polymer, or with its melt (C8H8)n. The efficiency of coverage exceeds 80% in most of cases, some of them approaching even 90%. No significant effect of the ratio reactive material/polymer seems to be observed. The degree of healing of the crack is defined in the paper. The method of highlighting the self-repairing effect is based on the amount of electricity passed through the sample. The new material has practically unchanged mechanical properties, a higher hydration capacity and a longer service life-cycle.

Keywords: *reactive grains, protective coating, self-repairing, new material*

[a] *Politehnica University of Bucharest, INCERTRANS SA, Academy of Romanian Scientists, Spl. Independentei 313, sector 6, ZipCode 060042, Bucharest, Romania*
[b] *Technical University of Civil Engineering, Blvd Lacul Tei 124, ZipCode 020396 Bucharest*
[c] *INCERTRANS SA, Transport Research Institute, Calea Grivitei 391-393, ZipCode 010719, Bucharest, Romania*
[d] *SW Umwelttechnik Romania, Str. Zavoiului, Nr. 1, com. Vanatorii Mici, jud. Giurgiu ZipCode 087253, Romania*
[*] *Corresponding author: miron.zapciu@upb.ro*

INTRODUCTION

1. State of the art

There are currently several attempts to make self-repairing concrete using different principles. Vascular recipes can be used inside the concrete, containing embedded resins or from an external source, additions of superabsorbent polymers, or even the use of bacteria encapsulated together with the necessary nutrients and which, when the crack appears, resume their metabolism, releasing CO_2, which carbonates the portlandite resulting from the hydration of the Portland cement and resulting in the clogging of the crack. There are also methods that involve the use of active hydraulic additives that, in the presence of portlandite, will develop hydro-compounds that can ensure the clogging of the crack, or fibers that reduce the width of the crack and allow natural concrete self-repair. The disadvantages are represented by the difficulty of implementing the adopted solutions which have been tested only in laboratory conditions and which do not fit for the implementation on real-site conditions.

There are attempts on the use of polymer-modified self-repairing bitumen (PmB), to increase the elasticity of road layers, to reduce wear and material fatigue at high temperatures. Polymer-based additives are generally used for modified bitumen. Of these additives, styrene-butadiene-styrene copolymers (SBS) are the most commonly used (WIPO patent with identification number WO 2017/116354 A1) [1].

Another example of autogenous healing, but of a cement composite, is made according to patent number 20080261027 from the USA [2], the claims being from The Regents of the University of Michigan. The patent relates to a self-healing cement composite and, in particular, to a fiber-reinforced cement-based composite, which has a self-controlled crack width dimensions from 50 μm to a maximum of 150 μm. Self-healing can occur within a variety of environmental conditions including that in which the material is damaged, as per example by tensile loading. Self-healing in this case was autogenic and observed by the test for analyzing the resistance of concrete to chloride ion penetration, according to the AASHTO T259-80 standard. The composite comprises hydraulic cement, water, sand, fly ash (pozzolanic additive) [19], water reducing agent and short and discontinuous fibers [3-5, 7-9]. The fibers are based on polyvinyl alcohol having diameters between 30 and 60 μm and are found in a percentage of 1.5% - 3.0% on the related composite volume. The use of superabsorbent polymer was reported too [6].

2. **Polymeric coated reactive grains** – Concept Presentation

The continued hydration of cement grains is considered an essential mechanism of chemical nature, responsible for generating the calcium silicate hydrates gels (CSH), superior to that of calcium carbonate precipitation:

they are not able just to seal the crack, however, by the means of a high bond strength to the crack walls, they may generate the mechanical recovery of the material, as well [10-13].

Another aspect relates to the currently cement production, based on fine clinker grains contents, with fast initial reactivity in order to reach the full-strength potential at the age of 28 days [14-17]. After the peak is reached, the hydration process experiences a sudden drop in the continuous hydration process, since the reactive basin is consumed.

The new concept of the authors about self-repairing is to increase the hydration capacity of the concrete using reactive grains addition, polymeric coated for reactivity conservation until the point when it becomes necessary: crack occurrence and consequently the necessity to seal/heal it, when humidity conditions are also ensured (Figure 1).

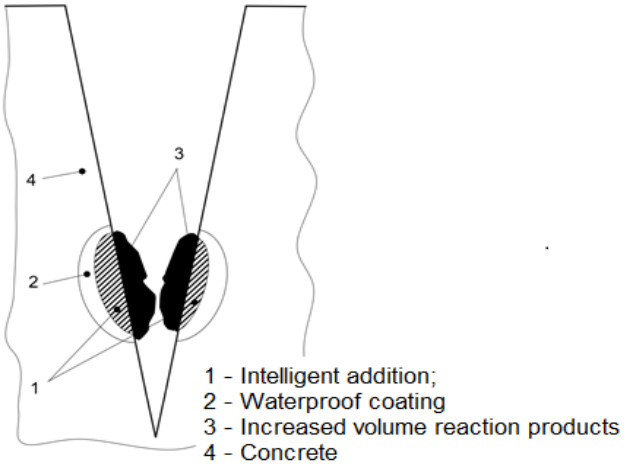

Figure 1. Representation of the concept for the reactive grains

Using polymeric coated reactive grains, the impermeable coating of a clinker material breaks when a crack appears in the material, allowing the reaction between water and cement stone components and, consequently, self-repairing due to the formation of a crack plugging product by generating the calcium silicate hydrates gels [12].

This addition of reactive grains has the following important advantages:

-increasing the service life for concrete used in reinforced concrete works in contact with aggressive agents;

-increasing the uptime between two repairs for reinforced concrete used in infrastructure works;

- the use of recyclable materials in making the smart addition;
- it is extremely practical, being adapted to site conditions.

The research was oriented so as to validate the followings:

- the materials which could be considered proper as reactive grain and protective polymeric cover;
- the encapsulation techniques from waterproofing capacity;
- the potential of self-repairing effect when crack is induced [18].

A smart addition material has been created (reactive grains + protective polymeric cover) capable of generating a self-repairing action after a long period of hydration in the mortar/concrete in wherein is added. The addition consists of an active hydraulic material wrapped in a waterproof polymer film, which breaks when the concrete crack crosses through the particle.

RESULTS AND DISCUSSION

1. Reactive grains covering degree

An active hydraulic material (Portland clinker) with the size of granules between 90 and 160 μm wrapped in a polymer film of a thickness of 4-7 μm has been used. Two metods were used: *Method 1* using polymer solution in an appropriate solvent and *Method 2* using melted polymer, (C8H8)n. After the achievement, the granules were passed through the 0,5 mm sieve for breaking the adhesions between the shells of the granules (Figure 2).

Covering Degree (CD, %) was determined by using conductivity test on suspensions of covered and uncovered clinker and the Equation (1):

$$CD(\%) = 100 \times \frac{Cond_{hp} - Cond_{h}}{Cond_{h}} \quad (1)$$

where:

$Cond_{hp}$ = conductivity of the coated grains suspension;

$Cond_{h}$ = conductivity of the uncoated grains suspension.

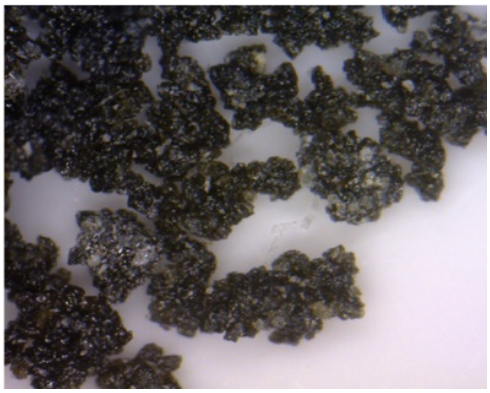

Figure 2. The grains wrapped in polymeric film

2. Conductivity results on reactive grains

Conductivity test on reactive grains suspension (1%) reveals an important variation in the first minute, and a much lower rate after (Figure 3). It was concluded that a conductivity measurement of suspension after 1 minute can offer a good information about the covering degree, as such the kinetic of the reaction depends of the contact area on phases.

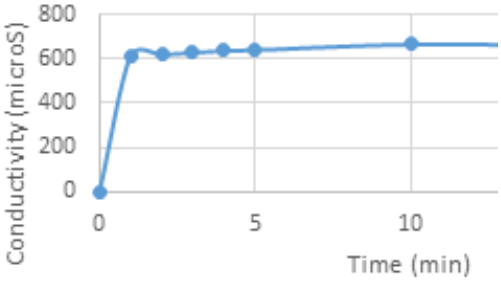

Figure 3. Level of conductivity during 10 min. for a suspension of uncoated reactive material (1%) in water

The conductivity results is proven to be a reliable efficiency of the smart grains addition covering, developed by the means of both methods. A number of 6 tested compositions, out of 10, reveal (Table 1) an efficiency of coverage exceeding 80%, three of them approaching even 90%. Considering the 10 experiments performed, no significative effect of the reactive material/polymer ratio seems to be observed.

Table 1. Coating degree results for different ratio clinker/polymer

Method	*No. of experiment*	*Ratio: Clinker / Polymer (%)*	*Degree of coating (%)*
Method 1 (PS-Polymer Solution)	1	54	83
	2	27	85
	3	18	88
	4	13.5	89
	5	9	85
	6	5	79
	7	10	66
	8	15	71
	9	20	70
Method 2 (MP- Melted Polymer)	10	11.3	87

The conductivity development over time, for the reactive grains, without coating (blue line) and the coated grains (Methods 1 and 2) is presented in the Figure 4.

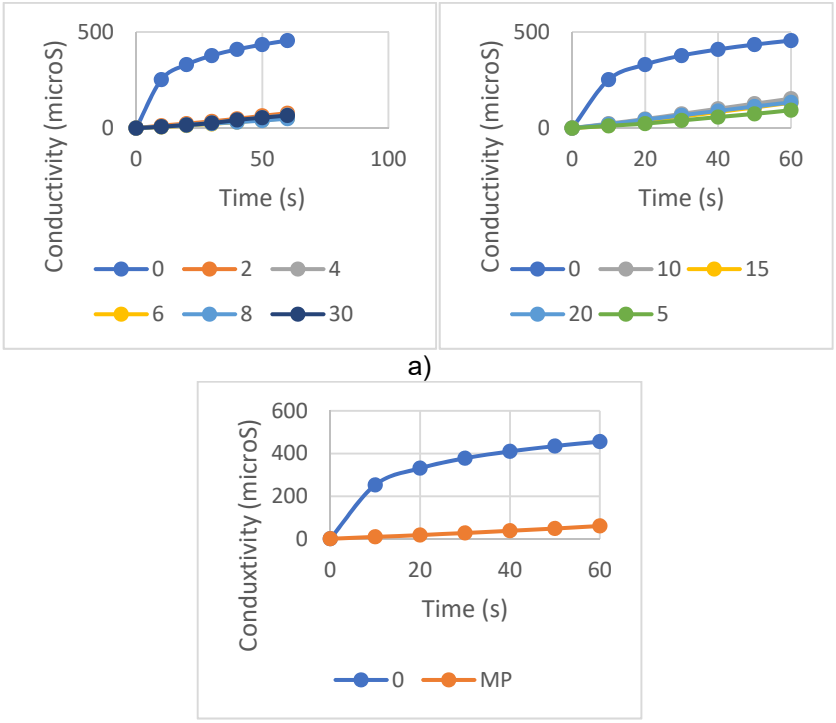

Figure 4. Variation of the conductivity during 1 min. for uncoated (0) and coated grains: a) using Method 1 (Polymer Solution) and b) Method 2 (Melted Polymer)

3) Results and discussion on self-repairing effect

In order to check the self-repairing effect of a smart addition grains, it has been carried out a related test.

The smart grains addition with a reactive material/polymer ratio of 9% was introduced into a standardised mortar performed, according to EN 196-1 standard, in different proportions. An CEM I52.5R cement was used to hydrate granules as much as possible and to reduce the natural self-repairing effect.

A degree of self-repairing (Healing Degree - HD) of the crack was defined as follows:

$$HD\ (\%) = 100*[(I_{fP} - I_{nP}) - (I_{fR} - I_{nR})] / (I_{fP} - I_{nP}) \qquad (2)$$

where:

I_{fP} = intensity of the current through the crack;

I_{nP} = intensity of the current through the uncracked aria;

I_{fR} = intensity of the current through the crack on the reference sample;

I_{nR}= intensity of the current through the uncracked aria on the reference sample.

The intensity of current through the crack I_c is the difference between intensity of the current on the cracked aria I_{fp} and uncracked I_{np} area.

Results for three samples are presented in the Figure 5 and reveals a good self-repairing properties of the smart addition grains.

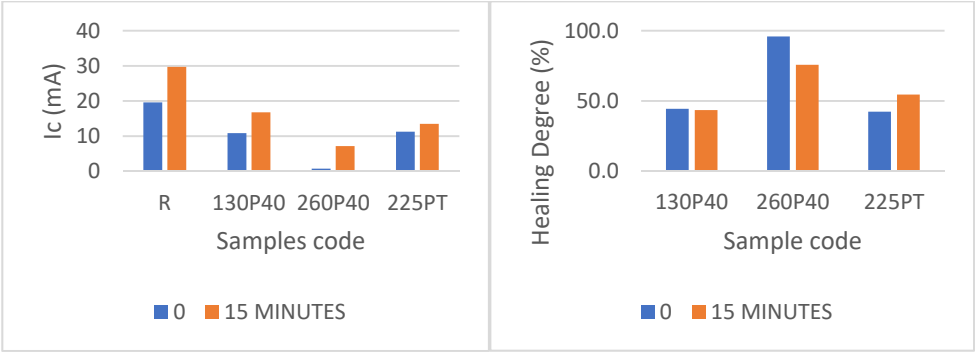

Figure 5. Intensity of current through crack after 0 and 15 minutes (left) and degree of healing (HD) of the crack (right)

For all 3 samples used, in which the smart grain dosage represents 130, 260 and 225 kg / m3, respectively. HD is around 50% and they have a maximum of 70% compared to the standard reference sample. The sample no.2, with an addition of 260 kg'm3, was the best composition on self-repair.

CONCLUSIONS

The material with a matrix based on cement, mortar or concrete, with self-repair properties (Fig. 1), is characterized by the fact that it contains the addition of reactive granules, encapsulated in our experiment with a polymeric film (C8H8)n.

The authors' recommendation is that the reactive granules have diameters in the range of 90-160 micrometers, their mass representing at least 80% of the total mass of the addition with self-repair properties. The total mass of the addition represents 5-10% of the total mass of the material with cement-based matrix and the following materials can be used: clinker, aluminous cement, blast furnace slag as ground cementitious material, hydraulically active materials (power plant ash, trass) or quicklime.

The material with a matrix based on cement, mortar or concrete, with self-repairing properties, is characterized in that the encapsulation with the polymer film is obtained by immersing the reactive granules in polystyrene solution, a solution that represents a maximum of 20% of the total mass of the addition with self-repair properties. The melting temperature of polystyrene was 240° C.

The self-repairing effect of intelligent addition grains has been proven on the mortars by electro diffusion of chloride ions. Crack healing degrees of more than 70% were obtained for some compositions.

The influence of the smart grains addition to mechanical resistance (resistance to static compression and bending test) of the material has been assessed using EN 196-1 standard and a small increase in all mechanicall performances was observed [18]; this demonstrates the lack of negative effects of the added grains on the mechanical strength of the material.

In order to implement the results of the research [20-21], it was necessary to establish the manufacture of a small size of a bridge beam using smart grains material. In the forthcoming work, in real operating and related exploitation situations, the behavior of this sample versus classical material will be compared.

EXPERIMENTAL SECTION

1. Procedure and requirements for obtaining test specimens

In order to demonstrate experimentally the self-repairing effect of new material an active hydraulic material was used, covered with a layer of waterproofing polymer and was tested its positive effect. The necessary test samples must be obtained after completing the following steps:

-obtaining granules of active hydraulic material with waterproofing coating;

-accelerated ageing of concrete;

-controlled cracking of the sample;

-use of an appropriate method for highlighting the self-healing effect;

- separation of the influence of the natural self-healing effect of concrete from that due to self-repairing addition.

The active hydraulic material must compulsory meet certain requirements:

- the reactive material generates new compounds by reaction with water or ions dissolved therein, compounds that will be stored in the crack and thus restricting the access of aggressive agents.

- the reactive material should not contain or generate sulphates, chlorides, alkalis or other aggressive concrete ions. The presence of sulphates can lead to the formation of ettringite with a remedial action by creating a barrier to water entering, but at the same time there is also the risk of an out-of-control reaction that can lead to the destruction of concrete.

- the reactive material must not negatively influence the hydration and hardening properties of Portland cement in case of accidental break-in of waterproof protection.

The following requirements must be met for the waterproof coating polymer:

- protect the reactive material from the water until the crack will crosses it;

- be adherent to reactive granules (adhesion to reactive material granules helps to withstand mechanical shocks during mixing);

- not negatively influence cement hydration processes;

- withstand efforts during the concrete preparation process;

- be resistant in the alkaline concrete environment;

- do not suffer positive volume variations in alkaline environment;

- be brittle so as to break and allow contact with the water to infiltrate;

- be available in large quantities;

- ability to be used in the technological processes – soluble in ordinary solvents or a reasonably low melting point;

- possibly to be a recyclable material to reduce costs and environment pollution.

For each sample were added 2.25 g polypropylene fibres so that the crack caused in the material does not lead to the complete rupture of the samples. Samples with dosages of 0 kg/m^3 smart addition grains were casted as the reference mortar R, with 130kg/m^3 smart addition as sample 130P40, 260 kg/m^3 as sample 260P40 and 225 kg/m^3 smart addition obtained by melting method as sample 225PT.

Fraction less than 0,5 mm from the standardized sand was partially removed in a volume equal to that of the smart addition grains used. The samples were casted into a classic 160x40x40 mm mould, modified by removing an intermediate wall. The mortar was compacted and stored 1 day according to EN 196-1 standard. Accelerated aging is obtained by a hygrothermal treatment at 80^{o}C in a water bath.

2. Experiment to control the crack of samples

The following procedure is used for controlled cracking of the sample: after 2 weeks of curing, mortar samples are removed from water bath and a 5 mm thick and 15 mm deep channel was cut with diamond disc saw in the median area, across the sample, to direct the crack. The sample was instrumented with a crack monitoring device mounted with axis at 15 mm from the bottom of the sample and comprising the median area where the cracking will occur. The sample is placed on two supports at a 100 mm apart and a force is applied via a roller in the median area (Figure 6).

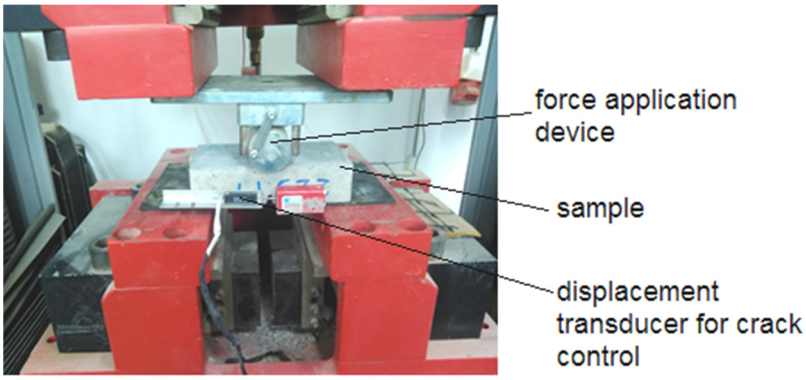

Figure 6. Experimental arrangement in order to obtaining a fixed crack width

The increase in force stops at the time of the crack appearing and then it adjusts its intensity until the desired opening is obtained. The test machine was turned off in this position and 2 metal fibers of appropriate size were applied to the side of the sample using appropriate adhesive. After hardening, the crack monitoring device was removed and two other fibers were applied in its place.

The samples are introduced into a water bath, but not in direct contact with water, to speed up the self-healing process. After an appropriate period, samples were extracted from the water bath and a channel with the same

specifications like the first one, centered at 27 mm from the end of the prisms was cutted.

The method of highlighting the self-repairing effect is based on the amount of electricity passed through the sample [20]. In order to highlight the influence of the crack on the transport of electric charges and implicitly the diffusion of chloride ions, the tests were carried out in areas with channels cut into samples, with or without crack.

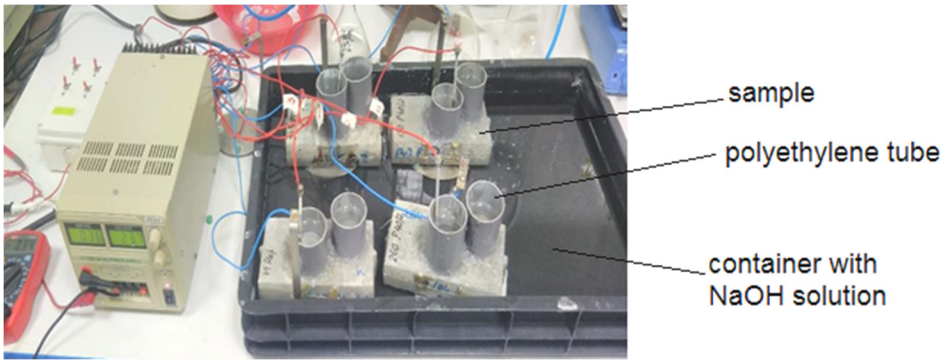

Figure 7. Experimental arrangement of the samples highlighting the self-repairing effect based on the amount of electricity passed through the sample

Two polyethylene tubes 50 mm in diameter were sticked on the casting face using a silicone seal, one in the central area above the crack and one above the channel centered at 27 mm from the prism end. All the four samples (Figure 7) were dried in an oven and saturated with water in vacuum at 20mm Hg. A 3% NaCl solution is inserted into the polyethylene tubes. The samples thus prepared were introduced in a 0.1% solution of NaOH were placed in a 0.1% NaOH solution in an insulating plastic container.

A 24V DC voltage was applied for 15 minutes and the intensity of the electrical current through the cracked I_{fP} and uncracked I_{nP} area of each sample was measured, including the I_{fR} and I_{nR} in reference sample R. The intensity of current through the crack I_c is the difference between intensity of the current flowing through the cracked (I_{fP}) and uncracked (I_{nP}) area.

3. Experimental validation of self-repairing effect using SEM

The action of intelligent addition grains has been validated by electronic microscopy (SEM) on sections obtained from the cracked and self-repaired area (Figure 8).

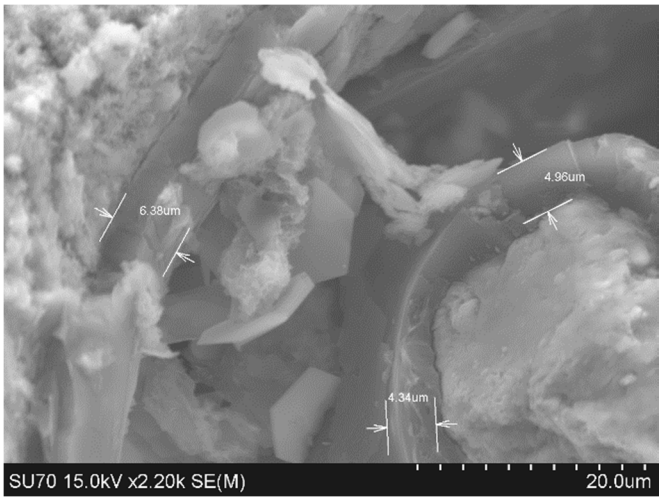

Figure 8. SEM capture; evaluation of the healing degree

A polymer coating of few micrometers thick (4.3 μm) and some products resulted from hydration could be viewed using SEM. Considering the largest uniaxial size of a polymer film-coated reactive addition granule equal to 193μm, respectively the uniaxial size of the crystallization zone of the hydrocomposites formed after the destruction of the polymer film (cured area ≈ 123μm), a 64% HD resulted for this sample.

It is emphasized that no microstructural elements were identified to highlight discontinuities or compositional heterogeneities of the samples and there is no suspicion about addition grains incompatibility in the cement matrix.

ACKNOWLEDGMENTS

This paper is supported by the Programme: "*Innovative solutions for transport infrastructure protection by the use of building materials with special self-maintenance and self-repair properties*", Programme code: 6 PS / 13.09.2019, financed by the Ministry of Education and Research.

REFERENCES

1. * * * WIPO *Patent number WO 2017/116354*, **2017**, pp. 8-10.
2. V. Li; E.H. Yang; *Patent number 20080261027*, USA, **2008**, pp. 5-9.
3. Ed. G. Nawy; *Concrete construction engineering handbook. 2nd Edition*, Boca Raton: Taylor & Francis Group, **2008**, pp. 15-19.
4. D. Snoeck; N. De Belie; *J. Mat. Civil Eng.* 04015086, **2015**, pp.1-11.

5. D. Snoeck; N. De Belie; *J. Mat. Civil Eng.*, **2015**, *28(1),* 50-86.
6. D. Snoeck; J. Dewanckel; V. Cnudde; N. De Belie; *Cement and Concrete Composites*, **2016**, *65*, 83-93.
7. M. Şahmaran; G. Yildirim; T.K. Erdem; *Cement and Concrete Composites*, 35(1), **2013**, pp.89-101.
8. P. Termkhajornkit; T. Nawa; Y. Yamashiro; T. Saito; *Cement and Concrete Composites*, 31(3), **2009**, pp.195-203.
9. K. Van Tittelboom; N. De Belie; *Materials*, 6(6), **2013**, pp. 2182-2217.
10. K. Van Tittelboom; E. Gruyaert; H. Rahier; N.De Belie; *Construction and Building Materials*, 37, **2012**, pp.349-359.
11. A. Witze; *Nature News*, **2017**, pp. 15-25.
12. * * * OSIM *Patent application no.A/00022*, **2020**, Bulletin of OSIM, RO-BOPI no.7/2020, pp. 31.
13. E.H. Yang; V.C. Li; *Cement and Concrete Research*, 42(8), **2012**, pp.1066-1071.
14. E.H. Yang; Y. Yang; V.C. Li; *ACI Materials Journal*, 104(6), **2007**, pp. 303-311.
15. G. Yildirim; M. Sahmaran; H.U. Ahmed; *Journal of Materials in Civil Engineering*, 27(6), **2014**, pp. 87-89.
16. G. Yildirim; M. Şahmaran; H.Ahmed; *Journal of Materials in Civil Engineering*, 27(6), **2014**.
17. Z. Zhang; S. Qian; H. Ma; *Construction and Building Materials*, 52, **2014**, pp.17-23.
18. C. Voinițchi; C. Baeră; M. Zapciu; C. Matei; H. Szilágyi; N. Ionescu; F. Tudorie; *Annals of the Academy of Romanian Scientists, Series on Engineering Sciences*, ISSN 2066-8570, Vol.12, No.1, **2020**, pp. 89-102.
19. A. Cuibus; M. Gorea; N. Har; Z. Kiss; Studia UBB Chemia, LIX, 4, **2014**, pp. 75-86.
20. * * * ASTM C1202-19 *Standard Test Method*, **2019.**
21. * * * Sectoral project 6PS/13.09.2019, financed by Ministry of Education and Research: Phase III, **2020**, Chapter: *Elaboration of the technology implementation manual*, pp. 11-15.

STUDIA UBB CHEMIA, LXVI, 4, 2021 (p. 267-276)
(RECOMMENDED CITATION)
DOI:10.24193/subbchem.2021.4.19

DRYING AND ENERGY RECOVERY OF SLUDGE

CORNEL SAVA[a,*], ELENA MARIA PICĂ[a]

ABSTRACT. This paper presents some of the results of research on the introduction of the operation of drying sludge from wastewater treatment in treatment plants. Graphical representations of the experimentally determined values demonstrate the possibility of continuing the process of decreasing the humidity of dehydrated sludge, by mechanical means.
Sludge drying is presented as a simple operation that can be easily introduced into the sludge treatment process.
The second part of the paper presents a machine that could be executed with relatively small amounts in each treatment plant in order to achieve the drying of dehydrated sludge.
The paper presents characteristics of dehydrated sludges in Cluj and Sălaj counties as well as chemical analyzes performed on dehydrated sludges.
In conclusion, the paper argues that dry sludge can be removed from the waste and turned into a material resource.

Keywords: *wastewater, wastewater treatment plants, sludge, waste, drying tunnel, dry mud, resource.*

INTRODUCTION

Wastewater collected through sewer systems built in the perimeter of urban and rural settlements is led to treatment plants. The concentration of substances in wastewater in mg/dm³ or g/m³, is the amount of substances contained in the unit volume. Mineral or organic substances are found in wastewater. The connections that exist in the wastewater have a decisive role in decantability. In the mixture formed using drinking water for hygienic or industrial purposes, water is found in several forms:

Free water not associated with solid particles: interstitial water, located in free spaces inside flakes and adherent water - which has adhered to the surface of solid particles,

Bound water is water that has interacted with the cells of living organisms.

[a] *Technical University of Cluj-Napoca, Building Services Engineering Department, Blvd. December 21, no. 128-130, 400604, Cluj-Napoca, România*
[*] *Corresponding author: sava.cornel47@yahoo.com*

The bonds that are established between water molecules and the cells of living organisms can be [1, 2]:

- Biological - intercellular water that represents a part of the cells linked by molecular forces in a stable phase,
- Chemical - intercellular water which is a part of the molecular crystal lattice also in a stable phase;
- Physical - in colloids the connection is maintained by the surface stresses present at the boundary between phases.

The stability of colloidal systems is ensured by factors that prevent particle agglomeration. The electrostatic repulsive forces are strong enough to prevent their agglomeration. In order for these particles to become large enough to be separated by sedimentation, a chemical treatment is required to cancel the interactions between the colloidal particles and water, making it possible to agglomerate them and deposit them on the decanter raft. The formation of aggregates begins with the proximity of particles, by reducing electrostatic repulsive forces.

RESULTS AND DISCUSSION

Coagulation can be considered as a first step in the wastewater treatment process. As a result of the deposition of coagulated particles on the decanter scrap in the treatment plants, results sludge. The resulting amount of sludge is directly related to the number of inhabitants and the specific water consumption. A consumption of 180 to 200 liters of water per inhabitant, attests to an increased urban comfort. The quantities of sludge resulting in several wastewater treatment plants in Cluj and Zalău counties are presented in Table 1.

Table 1. Sludge quantities in wastewater treatment plants

Town	The amount of sludge [t/day]	The amount of sludge [t/year
Cluj Napoca	70	7154
Dej	6.6	506
Zalău	10	913
Gherla	6	438

Moisture or water content varies depending on the nature of the sludge (mineral or organic) and the treatment stage from which it comes. In wastewater treatment plants, sludge can come from three sources [3, 4]:

1. The primary sludge is fresh sludge from the primary settling tank, has a gray color and contains household waste which decomposes easily,

2. Secondary sludge is sludge from the secondary settling tank after precipitation of activated sludge and separation of excess sludge. Excess secondary sludge has a brown color,

3. Precipitation sludge is sludge resulting from the chemical precipitation of phosphorus.

Sludge from wastewater treatment plants is collected and treated in complex systems to remove moisture. The primary sludge contains to a large extent solid organic matter and has the consistency of a dense liquid, with a water content between 93% and 97%.

The secondary sludge usually has a dry matter concentration of 0.7% and 7 Kg/m³, respectively.

The removal of water from the sludge is an important objective aimed at bringing the sludge to a state in which it can be stored and prepared for further processing.

In the treatment plants in Romania, the sludge dehydration takes place in the dehydration units where filter type equipment (belt press and polymer dosing) or centrifugal type equipment is used.

Table 2 presents the performances obtained in several treatment plants in Cluj and Sălaj counties.

Table 2. Treatment plants performances

Town	Humidity reduction (MS)
Cluj Napoca	28%
Dej	21%
Zalău	25%
Gherla	20%

Figure 1 shows the results obtained after drying the samples in spaces without ventilation, at a temperature of 50 °C.

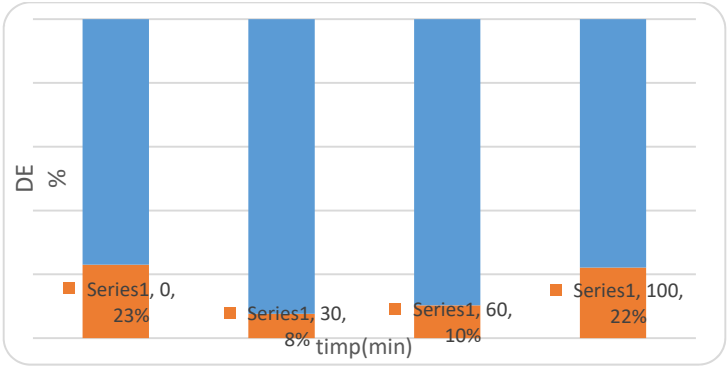

Figure 1. Sample drying results at 50 °C without ventilation

In Figure 2 we present the results of drying the samples under the same time conditions, but at a temperature of 100 ° C.

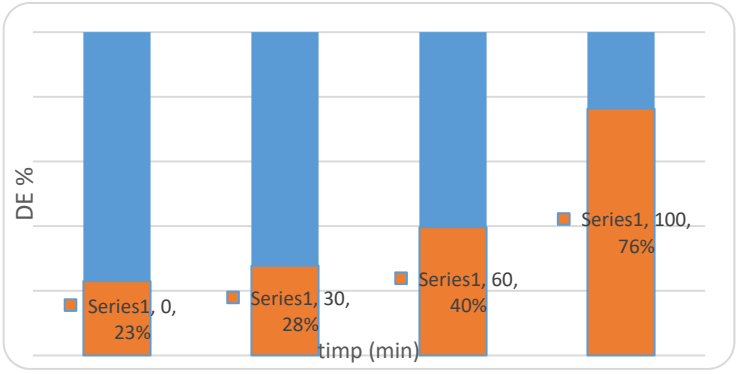

Figure 2. Drying results at 100 °C without ventilation

Doubling the temperature in an unventilated space has an insignificant influence on the degree of evaporation by comparison with the degree of evaporation obtained at 50 °C in a ventilated space.

The degree of evaporation obtained in unventilated space at 100 °C is comparable to the degree of evaporation obtained with only 50 °C in a ventilated space.

The experiment was done to show the importance of proper ventilation of the drying space [5].

Figure 3 shows the results of drying the samples at 50 °C in ventilated spaces.

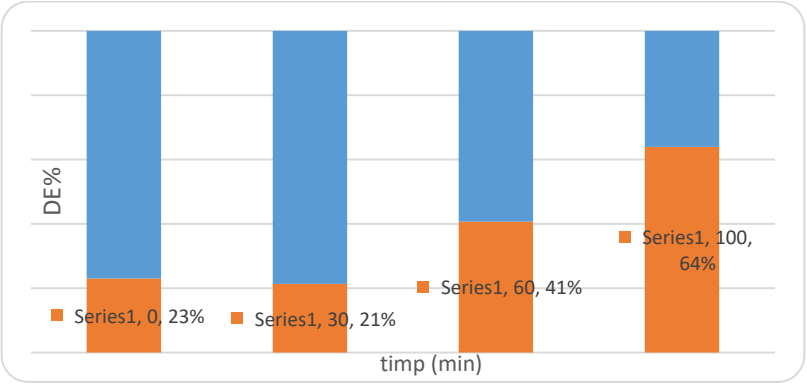

Figure 3. Samples drying results at 50 °C with ventilation

Ventilation of the drying space significantly increases the degree of evaporation, even in low temperature conditions.

Figure 4 shows the results of drying the samples under the same conditions, but at a temperature of 100 °C.

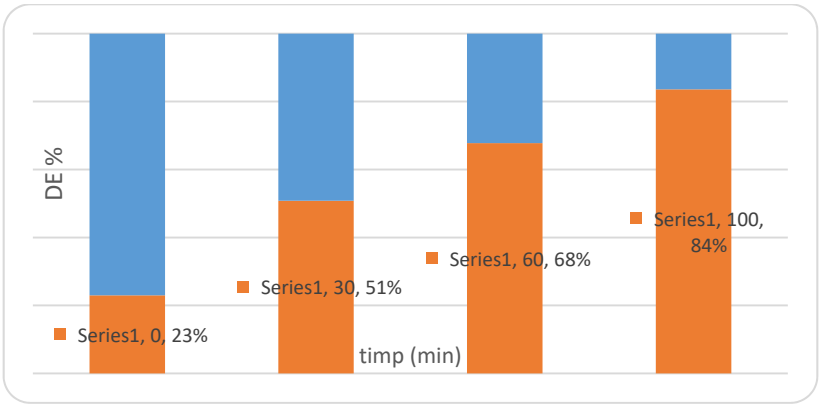

Figure 4. Drying results at 100 °C with ventilation

Doubling the temperature in ventilated areas significantly increases the degree of evaporation.

This experiment was selected as the starting point for the construction of a drying tunnel.

The values used in the construction of the graphical representations presented in fig.1-4 were obtained by introducing the results in equation (1) [6]:

$$DE = (G_{pi} - G_{pu}) / G_{pi} \times 100 \quad (1)$$

where:

DE = degree of evaporation;

G_{pi} = weight of the sample before drying;

G_{pu} = weight of the dry sample

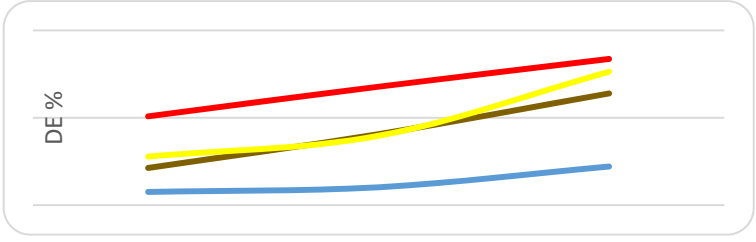

Figure 5. Graphical representation of the drying results of the ventilated and non-ventilated samples:- 100 °C with ventilation, - 100 °C without ventilation, - 50 °C with ventilation, - 50 °C without ventilation.

Figure 5 represent a comparison of the results by graphical representation, in temperature-time coordinates, in ventilated enclosures and unventilated enclosures.

The graphic representation explicitly shows the superiority of the ventilated drying spaces and the high efficiency for the temperature of 100 °C.

In support of the use of dry sludge as a resource, it is presented in tables no. 3 and 4 chemical elements contained in 7 samples of dehydrated sludge.

In Table 3 we present the results determined on 3 samples of dehydrated sludge and Table 4 shows the results for 4 samples of dehydrated sludge.

Tables 3 and 4 presents the results of chemical analyses performed in accordance with the regulations mentioned in the section Method of analysis. The determinations were performed on 7 different samples, to determine the elements contained in the dehydrated sludge. The percentage in which these elements are found in dehydrated sludge is very important for choosing the destination of dehydrated and dry sludge [7-9].

Table 3. Chemical analyses performed on sludge samples

Determined parameters	UM	Sample			Analysis method	Admitted limit*
		1	2	3		
Dry substance (DS)	%	17	11.82	18.77	STAS 12586-87	
Organic substance (OS)	%	82.5	77.24	83.15	STAS 12586-87	
Phosphorus	mg/kg ds	4864	4828.7	20567	SR ISO 11263/1998	
Cadmium	mg/kg ds	1.356	1.387	1.755	SR EN ISO 11047/1999	10
Copper	mg/kg ds	171.7	133.3	131.9	SR EN ISO 11047/1999	500
Nickel	mg/kg ds	22.35	23.26	16.64	SR EN ISO 11047/1999	100
Zinc	mg/kg ds	467.3	496.2	439.9	SR EN ISO 11047/1999	2000
Chromium	mg/kg ds	24.83	26.16	27.52	SR EN ISO 11047/1999	500
Lead	mg/kg ds	38.75	28.26	81.68	SR EN ISO 11047/1999	300
Calcium	%	1.206	1.376	0.7065	EPA 7000B	-
Potassium	%	1.008	0.670	0.4781	EPA 7000B	-

*according to OM no. 344/708/2004

Table 4. Chemical analyzes performed on samples of dehydrated sludge

Determined parameters	Unit	Sample				Analysis method	Admitted limit *
		1	2	3	4		
Total nitrogen	% (ds)	5.19	4.93	5.82	3.13	ISO 13878:1998	-
Arsenic	mg/kg ds	5.10	5.40	2.0	4.15	SR EN ISO 11885:2009	10
Cobalt	mg/kg ds	7.79	2.0	5.0	4.61	SR EN ISO 11885:2009	50
Mercury	mg/kg ds	0.32	0.80	0.47	0.80	SR EN ISO 11885:2009	5
AOX (adsorbable halogenated organic compounds)	mg/kg ds	0.94	4.64	15.95	2.26	SR EN ISO 8562:2005	500
PAH (polycyclic aromatic hydrocarbons)	mg/kg ds	0.092	0.147	0.012	0.008	SR EN ISO 17993::2004	5

*according to OM no. 344/708/2004

Chemical analyses performed on dehydrated sludge show that the heavy metal content cannot be influenced by dehydration and drying.

By drying at a temperature above 80 °C, eggs and bacilli that are dangerous to crops can be removed. For heavy metal content it is necessary to make laboratory determinations to be made available to those who are to approve the use of dry sludge for fertilizing agricultural land. The beneficial elements for fertilization are represented by the content of phosphorus, nitrogen, and potassium.

The chemical analyzes presented in Tables 3 and 4 show that dehydrated and dry sludge can be used without posing any danger to soils or to humans. All chemical elements are within the limits allowed by current legislation.

EXPERIMENTAL SECTION

Dehydrated sludges at the percentages of solid substance that were presented in Table 2, are stored in a buffer silo from which the supply can be made for their thermal recovery. The sludge can be transported by pumping or conveyors. Drying technology can allow drying between 75% and 90%, depending on the destination of the dried sludge. The drying tunnel is a mixed conduction / convection type machine, in which the dehydrated sludge

dries in a single pass. At the exit, the sludge can be in the form of granules or cakes. The sludge is heated by a fluid that transfers heat without coming into direct contact. For the drying tunnel to be effective, as shown in laboratory experiments, it must ensure the evacuation of evaporated water. The evacuation of water vapor can be done with a process gas, blown in the direction of movement of the sludge subjected to drying. The shape of the inner surfaces of the dryer must be so designed as to prevent the accumulation of sludge inside the machine.

Gas emissions to the atmosphere must be considered when constructing the drying tunnel. The gases produced inside the drying tunnel are fully recovered and passed through a condensing system. The liquid obtained is analyzed in the laboratory and the toxic elements neutralized [10].

Dry sludge is an easy product to use in many industries. Drying at high temperatures reduces the infectious potential of sludge, making it possible to use it in agriculture. If you opt for the energy recovery of sludge by incineration, the dry sludge is already ready for combustion. The sludge drying operation is an important step in diversifying the ways of capitalizing on this treatment product, which is now an important source of pollution [11-13].

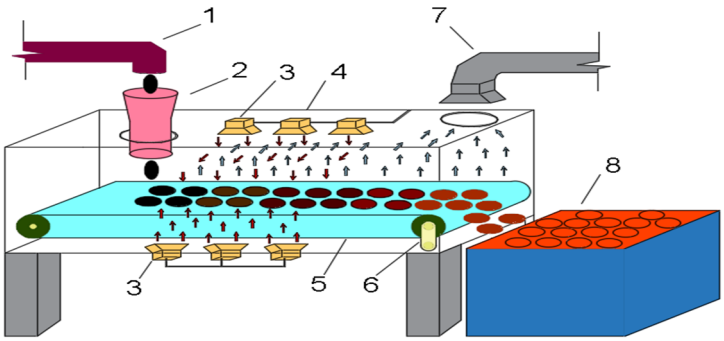

Figure 6. Dehydrated sludge drying tunnel
1.– Dehydrated sludge food basket; 2. - Mud steering funnel; 3. - Heating and ventilation system; 4. - Drying tunnel; 5. - Conveyor belt; 6. - Band drive drum; 7. - Vapor collection system; 8. - Dry sludge unloading container.

The equipment shown in Figure 6 is an original proposal that can achieve the drying of sludge as established experimentally. The drying tunnel allows adjustments and adaptations for all the main elements involved in the phenomenon of water evaporation. Thus, the degree of ventilation, drying time and working temperature can be easily adjusted [14].

Drying of dehydrated sludge is an operation that allows them to be removed from the category of environmentally hazardous waste and introduced into the category of resources usable in many areas.

Dry sludge becomes easy to store and is not dangerous for the environment [15].

CONCLUSIONS

Water removal by mechanical means is limited by the performance of the equipment. To further remove water from dehydrated sludge, this paper proposes an original method of drying sludge after it has come out of the dehydration equipment.

During the research, conditions like those encountered in the natural environment were created. Experiments have been created that can accurately highlight the factors involved in the complex phenomenon of water evaporation from dehydrated sludge.

To verify the method, samples were taken from the dehydrated sludge and weighed and dried. The samples were dried in different drying environments, namely ventilated drying spaces, and unventilated drying spaces.

Another direction of research was to establish the relationship between the time required for drying and the degree of evaporation. The samples were dried at different temperatures to determine how the temperature influences evaporation.

In all cases, the degree of evaporation was the difference in weight between the sample subjected to drying and the same dry sample.

For use, the dried sludge is subjected to chemical determinations showing the composition in favourable elements for use and toxic elements that do not allow its use as a resource.

ACKNOWLEDGMENTS

We thank Prof. Dr. Eng. Ovidiu Nemeș for the advice and encouragement that made it possible for this paper to be offered for consultation to those interested.

REFERENCES

1. B. Lyes, A. Patricia, L. Angélique, Review on fundamental aspect of application of drying process to wastewater sludge*,* Renewable and Sustainable Energy Reviews, Elsevier, **2013,** *30,* 29–43.
2. M. Henze, P. Harremoes, J. Jes LaCour Jansen, E. Arvin, Wastewater treatment: biological and chemical processes, Springer Berlin Heidelberg, Germany, 2001, 1-422.

3. T. Rusu, Technologies and equipment for water treatment and purification, U.T. Pres, Cluj-Napoca, România, **2008**, *Vol. I.*
4. D. Mamais, D. Jenkins, *Water Res.*, **1993**, *27,* 195–197.
5. P. Tudor, D. Florin, H. Anca, Ventilation and air conditioning installations, U.T. Pres, Cluj-Napoca, România, **2010**, Vol. 1, 1-348.
6. G. Olsson, B. Newell, Wastewater treatment systems: modelling, diagnosis and control, IWA publishing, London, United Kingdom, **1999**, 1-750.
7. B. Rao, L. Cao, *J. Agric. Eng.*, **2012**, *28*, 184–188.
8. A. Reyes, M. Eckholt, F.Troncoso, G. Efremov, *J. Drying Technol.*, **2004**, *22*, 35–50.
9. B. Lyes, *Renewable and Sustainable Energy Reviews*, **2012**, *16*, 1061–1073.
10. I. Vădan, A. C. Cziker, Modern energy conversion systems, U.T. Pres, Cluj-Napoca, România, 2017, 1-505.
11. *"ÖWAV-Arbeitsausschuss "Thermische Behandlung und Verwertung"*, **2006,** 1-4.
12. Horst Müller, *ÖWAV-Klärschlammtagung*, **2018,** 1-60.
13. B.C O'Kelly, *J. Air Waste Manag. Assoc.*, **2005**, 765.
14. V.L. Mathioudakis, A.G. Kapagiannidis, E. Athanasoulia, V.I. Diamantis, P. Melidis, A. Aivasidis, *Desalination***, 2009**, *248 (1–3)*, 733-739.
15. I. Leonard, M. Dumitru, V. Nicoleta, D. M. Motelică, T. Veronica, Methodology for using urban sludge in agriculture, Ed. Solness, Timișoara, România, **2007**, pp 1-193.

STUDIA UBB CHEMIA, LXVI, 4, 2021 (p. 277-282)
(RECOMMENDED CITATION)
DOI:10.24193/subbchem.2021.4.20

CHEMICAL AND THERMOGRAVIMETRY ANALYSIS FOR MUNICIPAL WASTE SLUDGE – CASE SCENARIO ANALYSIS

ADRIAN EUGEN CIOABLA[a,*], LAURENȚIU-VALENTIN ORDODI[b], GERLINDE RUSU[b]

ABSTRACT. The need for solutions in the sector of municipal waste management brings different problems which can be properly managed by using modern technologies, new ways to capitalize substrates and materials which in normal conditions are not potentially usable. The present study involves chemical and thermal analysis in order to determine the energetic potential and overall properties of one type of municipal waste sludge collected during summer in Caras-Severin County. For confidential reasons, the origin of the waste sludge will not be mentioned.

Keywords: *municipal waste sludge, chemical analysis, thermogravimetry*

INTRODUCTION

Waste management is currently one of the biggest problems in both small and large communities. Even if related with the produced waste, a large part can be further processed, separated and further recycled or used in different applications for energy conversion or industrial applications, still, there are large quantities of waste which have currently no solution in terms of large-scale processing and use for further benefits.

The exponential population growth, economic development, and rapid urbanisation are the key contributors to MSW generation [1]. Besides, the high consumption rate and consumer-based lifestyle have been the driving factors towards an increase in MSW generation [2,3]. This increased rate of MSW generation is one of the global issues that contribute to socio-economic and environmental problems [4]. These waste accumulations have caused severe ecological problems involving air and water pollution.

[a] *Politehnica University of Timisoara, Faculty of Industrial Chemistry and Environmental Engineering, 6 Vasile Parvan blvd., Timisoara, Romania*
[b] *Politehnica University of Timisoara, Faculty of Mechanical Engineering, 1 Mihai Viteazu blvd*
[*] *Corresponding author: adrian.cioabla@upt.ro*

Besides, uncontrolled increase in waste could trigger a shortage of waste disposal areas [5]. In 2018, an estimated average of 2 billion metric tons/year of waste was generated worldwide, which is predicted to rise to 3.40 billion tonnes by 2050 [6]

The environmental problem of waste, waste-related challenges and sustainable energy supply is being minimised through a range of approaches: AD, gasification, fermentation, pyrolysis, and liquefaction [7-9].

Municipal sewage sludge is an unavoidable by-product of wastewater treatment. An increase in the amount of sewage sludge produced has been observed for many years. The amount of generated sewage sludge is only 1–3% of the volume of flowing sewage [10].

Sewage sludge can be used in agriculture as a valuable source of nitrogen and phosphorus, for production of compost, and for the reclamation of degraded areas [11,12]. The choice of the method of sewage sludge management is particularly dictated by its quantity and properties [13]. Moreover, it is subject to legal regulations.

The source of heavy metals in sludge is wastewater, which is mainly generated by plants using galvanic processes, steel pickling, and the recycling of lead batteries.

In this regards, municipal waste waters and waste sludge are of interest in the present material, with impact on a case study in terms of potential uses for the test sludge in co-firing processes.

The present article will underline the base analysis for a proper prepared sludge sample having its origin in the SW part of the country (Banat Region, Caraș - Severin County). The material was analyzed in terms of physical and chemical properties for determining its possible applications. Conclusions were traced in this regard and further recommendations have been made, connected with the obtained results.

RESULTS AND DISCUSSIONS

After the laboratory determinations were made, the obtained results are presented below.

Table 1. Experimental results (part 1)

MATERIAL	Moisture content [%]	Ash content (db) [%]	Gross calorific value (db) [J/g]	Net calorific value (db) [J/g]
Waste sludge – Caras-Severin County	8.51	62.2	7883	7039

From the point of view of the ash content, it can be observed that the minerals inside the material are at a very high level, making it almost impossible to be used in co-incineration processes.

During the laboratory testing the material presented difficulties to be burned in order to determine its calorific value.

Table 2. Experimental results (part 2)

MATERIAL	Carbon content (db) [%]	Hydrogen content (db) [%]	Nitrogen content (db) [%]	Volatile matter content (db) [%]
Waste sludge – Caras-Severin County	18.4	3.5	2.12	36.1

The elements presented in the table above are in the normal range for this type of material, indicating relatively low potential for use in co-firing applications.

Table 3. Experimental results (part 3)

MATERIAL	Sulphur content (db) [%]	Chlorine content (db) [%]
Waste sludge – Caras-Severin County	1.5	0.12

A very interesting analysis represents the Sulphur and Chlorine contents. Unexpectedly, the Chlorine level is relatively low in this case, but the Sulphur level is high as percentage inside the analyzed sample. This aspect also makes the material not suitable for co-firing applications.

Table 4. Experimental results (part 4)

MATERIAL	Shrinking temperature ºC	Deformation temperature ºC	Hemisphere temperature ºC	Flow temperature ºC
Waste sludge – Caras-Severin County	930	1180	1230	1260

One interesting analysis that could not be made in Romania was the ash melting behaviour. This analysis indicates the way in which the material behaves inside the firing chamber at high temperatures.

The obtained values from measurements indicate a relatively high point of flowing temperature, which is a common factor for this type of material.

The thermo-gravimetrical analyses (TGA) were performed on TG 209 F1 Libra equipment (Netzsch) under nitrogen atmosphere and under dynamic conditions 10 K/min from 20 to 900 °C.

Table 5. TG curves specific points

Sample	Inflexion		Mass loss (%)		Residual mass (%)
	First step	Second step	25-150 ºC	150-600 ºC	
Waste sludge - Caras-Severin County	128.9	354	7.72	27	58.74

The TG curves present two degradation steps:

- the first degradation step occurs between 25 and 150 ºC and has a sharp mass loss being associated to water loss. The mass loss for the first degradation step is under 10% for the sample.

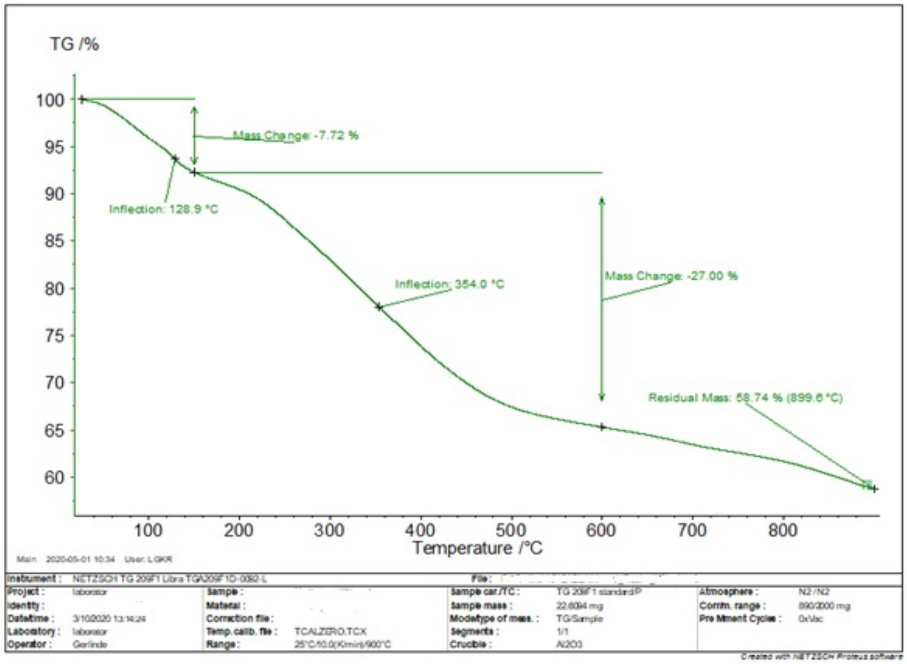

Figure 1. TG curves for analysed sample under nitrogen environment

- the second from 150 to 600 ºC is associated to thermal decomposition of the organic compounds of the samples. The mass loss is under 30% for the analyzed material. The high value for the residual mass (58%) probably denotes the high inorganic content for the sample.

CONCLUSIONS

The presented study involved the analysis of a sludge type of material in correlation to determining its properties from a chemical stand point and TG analysis.

Unfortunately, all the presented data (ash content, calorific value, sulphur content) prove that the analysed material is not suitable for co-firing applications. It also has a relatively low calorific level of energy. Usually, summer effluents are filled with high concentrations of organic mass which in turn raise the calorific value, but in this case the presented scenario proves the contrary.

The materials can be used as a base substrate for biogas production, but the estimated rate of success is debatable.

EXPERIMENTAL SECTION

The next paragraph will underline the overall presentation of the analysed waste sludge.

Table 6. General presentation of material

No.	MATERIAL	OBSERVATIONS	ORIGIN SOURCE AND DETAILS
1.	Waste sludge – Caras-Severin County	PRE-DRIED MATERIAL	Treatment plant

For the laboratory analysis, the next standards were used as methods.

- EN ISO 18134 – Solid biofuels – Determination of moisture content – Oven dry method (3);
- EN ISO 18122- Solid biofuels - Determination of ash content;
- EN 14918 - Solid biofuels –Determination of calorific value;
- EN ISO 16948 – Solid biofuels – Determination of total content of carbon, hydrogen and nitrogen

- EN ISO 16994 - Solid biofuels — Determination of total content of sulfur and chlorine
- EN ISO 18123 – Solid biofuels – Determination of the content of volatile matter.
- CEN/TS 15370 - Determination of ash melting behavior.

ACKNOWLEDGEMENT

The authors wish to thank the team from the *BEA Institut für Bioenergie – Viena, Austria,* for all the support given during the analysis made in the laboratory for the studied material.

REFERENCES

1. Kamaruddin MA; Yusoff MS; Rui LM; Isa AM; Zawawi MH; Alrozi R; *Environ Sci Pollut Control Ser*, **2017**, *24*, 26988–27020
2. Kumar A; Samadder S.; *Waste Manag,* **2017**, *69*, 407–422
3. Khan D, Kumar A; Samadder SR; *Waste Manag*, **2016**, *49*, 15–25
4. Klavenieks K; Dzene KP; Blumberga D; *Energy Procedia,* **2017**,*128*, 512–519
5. Kumar S; Smith SR; Fowler G; Velis C; Kumar SJ, Arya S; *R Soc Open Sci* **2017**, *4*, 160764, 1-14
6. Pham TPT; Kaushik R; Parshetti GK; Mahmood R; Balasubramanian R; *Waste Manag*, **2015**, *38*, 399–408
7. Rajendran K; Aslanzadeh S; Johansson F; Taherzadeh MJ; *Energy Convers Manag,* **2013**, *74*,183–191
8. Lee XJ; Ong HC; Gan YY; Chen W-H; Mahlia TMI; *Energy Convers Manag*, **2020**, *210*, 112707, 1-34
9. Silitonga AS; Mahlia TMI; Kusumo F; Dharma S; Sebayang AH; Sembiring RW; *Renew Energy*, **2019**, *133*, 520–527
10. Statistics Poland. Statistical Yearbook of the Regions 2019, Statistics Poland, Warsaw, **2020**, Poland
11. Farasat, S; Namli, A; *Fresen. Environ. Bull*, **2016**, *25*, 1484–1493
12. Lasaridi KE; Manios T; Stamatiadis S; Chroni C; Kyriacou A; *Sustainab.*, **2018**, *10*, 1-13
13. Latosi´nska, J; *Environ. Prot. Eng.,* **2017**, *43*, 105–122

STUDIA UBB CHEMIA, LXVI, 4, 2021 (p. 283-295)
(RECOMMENDED CITATION)
DOI:10.24193/subbchem.2021.4.21

THE STUDY OF THE RHEOLOGICAL BEHAVIOR AND THE OXIDATION STABILITY OF SOME COSMETIC EMULSIONS

ADELA MANEA[a], ANDRA TAMAȘ[a*], SABINA NIȚU[a], DELIA PERJU[a]

ABSTRACT. The paper presents the rheological behavior study of cosmetic emulsions as well as their oxidation stability. The influence of temperature and of the cooling rate was determined, as well as that of the active principles content on the rheological behavior, by setting the dependence between the shear stress τ and the shear rate $\dot{\gamma}$. The analysis of this dependence demonstrates that these emulsions present non-Newtonian behavior. The oxidation stability was monitored for 210 days by determining the peroxide value and the presence of initial and final oxidation products (by monitoring K_{232} and K_{270} values, respectively).

Keywords: *cosmetic emulsions, emulsifier, mathematical models, oxidation, rheological behavior, stability, viscosity, peroxide value*

INTRODUCTION

Emulsions are thermodynamically unstable colloidal systems, in which there are droplets of a liquid dispersed in a second immiscible fluid [1].Oil-in-water emulsions (O/W) are characterized by oil droplets dispersed in an aqueous continuous phase and are commonly used in various industrial applications, such as in food industry, pharmaceutical or cosmetic fields [2,3]. Cosmetics are more or less complex, stable and homogeneous mixtures, resulting from a formulation which consists in the association of a raw material with another one. These ingredients are subdivided into three categories: active principles, excipients and additives [4].

The use of bioactive extracts from a variety of botanicals in cosmetics accomplishes two functions: care of the body and as ingredients to influence the biological functions of the skin, providing the nutrients for healthy skin [5]. They possess various properties like photoprotection, antioxidant (vitamin C and E, tea polyphenols, resveratrol, pomegranate fruit extract), antiaging

[a] *Politehnica University Timisoara, Faculty of Industrial Chemistry and Environmental Engineering, 6 V. Pârvan Bd., RO-300223, Timisoara, Romania;*
* *Corresponding author: andra.tamas@upt.ro*

(oleanolic extract, boswellia), moisturizing (retinoids, alpha hydroxy acids, soy extract, aloe vera), astringent (arnica, cucumber), anti-irritant (coriander seed oil) antimicrobial activity [6] and anti-cellulite properties (caffeine) [7].

In order to obtain acceptable emulsions for cosmetic products, must be taken into account the incorporation of stabilizers (co-emulsifiers) to prolong storage stability, the selection of an effective preservation system to prevent their microbiological deterioration, as well as the introduction of other control substances (antioxidants, pH adjusters, thickening agents) [8].

Cosmetic emulsions can present instability during the storage, from chemical changes of the components, the presence of microorganisms or physical changes (mechanical or visual). The first two causes of instability are generally unacceptable.

In general, rheology is defined as a science that studies the interdependence between mechanical stress, the response of bodies and their properties. It establishes a series of mathematical models that describe the behavior of bodies subjected to stress, behavior determined by the dependence that exists between force (stress) and response (deformation, flow) [9].

Creams are semi-solid emulsions which contain mixtures of oil and water. Their consistency varies between liquids and solids. For this reason, the rheological characterization is more complicated because both rheological models for solids and those for liquids must be considered.

In cosmetic emulsions, rheological characterization is very important to ensure not only the flow control but also its absence when necessary. Thus, a cream must recover its structure and initial viscosity after being applied to the skin, without allowing it to flow or drip.

Also, rheological measurements are very useful to characterize the flow properties of emulsion systems and to predict their behavior during manufacturing, packing or final use [2].

The aim of this work is to analyse the rheological behavior of O/W emulsions. The influence of active principles content, the preparation temperature and the cooling rate were followed. The mathematical models which described the dependence $\tau = f(\dot{\gamma})$ were established. Also, it was studied the oxidation stability in time, depending on storage conditions.

RESULTS AND DISCUSSION

Rheological characterization

The influence of temperature on the rheological behavior was determined for all the samples. In Figure 1, the dependence between the shear stress τ and the shear rate $\dot{\gamma}$ is shown for emulsion A, at three temperature values.

It is observed that the dependencies between the shear stress and the shear rate are linear, with a non-zero intercept corresponding to a yield stress $\tau_0 \neq 0$. This behaviour is characteristic of non-Newtonian fluids (plastic Bingham) [10,11], which begin to flow only after the shear stress exceeds this threshold (critical value) [12].

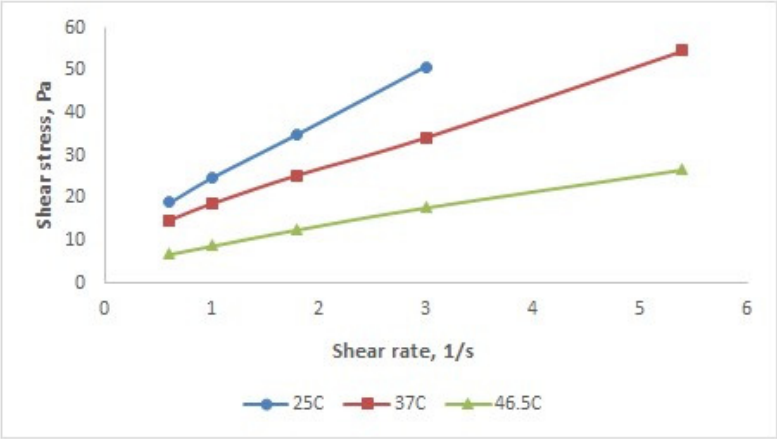

Figure 1. Shear stress (τ) *vs.* shear rate ($\dot{\gamma}$) for emulsion A

Using the TableCurve 2D program, the rheological equations corresponding to these dependences were established (Table 1), where η_p is the Bingham plastic viscosity. The plastic viscosity is the slope of the straight line, so that it can be stated that Bingham fluid has an initial shear stress threshold followed by a Newtonian flow [13,14].

Table 1. Rheological equations for emulsion A (Bingham model)

Temperature, ˚C	Eq. $\boldsymbol{\tau = \tau_0 + \eta_p \cdot \dot{\gamma}}$	R^2
25	$\tau = 11.17 + 13.24 \cdot \dot{\gamma}$	0.99969
37	$\tau = 9.98 + 8.23 \cdot \dot{\gamma}$	0.99927
46.5	$\tau = 4.81 + 4.11 \cdot \dot{\gamma}$	0.99651

It is found that increasing the temperature leads to both decreasing the yield stress (τ_0) and plastic viscosity (η_p), without changing the type of rheological behavior.

Because the curves $\tau = f(\dot{\gamma})$ obtained for emulsions B, C and D have a slightly different shape from the curves obtained for emulsion A, the rheological equations were deduced using both the Bingham model (Table 2)

and the Herschel-Bulkley model (Table 3). It is observed that they differ in the value of the flow index (n) which is equal to 1 for Bingham fluids and has subunit values in the case of Herschel-Bulkley model. In this latest model, k represents the consistency factor [11].

Table 2. Rheological equations for emulsions B, C and D (Bingham model)

Em.	Temperature, ˚C		
	25	37	46.5
	Eq. $\boldsymbol{\tau = \tau_0 + \eta_p \cdot \dot{\gamma}}$		
B	$\tau = 17.3 + 1.49 \cdot \dot{\gamma}$ (R^2=0.96868)	$\tau = 9.74 + 0.61 \cdot \dot{\gamma}$ (R^2=0.94597)	$\tau = 4.25 + 0.27 \cdot \dot{\gamma}$ (R^2=0. 88417)
C	$\tau = 9.46 + 13.61 \cdot \dot{\gamma}$ (R^2=0.99495)	$\tau = 5.15 + 6.35 \cdot \dot{\gamma}$ (R^2=0.99585)	$\tau = 2.31 + 0.75 \cdot \dot{\gamma}$ (R^2=0.9657)
D	$\tau = 20.9 + 6.56 \cdot \dot{\gamma}$ (R^2=0.98489)	$\tau = 11.48 + 3.6 \cdot \dot{\gamma}$ (R^2=0.9528)	$\tau = 3.59 + 0.7 \cdot \dot{\gamma}$ (R^2=0.97074)

Table 3. Rheological equations for emulsions B, C and D (Herschel-Bulkley model)

Em.	Temperature, ˚C		
	25	37	46.5
	Eq. $\boldsymbol{\tau = \tau_0 + k \cdot \dot{\gamma}^n}$		
B	$\tau = 13.08 + 5.29 \cdot \dot{\gamma}^{0.582}$ (R^2=0.99877)	$\tau = 5.92 + 3.80 \cdot \dot{\gamma}^{0.485}$ (R^2=0.99954)	$\tau = 0.04 + 4.14 \cdot \dot{\gamma}^{0.283}$ (R^2=0. 88417)
C	$\tau = 8.15 + 15 \cdot \dot{\gamma}^{0.937}$ (R^2=0.9951)	$\tau = 2.56 + 8.87 \cdot \dot{\gamma}^{0.838}$ (R^2=0.9979)	$\tau = 0.215 + 2.64 \cdot \dot{\gamma}^{0.585}$ (R^2=0.99481)
D	$\tau = 9.17 + 18.75 \cdot \dot{\gamma}^{0.454}$ (R^2=0.99799)	$\tau = 0.023 + 15.23 \cdot \dot{\gamma}^{0.399}$ (R^2=0.99711)	$\tau = 1.39 + 2.48 \cdot \dot{\gamma}^{0.594}$ (R^2=0.99336)

Bingham fluids do not have a constant viscosity but require a certain minimum value of the shear stress to initiate flow. The apparent viscosity η_a depends on the shear rate (rel.1), more exactly it decreases with shear rate increasing. As the shear rate tends to infinity, the viscosity reaches the limit value – the plastic viscosity η_p:

$$\frac{\tau}{\dot{\gamma}} = \eta_a = \frac{\tau_0}{\dot{\gamma}} + \eta_p \quad (1)$$

Thus, at 37˚C, the variation of the apparent viscosity as a function of the shear rate for these four emulsions is presented in Figure 2. It is observed that in the case of most viscous emulsions (C and D), due to the limitation of the viscosity range which can be determined by the device, the constant viscosity level (η_p) has not be reached.

Figure 3, comparatively shows the dependence $\tau = f(\dot{\gamma})$ for emulsion A (without the addition of active principles) and emulsion B (with the addition of 10% active ingredients), at two temperature values. It is observed that, at the same temperature, emulsion B has lower shear stress values than

emulsion A. This is also confirmed by the values of the yield stress and, respectively, plastic viscosity, which are lower in the case of emulsion B (Table 1 and 2).

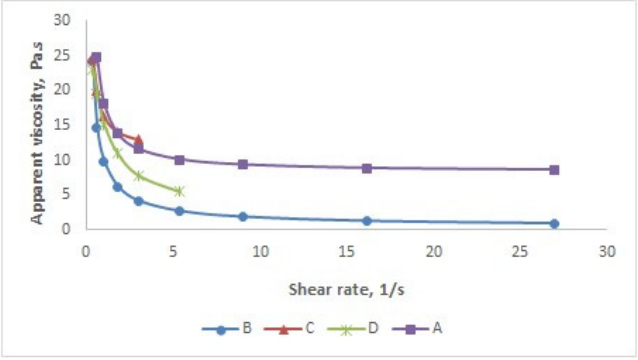

Figure 2. Apparent viscosity (η_a) *vs.* shear rate ($\dot{\gamma}$) for emulsions A, B, C and D at 37°C

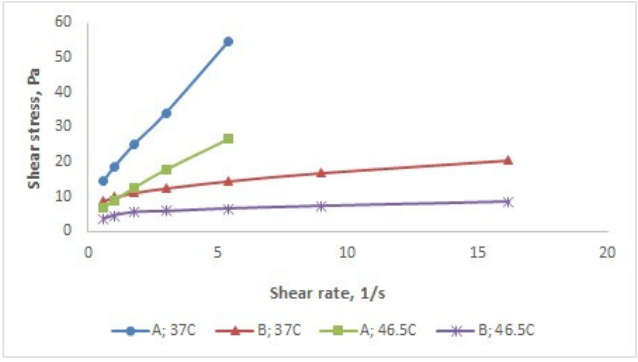

Figure 3. Shear stress (τ) *vs.* shear rate ($\dot{\gamma}$) for emulsions A and B

In order to establish the influence of the preparation temperature on the rheological behavior, emulsions with the same composition obtained at 70˚C (B) and, respectively, at 90˚C (C) were analysed. The dependence $\tau = f(\dot{\gamma})$, at two temperature values, is presented in Figure 4.

It is observed that the emulsion prepared at a higher temperature (emulsion C, 90˚C) has, at the same value of the temperature at which the measurement was performed, higher values of the shear stress compared to the emulsion prepared at 70˚C (B). This observation is also supported by the higher values of both the consistency factor (k) and the flow index (n) for the emulsion C (Table 3).

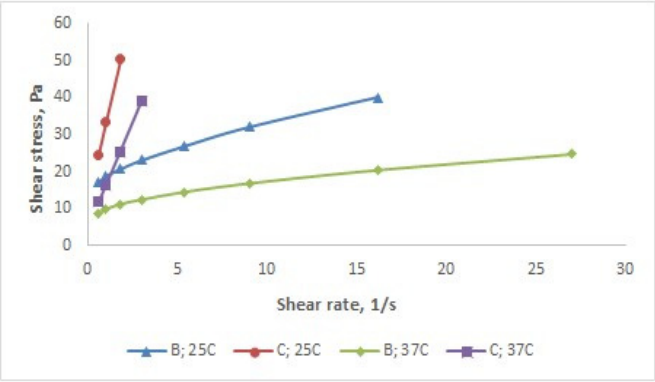

Figure 4. Shear stress (τ) *vs.* shear rate ($\dot{\gamma}$) for emulsions B and C

In order to establish the influence of the cooling rate on the rheological behavior, emulsions with identical composition were analysed: one of them was prepared at 70˚C and then was cooled slowly, in air, to 40°C under continuous homogenization (emulsion B), and the other one was suddenly cooled from 70˚C to 40°C in ice water (emulsion D). The variation of the apparent viscosity as a function of the shear rate for these emulsions is shown in Figure 5.

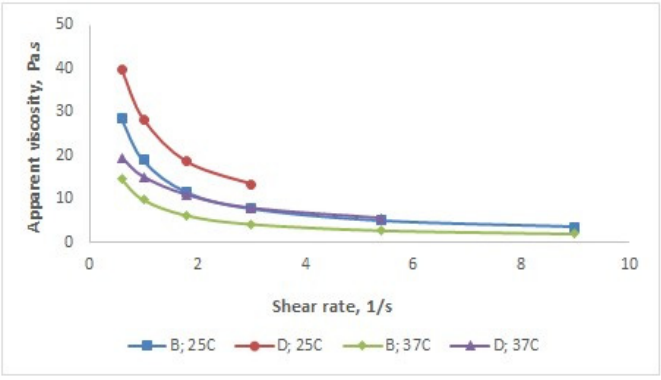

Figure 5. Apparent viscosity (η_a) *vs.* shear rate ($\dot{\gamma}$) for emulsions B and D

It is found that, at the same value of the shear rate and the same temperature, the values of the apparent viscosity are higher in the case of the suddenly cooled emulsion (D).

The oxidation stability

The oxidation stability of the emulsions was studied by determining the peroxide value (PV) and UV absorbances at 232 nm and 270 nm, respectively (K_{232}; K_{270}) for 210 days. Peroxide value is a parameter that gives the peroxides and hydroperoxides quantity formed in the first stage of oil oxidation [15]. These values are influenced by unsaturation degree of the oils, their storage conditions, temperature, light, air contact and the presence of some compounds with catalytic activity for oxidation [16]. K_{232} is related to the presence of hydroperoxides, conjugated dienes, carboxylic compounds and conjugated trienes. K_{270} is dependent on the secondary products formed from the oxidation products detected at 232nm [17].

The peroxide values of the emulsions exposed to air (A1-D1), slowly increased in the first period (180 days); after that, the increase becomes higher (Figure 6). These variations of the peroxide value demonstrate autocatalytic feature of the primary oxidation.

In the case of the emulsions that were not exposed to air (A-D), the curves PV *vs.* time are approximately horizontal (Figure 7). This is confirmed by the lack of the primary oxidation during the study. Comparatively, the peroxide value variation with time for B and B1 emulsions in the absence, respectively in the presence of the air is presented in Figure 8. The increase of the peroxide value due to air exposure was of 200% comparatively to that without air contact, at the end of the study.

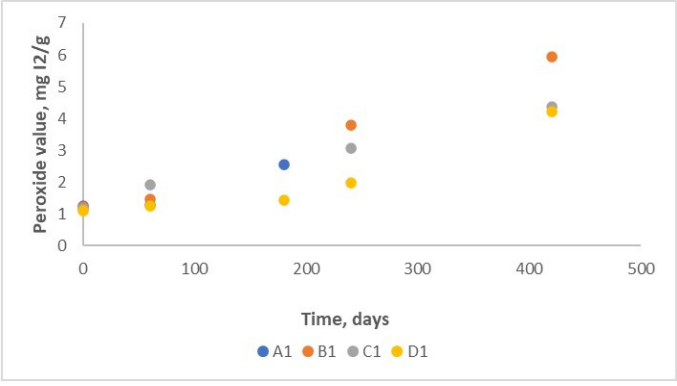

Figure 6. Peroxide value *vs.* time for emulsions A1-D1

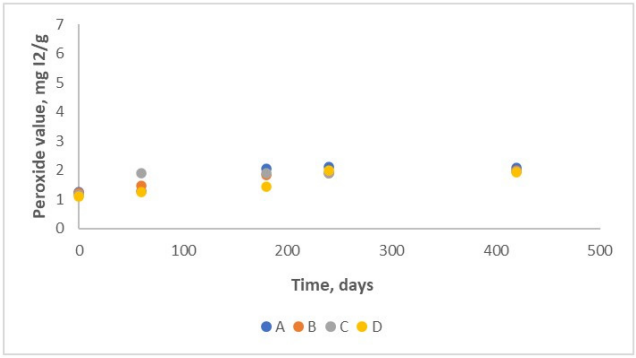

Figure 7. Peroxide value *vs.* time for emulsions A-D

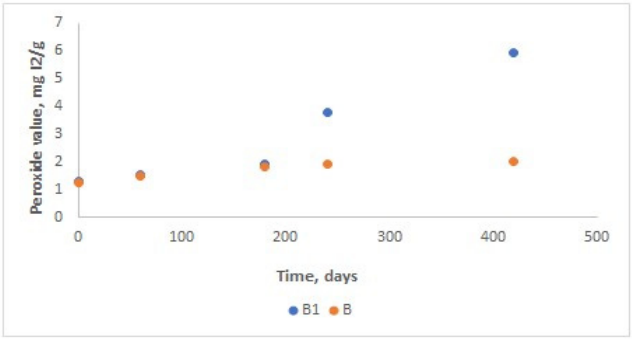

Figure 8. Peroxide value *vs.* time for emulsions B and B1

For the emulsions that have not come into contact with air, K_{232} and K_{270} remained at approximately constant values throughout the study period (Figures 9 and 10). This indicates the absence of secondary oxidation processes in the oil phase.

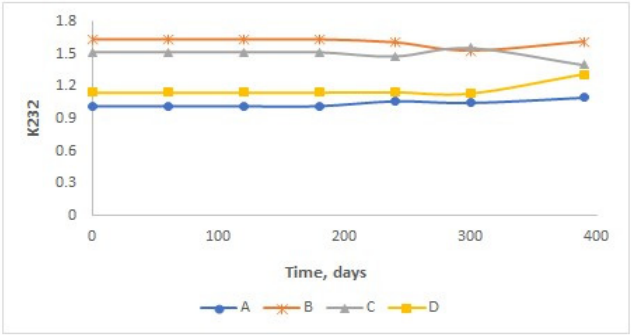

Figure 9. Spectrophotometric constant K_{232} for emulsions A-D

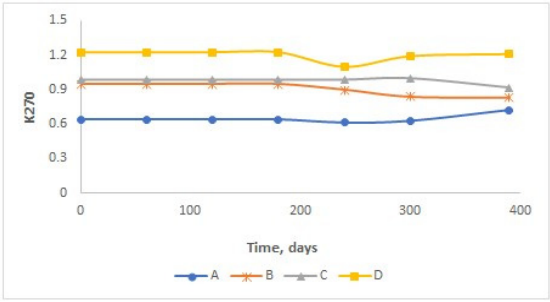

Figure 10. Spectrophotometric constant K_{270} for emulsions A-D

For the emulsions exposed to air contact, the K_{232} absorbance had constant values for approximately 200 days; after that, they recorded an increase. Variation of K_{270} was significantly reduced comparatively to K_{232}.

For the emulsions B and B1, in the absence, respectively in the presence of air, K_{232} and K_{270} variation during the study period is presented in Figures 11 and 12. According to these graphics, the secondary oxidation products are formed after 250 days.

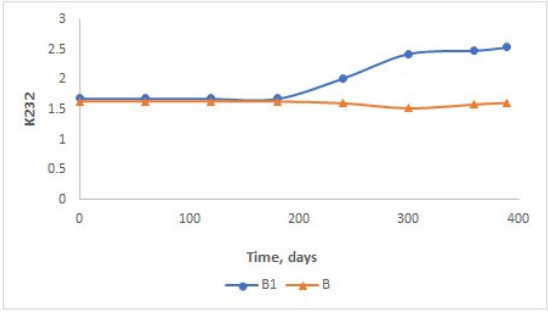

Figure 11. Spectrophotometric constant K_{232} for emulsions B and B1

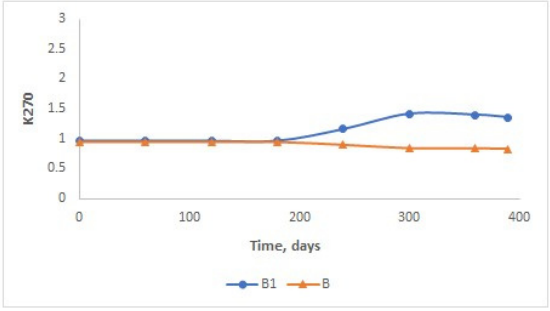

Figure 12. Spectrophotometric constant K_{270} for emulsions B and B1

CONCLUSIONS

The experimental results show that the rheological properties of the analysed emulsions are determined by the preparation conditions (temperature and cooling rate), by the temperature at which the measurements are made, as well as the presence in the composition of the active principles.

All the four emulsions show non-Newtonian behavior with yield stress and the obtained rheological equations fit into the Herschel-Burkley and/or Bingham mathematical models.

In the case of Bingham model, the values of the yield stress (τ_0) and of the plastic viscosity (η_p) decrease with increasing temperature. In the case of Herschel-Bulkley model, the yield stress varies similarly and the values of the consistency factor (k) are correlated with those of the flow index (n).

The decrease in the viscosity of the emulsions with active principles content in the aqueous phase is generated by the nature and concentration of the four incorporated active ingredients, the percentage of aqueous phase being the same in both emulsions.

The increase in the viscosity of the emulsion C could be the consequence of the partial evaporation of the aqueous phase due to the higher temperature at which it was prepared.

Regarding the maintenance of the stability and quality of cosmetic emulsions, it is extremely important the control of their storage conditions (temperature, light, humidity, etc). Evaluation of K_{232} and K_{270} values and peroxide value, respectively, are simple and accurate methods to predict the quality and oxidation stability of different compounds with oily phase content.

Properly preserved cosmetic emulsions, when not exposed to air, were shown to have high oxidation stability for the entire period of the study (420 days). There was no change in the peroxide value, K_{232} and K_{270} values, which indicate the absence of the primary oxidation and the lack of the secondary oxidation products.

The emulsions that were exposed to air, did not suffer any oxidation during the first 200 days. The increase of the peroxide value within the second period, indicates oxidation processes in the oily phase. Nevertheless, these values are relatively low, under 7mg I_2/g.

The values K_{232} and K_{270} for the samples exposed to air, increased moderately after 250 days. This increase confirms small quantities of secondary oxidation products.

EXPERIMENTAL SECTION

Preparation of the emulsions

Both the oily phase (1) and the aqueous phase (2) are heated to 70˚C (for emulsions A, B and D) and, respectively, to 90˚C (for emulsion C). Then, phase (1) was added over phase (2) and mixed for 10 minutes with a Lab High-shear Homogenizer, at 10000 rpm. After homogenization, emulsions A, B and C are gradually cooled to 40˚C, in air, under slower stirring (5000 rpm), and emulsion D is suddenly cooled in ice water to the same temperature.

After reaching the temperature of 40˚C, the active principles, phase (3), are added (in emulsions B, C and D). The active principle consists of: a) Lactobacillus ferment lysate filtrate – probiotic used in anti-aging creams; b) tea tree leaf extract (*Camellia Sinensis)*; c) pomegranate extract (*Punica Granatum)*; d) caffeine.

The composition of the studied emulsions is presented in Table 4.

Table 4. The composition of the analysed samples

Ingredients	Composition, wt %			
	A	B	C	D
Oily phase (1)				
Non-ionic emulsifier	5	5	5	5
Coco-Caprylate/Caprate (emollient / moisturizer)	10	10	10	10
Mixture of oils (sunflower, soybeans, olives, grape seeds)	4	4	4	4
Shea butter	5	5	5	5
Cocoa butter	4	4	4	4
Cetostearyl alcohol	2	2	2	2
Preservative	1.2	1.2	1.2	1.2
Aqueous phase (2)				
Glycerol	4	4	4	4
Sodium benzoate	0.4	0.4	0.4	0.4
Distilled water	64.4	54.4	54.4	54.4
Phase (3)				
Active principles	-	10	10	10

Rheological characterization

The experimental determinations for rheological characterization of the samples were carried out under thermostatic conditions (temperature range 25÷50°C), using a rotation viscometer Rheotest-2 with the system vat-drum S/S3, suitable for the viscosity range of these fluids and higher sensibility. The device allows the measurement of the torsion moment appeared thanks to the ring-shaped substance layer placed between a fixed cylinder and a rotating one with known revolution. The torsion moment is correlated with the shear rate.

Shear rate values were changed in the range 0.333÷27 s^{-1}.

Determination of peroxide value

The peroxide value was determined according to [16,18]: the sample (approximately 1g) is treated with a glacial acetic acid-chloroform (3:2, v/v) solution and then with a solution of KI. It was kept in the dark for 5 minutes followed by the titration with a standard solution of sodium thiosulfate 0.1N using starch as indicator.

Determination of Specific UV Extinction Coefficients (K_{232} and K_{270})

The measurement was performed through UV/VIS spectrophotometry with a UV/VIS Cary 60-Agilent Technologies spectrophotometer. Spectrophotometric analysis of the emulsions was performed in accordance with [17], which involves the determination of the specific extinction in cyclohexane at wavelength of 232 and 270 nm and the determination of the extinction coefficients K_{232} and K_{270}.

A mass of 0.25-0.3 g emulsion was weighted and dilluted to 1% in cyclohexane. Absorbance values were measured using a 1cm path length quartz cell at wavelength of 232 and 270nm. The extinction coefficients (K_λ) were calculated in accordance with Lambert-Beer law.

REFERENCES

1. F. Calvo; J.M.Gomez; L. Ricardez-Sandoval; O. Alvarez; *Chem.Eng.Res.Des.,* **2020**, *161*, 279-303
2. L. Gilbert; C.Picard; G. Savary; M. Grisel; *Colloids Surf., A*, **2013**, *421*, 150-163
3. P. Dubuisson; C.Picard: M. Grisel;G. Savary; *Colloids Surf., A*, **2018**, *536*, 38-46
4. J-B. Guillerme; C. Couteau; L. Coiffard; *Cosmetics*, **2017**; *4(3)*, 35-49
5. A.S. Ribeiro; M. Estanquiro; M.B. Oliveira; J.M.S. Lobo; *Cosmetics,* **2015**, *2*, 48-65
6. D. Chanchal; S.Swarnlata; *J.Cosmet.Dermatol.,* **2008**, *7*, 89-95
7. A. Herman; A.P.Herman; *Skin Pharmacol Physiol,* **2013**, *26,* 8-14
8. K. Sakamoto; R.Lochhead; H.Maibach; Y.Yamashita; *Cosmetic Science and Technology: Theoretical Principles and Applications,* 1st ed.; Elsevier, **2017**; pp.499-502
9. B. Ratner, A. Hoffman, F. Schoen, J. Lemons; *Biomaterials Science: An introduction to Materials in Medicine,* 2nd ed., Academic Press, **2004**, 23-31.
10. G. Schramm; *A Practical Approach to Rheology and Rheometry,* 2nd ed.; Thermo Electron Karlsruhe, **2004**; pp.15-30
11. A. Miclăuș; V. Pode; *Cazuri particulare de curgere a fluidelor ideale și reale. Elemente de reologie*, Ed. Casa Cărții de Știință, Cluj-Napoca, **2018**, pp.48-56

12. B.T. Zengeni; *Bingham Yield Stress and Bingham Plastic Viscosity of Homogeneous non-Newtonian Slurries*; Dissertation-Cape Peninsula University of Technology, **2016**, pp.9-22
13. H.F. George; F. Qureshi; Newton's law of viscosity, Newtonian and non-Newtonian fluids, in *Encyclopedia of Tribology,* Q.J. Wang, Y.W. Chung Eds.; Springer Science+Business Media, NY, **2013**, pp.2419-2424
14. R. Caenn; H.C.H. Darley; G.R. Gray; The rheology of drilling fluids, in *Composition and properties of drilling and completion fluids,* 6th ed; Gulf Professional Publishing, **2011**, Chapter 5, pp.183-185
15. E. Choe; D.B. Min; *Compr. Rev. Food Sci. Food Saf.,* **2006,** *5,* 169-186
16. M. Popa; I. Glevitzky; G-A. Dumitrel; M. Glevitzky; D. Popa; *Sci. Papers Ser. E*, **2017**, *VI*, 137-140
17. A. Malvis; P. Simon; T. Dubaj; A. Sladkova; A. Haz et al.; *Hindawi J.Chem.,* **2019**, Article ID 4567973
18. Official Methods of Analysis of AOAC International, edited by P. Cunniff, 16th ed., AOAC International, Arlington, **1995**, Method 965.33.

STUDIA UBB CHEMIA, LXVI, 4, 2021 (p. 297-308)
(RECOMMENDED CITATION)
DOI:10.24193/subbchem.2021.4.22

AN EXPERIMENTAL STUDY ON SPINNING DISC KEY PARAMETERS INFLUENCING ITS PERFORMANCE

EUGENIA TEODORA IACOB-TUDOSE[a]

ABSTRACT. The spinning disc technology (SD), with its enhanced fluid flow features, has been applied to an increasing number of fields lately. Experimental characterization of the flow on a smooth or radially/concentrically indented rotating disc, for different feeding liquid flow rates (30, 50, 70 L/h) and disc rotational speeds (200, 500, 800, 1100 rpm), using two types of feed distribution systems (one nozzle or four symmetrically distributed nozzles) has been performed, based on the pulse response technique. Based on the radial dispersion model, the Péclet number was determined for different experimental conditions and used to identify flow characteristics and to compare different spinning disc setups efficiencies. Based on the obtained experimental data, the large flowrate values and disc rotational speeds induce a flow regime closer to plug flow, however intense micromixing is achieved within an intermediate range of the studied parameters, when the turbulent wavy liquid film surface occurs, the micromixing is increased and thus, the SD technology is efficiently used. Certain flow characteristics can be achieved if the spinning disc is operated at specific parameter values.

Keywords: *spinning disc, feeding system, flowrate, rotational speed, identations*

INTRODUCTION

The spinning disc (SD) technology uses the centrifugal force action onto a liquid fed on a rotating disc, in order to form a thin film, characterized by intense micromixing induced by high shear rates and waves travelling on the liquid film surface [1]. Thus, enhanced transport properties [2-4] are obtained, suitable for fast gas-liquid reactions [5], homogeneous reactions and also for heterogeneous catalysis [6] or even enzymatic reactions [7] and also, for unit operations such as crystallization [8], extraction [9], boiling [10]

[a] *"Gheorghe Asachi" Technical University of Iasi, „Cristofor Simionescu" Faculty of Chemical Engineering and Environmental Protection, Department of Chemical Engineering, 73 Prof. Dr. Docent D. Mangeron Blvd., 700050, Iasi, Romania, e-mail: eugenia.iacob2017@gmail.com*

or condensation [11]. A large number of applications such as food, cosmetic and pharmaceutical product manufacturing [12,13,14], polymer production [15,16], treatment of industrial wastewaters for the degradation of some pollutants [17,18,19], nanoparticle manufacturing [20,12,21] prove the high versatility of the spinning disc technology.

This experimental study was initiated in order to explain some of the results obtained using SD technology in a laboratory setup in textile wastewater treatment [19] and to investigate key parameters influencing the disc performance. The residence time distribution (RTD) based on the pulse-response method was applied in the liquid film on a spinning disc, at different liquid flow rates and disc rotational speeds, with different liquid feeding systems (one orifice of different diameters and respectively, four symmetrically distributed orifice system), for a smoothed and respectively indented surface disc, in order to render information regarding the radial dispersion and also, the most suitable configurations to increase the SD technology efficiency.

The RTD can be a useful tool to investigate the mixing performance of a SD system, giving information related to the system's degree of dispersion (or Péclet number, high dispersion means low Péclet number, usually Pe<10 [22]) and also, allows comparisons regarding the efficiency of different experimental setups.

Some of the literature data suggest that depending on the feeding system used for liquid inlet on the disc, the convection structures of the liquid film are different which influences, in the end, the SD effectiveness. Specifically, if the liquid film is fed through the center of the disc than concentric waves are formed, developing in spiral waves towards the edge of the disc [23], while a liquid stream fed through one nozzle, above the disc induces standing waves formation [24] and also, spiral waves occurrence. The lastly mentioned setup was investigated in this work, using different diameter single orifice or four symmetrically distributed orifice systems in order to assess its effect on dispersion.

Furthermore, studies regarding the characteristics of the flow on a spinning disc found that large liquid flowrates and rotational speed values, low viscosity liquids would render a convection on the spinning disc closer to the plug flow [25, 26]. However, experimental data [19] obtained on SD technology applied in textile wastewater treatment indicate that a flow regime closer to plug flow is not always appropriate for attaining the best SD efficiency. The degree of dispersion and whether the plug flow is attained in our system can be revealed by calculating the Pe numbers for different working conditions from the RTD experimental data.

The diffusion equation for the tracer used flowing on the spinning disc is:

$$\frac{\partial C}{\partial t} = D\frac{\partial^2 C}{\partial r^2} - u\frac{\partial C}{\partial r} \quad (1)$$

Using some initial and boundary conditions for an open-open system and solving the above Equation (1), the normalized residence time distribution function E(θ) is obtained, with the normalized variance, σ_θ^2, given by [27, 28]:

$$\sigma_\theta^2 = \frac{2}{Pe} + \frac{8}{Pe^2} \quad (2)$$

where Pe is the Péclet number. Based on the experimental value σ_θ^2, using Equation (2), one can calculate the Pe number.

The tracer concentration obtained experimentally and the Equations (3) to (8) have been used to render respectively, the residence time distribution function, E(t), the normalized residence time distribution function, E(θ), the mean residence time, τ, the normalized mean residence time, θ, the variance, σ^2 and the normalized variance, σ_θ^2, as follows [28]:

$$E(t) = \frac{C(t)}{\int_0^\infty C(t)dt} \quad (3) \qquad E(\theta) = \tau E(t) \quad (4)$$

$$\tau = \frac{\int_0^\infty tC(t)dt}{\int_0^\infty C(t)dt} \quad (5) \qquad \theta = \frac{t}{\tau} \quad (6)$$

$$\sigma^2 = \frac{\int_0^\infty t^2 C(t)dt}{\int_0^\infty C(t)dt} - \tau^2 \quad (7) \qquad \sigma_\theta^2 = \frac{\sigma^2}{\tau^2} \quad (8)$$

where C(t) is salt concentration at time t. Randomly, for a few liquid flow rates and disc rotational speeds, the salt concentration time variation was checked in order to confirm a good reproducibility of the results.

RESULTS AND DISCUSSIONS

Residence time distribution curves can be symmetrical and narrow in the conditions of an ideal plug flow, in radial direction. In this case, dispersion is negligible. The more the flow deviates from this type of ideal convection, the more asymmetric and dispersed the residence time distributions.

1. One nozzle feeding system - influence of the nozzle diameter and liquid flowrate for smooth surface disc

Figure 1 (a)-(d) shows the normalized residence time distributions, E(θ), calculated at three different water flow rates of 10, 30, 50 L/h, for four constant disc rotational speeds of 200, 500, 1100, 2000 rpm, respectively, for a feeding inlet nozzle of 3.5 mm diameter. Absolutely all distributions have a characteristic, relatively symmetrical shape. At constant rotational speed, an increase in the flow rate from 10 L/h to 70 L/h renders slightly slender curves, indicating less dispersion, in agreement to Mohammadi's findings [25]. The longer tails, obtained for $\theta > 1$, suggest the persistence of the liquid on the spinning disc, fact confirmed experimentally by other literature studies that used flow visualization and found liquid dragging on the disc surface [24]. Similar curves for the normalized residence time distribution function were obtained for nozzles of 2.45 mm and respectively, 1.95 mm diameters, presented in figures 2 and 3, respectively, for three different liquid flow rates of 10, 50 and 70 L/h, at constant disc rotational speed of 200 and respectively, 2000 rpm.

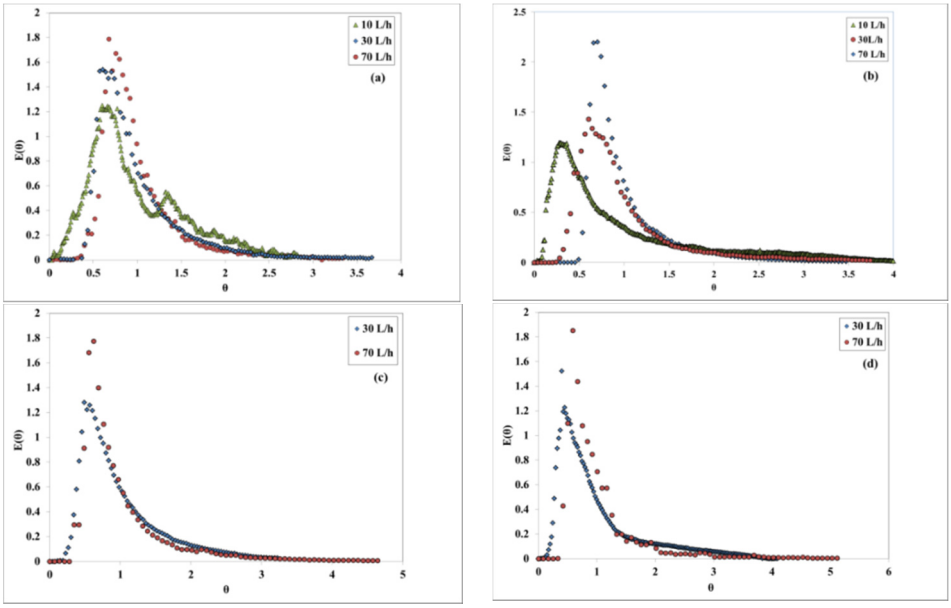

Figure 1. Influence of the liquid flowrate, at constant disc rotational speed, nozzle diameter ø 3.5 mm, smooth disc: (a) 200 rpm; (b) 500 rpm; (c) 1100 rpm; (d) 2000 rpm

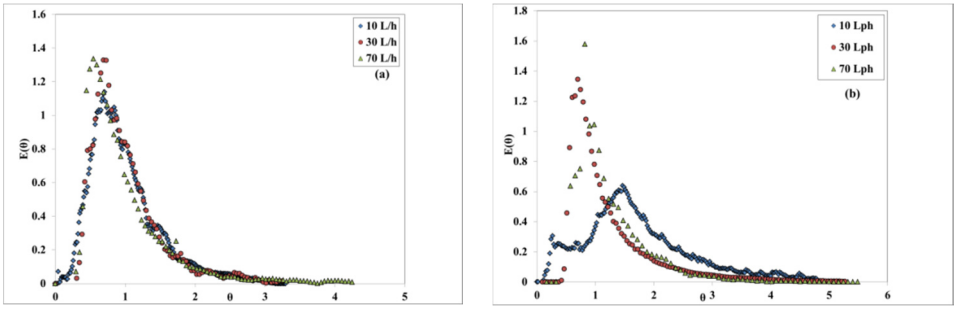

Figure 2. Influence of the liquid flowrate, at constant disc rotational speed, nozzle diameter ø 2.45 mm, smooth disc: (a) 200 rpm; (b) 2000 rpm

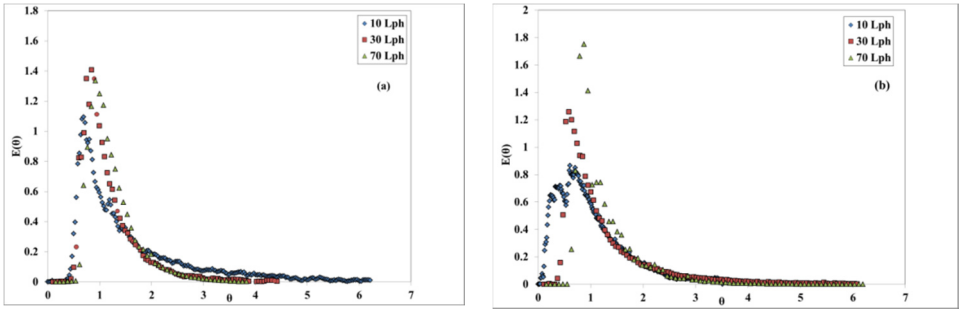

Figure 3. Influence of the liquid flowrate, at constant disc rotational speed, nozzle diameter ø 1.95 mm, smooth disc: (a) 200 rpm; (b) 2000 rpm

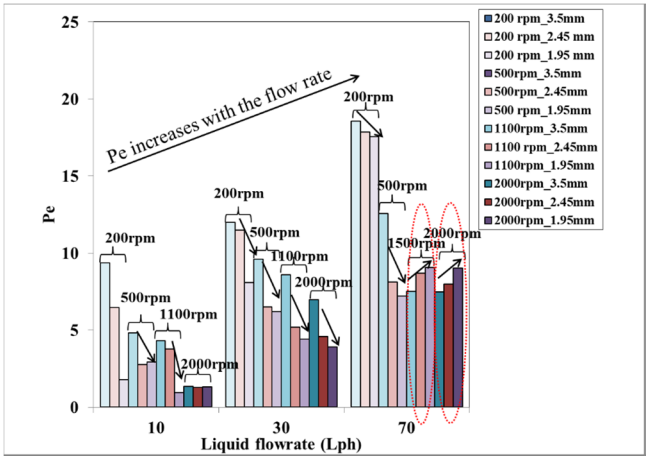

Figure 4. Comparison of different diameter feeding orifices with ø3.5, ø2.45 and ø1.95 mm on the spinning disc – smooth surface (Pe calculated based on the radial dispersion model)

A comparison between different orifice nozzle diameters, based on figures 1, 2 and 3 is difficult to make, thus, from the calculated normalized variance, σ_θ^2, using equation (8), the Péclet number was determined based on equation (2) and represented in figure 4 for different flowrates and disc rotational speeds.

The larger the orifice feeding diameter, the larger the Péclet number at lower flow rates of 10 and 30 L/h, at all investigated rotating speed ranging between 200 rpm and 1100 rpm. Smaller orifice diameter means larger velocity of the liquid jet on the spinning disc, thus, more dispersion on its surface. This result is similar to some other studies regarding a jet impinged, however, on an axially moving surface and found to experience greater dispersion at larger surface speeds [29]. Nevertheless, at 70 L/h, the trend is the same for the low range of rotational speed values of 200 and 500 rpm, but at larger rotating speeds of 1100 and 2000 rpm, Pe increases with the decrease of the orifice diameter, probably due to atomization occurrence which renders a lower liquid flow rate.

2. Four symmetrically distributed nozzle feeding system

2.1. Influence of the liquid flow rate and disc rotational speed

Figure 5(a)-(d) shows the normalized residence time distributions, E(θ), calculated at three different water flow rates of 30, 50, 70 L/h, for four constant disc rotational speeds of 200, 500, 800, 1100 rpm, respectively.

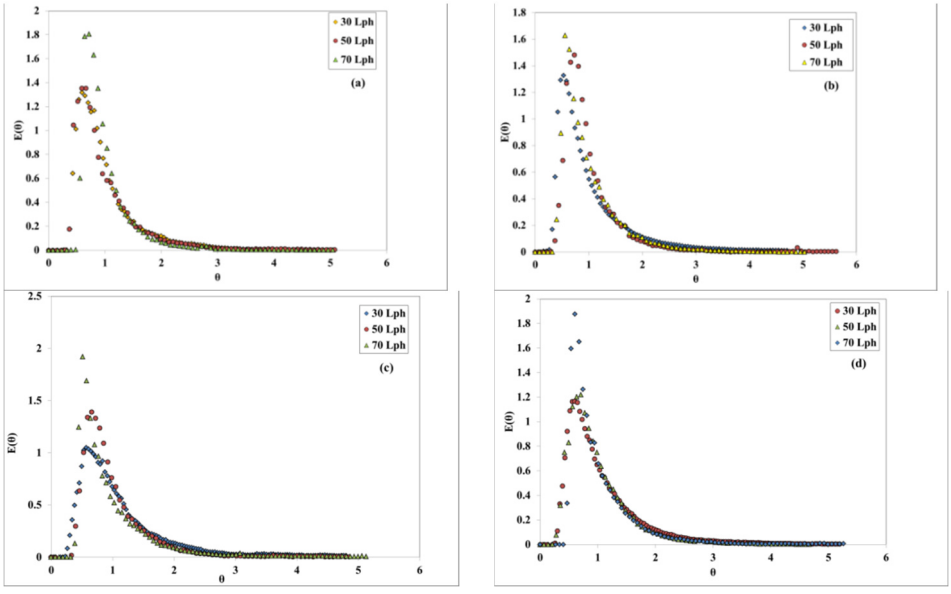

Figure 5. Influence of the liquid flowrate, at constant disc rotational speed, smooth disc: (a) 200 rpm; (b) 500 rpm; (c) 800 rpm; (d) 1100 rpm; four-point feeding system ø 1.75mm

One can observe for the four symmetrically distributed orifice feeding system of 1.75 mm diameter (the four nozzles of ø 1.75 mm have an equal area with the one ø 3.5mm nozzle) similar residence time distributions dependencies on liquid flow rate and disc rotational speed to the ones obtained with one nozzle feeding system. A comparison between the two equal flow areas feeding systems did not reveal significant differences, even though it is thought that the symmetrically distributed system should provide a more symmetric flow field on the disc than the one orifice system.

2.2. Influence of the disc surface

All the data presented to this point pertain to a smoothed spinning disc surface. The residence time distributions obtained on a radially and respectively, concentrically indented discs and comparisons to the smoothed surface disc are included in the following section.

2.2.1. Disc surface with radial indentations

The indentations on a surface are known to promote turbulence. The spiral movement of the liquid on the spinning disc hinted towards the use of a radially indented disc (Figure 10 (a)) that might promote additional mixing in comparison to a smooth surfaced disc, as long as the liquid flow on the disc does not have a strong radial component. Figure 6 (a), (b) shows the normalized residence time distribution obtained for a radially grooved disc, at three different flow rates of 30, 50 and 70 L/h and constant disc rotational speeds of 200 and 1100 rpm. For the grooved disc, similar distributions E(θ) in time and their dependence on the liquid flow rate, namely narrower curves for higher liquid flow rates, can be observed as for the smooth disc.

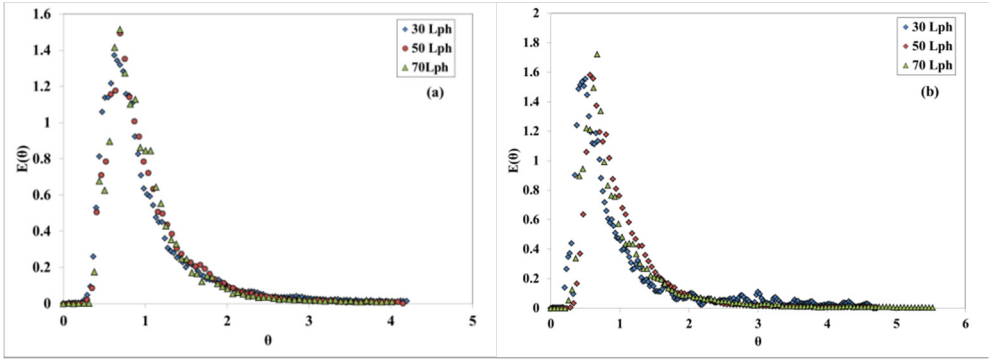

Figure 6. Influence of the liquid flowrate, at constant disc rotational speed, radially indented disc: (a) 200 rpm; (b) 1100 rpm.

In order to compare the dispersion for the two surfaces, the Péclet number was calculated from Eq. (2), based on the normalized variance, σ_θ^2, determined from experimental data, using Eq. (8). Figure 7 presents a comparison between the Pe numbers, for both smooth and radially grooved discs, at different liquid flow rates and rotational speeds. For liquid flow rates of 30 and 50 L/h, at all the investigated rotational speeds, the Pe number was slightly lower for the smooth disc than for the radially grooved disc, which indicates that the dispersion is lowered and the radial micromixing is enhanced for the indented disc.

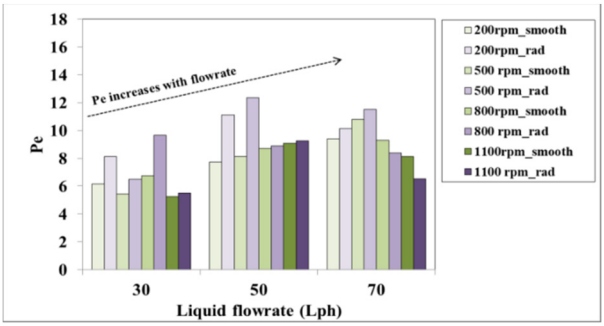

Figure 7. Comparison between smooth and radially indented discs based on calculated Pe number

At a liquid flow rate of 70 L/h, this trend was similar for rotational speeds of 200 and 500 rpm, while at 800 and 1100 rpm, the trend changed probably due to a combined increased liquid flow rate and rotational speed that possibly induced drainage through the radial grooves of the disc (the red dashed circles). Also, Figure 7 reveals an increased Pe number as the liquid flow rate increases, for most of the investigated rotational speeds, for both smooth and radially discs, which is consistent with the narrower residence time distribution curves obtained. Concluding the comparison between the two discs, one can use the radially indented disc to enhance the micromixing, especially at low to moderate rotational speeds and all investigated liquid flow rates.

2.2.2. Disc surface with concentric indentations

The concentrically indented disc should also promote intense micromixing, thus the disc of 20 cm with five concentrical grooves (Figure 10(b)) was used to obtain the residence time distribution. Figure 8 indicates that the plots have similar dependencies on the investigated liquid flow rates of 30, 50 and 70 L/h, at constant rotational speeds of 200 and 1100 rpm, as previously discussed.

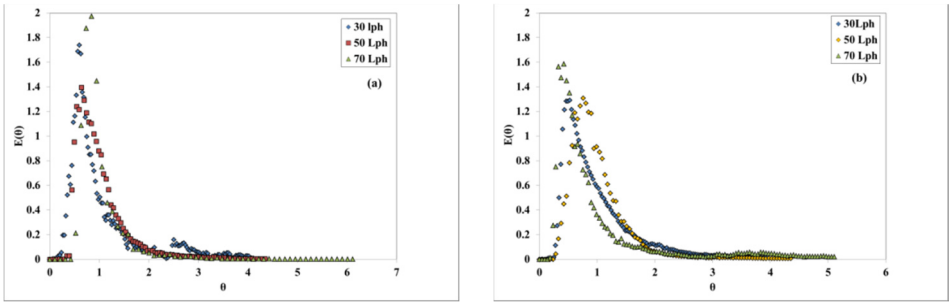

Figure 8. Influence of the liquid flow rate, at constant disc rotational speed, concentrically indented disc: (a) 200 rpm; (b) 1100 rpm

Comparison between the calculated Pe numbers using Eq.(2) (based on the normalized distribution, σ_θ^2, calculated with Eq.(8) from experimental data), for both smooth and concentrically grooved discs, at different liquid flowrates and rotational speeds are presented in figure 9. For 30 and 50 L/h liquid flowrates, the Pe number based on axial dispersion model for the grooved surface is slightly larger than for the smooth surface, for all investigated disc rotational speeds of 200, 500, 800 and 1100 rpm. These results are similar to Mohammadi's findings [25] that revealed, using the RTD analysis and the tanks-in-series model, at disc rotational speeds of 300 and 1200 rpm and a liquid flowrate of 15 mL/s (i.e. 54 L/h), that the concentrically indented disc is characterized by a larger number of tanks-in-series than a smooth surface disc, thus generates more micromixing. For this study, at larger liquid flowrates of 70 L/h, a similar trend is valid for 200, 500 and 800 rpm, however, at 1100 rpm, the trend is reversed, probably due to the atomization occurrence, which reduces the liquid flowrate on the discs (the red dashed circle in figure 9). In this case, the use of a concentrically indented disc promotes also more turbulence than the smoothed surface disc.

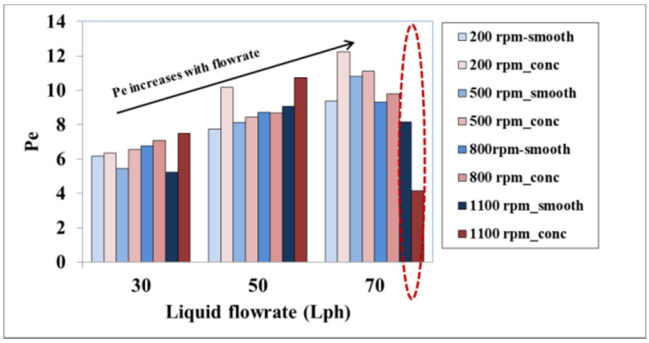

Figure 9. Comparison between smooth and concentrically indented discs based on calculated Pe number

A comparison between the radially and concentrically indented discs, regarding their efficiency in promoting turbulence is difficult to make, even though the Pe numbers for the radially grooved disc seem somewhat higher than for the concentrically grooved disc, however for both discs the Pe values lie within a range indicating mixed flow.

CONCLUSIONS

The pulse response technique was applied in order to characterize some of the flow features on a spinning disc of 20 cm diameter, with different water feeding systems, for different liquid flowrates and disc rotational speeds, in smooth and also indented, both radially and concentrically, disc setups. The experimental data indicated that for a smoothed surface disc, an increase in the liquid flow rate (10, 30, 70 L/h), at constant rotational speeds (200, 500, 1100 and 2000 rpm), causes a reduction in the dispersion. An increase in the disc rotational speed, within the low range (<800 rpm), induces a flow regime with less dispersion. However, within the high range values, atomization is prevalent and the RTD results can no longer be used. Furthermore, the chosen feeding system can induce less dispersion on the disc if larger diameter orifice is used. The Péclet numbers for the radially grooved disc, investigated for the first time, and also, for the concentrically grooved disc, are higher than for the smooth surface disc, especially in the low to moderate disc rotational speeds and for all investigated flow rates. Experimental data obtained at low flowrate and disc rotational speed values, using a smaller orifice diameter of the feeding system and a smoothed surface disc, indicate more dispersion, otherwise, the disc flow may be getting closer to a plug flow, even though the largest obtained Pe numbers in our system suggest still a reasonable amount of dispersion. These observations point out that that operating the SD within specified conditions would render certain flow characteristics, appropriate for the studied system.

EXPERIMENTAL SECTION

The experimental setup used to obtain all the experimental data is presented in Figure 10, together with detailed pictures of the radially (a) and respectively, concentrically (b) grooved discs. It consists of a spinning disc 3 driven by a variable speed, adjustable motor 5 through the coupling 4. The disc is placed in a case 6, provided with a cooling chamber 7 in case the liquid overheats. The tap water used in the experiment was supplied on the rotating disc via a metal rod 2, with one nozzle of different diameters (ø3.5, 2.45 and 1.95mm) or four symmetrically distributed nozzles, each of ø 1.75 mm diameter, from tank 10, using a pump 8, through flowmeter 9, which

measured the liquid flow rate, maintained constant by adjusting tap11. The spinning disc exit liquid was collected through a special machined piece which accommodated the conductometer probe 12, connected to the pre-calibrated conductivity meter 13 (Conductivity Meter 14, WTW 315i).

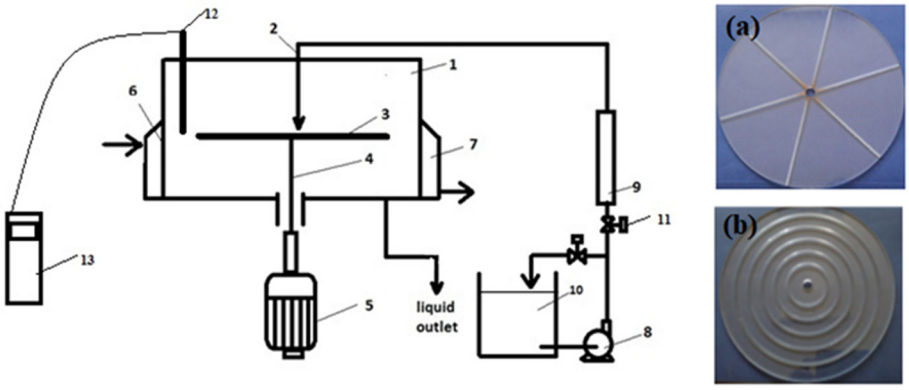

Figure 10. Experimental setup with spinning disc (a) radial grooves (b) concentric grooves

The disc rotational speed was measured using a laser tachometer with a precision of ± 0.1 rpm.

Once the steady state operating regime was reached, the pulse response technique was applied. It consisted of a 2 ml sodium chloride (NaCl) solution, 0.5 mol / L, injection directly into the disc inlet water jet within 1s. At the same time, the conductance values were recorded with a frequency of 1 Hz until the displayed value reached the very initial conductance value. Based on the calibration curve, previously obtained, the NaCl concentrations at the disc exit were calculated.

REFERENCES

1. A.I. Stankiewicz; J.A. Moulijn; *Chem. Eng. Prog.*, **2000,** *96*, 22-34.
2. R.J.J. Jachuck; C. Ramshaw; *Heat Recov. Syst.CHP*, **1994**, *14(5)*, 475-491.
3. I.S. Boiarkina; Norris, D. Patterson, *Chem. Eng. J.*, **2013**, 225, 752-765.
4. L-B Yao; W. Wu; X.-S. Wu; G.-W. Chu; Y. Luo; B.-C. Sun, *Chem Eng Process*, **2021**, 166, 108500-108521.

5. A. Chaudhuri; K.P.L. Kuijpers; R.B.J. Hendrix; P. Shivaprasad; J.A. Hacking; E.A.C. Emanuelsson; T. Noël; J. van der Schaaf, *Chem. Eng. J.*, **2020**, 400, 125875.
6. M. Vicevic; Jachuck R.J.J.; K.Scott, J.H. Clark; K. Wilson, *Green Chem*, 2004, 6, 533-537.
7. X. Feng; D.A. Patterson; M. Balaban; G. Fauconnier; E.A.C. Emanuelsson, *Chem. Eng. J.*, **2013**, 221, 407–417.
8. L. Cafiero; G. Baffi; A. Chianese; R. Jachuck, *Ind Eng Chem Res*, **2002**, 41(21), 5240-5246.
9. F. Visscher; J. van der Schaaf; M.H.J.M.de Croon; J.C.Schouten, *Chem. Eng. J.*, **2012**, 185-186, 267-273.
10. M.M. de Beer; J.T.F. Keurentjes; J.C. Schouten; J. van der Schaaf, *AIChE J.*, **2016**, 62 (10), 3763-3773.
11. M.M. de Beer; J.T.F. Keurentjes; J.C. Schouten; J. van der Schaaf, *AIChE J.*, **2016**, 62 (10), 3784-3796.
12. S. Sana; K. Boodhoo; V. Zivkovic, *Green Process Synth*, **2019**, 8, 507–515.
13. W.H. Khan; V.K. Rathod, *Chem. Eng. Proc.*, **2014**, 80, 1–10.
14. P. Oxley, C. Brechtelsbauer, Francois Ricard, Norman Lewis Industrial & Engineering Chemistry Research 39(7), 2000, 2175-2182.
15. K.V.K. Boodhoo; R.J. Jachuck; *Green Chem.*, **2002**, *2*, 235-244.
16. K.V.K. Boodhoo; R.J. Jachuck; *Appl. Therm. Eng.*, **2000**, *20(12)*, 1127-1146.
17. C.Y. Chang; N.L. Wu, *Ind. Eng. Chem. Res.*, **2010**, 49, 12173–12179.
18. A.Y. Zhang; M.H. Zhou; L. Han; Q.X. Zhou, *J. Hazard. Mater.*, **2011**, 186, 1374–1383.
19. E.T. Iacob-Tudose; C. Zaharia, *Appl Sc*, **2020**, *10*(23), 8687.
20. C. Ahoba-Sam, V.K. Boodhoo, U. Olsbye, K.J. Jens, *Materials*, **2018**, 11, 154.
21. M. Stoller, J.M. Ochando-Pulido, *Nanomaterials*, **2020**, 10, 1321.
22. Levenspiel, O. *Chemical reaction engineering*, 3, John Wiley & Sons, New York, USA, **1999**, p.259.
23. Woods, W. *The hydrodynamics of thin liquid films flowing over a rotating disc*, Ph.D.thesis, University of Newcastle upon Tyne, UK, **1995**.
24. Boiarkina, I.S. *Investigation of a Spinning Disc as a Thin Film Photocatalytic Reactor for the Degradation of Recalcitrant Wastewaters*, Ph.D. thesis, The University of Auckland, **2013**.
25. Mohammadi, S., Boodhoo, K.V.K., *Chem. Eng. J.*, **2012**, *207–208*, 885–894.
26. Boodhoo, K.V.K., Al-Hengari, S.R., *Chem. Eng. Technol.*, **2012**, *35(7)*, 1229-1234.
27. Bozga, G., Muntean, O. *Reactoare chimice (Chemical reactors)*, **1**, Ed.Tehnica, Bucuresti, Romania, 2000, p.169.
28. Coulson, J.M., Richardson, *J.F. Chemical Engineering*, 3, **3**, Elsevier Butterworth-Heinemann, Oxford, UK, 2007, p.90.
29. Moulson, J.B.T., Green, S.I., *Phys. Fluids*, **2013**, *25(10)*,102-106.

STUDIA UBB CHEMIA, LXVI, 4, 2021 (p. 309-328)
(RECOMMENDED CITATION)
DOI:10.24193/subbchem.2021.4.23

STATE OF THE SURFACE WATERS IN CROSS BORDER REGION OF EASTERN SERBIA AND CARAS SEVERIN COUNTY – MOLDOVA NOUA IN ROMANIA

ZORAN STEVANOVIĆ[a]*, RENATA KOVAČEVIĆ[a], RADMILA MARKOVIĆ[a], VOJKA GARDIĆ[a], BIANCA CONSTANTINA VULPE[bb], BIANCA BOROS[b], GHEORGHITA MENGHIU[b]

ABSTRACT. Bor, Krivelj, and Bela Rivers in Eastern Serbia belong to the watershed of Timok River, which is a tributary of Danube River. These Rivers flow near to the largest mining complex in Republic of Serbia. Rivers Bosneag, Radimna and Nera from the Romanian side in Caras Severin County near to Moldova Noua are also tributary of Danube and flow in area which is affected by spreading of dust from the abandoned flotation tailing of copper mine. This study includes environmental monitoring of the surface waters in considered Romania-Serbia cross border area during 2019-2020. Chemical analyses confirmed pollution mostly with heavy metals (Fe, Mn, Cu, Zn, As, Ni, Pb, Cd) closer to mines while with larger distance pollution decrease. The measured values were compared with Serbian and Romanian legislation which confirmed moderate and high pollution depending on category of surface waters. Measured Cd concentrations were of 9.51 - 5375 μg L^{-1} for the IV category of River water close to Bor mine. The main anthropogenic source in Eastern Serbia was Bor mine and smelter.

Keywords: *mining, surface waters, tailings, monitoring, pollution*

INTRODUCTION

Mining is one of the oldest industrial activities. The huge amounts of tailings that are created during the extraction and processing of ore represent a great danger to the environment and destroy agricultural land and forests.

[a] *Mining and Metallurgy Institute Bor, Zeleni bulevar 35, 19210 Bor, Serbia*
[b] *West University of Timisoara, Faculty of Chemistry, Biology, Geographic, Department of Biology-Chemistry, Oitz 4A, Timisoara, Romania*
* *Corresponding author: zoran.stevanovic@irmbor.co.rs*

The dust that the wind disperses from the tailings represent environment hazard by pollution of heavy metals ions. Tailings are also a source of Acid Mine Drainages (AMD) that contains high concentrations of metal cations, especially iron, and often toxic chemical elements such as arsenic [1]. AMD are one of the most significant environmental risks globally because they could be transported by surface waters on wider area, sometimes even out of the country. Hundreds of thousands of hectares of land and thousands of kilometers of watercourses around the world are threatened by the runoff of AMD [2]. Abandoned mines and tailings can generate acidic water for tens, hundreds, even thousands of years. Abandoned Richmond pyrite mine in California (USA) is estimated to generate an extremely acidic solution for the next 3,000 years [3], while a small zinc and copper mine in northwestern Ontario (Canada) is estimated to generate acidic mine waters in the next 10,000-35,000 years [4]. Although these are extreme examples, it is not uncommon for abandoned mine shafts and tailings to have the capacity to form acidic solutions over a period of hundreds of years. Surface and underground ore mining generally have serious negative impacts on the environment such as air pollution, land use and biodiversity and water availability. Also, some effluents generated in the mining industry contain large amounts of toxic substances (cyanides, heavy metals and other harmful and dangerous substances), which have serious human health and environmental hazards [5-7]. Based on possible hazards, waste mine water generated from active as well as abandoned mines is one of the main chemical threats to groundwater and surface water.

According to a study prepared for DG Environment, the European Commission, more than 4.7 billion tons of mining waste and 1.2 billion tons of flotation tailings were disposed of across the European Union [8]. Ten thousand active and abandoned mines are source for $5\text{-}10\times10^9$ m^3 of highly polluted AMD annually [9]. Global mining activities with technological processes of mineral processing and metal production generate several billion tons of solid inorganic waste or by-products, including liquid waste [10]. Balkan Peninsula was generally the main area in Europe for supply of copper, lead and zinc until 1990 [11] and many mines still are operational. Also, in this area exist and many abandoned mines and tailings which represent continuous environmental threat. Some previous environmental assessments on Balkan Peninsula show high mining impact on surface waters with coupling of findings from the natural science and socioeconomic approaches [12].

Due to a great negative impact of mining industry on water system, the aim of cross-border collaborative project (ROSNET2) was to perform the monitoring of surface waters close to active and abandoned mines in cross border area.

This paper includes results of environmental monitoring of the surface waters quality in considered Romania-Serbia cross border area during 2019-2020. The main objective was providing of timely response and warning for possible negative processes and accident situations and gain a complete insight into the state of the surface waters in Project area. All the results will be systematized and grouped in data base with updating possibility with new data and available to interested public.

RESULTS AND DISCUSSION

In Serbia, the most important copper mines are located in Eastern Serbia in Bor District. There are two mines with open pit exploitation (Veliki Krivelj and Cerovo), one undergrounds mine (Jama mine), two mineral processing plants in Krivelj and Bor and smelter for Cu concentrate. Certified geological reserves amount to approximately 3 billion tons of ore and they contain approximately 12 million tons of Cu. Confirmed reserves, with the average annual exploitation, guarantee copper production for the next 100 years. Long mining history resulted that in the immediate vicinity of Bor, exist huge quantities of open pit overburden and flotation tailings (> 2 billion tons) which contain hazardous and dangerous materials such as copper, nickel, arsenic, zinc, antimony, mercury, chromium, bismuth [13]. Waste Management Strategy of the Republic of Serbia for the Period 2010-2019 illustrates that 40000 ha of soil is polluted by mining operation, 7% being situated in Bor Region. Most of copper production of Serbia is located in Eastern Serbia and the total polluted surface of soil is 2784 ha. During the period 1933-1970, the flotation tailing completely degraded the valley of the Bor River which flows through the village near the Bor. Entire length of the Bor River flow to the empties into the Krivelj River, about 70 hectares of coastal land was polluted by the flotation tailings. It is estimated that the flotation tailings polluted even more than 2000 ha of the most fertile coastal land of the above rivers. In addition to the physical contamination of the coastal land of the Bor River valley by thousands of tons of flotation tailings, the Bor River is constantly polluted by waste water resulting from draining through the flotation tailings and open pit overburden [11].

Moldova Nouă is the second largest copper reserve in Romania (500 million tons of ore grading 0.35% copper) [14] and also the largest in considered cross border area. The operations were stopped but the environmental damages are still present. The tailings ponds from Moldova Nouă contain approximately 30 million m^3 of tailings covering an area of 130 ha with a height of most tan 20 meters [15]. One of the worst cases is represented by Tăuşani–Boşneag pond placed between Moldova Veche

town and Coronini village, Caraş-Severin County. Annual report concerning the state of the environment in Romania for 2019 illustrates that 24432 ha of soil are polluted by mining operations and 6639 ha of soil are polluted by heaps, tailings ponds, sterile deposits from floating and warehouses waste. The largest surfaces with polluted soil (23.2%) are registered in the area of the mines situated in the cross-border region of Romania and Serbia. The same report exposes the soil pollution affects about 0.9 million ha, the most destructive being the pollution with heavy metals (Cu, Pb, Zn, Cd) and sulphur dioxide. Additionally, the soil pollution with particles carried by the wind affects 0.363 million ha.

Flotation tailings are one of the sources for dust and AMD pollution. Two examples from both side of border (Tăuşani–Boşneag pond near Moldova Noua in Romania and old Bor flotation tailing in Bor) are presented in Figure 1.

a b

Figure 1. a) Tăuşani–Boşneag pond near Moldova Noua in Romania in windy conditions; **b)** Old Bor flotation tailing in Bor River valley

One type of pollution caused by flotation tailing is spreading of dust. Figure 1a shows spreading of the dust from the tailing in windy conditions. This dust usually contains small particles with heavy metal content which could be easily transferred into soil or surface waters and transported far away from the tailing. Both of presented mines are copper mines, where copper is in association with sulphur, iron, carbon and oxygen. In Serbia and Romania, copper mineralization is mostly porphyry type of deposits containing mostly sulphur minerals associated with pyrites that are one of the main sulfuric acid generators in contact with atmospheric precipitations. Consequently, Acid Mine Drainages generated from those kinds of waste materials is one of the main chemical threats to groundwater and surface water quality. AMD are, as a rule, acidic with pH value mostly between 2.5 and 4 due to an elevated concentration of sulphuric acid, as a second product of bacterial oxidation of sulphide minerals. Pyrite is the most abundant mineral in poly-metallic sulphide ore deposits and in mining waste dumps. The oxidation of

pyrite and copper minerals in an aqueous environment occurs via two simultaneous mechanisms, i.e., biochemical involving bacteria, and chemical way, can be described by the following stoichiometric reactions [16-18]:

(Bacterial) $2FeS_2 + 7.5O_2 + H_2O \rightarrow Fe_2(SO_4)_3 + H_2SO_4$ (1)

(Chemical) $2FeS_2 + 7Fe_2(SO_4)_3 + 8H_2O \rightarrow 15FeSO_4 + 8H_2SO_4$ (2)

(Chemical) $FeS_2 + Fe_2(SO_4)_3 \rightarrow 3FeSO_4 + 2S^0$ (3)

(Bacterial) $S^0 + H_2O + 1.5O_2 \rightarrow H_2SO_4$ (4)

Based on composition, heavy metal ions mobilization, surface water transportation on wider area and capacity of mine for generation, release of AMD that contained elevated concentrations of metals from mine wastes induces an environmental problem of global scale. The UN has even labelled AMD as the second biggest problem facing the world after global warming.

Locations of surface water sampling in Eastern Serbia are presented in Figure 2.

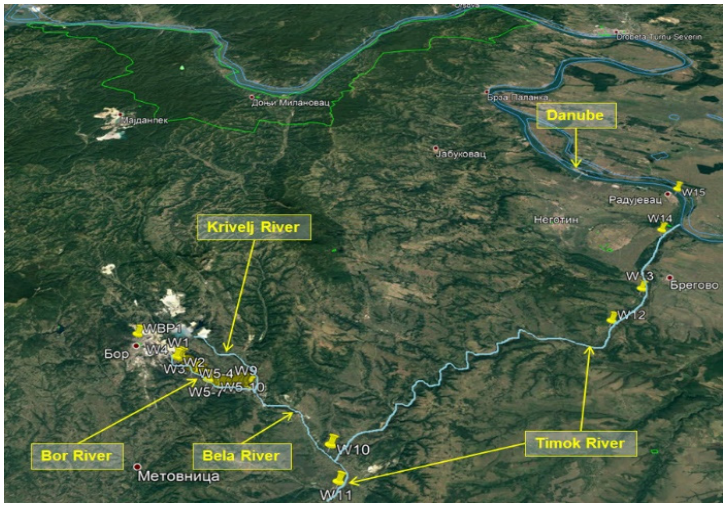

Figure 2. Surface water sampling – Eastern Serbia side

Locations of surface water samples are: (W1, W2) Robule accumulation; (W3) AMD from flotation tailing dam "RTH"; (W4) Industrial wastewater; (14 samples W5-1 - W5-14) Bor River before confluence with Krivelj River; (W6) Krivelj River, (W7) Bela River after the confluence of Bor and Krivelj River, (W8) Ravna River, (W9) Bela River after flows of Ravna River; (W10) Bela River before of confluence in Timok River; (W11) Timok River before confluence of Bela River; (W12) Timok River after confluence of Bela River (Rajac); (W13) Timok River (Mokranje-Negotin); (W14) Timok River (Bukovce); (W15) Danube River (Radujevac).

The results of chemical analyses of surface waters from the Serbian side and Maximum Allowed Concentrations (MAC) according to Serbian legislative are presented in Table 1.

Table 1. Chemical analyses of surface waters from the Serbian side

Category of surface water / Location	Parameter	Range (min-max)	Median	MAC	Content > MAC (%)[1]
IV From Bor city to the confluence Bor and Timok River Samples (W1 – W10)	Fe (mg L^{-1})	0.069-1231	134.9	2	**96**
	Mn (mg L^{-1})	1.8-115.8	5.9	1	**100**
	Cu (mg L^{-1})	0.089-318.7	50.6	1	**98**
	Zn (mg L^{-1})	0.28-43.2	7.5	5	**88**
	As (μg L^{-1})	<2.1-25058	385.4	100	**72**
	Ni (μg L^{-1})	7-16200	992	34	**91**
	Pb (μg L^{-1})	<2.1-3718	493	14	**83**
	Cd (μg L^{-1})	9.51-5375	715.8	0.9	**100**
	Cr (mg L^{-1})	<0.005-0.14	0.020	0.25	0
	Hg (μg L^{-1})	< 0.5	< 0.5	0.3	0
	SO_4^{2-} (mg L^{-1})	1246-13964	2179.0	300	**100**
III From the confluence Bor and Timok River up to the confluence of Timok and Danube River Samples (W12 – W14)	Fe (mg L^{-1})	<0.007-0.16	0.034	1	0
	Mn (mg L^{-1})	<0.006-0.78	0.47	0.3	**50**
	Cu (mg L^{-1})	<0.005-0.33	0.064	0.5	0
	Zn (mg L^{-1})	<0.005-0.76	0.30	2	0
	As (μg L^{-1})	<2.1-4.4	3.62	50	0
	Ni (μg L^{-1})	7-1600	362	34	**67**
	Pb (μg L^{-1})	<2.1-5.9	5.9	14	0
	Cd (μg L^{-1})	<1.1-47.0	25.8	0.6	**58**
	Cr (mg L^{-1})	<0.005	-	0.1	0
	Hg (μg L^{-1})	< 0.5	< 0.5	0.3	0
	SO_4^{2-} (mg L^{-1})	82.2-691.6	270.6	200	**50**
II Danube Sample (W15)	Fe (mg L^{-1})	<0.007-0.34	0.011	0.5	0
	Mn (mg L^{-1})	<0.006-1.6	0.33	0.1	**5**
	Cu (mg L^{-1})	<0.005-0.48	0.025	0.1	0
	Zn (mg L^{-1})	<0.005-0.037	0.037	0.3 - 2	0
	As (μg L^{-1})	<2.1-14.8	4.8	10	**15**
	Ni (μg L^{-1})	7-74	62	34	**30**
	Pb (μg L^{-1})	<2.1-5.5	5.5	14	0
	Cd (μg L^{-1})	<0.14-0.78	0.20	0.45	**5**
	Cr (mg L^{-1})	<0.005	-	0.05	0
	Hg (μg L^{-1})	< 0.5	< 0.5	0.3	0
	SO_4^{2-} (mg L^{-1})	26.7-1950	60.4	100	**40**

[(1)]Content > MAC (%) represent the percentage value of the number of the samples from the total number of taken samples that had measured values over MAC.

In Eastern Serbia, pH values for surface water samples from Bor city to the confluence of Bor and Timok River range from 1.77 to 7.72 indicating that most of the analyzed surface waters are strong acid water with pH values lower than 3.0 [19, 20]. According to Serbian legislation for surface water, in rivers from Bor city to the confluence Bor and Timok (IV water category), the content for almost all of the analyzed elements and sulfate are above the MAC [21].

Surface waters from Bor mining complex up to confluence with Timok River are extremely enriched with toxic elements such as arsenic and cadmium [22]. The manganese and cadmium concentrations in surface water samples from this area were above the MAC in all analysed samples (100% > MAC) as well as sulphate content. Exceedances of MAC values in these surface waters in a high percentage, above 70%, were also recorded for Cu (98.84%), Fe (96.51 %), Ni (91.86%), Zn (88.37%), Pb (83.72%) and As (72.09%). The only element with content below the MAC is chromium. As particular concern is the data for cadmium, the maximum detected value of this highly toxic metal is almost 5500 times higher than the MAC. Fe was the most abundant element in IV class of surface water samples with median value of 134mg L^{-1} and concentrations in range from 0.069 to 1231 mg L^{-1}.

The Median value [23, 24] is presented to indicate the central tendency of these highly scattered data. High presence of copper in IV class of surface water is also recorded with median value of 385.4 mg L^{-1} and concentration range from 0.089 to 318.7 mg L^{-1}. Considering recorded content, median value and percentage of samples with higher content than MAC, pollution main hazards are Cd, Mn, Cu, Fe, Ni, Zn, Pb and As. However, with addition consideration on pollutants impact on human health, the main risk is caused by Cd, As, Pb and Cu pollution. One of the highest pollution hazards represents Cadmium (Cd) with maximum recorded value of 5375 μg L^{-1} which is more than 5500 times higher than allowed concentration. Cd is a toxic heavy metal and its chronic exposure leads to antagonistic changes in living organisms when it enters the food chain [25]. It has gained the attention of scientists after a breakout of Itai-Itai disease in Japan that resulted from wastewater irrigation of agricultural lands [26]. In humans, Cd main intake occurs through food intake and once entered the human body Cd accumulates to a high level in several organs [27]. Cd is usually associated with chronic kidney disease, osteoporosis, diabetes, cardiovascular disease and cancer from long term exposure at levels above the MAC [28, 29]. Mining activity is one of the predominant sources of Arsenic (As) pollution. As is also extremely high pollution hazard with recorded 72.09 % of samples with increased values than MAC. Maximum recorded As value is more than 250 times higher than MAC. Arsenic is highly carcinogenic in waters [30], classified

by U.S. EPA as a Group A human carcinogen [31] and may cause serious diseases to humans [32, 33]. Lead (Pb) is the most toxic element that is present in the environment as a result of both natural and anthropogenic sources [34]. In case of Bor surrounding surface water the main source is, like for the other pollutants, huge mining activities. Pb was recorded in 83.72 % of samples with increased values than MAC with maximum recorded value of also more than 250 times higher than MAC. The primarily routes of lead exposure are through ingestion and inhalation. Once absorbed, lead binds to erythrocytes and travels in the blood to various tissues (liver, kidneys, lungs, brain, spleen, muscles, and heart) and moves further into bones and teeth, and may affect any organ or system in the body through fundamental biochemical processes [35, 36]. Even at low concentration, it can induce neurobehavioral dysfunctions, anaemia, cardiac dysfunction and vascular damage, kidney diseases, reproductive effects, bone toxicity and alters the major cellular functions [37-42]. Copper (Cu) is a most expected pollutant in Bor surrounding surface waters due to more than 115 years long history of copper mining in this area. Cu was recorded in 98.84 % of samples with increased values than MAC with maximum recorded value of more than 300 times higher than MAC. Human exposure to copper is similar to other metal ions, Cu being ingested with vegetables that extract it from soil solution via roots or by contaminated water and via the inhalation of particulate matter. Concerning human health, the toxicity of Cu is relatively low compared with other heavy metals, but excess copper accumulation in subjects following high-dose chronic exposure and in sensitive population's results in hepatic cirrhosis with jaundice, haemolytic anaemia, and degeneration of the basal ganglia, cardio toxicity, gastrointestinal disorders and central nervous system manifestations [43].

Samples from surface waters from rivers that belong to the III category (from the confluence Bor and Timok River to the confluence of Timok and Danube River) show that most of the elements and sulfates are below the MAC for the given category of surface waters. The manganese and sulphate content was exceeded in half of the analysed samples. The content of nickel and cadmium for this category of surface waters was exceeded in 66.67% and 58.33% of the analysed samples, respectively. The recorded concentrations of other considered elements were below the MAC values for this category of surface waters. Content of the main heavy metal polluter were dropped by increasing of distance from mining complex and by mixing of Bela River with Timok River. However, even in these surface waters, Cd was recorded with maximum concentration of over 70 times and median value of over 40 times higher than MAC for this category of surface waters. Nickel was recorded with maximum concentration of over 47 times and median value of over 10

times higher than MAC while manganese was recorded with maximum concentration of over 2 times and median value slightly higher than MAC.

The situation is even better with II category surface waters (Danube River) in which increased values of manganese and cadmium in 5%, arsenic in 15%, nickel in 30% and sulphate in 40% of the analysed samples were detected. Unlike IV class of surface waters, the maximum detected values of individual elements in II class of surface waters are not more than 2 times the MAC values.

Figure 3 illustrate as example trends of elements measured in higher concentrations (mg/l).

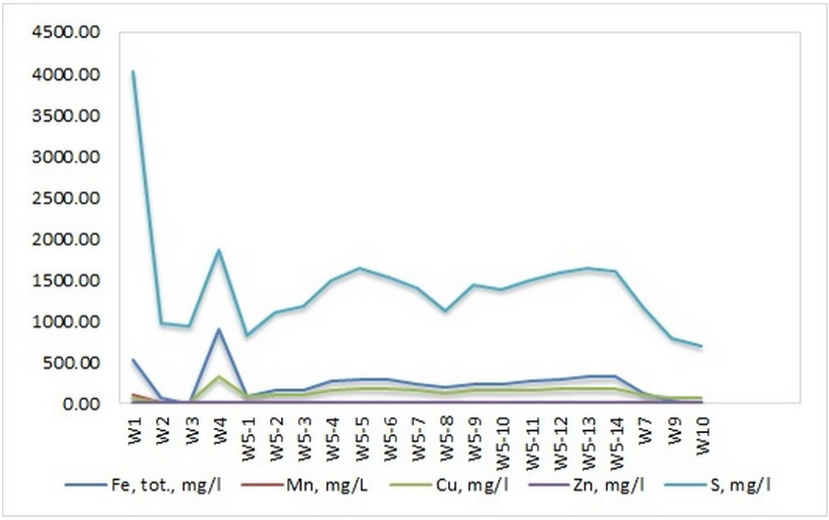

Figure 3. Trends of elements with higher concentrations – Eastern Serbia side

As it could be seen from the plot in Figure 3, pollutants show similar zigzag pattern, high concentrations of one species correspond to high concentrations of other species. These species show strong correlation indicating as the main source of pollution Bor mine and smelter [44, 45]. In addition, the relationships between species (Figure 4 - example for copper and zinc) were examined to evaluate relationships between the species that may indicate a common source.

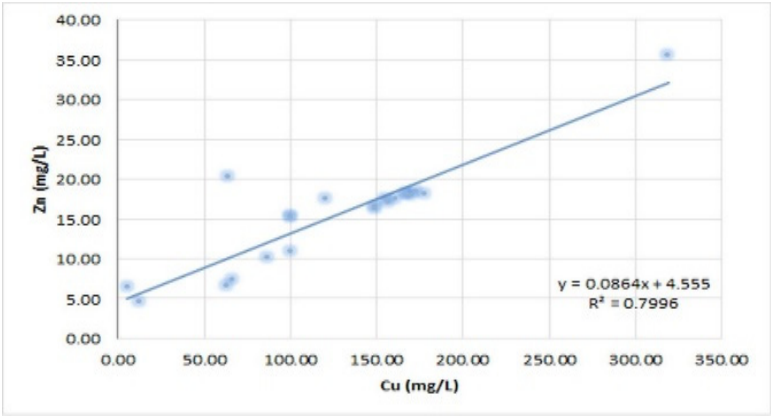

Figure 4. Cu and Zn concentrations relations – Eastern Serbia side

According to the scatter plot results, the coefficient of determination (R^2=0.7996) shows that almost 80% of concentrations of copper are well correlated with concentrations of zinc confirming the same anthropogenic source of pollution for this species. This may indicate that heavy metals in surface waters of III and IV category were originated from a single anthropogenic source of pollution. In case of Eastern Serbia, a copper smelter was the main source.

Figure 5 illustrate as example trends of elements measured in lower absolute concentrations (µg/l).

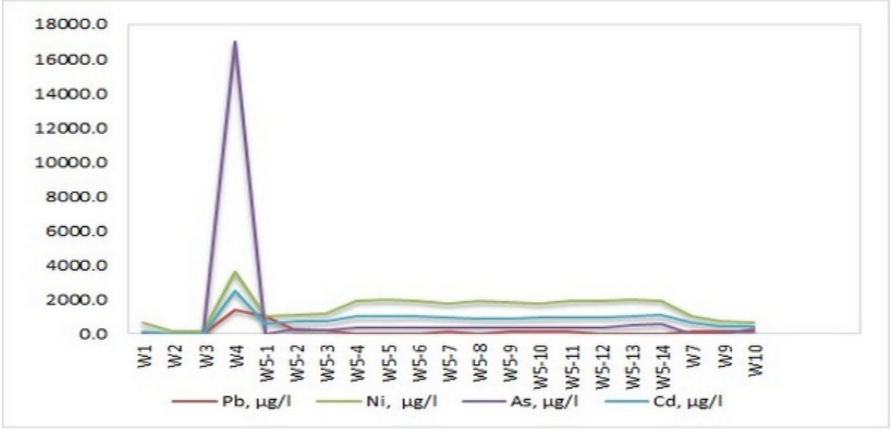

Figure 5. Trends of elements with lower absolute concentrations – Eastern Serbia

Heavy pollutants shown in Figure 5, with lower absolute concentrations but all above MAC values, show similar zigzag pattern like pollutants in Figure 3 indicating the single and common source of pollution.

Locations of surface water sampling in Caras Severin County near Moldova Noua in Romania are presented in Figure 6. Having on mind that copper mine from Romanian side is not in operational stage, water samples were taken for monitoring purposes at first. Sampling locations were chosen to cover surface waters in surrounding area where could be expected pollution by spreading of dust from the abandoned flotation tailing. Sequence of sampling was scheduled to cover different weather condition and seasons.

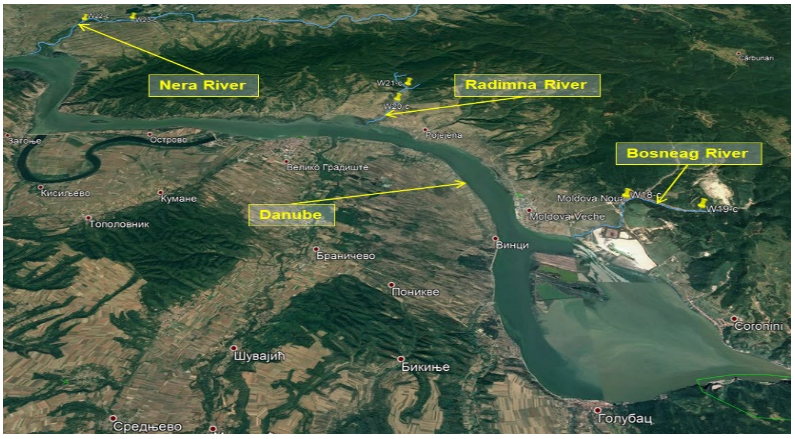

Figure 6. Surface water sampling – Romanian side

Locations of surface water samples are: (W18-c, W19-c) Bosneag River, Moldova Veche and upstream Moldova Veche; (W20-c, W21-c) Radimna River, Pojejena and upstream Pojejena; (W22-c, W23-c) Nera River, Socol and upstream Socol. Considered rivers from Romanian side cannot be polluted by AMD because they do not have direct contact with tailing material and they are not on downstream of possible AMD leaking from tailing but they can indicate pollution by spreading of dust from the tailing. This objective was chosen because of heavy spreading of dust from the abandoned tailing due to strong winds in this area.

The results of chemical analyses of surface waters from the Romanian side and MAC according to Romanian legislative [46] are presented in Table 2. All the results from the monitoring in scope of ROSNET2 are also available in created Knowledgebase [47].

Considered rivers in Caras Severin County near Moldova Noua in Romania mostly do not have acidic characteristics except slightly increased value than MAC for Bosneag River. This increased value (133.7 mg L^{-1}) is actually small and could not be stated as significant acidic characteristic. Probable reason for this value is vicinity of Bosneag River to flotation tailing.

Table 2. Chemical analyses of surface waters from the Romanian side

Category of surface water / Location	Parameter	Range (min-max)	Median	MAC	Content > MAC (%)
II Bosneag River Samples (W18c– W19c)	Fe (mg L^{-1})	0.0087-0.8903	0.4782	0.5	**50**
	Mn (mg L^{-1})	<0.0016-0.0583	0.0583	0.1	0
	Cu (mg L^{-1})	0.0284-0.1158	0.069	0.03	**75**
	Zn (mg L^{-1})	0.0252-0.0549	0.0472	0.2	0
	As (µg L^{-1})	<2.1-3.7	3.0	20	0
	Ni (µg L^{-1})	<3.6-4.2	4.2	25	0
	Pb (µg L^{-1})	<2.1-3.7	3.7	10	0
	Cd (µg L^{-1})	<0.14-0.39	0.26	1	0
	Cr (mg L^{-1})	<0.0017	/	0.05	0
	Hg (µg L^{-1})	< 0.5	< 0.5	0.3	0
	SO_4^{2-} (mg L^{-1})	78.5-295.8	133.7	120	**50**
II Radimna River Samples (W20c – W21c)	Fe (mg L^{-1})	0.1310-0.2652	0.2397	0.5	0
	Mn (mg L^{-1})	0.0106-0.0326	0.0230	0.1	0
	Cu (mg L^{-1})	0.0376-0.0546	0.0474	0.03	**100**
	Zn (mg L^{-1})	0.0176-0.0333	0.0216	0.2	0
	As (µg L^{-1})	<2.1	/	20	0
	Ni (µg L^{-1})	<3.6	/	25	0
	Pb (µg L^{-1})	<2.1	/	10	0
	Cd (µg L^{-1})	<0.14	/	1	0
	Cr (mg L^{-1})	<0.0017	/	0.05	0
	Hg (µg L^{-1})	< 0.5	< 0.5	0.3	0
	SO_4^{2-} (mg L^{-1})	21.9-30.3	24.8	120	0
II Nera River Samples (W22c-W23c)	Fe (mg L^{-1})	0.9895-1.1643	1.0292	0.5	**100**
	Mn (mg L^{-1})	0.0423-0.0524	0.0497	0.1	0
	Cu (mg L^{-1})	0.0136-0.0460	0.0317	0.03	**50**
	Zn (mg L^{-1})	<0.0062-0.0232	0.0109	0.2	0
	As (µg L^{-1})	<2.1	/	20	0
	Ni (µg L^{-1})	<3.6	/	25	0
	Pb (µg L^{-1})	<2.1	/	10	0
	Cd (µg L^{-1})	<0.14	/	1	0
	Cr (mg L^{-1})	<0.0017	/	0.05	0
	Hg (µg L^{-1})	< 0.5	< 0.5	0.3	0
	SO_4^{2-} (mg L^{-1})	21.6-29.6	24.8	120	0

Other two rivers have significantly lower values than MAC. The main way of pollution of these rivers is by spreading of dust from nearby flotation tailing in windy conditions. According to Romanian legislation for surface water, in considered rivers, the content for almost all of the analyzed elements is below the MAC [46] for this category of surface waters. The only exceptions are Fe and Cu which were with slightly increased concentrations probably because of windy weather before and during the sampling.

Maximum recorded concentration of iron was two times higher than MAC. Median value for Fe was below MAC for Bosneag River while for Nera River was two times higher but still with relatively low absolute concentrations. Possible reason for increased concentration of iron could be spreading of dust from nearby flotation tailing during windy weather. In recent researchers it was also noted that in general there are a trend of increasing of iron in river waters [48]. The possible causes of the increasing of Fe in the rivers are more elusive but probably also involve increased anaerobic microbial activity, considering the fact that water levels and temperature have increased during the period [49]. However, iron is not a strong hazardous element for human health, especially in recorded concentrations, but regarding of increased concentration it is expected that more attention will be given for clarification of noted increased transfer of Fe from soil to waters.

Increased copper concentrations were recorded in all considered rivers, with the highest content of Cu registered for Bosneag River, almost 4 times higher than MAC. However, median value was around 2 times higher than MAC. Having on mind that Bosneag River is closest to flotation tailing pond, probable reason for increased Cu concentration is spreading of dust from nearby flotation tailing during windy weather before and during sampling. Median value for Cu for Radimna River is 1.5 times higher than MAC and for Nera River is just slightly over MAC. These two rivers are located farther than Bosneag River from the flotation tailing which indicate similar reason for the measured Cu concentrations.

For the considered rivers on the Romanian side, it was important that no strong pollution with heavy metals was recorded. This is a consequence of the dominant dust pollution, and not AMD which is an incomparable higher danger than dust.

CONCLUSIONS

The present study is one of the broadest investigations of the multi-element content in surface waters generated from copper mining activities in the cross-border region of Romania and Serbia. It may thus represent a reference point for observed concentrations in future studies on considered area.

In Eastern Serbia, pH values for surface water samples from Bor city to the confluence of Bor and Timok River range from 1.77 to 7.72 indicating that most of the analyzed surface waters are strong acid water with pH values lower than 3.0. The recorded content of Cd, Mn, Zn, and Pb is above the MAC in almost all of the analyzed samples. Considering recorded content, median value and percentage of samples with higher content than MAC, pollution main hazards are Cd, Mn, Cu, Fe, Ni, Zn, Pb and As. However, with addition consideration on pollutants impact on human health, the main risk is caused by Cd, As, Pb and Cu pollution.

Samples from surface waters from rivers that belong to the III (Timok River) category show moderate pollution for the given category of surface waters. The manganese and sulphate content were exceeded in half of the analysed samples while nickel and cadmium exceeded in slightly higher percentage. The recorded concentrations of other considered elements were below the MAC values for this category of surface waters. Content of the main heavy metal polluter were dropped by increasing of distance from mining complex and by mixing of Bela River with Timok. However, based on recorded contents, on a longer distance from Bor mine, the main polluter were Cd and Ni.

In samples that belong to II category surface waters (Danube) was detected increased values of manganese, cadmium, nickel, arsenic and sulphate. However, the maximum detected values of individual elements in these surface waters are not more than 2 times over the MAC for this category of surface water. Having on mind that median values for the most hazardous elements, As and Cd is below median value and with low absolute concentrations, these single results could not be considered as pollution indicator.

Decreases in the concentrations of Fe, Cu, As, and Pb in surface river waters from confluence of Bela and Timok river were mainly due to precipitation of this metal ions on the river bed. On the other hand, Cd, Ni and Mn stayed in increased concentrations even in III category surface waters indicating dilution of these elements and longer transportation by water ways.

Trends in concentrations of ions in surface waters of IV category in Eastern Serbia indicated that all considered heavy metals originate from a Bor mine and smelter as a main anthropogenic source.

Considered rivers on Romanian side, in Caras Severin County near Moldova Noua, do not have acidic character and there was not recorded strong pollution with heavy metals. Slightly raised concentrations were recorded only for iron and copper while slightly increased content of SO_4^{2-} ions were recorded only in Bosneag River, probably as a consequence of vicinity to flotation tailing.

Comparing pollution in rivers surrounding Moldova Noua in Romania where the largest environmental impact is spreading of the dust from flotation tailing and rivers surrounding Bor in Eastern Serbia with combined AMD, tailing leaking and dust spreading environmental impact, it is clear that strongest environmental impact on surface rivers have AMD. Moreover, due to mobility potential and water ways transportation of the diluted ions, AMD have the significant environmental impact on wider area, in case of Bor mine, on cross border area.

EXPERIMENTAL SECTION

Considered Romanian Serbian Cross border area is presented in Figure 7. Project includes area of mine Moldova Nouă from the Romanian side and Eastern Serbia area from the active copper mine in Bor, all the way to the confluence of the Timok into the Danube near Radujevac. This area was chosen because both mine locations have negative impact on surface water system which flow in both cases to Danube. Rivers Bosneag, Radimna and Nera from the Romanian side in Caras Severin County near Moldova Noua are also tributary of Danube River and flow in area which is affected by spreading of dust from the abandoned flotation tailing of copper mine. Bor, Krivelj, and Bela Rivers in Eastern Serbia belong to the watershed of Timok River, which is also a tributary of Danube River. All mentioned Rivers flow near to the largest mining complex in Republic of Serbia where mining activities continuously exist for more than 115 years.

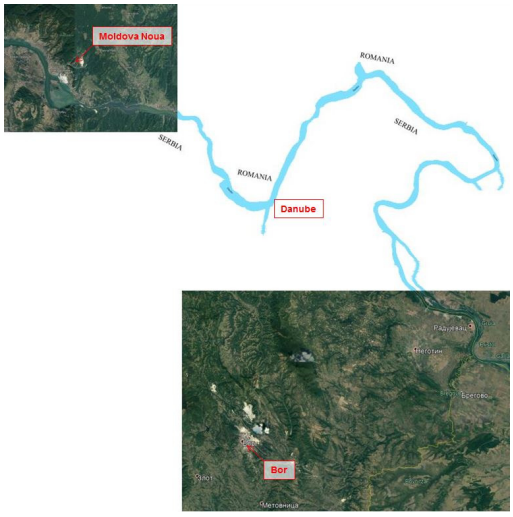

Figure 7. Romanian Serbian Cross border ROSNET2 Project area

Sampling locations are presented on Figures 2 and 6. During sampling was recorded GPS data for each sampling point and noted: sampling method, time, air and water temperature, color and odor of water, redox potential, pH value, DO (dissolved oxygen) and electro conductivity. Before sampling of surface waters on site, all bottles for storing of samples were treated with 3% HNO_3 (30-40 ml) during 6 days. Surface water sampling was performed with containers (cans of 1 L) which were rinsed three times in the river or water that will be sampling before sampling. One part of sample was poured into a container for measuring pH and temperature (also three times rinsed with water sample before performing measuring). After measuring the contents of containers were discarded. Other part of samples in quantity of exactly 50 ml was poured by syringe in bottles which already contains 63% 2.5 ml HNO_3, sealed and labelled. After packing, on site samples were transferred to chemical laboratory.

Samples were analyzed in chemical laboratory of Mining and Metallurgy Institute Bor with ICP-MS (Agilent Technologies 7700 Series, Singapore, Republic of Singapore); ICP-OES (Spectro Arcos, Kleve, Germany) and FIMS (Flow Injection Mercury System) 100 (Perkin Elmer, Norwalk, USA). Used techniques per elements with operating conditions are given in Table 3.

Table 3. Operating conditions for the analysis of the elements

Determined elements	Technigue	Operating conditions	
Hg	FIMS-AAS	Integration time (s)	20
		Data Processing	Peak Height, Smoothing: 0.5 s or 19 points
		Lamp	HCL
		Slit (nm)	0.7
		Wavelength (nm)	253.7
Cr, Cu, Fe, Mn, S, Zn	ICPOES	RF Power (W)	1450
		Coolant flow (L/min)	13
		Nebulizer flow (L/min)	0.75
		Auxiliary flow (L/min)	1.0
		Plasma, torch	Quartz, demountable, 2.0 mm injector tube
		Spray chamber	Scott
		Nebulizer	Cross-flow
		Sample aspiration rate	2 mL/min
		Wavelength (nm)	Cr-267.716 nm; Cu-324.754 nm; Fe-259.941; Mn-257.611; Mo-202.095 nm; Se-196.090 nm; S-180.731 nm; Zn-213.856 nm

Determined elements	Technigue	Operating conditions	
As, Cd, Ni, Pb	ICPMS	RF Power (W)	1550
		RF matching (V)	1.8
		Sample depth (mm)	10
		Carrier gas (L/min)	1.0
		Nebulizer pump speed (L/min)	0.1
		Spray chamber temperature (^{0}C)	2.0
		Peak pattern (point)	1.0
		Reaction gas cell flow (mL/min)	He-4.5
		Mass/Cell mode	As-75 He; Cd-111-No gas; Ni-60-No gas; Pb-208-No gas

ICP-OES surface waters analyses were performed according to (ISO 11885:2011) [50]. ICP-MS analysing were performed according to (ISO 17294:2016) [51].

The accuracy and the precision of the ICPMS and ICPOES methods were investigated analysing the two Standard Reference Material, NIST 1640a (Trace elements in natural water) and LGC Standard Reference Material VHG-QWPTM-15 (Water Pollution Trace metals). In Table 4 are given measured and certified concentrations with recovery rates for both used CRM.

Table 4. Measured and certified concentrations for both used CRM

Element	NIST 1640a				VHG-QWPTM-15			
	Certifed Value (μg L^{-1})	Found Value (μg L^{-1})	QC Acceptance Limits (μg L^{-1})	Recovery (%)	Certifed Value (μg L^{-1})	Found Value (μg L^{-1})	QC Acceptance Limits (μg L^{-1})	Recovery (%)
As	8.075	11.350	±0.070	140.6	516	497	451-568	96.3
Cd	3.992	3.980	±0.074	99.7	212	211	188-227	99.6
Cr	40.54	47.67	±0.30	117.6	113	112	103-123	99.1
Cu	85.75	110.82	±0.51	129.2	132	140	120-144	106.1
Fe	36.8	39.3	±1.8	106.8	3400	3514	3080-3770	103.4
Pb	12.101	11.421	±0.050	94.4	993	1008	899-1080	101.6
Mn	40.39	44.86	±0.36	111.1	1790	1769	1660-1970	98.8
Mo	45.60	44.92	±0.61	98.6	141	139	127-152	98.6
Ni	25.32	29.00	±0.14	114.6	630	617	572-687	97.9
Se	20.13	20.70	±0.17	102.8	440	424	458-582	96.4
Zn	55.64	51.27	±0.35	92.1	485	476	438-534	98.1

As shown in Table 4, the measured values and the certified values are in good agreement for all the certified concentrations for SRM LGC VHG-QWPTM-15. The Recovery for SRM NIST 1640a for As, Cd, Ni and Pb lies in the range 94.4-140.6%.

After chemical analyses, results were used for further calculations and environmental evaluation. Sample residues were stored in Mining and Metallurgy Institute Bor.

ACKNOWLEDGMENTS

This work was financially supported by the EU under Interreg – IPA CBC Romania-Serbia Programme and co-financed by the partner states in the Programme. Project ROmania Serbia NETwork for assessing and disseminating the impact of copper mining activities on water quality in the cross-border area (RoS-NET2) eMS code RORS - 337. The authors are also grateful for funding by Ministry of Education, Science and Technological Development Serbia, by Registration No. 451-03-9/2021-14/200052

REFERENCES

1. Đorđijevski S.; Ishiyama D.; Ogawa Y.; Stevanović Z.; *Environ Sci Pollut R*, **2018**, *25(25)*, 25005-25019.
2. Johnson D.B.; Hallberg K.B.; *Sci Tot Environ,* **2005**, *338*, 3-14.
3. Nordstrom D.K.; Alpers C.N.; *Proc Natl Acad Sci USA*, **1999**, *96(7)*, 3455-3462.
4. Blowes T.A.; Jambor D.W.; Scott J.L.; *Can Geotech J*, **1994**, *31*, 502-512.
5. Azapagic A.; *J Clean Prod*, **2004**, *12*, 639-662.
6. ICME and UNEP; Case Studies on Tailings Management. International Council on Metals and the Environment and United Nations Environment Programme 1998, **1998**, p.58.
7. Akcil A.; Koldas S.; *J Clean Prod*, **2004**, *14*, 1139-1145.
8. Charbonier B.; *Management of mining, quarrying, and ore-processing waste in the European Union 2001*, BRGM, **2001**, 29.
9. Dimitrijević M.D.; *Bakar*, **2012**, *37 (1)*, 33-44.
10. Iakovleva, E. Mäkilä; Salonen E.; Sitarz M.; Wang S.; Sillanpää, M.; *Ecol Eng*, **2015**, *81*, 30-40.
11. Stevanović Z.; Obradović Lj.; Marković R.; Jonović R.; Avramović Lj.; Bugarin M.; Stevanovic J.; *Waste Water - Treatment Technologies and Recent Analytical Developments*, Fernando Sebastian García, Einschlag and Luciano Carlos, IntechOpen, London, **2013**, DOI: 10.5772/51902.
12. Zobrist J.; Sima M.; Dogaru D.; Senila M.; Yang H.; Popescu C.; Roman C.; Bela A.; Frei L.; Dold B.; Balteanu D.; *Environ Sci Pollut R*, **2009**, 16, 14-26.

13. Markovic Z.S.; *Environmental and Food Safety and Security for South-East Europe and Ukraine*, Vitale K., Springer, Dnepropetrovsk, Ukraine, **2011**, 129-136.
14. Moldova Noua Mine;
15. Popescu F.; *Proc Technol*, **2016**, *22*, 440-444.
16. Dimitrijević M.D.; Antonijević M.M.; Dimitrijević V.Lj.; *Hem Ind*, **2002**, *56*, 299-316.
17. Abraitis P.K.; Pattrick R.A.D.; Vaughan D.J.; *Int J Miner Process*, **2004**, *74*, 41-59.
18. Gorgievski M.; Božić D.; Stanković V.; Bogdanović G.; *J Hazard Mater*, **2009**, *170*, 716-721.
19. Wang A.; Zhou K.; Zhang X.; Zhou D.; Peng C.; Chen W.; *Chem Eng J*, **2019**, *373*, 23-30.
20. R. Markovic; M. Bessho; N. Masuda; Z. Stevanovic; D. Bozic; T. Apostolovski Trujic; V. Gardic; *Appl. Sci.*, **2020**, *10(17)*, 5925.
21. Regulation on hazardous substances in waters ("Offic. Gaz. SRS", 31/82).
22. Lyn P.; *Altern Med Rev*, **2003**, *Vol.8, Issue 2*, 106-128.
23. Jordan E.; *Combined Sewer Overflow Toxic Pollutant Study*, U.S. Environmental Protection Agency, Washington, USA, **1984**, 60-67.
24. Goovaerts P.; *Encyclopedia of Environmental Health*, Ed. J.O. Nriagu, Elsevier: Amsterdam, Nederland, **2011**, 701-714.
25. Mahmood Q.; Mahnoor A.; Shahreen S.; Hayat M.T.; Ali S.; *Cadmium Toxicity and Tolerance in Plants*, Ed. Hasanuzzaman M.; Vara M.N., Elsevier: Amsterdam, Nederland, **2019**, 141-161.
26. Aoshima K.; *J Soil Sci Plant Nutr*, **2016**, *62*, 319–26.
27. Pan J.L.; Plant J.A.; Voulvoulis N.; Oates C.J.; Ihlenfeld C.; *Environ Geochem Hlth*, **2010**, *32*, 1–12.
28. Chunhabundit R.; *Toxicol Res,* **2016**, *32(1)*, 65-72.
29. Khan M.A.; Khan S.; Khan A.; Alam M.; *Sci Total Environ*, **2017**, *601*, 1591–1605.
30. Tabassum R.A.; Shahid M.; Dumat C.; *Environ Sci Pollut Res*, **2019**, *26*, 20018–20029.
31. U.S. Environmental Protection Agency; *Integrated Risk Information System (IRIS) on Arsenic*, National Center for Environmental Assessment, Office of Research and Development, Washington, DC. **1998**.
32. Watanabe T.; Hirano S.; *Arch Toxicol*, **2013**, *87*, 969-979.
33. Ebert F.; Weiss A.; Bültemeyer M.; Hamann I.; Hartwig A.; Schwerdtle T.; *Mutat Res*, **2011**, *715*, 32-41.
34. Wani A.L.; Anjum A.; Usmani J.A.; *Interdiscip Toxicol*, **2015**, *8(2)*, 55–64.
35. Meyer P.A.; Brown M.J.; Falk H.; *Mutat Res*, **2008**, *659(1-2)*, 166-175.
36. Nasiruddin R.M.; Tangpong J.; Rahman M.; *Toxicol Rep*, **2018**, 704-713.
37. Dórea J.G.; *Environ Res*, **2019**, 177:108641.
38. Bikash D.; Singh W.S.; Manna K.; *Indian J. Medical Spec*, **2019**, 10(2):66.
39. Kwon S.Y.; Bae O.N.; Noh J.Y.; Kim K.; Kang S.; Shin Y.J.; *Environ Health Perspect*, **2015**, 123:120-7.
40. Vigeh M.; Smith D.R.; Hsu P.C.; *Iran J Reprod Med*, **2011**, 9:1-8.
41. Bhardwaj P.; Rai D.V.; *Int J Res Med Sci*, **2016**, 4:177-80.
42. Gillis B.S.; Arbieva Z.; Gavin I.M.; *BMC Genomics*, **2012**, 13:344.

43. Harris Z.L.; Gitlin J.D.; *Am J Clin Nutr*, **1996**, *63*, 836S-841S.
44. Sánchez-Rodas D.; Sánchez de la Campa M.; de la Rosa Jesus A.D.; Oliveira V.; Gómez-Ariza J.L.; Querol X.; Alastuey A; *Chemosphere*, **2007**, *66*, 1485-1493.
45. Kovacevic R.; Jovasevic-Stojanovic M.; Tasic V.; Milosevic N.; Petrovic N.; Stankovic S.; Matic-Besarabic S.; *Chem Ind Chem Eng Q - CICEQ*, **2010**, *16*, 269–279.
46. The Romanian Ministry of Environment and Water Management. Order no 161/2006 for the approval of the Normative on the Classification of Surface Water Quality to establish the ecological status of the water bodies. *Official Journal of Romania*, No. 11/13.06.2006 (in Romanian).
47. Ostafe V.; Stevanovic Z.; Popovici Sturza C.; Isvoran A.; *New Front Chem*, **2021**, *30(1)*, 1-7.
48. Ekstrom A.A.; Regnell O.; Reader H.E.; Anders Nilson P.; Lofgren S.; Kritzberg E.; *J Geophys Res-Biogeo*, **2016**, *Vol.121(2)*, 479-493.
49. Sarkkola S.; Nieminen H.; Koivusalo A.; Laurén P.; Kortelainen T.; Mattsson M.; Palviainen S.; Piirainen M.; Finer L.; *Sci. Total Environ.*, **2013**, 463–464.
50. Water quality - Determination of selected elements by inductively coupled plasma optical emission spectrometry (ICP-OES) (ISO 11885:2011).
51. Water quality – Application of inductively coupled plasma mass spectrometry (ICP-MS) (ISO 17294:2016).

STUDIA UBB CHEMIA, LXVI, 4, 2021 (p. 329-339)
(RECOMMENDED CITATION)
DOI:10.24193/subbchem.2021.4.24

MODELING AND EXPERIMENTAL DATA VALIDATION OF VAPOR LIQUID EQUILIBRIA (VLE) FOR ABSORPTION AND DISTILLATION

M. ASLAM ABDULLAH[a], BANDARU KIRAN[a]*

ABSTRACT. The model combing the method UNIFAC with various model methods was applied for calculation of activity coefficients in an VLE model for hexaflourobenzene(1) benzene(2) at 333.15K, butanol(1) tetrachloroethene(2) at 101.08 kPa, carbondioxide(1) 3-pentanol(2) at 313.2K and other system compounds. The simulated results represent the overall average relative deviation below 0.5% which is comparable to the results presented by other authors in the literature. The data and results obtained for the systems are compared with the compositions predicted by the model and the sensitivity of the model parameters towards the composition data was analyzed through simulation techniques. The results predicted that overall error convergence was found to be less than 0.5 %.

Keywords: *Activity coefficient, VLE, Models, convergence*.

INTRODUCTION

A number of thermodynamic models have been proposed in different literatures. VLE models are based on fundamental equations for phase and chemical equilibria [1] and differ in the activity coefficient model is reported [2]. Since the EOS [3] for the calculation of fugacity coefficient in the liquid phase is relatively well established, the activity coefficients were identified as the key variables of the VLE models [4, 5]. Rigorous modeling and simulation of activity coefficients in this type of compounds is a challenge because the physical phenomena to be described as complex. In addition, the parameter regression is found to be difficult. The recent modeling is successful in data representation and interpretation of experimental data. However, the optimal approach is still uncertain except for reliable predictions. However, most of the mixtures encountered industrially are non – ideal. The non-ideality can be described by any of the several G^E models and EOS methods [6-8].

[a] *School of Chemical Engineering, Vellore Institute of Technology, Vellore, Tamil Nadu, India-632014.*
[*] *Corresponding author: kiran.chemengg@gmail.com*

THERMODYNAMIC PROPERTY METHODS FOR MODELING

ACTIVITY COEFFICIENT MODELS

In the literature several activity coefficient models are proposed and the oldest of the equations still in common use is that of Margules [9].

$$\left(\frac{G^E}{RT}\right)_{CAL} = x_1 x_2 \left[A_{21} x_1 + A_{12} x_2\right] \tag{1}$$

Van Laar equations are originally based on the Van der Waals equation of state but now these are regarded as pure empirical equations. Margules and Van Laar models can be expressed in linear form.

$$\left(\frac{G^E}{RT}\right)_{CAL} = \left[\frac{A'_{12} A'_{21}}{A'_{12} X_1 + A'_{21} X_2}\right] X_1 X_2 \tag{2}$$

Linear form of Van Laar model [10]

$$\left(\frac{G^E}{RT}\right)_{CAL} = \frac{1}{\left(\frac{1}{x_1 A_{12}} - \frac{1}{x_2 A_{21}}\right)} \tag{3}$$

Three parameter form of Van Laar equation [10]

$$\left(\frac{G^E}{RT}\right)_{CAL} = \frac{1}{\left(\frac{1}{x_1 A_1} - \frac{1}{x_2 A_2}\right)} + A_3 x_1 x_2 \left(x_1^2 - x_2^2\right) \tag{4}$$

Power series expression for the excess Gibbs energy and the corresponding activity coefficients for three parameter model [9] represented below.

$$\left(\frac{G^E}{RT}\right)_{CAL} = X_1 X_2 \left[B + C\left(X_1 - X_2\right)\right] \tag{5}$$

$$\left(\frac{G^E}{RT}\right)_{CAL} = x_1 x_2 \left[A_1 + A_2\left(x_1 - x_2\right) + A_3\left(x_1 - x_2\right)^2\right] \tag{6}$$

The model developed using volume fractions as measures of composition [11].These equations appear to take into account an important difference between molecules and should possibly have received more attention.

$$\Phi_1 = \frac{X_1 V_1}{X_1 V_1 + X_2 V_2} \quad (7) \qquad \Phi_2 = \frac{X_2 V_2}{X_1 V_1 + X_2 V_2} \quad (8)$$

$$\left(\frac{G^E}{RT}\right)_{CAL} = \Phi_1 \Phi_2 \left(X_1 V_1 + X_2 V_2\right)\left[A_{12} + \left(\Phi_1 - \Phi_2\right)A_{21}\right] \quad (9)$$

Equation for excess Gibbs–energy [11].

$$\left(\frac{G^E}{RT}\right)_{CAL} = x_1 x_2 A_{12} \frac{\left(\partial_1 - \partial_2\right)^2}{RT\left(\frac{1}{V_1 x_1} + \frac{1}{+V_2 x_2}\right)} \quad (10)$$

Expression for the excess Gibbs free energy [12] and substituting local compositions in the Flory– Huggins equations for polymer solutions. Wilson equations are not suitable for partially miscible systems [13]

$$\Lambda_{12} = \frac{V_2}{V_1} EXP\left(-\frac{A_{12}}{RT}\right) \quad (11) \qquad \Lambda_{21} = \frac{V_1}{V_2} EXP\left(-\frac{A_{21}}{RT}\right) \quad (12)$$

$$\left(\frac{G^E}{RT}\right)_{CAL} = -X_1 \ln\left(X_1 + \Lambda_{12} X_2\right) - X_2 \ln\left(X_2 + \Lambda_{21} X_1\right) \quad (13)$$

$$\tau_{21} = \frac{A_{21}}{RT} \quad (14) \qquad \tau_{12} = \frac{A_{12}}{RT} \quad (15) \qquad G_{12} = EXP\left(\tau_{12}\right) \quad (16) \qquad G_{21} = EXP\left(\tau_{21}\right) \quad (17)$$

Flory and Huggins equation

$$\Phi_1 = \frac{x_1 V_1}{x_1 V_1 + x_2 V_2} \quad (18) \qquad \Phi_2 = \frac{x_2 V_2}{x_1 V_1 + x_2 V_2} \quad (19)$$

$$\left(\frac{G^E}{RT}\right)_{CAL} = x_1 x_2 \left[\frac{G_{21} \ln\left(G_{21}\right)}{x_1 + x_2 G_{21}} + \frac{G_{12} \ln\left(G_{12}\right)}{x_2 + x_1 G_{12}}\right] \quad (20)$$

Studied the properties of Wilson equation and the equation has been the starting point for a class of activity coefficient equations collectively known as local–composition equations [14].

$$\Lambda_{12} = \frac{V_2}{V_1} EXP\left(-\frac{A_{12}}{RT}\right) \quad (21) \qquad \Lambda_{21} = \frac{V_1}{V_2} EXP\left(-\frac{A_{21}}{RT}\right) \quad (22)$$

$$\left(\frac{G^E}{RT}\right)_{CAL} = X_1 \ln\left(\frac{1}{X_1 + \Lambda_{12}X_2}\right) + X_2 \ln\left(\frac{1}{X_2 + \Lambda_{21}X_1}\right) - \frac{X_1X_2\Lambda_{12}\ln(\Lambda_{12}\Lambda_{21})}{X_1 + \Lambda_{12}X_2} \quad (23)$$

The Non Random Two Liquid (NRTL) equation using Scott's two liquid theories and taking into account non–randomness of mixing are follows [15, 16].

$$\Lambda_{12} = \frac{V_2}{V_1}\mathrm{EXP}\left(-\frac{A_{12}}{RT}\right) \quad (24) \qquad \Lambda_{21} = \frac{V_1}{V_2}\mathrm{EXP}\left(-\frac{A_{21}}{RT}\right) \quad (25)$$

$$\left(\frac{G^E}{RT}\right)_{CAL} = X_1 \ln(X_1 + X_2\Lambda_{21}) + X_2 \ln(X_2 + X_1\Lambda_{12}) \quad (26)$$

Modified form of Wilson equation by combining Flory–Huggins term and Wilson equation and incorporating molar volume ratios

$$\Lambda_{12} = \frac{V_2}{V_1}\mathrm{EXP}\left(-\frac{A_{12}}{RT}\right) \quad (27) \qquad \Lambda_{21} = \frac{V_1}{V_2}\mathrm{EXP}\left(-\frac{A_{21}}{RT}\right) \quad (28)$$

$$\Phi_1 = \frac{X_1R_1}{X_1R_1 + X_2R_2} \quad (29) \qquad \Phi_2 = \frac{X_2R_2}{X_1R_1 + X_2R_2} \quad (30)$$

$$\left(\frac{G^E}{RT}\right)_{CAL} = X_1 \ln\left(\frac{\Phi_1}{X_1}\right) + X_2 \ln\left(\frac{\Phi_2}{X_2}\right) + X_1 \ln\left(\frac{X_1R_1 + X_2R_2}{X_1R_1 + X_2R_2\Lambda_{12}}\right) + X_2 \ln\left(\frac{X_1R_1 + X_2R_2}{X_2R_2 + X_1R_1\Lambda_{21}}\right) \quad (31)$$

The UNIQUAC (Universal Quasi–chemical) equation based on Guggenheim's quasi–chemical analysis generalized through introduction of the local area fraction as the primary concentration variable [17, 18].

$$\tau_{12} = \mathrm{EXP}\left(-\frac{A_{12}}{RT}\right) \quad (32) \qquad \tau_{21} = \mathrm{EXP}\left(-\frac{A_{21}}{RT}\right) \quad (33) \qquad \Phi_1 = \frac{X_1R_1}{X_1R_1 + X_2R_2} \quad (34)$$

$$\Phi_2 = \frac{X_2R_2}{X_1R_1 + X_2R_2} \quad (35) \qquad \theta_1 = \frac{X_1Q_1}{X_1Q_1 + X_2Q_2} \quad (36) \qquad \theta_2 = \frac{X_2Q_2}{X_1Q_1 + X_2Q_2} \quad (37)$$

$$\left(\frac{G^E}{RT}\right)_{CAL} = X_1 \ln\left(\frac{\Phi_1}{X_1}\right) + X_2 \ln\left(\frac{\Phi_2}{X_2}\right) - \left(\frac{Z}{2}\right)\left[X_1 Q_1 \ln\left(\frac{\theta_1}{\Phi_1}\right) - X_2Q_2 \ln\left(\frac{\theta_2}{\Phi_2}\right)\right] - X_1 Q_1 \ln(\theta_1 + \theta_2\tau_{21}) - X_2 Q_2 \ln(\theta_2 + \theta_1\tau_{12}) \quad (38)$$

Suggested modification in the Wilson equation to give weightage to the molar volumes of the components are given below [19].

$$\tau_{12} = \frac{V_2}{V_1} EXP\left(-\frac{A_{12}}{RT}\right) \quad (39) \qquad \tau_{21} = \frac{V_1}{V_2} EXP\left(-\frac{A_{21}}{RT}\right) \quad (40)$$

$$\left(\frac{G^E}{RT}\right)_{CAL} = X_1 \ln\left(\frac{X_1 + \left(\frac{V_2}{V_1}\right)X_2}{X_1 + X_2\tau_{12}}\right) + X_2 \ln\left(\frac{X_2 + \left(\frac{V_1}{V_2}\right)X_1}{X_2 + X_1\tau_{21}}\right) \quad (41)$$

The following is the two forms to represent the VLE data of alcohol – hydrocarbon mixtures obtained at 313.15 K [20 - 23]

$$\left(\frac{G^E}{RT}\right)_{CAL} = \frac{x_1 x_2}{A_{12} + A_{21}(2x_1 - 1)} \quad (42)$$

PREDICTIVE MODELS

Estimation of thermodynamic properties of liquid mixtures from group contributions was first suggested [24] used group contributions to correlate heats of mixing. (a) UNIFAC (UNIQUAC Functional group Activity Coefficients) (b) Derr and Deal (1969) extended the Analytical Solution of Groups (ASOG) method (c) Equations of state.

(i) Equation of State for Simple Molecules

The van der Waals equation of state was the first equation capable of representing vapour-liquid coexistence [25, 26]

$$P = \frac{RT}{V - b} - \frac{a}{V^2} \quad (43)$$

The van der Waals equation can be regarded as a “hard-sphere (repulsive) + attractive” term equation of state composed from the contribution of repulsive and attractive intermolecular interactions, respectively.

(ii) PARAMETER ESTIMATION

The estimation parameters in the G^E models [27] and EOS methods had received wide attention since the parameters in a given model contain concisely the information on the composition dependent behavior [28] of the solution. The following methods appear to be more popular. The popular

optimization methods are Genetic Algorithm, Simulated Annealing Goldstein and Price, Greenstadt and Goldfarb, Approximation of Hessian, Zoutendijk's. Hook and Jeeves, Neldermead Simplex Method

(iii) **MODEL VALIDATION**

Activity Coefficient Models [29, 30] **Algorithm**

Step 1. Read P_c, V_c, T_c, ω, R, Q (UNIQUAC) for components 1 and 2
Step 2. Read Antoine constants A, B, C for components 1 and 2. Read T, P, x, y data and number of point's 'n'
Step 3. Calculate saturated molar volume V for components 1 and 2 using Racket equation
Step 4. Calculate using Tsonpolous correlation for components 1 and 2 by assuming vapor phase is ideal
Step 5. Minimize the objective function using optimization methods
Step 6. Calculate the absolute average deviation

EOS Models Algorithm for Peng Robinson and Margules mixing Rule

Step1. Read T_c, P_c, ω for components 1 and 2
Sgtep 2. Read T, P, x, y data. Find the values of the mixing rules using Margules Equation
Step 3. The below function is minimized using Hooke & Jeeves optimization method
Step 4. The optimum values of k_1, k_2 and k_3 are found
Step 5. The predicted vapor composition can be evaluated using the following correlation [31 - 34]

$$\ln\phi_i^V = \frac{b_i}{b_{vap}}\left(Z_{vap}-1\right)-\ln\left(Z_{vap}-\beta_{vap}\right)-\frac{q_{vap}}{2\sqrt{2}}\left(\frac{2\sum_{j=1}^{c} x_j a_{ij}}{a_{vap}}-\frac{b_i}{b_{vap}}\right)I_V \qquad (44)$$

RESULTS AND DISCUSSION

The modeling and simulation of VLE models (Table 1, 2, 3, and 4) for various chemical compounds are studied and are compared with the experimental results. The results predict that error of convergence is less than 0.5%. The phase diagrams [35] are drawn by plotting the data of experimental and model predicted data, which are shown in the figure 1.

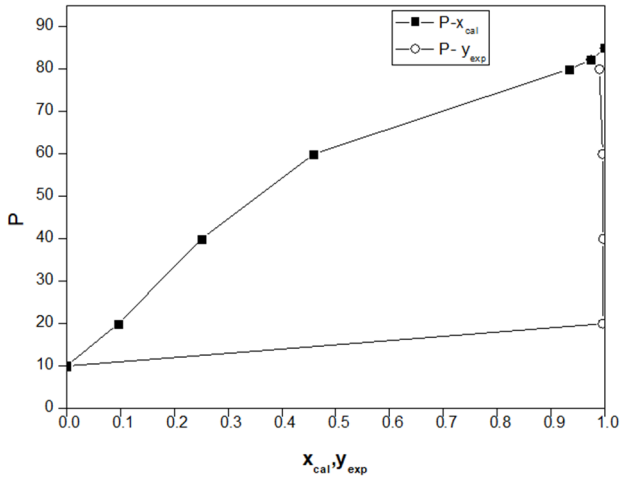

Figure 1. P-X-Y plot for experimental and predicted given in Table 4

Table 1. Objective functions for activity coefficient models and equation of state models

Objective functions for activity coefficient models	
$\sum_{i}^{n}\left[\frac{G^{E}_{EXP}}{RT}-\frac{G^{E}_{CAL}}{RT}\right]^{2}$ (45)	$\sum_{i}^{n}\left[\left(\frac{(\gamma_{1EXP}-\gamma_{1\,CAL})}{(\gamma_{1EXP})}\right)^{2}+\left(\frac{(\gamma_{2EXP}-\gamma_{2CAL})}{(\gamma_{2EXP})}\right)^{2}\right]$ (46)
$\sum_{i}^{n}\left[(\gamma_{1EXP}-\gamma_{1\,CAL})^{2}+(\gamma_{2EXP}-\gamma_{2CAL})^{2}\right]$ (47)	$\sum_{i}^{n}\left[(y_{EXP}-y_{CAL})^{2}+(P_{EXP}-P_{CAL})^{2}\right]$ (48)
$\sum_{i}^{n}(y_{EXP}-y_{CAL})^{2}$ (49)	$\sum_{i}^{n}(P_{EXP}-P_{CAL})^{2}$ (50)
Objective functions for equation of state	
$\sum_{i}^{n}\left[(\varphi_{1}^{vap}*y_{1}*P-\varphi_{1}^{liq}*x_{1}*P)^{2}+(\varphi_{2}^{vap}*y_{2}*P-\varphi_{2}^{liq}*x_{2}*P)^{2}\right]$ (51)	

Table 2. Component system 1: Hexafluorobenzene (1) Benzene (2) at 333.15 K

P_{exp}, atm	x	y_{exp}	ycal				
			Ideal vapor	Correlation	Prediction	PR-EOS	SRK-EOS
			NELD-MCLC	ZOUT-NRTL	POLA-UNQ1	SWTR-PRSV-7	MARG-HAKP-7
0.52160	0.0000	0.0000	0.000000	0.000000	0.000000	0.000000	0.000000
0.52570	0.0941	0.0970	0.096541	0.095746	0.096470	0.097118	0.097109
0.52568	0.1849	0.1788	0.177904	0.177742	0.177621	0.178485	0.178546
0.52287	0.2741	0.2567	0.255947	0.256227	0.255765	0.256388	0.256417
0.51818	0.3648	0.3383	0.338211	0.338493	0.338251	0.338498	0.338394
0.50989	0.4538	0.4237	0.424064	0.423824	0.423828	0.424228	0.424015
0.50773	0.5266	0.4982	0.498493	0.498231	0.498175	0.498610	0.498415
0.50350	0.6013	0.5783	0.578339	0.577842	0.577462	0.578438	0.578412
0.49974	0.6894	0.6760	0.675496	0.674796	0.673922	0.675604	0.675888
0.49757	0.7852	0.7824	0.781704	0.780786	0.779786	0.781831	0.782265
0.49794	0.89600	0.8996	0.899691	0.898726	0.898377	0.899793	0.899623
0.50155	1.0000	1.0000	1.000000	1.000000	1.000000	1.000000	1.000000
ΔY			0.000349	0.000624	0.000818	0.000265	0.000138

Table 3. Component system 2–Butanol (1) Tetracholoroethene (2) at 101.08 kPa

T_{exp}, K	x	y_{exp}	y_{cal}			
			Correlation	Prediction	PR-EOS	SRK-EOS
			POWE-SCHA	PNO2-MALA	SWTR-BOUM-7	SWTR-PARE-9
394.25	0.0000	0.0000	0.000000	0.000000	0.000000	0.000000
387.65	0.0380	0.2050	0.192768	0.193936	0.204900	0.204809
380.25	0.1170	0.4030	0.400829	0.401654	0.403970	0.404597
376.65	0.1820	0.4910	0.491572	0.491092	0.489515	0.489859
374.05	0.2630	0.5590	0.561726	0.560027	0.559623	0.558700
372.55	0.3480	0.6100	0.609357	0.607066	0.610110	0.608314
371.35	0.4720	0.6620	0.655817	0.653841	0.659451	0.658476
370.95	0.5200	0.6720	0.670137	0.668674	0.673110	0.673327
370.55	0.5680	0.6820	0.683975	0.682994	0.685076	0.686802
370.35	0.6120	0.6970	0.697293	0.696545	0.697287	0.699782
370.25	0.6620	0.7130	0.713689	0.713194	0.712832	0.715683
370.25	0.8240	0.7880	0.791115	0.790386	0.785333	0.787435
370.75	0.8850	0.8360	0.840070	0.838996	0.835602	0.835619
371.35	0.9330	0.8890	0.892802	0.891630	0.890318	0.888928
371.65	0.9700	0.9460	0.945899	0.945015	0.944175	0.942971
372.45	0.9920	0.9840	0.984445	0.984151	0.984374	0.983774
372.65	1.0000	1.0000	1.000000	1.000000	1.000000	1.000000
ΔY			0.002459	0.002333	0.001004	0.001430

Table 4. Component system 3: Carbon dioxide (1) 3–Pentanol (2) at 313.2 K

P_{exp}, bar	x_{cal}	y_{exp}	y_{cal}	
			PR-EOS	SRK-EOS
			MARG-PRSV -4	MARG-THRO-5
10.0000	0.00000	0.0000	0.000000	0.000000
20.0000	0.09600	0.9960	0.996000	0.996000
40.0000	0.25100	0.9970	0.997000	0.997000
60.0000	0.45900	0.9960	0.996000	0.996000
80.0000	0.93300	0.9900	0.989999	0.989999
82.2000	0.97400	0.9740	0.974000	0.974000
85.0000	1.00000	1.0000	1.000000	1.000000
AAD in y			0.000000	0.000000

Table 5. Different component systems property model data

System Name	Temp/Pres	Δy		
		PR–EOS	DECHEMA	PR – Mathias
Methanol(1) Acetonitrile(2)	303.15 K	0.005162	0.0043(Uniq)	0.005097
Methanol(1) 1,2–Dichloroethane(2)	323.15 K	0.004235	0.0031(Marg)	0.000776
2–Methyl1propanol(1) 3–Methylbutanol(2)	353.15 K	0.007487	0.0090(NRTL)	0.002130
Propionicaldehyde(1) Methanol(2)	318.15 K	0.005853	0.0058(Uniq)	0.003616
Benzene(1) 1–Butanol(2)	1.0132 bar	0.003308	0.0023(Vanl)	0.001972
Ethylacetate(1) 2–Methoxyethanol(2)	1.0132 bar	0.004412	0.0043(Wils)	0.004190
Ethanol(1) Ethylbenzene(2)	1.0132 bar	0.011148	0.0026(NRTL)	0.000535
Ethanol(1) Tetrachloroethylene(2)	1.0132 bar	0.007672	0.0055(Uniq)	0.003978

NOMENCLATURE

G^E – Gibbs free energy
A – Activity coefficients
T – Temperature ^oC
R – Gas constant
X – Vapor moles
γ- Phase coefficients
p – Pressure, kpa
B, C, k, ω, Ø – constants
Λ – Excess free energy mixing
V – Molar volume ratios

CONCLUSIONS

In this study, model combing the method UNIFAC with various model methods was applied for calculation of activity coefficients in an VLE model for hexaflourobenzene(1) benzene(2) at 333.15K, butanol(1) tetrachloroethane (2) at 101.08 kPa, carbon dioxide(1) 3-pentanol(2) at 313.2K and other system compounds. The relative deviation between predicted and experimental values is below 0.5% error, which shows the comparable to the results given in paper with the literature available. The data and results obtained for the systems are compared with the compositions predicted by the model and the sensitivity of the model parameters towards the composition data was analyzed through simulation techniques. The results predicted that overall error convergence was found to be less than 0.5 % and commendable results obtained.

REFERENCES

1. K. Liu; T. Zhang; Y. Ma; J. Gao; D. Xu; L. Zhang; Y. Wang; *The J. Chem. Therm*., **2020**,144,106075
2. A.W. Islam; Md. H. Rahman; *The J. Chem.Therm*., **2012,** *44***(1), 31-37**
3. J.P.H. Luis; A.F. Jorge; A. Velasquez; *Fluid Phase Equilib*., **2021**, *546***, 113123**
4. P.A. Ravi; P.A. Venkateswara R; Proceedings of the Symp on adv in *Chem. Eng*., **1997**, BARC, Mumbai (2), 83–89
5. P.A. Ravi; B.J. Srinivasa; K. Aravind; B. Naidu; Proceedings of ECCE – 6, Copenhagen, (2007), 2-67
6. D.B. Ashok; R.C. Trupathi; Optimization concepts and applications in Engineering. Pearson Education Asia, Singapore, 1999, 1-14
7. R. Venkateswara; P.A. Ravi; *The Can. J. Chem. Eng*., **1984**, *62*(1), 142-148
8. C. Tsonopoulos. *AIChE J*., **1974**, *20*(2), 263-272
9. O. Redlich; A.T. Kister; *J. Chem. Phy*.,**1947**, *15,* 849
10. C. Black; *Int. J. Therm*., **1986**, *7*, 987-1002
11. G. Scatchard; W.J. Hamer; *J. Am. Chem. Soc.*, **1935**, *57*, 1805-1809
12. G.M. Wilson; *J. Ame. Chem. Soc*., **1964**, *86*(2), 127-130
13. H.C. Carlson; A.P. Colburn; *Ind. Eng. Chem*., **1942**, *34*(5),581-589
14. J.F. Heil; J.M. Prausnitz;. AIChE J.., **1966**, *12*(4), 678-685
15. H. Renon; J.M. Prausnitz; *AIChE. J*., **1968**, *14*(1), 135-144
16. A. Vetere; *Fluid Phase Equilib*., **2000**, *173* (1), 57 – 64
17. D.S. Abrams; J.M. Prausnitz; *AIChE J*., **1975**, *21* (1), 116-128
18. K. Noda; J. Ishida; *J. Chem. Eng. Japan*., **1980**, *13*, 334-336
19. T. Tsuboka; T. Katayama; *J. Chem. Engg. Japan*., **1975**, *8*(3), 181-187
20. I. Nagata; Fluid Phase Equilib., **1985**, *19*(3), 153-174
21. I. Nagata; K. Gotoh; *Thermochemi. Acta*., **1995**, *258*, 77-107

22. I. Nagata; T. Ohta; S. Nakagawa;. *J. Chem. Eng. Japan*., **1976**, *9*(4), 276-281
23. P. Oracz; S. Warycha; *Fluid Phase Equilib*. **1997**, *137* (1-2), 149-162
24. H.G. Racket; *J. Chem. Eng. Data*., **1967**, *12*(1), 66-69
25. O. Tatsuhiko; Fluid Phase Equilib.,**1997**, *129* (1-2), 89-103
26. O. Jose; Valderrama; *Ind. & Engg. Chem. Res*., **2003**, *42*(8), 1603-1618
27. J. Huang; L. Lee. *Fluid Phase Equilib*., **1996**,*121* (1-2), 27-43
28. J.H. Vera; S.G. Sayegh; G.A. Ratcliff; *Fluid Phase Equilib*., **1977**, *I* (2), 113-135
29. W.W. Focke; *AIChE J*., **2000**, *12*, 35-46
30. C.V. Epaminondas; P.T. Dimitrios;. *Ind. Eng. Chem. Res*., **1996**, *35*(4), 1438-1445
31. A.N. Andiappan; Y. Mclean; *The Can. J. Chem. Engg*., **1972**, *50* (3), 384-389
32. R.W. Hanks; L.T. Romeo; J.C. James; *Thermochim. Acta*., **1978**, *27* (1-3), 9-18
33. R.S. Poston; J.J. McKetta; *J. Chem. Eng. Data*., **1966**, *11*(3),364-365
34. C.K.R. Himesh; C.A. Eckert; 71st National Meets of AIChE, Tulsa, Okla., 1974, 32, 178
35. I. Nagata; K. Tamura; *Fluid Phase Equilib*., **1997** *135*(2), 209 – 226

STUDIA UBB CHEMIA, LXVI, 4, 2021 (p. 341-353)
(RECOMMENDED CITATION)
DOI:10.24193/subbchem.2021.4.25

DFT STUDY OF GEOMETRIC ISOMERIZATION AND KETO–ENOL TAUTOMERIZATION OF DIHYDROXYFUMARIC ACID

NATALIA BOLOCAN[a,*], GHEORGHE DUCA[b]

ABSTRACT. A total of 45 isomers of dihydroxyfumaric acid (DHF), including 23 keto and 22 enediol forms, were identified and their geometrical isomerization and tautomerization was studied at the B3LYP level of theory using the 6–311++G(2df,2p) basis set in the gas phase and aqueous solution, and three most stable enediol structures were identified. Interconversions between the enediol forms and the keto forms proceed through two paths: (1) proton transfer (E_a ≈ 135–160 kJ mol^{-1}) and (2) internal rotation (E_a ≈ 0.15–75 kJ mol^{-1}). Keto–enol tautomeric reactions of dihydroxyfumaric acid were investigated for the three most stable enediol structures. It was found that the activation energy and the free activation energy is in the range of 230–310 kJ mol^{-1} for the gas phase and by 50-80 kJ mol^{-1} lower in water, and TSs structures reveal that the carboxylic oxygen that forms the hydrogen bond in the enediol structure is involved in the mechanism of proton transfer. Furthermore, equilibrium constants have been calculated, along with the forward and reverse reaction rates for the isomerization and tautomerization reactions of the three most stable enediol structures, in gas and water.

Keywords: *dihydroxifumaric acid, keto-enol tautomerism, dft study.*

INTRODUCTION

Dihydroxyfumaric acid is the traditional name for (2E)–2,3–dihydroxybut–2–enedioic acid, first obtained by Fenton in the 1890s [1]. It is an organic acid formed from tartaric acid by dehydrogenation or slow oxidation, a proven intermediate in the cycles of di– and tricarboxylic acids, and the glyoxalic acid via the tartaric acid transformation cycle.

[a] *Laboratory of Physical and Quantum Chemistry, Institute of Chemistry, 3 Academiei str., Chisinau, MD 2028, Moldova*
[b] *Research Center of Physical and Inorganic Chemistry, Institute of Chemistry, 3 Academiei str., Chisinau, MD 2028, Moldova*
** Corresponding author: natalia.bolocan@ichem.md*

An important intermediate in vegetal and living organisms, DHF recently became a molecule of interest in the scientific world, mainly due to Eschenmoser's proposal [2] that glyoxylate and DHF (its dimer) could have served as primary molecules in the synthesis of organic macromolecules in the constraints of prebiotic chemistry. Furthermore, our previous investigations showed that DHF and some of its salts and derivatives have wide practical applications and may be successfully used for the enhancement and preservation of wines [3,4], as inhibitors of nitrosoamines formation in vitro [5,6] and in vivo [7,8], as well as efficient scavengers of DPPH and ABTS free–radicals [9].

In spite of the interest recently attracted by DHF and its potential practical uses in various fields, to the best of our knowledge, to date there are no published theoretical investigations of the DHF conformational isomerism. Moreover, although there is evidence that keto–enol tautomerism is one of the most commonly studied forms of prototropy [10], studies of the DHF molecule are very sparse: keto–enol tautomerization of DHF acid was studied experimentally by Fleury and Souchay [11] in the 1960's, by Souza *et al.* in the 1980's during their investigations of DHF decarboxilation [12], and by Travin *et al.* in the 1980's during a kinetic investigation of the uranyl ion-DHF complex [13]. In this context, the present research was undertaken to provide valuable data for further use in both theoretical and practical areas.

In the case of DHF, various conformations are possible for the two tautomeric forms, due to the intramolecular rotations along the single C–C bonds and due to the possible *syn*– and *anti*– periplanar orientation of the hydroxyl hydrogen with respect to the keto oxygen.

RESULTS AND DISCUSSION

Thermodinamically stable isomers

The calculated harmonic vibrational frequencies at the B3LYP/6–311++G(2df,2p) level of theory revealed that there are 22 enediol and 23 keto optimized structures of DHF at stationary points in the gas phase. The most stable enediol and keto structures are presented in Figure 1, and cartesian coordinates of all 45 optimized structures, for the gas phase and the aqueous medium, are available in Supplementary material. The isomers are nominated and arranged from the most stable isomer to least stable one (according to Gibbs free energy calculations). We nominate the enediol isomers as E1–E22, and the keto forms as K1–K23.

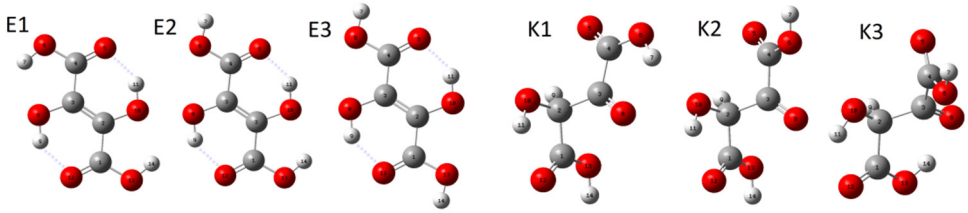

Figure 1. Optimized structures of the most stable enediol and keto isomers of dihydroxyfumaric acid

The electronic energy (E), enthalpy (H) and Gibbs energy (G) of each conformer were calculated at 298.15 K. Using the energy of E1 as the reference point for gas calculations, and the energy of E2 as the reference point for calculations in the aqueous medium, all values obtained for ΔE, ΔH and ΔG are listed together in Table 1 for comparison.

Table 1. Relative energies (kJ mol^{-1}) with respect to the most stable enediol (E1), of the enediol (E1–E22) and keto (K1–K23) isomers of dihydroxyfumaric acid, at 298.15 K. In gas phase, the total energy values for E1 are as follows: E =–606.1440772 a.u., H = –606.04156958 a.u., G = –606.08507874 a.u. In water, the total energy values for E2 are as follows: E =–606.15927423 a.u., H = –-606.05902544 a.u., G = –606.10366354 a.u.

Enediol isomers	*ΔE*		*ΔH*		*ΔG*		Keto isomers	*ΔE*		*ΔH*		*ΔG*	
	Gas	Water	Gas	Water	Gas	Water		Gas	Water	Gas	Water	Gas	Water
E1	0.00	0.59	0.00	0.53	**0.00**	0.48	*K1*	54.34	34.66	53.13	37.51	46.70	32.52
E2	5.18	0.00	5.26	0.00	5.07	**0.00**	*K2*	58.64	35.61	56.85	38.70	49.52	33.92
E3	10.42	0.01	10.54	0.58	10.05	1.24	*K3*	58.32	39.02	55.89	40.65	50.63	36.63
E4	15.46	10.54	15.89	10.62	14.90	7.59	*K4*	63.37	37.36	61.15	40.60	53.27	35.28
E5	24.33	16.07	24.74	121.6	22.99	12.41	*K5*	60.67	36.20	59.55	40.97	54.84	39.55
E6	26.66	9.24	26.21	9.40	25.05	8.73	*K6*	64.46	39.49	63.45	43.18	56.37	39.90
E7	30.59	9.86	30.13	10.23	28.65	9.78	*K7*	62.83	39.97	61.77	42.57	56.44	37.42
E8	39.95	21.39	36.73	22.46	37.36	20.86	*K8*	63.22	37.76	61.88	40.41	56.57	36.34
E9	38.07	21.40	38.45	22.44	35.88	20.64	*K9*	69.15	40.00	67.44	43.32	59.48	39.07
E10	40.46	19.58	39.97	22.15	36.67	21.80	*K10*	62.96	37.80	61.29	38.98	59.54	38.91
E11	41.07	15.73	40.10	17.01	37.41	17.04	*K11*	72.92	42.22	70.65	45.44	62.30	38.46
E12	42.66	16.56	41.89	17.55	38.49	17.05	*K12*	68.81	36.57	67.31	38.73	62.73	37.59
E13	44.21	16.92	43.85	18.60	41.44	19.35	*K13*	71.95	39.77	70.31	42.69	63.04	37.76
E14	44.48	18.59	41.31	20.11	42.81	20.11	*K14*	70.45	35.84	68.97	35.38	63.36	35.64
E15	50.37	21.17	49.91	23.43	46.55	23.39	*K15*	72.24	38.18	70.39	40.77	64.11	35.20
E16	51.27	22.88	50.94	24.73	47.16	24.50	*K16*	78.83	46.30	76.76	48.72	69.98	50.32
E17	51.07	21.12	50.42	22.72	47.60	23.02	*K17*	82.73	41.31	80.28	44.87	71.19	39.40
E18	51.53	20.59	50.65	21.96	48.16	22.08	*K18*	80.28	40.14	77.79	42.13	72.48	36.55
E19	52.67	26.93	52.13	29.29	48.46	29.32	*K19*	83.40	39.57	80.76	41.98	73.69	36.00
E20	59.99	19.98	59.70	22.15	58.37	23.85	*K20*	80.71	45.73	78.31	47.93	74.03	46.49
E21	66.16	33.48	64.68	34.09	60.06	32.14	*K21*	83.82	37.52	81.62	40.73	74.26	36.99
E22	72.94	27.95	72.89	32.85	70.64	33.78	*K22*	82.55	44.38	80.86	46.49	75.24	43.81
							K23	112.03	56.13	110.6	59.01	104.8	57.63

Results show that the enediol forms of DHF are more stable than the keto forms, both in gas phase and in water.

In the gas phase, the enediol structure E1 of DHF is the most stable form and represents the global minimum in the potential energy curve of DHF acid. It should be mentioned here that its Gibbs free energy is lower than that of the most stable keto structure K1 by 46.7 kJ mol^{-1} at the DFT(B3LYP) level. The stability of E1 may be attributed to the presence of the intramolecular hydrogen bonding effect present in the E1 structure more than in others, and to stabilizing orbital interactions due to the *anti*– periplanar orientation of the hydroxyl hydrogen with respect to the keto oxygen.

In water, the most stable isomer is E2. It should be mentioned here that its Gibbs free energy is lower than that of the most stable keto structure K1 by 32.7 kJ mol^{-1} at the DFT(B3LYP) level.

The Boltzmann distribution according to Eq. 1. shows that in gas phase, 99.78% of DHF are represented by only 3 enediol structures: the most stable isomer E1 accounts for 87.4%, followed by isomer E2 with a relative abundance of 10.98%, then isomer E3 - 1.4%. In aqueous solution, the three most stable enediolic forms account for 97.3% of the acid, with the following relative abundance indices: the most stable isomer E2 accounts for 38.4%, followed by E1 - 31.8% and E3 - 27.1%.

Comparison of some geometrical parameters of enediol and keto structures

The enediol structures of DHF are almost completely planar, except for structures E20 and E22, which suffer from atom–atom repulsion. This planarity of enediol structures is probably a consequence of intramolecular interactions between the enolic –OH groups and the C=O or –OH of the carboxylic groups which lead to electron delocalization in the molecule. Selected geometrical parameters for the four most stable enediol and keto structures are available in Supporting information.

The three most stable enediol structures of DHF are characterized by dihedral angles deviations of no more than 0.1°, while in all other enediol isomers structures (except for E20 and E22) the discussed dihedral angles deviations are a bit larger, but do not exceed 1° from planarity. The most significant deviations are present in structures E20 and E22: up to -3.8° and -2.4° for the (O8C3C2C1) angle, -16.1° and -3.8° for the (O8C3C4O5) angle, -17.3° and -3.2° for the (O6C4C3C2) angle and -179.1° and -166.8° for the (O10C2C1O13) angle. E20 and E22 are the only enediol structures which deviate significantly from planarity because the *anti*– periplanar oriented hydroxyl hydrogens (with respect to the keto oxygen) of the two carboxylic

groups on both ends of the molecule force the enolic hydrogen atom out of the plane almost perpendicularly, with the (C1C2O10H11) dihedral angle being 94.1° and 72.9° for the E20 and E22, respectively.

TABLE 2. Select dihedral angles (in °) and dipole moments (in Debye) of the four most stable enediol and four most stable keto isomers of DHF, in gas

Isomer	dihedral (O10C3C2O8) angle	dihedral (O10C2C1O12) angle	dihedral (O10C3C2C1) angle	dihedral (O5C4C3O8) angle	Dipole moment
E1	180.0	– 0.1	– 0.0	180.0	0.00132
E2	180.0	– 0.0	– 0.1	– 180.0	3.10558
E3	180.0	– 0.0	– 0.0	180.0	0.00107
E4	179.9	– 180.0	– 0.1	0.1	0.00262
K1	93.6	– 6.2	– 26.8	– 8.9	3.17906
K2	116.1	– 35.8	– 4.5	– 13.6	0.81446
K3	171.8	– 82.8	47.0	11.6	1.66599
K4	130.6	133.8	9.0	– 18.3	3.19301

The keto structures are twisted with the dihedral (O10C2C3O8) angle ranging between 88.8° to 175.6°. The other dihedral angles deviate from planarity by up to 85.7° in some keto structures. This variation of the dihedral angles, however, only slightly influences other bond lengths and angles.

Barriers of Rotation and Tautomerization

Transition states of interconversions between the enediol and the keto isomers

All TS structures related to the interconversion of the enediol forms and the keto forms of DHF acid were identified, and select TSs are presented in Figure 2. Table 3 presents the activation energy (E_a), imaginary frequency (ν), and Gibbs free activation energy ($\Delta G^{\#}$) for interconversions of select enediol and keto forms. The enthalpy activation energy ($\Delta H^{\#}$) has been calculated as well, and its values were almost equal to $\Delta G^{\#}$.

Interconversions between the enediol forms and between the keto forms take place through both proton transfer and internal rotation (C–C and O–H rotation) pathways. In enediol-enediol transformations, the activation energies of proton transfer are in the range of 135–160 kJ mol^{-1} and for the rotational path are in the range 5–75 kJ mol^{-1}. For interconversions between the keto forms, activation energies are in the range of 139–153 kJ mol^{-1} for the proton transfer path and of 0.15–52 kJ mol^{-1} for the rotational path.

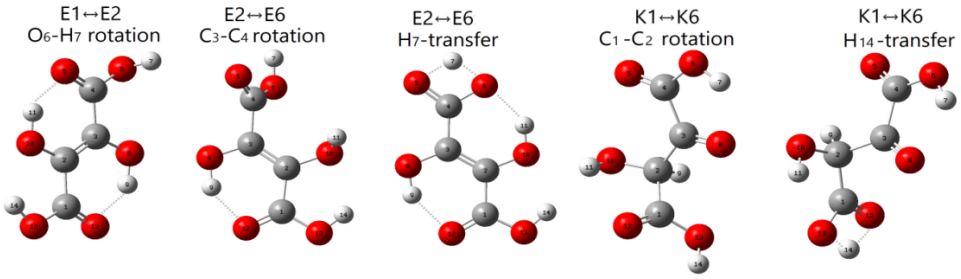

Figure 2. Optimized geometries of selected TSs of enediol–enediol and keto-keto interconversions

In the case of enediol and keto isomers bearing at least one carboxylic group with a *syn*- periplanar oriented hydrogen, there are a number of transformations that take place through both pathways, proton transfer and C–C rotation, and these interconversions may be regarded as competitive reactions.

These are: E2 ↔ E6, E3 ↔ E7, E5 ↔ E10, E7 ↔ E18, E8 ↔ E13, E9 ↔ E19, E11 ↔ E17, E12 ↔ E14, E12 ↔ E15, E14 ↔ E16, E15 ↔ E16, E19 ↔ E21 and K1 ↔ K6, K2 ↔ K4, K2 ↔ K9, K4 ↔ K11, K7 ↔ K8, K9 ↔ K11, K12 ↔ K22, K13 ↔ K15, K13 ↔ K17, K14 ↔ K21, K15 ↔ K19, K17 ↔ K19.

However, the activation energies for H–transfer processes are significantly higher than for the C–C rotational path, and the ratios of k_p/k_r (k_p and k_r are the rate constants of the proton transfer and the rotational paths, respectively) are obtained zero at 298.15K in the gas phase, based on the Arrhenius rate constant equation, if the same value of A is considered for both paths.

Therefore, we may conclude that the above-mentioned interconversions take place in gas phase through the C–C rotational paths, and proton transfer processes can not occur simultaneously.

Imaginary frequencies (ν, in cm^{-1}) of select TS structures for enediol–enediol and keto–keto interconversions are tabulated in Table 3. As expected, the C–C internal rotation has the minimum frequency (around – 40 cm^{-1} – 100 cm^{-1}), being almost a pure rotational vibration. Also, the imaginary frequency of the proton transfer reaction is around –1900 cm^{-1}, a stretching vibration frequency. In the case of O–H rotation, the imaginary frequency values are between pure rotation and pure stretching vibrations, usually in the range of –200 cm^{-1} …–600 cm^{-1}, slightly higher in the case of carboxylic O–H rotations. This is probably due to the fact that there are a lot of hydrogen bonds/interactions and electron delocalization sites in DFH isomers, and the rotation of a hydrogen atom may break a hydrogen bond and start the formation of another hydrogen bond, therefore, the O–H rotation is mixed with a stretching vibration and its

Table 3. Activation energy, E_a, Gibbs free activation energy, $\Delta G^{\#}$ (KJ mol^{-1}), and imaginary frequency, v (scaled by 0.967[16]) (cm^{-1}), for select interconversions between enediol isomers and between the keto forms.

TS	v		E_a		$\Delta G^{\#}$	
	Gas	Water	Gas	Water	Gas	Water
Enediol–enediol interconversions						
			O–H rotation			
E1 → E2	–607.01	-426.97	52.19	41.42	47.50	39.90
E2 → E1			47.01	42.01	42.43	40.38
E2 → E3	–601.56	-575.23	51.71	41.52	47.01	40.19
E3 → E2			46.47	41.53	42.03	38.96
E6 → E17	–374.78	-324.1	45.17	30.02	40.43	29.94
E17 → E6			20.76	18.13	17.87	15.66
			C–C rotation			
E9 → E19	-46.23	-62.20	48.11	34.25	65.83	33.71
E19 → E9			37.24	26.47	7.46	25.32
E2 → E6	–52.04	-72.12	52.64	33.45	49.31	35.09
E6 → E2			31.15	24.21	29.34	26.36
			H–transfer			
E2 → E6	–1,875.32	-1997.15	158.92	164.36	145.82	154.28
E6 → E2			137.43	155.12	125.85	145.54
E3 → E7	–1,873.71	-1995.14	156.93	163.68	143.84	152.10
E7 → E3			136.76	153.81	125.23	143.56
Keto–keto interconversions						
			O–H rotation			
K1 → K2	–487.93	-520.06	48.76	44.06	43.87	39.81
K2 → K1			44.46	43.11	41.04	38.41
K1 → K16	–492.33	-507.37	44.33	43.50	40.64	37.71
K16 → K1			28.18	31.86	25.91	19.91
K11 → K22	–481.19	-536.29	41.57	41.00	37.88	36.35
K22 → K11			31.94	38.83	24.94	31.00
			C–C rotation			
K1 → K6	–73.29	-56.36	22.84	14.15	23.87	15.10
K6 → K1			12.72	9.32	14.19	7.71
K1 → K12	–69.77	-215.90	23.62	17.50	23.73	18.20
K12 → K1			9.15	15.59	7.70	13.13
			H–transfer			
K1 → K6	–1,887.85	-1936.46	162.29	167.03	148.58	156.83
K6 → K1			152.17	162.20	138.90	149.44
K2 → K4	–1,887.49	-1938.56	167.09	168.40	153.19	155.58
K4 → K2			162.36	166.65	149.43	154.22

frequency is higher than that for C–C rotational vibration. Calculation results for the aqueous medium show that imaginary frequencies for O-H and C-C rotations are lower in water than in gas, while for H-transfer reactions, imaginary frequencies are higher in water than in gas, both for enediol-enediol and keto-keto interconversions. Also, the activation energies of H-transfer reactions are higher for water, than for gas, probably due to the stabilization of the structures by additional hydrogen bonds with water molecules from the implicit solvent medium.

Keto–enol tautomerism of DHF acid

Keto–enol tautomerization was investigated for the three most stable enediol structures that account for 99.76% of DHF in the gas phase, and 97.3% in aqueous medium. Optimized TS structures in gas phase are shown in Fig. 3, and all cartesian coordinates are presented in supplementary material.

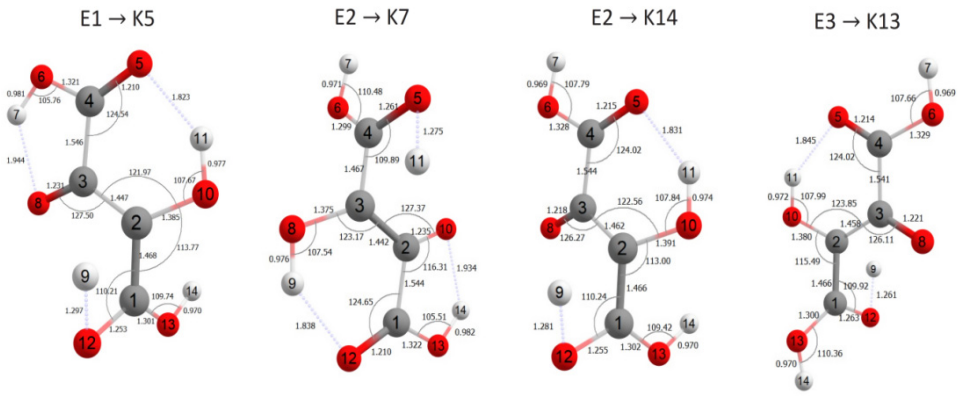

Figure 3. Optimized TS structures of TSs in the keto–enol tautomerism of the three most stable enediol isomers of DHF, in the gas phase

Energy barriers of the keto–enol tautomerization process were computed using the energy differences between local minimum structures (Table 1) and transition states. The only route for the keto–enol tautomerism is through proton transfer. Table 4 presents the activation energy, E_a, imaginary frequency, ν, and Gibbs free activation energy, $\Delta G^{\#}$ of the keto–enol interconversions calculated at the B3LYP level of theory at 298.15 K. As expected, the barriers for enediol → keto conversions exceed those for the reverse keto → enediol transitions, in gas and in water, by around 50 kJ mol^{-1}.

Table 4. Activation energy, E_a, imaginary frequency, ν (scaled by 0.967[16]) (cm^{-1}), and Gibbs free activation energy, $\Delta G^{\#}$, for the keto–enol tautomerism of the three most stable enediol forms, in gas and solvent (water).

Reaction	ν (cm^{-1})		E_a (kJ mol^{-1})		$\Delta G^{\#}$ (kJ mol^{-1})	
	Gas	*Water*	*Gas*	*Water*	*Gas*	*Water*
E1 → K5	–1813.03	–1881.78	293.46	236.07	275.13	212.88
K5 → E1			232.79	175.41	220.29	158.05
E2 → K7	–1791.89	–1885.58	291.07	228.97	272.36	206.85
K7 → E2			233.42	171.31	220.99	155.48
E2 → K14	–1819.46	–1899.57	309.94	239.55	289.43	216.36
K14 → E2			244.66	174.27	231.14	158.07
E3 → K13	–1805.39	–1895.83	308.11	232.14	287.50	209.61
K13 → E3			246.58	170.60	234.51	156.63

The activation energies for the keto–enol tautomerism are up to 20–fold greater than those for the interconversions of the enediol–enediol or keto–keto forms, which may be explained by the fact that the mechanism of the keto–enol tautomerism is more complex and involves more atoms, as well as a geometrical rearrangement of the molecule. It should be mentioned here that E_a and $\Delta G^{\#}$ are lower by 50-80 kJ mol^{-1} in water, than in gas, indicating that water influences the H-transfer process, making it easier. The TSs structures reveal that the carboxylic oxygen that forms the hydrogen bond in the enediol structure is involved in the mechanism of proton transfer.

Table 5 summarizes kinetic and thermodynamic data for the transition states of isomerization and tautomerization reactions of the three most stable enediol forms, in the gas phase and in water. In the gas phase, E1 is the most stable species and isomerization reactions E1 ↔ E2 and E2 ↔ E3 are characterized by equilibrium constants of 0.13. In water, the most stable isomer is E2, and isomerization reactions E1 ↔ E2 and E2 ↔ E3 are characterized by equilibrium constants of 1.21 and 0.61, respectively. Results show that the presence of solvent (water) influences both, thermodinamic and kinetic parameters. In aqueous solution, the ΔE, ΔH, ΔG, $\Delta G_1^{\#}$ and $\Delta G_2^{\#}$ decrease by around 2-7 kJ mol^{-1} in isomerization reactions and by around 10-30 kJ mol^{-1} in tautomerism reactions. In the gas phase, equilibrium constants of keto-enol transformations E1 ↔ K5, E2 ↔ K7, E2 ↔ K14 and E3 ↔ K13 equal to 2.46 x 10^{-10}, 10.29 x 10^{-10}, 0.61 x 10^{-10} and 5.21 x 10^{-10}, respectively. In water, these values are of 1.41 x 10^{-7}, 2.73 x 10^{-7}, 5.61 x 10^{-7}, 3.93 x 10^{-7}, respectively, showing a significant increase in the values of direct reactions.

Table 5. Kinetic and thermodynamic data for the transition states of isomerization and tautomerization of the three most stable enediol forms, in the gas phase and in water. All energetic data have been reported in kJ mol^{-1} and the rate constants in s^{-1}. [a]

	Isomerism				Keto-enol tautomerism							
	E1 ↔ E2		E2 ↔ E3		E1 ↔ K5		E2 ↔ K7		E2 ↔ K14		E3 ↔ K13	
	Gas	Water	Gas	Water	Gas	Water	Gas	Water	Gas	Water	Gas	Water
ΔE	5.18	-0.59	5.24	-0.01	60.67	35.61	57.66	39.97	65.28	35.84	61.54	39.78
ΔH	5.26	-0.53	5.27	0.58	59.55	40.44	56.50	42.57	63.70	35.38	59.77	42.12
ΔG	5.07	-0.48	4.98	1.24	54.84	39.07	51.30	37.42	58.29	35.64	52.99	36.52
Keq	0.13	1.21	0.13	0.61	2.46×10^{-10}	1.41×10^{-7}	10.29×10^{-10}	2.73×10^{-7}	0.61×10^{-10}	5.61×10^{-7}	5.21×10^{-10}	3.93×10^{-7}
$\Delta G^{\#}_1$	47.50	39.90	47.01	40.19	275.13	261.20	272.36	260.72	289.43	270.23	287.50	267.22
$\Delta G^{\#}_2$	42.43	40.38	42.03	38.96	220.29	222.13	220.99	223.29	231.14	234.59	234.51	230.70
k_1	2.96×10^{4}	6.29×10^{5}	3.61×10^{4}	55.98×10^{4}	3.91×10^{-36}	1.01×10^{-33}	1.19×10^{-35}	1.23×10^{-33}	1.22×10^{-38}	2.66×10^{-35}	2.66×10^{-38}	8.96×10^{-35}
k_2	2.29×10^{5}	5.18×10^{5}	2.69×10^{5}	9.19×10^{5}	1.59×10^{-26}	71.85×10^{-26}	1.19×10^{-26}	4.49×10^{-27}	1.99×10^{-28}	4.70×10^{-29}	5.11×10^{-29}	2.26×10^{-28}

[a] *$\Delta G^{\#}_1 = G_{TS} - G_{reactant}$, $\Delta G^{\#}_2 = G_{TS} - G_{product}$, k_1 - rate of forward reaction, k_2 - rate of reverse reaction.*

CONCLUSIONS

In the course of this research, 45 isomers of dihydroxyfumaric acid have been identified, including 23 keto and 22 enediol forms, and their geometrical isomerization and tautomerization was studied at the B3LYP level of theory using the 6–311++G(2df,2p) basis set in the gas phase.

It was found that three enediol structures account for 99.96% of the dihydroxyfumaric acid in the gas phase, according to the following distribution: E1 – 87.4%, E2 – 10.98%, E3 – 1.4%. In aqueous medium, these structures account for 97.3% of the acid, with the following relative abundance indices: E1 – 31.8%, E2 – 38.4%, E3 – 27.1%.

The activation energy (E_a), imaginary frequency (ν), and Gibbs free activation energy ($\Delta G^{\#}$) were calculated for enediol–enediol and keto–keto interconversions. These interconversions proceed through internal rotation (E_a ≈ 0.15–75 kJ mol^{-1}), because proton transfer requires a significantly higher activation energy (E_a ≈ 135–160 kJ mol^{-1}), in the gas phase and aqueous solution.

Keto–enol tautomeric reactions of dihydroxyfumaric acid were investigated for the three most stable enediol structures. The activation energies of the keto–enol interconversions are in the range of 230–310 kJ mol^{-1} in the gas phase, which is on average, up to 20–folds greater than the activation energies of the enediol or keto interconversions between themselves. In water, this process unfolds easier, and E_a and $\Delta G^{\#}$ are lower by 50-80 kJ mol^{-1}. Kinetic and thermodynamic calculations were performed for the transition states of isomerization and tautomerization reactions of the three most stable enediol forms, in the gas phase and in water, equilibrium constants have been identified, along with the forward and reverse reaction rates.

In conclusion, this research presents important information regarding the isomerization and tautomeriztion reactions of difydroxyfumaric acid, which broaden the understanding of these processes in gas and water.

THEORETICAL APPROACH AND METHODS

All geometry optimizations were done by density functional theory (DFT), which give reliable thermodynamic data for molecules and systems with hydrogen bonding, when employed with a large and reasonable basis set [14]. Therefore, the geometries of all possible tautomers–rotamers of DHF and the relevant transition states (TSs) were optimized at the B3LYP/6–311++G(2df,2p) level. All calculations were carried out using the ORCA quantum chemistry package [15], without any symmetry constraints. The absence of imaginary frequencies in the vibrational spectra confirmed that calculated isomer structures were energy minimums.

The Nudged Elastic Band method (as implemented in the ORCA software [15]) was used as a first step to find TSs, which were further optimized and studied at the B3LYP/6–311++G(2df,2p) level, as mentioned above. Transition states were verified with frequency calculations, and were characterized by the existence of only one imaginary frequency for motion along the reaction coordinate.

The effect of water, as the solvent, on the isomerism and tautomerism reactions was calculated using the SMD model, as implemented in ORCA [15].

The Boltzmann equation (Eq.1) was used to calculate the relative abundances (RA) of the enediol and keto isomers, using the internal energy corrected for the zeropoint energy (ZPE).

$$RA = exp\,(-\Delta E/RT) \qquad \text{(Eq. 1)},$$

where $\Delta E = \Delta E_{el} + \Delta ZPE$.

Rate constants were calculated by canonical TS theory using Eyring equation

$$k = \frac{k_B T}{h}\, e^{-\Delta G^{\#}/RT} \quad \text{(Eq.2)},$$

where $\Delta G^{\#}$ is the Gibbs energy of activation, $k_B$is Boltzmann's constant, and h is Planck's constant.

The equilibrium constant K_{eq} is given by the following equation:

$$K_{eq} = exp\,(-\Delta G/RT) \quad \text{(Eq.3)},$$

where $\Delta G = G_{298}^{products} - G_{298}^{reactants}$and individual thermodynamic parameters are $G_{298} = H_{298} - TS_{298}$, $H_{298} = E_{el} + E_{vib} + E_{rot} + E_{trans} + ZPE + k_B T$ and $S_{298} = S_{el} + S_{vib} + S_{rot} + S_{trans}$. All calculations were carried out at 298.15K and 1.0 atm.

AUTHOR CONTRIBUTIONS

Natalia Bolocan: Conceptualization, investigation, writing-original draft preparation and editing.
Gheorghe Duca: Conceptualization, supervision, writing - review and editing.

FUNDING INFORMATION

National Research Project REDOX No. 20.80009.5007.04

REFERENCES

1. a) H.J.H. Fenton; *J. Chem. Soc. Trans.,* **1894**, *65*, 899 – 910; b) H. J. H. Fenton, *J. Chem. Soc. Trans.,* **1905**, *87*, 804 – 818.
2. A. Eschenmoser; *Chem. Biodivers.,* **2007**, *4*, 554 – 573.
3. A. Sychev; G. Duca; *Fruit growing, Viticult. vinif. Mold.,* **1985**, *12*, 39-41 (in Romanian).
4. G. Duca; *Homogeneous Catalysis with Metal Complexes: Fundamentals and Applications*; Springer-Verlag Berlin Heidelberg, **2012**; Vol. XII, 478 p.
5. I. Stepanov; S.G. Carmella; S.S. Hecht; G. Duca; *J. Agric. Food Chem.,* **2002**, *50 (10)*, 2793-2797.
6. Gh. Duca; *Free radicals in natural water,* in *Free Radicals in Biology and Environment*; F. Minisci Ed.; Springer Dordrecht, NATO ASI Series, **1997**, pp. 475-489.
7. D. Porubin; *Chem. J. Mold.,* **2007**, *2*, 3–7.

8. D. Porubin; S. Hecht; ZZ. Li; M. Gonta; I. Stepanov; *J. Agric. Food. Chem.,* **2007**, *55 (17)*, 7199–7204.
9. N. Secara; G. Duca; L. Vlad; F. Macaev; *Chem. J. Mold.,* **2010**, *5 (2)*, 59–67.
10. E.D. Raczynska; W. Kosinska; B. Osmiałowski; R. Gawinecki; *Chem. Rev*. **2005**, *105*, 3561−3612.
11. P. Souchay; D. Fleury; M. Fleury; *C. R. Acad. Sc. Paris*, **1967**, *264, C*, 2130–2133.
12. D. Sazou; P. Karabinas; D. Jannakoudakis; *J. Electroanal. Chem.,* **1984**, *176*, 225–234.
13. S.O. Travin; T.D. Kemp; P. Mur; *Khim. Fiz. (USSR),* **1986***, 5 (10*), 1393-1404.
14. J. Tirado–Rives; W. Jorgensen; *J. Chem. Theory Comput.,* **2008**, *4*, 297–306.
15. F. Neese; F. Wennmohs; U. Becker; C. Riplinger; *J. Chem. Phys.,* **2020**, *152*, 224108.
16. M.P. Andersson and P. Uvdal, *J. Phys. Chem. A*, **2005**, *109 (12)*, 2937–2941.

STUDIA UBB CHEMIA, LXVI, 4, 2021 (p. 355-368)
(RECOMMENDED CITATION)
DOI:10.24193/subbchem.2021.4.26

DETERGENT AIDED REFOLDING AND PURIFICATION OF RECOMBINANT XIAP FROM INCLUSION BODIES

KATALIN NAGY[a], ZITA KOVÁCS[b], ILDIKÓ MIKLÓSSY[c]*, PÁL SALAMON[b], CSONGOR-KÁLMÁN ORBÁN[c], BEÁTA ALBERT[b,c], SZABOLCS LÁNYI[a,c]

ABSTRACT. Human proteins expressed in prokaryotic systems tend to form inclusion bodies. Proteins in inclusion bodies are inactive and the refolding of these densely packed protein molecules is affected by several factors depending on the applied refolding technique. To obtain the active form of protein the most common technique is denaturation of the protein aggregates followed by refolding of inclusion proteins. Conventional denaturants for solubilization are urea, guanidine hydrochloride and sodium dodecyl sulphate (SDS), while refolding can be achieved by several techniques found in the literature. In our study, the recombinant GST-tagged XIAP (X-linked Inhibitor of Apoptosis protein) construct was expressed as inclusion bodies. The protein was solubilized with high efficiency using N-Lauroylsarcosine (ionic detergent). A chromatography-based method using different ratios of detergents was investigated for the refolding process. Batch mode affinity purification was successfully executed using Glutathione Sepharose 4B resin and TritonX-100, n-octyl β-D-thio-glucopyranoside (OTG) and 3-[(3-cholamidopropyl) dimethylammonio]-1-propanesulfonate hydrate (CHAPS) detergents in the appropriate ratio. Finally, the refolded protein was purified by size-exclusion chromatography and investigated by western blot analysis.

Keywords: *XIAP, inclusion body, solubilization, refolding, detergents, affinity chromatography*

[a] *University POLITEHNICA of Bucharest, Faculty of Applied Chemistry and Materials Science, Str. Gh. Polizu, Nr. 1-7, Sector 1, 011061 Bucuresti, Romania*
[b] *University of Pécs, Faculty of Sciences, Ifjúság útja 6., 7624 Pécs, Hungary*
[c] *SAPIENTIA Hungarian University of Transylvania, Faculty of Economics, Socio-Human Sciences and Engineering, Department of Bioengineering, 1 Libertatii Square, RO-530104, Miercurea Ciuc, Romania*
**Corresponding author: miklossyildiko@uni.sapientia.ro*

INTRODUCTION

In multicellular organisms, apoptosis represents genetically programmed cell death. Apoptotic regulation has been involved in many human diseases, including cancer, autoimmune disease, inflammation and neurodegradation [1–3]. Discovering critical apoptosis regulators could be an efficient strategy for the development of new therapies. Two main apoptotic pathways are known: the intrinsic (mitochondrial) and the extrinsic pathways [4,5]. The two pathways are linked and the molecules in one pathway can influence the other pathway, while both proceed via activating caspases [6]. The most potent caspase inhibitor in the IAP family is human X-linked inhibitor of apoptosis protein (XIAP), contains 3 BIR domains (Baculovirus IAP Repeat) in the N-terminal region and a RING do-main endowed with E3 ubiquitin ligase activity, in the C-terminal region. The functional features of these structural domains have been studied in detail: BIR2 domain inhibits caspase-3 and caspase-7, whereas BIR3 domain inhibits caspase-9. According to the literature high levels of e have been found in several cancer cell lines [7], while gene expression analysis of XIAP didn't show high level of mRNA [8]. This indicates that XIAP is probably regulated by post translational mechanisms. In this case, the physiological amount of Smac-DIABLO released from the mitochondria may not be sufficient to overcome the inhibitory effect of XIAP on the caspases, thus preventing apoptosis. Inactivation of overexpressed XIAP by Smac mimetic molecules may relieve caspase binding, thereby promoting apoptosis in malignant cells [9–17].

For over two decades, bacterial expression systems are useful in biotechnologies for investigation of biologically active human proteins, for development of therapeutic drugs and biomaterials [18]. The gram negative bacterium *Escherichia coli* (*E.coli*) is widely used for recombinant protein production. *E. coli* expression system remains the preferred host of choice being a well-established host with short culture time, cultivable on low cost media and characterized by easy genetic manipulation. The number of frequently used expression plasmid copies within the cell can range from one to several hundreds. Several studies have shown high expression levels of proteins using isopropyl b-D-1-thiogalactopyranoside (IPTG) inducible systems. The production process requires the accomplishment of three steps: expression, solubilization and purification [19]. However, when eukaryotic proteins are overexpressed in *E. coli* hosts, they often form inclusion bodies. XIAP is a cysteine rich protein (20 cysteines), moreover, containing a RING domain and increases its tendency to aggregation when overexpressed.

Proteins in inclusion bodies are inactive and the refolding of these densely packed protein molecules is affected by several factors depending on the applied refolding technique. To obtain the active form of the target protein the most common technique is denaturing, then refolding of inclusion proteins. On one hand, conventional solubilizing denaturants are urea, guanidine hydrochloride and sodium dodecyl sulphate (SDS), and refolding of solubilized proteins several methods found in literature are used [18,20–25]. On the other hand, natively folded proteins can be extracted from inclusion bodies using mild detergents, such as N-Lauroylsarcosine, known also as sarkosyl L [26–29].This detergent has many desirable properties: it is non-denaturing, it forms micelles that are small in size, it does not interfere with spectroscopic concentration measurements, and it is of low cost. The refolding protocol developed by Massiah et al. is a rapid, simple, and efficient method for recovering glutathione S-transferase (GST) and Hisx6-tagged maltose binding protein (MBP) fusion proteins from inclusion bodies [30]. N-Lauroylsarcosine has a negatively charged carboxylate group similar to SDS, while it does not have a similar denaturing effect and it is used in many studies to solubilize proteins from inclusion bodies. Lysis buffers usually contain low percentages, 0.1% to 2%, of N-Lauroylsarcosine [31]. Mixed micelle systems are successfully used in detergent and mi-celle-assisted protein refolding procedures, the proposed mechanism of action being the simultaneous availability of transient polar and non-polar interaction sites which reduce hydrophobic interactions between folding intermediates [32]. Triton X-100 (4-(1,1,3,3-Tetramethylbutyl)phenyl-polyethylene glycol) is a non-ionic mild detergent used for cell lysis, cell membrane disruption and enhancing protein solubility [33]. CHAPS, namely 3-[(3-cholamidopropyl) dimethylammonio]-1-propanesulfonate is a zwitterionic detergent with non-denaturing properties used also for enhancing protein solubility. The above mentioned research group have observed that using both Triton X-100 and CHAPS in a specific ratio can enhance purification yield of sarcosyl solubilized proteins [29]. The exact mechanism of action of N-Lauroylsarcosine, Triton X-100 and CHAPS is not known, while on the basis of literature sources, it can be presumed that N-Lauroylsarcosine molecules disrupt aggregation and encapsulate proteins, while Triton X-100 and CHAPS with low critical micelle concentrations (CMC, 0.25 mM and 6–10 mM) form large mixed micelles or bicelles that incorporate N-Lauroylsarcosine molecules from the solution facilitating proper protein refolding [29].

The aim of our study was to develop a detergent and micelle-assisted, chromatography-based modified procedure for XIAP, and to investigate the effect of n-Octyl β-D-thioglucopyranoside (OTG) on protein refolding.

RESULTS AND DISCUSSION

In our work, we present a straightforward solubilization and detergent assisted refolding procedure for the recovery of native recombinant GST tagged XIAP protein. XIAP contains a RING domain and 20 cysteine residues, and its GST-fusion construct is expressed in *E. coli* as inclusion bodies by standard expression protocols, which can be effectively solubilized by *N*-Lauroylsarcosine according to our results. For the refolding of the protein, we used a detergent and micelle-assisted, chromatography-based modified procedure, which was optimized for XIAP and possibly, other RING domain containing proteins.

Expression of GST-XIAP and solubilization with N-Lauroylsarcosine

For expression of the target GST-tagged XIAP recombinant protein, the *E. coli BL21(DE3)Rosetta plysS* strain was successfully used, the highest protein quantity being achieved at 18 °C in a 8 hours period, using 0.2 mM inducer concentration [34]. The apparent molecular weight of the overexpressed protein was 80 kDa based on SDS-PAGE analysis, consistent with the calculated molecular mass of the XIAP-GST construct (78 kDa). Electrophoretic bands present in samples taken after (Figure 1. lane 2.) in comparison, to samples taken before (Figure 1. lane 1.) the induction of expression, analyzed by SDS-PAGE, provide confirmation of target protein expression. After cell lysis, the analyzed bacterial supernatant (Fig. 1, lane 3) and pelleted fraction (Fig. 1, lane 4), show the target protein aggregated in inclusion bodies. Natively folded proteins can be extracted from inclusion bodies using mild detergents such as *N*-Lauroylsarcosine, in our case, in a first experiment, the solubilization step was carried out according to the protocol developed by Massiah's group [31]. The results suggest that virtually the total amount of the insoluble XIAP-GST was solubilized successfully at 10% *N*-Lauroylsarcosine added to the lysis buffer. Figure 1. lane 6. shows inclusion body supernatant after solubilization, while lane 7. shows the pellet after solubilization.

Knowing that mild solubilization of inclusion body aggregates is the key for improving recovery of bioactive proteins, we continued our work with assessment of *N*-Lauroylsarcosine concentration effect on solubilization yield of our target protein. The refolding protocol, based on the solubilization of proteins without chaotropic agents was optimized and used for the XIAP-GST construct. According to literature low concentrations of *N*-Lauroylsarcosine have been used to solubilize proteins expressed in bacteria grown in LB media [35,36]. In addition, Massia's grup concluded that GST tagged proteins expressed in bacteria grown in the M9 minimal medium, low concentrations (0.3-2%) of *N*-Lauroylsarcosine are less effective [31]. We hypothesized that,

less than 10% of *N*-Lauroylsarcosine will already be appropriate for solubilisation of inclusion bodies. Our results demonstrated that, decresing concentrations of *N*-Lauroylsarcosine from 2% to 4%, as Figure 2. shows, we did not observe significant differences in total solubilized protein quantities. Based on our results, we can declare that solubilization with 2% *N*-Lauroylsarcosine already was appropriate.

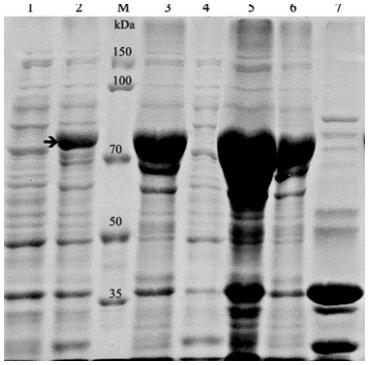

Figure 1. 10 % SDS-PAGE analysis of XIAP-GST expressed in *E. coli* at 18 °C (Lane 1: uninduced total cell lysate; lane 2: total cell lysate afterinduction with 0.2 mM IPTG after 8 hours of culture; lane M: Protein molecular weight marker (Novagen, Sigma Aldrich); lane 3: cell lysate after homogenization; lane 4: supernatant after centrifugation; lane 5: pellet after centrifugation; lane 6: supernatant after solubilization with 10% N-Lauroylsarcosine; lane 7: pellet after solubilization. Proteins stained with Coomassie Brilliant Blue R250).

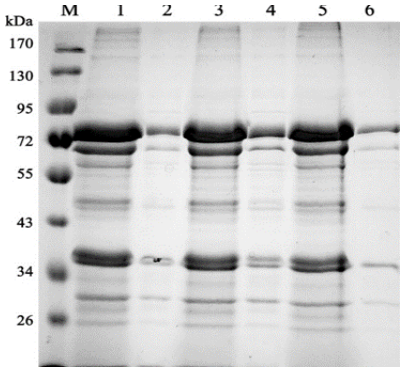

Figure 2. 10 % SDS-PAGE analysis of solubilized XIAP-GST inclusion bodies with different concentration of *N*-Lauroylsarcosine (Lane M: Protein molecular weight marker (*Thermo Scientific*); lane 1: 3% *N*-Lauroylsarcosine supernatant; lane 2: 3% *N*-Lauroylsarcosine pellet; lane 3: 4% *N*-Lauroylsarcosine supernatant; lane 4: 4% *N*-Lauroylsarcosine pellet; lane 5: 2% *N*-Lauroylsarcosine supernatant; lane 6: 2% *N*-Lauroylsarcosine pellet).

Solubilized protein fractions were further analyzed by electrophoretic microchip using a 2100 Bioanalyzer and the Protein 230 kit for molecular weight determination and protein quantitation. As Fig. 3 shows, the apparent molecular weight of the target protein was about 80.4 kDa based on the electrophoregram, consistent with the calculated molecular mass of the XIAP-GST construct (78 kDa), while the solubilized XIAP-GST concentration is 1.025 µg/µl. In total, we obtained 19.62 mg (98.1%) solubilized XIAP-GST.

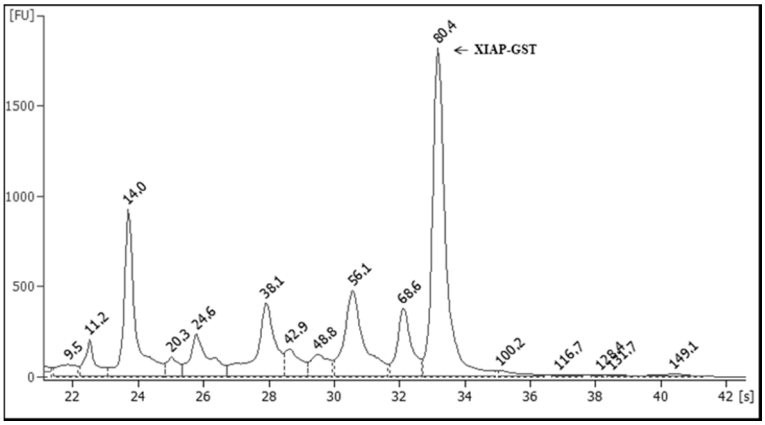

Figure 3. Protein electrophoretic microchip analysis of supernatant after solubilization with *N*-Lauroylsarcosine.

Refolding the XIAP-GST protein by detergent-aided affinity chromatography and gel-filtration

Removal of *N*-Lauroylsarcosine is necessary for efficient affinity purification and refolding of the target protein [37]. There are several studies in the literature for removal of *N*-Lauroylsarcosine by dilution and dialysis [19,38]. The CMC of *N*-Lauroylsarcosine is >0.5% (14 mM) and at lower concentrations (0.1-1%) it is removable by dialysis [33]. A low CMC indicates that the equilibrium between detergent monomers and detergent micelles is almost completely on the micelle side, and that the micelles are of large size, while only detergent monomers can diffuse easily into the surrounding buffer. Removal of detergents with CMC >5 mM is not possible by dialysis. In addition, *N*-Lauroylsarcosine may be sequestered by adding a nonionic detergent, for example OTG, in at least a 5-fold weight excess over the *N*-Lauroylsarcosine [37].

Optimizing refolding conditions for the recombinant XIAP-GST was carried out by adding TritonX-100, CHAPS and OTG in the appropriate ratios, testing 6 different refolding conditions, as stated in the Materials and methods

section (pairwise use of Triton X-100, CHAPS or OTG), prior to affinity purification performed in batch mode. All three detergents (TritonX-100, CHAPS and OTG) facilitated binding of the XIAP-fused GST to the GSH Sepharose matrix. No protein precipitation was observed in case of conditions 1, 2, 4, 5, 6, while in case of condition 3 (Figure 3. lane 3), using the highest concentrations of TritonX-100 and 30 mM CHAPS, almost the total amount of the target protein precipitated. Purification of the refolded protein was followed by SDS-PAGE as presented in Figure 4. Based on band widths of the purified fractions separated on SDS-PAGE gel, refolding aided by 2% Triton X-100 and 20% CHAPS (Figure 4. lane 2) can be considered to be most adequate for XIAP-GST in our experimental setting. Except for refolding condition 3, with 3% TritonX-100 and 30% CHAPS, in all other cases virtually all proteins were purified by affinity chromatography.

In summary, detergent aided refolding and purification experiments can be considered successful. The highest efficiency, i.e. 92.34% (3.02 mg) of refolded protein, was achieved using 2% TritonX-100 and 20 mM CHAPS. In terms of efficiency, refolding and purification performed with 1% Triton X-100 resulted in the next highest yield – 82.15% protein (2.68 mg) with the addition of 10 mM CHAPS, and 79.86% with 1.5% OTG (2.61 mg). We recorded a slightly reduced efficiency, 73.03% refolded protein (2.39 mg), in case of 1% TritonX-100 and 1% OTG, and 72.12% refolded protein (2.36 mg) using 10 mM CHAPS and 1% OTG. Further purification protocol was performed using 2% TritonX-100 and 10 mM CHAPS in order to obtain a high purity protein solution.

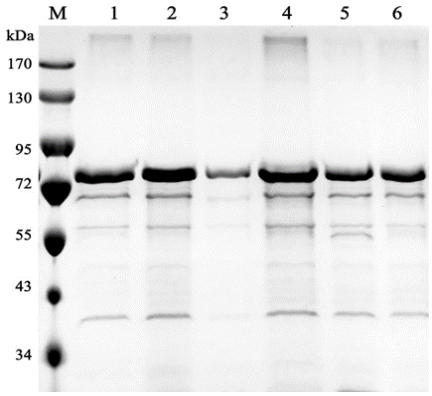

Figure 4. Batch purification of XIAP-GST protein refolded under different detergent-aided conditions (Lane M: Protein molecular weight marker (*Thermo Scientific*); lane 1: 1% TritonX-100 and 10 mM CHAPS; lane 2: 2% TritonX-100 and 20mM CHAPS; lane 3: 3% TritonX-100 and 30mM CHAPS; lane 4: 1% TritonX-100 and 1% OTG; lane 5: 1% TritonX-100 and 1.5 % OTG; lane 6: 10 mM CHAPS and 1% OTG).

However, based on our findings, several other tested conditions yielded similar refolding efficiencies, in a range of 92.34%-72.12% refolded XIAP-GST. Refolding conditions were tested in triplicates. Thus, for refolding of the protein, a detergent and micelle-assisted, chromatography-based procedure was established. The refolding procedure was carried out using different ratios of detergents, with affinity purification successfully executed using Glutathione Sepharose 4B resin and detergents in the appropriate ratios. These detergent mixtures (presented in Materials and Methods section) were set up as follows: from first to third mixture effectiveness of Triton-X and CHAPS was investigated, then another non-ionic detergent (OTG) effect to protein refolding was tested by mixtures fourth and fifth. Based on our results in case of two non-ionic detergents we recorded a slightly reduced efficiency. Finally, we investigated CHAPS and OTG detergent mixtures as new potential refolding process.

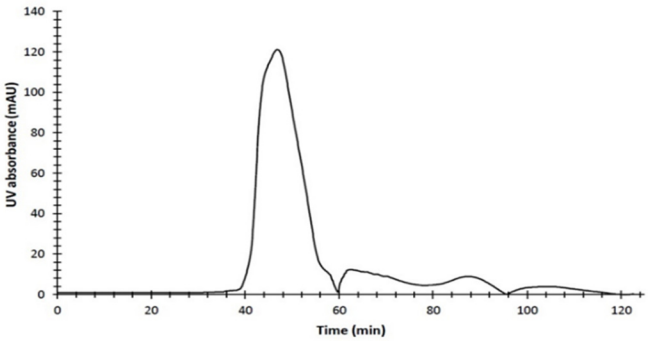

Figure 5. Elution profile of refolded XIAP-GST after separation on a HiLoad 16/600 Superdex 75 pg column. Detection was performed at 280 nm.

For further purification of the target protein we performed size-exclusion chromatography, using HiLoad 16/600 Superdex 75 pg column. The column was first loaded with Tris-HCl buffer, followed by sample injection to column. Figure 5. shows the elution profile of XIAP-GST, according to which, this purification step was very efficient, and resulted in a 97% efficiency purification of refolded protein. The overall yield of refolded protein was 17.57 mg/200 ml *E. coli* culture.

Identification of the refolded protein

A WB analysis was performed to confirm the refolding of recombinant XIAP-GST. Western blot analysis indicated the authenticity of refolded and purified protein [39–41]. Proteins were immunodetected using an anti-XIAP

antibody, which reacts with an epitope located in the C-terminal region encoded by amino acids 352-449 of XIAP. The UBA region of the protein is responsible for interactions with e.g NFκB and other mono-or diubiquitiladed proteins [42].

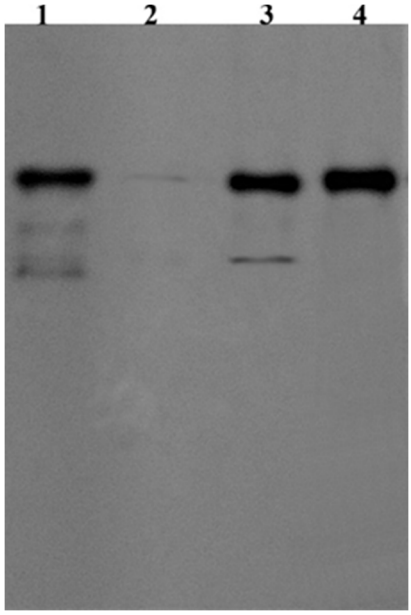

Figure 6. WB analysis of XIAP-GST protein. Lane 1: Refolded and purified XIAP-GST from experiment 2 (lane 2: unfolded GST-XIAP; lane 3: XIAP-GST after size exclusion chromatography; lane 4: Recombinant XIAP-GST from commercial source).

Based on the above, we used western blotting to characterize structural epitopes of metastable folding intermediates, while the specificity of antibodies to folding intermediates allows to identify protein folding. As a control sample, recombinant XIAP-GST (84 kDa) obtained from commercial sources was used to identify our refolded protein. In addition, our blotting experiment was designed by using non-denaturing conditions. Fig.6 shows the WB analysis of refolded XIAP-GST. As these results show, we can declare that solubilization and refolding of XIAP-GST was successful, as both the refolded protein and the commercial protein show similar profiles after separation and identification by the specific antibodies. In addition, in case of unfolded protein (Fig.6, lane 2.) there is no visible protein after western blotting, while this can also be considered as a proof that only refolded proteins were immunodetected.

CONCLUSIONS

In vitro refolding of inactive protein aggregates is affected by several factors, depending on the applied refolding technique and in most cases, has to be customized for the specific protein. In our study, we present a quick and straightforward solubilization and detergent assisted refolding procedure using detergents for the recovery of native recombinant GST tagged XIAP protein.

According to the data presented above, XIAP-GST can be effectively solubilized by 2% N-Lauroylsarcosine, while 92.34% of the protein can be refolded using 2% TritonX-100 and 20 mM CHAPS during affinity purification. However, Size-exclusion chromatography assured a purification of 97% of the refolded protein solution, thus obtaining an overall yield of 17.57 mg refolded, purified XIAP-GST starting from 200 ml bacterial culture.

EXPERIMENTAL SECTION

Materials and instruments

All molecular reagents and chemicals, unless stated otherwise, were purchased from commercial sources (Sigma Aldrich, Merck, BioLabs and Thermo Scientific™). *E. coli BL21 (DE3) Rosetta plysS* was obtained from Thermo Scientific. The pGEX6p1-GST-XIAP recombinant plasmid was a kind gift from Attila Reményi (*Eötvös Loránd* University, Budapest, Hungary) [43]. The recombinant GST-XIAP used as control for western blot analysis was obtained from commercial sources (Merck). The electrophoresis apparatus was from Bio-Rad (Bio-Rad Mini ProteanTetraCell). Sorvall LYNX 6000 super speed centrifuge (Thermo Scientific) was used for centrifugation. Batch purification of proteins was executed using Glutathione Sepharose 4B affinity chromatography resin (GE Healthcare). All chromatography experiments were performed using an AKTA FPLC system (Amersham Pharmacia Biotech). Hi Load 16/600 Superdex 75 pg column was purchased from GE Healthcare. For chip electrophoresis assays a 2100 Bioanalyzer Instrument (Agilent) and Protein 250 Kit (Agilent) were used.

Protein expression and preparation of inclusion bodies

The nucleotide sequence encoding XIAP (NM_001167.4) was fused with GST. The pGEX6p1-GST-XIAP recombinant plasmid was transformed into competent *E. coli BL21 (DE3) Rosetta plysS* cells and plated on Luria Bertani (LB) agar containing 100 μg/ml ampicillin and 34 μg/ml chloramphenicol. A single colony was used to inoculate 5 ml LB-ampicillin medium and grown

for 8 h at 37 °C and 250 rpm in an orbital shaker. Then, 1 ml of the inoculum culture was transferred to 200 ml of the M9 minimal medium containing 100 µg/ml ampicillin and 34 µg/ml chloramphenicol and cultured under the same conditions until the OD_{600} value reached 0.7. The culture temperature was decreased to 18 °C and 0.2 mM IPTG was added to induce the expression of the recombinant protein [34]. The culture was incubated for 8 h at 18 °C in an orbital shaker. The cells were harvested by centrifugation at 4500 rpm for 10 min at 4 °C. Total protein was analyzed by 10 % (w/v) SDS–PAGE.

Recovery of inclusion bodies

Three grams of harvested cells were suspended in 30 mL lysis buffer (50 mM Tris HCl, 200 mM NaCl and 2 mM DTT, pH 7.8). Lysozyme (1 mg/mL) was added to the cell suspension and incubated for 30 minutes at 4 °C, in an orbital shaker. Afterwards, DNase I (0.1 mg/ml final concentration) was added to the cell suspension. After 30 minutes of incubation, cells were homogenized with a high-pressure homogenizer (LM10 Microfluidizer) at 18,000 psi for two cycles. The cell lysate was centrifuged for 20 minutes at 15,000 x g, at 4 °C, and pellets were collected and washed with ultra-pure water twice.

Solubilization of inclusion bodies

Solubilization of the target protein was carried out by adding *N*-Lauroylsarcosine in different concentrations (2%, 3%, 4% and 10%) to the above mentioned lysis buffer. These suspensions were incubated at room temperature with gentle stirring for 1 h, followed by centrifugation at 10,000×g for 15 min. The supernatant containing the target protein was immediately subjected to the refolding procedure. The solubilized protein fractions were analyzed by 10 % (w/v) SDS–PAGE.

Refolding and purification

Qualitative analysis of total protein was executed by protein chip analysis. The experiment was carried out according to Protein 230 Kit (Agilent) experiment description using Bioanalyzer 2100. Optimizing refolding conditions for the recombinant XIAP-GST was carried out using TritonX-100, CHAPS and OTG in different ratios. Solubilized proteins were refolded using 6 different conditions, as follows:

1: 1% TritonX-100 and 0.61% (10 mM) CHAPS; ***2***: 2% TritonX-100 and 1.22% (20mM) CHAPS; ***3***: 3% TritonX-100 and 4.83% (30mM) CHAPS; ***4***: 1% TritonX-100 and 1.5% OTG; ***5***: 1% TritonX-100 and 1 % OTG; ***6***:

0.61% (10 mM) CHAPS and 1% OTG. Refolding conditions were tested in triplicates. The detergents were added carefully to the solubilized protein with slow mixing, at room temperature. Refolded proteins were purified on Glutathione Sepharose 4B resin. Solubilized proteins were incubated for 2 hours with the glutathione beads at room temperature with gentle mixing. Purification of the refolded proteins was carried out according to the manufacturer's (GE Healthcare) instructions and was followed by 10 % SDS-PAGE. Elution of the protein was carried out by 50 mM Tris-HCl buffer, pH 8.0, containing 20 mM reduced glutathione. The eluted fractions were stored at 4 °C and analyzed by 10% SDS-PAGE. Protein concentrations were determined spectroscopically (at 280 nm) using Genova Nano micro-volume spectrophotometer. Purified proteins were dialyzed for 48 h in 50 mM Tris-HCl buffer, pH 7.8 with three changes. For further purification of the target protein we performed by size-exclusion chromatography using a HiLoad 16/600 Superdex 75 pg column at 1 ml/min flow rate. The column was first loaded with 2 column volumes of 50 mM Tris-HCl, pH 7.8 buffer, followed by sample injection. Elution was monitored at 280 nm. The eluted fractions were stored at 4 °C and analyzed by 10 % SDS-PAGE. All samples were analyzed by based the Laemmli protocol SDS-PAGE with a 5% (w/v) stacking gel and a 10% (w/v) resolving gel at a constant voltage of 120V [44].

Western Blot analysis

Western Blot (Mini Trans-Blot®, Bio-Rad) analysis was performed to confirm the refolding of XIAP-GST. Recombinant XIAP-GST proteins were separated by electrophoresis, using native PAGE and then transferred by wet transfer onto PVDF membrane. The transfer buffer contained 25 mM Tris-HCl, 192 mM glycine, 0.7 % acetic acid at pH=7.4. The membrane was incubated at 4°C overnight with a monoclonal anti-XIAP antibody, clone 2F1 (Abcam), at a dilution rate of 1:1000 in TBS buffer. After washing 4 times with TBS for 15 min each, the membrane was incubated with Goat Anti-Mouse IgG H&L (HRP) secondary antibody (Abcam) diluted 1:1000 in TBS. The next step was washing 4 times with TBS for 15 min each. Finally, the protein was detected using the Pierce™ ECL substrate (Thermo Scientific), and the membrane was visualized using X-ray film (dark room technique).

ACKNOWLEDGMENTS

This research was financially supported by the Department of Bioengineering, Sapientia Hungarian University of Transylvania.

REFERENCES

1. C.M. Croce; J.C. Reed; *Cancer Res.*, **2016**, *76*, 5914–5920
2. M.J. Roy; A. Vom; P.E. Czabotar; G. Lessene; *Br. J. Pharmacol.*, **2014**, *171*, 1973–1987
3. R. Singh; A. Letai; K. Sarosiek; *Nat. Rev. Mol. Cell Biol.*, **2019**, *20*, 175–193
4. P.J. Burke; *Trends in Cancer.*, **2017**, *3*, 857–870
5. F. Cairrao; P.M. Domingos; *Encycl. Life Sci. (ELS), John Wiley Sons, Ltd Chichester.*, **2010**, pp. 1-8
6. Y. Estornes; M.J.M. Bertrand; *Semin. Cell Dev. Biol.*, **2015**, 39, 106–114
7. R. Saraei; M. Soleimani; A.A. Movassaghpour Akbari; M. Farshdousti Hagh; A. Hassanzadeh; S. Solali; *Biomed. Pharmacother.*, **2018**, *107*, 1010–1019
8. P. Hundsdoerfer; I. Dietrich; K. Schmelz; C. Eckert; G. Henze; *Pediatr Blood Cancer.*, **2009**, *55*, 260–266
9. H. Sun; L. Liu; J. Lu; S. Qiu; C.Y. Yang; H. Yi; S. Wang; *Bioorganic Med. Chem. Lett.*, **2010**, *20*, 3043–3046
10. R. Feltham; B. Bettjeman; R. Budhidarmo; P.D. Mace; S. Shirley; S.M. Condon; S.K. Chunduru; M.A. McKinlay; D.L. Vaux; J. Silke; C.L. Day; *J. Biol. Chem.*, **2011**, *286*, 17015–17028
11. G. Garg; S. Vangveravong; C. Zeng; L. Collins; M. Hornick; Y. Hashim; D. Piwnica-Worms; M.A. Powell; D.G. Mutch; R.H. Mach; W.G. Hawkins; D. Spitzer; *Mol. Cancer.*, **2014**, *13*, 1–13
12. L. Bai; D.C. Smith; S. Wang; *Pharmacol. Ther.*, **2014**, *144*, 82–95
13. A. Tchoghandjian; A. Soubéran; E. Tabouret; C. Colin; E. Denicolaï; C. Jiguet-Jiglaire; A. El-Battari; C. Villard; N. Baeza-Kallee; D. Figarella-Branger; *Cell Death Dis.*, **2016**, *7*, 1–10
14. S. Fulda; *Clinical Cancer Research,* **2015**, *21*, 5030–5037
15. L. Manzoni; D. Gornati; M. Manzotti; S. Cairati; A. Bossi; D. Arosio; D. Lecis; P. Seneci; *Bioorganic Med. Chem. Lett.*, **2016**, *26*, 4613–4619
16. A.C. West; B.P. Martin; D.A. Andrews; S.J. Hogg; A. Banerjee; G. Grigoriadis; R.W. Johnstone; J. Shortt; *Oncogenesis.*, **2016**, *5*, e216-6
17. K. Welsh; S. Milutinovic; R.J. Ardecky; M. Gonzalez-Lopez; S.R. Ganji; P. Teriete; D. Finlay; S. Riedl; S.I. Matsuzawa; C. Pinilla; R. Houghten; K. Vuori; J.C. Reed; N.D.P. Cosford; *PLoS One.*, **2016**, *11*, 1–19
18. D.M. Francis; R. Page; *Curr. Protoc. Protein Sci.*, **2010**, 61, 5.24.1-5.24.29
19. H. Yamaguchi; M. Miyazaki; *Biomolecules.*, **2014**, *4*, 235–251
20. E. Kovács; L. Szilágyi; G. Koncz; *Appl. Biochem. Biotechnol.*, **2013**, *170*, 819–830
21. C.J. Jeffery; *Curr. Protoc. Protein Sci.*, **2016**, *83*, 29.15.1-29.15.15
22. A. Mohammadian; H. Kaghazian; A. Kavianpour; R. Jalalirad; *Chem. Technol. Biotechnol.*, **2018**, *93*, 1579–1587
23. A. Basu; X. Li; S.S.J. Leong; *Appl. Microbiol. Biotechnol.*, **2011**, *92*, 241–251
24. G. Gieseler; I. Pepelanova; L. Stuckenberg; L. Villain; V. Nölle; U. Odenthal; S.

Beutel; U. Rinas; T. Scheper; *Appl. Microbiol. Biotechnol.*, **2017**, *101*, 123–130
25. A.A. Padhiar; W. Chanda; T.P. Joseph; X. Guo; M. Liu; L. Sha; S. Batool; Y. Gao; W. Zhang; M. Huang; M. Zhong; *Appl. Microbiol. Biotechnol.*, **2018**, *102*, 2363–2377
26. J. Zhang; X. Lv; R. Xu; X. Tao; Y. Dong; A. Sun; D. Wei; *Appl. Microbiol. Biotechnol.*, **2015**, *99*, 6705–6713
27. K. Babaei Sheli; M. Ghorbani; A. Hekmat; B. Soltanian; A. Mohammadian; R. Jalalirad; *Biotechnol. Reports*., **2018**, *19*, e00259
28. A. Ghoshal; S.S. Ghosh; *Appl. Biochem. Biotechnol.*, **2014**, *175*, 2087–2103
29. F. Naz; M. Asad; P. Malhotra; A. Islam; F. Ahmad; M.I. Hassan; *Appl. Biochem. Biotechnol.*, **2014**, *172*, 2838–2848
30. H. Tao; W. Liu; B.N. Simmons; H.K. Harris; T.C. Cox; M.A. Massiah; *Biotechniques*., **2010**, *48*, 61–64
31. M.A. Massiah; K.M. Wright; H. Du; *Curr. Protoc. Protein Sci.*, **2016**, *84*, 6.13.1-6.13.24
32. R.R. Burgess; Chapter 17 Refolding Solubilized Inclusion Body Proteins, in: Methods Enzymol., 1st ed., Elsevier Inc., **2009**, pp. 259–282
33. G. Zardeneta; P.M. Horowitz; *Anal. Biochem.*, **1994**, *223*, 1–6
34. K. Nagy; Z. Kovács; P. Salamon; C.K. Orbán; S. Lányi; B. Albert; *Stud. Univ. Babes-Bolyai Chem.*, **2019**, *64*, 101–110
35. S. Frankel; R. Sohn; L. Leinwand; *Proc. Natl. Acad. Sci. U. S. A.*, **1991**, *88*, 1192–1196
36. Q. Zhuo; J.H. Piao; R. Wang; X.G. Yang; *Protein Expr. Purif.*, **2005**, *41*, 53–60
37. D. Kumar; *Ref. Modul. Life Sci.*, **2018**, 1–17
38. S.A. Frankel; A. Leinwand, Leslie; Solubilization of protein after bacterial expression using Sarkosyl,*U.S. Patent,* **1993**, 1–5
39. D. Nasrabadi; S. Rezaeiani; A. Sayadmanesh; M.B. Eslaminejad; A. Shabani; *Avicenna J. Med. Biotechnol.*, **2018**, *10*, 202–207
40. A.K. Patra; G.K. Gahlay; B.V.V. Reddy; S.K. Gupta; A.K. Panda; *Eur. J. Biochem.*, **2000**, *267*, 7075–7081
41. W. Li; Y. Yuan; Z. Luo; X. Zheng; L. Zhao; W. Duan; Y. Yu; *Biosci. Biotechnol. Biochem.*, **2010**, *74*, 1173–1180
42. M.K. Tse; S.K. Hui; Y. Yang; S.T. Yin; H.Y. Hu; B. Zou; B.C.Y. Wong; K.H. Sze; *PLoS One*., **2011**, *12*, e28511
43. A. Takeda; T.K. Oberoi-Khanuja; G. Glatz; K. Schulenburg; R. Scholz; A. Carpy; B. Macek; A. Remenyi; K. Rajalingam; *EMBO J.*, **2014**, *33*, 1784–1801
44. U.K. Laemmli; *Nature*., **1970**, *227* (5259), 680–685

STUDIA UBB CHEMIA, LXVI, 4, 2021 (p. 369-382)
(RECOMMENDED CITATION)
DOI:10.24193/subbchem.2021.4.27

ANTIMICROBIAL ACTIVITY OF EXPERIMENTAL ENDODONTIC SEALER BASED ON BIOCERAMIC NANOMATERIALS

LUCIA IACOBINA TIMIS[a]*, MARIA GOREA[b]*, CARMEN COSTACHE[c], IOANA ALINA COLOSI[c], PAVEL ȘCHIOPU[c], PAUL-ȘTEFAN PANAITESCU[c], ADA DELEAN[a], DINU IULIU DUMITRASCU[d], RADU SEPTIMIU CÂMPIAN[e]

ABSTRACT. The aim of this work was to evaluate the antimicrobial effectiveness of a bioceramic experimental endodontic sealer (EES), alongside with its components. As a novelty, magnesium silicate was incorporated into the experimental material, in order to improve the mechanical performance of the product. The main oxide components, tricalcium silicate (Ca_3SiO_5) and magnesium silicate (Mg_2SiO_4) were synthesized in nanoparticles from specific precursors by a sol-gel method. To compare the efficiency of the new developed product, commercially available materials, with similar chemical composition, used in everyday practice, were also tested: BC Sealer, MTA Bioceramic Root Canal Sealer, and MTA Fillapex. The method employed for the present study was the agar well diffusion test (ADT). The selected microbial strains were *Enterococcus faecalis* and *Candida albicans*, frequently associated with persistent infection and recurrent infections of the endodontic space, as well as periapical pathologies refractory to endodontic treatment. Measurements of the inhibition areas were performed at 24-hour intervals for 7 consecutive days. Tricalcium silicate and all tested endodontic sealers revealed antimicrobial effectiveness against *Candida albicans* at 24 hours after placement, with a prolonged activity, for up to 7 days. The study revealed no antibacterial effect against *Enterococcus faecalis* at 24 hours nor in the following 7 days, for any of the tested samples.

Keywords: *antimicrobial activity, bioceramic, endodontic sealer, tricalcium silicate*

[a] *Iuliu Haţieganu University of Medicine and Pharmacy, Faculty of Dentistry, Department of Odontology, 33 Calea Moţilor str., RO-400001 Cluj-Napoca, Romania.*
[b] *Babeş-Bolyai University, Faculty of Chemistry and Chemical Engineering, 11 Arany Janos str., RO-400028, Cluj-Napoca, Romania.*
[c] *Iuliu Haţieganu University of Medicine and Pharmacy, Faculty of Medicine, Department of Molecular Sciences, Division of Microbiology, 6 Louis Pasteur str., RO-400349, Cluj-Napoca, Romania.*
[d] *Iuliu Haţieganu University of Medicine and Pharmacy, Faculty of Medicine, Department of Anatomy and Embryology, 3-5 Clinicilor str., RO-400006 Cluj-Napoca, Romania.*
[e] *Iuliu Haţieganu University of Medicine and Pharmacy, Faculty of Dentistry, Department of Oral Rehabilitation, 15 Victor Babeş str., RO-400012, Cluj-Napoca, Romania.*
** Corresponding author: maria.gorea@ubbcluj.ro, Timis.Lucia@umfcluj.ro*

INTRODUCTION

The success of the endodontic treatment is given by the absence of acute or chronic apical periodontitis in endodontically treated teeth. This goal can be achieved by eliminating microorganisms and their by-products from the root canal and avoiding further recontamination [1-3].

Endodontic obturating materials that exhibit antimicrobial properties may be helpful in reducing the contamination of the endodontic space, thus increasing the success rate of the treatment.

Currently, a great number of endodontic sealers are available for clinical use. According to their composition and based on its main component, they belong to one of the following groups: zinc oxide eugenol, calcium hydroxide, epoxy resin, silicone, glass ionomer, methacrylate resin, calcium phosphate or calcium silicate based materials.

The chemical composition of endodontic sealers can influence the products' antimicrobial properties [4,5]. Most endodontic sealers that present significant antimicrobial properties also exhibit an irritating or toxic effect upon the periapical tissues and oral mucosa, especially those containing epoxy resins, methacrylate resins, formaldehyde, or eugenol [1]. Consequently, the aim to produce the least possible harm to the surrounding tissues is often hard to achieve, as root canal obturating materials are placed in proximity to the periapical area.

The development of bioceramic nanomaterials based on calcium silicates and calcium phosphates marked a new stage both in medicine and dentistry. In addition to their superior physical properties, they are biocompatible, being very well tolerated by the periapical tissues, and bioactive, inducing bone healing and regeneration [6,7].

Bioceramic endodontic sealers have been developed as an alternative to conventional materials used for root canal obturation since 2007. Their main constituents, calcium silicates, calcium phosphates, or both, are combined with one or more of the following components: calcium hydroxide, zirconium oxide, bismuth oxide, calcium sulphate, tricalcium aluminate, resins, calcium salicylate, mineral trioxide aggregate [8,9].

TotalFill BC sealer (FKG, Switzerland) is a premixed ready to use hydrophilic sealer based solely on inorganic compounds. It presents an increased biocompatibility due to its composition, and a success rate of 90.9% in nonsurgical endodontic treatments [10]. It has an alkaline pH, due to OH^- ion release, and superior bioactivity compared to other materials, including the ones in its class [11].

MTA Bioceramic Sealer (Henry-Schein, USA) and MTA-Fillapex (Angelus, Brazil*)* are both formulated as two paste systems, designed to be mixed prior to their placement inside the root canal. They have similar composition, consisting of mineral trioxide aggregate as a source for calcium silicates and R_20_3 (mainly Bi^{3+}) associated with organic resins: salicylate resin and diluting or base resins. Their bioactivity and biocompatibility are proven to be inferior compared to resin-free bioceramic materials, but still, superior to other classes [12,13].

Various studies were performed upon different types of pathogens, in order to assess the antimicrobial effect of commercial endodontic sealers. Agar diffusion test (ADT) was the most used. The results for bioceramic sealers are subject to controversies. Some studies revealed their long-term antimicrobial properties [14], while others only revealed a short-term effect [15], or even none [4].

Enterococcus faecalis, a facultative anaerobic bacterium, holds the ability to penetrate dentinal tubules, form biofilms, survive nutritional deprivation and resist antimicrobial sealers, thus generating persistent periapical infections [16,17].

Candida albicans, an opportunistic yeast, manifests high resistance in the oral cavity and has an affinity to dentin, penetrating dentinal tubules. It can survive in hostile environments and is involved as causal agent of endodontic treatment failures [18,19].

The coexistence of *E. faecalis* and *C. albicans* has been observed, the two microorganisms being co-isolated in 10% of the periapical and root canal infections and in 40% of the oral lesions [20]. Fungal-bacterial interactions are deemed problematic because the presence of *C. albicans* was proven to increase the metabolic activity of the biofilm, indicating its fast growing and colonisation, with an increased resistance to antimicrobial treatment [21].

The aim of this in vitro study was to evaluate the antimicrobial properties of an experimental bioceramic sealer (EES) as well as the individual properties of its main components: tricalcium silicate (Ca_3SiO_5), zirconium dioxide (ZrO_2), magnesium silicate (Mg_2SiO_4) and zinc chloride ($ZnCl_2$). Similar commercially available bioceramic sealers were tested for comparison: BC Sealer, MTA Bioceramic Root Canal Sealer, and MTA Fillapex.

The study was performed using the agar diffusion test (ADT) on strains of pathogens incriminated in inducing periradicular infections resistant to treatment: *Enterococcus faecalis and Candida albicans.* The properties were evaluated on a 7-day period starting at 24 hours after placement.

RESULTS AND DISCUSSIONS

All tested endodontic sealers' antimicrobial activity was assessed by measuring the diameters of the inhibition zones that could be observed around each well, at 24-hour intervals for 7 consecutive days.

Duplicate measures were averaged, and Friedman test was used to determine the significance of the difference between the tested materials. Post-hoc analysis was performed using Dunn pairwise comparisons with Bonferroni correction for multiple testing.

Candida albicans

All commercially available sealers, as well as tricalcium silicate and the experimental composition (EES) displayed consistent growth inhibition for *C. albicans,* as presented in Figure 1.

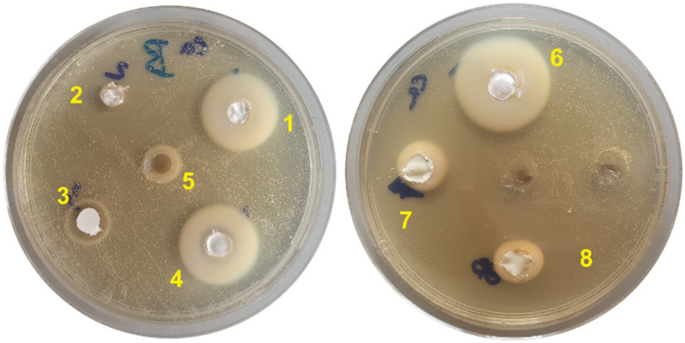

Figure 1. ADT of multiple sealers on *Candida albicans* inoculated plate: 1 - Tricalcium silicate (Ca_3SiO_5), 2 - Magnesium silicate (Mg_2SiO_4), 3 - Zirconium dioxide (ZrO_2), 4 - Experimental sealer (EES), 5 – Zinc chloride ($ZnCl_2$), 6 - TotalFill BC Sealer, 7 - MTA Bioceramic Sealer, 8 - MTA-Fillapex.

Mean values of the diameters of the inhibition zones were calculated for each sample and presented in Table 1.

Friedman test showed significant differences between the medians of the measurements ($\chi^2 = 27.07$, $p < 0.05$), as presented in Figure 2.

Table 1. Average measurements of the zones of *C. albicans* diameters of inhibition zones (mm).

Sealer	Day 1	Day 2	Day 3	Day 4	Day 5	Day 6	Day 7	Median
Tricalcium silicate ***(Ca_3SiO_5)***	20.3	20.0	20.5	20.7	20.4	20.2	21.0	20.4
Magnesium silicate ***(Mg_2SiO_4)***	0.0	0.0	0.0	0.0	0.0	0.0	0.0	0.0
Zirconium dioxide ***(ZrO_2)***	0.0	0.0	0.0	0.0	0.0	0.0	0.0	0.0
Experimental sealer ***(Ca_3SiO_5, Mg_2SiO_4, ZrO_2, $ZnCl_2$)***	20.0	20.0	20.0	20.3	20.3	20.1	21.2	20.1
Zinc chloride ***($ZnCl_2$)***	0.0	0.0	0.0	0.0	0.0	0.0	0.0	0.0
TotalFill BC Sealer	26.0	24.0	24.0	24.5	24.9	25.1	25.5	24.9
MTA Bioceramic Sealer	25.7	22.0	24.0	22.0	22.5	22.1	24.0	22.5
MTA-Fillapex	25.0	21.5	22.0	20.8	21.2	21.1	23.3	21.5

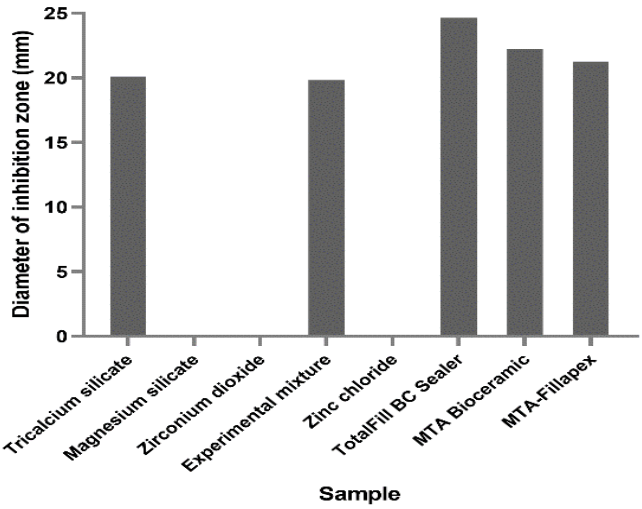

Figure 2. Medians of the measurements of *C. albicans* diameter of inhibition zone.

Regarding the antifungal effect against *C. albicans,* tricalcium silicate showed no significant statistical difference from MTA-Fillapex (p=1) and MTA Bioceramic Sealer (p=0.068). The experimental sealer showed no statistically significant difference compared to MTA-Fillapex (p=0.346). MTA Bioceramic Sealer performed better than the experimental sealer (p<0.05). TotalFill BC Sealer performed better than both tricalcium silicate (p<0.05) and the experimental sealer (p<0.05). There was no statistical difference between tricalcium silicate and the experimental sealer's ability to inhibit the growth of C. *albicans* (p=1), suggesting that Tricalcium silicate's inhibitory activity remains constant even when present as part of this composition. Zinc chloride $ZnCl_2$ solution produced no inhibition zones. Further studies are needed to better understand Tricalcium silicate's inhibitory action upon *C. albicans* and how this effect is influenced by its concentration in the sealing material.

Fungi are common inhabitants of the gastrointestinal tract and the oral cavity in the human body. Therefore, they can be present in the microbiota of infected root canal. *Candida albicans* is the yeast most isolated from these infections [22,23]. It has an affinity to dentin, is able to penetrate dentinal tubules, and can adapt to different environments [24].

The pathogenicity of *C. albicans* is further increased by its ability to form biofilms, thus becoming 10-100 times more resistant to common medication than planktonic cells. Like *E. faecalis*, it is often responsible for persistent endodontic related infections that are reluctant to treatment [25].

There is a consensus in literature regarding the antifungal properties of bioceramic sealers. Tested bioceramic sealers exhibited antimicrobial effect against strains of *Candida albicans* on ADT. Authors have described them having moderate activity, but still not as significant as other classes, like epoxy resin materials [26], or zinc oxide eugenol materials [15], more pronounced that methacrylate-based materials [27].

The present study revealed antifungal activity against *C. albicans* for all commercial endodontic sealers along with calcium silicate and experimental sealer. The effect was present at 24 hours after placement and it was maintained for the entire period of the study (7 days).

Enterococcus faecalis

The antimicrobial activity upon *Enterococcus faecalis* was not observed at 24 hours or in the following 7 days, neither for the commercial sealers, nor for the experimental material, or its components (Figure 3).

There is no information on the possible activity during the first 24 hours because this didn't represent the purpose of our research.

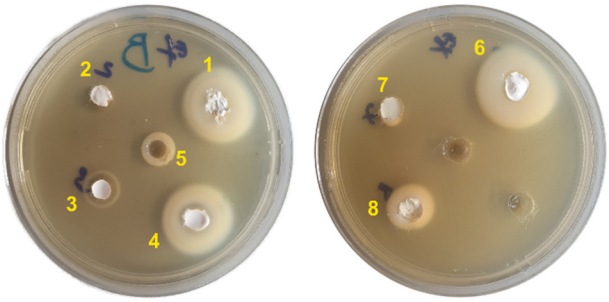

Figure 3. ADT of multiple sealers on *Enterococcus faecalis* inoculated plate: 1 - Tricalcium silicate (Ca_3SiO_5), 2 - Magnesium silicate (Mg_2SiO_4), 3 - Zirconium dioxide (ZrO_2), 4 - Experimental sealer (EES), 5 – Zinc chloride ($ZnCl_2$), 6 - TotalFill BC Sealer, 7 - MTA Bioceramic Sealer, 8 - MTA-Fillapex

Enterococci are a group of opportunistic pathogens found in the gastrointestinal tract [28]. Among these cocci, *E. faecalis* is of interest because, if present in the microbiota of infected root canals, in most of the cases it is associated with chronic apical periodontitis, especially with cases that are refractory to endodontic treatment [29,30]. It is a gram positive facultative anaerobic bacterium that can penetrate deep into dentinal tubules and form biofilms. *E faecalis* can tolerate increased pH, up to 11.5, and prolonged starvation. Due to its virulence factors and biofilm formation the microorganism is resistant to many intracanal medicaments, including antibiotics and calcium hydroxide [31,32].

Various studies using the diffusion method on Muller-Hinton agar were performed to assess the antimicrobial properties against *E. faecalis* of available commercial endodontic sealers.

Following a systematic review, AlShwaimi et al [33] concluded that, even though many of the studies investigated reported some form of antibacterial activity against *E. faecalis*, it typically only persisted for up to 24 hours, depending on the analysed endodontic material. The activity was usually lost after the material was set, with no observable inhibition zones from day 2 to 7 [33].

Conventional materials like zinc-oxide-eugenol or epoxy resin-based sealers are known to exhibit strong antibacterial effect against *E. faecalis* [34]. Nonetheless, they are toxic, cytotoxic, or mutagenic for human cells, especially the ones containing formaldehyde [35].

Bioceramic materials are newly introduced on the market, and there isn't enough available data. Our study revealed no antibacterial effect against *E. faecalis* at 24 hours, for all the tested samples. Similar studies in the literature show conflicting evidence [16]. This may be due to different

investigation methods, materials or bacterial strains used, duration of the research, concentration of *E. faecalis*, or method of inoculation.

It might also be possible they do not present a pronounced antibacterial effect against *E. faecalis*, thus different results of the studies performed to date. A standardized method would be necessary when investigating this bacterium, as different tests can offer different results.

The fact that the antimicrobial activity upon *E. faecalis* was not noticeable when studies using the ADT method were performed, as opposed to some cases when DCT was used, can lead to the encouraging inference that bioceramic sealers might have some weak inhibitory effect on this class of enterococci. Comparative studies that used ADT and DCT methods revealed the antimicrobial effect in the latter [4].

Antimicrobial activity is a desired property of root canal obturating materials, as they may entomb and neutralize the residual micro-organisms remaining after chemo-mechanical instrumentation. However, materials exhibit such properties on a limited number of species, and for a limited amount of time.

It is known that antibacterial properties of endodontic sealers are at their highest levels immediately after preparation and decreases in time, as the material sets [27]. Consequently, most of the antimicrobial ADT studies were performed on freshly mixed endodontic sealers evaluating their activity shortly after placement, or at different time intervals mostly within the first 24 hours [36]. This would be relevant if the in vivo setting time would be comparable to the sealers producer's statement. However, Allan et al (2001) evaluated the setting time of different endodontic sealers both under bench-top conditions and under simulated clinical conditions. Their study revealed that, in simulated clinical conditions, all investigated materials were only partially set after 1 week, and requested at least 4 weeks for complete setting, considerably longer than the time required for in vitro setting [37].

Following this, while the material is not completely set, in areas where its pasty consistency is maintained, it may be possible for it to still exhibit antimicrobial properties. Taking this into consideration, our study upon the antimicrobial activity was conducted for a period of 7 days.

Bioceramic endodontic sealers are considered the best alternative for obturating root canals due to their superior properties. Regarding their antimicrobial activity, they might not possess such an increased effect compared to other classes of endodontic sealers, but they have the benefit of being the most biocompatible of all, and this should make them the materials of choice. Therefore, it is important not to fully rely on the ability of endodontic materials to neutralize the microorganisms from infected root canals. It is desirable to ensure that *E. faecalis*, and *C. albicans* are eliminated before performing the obturation with bioceramic materials by using other

means of decontamination: chlorhexidine 2%, chitosan, propolis, MTAD, photon-induced photoacoustic streaming (PIPS), quaternary ammonium silane (k21) [38-42].

CONCLUSIONS

Analysing the results of the study it was concluded that experimental endodontic sealers' (EES) antimicrobial behaviour upon the tested strains was comparable to similar bioceramic materials available on the market.

Antifungal properties against *C. albicans* were observed for all commercial sealers as well as for tricalcium silicate and the experimental composition (EES), for up to 7 days.

The measurements performed to determine the samples' effects upon *E. faecalis* after the first 24 hours were not encouraging, as no inhibitory activity was detected for any of the materials tested.

More sensitive testing methods might be needed to accurately assess the effectiveness of bioceramic materials against microorganisms. We intend to further evaluate the experimental sealer and using the DCT (direct contact test) method, for a more accurate conclusion regarding its activity in relation to microorganisms.

This line of research should be further pursued, since the new bioceramic material is based on compounds that are nontoxic, biocompatible, and bioactive: tricalcium silicate and magnesium silicate.

EXPERIMENTAL SECTION

Experimental endodontic sealer (EES)

The main constituents of the experimental endodontic sealer were tricalcium silicate, magnesium silicate (forsterite), and zirconium oxide.

Nano-sized tricalcium silicate Ca_3SiO_5 was obtained using the sol-gel method from $Ca(NO_3)_2x4H_2O$ -calcium nitrate tetra hydrate (Merck) and TEOS - $C_8H_{20}O_4Si$-tetraethyl orthosilicate (Merck), molar ratio $CaO:SiO_2$ was established at 3:1. As pH regulators ethanol (C_2H_5OH) and nitric acid (HNO_3) were used [43].

Forsterite nano powder was synthesized by sol gel method using magnesium nitrate hexahydrate $Mg(NO_3)_2x6H_2O$ (Merck) and tetraethyl orthosilicate $C_8H_{20}O_4Si$ (Merck), in a molar ratio Mg:Si of 2:1. Nitric acid was used as a pH regulator [44].

Both nanomaterials were synthesized and characterised in the laboratory. Their biocompatibility and physical properties were investigated [43, 44].

The bioceramic experimental endodontic sealer (EES) was formulated as a two-component powder-liquid material. The solid component consists of 74% tricalcium silicate (Ca_3SiO_5); 25% magnesium silicate (Mg_2SiO_4), and 1% zirconium dioxide (ZrO_2). In order to obtain the pasty consistency required, 2% Zinc chloride ($ZnCl_2$) solution was added as the liquid component.

Antimicrobial properties

Agar well diffusion test (ADT) was used to determine the antimicrobial properties of the experimental sealer and its individual components and compare them to available commercially endodontic sealers. This is a modified version of the widely used disk diffusion antibiotic susceptibility test, adapted for semisolid substances [45], being the most used method to assess the antimicrobial activity of endodontic sealers [16]. The specific protocol employed in this study was adapted from Gürel et al [18].

Eight samples were tested: tricalcium silicate, magnesium silicate, zirconium dioxide (Merk, Germany), zinc chloride (Merk, Germany), experimental endodontic sealer (EES), TotalFill BC Sealer (FKG, Switzerland), MTA Bioceramic Sealer (Henry-Schein USA), MTA-Fillapex (Angelus, Brazil*).* The similarity between the tested sealers and the experimental material consists in their composition being based on calcium silicates as major compounds, with or without resins addition. Their composition, as indicated by the producer, is shown in Table 2.

Two microbial strains were used: *Enterococcus faecalis* ATCC 29212 (American Type Culture Collection), and *Candida albicans* ATCC 10231. *E. faecalis* was inoculated on Columbia agar with 5% sheep blood (Bio-Rad, Marnes la Coquette,France) and incubated aerobically for 24 h at 37°C. *C. albicans* was inoculated on Sabouraud chloramphenicol gentamicin agar (Bio-Rad, Marnes la Coquette,France) for 48 h at 37°C.

Suspensions (in 0.9% saline) with an optical density of 0.5 McFarland ($1.5x10^8$ CFU/mL, colony formation units) were prepared from 24 hours colonies of *E. faecalis* and 48 hours colonies of *C. albicans*. The optical density was controlled using a densitometer (DEN-1 McFarland Densitometer, Biosan SIA, Riga, Latvia).

Mueller-Hinton agar plates (Merck KGaA, Darmstadt, Germany) were used for antimicrobial activity testing. Five equally spaced wells with a diameter of 6 mm and a depth of 3 mm, were punched in each Mueller-Hinton agar plate using a sterile cork borer.

Table 2. Chemical composition of the tested samples.

No	Sample	Form of presentation	Composition
1	Tricalcium silicate (Ca_3SiO_5)	Powder-liquid system	Tricalcium silicate (Ca_3SiO_5) Zinc chloride ($ZnCl_2$) 2% solution
2	Magnesium silicate (Mg_2SiO_4)	Powder-liquid system	Magnesium silicate ((Mg_2SiO_4) Zinc chloride ($ZnCl_2$) 2% solution
3	Zirconium dioxide (ZrO_2) (Merk, Germany)	Powder-liquid system	Zirconium dioxide (ZrO_2) Zinc chloride ($ZnCl_2$) 2% solution
4	Experimental endodontic sealer (EES)	Powder-liquid system	Tricalcium silicate (Ca_3SiO_5) Magnesium silicate Mg_2SiO_4) Zirconium dioxide (ZrO_2) Zinc chloride ($ZnCl_2$) 2% solution
5	Zinc chloride ($ZnCl_2$) 2% solution (Merk, Germany)	Single component liquid	Zinc chloride ($ZnCl_2$) 2% solution
6	TotalFill BC Sealer (FKG, Switzerland)	Single component paste	Zirconium oxide Tricalcium silicate Dicalcium silicate Calcium hydroxide
7	MTA Bioceramic Sealer (Henry Schein USA)	Two paste system	Paste A: Salicylate resin, Natural resin, Calcium tungstate, Nanoparticulated silica Paste B: Diluting resin Mineral trioxide aggregate Titanium dioxide Silicon dioxide
8	MTA-Fillapex (Angelus, Brazil)	Two paste system	Paste A: Salicylate resin, Bismuth trioxide, Fumed silica Paste B: Mineral trioxide aggregate, Fumed silica, Titanium dioxide, Base resin

The Mueller-Hinton plates were inoculated with the prepared suspensions. The wells were then filled with the materials to be tested. The solvent was also used on its own as negative control, being deposited in a dedicated well.

The plates were subsequently incubated aerobically at 37 °C for 7 days. The antimicrobial agent, where present, diffused in the agar medium and inhibited the growth of the tested microbial strain. The diameter of the inhibition zone was measured recorded and compared every 24 h using an electronic calliper with an accuracy of ± 0.2 mm).

ACKNOWLEDGMENTS

This work was supported by PhD Research Project no. PCD 1033/66/January 13, 2021, offered by Iuliu Hațieganu University of Medicine and Pharmacy, Cluj-Napoca, Romania.

REFERENCES

1. D.A. Fonseca; A.B. Paula; C.M. Marto; A. Coelho; S. Paulo; J.P. Martinho; E. Carrilho; M.M. Ferreira; *Materials (Basel),* **2019**, 12(24), 4113.
2. E. Carlos; H. Roberto; R.A.E. Cyntia; H.G.A. Ana; D.S. Manoel; D.P. Jesus; *Braz. Dent. J*., **2014**, 25, 25–31.
3. K. Ruksakiet; L. Hanák; N. Farkas; P. Hegyi; W. Sadaeng; L.M. Czumbel; T. Sang-Ngoen; A. Garami; A. Mikó; G. Varga; Z. Lohinai; *J. Endod*., **2020**, 46(8), 1032-1041.
4. C. Poggio; F. Trovati; M. Ceci; M. Colombo; G. Pietrocola; *J. Clin. Exp. Dent.,* **2017**, 9(6), e743-e748.
5. Y. Huang; X. Li; P. Mandal; Y. Wu; L. Liu; H. Gui; J. Liu; *BMC Oral Health,* **2019,** 19(1), 118.
6. L. BIZO; K. SABO; R. BARÁBAS; G. KATONA; L. BARBU-TUDORAN; A. BERAR; Studia UBB Chemia, **2020**, LXV(1), 137-148.
7. D.G. Olaru; A. Olaru; G.H. Kassem; M.V. Popescu-Drigă; L.R. Pinoşanu; D.I. Dumitrascu; E.L Popescu; D.M. Hermann; A. Popa-Wagner; *Rom. J. Morphol. Embryol.,* **2019**, 60(3), 787-792.
8. S. Jitaru; I. Hodisan; L. Timis; A. Lucian; M. Bud; *Clujul Med.,* **2016**, 89(4), 470–473.
9. D.G. Seo; D. Lee; Y.M. Kim; D. Song; S.Y. Kim; *Materials (Basel)*, **2019**, 12(15), 2482.
10. P.J. Penha da Silva; M.F. Marceliano-Alves; J.C. Provenzano; R.L.A. Dellazari; L.S. Gonçalves; F.R.F. Alves; *Eur. J. Dent*., **2021**, 15(3), 475-480.
11. M.A. Elsayed; E.E. Hassanien; A.A.E. Elgendy; *Eur. Endod. J*., **2021**, 6(2), 183-188.
12. G. Sfeir; C. Zogheib; S. Patel; T. Giraud; V. Nagendrababu; F. Bukiet; *Materials (Basel),* **2021**, 14(14), 3965.

13. L.B. Mestieri; A.L. Gomes-Cornélio; E.M. Rodrigues; L.P. Salles; R. Bosso-Martelo; J.M. Guerreiro-Tanomaru; M. Tanomaru-Filho; J. Appl. Oral. Sci., **2015**, 23(5), 467-471.
14. P. Mangat; A. Dhingra; S. Muni; H.K. Bhullar; *J. Conserv. Dent.,* **2020**, 23(6), 571-576.
15. G. Singh; I. Gupta; F.M.M. Elshamy; N. Boreak; H.E. Homeida; *Eur. J. Dent*., **2016**, 10(3), 366-369.
16. M. Šimundić Munitić; T. Poklepović Peričić; A. Utrobičić; I. Bago; L. Puljak; *PLoS One*, **2019**, 14(10), e0223575.
17. L.W. Lee; Y.L. Lee; S.H. Hsiao; H.P. *Lin; J. Formos. Med. Assoc.,* **2017**, 116(6):448-456.
18. M. Gürel; E.Ö. Demiryürek; T. Özyürek; T. Gülhan; *Int. J. Appl. Dent. Sci*., **2016**; 2(3), 19-22.
19. T.M.T. Waltimo; E.K. Sirén; H.L.K. Torkko; I. Olsen; M.P.P. Haapasalo; *Int. Endod. J.*, **1997**, 30(2), 96-101.
20. D. Montelongo-Jauregui; J.L. Lopez-Ribot; *J. Fungi (Basel)*, **2018,** 4(4), 122.
21. T. Young; O.A. Alshanta; R. Kean; D. Bradshaw; J. Pratten; C. Williams; C. Woodall; G. Ramage; J.L. Brown; *Microorganisms,* **2021**, *9*(1), 59.
22. A. Alberti; S. Corbella; S. Taschieri; L. Francetti; K.S. Fakhruddin; L.P. Samaranayake; *PLoS One*, **2021**;16(7), e0255003.
23. O.A. Alshanta; S. Shaban; C.J. Nile; W. McLean; G. Ramage; *Antibiotics (Basel)*, **2019,** 8(4), 204.
24. J.F. Jr Siqueira; B.H. Sen; *Oral Surg. Oral Med. Oral Patho.l Oral Radiol. Endod. **2004**, 97(5), 632-641.*
25. Y.J. Yoo; A.R. Kim; H. Perinpanayagam; S.H. Han; K.Y. Kum; *Microorganisms,* **2020**, 8(9), 1300.
26. F. Jafari; S. Jafari; H. Samadi Kafil; T. Momeni; H. Jamloo; *Iran. Endod. J.,* **2017**, 12(1), 98-102.
27. R.K. Rathod; P.D Taide; R.D. Dudhale; *Niger. J Surg*., **2020**, 26(2), 104-109.
28. D. Djorić; N.E. Minton; C.J. Kristich; *Mol. Oral. Microbiol*., **2021**, 36(2), 132-144.
29. C. Tennert; M. Fuhrmann; A. Wittmer; L. Karygianni; M.J. Altenburger; K. Pelz; E. Hellwig; A. Al-Ahmad; *J. Endod***, 2014**, 40(5), 670-677.
30. R. Vidana; Å. Sullivan; H. Billström; M. Ahlquist; B.Lund; *Letters in Applied Microbiology*, **2011**, 109-115.
31. P.H. Ferrari; S. Cai; A.C. Bombana; *Int. Endod. J.,* **2005**, 38(6), 372-380.
32. P.N Nair; *Int. Endod. J*., **2006**, 39(4), 249-281.
33. E. AlShwaimi; D. Bogari; R. Ajaj; S. Al-Shahrani; K. Almas; A. Majeed; *J. Endod*., **2016**, 42(11), 1588-1597.
34. I.M. Saleh; I.E. Ruyter; M. Haapasalo; D. Ørstavik*; Int. Endod. J., **2004**, 37(3), 193-198.*
35. A. Kaur; N. Shah; A. Logani; N. Mishra; *J. Conserv. Dent.,* **2015**, 18(2), 83-88.
36. M. Šimundić Munitić; A. Budimir; S. Jakovljević; I. Anić; I. Bago; *Acta Stomatol. Croat.,* **2020**, 54(1), 3-9.
37. N.A. Allan; R.C. Walton; M.A. Schaeffer; *J. Endod*., **2001**, 27(6), 421-423.

38. N. Ballal; M. Kundabala; K. Bhat K; S. Acharya; M. Ballal; R. Kumar; P. Prakash; *Aust. Endod. J.*, **2009,** 35(1), 29-33.
39. S. Arslan; H. Ozbilge; E.G. Kaya; O. Er; *Saudi Med. J.*, **2011**, 32(5), 479-83.
40. B.M. Newberry; S. Shabahang; N. Johnson; R. M. Aprecio; M. Torabinejad; *J. Endod.* **2007**, 33(11), 1352-1354.
41. N. Mandras; D. Pasqualini; J. Roana; V. Tullio; G. Banche; E. Gianello; F. Bonino; A.M. Cuffini; E. Berutti; M. Alovisi*; J. Clin. Med*., **2020**, 9(12), 3915.
42. E.S.K. Kok; X.J. Lim; S.X. Chew; S.F. Ong; L.Y. See; S.H. Lim; L.A. Wong; F. Davamani; V. Nagendrababu; A. Fawzy; U. Daood; *BMC Oral Health*, **2021**, 21(1), 116.
43. L. Timiş; A. Avram; M. Gorea; L. Bizo; S. Cîmpean; R. Câmpian; *Studia UBB Chemia*, **2020**, 65, 157-169.
44. M. Gorea; M.A. Naghiu; A. Avram; I. Petean; M. Tomoaia-Cotisel; *Studia UBB Chemia*, **2019**, 64, 383-392.
45. M. Balouiri; M. Sadiki; S.K. Ibnsouda; *J. Pharm. Anal*., 2016, 6(2), 71-79.

STUDIA UBB CHEMIA, LXVI, 4, 2021 (p. 383-396)
(RECOMMENDED CITATION)
DOI:10.24193/subbchem.2021.4.28

INFLUENCE OF HIGH SALINITY AND S-METHYLMETHIONINE ON SOME HEALTH-PROMOTING METABOLIC PROPERTIES OF GARDEN ROCKET LEAVES

LASZLO FODORPATAKI[a,b,c] *, MARTIN IAKAB[c], BERNAT TOMPA[a]

ABSTRACT. Production of health-promoting substances in plants' metabolism may be modulated by treatment with chemical stress factors and natural bioactive compounds, which enhance stress tolerance through stimulation of biosynthesis of several protective metabolites. The aim of this work is to reveal metabolic interactions between high salinity stress (exerted by the presence of 100 mM NaCl in the mineral nutrient solution) and treatment of plants with 0.1 mM S-methylmethionine (also known as vitamin U). This plant-derived bioactive compound enhances the production of antioxidants such as carotenoids, ascorbate and other phenoloids in leaves of rocket plantlets exposed to salt stress, while reducing the concentration of toxic malondialdehyde and related catabolic products of membrane lipid peroxidation. Thus, a suitable combination of high salinity and plant hardening with S-methylmethionine may improve the quality of fresh rocket leaves upon human and animal consumption.

Keywords: *ascorbate, carotenoids, phenoloids, lipid peroxidation, salt stress*

INTRODUCTION

Treatment of crop plants with chemical stress factors and bioactive compounds modulates several metabolic processes, thus enhancing tolerance and resulting in accumulation of protective substances which possess health-promoting qualities upon human consumption [1, 2, 3, 4]. Environmental stresses may elicit the biosynthesis of several metabolites in plants, including

[a] *Babeş-Bolyai University, Faculty of Biology and Geology, 1 M. Kogalniceanu St., RO-400084, Cluj-Napoca, Romania*
[b] *Babeş-Bolyai University, Centre of Systemic Biology, Biodiversity and Bioresources, 1 M. Kogalniceanu St., RO-400084, Cluj-Napoca, Romania*
[c] *Sapientia Hungarian University of Transylvania, Department of Horticulture, 1C Sighisoarei Rd, RO-540485, Targu Mures, Romania*
** Corresponding author: lfodorp@gmail.com*

a wide range of bioactive molecules which contribute to the nutraceutical value of plant-derived foods. Beside controlled abiotic stressors, natural biostimulants can also be used to improve the quantity and nutritional quality of crops, by inducing directed metabolic changes in plant cell, with no need to genetically manipulate the plant material. Application of small amounts of biostimulants is also one of the most promising alternatives to cope with yield losses caused by environmental stress factors (such as drought, extreme temperatures, high salinity, soil contamination with heavy metals, pollutant gases in the atmosphere), excluding the extensive use of pesticides and artificial fertilizers [5, 6].

One of the most frequent chemical factors which may severely impair growth and yield of crop plants is salinity stress, caused by elevated sodium chloride concentration of the water in the soil which surrounds the root system. The short-term effect of high salinity is inhibition of growth, due to an osmotic imbalance related to water loss of root cells into the more concentrated solution of the rhizosphere. This can be compensated with osmotic adjustments, through up-regulation of the biosynthesis of certain compatible solutes, such as free proline, glycine betaine, sucrose, trehalose, sorbitol etc. This leads to the recovery of water balance of plant tissues but needs an input of extra energy for the antistress reactions [7, 8]. The main long-term effect of salt stress is ion toxicity induced by over-accumulation of the sodium ions in the cells, which leads to an imbalance in the homeostasis of inorganic ions needed for normal metabolic processes. This is related to the uptake antagonism of sodium with essential potassium and calcium ions, as well as to the inhibition of several enzymes which necessitate potassium ions for their proper functioning. The main reaction of plants to this ion toxicity is sequestration of sodium ions inside the vacuole, where no enzyme-catalyzed biochemical reactions occur [9, 10]. A side effect of severe or prolonged salt stress is the accumulation of harmful reactive oxygen species (hydrogen peroxide, singlet oxygen, superoxide and hydroxyl radicals). This causes an oxidative stress, which can be counteracted by activation of the non-enzymatic and enzymatic constituents of the antioxidative defense system. As several antioxidants (e. g. vitamin C or ascorbic acid, carotenoids as precursors of vitamin A, vitamin E or tocopherol, certain flavones, flavonols, proanthocyanidines, polyphenols etc.) which accumulate in plants as a result of stress defense are appreciated as health-related compounds in the human diet, salt stress can be used for enhancing the nutritional quality of fresh vegetables [11, 12]. Oxidative stress is generally associated with peroxidation of un-saturated fatty acids in membrane lipids, which affects selective membrane permeability and results in generation of toxic degradation products (mainly malondialdehyde), thus a specific component of stress tolerance is membrane protection against lipid peroxidation [13, 14].

Apart from adverse developmental conditions, plant metabolism can also be modulated by treatments with various bioactive phytochemicals. These compounds are non-nutrient plant molecules which trigger natural defense mechanisms, thus only small amounts are needed to promote growth, to enhance nutrient use efficiency, to improve crop productivity and to increase tolerance against stress factors. As modulators of physiological processes in plants, they may induce or enhance the biosynthesis of specific secondary metabolites (e. g. phenolic compounds through the shikimate pathway or terpenoids through the mevalonate pathway) to cope with stressful growth conditions, thus enriching vegetables and fruits in compounds with high nutraceutical value. As compared to complex product mixtures with a combination of several organic compounds (e. g. seaweed extracts, protein hydrolysates), pure organic active compounds present several advantages, since their optimal concentrations, physiological effects and action mechanisms can be determined more accurately. The most promising bioactive compounds which trigger metabolic defense against various abiotic stresses in plants are certain proteinogenic and non-proteinogenic amino acids, polyamines, oligopeptides, oligosaccharides and vitamins [3]. One of the less studied, but apparently very efficient natural bioactive compounds is S-methylmethionine, an amino acid derivative also known as vitamin U [15, 16]. It is involved in important reactions of methylation related with detoxification of harmful organic pollutants and toxic metabolites, being ubiquitous in flowering plants. It increases tolerance of plants to extreme temperatures, to certain virus infections and to heavy metal toxicity, e. g. by stimulating the phenyl-propanoid pathway which provides plant cells with several protective molecules, including antioxidants and antimicrobial agents [6, 17, 18, 19].

Plant metabolites induced by environmental stress factors and by exogenous application of bioactive compounds exert their health-promoting effects especially upon consumption of fresh leafy vegetables in form of salads. Such vegetables include various cultivars of lettuce, spinach, artichoke, sorrel. At present, garden rocket (*Eruca sativa*), also known as rucola or arugula, is becoming a more and more popular leaf vegetable with a tart, bitter and peppery flavor. It is used for centuries in the Mediterranean and Asian traditional cuisine, but there is very scarce information about the impact of controlled growth conditions on its nutraceutical value [4, 20].

On the basis of the above-mentioned facts, the aim of this study is to reveal metabolic impacts of high salinity and of the application of S-methylmethionine, separately and in combination, on garden rocket plants and on the content of their leaves in organic compounds with relevance for human consumption, such as carotenoids and other photosynthetic pigments, phenolic compounds, ascorbic acid, products of membrane lipid peroxidation.

Results of these investigations may contribute to the improvement of nutraceutical quality of the garden rocket as a healthy fresh vegetable.

RESULTS AND DISCUSSION

Carotenoids represent a large group of lipophilic plant pigments (tetraterpenes) with antioxidant properties, being able to annihilate such harmful reactive oxygen species as hydroxyl radicals, alkyl-peroxyl radicals and singlet oxygen [21]. Their amount in rocket leaves was significantly increased by exposure for one week to high salinity generated with 100 mM NaCl, and it was further elevated when salt stress was combined with addition of 0.1 mM S-methylmethionine to the aqueous solution used for watering the plantlets (Fig. 1). SMM applied under normal growth conditions did not cause any significant change in carotenoid content.

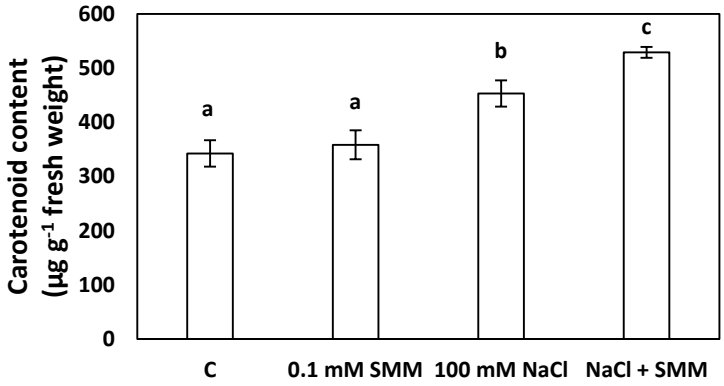

Figure 1. Influence of S-methylmethionine (SMM) and of high salinity, applied separately and in combination, on the carotenoid content of garden rocket leaves, after one week of treatment (n = 10, vertical bars represent ±SE from the means, different letters indicate statistically significant differences at $P < 0.05$)

Stimulation of carotenoid synthesis by salt stress is most probably due to the oxidative burst generated by the persistence of high salinity for several days. When salt tolerance is developed by hardening, plants activate their antioxidative protection, and carotenoids represent a distinct category of non-enzymatic antioxidants, acting specifically in the photosynthetic apparatus located in the thylakoid membranes of chloro-plasts [22]. When stress tolerance becomes enhanced by exogenously supplied bioactive compounds, such as vitamin U (SMM), a more efficient antioxidative protection is associated

with a further increment of the carotenoid pigment content of leaves. These results are in agreement with those reported by [4, 11], where enrichment of the irrigation water with NaCl increased the total carotenoid content (particularly the amounts of lutein and β-carotene) in lettuce leaves. Similar results were also reported for canola leaves, when plants were primed with vitamin U before being exposed to low temperature stress [17]. Due to the fact that α-carotene, β-carotene and β-cryptoxanthin are provitamin A carotenoids that can be converted by the human body into vitamin A (retinol), while many other carotenes (e. g. lycopene) and xanthophylls (e. g. lutein, zeaxanthin, antheraxantin) are effective antioxidants, their increased quantity enhances the health-promoting quality of rocket leaves in the human diet [3, 23].

In contrast with carotenoids, chlorophylls (being the main photosynthetic pigments of plants) may act as prooxidants, because upon absorption of light energy (especially under high photon flux densities) they lead to generation of singlet oxygen in the thylakoid membranes. Thus, a decreased ratio between prooxidant chlorophylls and antioxidant carotenoids confers a lowered risk of oxidative stress associated with metabolic imbalance due to unfavorable growth conditions [21]. While treatment of rocket plants with 0.1 mM S-methylmethionine resulted in a moderate, but statistically significant increment of the chlorophylls to carotenoids ratio in leaves, salt stress induced for one week with 100 mM NaCl led to a decrement of this ratio from more than 3 to values approaching 2 (Fig. 2).

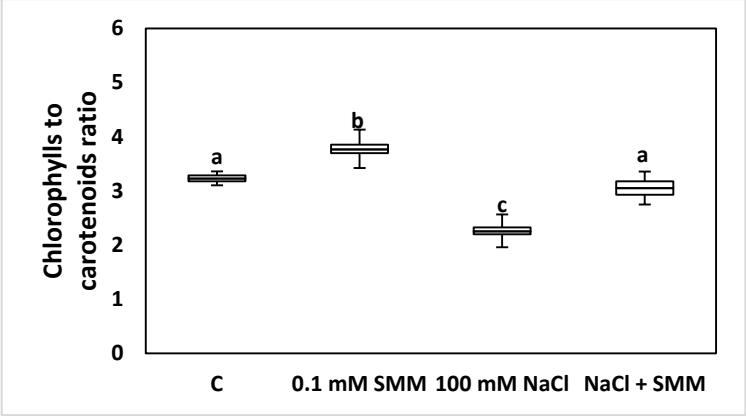

Figure 2. Changes of the chlorophylls to carotenoids ratio in leaves of rocket plants grown under constant light intensity and treated for one week with S-methylmethionine (SMM), high salt concentration and a combination of the former two chemical factors (n = 10, vertical bars represent ±SE from the means, different letters indicate statistically significant differences at $P < 0.05$)

When SMM treatment was applied to reduce the negative impact of high salinity, the chlorophylls to carotenoids ratio was restores to a level very close to the one that could be determined in the control plants. Because light intensity may considerably influence the chlorophyll and carotenoid pigment content of leaves, the plants were grown under constant photon flux density during the photoperiods. Increment of the chlorophylls to carotenoids ratio by SMM can be explained by the fact that this bioactive compound induced a moderately higher chlorophyll content of leaves (data not shown) but did not influence the amount of carotenoids. When SMM was applied simultaneously with salt stress, it totally annihilated the decreasing effect of high salinity on this ratio. Down-regulation of chlorophyll biosynthesis and up-regulation of chlorophyll degradation, as well as stimulation of carotenoid production as part of the antioxidative defense mechanism, was documented for several other crop plants, such as lettuce, broccoli, cauliflowers, tomato, pepper and melon fruits [4, 5, 9]. Interaction of SMM with salt stress on chlorophyll metabolism (in the porphyrin pathway) and on the metabolism of carotenoids (in the mevalonate pathway) is poorly documented in the literature. Similar results were reported when canola plants were treated with 1 mM SMM upon exposure to two different salt concentrations (60 mM and 120 mM NaCl) [24].

Phenoloids represent a large group of plant metabolites, many of them being produced as signaling molecules or defense effectors under various environmental stress conditions. Their biosynthesis in plants proceeds through the shikimate pathway, and in some cases the malonate pathway also has a contribution to it. By modulation of these biosynthetic pathways, plant exhibit a metabolic plasticity that results in increased tolerance to adverse developmental conditions. The main groups of plant phenolic compounds are water-soluble simple phenoloids (e. g. coumarins), flavonoids (anthocyanins, flavones, flavonols, flavanols, flavanones, isoflavones), hydrolysable tannins, as well as complex tannins and condensed phenylpropanoids, which are not soluble in water. Several different representatives have antioxidant properties, while others exert other health-protective effects upon ingestion. In plants, their aromatic rings also confer protection against ultraviolet radiations [9, 26]. This is the reason why the variation of overall phenoloid content of rocket leaves was selected as a possible biochemical marker of tolerance against the oxidative stress associated with high salinity, as well as of the benefic influence of vitamin U on protective processes. After seven days of treatment, 0.1 mM SMM increased the phenoloid content of rocket leaves by about 20% (Fig. 3). This increment was even more pronounced upon long-term salt stress, while the highest phenoloid content (approximately two times higher than in the control) was measured when high salinity was combined with SMM treatment.

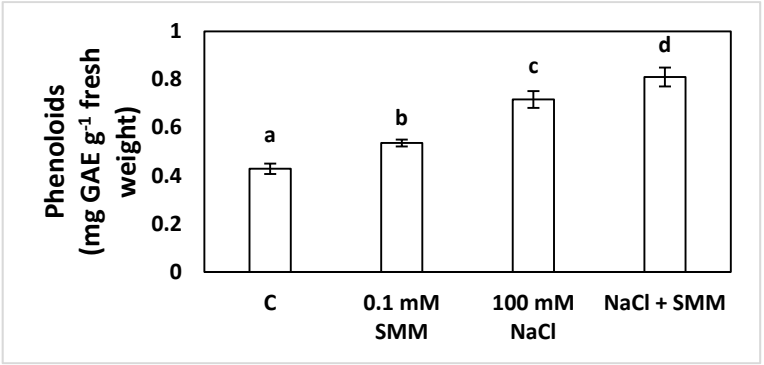

Figure 3. Phenoloid content of garden rocket leaves, expressed as gallic acid equivalents (GAE), upon exposure for seven days to 0.1 mM S-methylmethionine (SMM), to high salinity induced with 100 mM NaCl, and to the combination of the former two chemical agents (n = 10, vertical bars represent ±SE from the means, different letters indicate statistically significant differences at $P < 0.05$)

Experiments performed with maize plants exposed to low temperature have shown that the phenylpropanoid pathway is stimulated by S-methylmethionine [6]. This bioactive compound also induced an increased phenoloid content of lettuce leaves exposed for six days to 75 mM and 150 mM NaCl but did not cause any significant increment in the overall phenolic compound content if salt stress was imposed for a shorter period of time (three days instead of six days) [11]. These data are in agreement with those experiments which demonstrated that phenolic compounds accumulate under stress conditions later than other non-enzymatic antioxidants, being responsible mainly for the reestablishment of redox homeostasis after prolonged exposure to adverse conditions, when the other ways of antioxidative defense have become weakened [10, 28, 29]. It was also demonstrated that the highest antioxidant capacity is possessed by phenolic compounds with several hydroxide groups linked to the aromatic ring [29, 30].

The ascorbic acid (vitamin C) content, which represents a major indicator of health-promoting quality of plant materials, was not significantly influenced by S-methylmethionine, but when this bioactive compound was supplied to salt-stressed rocket plants, the vitamin C content of leaves was increased by about 30% (Fig. 4). The long-term exposure of plantlets to high salinity also led to a statistically significant elevation of ascorbate content, and this increment was further intensified by SMM, probably as a result of stimulation of antioxidative protection upon the installation of oxidative stress conditions associated with sustained salt stress.

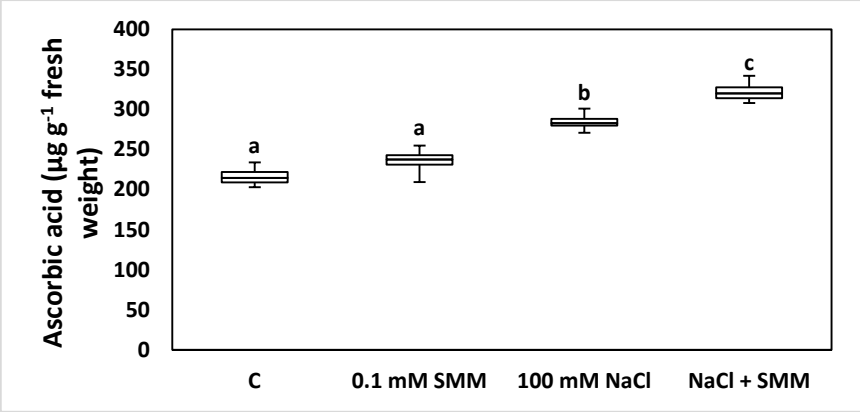

Figure 4. Variations in the ascorbic acid content of garden rocket leaves after seven days of treatment with 0.1 mM S-methylmethionine (SMM), with 100 mM NaCl, and with the combination of the former two chemical agents (n = 10, vertical bars represent ±SE from the means, different letters indicate statistically significant differences at $P < 0.05$)

In lettuce leaves 0.25 mM and 2 mM SMM moderately increased the vitamin C content and compensated for its significant reduction by development at 5°C [17]. Priming of lettuce plantlets with 0.05 mM SMM for three days prior to exposure to salt stress resulted in an increment of ascorbate content until the third day of salt treatment, and remained stabilized at this higher level during the following three days [11]. These results suggest that SMM may enhance the antioxidative defense of plants through the triggering of an up-regulation of ascorbate biosynthesis under adverse growth conditions, such as high salinity and low temperature. Increased ascorbic acid quantities were also reported in leaves of five weeks old lettuce plants exposed to chilling stress and heat shock, a positive correlation between the overproduction of hydrogen peroxide and vitamin C content being established [26]. In soybean varieties differing in flavonoid content increased levels of UV-B radiation decreased ascorbate content and increased dehydroascorbate content, in relation with an enhanced oxidative stress [30]. It was also shown that under the influence of various inhibitors of enzymatic browning in lettuce leaves, increased ascorbic acid content protected phenolics from oxidation [28]. Thus, it seems that vitamin C content of leaves can be increased by exposure for several days to mild stress conditions and by application of bioactive compounds, especially when these are used simultaneously with or prior to stress factors. This increases the nutritional value of freshly consumed vegetables.

Whenever metabolic impairments result in over-accumulation of reactive oxygen species, oxidative membrane damage occurs. This affects the structural and functional properties of membrane lipide and membrane-associated proteins, leading to the loss of selective permeability of membranes and to toxic products of peroxidation of unsaturated fatty acids present in membrane lipids [31]. Highly toxic products of lipid peroxidation, referred to as thiobarbituric acid-reactive substances (TBARS), the mostly dangerous one being malondialdehyde, were generated in increased amounts in the living cells of rocket plants exposed for seven days to 100 mM NaCl (Fig. 5). This indicates that long-term exposure to high salinity causes oxidative stress which damages biomembranes.

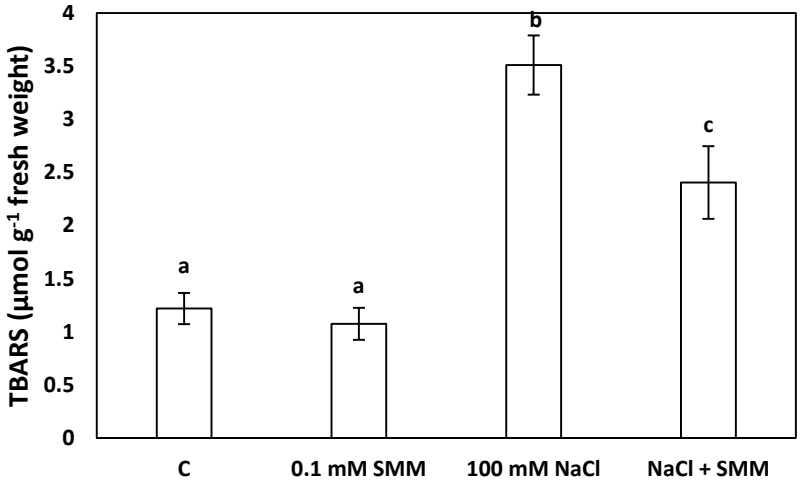

Figure 5. Influence of high salinity and treatment with S-methylmethionine (SMM) on the amount of thiobarbituric acid-reactive substances (TBARS) resulted from oxidative damage of membrane lipids in rocket plants (n = 10, vertical bars represent ±SE from the means, different letters indicate statistically significant differences at $P < 0.05$)

The generated TBARS may damage proteins and nucleic acids in plants as well as in humans, upon consumption of plants as part of the diet. This is one reason why it is important to reduce the TBARS content of crop plants grown under harmful conditions. This can be achieved by supplying 0.1 mM SMM to salt-stressed plants, the treatment being able to significantly reduce the toxic TBARS content. Because SMM did not induce oxidative stress, it did not cause changes in the very low TBARS content characteristic for the unstressed control plants. But it significantly diminished the TBARS

production in salt-stressed plants (Fig. 5), thus reducing the amount of undesirable toxic products of lipid peroxidation. These results suggest that SMM may enhance the capacity of the enzymatic and/or non-enzymatic components of the antioxidative protection system to reduce the concentration of reactive oxygen species generated due to metabolic imbalances. Similar results were obtained when canola plants were grown on substrates with different salt concentrations. The degree of oxidative membrane damage was proportional with the level of salinity, being lower at 60 mM NaCl than at 120 mM NaCl. Exogenously applied SMM (1 mM, by leaf spraying) totally annihilated the increment of TBARS production generated by 60 mM NaCl and partly reduced the concentration of toxic products of lipid peroxidation when plants were exposed to a more severe salt stress induced with 120 mM NaCl [24]. Increased lipid peroxidation was also reported when plants were exposed to soil pollution with water-soluble forms of various heavy metals, to intense UV-B radiations, to air pollution with ozone and nitrogen oxides, to severe drought or to extreme temperatures [5, 13, 31, 33].

CONCLUSIONS

High salinity stress caused by the presence of 100 mM NaCl in the aqueous solution around the root system, increased carotenoid content, total phenoloid content, ascorbic acid content and the amount of toxic derivatives of lipid peroxidation in young leaves of garden rocket plants. S-methylmethionine or vitamin U, as a natural metabolic product of plants, applied exogenously in the concentration of 0.1 mM, acting as a bioactive compound that counteracts negative effects of salt stress, induced a further increment in the carotenoid pigment, phenoloid and ascorbic acid content, thus contributing to an enhanced antioxidative protection of leaf cells. Furthermore, this amino acid derivative reduced the production of malondialdehyde and other thiobarbituric acid-reactive substances generated upon oxidative damage of membrane lipids. All these metabolic changes increased the health-promoting quality of fresh rocket leaves upon human consumption.

This is a novel contribution to cost-effective modulation of biochemical processes in the metabolism of garden rocket plants, in order to increase the content of certain antioxidants (carotenoids, phenoloids, ascorbic acid) in leaves, and to annihilate negative effects of high salinity with the use of a plant-derived bioactive compound (S-methylmethionine), thus avoiding pesticides and genetic manipulations in the attempt to improve yield and nutraceutical quality of this leafy vegetable.

EXPERIMENTAL SECTION

Garden rocket or "rucola" (*Eruca sativa* Mill.) belongs to the cabbage and mustard family (Brassicaceae), possessing a specific metabolic pathway for the synthesis of sulfur-containing glucosinolates. Because they confer a peppery flavor to the leaves, rocket plants are widely used as salad vegetables in the health-promoting human diet. Garden rocket seeds were germinated in pots with perlite as a soil substitute, and plantlets were watered twice a week with Hoagland's mineral nutrient solution [11], being grown in an environmental chamber (Sanyo MLR-351H) under a photosynthetically active photon flux density of 330 μmol m^{-2} s^{-1} for a daily photoperiod of 14 h, at 22°C in the light period and 18°C in the dark period, the relative air humidity being maintained at 70%. Three weeks old plantlets were exposed for seven days to different salt and triacontanol treatments: control plants were watered with Hoagland's basal solution, salt-stressed plants were subjected to the presence of 100 mM NaCl dissolved in the nutrient solution, treatment with vitamin U was achieved with 0.1 mM S-methylmethionine (SMM) added to the nutrient medium, while salt-stressed and vitamin U-treated plants received the mineral nutrient medium with the simultaneous addition of 100 mM NaCl and 0.1 mM SMM. The concentrations were selected from previous experiments (100 mM NaCl induces a moderate salt stress in rocket plants, and 0.1 mM is a concentration of SMM which does not exert any detectable negative effect during early developmental stages of plants). Each of the four experimental variants was set in ten separate repetitions, with one plant per pot. Parts of the second fully expanded leaf from the top of the stem were used for biochemical determinations.

The quantity of photosynthetic pigments (chlorophyll *a*, chlorophyll *b* and carotenoids) was determined photometrically (with a Jasco V750 UV-Vis spectrophotometer). In a pre-chilled mortar 0.25 g fresh weight of leaves were homogenized in 5 mL of 80% (v/v) acetone. The supernatant resulting from centrifugation of the acetonic extract for 10 min at 4000g was used for absorbance measurements at the wavelengths of 663 nm, 646 nm and 470 nm. The reference sample consisted of acetone 80%. The quantities of chlorophyll *a*, chlorophyll *b* and carotenoid pigments were determined based on the absorbance values measured at the three above-mentioned wavelengths, being expressed as mg per gram leaf fresh weight, according to [22].

The total phenolics content of rocket leaves was determined photometrically, using the Folin-Ciocâlteu reagent method [25, 26]. 1 g fresh leaf was homogenized in a mortar with 6 mL 80% (v/v) acetone, the mixture was incubated in darkness at 4°C overnight, then it was centrifuged at 2000g for 3 min. 0.2 mL of supernatant was supplemented with 1 mL of 10% (v/v) Folin-

Ciocâlteu reagent. After 5 min, 0.8 mL of 7.5% (w/v) sodium carbonate was added to the previous mixture. After incubation in the dark at 45°C for 15 min, the absorbance of the resulting blue solution was measured at 765 nm (with a Jasco V750 UV-Vis spectrophotometer). A blank was prepared with 0.2 mL of 80% (v/v) acetone. A gallic acid standard curve was prepared from a freshly made stock solution of 1 mg mL^{-1} gallic acid in 80% (v/v) acetone, and the total phenoloid content of leaves was expressed in gallic acid equivalents on a fresh weight basis [27, 30].

Extraction and determination of the ascorbic acid content of rocket leaves was performed according to [32]. 0.5 g of freshly harvested leaf blades were homogenized in a prechilled mortar with 4 mL of 6% (w/v) trichloroacetic acid. The mixture was centrifuged at 16500g and 4°C for 15 min, and 0.2 mL of supernatant was supplemented with a mixture of trichloroacetic acid, ortophosphoric acid, dithiothreitol, ferric chloride, N-ethylmaleimide, ethanolic solution of 2,2'-dipyridyl, all of these being dissolved in sodium phosphate buffer (pH 7.4). After one hour of incubation at 42°C the absorbance of the solution was measured at 525 nm with a spectrophotometer. The oxidized form of vitamin C (dehydroascorbate) was converted by dithiothreitol into the reduced form, thus after incubation the total ascorbic acid content of samples was present in its reduced state. This reduced form of ascorbic acid generated ferro ions from the ferric chloride, and the ferro ions gave a colored product with 2,2'-dipyridyl. The quantity of ascorbic acid in the leaf samples was determined through a calibration curve obtained with known concentrations of pure ascorbic acid [31, 32].

Oxidative membrane damage was evaluated through the generation of malondialdehyde and other related thiobarbituric acid-reactive substances (TBARS) because of peroxidation of unsaturated fatty acids from the lipid bilayer of cell membranes [2, 14]. 0.5 g fresh weight of leaf blades were homogenized in a pre-chilled mortar with 5 mL of 0.1% (w/v) trichloroacetic acid. The homogenate was centrifuged at 15000g for 15 min, then 2 mL of the supernatant was supplemented with 4 mL of 10% (w/v) trichloroacetic acid in which 0.5% (w/v) 2-thiobarbituric acid was dissolved previously. The mixture was heated at 95°C for 30 min, then cooled in an ice bath. The solution that turned light red was centrifuged at 10000g for 5 min and the absorbance of the supernatant was measured at 532 nm and 600 nm. The value obtained at 600 nm (related to the presence of interfering anthocyanins) was deduced from the one measured at 532 nm. TBARS concentration of the leaf samples was calculated using the extinction coefficient of 155 mM^{-1} cm^{-1} [14, 31].

Experiments were performed with ten plants for each treatment, while measurements had three technical repetitions for every plant material. The R statistical package (R Core Team 2019) was used for statistical data analyses. Normality of data distribution was evaluated with the Shapiro-Wilk test, and Bartlett's test was used for analysis of the homogeneity of variances. Data were represented as the mean ± standard error (SE). Significant differences were determined with the one-way ANOVA and the post-hoc Tukey HSD test, differences being considered significant at $P < 0.05$.

ACKNOWLEDGMENTS

This research was partly supported by the Institute of Advanced Studies in Science and Technology of the "Babeș-Bolyai" University in Cluj-Napoca, Romania, through a fellowship for excellence in research, awarded in 2020 to M. Sc. student Bernat Tompa.

REFERENCES

1. R. Bulgari; G. Franzoni; A. Ferrante; *Agronomy*, **2019**, *9*, 306-316
2. P. du Jardin; L. Xu; D. Geelen; Agricultural functions and action mechanisms of plant biostimulants (PBs). In *The Chemical Biology of Plant Biostimulants*, D. Geelen; L. Xu, Eds.; Wiley Online Books, Hoboken, USA, **2020**, Chapter 1, pp. 1-30
3. A.L. Garcia-Garcia; F.J. Garcia-Machado; A.A. Borges; S. Morales-Sierra; A. Boto; D. Jimenez-Arias; *Front. Plant Sci.*, **2020**, *11*, 575829
4. S. Toscano; A. Trivellini; G. Cocetta; R. Bulgari; A. Francini; D. Romano; A. Ferrante; *Front. Plant Sci.*, **2019**, *10*, 1212
5. C. Kaya; M. Ashraf; O. Sonmez; A.L. Tuna; T. Polat; S. Aydemir; *Acta Physiol. Plant.*, **2015**, *37*, 1729-1741
6. K. Paldi; I. Racz; Z. Szigeti; S. Rudnoy; *Biol. Plant.*, **2014**, *58*, 189-194
7. E. Blumwald; *Curr. Opin. Cell Biol.*, **2000**, *12*, 431-434
8. D. Rhodes; A. Nadolska-Orczik; P.J. Rich; Salinity, osmolytes and compatible solutes. In *Salinity:Environment-Plant-Molecules*, A. Lauchli; U. Luttge, Eds.; Kluwer Academic Publishers, Dordrecht, the Netherlands, **2002**, pp. 181-204
9. C. Ouhibi; H. Attia; F. Rebah; N. Msilini; M. Chebbi; J. Aarrouf; L. Urban; M. Lachaal; *Plant Physiol. Biochem.*, **2014**, *83*, 126-133
10. C. Sgherri; U. Perez-Lopez; F. Micaelli; J. Miranda-Apodaca; A. Mena-Petite; A. Munoz-Rueda; M. F. Quartacci; *Plant Physiol. Biochem.*, **2017**, *115*, 269-278
11. L. Fodorpataki; B. Holinka; E. Gyorgy; Priming with S-methylmethionine increases non-enzymatic antioxidant content of lettuce leaves exposed to salt stress**.** In *Controlled Environment Agriculture*, M. Asaduzzaman, Ed.; Nova Science Publishers, New York, USA, **2016**, Chapter 6, pp. 133-164
12. J. Zhu; *Trends Plant Sci.*, **2001**, *6*, 66-72

13. A. Baryla; C. Laborde; J.-L. Montillet; C. Triantaphylides; P. Chagvardieff; *Env. Poll.*, **2000**, *109*, 131-135
14. N. Jambunathan; *Meth. Mol. Biol.*, **2010**, *639*, 291-298
15. A.D. Patel; N.K. Prajapati; *J. Chem. Pharm. Res.*, **2012**, *4*, 209-215
16. P. Ranocha; S.D. McNeil; M.J. Ziemak; C. Li; M.C. Tarczynski; A.D. Hanson; *Plant J.*, **2001**, *25*, 575-584
17. L. Fodorpataki; K. Molnar; B. Tompa; S.R.C. Plugaru; *Not. Bot. Horti Agrobot.*, **2019**, *47*, 592-598
18. E. Ludmerszki; K. Paldi; I. Racz; Z. Szigeti; S. Rudnoy; *Appl. Ecol. Environ. Res.*, **2014**, *12*, 777-785
19. C. Olah; E. Ludmerszki; I. Racz; G. Balassa, S. Rudnoy; *Russ. J. Plant Physiol.*, **2018**, *65*, 63-68
20. G. Cocetta; S. Mishra; A. Raffaelli; A. Ferranta; *J. Plant Physiol.*, **2018**, *231*, 261-270
21. N. Smirnoff; Ascorbate, tocopherol and carotenoids: metabolism, pathway engineering and functions. In *Antioxidants and Reactive Oxygen Species in Plants*, N. Smirnoff, Ed.; Blackwell Publishers, Oxford, United Kingdom, **2005**, pp. 53-86
22. H.K. Lichtenthaler; A.R. Wellburn; *Biochem. Soc. Trans.*, **1983**, *11*, 591-592
23. S.S. Gill; N. Tuteja; *Plant Physiol. Biochem.*, **2010**, *48*, 909-930
24. L. Fodorpataki; K. Molnar; B. Tompa; C. Bartha; *Intl. J. Agric. Biol.*, **2021**, *25*, 11-19
25. Z. Louail; N. Djemouai; S. Krimate; K. Bouti; S. Bouti; H. Tounsi; A. Kameli; *Anal. Univ. Oradea*, **2020**, *27*, 215-223
26. M.-M. Oh; E.E. Carey; C.B. Rajashekar; *Plant Physiol. Biochem.*, **2009**, *47*, 579-583
27. V. Mulabagal; M. Ngouajio; A. Nair; Y. Zhang; A.L. Gottumukkala; M.G. Nair; *Food Chem.*, **2010**, *118*, 300-306
28. A. Altunkaya; V. Gokmen; *Food Chem.*, **2008**, *107*, 1173-1179
29. R. Llorach; A. Martinez-Sanchez; F.A. Tomas-Barberan; M.I. Gil; F. Ferreres; *Food Chem.*, **2008**, 1028-1038
30. V.L. Singleton; R. Orthofer; R.M. Lamuela-Raventos; *Meth. Enzymol.*, **1999**, *299*, 152-178
31. S.K. Panda; I. Chaudhury; M.H. Khan; *Biol. Plant.*, **2003**, *46*, 289-294
32. K. Kampfenkel; M. van Montagu; D. Inze; *Anal. Biochem.*, **1995**, *225*,165-167
33. C. Xu; S. Natarajan; J.H. Sullivan; *Env. Exp. Bot*, **2008**, *63*, 39-48
34. K. Molnar; B. Biro-Janka; I.I. Nyaradi; L. Fodorpataki; B.E. Varga; J. Balint; M.M. Duda; *Acta Biol. Maris.*, **2020**, *3*, 48-55

STUDIA UBB CHEMIA, LXVI, 4, 2021 (p. 397-404)
(RECOMMENDED CITATION)
DOI:10.24193/subbchem.2021.4.29

THE DYNAMICS OF HEMERYTHRIN AND HEMERYTHRIN DERIVATIVES

FRANCISCO CARRASCOZA[a,b,c], ADRIAN M.V. BRÂNZANIC[a,d], RADU SILAGHI-DUMITRESCU[a]

ABSTRACT. The non-heme diiron protein hemerythrin (Hr) has been considered as a possible alternative for semi-artificial oxygen carriers ("blood substitutes"). Studies on the stability of its octameric structure have been attempted by attaching spin labels to analyze its electron paramagnetic spectroscopy (ESR) signals. Reported here are molecular dynamics results of Hr bound with 1-oxyl-2,2,5,5-tetramethylpyrroline-3methyl (MTSSL) at the Cys51 position. Our results show that the Hr-MTSSL complex is less stable than its native form. These findings help to explain ESR signals obtained experimentally. Also, these results are crucial to understand the limitations of PEGylated spin labels for protein structural analysis and suggest the need or further exploration of other alternatives.

Keywords: *hemerythrin, molecular dynamics, spin label, blood substitute, diiron*

INTRODUCTION

Hemerythrin (Hr) is a homo-octameric alpha-helical protein with a non-heme diiron active site found in marine worms or bacteria, and has been studied as a potential alternative to hemoglobin as starting material for semi-artificial oxygen carriers (SARTOC, or "blood substitutes") either in PEGylated form or in glutaraldehyde-polymerized form.[1–8] The stability of these materials under physiologically relevant conditions has received little attention so

[a] *Babeş-Bolyai University, Faculty of Chemistry and Chemical Engineering, 11 Arany Janos str., RO-400028, Cluj-Napoca, Romania*
[b] *Institute of Computer Science, Poznan University of Technology, Ul. Piotrowo 2, 61-138, Poznan, Poland*
[c] *European Centre for Bioinformatics and Genetics ECBiG, Ul. Piotrowo 2, 61-138, Poznan, Poland*
[d] *Babeş-Bolyai University, Institute of Interdisciplinary Research in Bio-Nano-Sciences, 42 Treboniu Laurian str., RO- 400271, Cluj-Napoca, Romania*
[*] *Corresponding author: radu.silaghi@ubbcluj.ro*

far. Recently, (1-oxyl-2,2,5,5-tetramethylpyrroline-3methyl)methanethiosulfonate (MTSSL) has been attached at the Cys51 position of each monomer of Hr in order to analyze EPR signals that can render information about the stability of the Hr octameric structure.[9,10]

Earlier, all-atom molecular dynamics on Hr has been performed to explore dioxygen permeation to its diiron active site – but mostly as a reference to methane monooxygenase pathways.[11] On the other hand, more relevant for SARTOC would be solvent accessibility (hence the polarity) of the oxy-diiron site, since this would control the autooxidation rate which is in turn responsible for a good part of the side effect of SARTOC candidates.[8,12–15]

Reported here is a theoretical attempt to explore the behavior of MTSSL-labeled Hr. Using molecular dynamics we try to understand the experimental results, and to describe whenever MTSSL label can be a suitable compound to analyze Hr in vitro. Our results show that when the octameric Hr is fully PEGylated, there is a pattern of decreased stability, probably due to the inter monomer clashes induced by the spin label. This can be a suitable explanation for the observed EPR signals.[9] These findings may be of interest also in understanding how certain cross-linkers used in blood substitutes affect Hr and hemoglobin derivatives in its relationship structure and behavior.

RESULTS AND DISCUSSION

One goal of MD simulations with Hr is to establish the degree of mobility within the monomer, and the manner in which chemical derivatization with PEG or with MTSSL (spin label) would affect the results. Measurements of distances and volumes intra and inter monomer were thus taken in order to observe the effect of the label across the time. Thus, Figure 1 reveals that the spin-labeled cysteine residue lies sufficiently close to the inter-monomer interface in order to disrupt monomer-monomer interactions. Indeed, the distance between the α carbons of labeled Cys51 (Cyx51) in one chain and Asp23 in the neighboring chain, is on average 5 Å longer in the spin-labelled structure – an increase sufficient to disrupt most of the typical intermolecular forces (hydrogen bonds and hydrophobic interactions especially). This difference is already seen in the geometry-optimized structures, and is maintained throughout the 5 nanoseconds of MD simulation – albeit with a slight decrease in time.

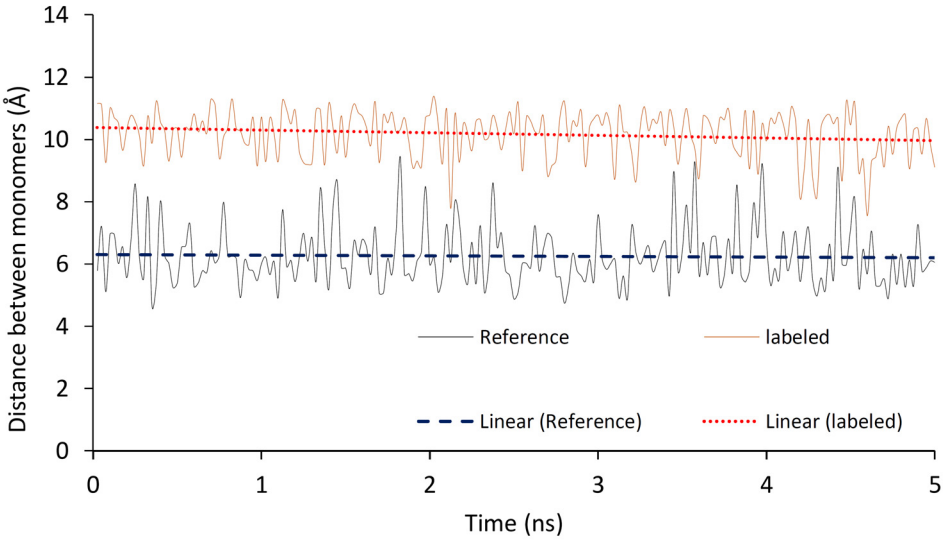

Figure 1. Distance between two monomers in Hr octamer; native and MTSSL-labeled Hr are shown. The distance is measured between CYX50 Cα and Asp23 Cα Chains A and B, respectively, in Hr octameric model. Black/Blue lines shows data and trend for Hr octamer model of reference. Brown/Red lines shows data and trend for Hr octamer model with MTSSL label.

The measured volume of the native octamer, at 110264 Å^3, was almost 3000 Å^3 smaller than of the MTSSL-labeled octamer (at 113082 Å^3) – most of which can be assigned to the spin label itself. Likewise, there is an average ~200 Å^2 increase in solvent accessible surface (SAS) per monomer in the MTSSL-labeled octamer compared to the native form, cf. Table 1.

Table 1. SAS analysis for the average post MD of octameric structures (in Å2).

Structure	Chain	Native	MTSSL
Monomer	A	4714	5042
Monomer	B	4697	4829
Monomer	C	4677	4796
Monomer	D	4901	4776
Monomer	E	4791	4594
Monomer	F	4842	5096
Monomer	G	4722	4824
Monomer	H	4819	5251
Average		4770	4901

Solvent Accessible Surface area measurements for the iron, for its amino acid ligands, and for Cys51, are listed in Table 2. For the diiron site (ligands included), this is an important issue since the autoxidation rate of the iron-dioxygen complex in all oxygen –carrying proteins (Hr included)[16] is directly correlated with solvent exposure. This correlation is of course expected since liberation of molecular oxygen from the Fe(II)-dioxygen complex implies a neutral hydrophobic departing ligand, while autoxidation implies the departure of a polar or anionic superoxide – hence favored by more hydrophilic/solvent-exposed environments.

In line with the data shown above, position 51 obviously increases its SAS when labeled. In the native form, its SAS is reduced to virtually zero, meaning that the residue is in a hydrophobic area – while the labeling leads to a notable solvent exposure (40.7 $Å^2$ cf.Table 2), meaning that the presence of the spin label MTSSL creates space in between monomers leading to access of water.

Meanwhile, at the active site, the environment is seen to indeed change for some of the residues and only slightly for the iron. Indeed, the latter is as expected almost entirely non- exposed to solvent – a logical fact for a dioxygen-carrying protein as discussed above. Nevertheless, a slight increases in SAS of ~3 $Å^2$ is still seen the MTSSL-labelled octamer versus the native version. Small changes are also seen in the solvent exposures of the amino acids serving as ligands to the iron; on average, the total increase is of ~19 $Å^2$ – a very small value but nevertheless one that distinctly warns of the effects that chemical derivatization (or indeed other changes, such as site-directed mutagenesis) may have on the diiron site in Hr even when these changes occur relatively far from the first coordination sphere. In this respect the behavior of the respective iron-ligated amino acids does differ qualitatively: while His77 sees its SAS reduced by 10 $Å^2$ to zero when labeled in the octameric form, His54 and His73 see even more dramatic changes in the opposite directions – with the rest of the amino acids contributing much less. Perhaps of note is also the fact that these changes are not intrinsic to the monomer, but are rather the effect of the octameric environment. Indeed, the SAS of the iron ligands changes by very little in the opposite direction (increased hydrophobicity for MTSSL-Hr compared to native Hr) when the MD simulation is performed on isolated monomers, as opposed to octamers.

Table 2. SAS for selected residues inside averaged structures obtained from the sampling of Hr molecular dynamics monomers (mon) and octamers (oct) with MTSSL label (MTSSL) and without (native). Measurements are reported in Å^2.

Structure	Fe1	Fe2	Fe1[a]	Fe2[a]	His 25	His 54	Glu 58	His 73	His 77	His 101	Glu 106	51[b]
mon-nat	0.0	0.6	0.0	0.6	2.8	1.1	0.0	9.3	9.7	7.6	0.0	11.3
mon-MTSSL	0.0	0.0	0.0	0.0	1.0	1.0	0.0	8.7	3.6	7.9	0.1	94.0
oct-nat	0.0	0.4	0.0	0.4	1.7	0.9	0.0	0.8	9.5	6.0	0.0	0.1
oct-MTSSL	0.0	1.1	0.1	2.2	1.4	10.2	0.3	14.2	0.0	10.9	0.5	40.7

[a] Averaged measurement of SAS for the octamer structures.
[b] Position 51 in the protein, either Cys or Cys-MTSSL.

CONCLUSIONS

The first MM study of hemerythrin is reported here. The data provide support for interpreting experiments where Hr is a template or starting material for blood substitutes – hence, in multimeric form and chemically derivatized with polyethylene glycols, spin labels, or other reagents. Derivatization with a spin label at the native Cys51 position in Hr, is found to destabilize the octameric structure and to lead to a slight increase in solvent accessibility of the diiron center. Both of these consequences of the chemical derivatization would be functional disadvantages for an oxygen-carrying protein. This puts some limitations on the relevance of the EPR spin labeling studies with Hr, and also suggests the need for a careful investigations of the effects of the PEGylation procedures in the context of blood substitute candidates.

EXPERIMENTAL SECTION

Classical molecular dynamics simulations were performed using YASARA.[17] Monomeric and octameric hemerythrin structures were modeled using the X-ray diffraction based structure PDB ID 1I4Y[18] from *Phascolopsis gouldii* wild type retrieved from the Protein Data Bank[19] website. In the case of the MTSSL-labeled Hr structures, the MTSSL model (cf. Figure 2) was created using GaussView version 5;[20] its geometry was energetically taken to a minimum at the semiempirical PM6 level of theory.[21]

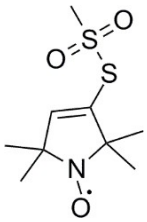

Figure 2. MTSSL, Full IUPAC nomenclature name:
(1-Oxyl-2,2,5,5-tetramethylpyrroline-3- methyl) methanethiosulfonate.

This model was then attached to each one of the monomers in Cys51 position of hemerythrin, yielding the structures illustrated in Figure 3 and Figure 4.

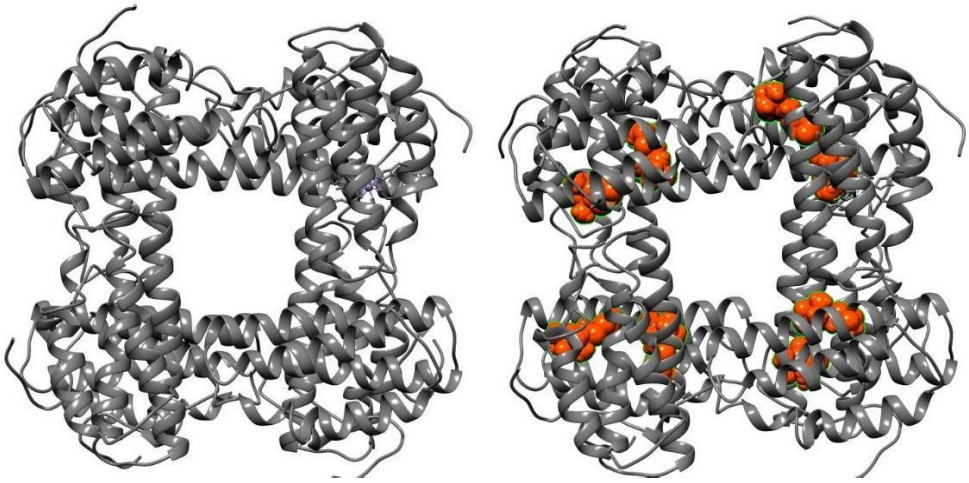

Figure 3. Left: Hr octamer, in ribbon representations. Right: Hr-octamer-MTSSL labelled at Cys51 position of each monomer. Hr represented in gray ribbons, MTSSL label in orange VDW spheres. All graphics have been constructed using UCSF Chimera software program.[22]

All simulations were carried out using the AMBER 03 force field as implemented in YASARA.[23] Long-range interactions were treated with the Particle Mesh Ewald[24] algorithm with a cut off value of 10.48 Å. Periodic boundary conditions were defined using a water filled box of 10 Å distance from all the amino acids of the protein. Each system was solvated with TIP3P water molecules model.[25] Counter-ions of NaCl were randomly placed in the box to neutralize the system to physiological pH 7.4. Each system was subjected first to steepest descent minimization, this is

hereafter referred to as the initial structure. After removing conformational stress through equilibration simulations, sampling was carried out with a time step of 0.5 fs and with snapshots saved in the trajectory every 3 ps. All simulations were carried out at constant pressure and temperature (NPT) conditions at 298 K, for a period of 1 ns. After 10 ns MD simulations, were sampled. RMSD deviation for the trajectory was measured taking as reference the structure with minimum energy obtained during the trajectory, and for other calculations (for instance SAS and molecular volume) an averaged structure was obtained discarding the 5 nanoseconds of equilibration time and the first nanosecond of sampling.

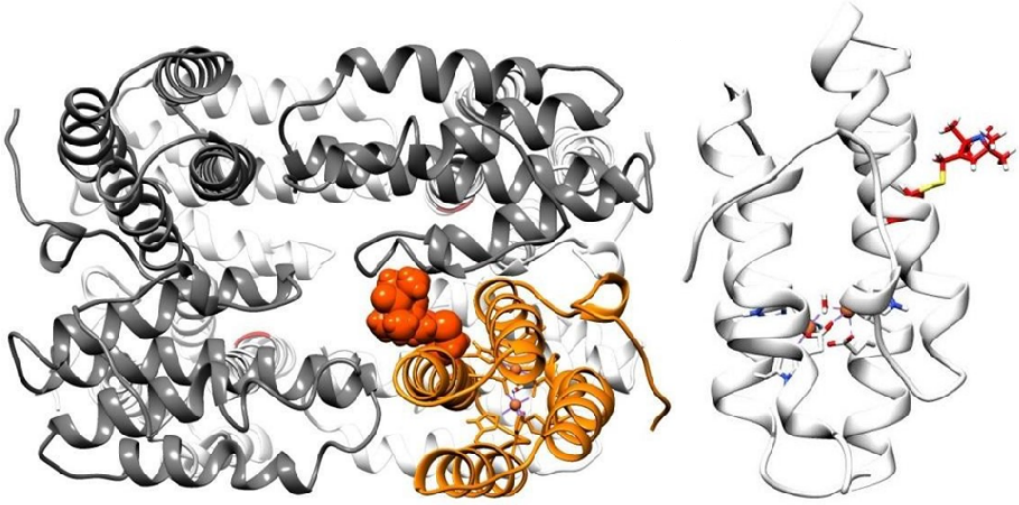

Figure 4. Left: Hr monomer-MTSSL (orange ribbons with MTSSL label in orange VDW surfaces) labeled at Cys51 position interacting with neighbor monomers (gray ribbons). Hr back monomers (not neighbors, not interacting with MTSSL label) are represented in withe ribbons for clarity. Right: Hr monomer (in white ribbons) MTSSL label in red ball and sticks, metallic center, Fe(Cl)-OH-Fe, represented in balls and sticks.

ACKNOWLEDGMENTS

Funding from the Romanian Ministry of Education and Research (PN-III-P2-2.1-PED2019-2293) is gratefully acknowledged. Infrastructure from the Babes-Bolyai University and from the European Centre for Bioinformatics and Genomics affiliated to Poznan University of Technology (Poznan, Poland) was used in this work.

REFERENCES

1. D. Hathazi; A. C. Mot; A. Vaida; F. Scurtu; I. Lupan; E. Fischer-Fodor; G. Damian; D. M. Kurtz Jr.; R. Silaghi-Dumitescu; *Biomacromolecules* **2014**, *15***,** 1920–1927.
2. S. V Kryatov; E. V Rybak-Akimova; S. Schindler; *Chem Rev* **2005**, *105*, 2175–2226.
3. E. Fischer-Fodor; A. Mot; F. Deac; M. Arkosi; R. Silaghi-Dumitrescu; *J Biosci* **2011**, *36***,** 215–221.
4. M. Arkosi; F. Scurtu; A. Vulpoi; R. Silaghi-Dumitrescu; D. M. Kurtz Jr.; *Artif Cells Blood Substitutes Biotechnol* **2017**, *45***,** 218–223.
5. A. C. Mot; A. Roman; I. Lupan; D. M. Kurtz Jr.; R. Silaghi-Dumitrescu; *Protein J* **2010**, *29*, 387–393.
6. V. A. Toma; A. D. Farcas; I. Roman; B. Sevastre; D. Hathazi; F. Scurtu; G. Damian; R. Silaghi-Dumitrescu; *Int J Biol Macromol* **2017**, *107*, 1422–1427.
7. F. Scurtu; B. Tebrean; M. K. Árkosi; A. Ionele; R. Silaghi-Dumitrescu; *Stud Univ Babes-Bolyai Chem,* **2019**, *64(2)*, 421-434.
8. D. Hathazi; F. Scurtu; C. Bischin; A. Mot; A. Attia; J. Kongsted; R. Silaghi-Dumitrescu; *Molecules* **2018**, *23*, E350.
9. I. M. Takacs; A. Mot; R. Silaghi-Dumitrescu; G. Damian; *J Mol Struct* **2014**, *1073***,** 18–23.
10. M. I. Takacs; A. Mot; R. Silaghi-Dumitrescu; G. Damian; *Stud Univ Babes-Bolyai Chem* **2013**, *58***,** 61–69.
11. F. Pietra; *Chem Biodivers* **2017**, *14*, e1600158.
12. J. Dunne; A. Caron; P. Menu; A. I. Alayash; P. W. Buehler; M. T. Wilson; R. Silaghi-Dumitrescu; B. Faivre; C. E. Cooper; *Biochem J* **2006**, *399*, 513–524.
13. A. I. Alayash; *Free Radic Res* **2000**, *33*, 341–348.
14. A. I. Alayash; *Trends Biotechnol.* **2014**, *32*, 177–185.
15. D. A. Svistunenko; A. Manole; *J Biomed Res* **2020**, *34***,** 281–291.
16. D. M. Kurtz; *Essays Biochem* **1999**, *34***,** 85–100.
17. E. Krieger; G. Vriend; *Bioinformatics* **2014**, *30***,** 2981–2982.
18. C. S. Farmer; D. M. Kurtz Jr.; Z. J. Liu; B. C. Wang; J. Rose; J. Ai; J. Sanders-Loehr; D. M. Kurtz Jr.; Z. J. Liu; B. C. Wang; J. Rose; J. Ai; J. Sanders-Loehr; *J Biol Inorg Chem* **2001**, *6*, 418–429.
19. H. M. Berman; J. Westbrook; Z. Feng; G. Gilliland; T. N. Bhat; H. Weissig; I. N. Shindyalov; P. E. Bourne; *Nucleic Acids Res* **2000**, *28*, 235–242.
20. R. Dennington; T. Keith; J. Millam; *Semichem Inc., Shawnee Mission, KS* **2009**, Semichem Inc.
21. J. P. Stewart; *J Mol Model* **2007**, *13*, 1173–1213.
22. E. G. Pettersen; T. D. Goddard; C. C. Huang; G. S. Couch; D. M. Greenblatt; E. C. Meng; T. E. Ferrin; *J Comput Chem* **2004**, *25*, 1605–1612.
23. Y. Duan; C. Wu; S. Chowdhury; M. C. Lee; G. Xiong; W. Zhang; R. Yang; P. Cieplak; R. Luo; T. Lee; J. Caldwell; J. Wang; P. Kollman; *J Comput Chem* **2003**, *24*, 1999–2012.
24. U. Essmann; L. Perera; M. L. Berkowitz; T. Darden; H. Lee; L. G. Pedersen; *J Chem Phys* **1995**, *103*, 8577–8593.
25. W. L. Jorgensen; *J Am Chem Soc* **1981**, *103*, 335–340.